224
8/22/69

HOME
HELP

950

MASTER

ORNL-4396
UC-80 – Reactor Technology

MOLTEN-SALT REACTOR PROGRAM
SEMIANNUAL PROGRESS REPORT
FOR PERIOD ENDING FEBRUARY 28, 1969

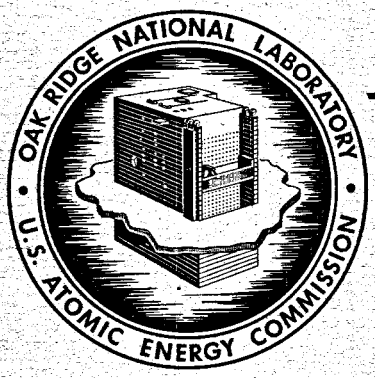

OAK RIDGE NATIONAL LABORATORY
operated by
UNION CARBIDE CORPORATION
for the
U.S. ATOMIC ENERGY COMMISSION

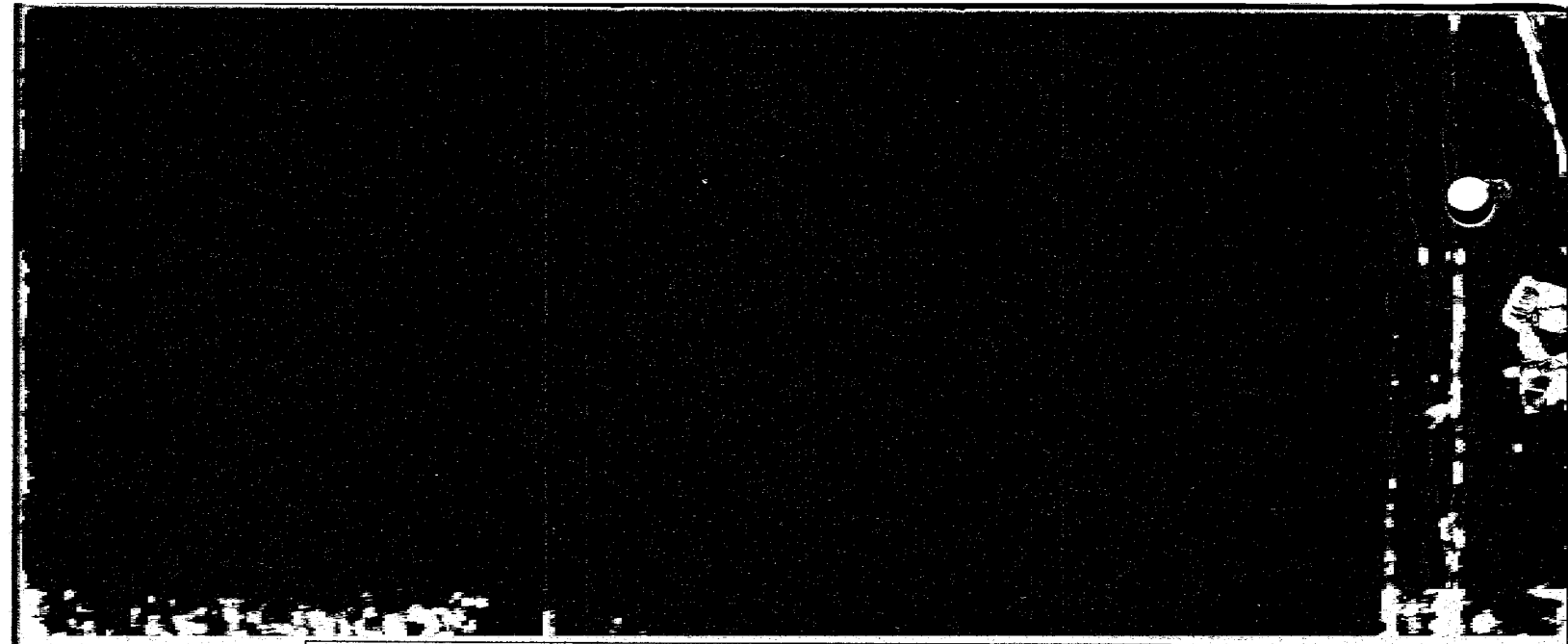

Printed in the United States of America. Available from Clearinghouse for Federal Scientific and Technical Information, National Bureau of Standards, U.S. Department of Commerce, Springfield, Virginia 22151
Price: Printed Copy $3.00; Microfiche $0.65

ORNL-4396
UC-80 – Reactor Technology

Contract No. W-7405-eng-26

MOLTEN-SALT REACTOR PROGRAM

SEMIANNUAL PROGRESS REPORT

For Period Ending February 28, 1969

M. W. Rosenthal, Program Director

R. B. Briggs, Associate Director
P. R. Kasten, Associate Director

AUGUST 1969

OAK RIDGE NATIONAL LABORATORY
Oak Ridge, Tennessee
operated by
UNION CARBIDE CORPORATION
for the
U. S. ATOMIC ENERGY COMMISSION

This report is one of a series of periodic reports in which we describe the progress of the program. Other reports issued in this series are listed below. ORNL-3708 is especially useful because it gives a thorough review of the design and construction and supporting development work for the MSRE.

ORNL-2474	Period Ending January 31, 1958
ORNL-2626	Period Ending October 31, 1958
ORNL-2684	Period Ending January 31, 1959
ORNL-2723	Period Ending April 30, 1959
ORNL-2799	Period Ending July 31, 1959
ORNL-2890	Period Ending October 31, 1959
ORNL-2973	Periods Ending January 31 and April 30, 1960
ORNL-3014	Period Ending July 31, 1960
ORNL-3122	Period Ending February 28, 1961
ORNL-3215	Period Ending August 31, 1961
ORNL-3282	Period Ending February 28, 1962
ORNL-3369	Period Ending August 31, 1962
ORNL-3419	Period Ending January 31, 1963
ORNL-3529	Period Ending July 31, 1963
ORNL-3626	Period Ending January 31, 1964
ORNL-3708	Period Ending July 31, 1964
ORNL-3812	Period Ending February 28, 1965
ORNL-3872	Period Ending August 31, 1965
ORNL-3936	Period Ending February 28, 1966
ORNL-4037	Period Ending August 31, 1966
ORNL-4119	Period Ending February 28, 1967
ORNL-4191	Period Ending August 31, 1967
ORNL-4254	Period Ending February 29, 1968
ORNL-4344	Period Ending August 31, 1968

Contents

INTRODUCTION xi

SUMMARY xiii

PART 1. MOLTEN-SALT REACTOR EXPERIMENT

1. MSRE OPERATIONS 1
   1.1 Chronological Account of Operations and Maintenance 1
   1.2 ^{233}U Zero-Power Tests 5
      1.2.1 Critical Experiment 5
      1.2.2 Control Rod Calibration 7
      1.2.3 Temperature Coefficient of Reactivity 8
      1.2.4 Concentration Coefficient of Reactivity 9
   1.3 Operations Analysis 9
      1.3.1 System Dynamics 9
      1.3.2 Gas in the Fuel Salt 11
      1.3.3 Neutron and Pressure Noise Measurements 16
      1.3.4 Perturbations in Nuclear Power 16
      1.3.5 Salt Transfer to Overflow Tank 21
      1.3.6 Thermal-Convection Heat-Removal Test 22
      1.3.7 Radiation Heating 23
      1.3.8 Thermal Cycle History 23
   1.4 Equipment 24
      1.4.1 ^{233}U Loading Equipment 24
      1.4.2 Salt Samplers 25
      1.4.3 Control Rods and Drives 26
      1.4.4 Off-Gas System 27
      1.4.5 Component Cooling System 28
      1.4.6 Containment and Ventilation 28
      1.4.7 Electrical System 28
      1.4.8 Heaters 29
      1.4.9 Other 29

2. COMPONENT DEVELOPMENT 30
   2.1 Freeze-Flange Thermal-Cycle Test 30
   2.2 Pumps 31
      2.2.1 Mark 2 Fuel Pump 31
      2.2.2 Oil Pump Endurance Test 32

3. INSTRUMENTATION AND CONTROLS 33
3.1 MSRE Operating Experience 33
3.2 Controls System Design 33
3.3 MSRE Computer System 33

4. MSRE REACTOR ANALYSIS 35
4.1 Long-Term Isotopic Changes and Reactivity Effects During Operation with ^{233}U 35
4.2 Analysis of Zero-Power Rod-Calibration Experiments 37
4.2.1 Rod-Drop Experiments 38
4.2.2 Reactivity Effect of Excess Uranium 40
4.2.3 Summary of Rod-Calibration Information 41
4.3 Calculations of Reactivity Variations from Power-Time Records 43
4.4 Theoretical Analysis of Dynamics with ^{233}U Fuel 45

PART 2. MSBR DESIGN AND DEVELOPMENT

5. DESIGN 49
5.1 General 49
5.2 Plant Layout 49
5.3 Reactor 52
5.4 Primary Heat Exchangers 57
5.5 Steam Generator and Superheater 57
5.6 Steam Reheater 59
5.7 Removal of Reactor Afterheat 59
5.7.1 Introduction 59
5.7.2 Sources of Afterheat 59
5.7.3 Heat-Removal Systems 60
5.8 Distribution of Noble-Metal Fission Products and Their Decay Heat 62
5.9 Reactor Temperatures, Flows, and Heat Transfer 64
5.9.1 Reactor Core 64
5.9.2 Flow and Temperature in Radial Reflector 67
5.9.3 Flow and Temperature in Axial Reflectors 69
5.9.4 Vessel Temperatures 70
5.10 Estimated Costs of 1000 Mw (electrical) MSBR Power Station 70
5.11 MSBE Design 71
5.11.1 Introduction 71
5.11.2 Description of Reactor Plant 74

6. REACTOR PHYSICS 76
6.1 Physics Analysis of MSBR 76
6.1.1 Optimization of the MSBR 76
6.1.2 The One-Fluid MSBR Reference Design 77
6.1.3 Nuclear Design Studies 77

6.1.4 Optimum Thorium Concentration in MSBR 80
6.1.5 Improvements in Computational Tools 82
6.1.6 Gamma and Neutron Heating in MSBR 83
6.2 Physics Analysis of MSBE 84
6.2.1 MSBE Design Studies 84
6.3 MSBR Experimental Physics 87
6.3.1 Initial Results of the Experiment to Measure $\alpha(^{235}U)$ in the MSRE 87

7. SYSTEMS AND COMPONENTS DEVELOPMENT 90
7.1 Off-Gas System 90
7.1.1 Volume Holdup Tank 90
7.2 Noble-Gas Migration in the MSBR 92
7.2.1 Contribution of the Noble Gases to Afterheat in the Graphite 92
7.2.2 Distribution of Decay Heat in the MSBR Off-Gas System 94
7.3 Bubble Generator 95
7.4 Bubble Separator 96
7.5 Molten-Salt Steam Generator Test Stand 98
7.6 Sodium Fluoroborate Circulating Test Loop 98
7.6.1 Pumping Characteristics of Sodium Fluoroborate Salt 100
7.6.2 Control of Salt Composition 100
7.6.3 Corrosion Product Deposition 102
7.6.4 Gas System Studies 102
7.7 MSBR Pumps 106
7.7.1 MSBR Primary-Salt Pump 106
7.7.2 Pump Program for the Molten-Salt Breeder Experiment 108
7.7.3 MSBE Salt Pump Test Stand 109
7.7.4 ALPHA Pump 109
7.8 Remote Welding 109

8. MSBR INSTRUMENTATION AND CONTROLS 113
8.1 Control System Analysis 113
8.2 Calculations of Neutron Decay After Shutdown 115
8.2.1 Calculation of the Effect of the Beryllium Photoneutron Reaction on Neutron Density After Shutdown 115
8.2.2 Calculation of Neutron Density Following Loss of Primary Flow 115
8.3 Dynamic Analysis of MSBR Steam Generator 116
8.4 High-Temperature Resistance Thermometer Evaluation 116

9. HEAT TRANSFER AND THERMOPHYSICAL PROPERTIES 119
9.1 Heat Transfer 119
9.2 Thermophysical Properties 122
9.2.1 Thermal Conductivity 122
9.3 Mass Transfer to Circulating Bubbles 124

PART 3. CHEMISTRY

10. CHEMISTRY OF THE MSRE 129

10.1 A Material Balance for the MSRE Fuel Salt 129

10.2 MSRE Fuel Circuit Corrosion Chemistry 130

10.3 Adjustment of $U^{3+}/\Sigma U$ Concentration of the MSRE Fuel Salt 133

10.4 Examination of Simulated MSRE Fuel Mixture for Foam-Producing Properties 135

10.5 Foaming Behavior in Molten Salts 137

11. FISSION PRODUCT BEHAVIOR 138

11.1 Fission Product Behavior in the MSRE 138

11.1.1 Examination of Graphite Surveillance Specimens 138

11.1.2 Distribution of Fission Products in the MSRE 138

11.1.3 Fission Product Inventory During ^{233}U Operation 138

11.1.4 Response of ^{95}Nb Activity to Fuel Redox Chemistry 139

11.1.5 MSRE Off-Gas Analyzer-Sampler 140

11.1.6 Examination of Material Recovered from MSRE Off-Gas Line 143

11.2 Fission Product Volatilization Tests 145

11.2.1 Chemical Probe Tests 145

11.2.2 Electric Charge of the Radioactive Aerosols 148

11.2.3 Electron Microscope Tests 148

11.2.4 Aerosol Deposition from a Helium Stream 148

11.2.5 Closed-Tube Diffusion Tests 150

11.2.6 Volatilization of MSRE Salt in the Absence of Radioactivity 150

11.2.7 Summary and Interpretation of Hot-Cell Test Results 151

11.2.8 Attempt to Sample Foam in Pump Bowl 151

11.3 Laboratory Tests on Aerosol Formation Over Molten Salts and Transfer of Niobium from Salt to Bismuth 153

11.4 The Chemistry of the Noble Fission Product Fluorides 157

11.4.1 Molybdenum Fluoride Synthesis, Characterization, and Stability 157

11.4.2 Mass Spectrometric Studies of Fluorides 159

12. PHYSICAL CHEMISTRY OF MOLTEN SALTS 163

12.1 CeF_3 Solubility in Molten Mixtures of LiF, BeF_2, and ThF_4 163

12.2 Correlation of CeF_3 Solubility with Solvent Composition 164

12.3 Zone Melting of Fluoride Salts 166

12.3.1 Phase Behavior 167

12.3.2 Zone Melting 168

12.3.3 Cyclic Slow Cooling 168

12.3.4 Cerium 168

12.4 Behavior of CeF_3 in the Fractional Crystallization of ThF_4 from LiF-BeF_2-ThF_4 Melts 168

12.5 Properties of the Alkali Fluoroborates 169

12.5.1 Phase Relations in Fluoroborate Systems 169

12.5.2 The System Na-KF-BF_3 170

12.5.3 The System KF-KBF_4 170

12.5.4 The System $NaBF_4$-KBF_4 171

12.5.5 The System NaF-$NaBF_4$ 171

12.6 Limits of Miscibility in Molten Salt Systems: KBF_4-LiF, Li_2BeF_4-KI, and Li_2BeF_4-KBF_4 171
12.6.1 The System KBF_4-LiF 171
12.6.2 The System Li_2BeF_4-KI 172
12.6.3 The System Li_2BeF_4-KBF_4 172
12.7 Solubility of Thorium Metal in Molten Lithium Fluoride–Thorium Fluoride Mixtures 172
12.8 The Crystal Structure of KBF_4 173
12.9 Densities of Molten Salts 174
12.10 Spectroscopy of Fluoride Media 175
12.10.1 The Diamond-Windowed Cell 175
12.10.2 Salt Purification for Fluoride Spectroscopy 175
12.11 The Distribution of U^{4+} Between Molten LiF-BeF_2-ThF_4-UF_4 and a (U-Th)O_2 Solid Solution 176
12.12 An Ni-NiO-BeO Electrode as a Reference Electrode in Molten Fluorides 178
12.13 Emf Measurements with Concentration Cells with Transference in Molten Mixtures of LiF and BeF_2 180
12.14 Electrical Conductance of Molten KNO_3 182
12.15 Electrical Conductance of Molten Beryllium Fluoride 184

13. CHEMISTRY OF MOLTEN-SALT REACTOR FUEL REPROCESSING TECHNOLOGY 187
13.1 Simultaneous Extraction of Zirconium and Uranium and of Zirconium and Protactinium 187
13.2 Protactinium Studies in the High-Alpha Molten-Salt Laboratory 188
13.3 Further Studies of the Reductive Extraction of Protactinium from Single-Fluid MSBR Fuel Salt by Thorium in Molten Bismuth 189
13.4 Reductive Extraction of Rare Earths from Molten Mixtures of LiF, BeF_2, and ThF_4 into Bismuth 191
13.5 Metal Phases Other than Bismuth for Rare-Earth Extraction 192
13.6 Separation of Cerium from Thorium in Bismuth by Cold Zone Deposition of Thorium Bismuthide 193
13.7 Extraction of Thorium by Electrolytic Reduction into Flowing Liquid Lead from Molten Mixtures of LiF, BeF_2, ThF_4, and Rare-Earth Fluorides 195

14. DEVELOPMENT AND EVALUATION OF ANALYTICAL METHODS FOR MOLTEN-SALT REACTORS 197
14.1 Determination of Oxide in MSRE Fuel 197
14.2 Determination of the Oxidation State of Constituents of MSRE Fuel 197
14.2.1 Determination of Total Reducing Power of MSR Salts 197
14.2.2 Determination of U(III) in Radioactive MSRE Fuel by a Hydrogen Reduction Method 199
14.2.3 Voltammetric Determination of U(IV)/U(III) Ratios in MSRE Fuel 200
14.3 Emf, Voltammetric, and Spectrophotometric Measurements on the U(IV)/U(III) Couple in Molten LiF-BeF_2-ZrF_4 201
14.4 Emf Measurements in Molten Fluorides 202
14.5 Development of a Molten-Salt Spectrophotometric Facility for Hot-Cell Use 202

14.6 Absorption Spectra of 3*d* Transition-Metal Ions in Molten LiF-BeF_2 204
14.7 Effect of Reductants on Metal-Fluoride-Salt Wetting Behavior 205
14.8 Determination of Contaminants in the Blanket Gas of $NaBF_4$ Tests 205
14.9 Determination of Bismuth in MSRP Salts 208
14.9.1 Polarography 208
14.9.2 Spectrophotometry 208
14.9.3 Emission Spectrography 208
14.9.4 Polarographic Shipping 208
14.9.5 Isotopic Exchange 208

PART 4. MOLTEN-SALT IRRADIATION EXPERIMENTS

15. MOLTEN-SALT CONVECTION LOOP IN ORR 210
15.1 Studies of Surface Wetting of Graphite by Molten Salt 210

PART 5. MATERIALS DEVELOPMENT

16. MSRE SURVEILLANCE PROGRAM 211
16.1 Examination of Particles Removed from Pump Bowl with Magnets 211
16.1.1 Observations on Particles from Magnet FP-15-53 212
16.1.2 Observations on Particles from Magnet FP-16-2 213

17. GRAPHITE STUDIES 214
17.1 Fundamental Studies of Radiation Damage Mechanisms in Graphite 214
17.2 Graphitization Chemistry and Binder System Development 215
17.3 Hot Pressing of Graphite Pellets Using Various Binders 216
17.4 Procurement and Physical Property Measurements on New Grades of Graphite 217
17.5 Physical Properties of Graphites 219
17.6 X-Ray Studies 219
17.7 Electron Microscopy of Graphite 221
17.8 Gas Impregnation of Graphite with Carbon 221
17.9 Graphite Irradiation in HFIR 224
17.10 Calculation of Lifetime and Induced Stresses in MSBR Cores 229

18. HASTELLOY N 232
18.1 Influence of Titanium and Carbon on the Mechanical Properties of Nickel-Base Alloys 232
18.2 Aging of Modified Hastelloy N 233
18.3 Influence of Irradiation Temperature on the Creep-Rupture Properties of Hastelloy N 235
18.4 Electron Microscopy Studies 240
18.5 Measurement of Residual Stresses in Hastelloy N Welds 242
18.6 Corrosion Studies 243
18.6.1 Fuel Salts 243
18.6.2 Fertile-Fissile Salts 243

18.6.3 Blanket Salts 245
18.6.4 Coolant Salts 246
18.6.5 Comparison of the Kinetic Behavior of Nickel- and Iron-Based Alloys in Molten Fluoride Salts 248
18.7 Forced Convection Loop 253
18.8 Oxidation of Hastelloy N 254

19. SUPPORT FOR CHEMICAL PROCESSING 261
19.1 Graphite–Hastelloy N Transition Joint Development 261
19.2 Development of Corrosion-Resistant Brazing Alloys for Molybdenum 261
19.3 Examination of Mo-TZM Capsule 262
19.4 Bismuth Corrosion Studies 264

20. SUPPORT FOR COMPONENTS DEVELOPMENT PROGRAM 267
20.1 Remote Welding Development 267
20.2 Thermal Cycling Tests on Coated Bearing Specimens 267

PART 6. MOLTEN-SALT PROCESSING AND PREPARATION

21. FLOWSHEET ANALYSIS 270
21.1 Proposed Reductive Extraction Processing Flowsheet for a Single-Fluid MSBR 270
21.2 Protactinium Removal from a Single-Fluid MSBR 272
21.3 Removal of Rare Earths from a Single-Fluid MSBR 273
21.4 Material Balance Calculations 275
21.4.1 MSBR Nuclear Data Compilation 275
21.4.2 MSBR Material Balance Calculations 275
21.4.3 MSBR Processing Plant Design Calculations 277

22. MEASUREMENT OF DISTRIBUTION COEFFICIENTS IN MOLTEN-SALT–METAL SYSTEMS 279
22.1 Extraction of Uranium, Zirconium, Protactinium, and Plutonium from Single-Fluid MSBR Fuels 279
22.2 Solubility of Protactinium in Bismuth 282
22.3 Extraction of Thorium and Rare Earths from Single-Fluid MSBR Fuels 284
22.4 Metal Transfer Process Studies 285
22.5 Effect of Other Components on the Solubility of Thorium in Bismuth 287

23. ENGINEERING DEVELOPMENT OF PROCESS OPERATIONS 288
23.1 Electrolytic Cell Development 288
23.1.1 Quartz Static Cell Experiments 288
23.1.2 All-Metal Static Cell Experiment 291
23.2 Reductive Extraction Engineering Studies 291
23.3 Simulated Molten-Salt–Liquid-Bismuth Contactor Studies 293
23.4 Design of a Continuous Electrolytic Cell Testing System 296
23.5 Experimental Facilities for Reductive Extraction Development Work 297

24. DISTILLATION OF MSRE FUEL CARRIER SALT 298

ORGANIZATION CHART 301

Introduction

The objective of the Molten-Salt Reactor Program is the development of nuclear reactors which use fluid fuels that are solutions of fissile and fertile materials in suitable carrier salts. The program is an outgrowth of the effort begun over 19 years ago in the Aircraft Nuclear Propulsion program to make a molten-salt reactor power plant for aircraft. A molten-salt reactor – the Aircraft Reactor Experiment – was operated at ORNL in 1954 as part of the ANP program.

Our major goal now is to achieve a thermal breeder reactor that will produce power at low cost while simultaneously conserving and extending the nation's fuel resources. Fuel for this type of reactor would be $^{233}UF_4$ dissolved in a salt that is a mixture of LiF and BeF_2, but it could be started up with ^{235}U or plutonium. The fertile material would be ThF_4 dissolved in the same salt or in a separate blanket salt of similar composition. The technology being developed for the breeder is also applicable to high-performance converter reactors.

A major program activity is the operation of the Molten-Salt Reactor Experiment. This reactor was built to test the types of fuels and materials that would be used in thermal breeder and converter reactors and to provide experience with the operation and maintenance of a molten-salt reactor. The MSRE operates at 1200°F and at atmospheric pressure and produces about 8.0 Mw of heat. The initial fuel contained 0.9 mole % UF_4, 5 mole % ZrF_4, 29 mole % BeF_2, and 65 mole % ^7LiF, a mixture which has a melting point of 840°F. The uranium was about 33% ^{235}U.

The fuel circulates through a reactor vessel and an external pump and heat exchange system. All this equipment is constructed of Hastelloy N, a nickel-molybdenum-iron-chromium alloy with exceptional resistance to corrosion by molten fluorides and with high strength at high temperature. The reactor core contains an assembly of graphite moderator bars that are in direct contact with the fuel. The fuel salt does not wet the graphite and therefore does not enter the pores. Heat produced in the reactor is transferred to a coolant salt in the primary heat exchanger, and the coolant salt is pumped through a radiator to dissipate the heat to the atmosphere.

Design of the MSRE started in the summer of 1960, and fabrication of equipment began early in 1962. Pre-nuclear testing was begun in August of 1964, and, following some modifications, the reactor was taken critical on June 1, 1965. Zero-power experiments were completed early in July. After additional modifications, maintenance, and sealing of the containment, operation at a power of 1 Mw began in January 1966.

At the 1-Mw power level, trouble was experienced with plugging of small ports in control valves in the off-gas system by heavy liquid and varnish-like organic materials. These materials are believed to be produced by radiation polymerization of a very small amount of oil that vaporizes after leaking through a gasketed seal into the tank of the fuel circulating pump. This difficulty was overcome by installing a specially designed filter in the off-gas line.

Full power was reached in May 1966, and the plant was operated at full power for about six weeks. Then one of the radiator cooling blowers (which were left over from the ANP program) broke up from mechanical stress. While new blowers were being procured, an array of graphite and metal surveillance specimens was taken from the core and examined.

Power operation was resumed in October 1966 with one blower; then in November the second blower was installed, and full power was again attained. After a shutdown to remove salt that had accidentally gotten into an off-gas line, the MSRE was operated in December and January at full power for 30 days without interruption. The next power run was begun later in January and was continued for 102 days, until terminated to remove a second set of graphite and metal specimens. An additional operating period of 46 days during the summer was interrupted for maintenance work on the sampler-enricher when the cable drive mechanism jammed.

In September 1967, a run was begun which continued for six months, until terminated on schedule in March 1968. Power operation during this run had to be interrupted once when the reactor was taken to zero power to repair an electrical short in the sampler-enricher.

Completion of this six-month run brought to a close the first phase of MSRE operation, in which the objective was to demonstrate on a small scale the attractive features and technical feasibility of these systems for civilian power reactors. We believe this objective has been achieved and that the MSRE has shown that molten-fluoride reactors can be operated at temperatures above 1200°F without corrosive attack on either the metal or graphite parts of the system, that the fuel is completely stable, that reactor equipment can operate satisfactorily at these conditions, that xenon can be removed rapidly from molten salts, and that, when necessary, the radioactive equipment can be repaired or replaced.

The second phase of MSRE operation began in August 1968, when a small facility in the MSRE building was used to remove the original uranium charge from the fuel salt by treatment with gaseous F_2. In six days of fluorination, 219 kg of uranium was removed from the molten salt and loaded onto absorbers filled with sodium fluoride pellets. The decontamination and recovery of the uranium were very good.

While the fuel was being processed, a charge of ^{233}U that had been made in the Savannah River reactors was converted to UF_4-LiF enriching salt in ORNL's Thorium-Uranium Recycle Facility. The enriching salt was added to the original carrier salt, and in October 1969 the MSRE became the world's first reactor to operate on ^{233}U. The nuclear characteristics with the ^{233}U were close to the predictions, and, as expected, the reactor was quite stable. One surprise was a considerable increase in the amount of gas entrained in the salt, which made the reactor power very noisy. A slight reduction in the pump speed eliminated the gas. We are investigating why the gas behavior was different after the fuel was processed.

A large part of the Molten-Salt Reactor Program is now being devoted to future molten-salt reactors. Conceptual design studies are being made of breeder reactors, and an increasing amount of work on materials, on the chemistry of fuel and coolant salts, and on processing methods is included in the research and development program.

Until recently, most of our work on breeder reactors was aimed specifically at two-fluid systems in which graphite tubes would be used to separate uranium-bearing fuel salts from thorium-bearing fertile salts. We think attractive reactors of this type can be developed, but several years of experience with a prototype reactor would be required to prove that graphite can serve as piping while exposed to high fast-neutron irradiations. As a consequence, a one-fluid breeder was a long-sought goal.

About a year ago two developments established the feasibility of a one-fluid breeder. The first was demonstration of the chemical steps in a process which uses liquid bismuth to extract protactinium and uranium selectively from a salt that also contains thorium. The second was the recognition that a fertile blanket can be obtained with a salt that contains uranium and thorium by reducing the graphite-to-fuel ratio in the outer part of the core. Our studies show that a *one-fluid, two-region* breeder can be built that has fuel utilization characteristics approaching those of our two-fluid designs and probably better economics. Since the graphite serves only as moderator, the one-fluid reactor is more nearly a scaleup of the MSRE.

These features caused us to change the emphasis of our breeder program from the two-fluid to the one-fluid breeder. Most of our design and the development effort are now directed to the one-fluid system.

Summary

PART 1. MOLTEN-SALT REACTOR EXPERIMENT

1. MSRE Operations

This report period covered the loading of ^{233}U, zero-power experiments with the new fissile material, and the resumption of full-power operation.

Criticality was attained by melting UF_4-LiF eutectic salt containing 33.3 kg of uranium (91% ^{233}U) into the carrier salt from which the original uranium had been stripped. The critical loading was only 1% less than predicted. Reactivity coefficients and control rod worth were also in acceptable agreement with predictions. Dynamics tests showed that the system was stable at all power levels, and the experimental transfer functions fitted the theoretical curves.

Shortly after the beginning of fuel-salt circulation, beryllium metal was exposed to the salt to increase the reducing power. At that time the amount of blanket gas entrained in the circulating fuel increased from less than 0.1 vol % to about 0.6 vol % and remained there. Various experiments were done in efforts to elucidate the effect of the beryllium. The entrained gas was practically eliminated from the fuel loop by operating the pump at slightly reduced speed.

During the approach to power, small perturbations were observed in the nuclear power and some other system variables. These were tentatively ascribed to gradual accumulation and sudden release of gas from somewhere in the core. The perturbations ceased when the circulating void fraction was reduced.

The fuel off-gas line partially plugged near the pump bowl during the zero-power experiments, and an accumulation of frozen salt mist was removed before the beginning of power operation.

Component performance was generally good, but a loose gear in the fuel-sampler drive mechanism caused a three-week shutdown in December, delaying the start of power operation. At the end of the period, fuel had been in the core continuously for 47 days, during which time the integrated power amounted to 747 equivalent full-power hours.

2. Component Development

The MSRE-type freeze flange undergoing thermal cycle testing was inspected after 321 cycles. The crack observed first after 268 cycles had extended only slightly. Cycling was resumed.

The mark 2 fuel pump, which features a deeper bowl, began test operation with molten salt and accumulated a total of 4000 hr. The only difficulty was periodic plugging of the off-gas line with what appeared to be frozen salt mist.

3. Instrumentation and Controls

Daily tests of rod-scram relays turned up no more failures. (Three of fifteen failed in the previous six months.) Two fission chamber failures occurred after nine months and one year of service respectively. The improvement over the three-month average life was attributed to improved sealing against water intrusion. Neutron chambers were installed in the drain tank cell for the ^{233}U loading and were afterwards removed. Only minor modifications were made in the instrumentation and controls.

A moderate number of minor failures occurred in the on-line digital computer. Numerous software changes were made in support of reactor operations and experiments. The conversational-mode calculational language FOCAL was adapted to the BR-340, making possible engineering calculations in the background time interspersed with the routine monitoring and computing operations of the computer.

4. MSRE Reactor Analysis

Nuclide changes and reactivity effects during extended power operation with ^{233}U were computed using updated cross-section data. The computed distribution of fissions was 94% in ^{233}U, 4% in ^{239}Pu, and 2% in ^{235}U at the beginning, with the ^{239}Pu fissions slowly decreasing and the ^{233}U fissions increasing with integrated power. The reactivity effect of long-term changes in nuclides (exclusive of uranium burnup) was computed to be $-1.1 \times 10^{-7}\ \delta k/k$ per megawatt-hour.

Analysis of rod-drop experiments gave a total worth of one control rod, near the minimum critical uranium loading, of 2.58 ± 0.05% $\delta k/k$. The uranium concentration coefficient of reactivity was inferred to be about 5% smaller than had been predicted. New rod-calibration curves for use in the on-line reactivity balance calculations were derived from the experiments.

A method for the calculation of time variations in reactivity corresponding to specified variations in the fission rate was developed and used to analyze some observed "blips" in the MSRE power level.

Theoretical analysis of the dynamic stability of the MSRE with ^{233}U fuel was extended to obtain the power dependence of all the eigenvalues of the system mathematical mode. The dependence exhibited the expected tendency of the system to become more sluggish in returning to its original state at lower power levels.

PART 2. MSBR DESIGN AND DEVELOPMENT

5. Design

Design study of a 1000 Mw (electrical) MSBR power station was continued. The plant layout remains essentially the same except that the reactor cell diameter was increased to 66 ft to accommodate a larger reactor vessel. The cell wall construction was modified to provide double containment of the radioactive systems.

The size of zone I of the reactor core was increased to 14 ft diam X 13 ft high, and other dimensions were adjusted to reduce the damage neutron flux to assure a 4-year life for the core graphite and a 30-year life for the reflector graphite. The latter will then not require provisions for routine replacement.

The undermoderated region surrounding the most active portion of the core was redesigned to use 2-in. by 10-in. by 14-ft-long slabs of graphite rather than graphite spheres. This region contains 37% by volume of salt as in the previous concepts.

The reflector graphite was redesigned to make use of larger pieces and to assure a well-defined passage for flow of fuel salt to cool the reactor vessel wall. The fuel salt will flow radially inward from the wall annulus to cool the reflector graphite.

Axial reflectors were added at the top and bottom to improve the nuclear performance and to reduce the damage flux on the Hastelloy N vessel heads. The lifting rods used to remove the entire core assembly for graphite replacement are now removable to eliminate the poisoning effect during normal operation.

The top of the primary heat exchanger was modified to use L-shaped tubes and a vertical tube sheet. The upper portion of the tubing contains a sine-wave bend to reduce the stresses due to thermal expansion. The heat exchanger design assumes use of tubing with a knurled groove to enhance the heat transfer on both inside and outside.

The removal of reactor afterheat has been analyzed in more detail. The normal method is to continue circulation of both the primary and secondary salts and to transfer the heat to the steam system. The fuel salt can be drained to a tank provided with cooling thimbles, and the residual heat due to deposited fission products in the core can be removed by circulating nitrogen with the fuel-salt pumps.

More detailed studies were completed on the temperature distributions within the reactor. It was found that the maximum core graphite temperature would be 1307°F, occurring about 1 ft above midheight in the reactor. The maximum temperature in the radial reflector graphite was found to be 1363°F. Vessel wall temperatures were also analyzed and found to be within acceptable limits.

The MSBR station cost estimates were revised to more nearly reflect 1969 costs. At a construction cost of about $160.00 per kilowatt and a production cost of 4 mills/kwhr, the MSBR compares favorably with our estimates of costs for water reactors.

Some conceptual design studies were begun for a molten-salt breeder experiment. The objectives proposed for the experiment can be accomplished with a reactor with a power in the range of 100 to 200 Mw (thermal).

6. Reactor Physics

Recent optimization studies of molten-salt breeder reactor configurations have been based on a figure of merit which places greater weight on fuel specific power than does the annual fuel yield. In addition, a limitation on the maximum fast-neutron flux in the graphite may now also be imposed as a constraint on the optimization.

Since the previous progress report, we have found that the core of the 1000 Mw (electrical) single-fluid MSBR can be enlarged so as to extend the useful life of the graphite from two to four years with only a slight penalty in breeding performance. Additional modifications have been made to provide proper cooling of the reflector and to limit the fast-neutron flux in the reflector to a level that should not require replacement of the reflector during the life of the reactor. Finally, further detailing of the reactor design has resulted in other upward revisions in the estimated salt inventory. In all, the salt volume in our present MSBR configu-

ration is about 20% greater than reported previously. In the aggregate, these changes result in a reactor having a breeding ratio of 1.065, fissile material inventory of 1470 kg (including protactinium), annual fuel yield 3.34%, and a useful core life of four years at 0.8 plant factor.

A new analysis of the effect of thorium concentration on MSBR performance was carried out in terms of the new figure of merit and with careful adjustment of neutron cross sections to fit each case being considered. We find that 12 mole % of thorium in the salt is very nearly optimum in terms of breeding performance.

Improved digital computer codes for preparation of the neutron cross sections required in multigroup flux calculations and for carrying out multigroup two-dimensional neutron diffusion calculations have been put into use in the MSR program during the last several months. They have greatly facilitated the explicit two-dimensional calculations which are necessary to check the 2-D synthesis calculations used in the ROD optimization code and which are also employed in analysis of tentative configurations for a molten-salt breeder experiment.

Neutron transport codes have been adapted to calculate also the transport of gamma rays whose sources depend in part on the computed neutron fluxes. This computational tool allows one to calculate gamma heating in complex, multizoned reactor configurations without recourse to approximate buildup factor methods whose use is questionable in such configurations. The codes were used to obtain heating distributions in the MSBR.

Further analysis of possible configurations for a molten-salt breeder experiment shows that both the target maximum damage flux of 5×10^{14} neutrons cm^{-2} sec^{-1} (>50 kev) and an initial breeding ratio (with ^{233}U fuel) greater than unity can be achieved with a reactor power less than 200 Mw (thermal). If one accepts a breeding ratio only slightly less than unity, the target damage flux can be achieved with a reactor power of 100 Mw (thermal).

The experiment to measure the spectrum-averaged values of α (the capture-to-fission cross-section ratio) for both ^{235}U and ^{233}U in the MSRE is progressing well, and has reached the point where comparisons between measured and calculated values can be made for the ^{235}U samples. Tentatively, the agreement seems excellent, the measured value of $\overline{\alpha}_{25}$ being about 3.5% lower than the calculated value based on the ENDF/B cross-section library. Though the experimental errors have not been fully assessed, this difference is about the same as the expected accuracy of the measurements. This level of accuracy in the measurement of α contributes about 0.7% uncertainty in η for ^{235}U, but would correspond to about 0.4% uncertainty in η for ^{233}U.

7. Systems and Components Development

Studies on the off-gas system were continued, and a preliminary design concept for the volume holdup tank is presented. This tank provides about 1 hr holdup for all gases leaving the reactor and employs a circulating coolant which receives the solid fission products from an impaction separator and absorbs the energy from these and the decay of the noble gases. The system must reject a maximum of 18 Mw of decay heat.

The ^{135}Xe distribution calculations were extended to include the other noble-gas fission products, of which there are over 30 kryptons and xenons. The fluxes of these isotopes to the circulating gas bubbles, to the graphite, out of the reactor, and to the noble-gas removal system were calculated for conditions of the graphite coating and the noble-gas stripping system which yielded a ^{135}Xe poison fraction of 1.27 and 0.56%. The flux of the fission product gas to the graphite for the latter case was used to calculate the afterheat in the graphite after about two years of continuous operation at full power. Heat is released at the rate of 1 Mw 10 min after shutdown and has decayed to less than 0.15 Mw 10 hr later. An estimate was made of the distribution of about 21 Mw of decay heat in the off-gas system, including about 9 Mw of heat from the decay of noble metals.

Studies were started on a bubble generator that resembles an inverted venturi and consists of a teardrop inside a straight section of pipe. It was found that the primary mechanism for generating small bubbles is the use of the energy in the turbulent field in the diffuser. Coalescence of the small bubbles was found to increase as the void fraction in a water stream increased much above 0.1%; however, it was indicated that higher fluid velocities would inhibit coalescence, and this will be checked. A third set of vanes for the vortex type of in-line bubble separator was made as a scaled-up version of an earlier model used on another experiment and for which there was satisfactory performance. This model appears to confirm the earlier experience, but testing was just begun at the end of the period.

A request for directive for a molten-salt steam generator test stand was sent to the AEC for approval and authorization of expenditures. The test stand will have a capacity of 3 Mw and will consist of a molten-salt pump loop with a gas-fired heat source and a water-steam loop capable of operating at subcritical and supercritical pressures. The test stand will be used

to gain fundamental engineering data and to investigate ideas for generating steam with molten salt.

The sodium fluoroborate test loop was operated almost continuously from August 19, 1968, to November 4, 1968. During this period work was completed on pump cavitation tests, studies were continued on methods of controlling salt composition and on restrictions in the off-gas line, and initial tests were made with a cold finger to investigate cold-zone deposition of corrosion products. During November and December a test section was installed in the off-gas line at the pump bowl outlet to provide pressure and temperature profile data and to permit installation of various traps and filters. The loop was restarted on December 19, 1968, and circulation has continued without interruption through February 1969. Cumulative circulating time is 4600 hr, of which 3600 hr have been with the clean batch of salt. In general, the test work has produced no evidence of any problem which would preclude the use of $NaBF_4$-NaF eutectic as a reactor coolant.

Results of the cavitation tests with the clean charge of salt appear consistent with the notion that cavitation inception for the PK-P pump operating with sodium fluoroborate can be correlated on the basis of net positive suction head and vapor pressure.

It was concluded that control of the fluoroborate salt composition at the eutectic point will be easy, provided a suitable method can be established for monitoring the salt composition. Four monitoring methods have been under consideration. Of these, the one with the most promise uses the partial pressure of BF_3 over the salt, as indicated by the thermal conductivity of the off-gas stream, to calculate the salt composition.

The cause of gas-system restrictions was traced to accumulations of salt mist at the pump bowl off-gas nozzle and in the control valve. The test data indicate that the trouble can be eliminated by the use of a special hot trap at the pump bowl outlet and a high-efficiency filter immediately downstream of the hot trap.

The conceptual layout of a primary-salt pump for the molten-salt breeder reactor has been further defined to consider the problems incurred by system thermal expansion, coupling the drive motor to the pump, pump containment requirements, and shaft seal oil leakage. The plan to obtain the participation of the United States pump industry in the Molten-Salt Breeder Experiment (MSBE) salt pump program is progressing. The specification for the MSBR primary-salt pump was revised in the light of project and pump manufacturer comments. An evaluation team was selected, and they visited pump manufacturers to determine their interest and capabilities in the salt pump program. A request for proposal is being prepared for submittal to pump manufacturers. A request for directive based on preliminary design and cost estimates was prepared for the MSBE salt pump test stand, and a draft of the system design description was also prepared for it. Design work was initiated for a small pump for laboratory applications. It will be designed for molten salt and liquid metal at temperatures to 1400°F, flow capacities to 30 gpm, and head capability to 300 ft.

We completed the fabrication and started the testing of the automated cutting and welding equipment based on the design developed by the Air Force and the North American Rockwell Corporation. Initial tests of the equipment were performed with a welding programmer loaned to us by the Air Force, and these tests, performed without benefit of operating experience or equipment debugging, gave very encouraging results. This is the first of tests to establish the feasibility of remote welding for molten-salt reactors. A detailed "Proposal for the Development of a Remote Control System for Cutting and Welding Radioactive Pipe and Vessels" was submitted to the Director, Division of Reactor Development and Technology. The program covers a five-year, $3,000,000 development program to adapt the orbital equipment to fully remote operation in high radiation fields. The equipment, once developed, would have application for maintenance of most operating reactors.

8. MSBR Instrumentation and Controls

The preliminary investigation of an overall plant control system of the single-fluid 1000 Mw (electrical) MSBR was completed. This investigation included, in addition to the studies previously reported, simulations of the reactor heat transfer, nuclear kinetics, and a reactivity control system. The secondary-salt flow rate was altered at a rate proportional to the error in steam temperature, as suggested by previous studies, to achieve closer control of steam temperature.

Several transient cases were run with this model, including step and ramp changes in power demand and reactivity and step loss of one secondary-salt coolant loop. Normally anticipated ramp changes in load demand resulted in less than 10°F temperature change at the turbine throttle. Large load changes such as a 50% loss of load, however, resulted in throttle temperature variations of about 150°F. Control reactivity requirements were less than 0.075% $\delta k/k$ for the above cases with rates of about 0.003%/sec $\delta k/k$. The results

also indicate that for large load changes it may be necessary to vary primary-salt flow as well as secondary-salt flow to reduce the temperature variations on the reactor and heat exchanger.

The calculation of the decay of neutron density in the MSBR following shutdown was extended to investigate the effects of the loss of all primary-salt flow. The curves included indicate the integral of reactor power for the first 5 min after flow interruption for various rates and amounts of negative reactivity insertion. The effect of delaying control rod action is also shown.

The effect of the photoneutron reaction from beryllium on neutron density following shutdown was calculated and found to be negligible.

A dynamic analysis of a steam generator for the MSBR was performed at ORNL. A more extensive analysis is being carried on under subcontract with the University of Illinois at the university's hybrid computation facility.

Investigation of the stability of resistance thermometers to gross shifts in calibration under conditions of prolonged operation at high temperature with occasional wide variations in temperature was continued. The testing of two sets of thermometers seemed to indicate that cycling between room temperature and 1500°F, the maximum rated temperature, or extended operation at 1500°F would stabilize the thermometers.

9. Heat Transfer and Thermophysical Properties

Heat Transfer. – Studies were continued with a proposed MSBR fuel salt (LiF-BeF_2-ThF_4-UF_4, 67.5-20-12-0.5 mole %) using the pressurized flow system and a small-diameter resistance-heated Hastelloy N test section. In the recent experiments care was taken to minimize errors due to nonuniform heat loss, faulty thermocouple installation, and erratic readout, although there remained a possibility that the flow may have been affected by a repair weld near one end of the test section. Whereas wall temperature patterns in the laminar flow regime were consistent with the expectation of fully developed flow beyond a rather well-defined entrance region, the patterns in the high transition and turbulent flow regimes continued to reveal irregularities indicative of a laminar-turbulent transition extending to the outlet of the test section. Variation in the heat flux by a factor of 10 produced no significant change in the relative amplitude of the irregularities in wall temperature. Comparison of experimentally determined Nusselt moduli near the exit of the test section with those predicted by the accepted correlations indicated a dependence on Reynolds modulus which was greater than would be expected for fully developed turbulent flow. A system identical geometrically (except for the weld repair) to that used in the MSBR fuel salt experiments was operated with the salt Hitec (KNO_3-$NaNO_2$-$NaNO_3$, 44-49-7 mole %). Not only were the wall temperature patterns indicative of developed turbulent flow, but the Nusselt moduli agreed well with accepted correlations. The next phase in the experimental program will involve heat transfer measurements with the MSBR fuel salt in the same apparatus used for the experiments with Hitec.

Thermophysical Properties. – Preliminary thermal conductivity measurements in both the solid and liquid states have been made for a proposed MSBR fuel salt (LiF-BeF_2-ThF_4-UF_4, 67.5-20-12-0.5 mole %), using the variable-gap apparatus. The conductivity of the solid decreased linearly from about 0.026 w cm^{-1} $(°C)^{-1}$ at 290°C to about 0.014 w cm^{-1} $(°C)^{-1}$ at the melting point, 480°C. The ratio of liquid to solid conductivity at the melting point was 0.84, in good agreement with data for other salt mixtures. Over the range of temperature from the melting point to 860°C, the thermal conductivity of the proposed MSBR fuel salt was found to lie between that of the MSRE fuel and coolant salts, displaying a maximum of 0.0138 w cm^{-1} $(°C)^{-1}$ at about 650°C.

Despite the added difficulties in making conductivity measurements in the solid state and the associated sources of error, the measured thermal resistance displayed the same consistency as a function of gap width as observed for liquid samples and indeed yielded the same values for the fixed resistances associated, for example, with gas or surface corrosion films. Thus future experiments will include measurement of thermal conductivity in both solid and liquid states.

Mass Transfer to Circulating Bubbles. – Design of the facility for investigating mass transfer of oxygen (simulating ^{135}Xe) from glycerol-water solutions (simulating molten salt) to helium has been completed, and construction is progressing. It has been decided to use the variable-area nozzle method under development by Kedl for bubble generation. Tests of a conical screen bubble separator are encouraging. A semiempirical dispersion criterion for bubbles in a turbulently flowing stream has been developed which relates bubble and pipe sizes and liquid properties to the Reynolds modulus. Application of this criterion to the mass transfer experiment has delineated the range of Reynolds and Schmidt moduli for which fully dispersed bubble flow can be expected and has indicated that vertical orientation of the test section will probably be necessary to obtain meaningful data in the low Reynolds modulus range.

PART 3. CHEMISTRY

10. Chemistry of the MSRE

A material balance for fuel and flush salts was established from analytical chemical and physical property data for the entire period of MSRE operations with ^{235}U fuel. The results, which were consistent with on-site estimates, were used as base-line data for ^{233}U experiments. Generalized corrosion occurred rapidly at the beginning of ^{233}U operations because of the presence of Fe^{2+} as a contaminant in the reconstituted fuel salt, but the corrosion was checked completely by adjustment of $U^{3+}/\Sigma U$ concentration during the early stages of these operations. Anomalous development of a larger void fraction than had been observed previously in the fuel salt was investigated by laboratory experiments intended to simulate partially the conditions in the MSRE fuel pump. Foam development, thought to be a significant factor, was not observed. In other experiments foam behavior in molten salts was studied in glass apparatus with high-speed photography.

11. Fission Product Behavior

Additional results of postirradiation examination of the third surveillance specimen assembly confirmed that local variation in graphite porosity significantly affects diffusion of activities through salt-graphite interfaces.

Programs were developed for calculation of fission product inventories during ^{233}U operation of the MSRE. Discovery that the ^{95}Nb oxidation-reduction equilibrium provides a sensitive measure of the redox potential of the fuel salt identified its potential use as a corrosion indicator in molten-salt reactors.

Operation of the MSRE off-gas sampler-analyzer showed the presence of 1 to 3 g/day of hydrocarbons in the stream. Mass spectrometric analysis of samples taken during power operations with ^{235}U and ^{233}U showed appropriate response of xenon and krypton isotopic ratios to the fuel used.

Transport properties of fission products which "volatilize" from the surface of radioactive salt mixtures were studied in both hot-cell tests and via tracer experiments using chemical traps and probes. The aerosol particles produced were found to have average diameters of 4 to 20 A.

The chemistry of the noble metal fission product fluorides was investigated in laboratory experiments. The fluorides and oxyfluorides of niobium, molybdenum, and ruthenium were prepared and characterized. Their stabilities were determined using mass spectrometric methods.

12. Physical Chemistry of Molten Salts

The solubilities and heats of solution of CeF_3 in $LiF\text{-}BeF_2\text{-}ThF_4$ and $LiF\text{-}ThF_4$ mixtures were determined at 600 and 800°C. Solubility of CeF_3 was correlated with solvent composition and found to depend on the sum of BeF_2 and ThF_4 concentrations.

Zone melting and cyclic slow-cooling experiments were conducted with $LiF\text{-}BeF_2\text{-}ThF_4$ mixtures (72-16-12 and 57-33-10 mole % with 0.3 and 0.025 mole % CeF_3 added). Behavior was consistent with published and recent phase studies of the solubility of CeF_3 in the $LiF\text{-}BeF_2\text{-}ThF_4$ system. Cyclic slow cooling provided equal or better thorium separation than zone melting, although appreciable separations were not obtained for thorium or cerium in the $LiF\text{-}BeF_2\text{-}ThF_4$ (72-16-12 mole %) mixture.

Studies of the equilibrium phase behavior in the system $NaF\text{-}KF\text{-}BF_3$ were continued. Liquid-liquid immiscibility in the systems $LiF\text{-}KBF_4$, $Li_2BeF_4\text{-}KI$, and $Li_2BeF_4\text{-}KBF_4$ was observed in accord with prediction. Composition-temperature relationships of the conjugate monotectic liquids were established. The crystal structure of the low-temperature form of KBF_4 was determined from three-dimensional x-ray diffraction data.

The solubility of thorium metal in molten $LiF\text{-}ThF_4$ (73-27 mole %) at 620°C was established as 0.1 mole %. Densities of molten MSR fuel and coolants were measured at their typical operating temperatures with heretofore unprecedented accuracy. The establishment of a program for the investigation of visible-ultraviolet absorption spectroscopy in molten fluorides was completed, including the development of the diamond-windowed spectrophotometric cell which is unreactive to fluorides and the production of fluoride solvents and solutes of the purity required for spectroscopy.

The distribution of U^{4+} between molten $LiF\text{-}BeF_2\text{-}ThF_4\text{-}UF_4$ and a $(U,Th)O_2$ solid solution was investigated for possible application to molten-salt reactor fuel reprocessing. The exchange process was found to be rapid and reversible.

Efforts were continued to develop an Ni-NiO-BeO electrode as a reference electrode in molten fluorides. The results obtained were reproducible but were not in agreement with cell potentials calculated from available thermochemical data. Transference numbers were measured in molten mixtures of LiF and BeF_2. It was found that $t_{Li^+} = 1.0 \pm 0.05$ in the range $0.3 < x_{BeF_2} < 0.5$, and possibly over the entire concentration range. The mobility of the beryllium ions is zero within experimental error. The suitability of molten potassium nitrate for use as a molten-salt conductance standard in

cell-constant determinations has been demonstrated. The specific conductance is well represented (σ = 0.0008) by the equation

$$K = -0.7098 + 4.6203 \times 10^{-3} t(°C) - 2.0221 \times 10^{-6} t^2 .$$

As part of a continuing investigation of electrical conductivities in the molten LiF-BeF_2 system, preliminary results are reported for the temperature dependence of pure molten beryllium fluoride over the range 530–685°C.

13. Chemistry of Molten-Salt Reactor Fuel Reprocessing Technology

Development chemistry for molten-salt reactor fuel reprocessing technology has been devoted to the reductive extraction concept whereby constituents of the fuel are selectively extracted into molten bismuth containing either lithium or thorium as the reducing agent. The chemical feasibility of ^{233}Pa isolation has been demonstrated by a process which also requires the prior reduction of uranium from the salt mixture and its subsequent oxidation into the salt effluent of a ^{233}Pa extraction column. Recent studies have examined the effects of metal additives to bismuth, and varied process applications to achieve improved rare-earth separations.

14. Development and Evaluation of Analytical Methods for Molten-Salt Reactors

The oxide content of the ^{233}U fuel in the MSRE was found to be 61 ppm, essentially identical to that of the ^{235}U fuel. The oxide apparatus is expected to require major repairs shortly but will probably last through the MSRE operations. Three approaches were studied as possible methods for the determination of U(III) in the radioactive MSRE fuel. Of these the total reducing power and hydrogen transpiration methods were found to be impractical for the analysis of the ^{233}U fuel at this time. A voltammetric method in which the potential of a noble electrode poised by the U(IV)/U(III) couple is measured vs the position of the U(IV)→U(III) voltammetric wave offers the possibility of more immediate measurements. The technique requires the insertion of three platinum electrodes in the salt. An apparatus has been designed that will permit the insertion of electrodes in MSRE fuel that is remelted in the original sampling ladle. Tests with simulated fuel have demonstrated that U(IV)/U(III) ratios can be maintained for several hours and that the frozen salt could be exposed to the atmosphere for periods necessary for hot-cell transfers without significant loss of U(III).

The accuracy of the measurements was established in separate experiments in which MSRE-type melts containing U(IV)/U(III) in ratios from 7 to 140 were measured voltammetrically and potentiometrically vs an Ni/NiF reference. The melts were simultaneously sampled for a spectrophotometric determination of U(III) concentrations. Satisfactory agreement was obtained between the voltammetric and spectrophotometric determinations. Also, the potentiometric measurements were in agreement with values calculated from reported values of free energies. Potentiometric measurements vs the Ni/NiF reference electrode are also reported for Be(II)/Be, Zr(IV)/Zr, and corrosion product couples in LiF-BeF_2-ZrF_4 and for the Fe(II)/Fe and Fe(III)/Fe(II) couples in LiF-NaF-KF. A pronounced cathodic shift of the Fe(III)/Fe(II) couple in LiF-NaF-KF indicates a strong complexing of Fe(III) by free fluoride in the melts.

It appears that the facility for the spectrophotometry of radioactive molten fluoride salts can be completed as scheduled. Delivery of the optical system has been scheduled for August. Three of the major salt-handling components, the optics furnace, its top assembly, and the transport container, have been fabricated and subjected to preliminary testing and modification. The sample loading furnace is almost completed. A hot cell has been decontaminated, and the necessary in-cell services are being designed. The successful sampling of fluoride melts for the determination of U(III) by a technique similar to the one to be used in the hot cell confirmed the validity of the method designed for radioactive samples. These experiments also demonstrated the use of the absorption of U(IV) to determine the path length of melts in windowless cells.

Absorption spectra in molten Li_2BeF_4 are summarized for a variety of $3d$ transition-metal ions. All of these spectra, which include a representative of each configuration except $3d^5$, are consistent with ions situated in high symmetry, either octahedral or distorted octahedral. Cobalt(II) maintains high symmetry even in melts enriched in BeF_2.

Observations of wetting and nonwetting behavior of LiF-BeF_2 melts in various container materials were accumulated and analyzed. Conditions found necessary for wetting to occur include an electrically conductive container together with an active metal in contact with a melt containing one or more soluble species of the active metal. Sparingly soluble oxides did not cause wetting.

Liquid contaminants in the He-BF_3 cover gas of the circulating $NaBF_4$ loop have been tentatively identified as hydrolysis products of BF_3. An apparatus has been assembled to study these materials and to develop techniques for their removal from off-gas systems.

A variety of analytical techniques are being tested for the determination of traces of bismuth in MSRP salts. Presently, the detection limit for the iodide spectrophotometric method is 10 ppm. Emission spectrographic, polarographic stripping, and isotope exchange methods are being investigated for determinations at the 1-ppm level or lower.

PART 4. MOLTEN-SALT IRRADIATION EXPERIMENTS

15. Molten-Salt Convection Loop in the ORR

Wetting studies indicated that very stringent gas purification measures will have to be used in future small-scale experiments, such as the in-pile thermal convection autoclave, if wetting by the salt and concomitant confusion of the experimental results are to be avoided. Titanium or uranium metal hot trapping at the points of entry of gas streams into the loop are indicated as minimum requirements.

PART 5. MATERIALS DEVELOPMENT

16. MSRE Surveillance Program

Several magnetic particles were removed from the MSRE pump bowl with a permanent magnet. These particles were mixtures of iron and nickel with trace amounts of chromium and molybdenum and ranged from 20 to $<1\ \mu$ in size.

17. Graphite Studies

Several new graphites were obtained for evaluation. These materials have been characterized by the measurement of several physical properties and have been included in other phases of our program. The techniques were developed for making several physical property measurements on graphite, including thermal conductivity, electrical resistivity, anisotropy by x-ray diffraction, and structure studies by transmission electron microscopy. Several graphites have been irradiated to a fluence of 2.5×10^{22} neutrons/cm^2 (>50 kev) at 715°C. Dimensional measurements indicate that (1) the maximum density and the associated fluence are inversely proportional to the original density, (2) the crystallite growth rates at maximum density are dependent only on the preferred orientation, and (3) grades H337, H364, and AXF show an initial delay before densifying and offer improved dimensional stability.

Our graphite sealing studies have concentrated on optimizing the processing parameters for various graphite substrates. Some sealed AXF samples were irradiated to a maximum fluence of 1.3×10^{22} neutrons/cm^2 (>50 kev). Although the permeabilities increased, one sample had a helium permeability of at least 1.7×10^{-7} cm^2/sec. Other samples have been sealed and are being irradiated.

18. Hastelloy N

Titanium and carbon additions improved the mechanical properties of a base alloy of Ni–12% Mo–7% Cr. Samples of Ni–12% Mo–7% Cr–0.05% C containing various amounts of titanium were aged for various times at 650 and 760°C. Mechanical property tests showed that changes took place, but these changes were not sufficient to account for the variations noted over this temperature range during irradiation. Electron microscopy revealed that the good properties were associated with a fine MC-type precipitate and that the poorer properties were noted at higher temperatures, where a coarse M_2C-type carbide was formed. The MC-type carbide can be stabilized with higher concentrations of Ti, Hf, Nb, Zr, and Y, and postirradiation creep tests show that good properties result.

Our corrosion studies continued to affirm the excellent compatibility of Hastelloy N with the lithium-beryllium-fluoride salts. A loop constructed of type 304L stainless steel has a higher, but acceptable, corrosion rate and has operated for over six years without difficulty. Our proposed coolant salt, sodium fluoroborate, is somewhat more aggressive, but our thermal convection loops indicate that acceptable corrosion rates are attainable when the water content of the salt is low. We have operated a pumped loop of Hastelloy N containing sodium fluoroborate for about 1500 hr. The salt composition has shown some erratic changes in metallic impurities, but operation has proceeded without difficulty.

19. Support for Chemical Processing

Molybdenum and graphite seem compatible with fuel salts and with bismuth and are potentially useful construction materials for a chemical processing plant for MSBR's. The primary remaining problem is fabri-

cation, since both materials are difficult to join. Techniques have been developed for brazing both materials, but these joining materials may not be compatible with bismuth. We are also examining the possibility of coating iron-base alloys with molybdenum to prevent temperature-gradient mass transfer of the iron by the bismuth.

20. Support for Components Development Program

We have procured some of the equipment necessary for making welds in Hastelloy N by processes that are potentially useful for remote applications. Useful experience has also been gained through the use of some automatic welding equipment that utilizes the MIG welding process.

Several plasma-sprayed bearing surfaces on Hastelloy N have received cursory evaluation. The coatings did not spall during thermal cycling, but several small flaws did develop.

PART 6. MOLTEN-SALT PROCESSING AND PREPARATION

21. Flowsheet Analysis

The proposed process flowsheet for a 1000 Mw (electrical) single-fluid MSBR includes a system for ^{233}Pa isolation based on reductive extraction using molten bismuth. The salt is processed at a rate equivalent to 1 reactor volume in three days. Calculations using revised equilibrium distribution data show the system to be theoretically practical. The flowsheet also includes a system for rare-earth removal which processes the contents of the reactor on a 30-day cycle. Calculations indicate that a cascade of perhaps 24 stages will be necessary to effect rare-earth removal with bismuth flow rates as high as 15 gpm. An important variable in this calculation was the fraction of thorium electrolyzed from the salt as it passed through the electrolytic cell unit. A computer code has been developed to perform steady-state material balance calculations which describe the nuclear, chemical, and physical processes occurring in the fuel of an MSBR.

22. Measurement of Distribution Coefficients in Molten-Salt–Metal Systems

Distribution of uranium, protactinium, plutonium, thorium, rare earths, and other fission products between molten fluoride salts and liquid bismuth solutions is being studied in support of a reductive extraction process for single-fluid MSBR fuels. Equilibrium data were obtained with a variety of LiF-BeF_2-ThF_4 salts at 600°C. These data show that uranium and zirconium will coextract but that they should be easily separated from protactinium. Plutonium can probably be separated from protactinium if the reductant concentration in the metal phase is very low. Protactinium should be easily separated from the rare earths and thorium; the Pa-Th separation factors were 2000 to 4400 with the salt compositions used. The rare-earth–thorium separation will be much more difficult; separation factors were in the range of 1.0 to 3.5. A metal transfer process is being evaluated as an alternative to reductive extraction for the rare-earth–thorium separation.

The mutual solubilities of nickel and thorium in bismuth were determined at 600°C. The results can be expressed as a mole fraction solubility product $K_{xp} = 6.2 \times 10^{-7}$.

23. Engineering Development of Process Operations

Electrolytic cells will be required for operation of reductive extraction systems in an MSBR fuel processing plant. The cells will be used to oxidize materials in bismuth streams effluent from extraction contactors as well as for reducing lithium and thorium into bismuth streams which are fed to the contactors. Experiments have been carried out in quartz cells (4 in. OD) which used bismuth pools as the electrodes and 66-34 mole % LiF-BeF_2 as the electrolyte. Current densities up to 4.5 amp/cm^2 were observed. The current was linearly dependent on applied voltage, which suggests that there is essentially no limiting current in the range covered by the experiments. Corrosive conditions will exist in the vicinity of anodic surfaces, and it is planned that such surfaces be protected by a frozen salt layer. A small all-metal static cell has been installed for study of this method of operation.

Equipment has been installed for semicontinuous engineering experiments on reductive extraction. The equipment allows purification and countercurrent contact of up to 15 liters each of molten salt and bismuth containing thorium through a 0.82-in.-ID, 2-ft-long column packed with ¼-in. right circular cylinders. Preliminary testing and degassing of the equipment has begun, and charging of bismuth and molten salt (72-16-12 mole % LiF-BeF_2-ThF_4) will have been completed soon.

The hydrodynamic properties of contactors are being studied in simulated systems using water and mercury.

Quantitative measurements have been made of flooding rates, pressure drop, and dispersed phase (Hg) holdup. Information was also obtained on flow patterns and drop sizes. Four packing materials and one baffled cartridge have been studied in a 1-in.-ID column. A mathematical model describing the hydrodynamic aspects of a dispersed-flow column was developed.

A system is being built to allow the steady-state testing of a variety of electrolytic cell designs. Provision is made for circulating up to 0.5 gpm of bismuth and 0.25 gpm of salt through the cell containment vessel, for sampling the inlet and outlet streams from the cell, and for visually observing operation of the cell.

24. Distillation of MSRE Fuel Carrier Salt

An experimental molten-salt still is being installed at the MSRE for demonstrating low-pressure, high-temperature distillation of 48 liters of irradiated MSRE fuel carrier salt. Minor equipment modifications suggested by nonradioactive tests were made. A condensate sampler similar to equipment used for addition of ^{233}U to the fuel drain tanks was built.

The still was tested by transferring 16 liters of nonradioactive salt into the system and distilling about 2 liters of this salt.

Part 1. Molten-Salt Reactor Experiment

P. N. Haubenreich

Loading of ^{233}U into the MSRE commenced a few days after the beginning of the six-month period reported here. Part 1 of this report describes the critical experiment, the zero-power determinations of nuclear characteristics, and, finally, operation at full power of the world's first ^{233}U-fueled reactor. Results are reported which show the adequacy of the nuclear data and the procedures used to predict the characteristics of the system with ^{233}U. An experiment to measure accurately the capture-to-fission ratio of ^{233}U in a molten-salt reactor neutron spectrum was in progress at the end of the report period. Results of dynamics tests showed the expected response and proved the system to be quite stable and easy to control, despite the very low delayed neutron fraction of ^{233}U. Beginning early in the ^{233}U operation, the amount of gas entrained in the pump and circulating with the fuel was higher than ever before. Fuel chemistry in the aftermath of processing and its possible relation to the gas entrainment are discussed in Part 3 of this report. One effect of the higher gas content (up to 0.7 vol %) was sporadic small perturbations in salt level and nuclear power. Analysis of the perturbations, described in Part 1, shows that their effects are too small to affect the operation or the life of the reactor, and the cause is probably related to the specific situation in the MSRE which permits gas to cling in the core. Development work directly related to the MSRE is also described in Part 1.

1. MSRE Operations

P. N. Haubenreich

1.1 CHRONOLOGICAL ACCOUNT OF OPERATIONS AND MAINTENANCE

J. L. Crowley T. L. Hudson
J. K. Franzreb A. I. Krakoviak
R. H. Guymon R. B. Lindauer
P. H. Harley M. Richardson
B. H. Webster

At the end of August 1968, the fuel salt had just been fluorinated to remove the 33%-enriched ^{235}U that had fueled the reactor since the nuclear startup in June 1965, and reduction of the corrosion product fluorides was under way.[1] After treatment with hydrogen and finely divided zirconium, the salt was passed through a filter and returned to the reactor drain tanks on September 8. Samples showed acceptably low concentrations of corrosion products, thus clearing the way for use of the carrier salt for the operation with ^{233}U. The principal reactor-associated activities for this report period are shown graphically in Fig. 1.1.

The amount of uranium (91% ^{233}U) which had to be added to attain criticality at the reference condition (1200°F, rods fully withdrawn, no circulation) was predicted to be 33.9 kg. Equipment had been attached to drain tank 2 to permit addition of batches of enriching salt containing up to 7 kg of uranium. Three batches totaling 21 kg of uranium were added before the salt was pushed up into the fuel loop to determine the neutron multiplication. This was repeated after the addition of one more 7-kg batch. The final addition through the drain tanks was 5 kg of uranium, bringing the total added to 32.9 kg. When the core was filled

[1] *MSR Program Semiann. Progr. Rept. Aug. 31, 1968*, ORNL-4344, pp. 1–11.

after this addition, extrapolation of the subcritical multiplication indicated that only 0.35 kg more uranium was required. A capsule of enriching salt containing 96 g of uranium was added through the sampler-enricher to check out its operation and to refine the extrapolation to the critical loading. Then the salt was drained and secured in drain tank 1.

As long as uranium was being loaded into the drain tank, the drain-tank cell could not be sealed. Therefore, before the reactor was taken critical, the loading equipment was removed from FD-2, the cell was sealed, and the containment was leak-tested at 20 psig. The critical experiment was then resumed, with uranium being added, 96 g at a time, through the sampler-enricher directly into the circulating fuel salt. On October 2 criticality was attained after the addition of 33.29 kg of uranium, slightly less than had been predicted originally. Capsule additions continued for the next 38 days, by which time a total of 27 capsules had been added and one control rod had been almost fully inserted. Initial criticality had been attained after 4 capsules. After 6 capsules the reactor was critical with the fuel circulating. On October 8, after the addition of the tenth capsule, the reactor power was raised to 100 kw to observe the dynamics. This was the first time that a ^{233}U-fueled reactor had ever operated at significant power, and the occasion was marked by a ceremony including AEC Chairman Glenn Seaborg and Commissioner Wilfred Johnson, among others. Chairman Seaborg, who headed the team that had discovered ^{233}U, was at the controls when the power was raised. At his side was R. W. Stoughton, of the ORNL Chemistry Division, who with Seaborg and J. W. Gofman first identified ^{233}U on February 2, 1942.

After each of the capsule additions subsequent to initial criticality, the critical control rod position and the rod sensitivity were measured with and without the fuel circulating. Two sets of rod-drop tests were done to obtain total rod worth. After the last addition the critical rod position was determined at temperatures

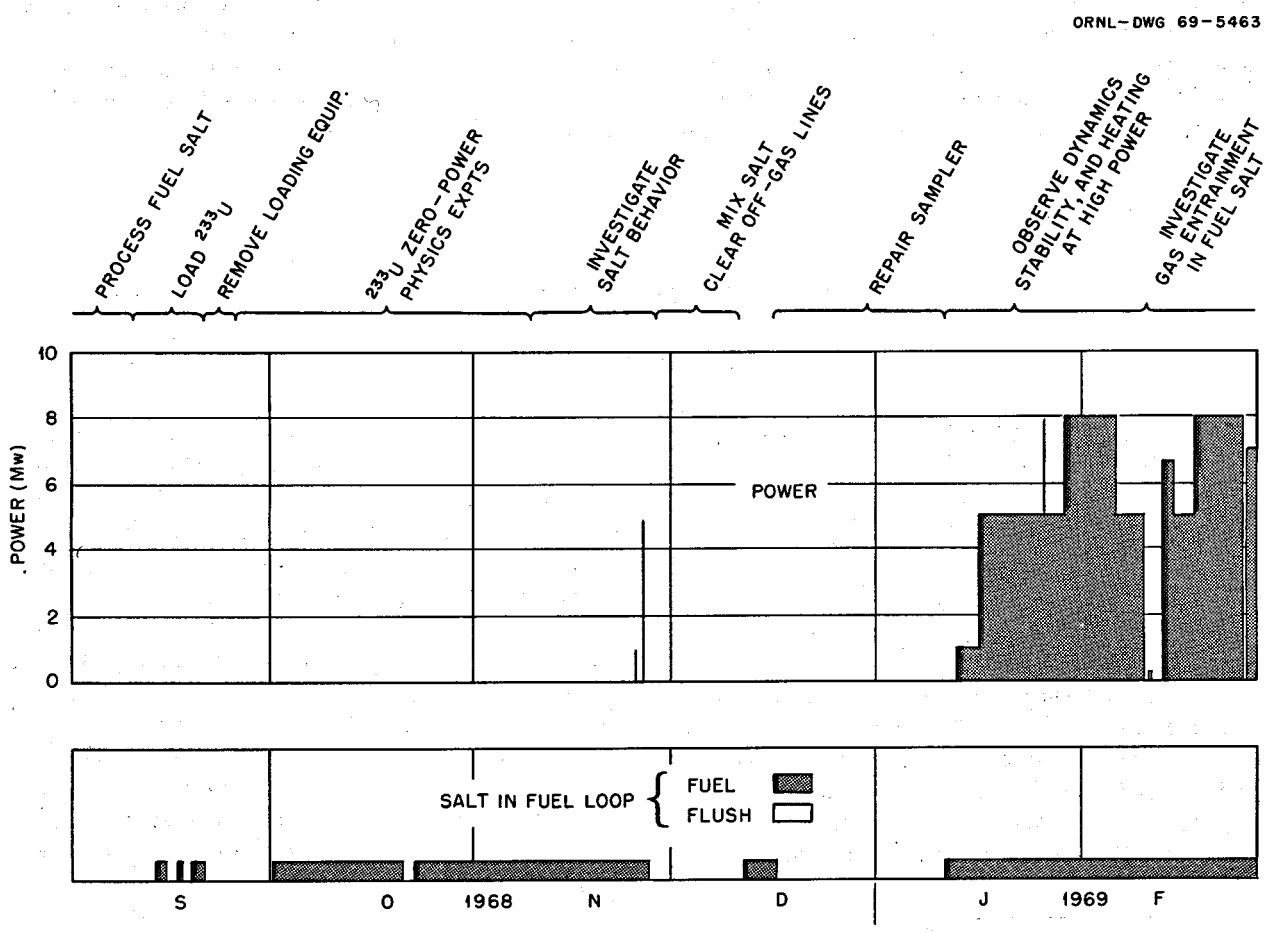

Fig. 1.1. MSRE Operations, September 1968–February 1969.

from 1175 to 1225°F, with and without the fuel circulating.

The fuel was circulated for two months during the course of the uranium additions and reactivity measurements. (There was a one-day interruption when the fuel drained following an instrument power failure.) Throughout this period there was abundant evidence of an unusual amount of gas entrainment in the circulating fuel – about 0.5–0.7 vol % compared with <0.1 vol % during the years of operation with ^{235}U. This was manifested most clearly as a change in pump-bowl level after start or stop of fuel circulation, but also showed up in the effects of pressure and fuel circulation on reactivity. A dependence of the core bubble fraction on fuel temperature showed up as a difference in the temperature coefficients of reactivity measured with the fuel circulating and with it stationary and practically free of gas.

Examination of records of pump-bowl level showed that the increased amount of gas in the fuel loop had started rather suddenly on September 15, after about 16 hr of fuel circulation. Comparison of pressures on the two bubblers in the pump bowl showed that the density of the fluid several inches below the surface decreased by about 20% at the same time. Subsequently the transfer of salt into the overflow tank was abnormally high. These changes occurred 2 hr after the start of a 12-hr exposure of a beryllium rod in the pump bowl. (The 21 kg of uranium that had been added to this point was practically all in the U^{4+} state, and the beryllium was intended to reduce some to U^{3+} so as to provide a reducing environment to forestall corrosion.) The correlation of the gas changes with the exposure of beryllium metal was confirmed on October 13, when another beryllium rod was immersed in the pump bowl for 10 hr. During this interval the pump-bowl level and the reactivity showed the circulating bubble fraction changing erratically between 0.3 and 0.6 vol %. The gas fraction remained high after the beryllium was removed, and the rate of transfer to the overflow tank was as high as 29 lb/hr. (It had gotten down to about 4 lb/hr before this second beryllium addition.) Also, during the following day, pressure drops began to show a restriction in the fuel off-gas line near the pump bowl. In order to investigate these phenomena, reactor operation was continued, at very low power (about 50 w), for almost three weeks after the last uranium addition.

The nickel cages in which the beryllium rods were suspended in the fuel salt had come out with deposits of magnetic material that proved to be mixtures of iron, chromium, and nickel. This was taken to mean that the corrosion product fluorides had not been completely reduced in the chemical processing and that some had been reduced by the beryllium. Magnets lowered into the pump bowl brought out samples of the magnetic powder, suggesting that the reduced metals tended to float in the pump bowl. Because it appeared that the reduction achieved by the first two beryllium rods was mainly of iron and chromium, a third rod was exposed on November 15 to reduce some U^{4+} to U^{3+}. Again there were effects on the gas in the pump bowl and in the loop. A week later an experimental assembly of alternate short sections of beryllium rod and permanent magnets was exposed in a nickel cage. Examinations through the sampler-enricher periscope after 5 min, 1 hr, and 6 hr showed only small amounts of metal powder on the assembly.

A shutdown had been scheduled before the beginning of sustained power operation, and on November 28 the fuel and coolant salts were drained. The original purpose was to mix the fuel salt in the loop and in the drain tank, which by now had different uranium concentrations as a result of the capsule additions. But the pressure drop across restriction in the off-gas line at the fuel-pump bowl had gradually increased to about 4 psi, so the reactor cell was opened, and the line was rodded out with a flexible tool designed to retrieve some of the plugging material. The deposit appeared to be mostly frozen salt mist. The coolant was drained, because for some months there had been indications of partial obstructions in the off-gas line from this system, presumably from oil residues, and heaters and an oil trap had been designed to be installed near the coolant pump. Cleanout of the coolant off-gas line revealed deposits ranging from tarry near the pump to light oil farther away.

On December 12 fuel circulation started for run 16. The intended approach to full power was delayed, however, because the analog input system for the on-line computer, which was needed for the dynamics tests, was not operating properly. After five days of operation at 10 kw while the computer problems were being worked on, the fuel sampler drive became inoperative. In order to gain access to the drive unit, it was necessary to drain the fuel and remove the shield blocks over the reactor.

A temporary containment enclosure and shielding were set up, and the drive was lifted part way out of the sampler shield so repairs could be made. These consisted in cutting into the drive box and welding a loose gear to its shaft and then patching the containment box.

Before the reactor was started up again, control rod drive No. 3 was inspected and worked on. Although the

drop time for this rod was still acceptable, it had crept up gradually over the previous several months. Analysis of acceleration and examination of the drive and the rod itself showed only a general increase in stiffness or drag. A small weight added to the drive produced quite satisfactory performance.

Maintenance was completed and nuclear operation was resumed on January 12. The first day was spent at very low power, confirming the earlier temperature coefficient measurement. Then the power was raised to 1 Mw, where it was held for dynamics tests, observation of nuclear heating, and fuel sampling. On January 17 the power was stepped up to 5 Mw.

With the beginning of 5-Mw operation, a new phenomenon was noted. This was the occurrence of small perturbations, at a frequency of 10 to 20 per hour, that affected the nuclear power, the fuel-pump level and pressure, and temperatures in the reactor outlet. The perturbations, or "blips," were too small to be of immediate consequence, but intensive efforts were started to determine the mechanism (see Sect. 1.3.4).

Analysis of the behavior of the several signals during typical blips indicated that the reactivity perturbations (about 0.01 to 0.02% $\delta k/k$) were most probably caused by a temporary reduction in the amount of gas held up in the reactor core. Furthermore, examination of recorded data showed that a peculiar behavior of the salt level in the annulus of the reactor access nozzle which accompanied the reactivity perturbation had begun on September 15, when the gas fraction in the circulating salt had increased. Operation at 1, 3, and 5 Mw with sensitive instrumentation showed that the frequency with which the disturbances occurred and the amount of reactivity associated with them were independent of power. Further evidence that the blips were related to gas in the core came when a beryllium rod was exposed to the salt on January 24. For several hours while the beryllium was in, the gas fraction in the loop was about half what it had been and there were no blips. The gas and the blips came back after the beryllium was removed.

After the conclusion that the blips were not evidence of some potentially damaging situation, the reactor was taken to full power of 8 Mw on January 28. Tests at this level showed, as they had at lower powers, that the dynamic response of the reactor system was quite close to predictions. The small delayed neutron fraction of ^{233}U was more than offset by the longer neutron lifetime and larger negative temperature coefficient of reactivity with the more dilute fuel, making the system more strongly damped and giving a larger stability margin than in the ^{235}U operation.

After a total of nine days at full power, the power was reduced to 5 Mw to permit operation at lower fuel temperature without getting the coolant radiator below 1000°F. Variation of fuel temperature, pressure, and salt level showed slight effects on gas in the loop. The effect of these variables on blips seemed to be overshadowed by a gradual decline in frequency and size.

Gas in the fuel loop is a result of injection of bubbles into the salt in the pump bowl by the jets from the xenon stripper. It appeared therefore that the amount of gas could be drastically reduced by slowing down the pump to cut the velocity of the jets and the flow of salt into the pump suction. While a variable-frequency power supply for the fuel pump was being set up and checked out, a thermal convection experiment was run on February 12. The fuel pump was turned off, the reactor was taken critical, and the heat load was gradually increased by raising the radiator doors. The reactor was operated at various powers up to 350 kw and thermal convection circulation rates up to about 30 gpm, for a total of 6 hr. The nuclear power followed the heat load without control rod adjustment, and there were no blips. (The blip frequency with forced circulation and entrained gas just before the experiment had been around five per hour.)

After the thermal convection experiment, normal high-power operation was resumed and continued until the variable-frequency pump power supply could be put into service. This was ready on February 27. Starting at half speed, the pump was brought up in steps to full speed while the reactor was held at 10 kw to observe the noise in the nuclear power. At half speed, the salt level, the reactivity, and the neutron noise showed practically no bubbles in the loop. A rather sharp threshold occurred between 90 and 95% of full flow, where all indications showed bubbles appearing in the fuel loop. The power supply was dropped back to 50 cps (83% of full flow), and the power was raised to 7 Mw. For the next five days, operation continued at these conditions. The neutron noise (the small, random fluctuations in power) was far less than had been observed in ^{233}U operation, and there were no blips. The pump speed was then returned to normal, the bubbles and noise came back, and blips began to occur again. A discussion of this and other evidence on the blips is given in Sect. 1.3.4.

At the end of February the reactor had been operating continuously for 47 days. A restriction had built up again in the fuel off-gas line at the pump bowl, becoming detectable on January 17 and gradually increasing until February 27, when it blew out with an 8-psi ΔP across it. Partial restrictions, believed to be organics, appeared in the coolant off-gas line and at the

entrance to the main charcoal bed and were relieved by application of heat. Otherwise there was nothing threatening a shutdown.

Operating statistics at the end of February are given in Table 1.1.

1.2 ^{233}U ZERO-POWER TESTS

J. R. Engel

The program of zero-power tests with ^{233}U was very similar to that followed during the initial experiments with the ^{235}U fuel. The purpose was to first establish the critical fuel loading under the simplest attainable conditions and then measure the control rod worth and the temperature and fuel-concentration coefficients of reactivity. We originally planned to measure the loss of delayed neutrons due to circulation of the precursors, but the high circulating void fraction and the attendant "noise" that it produced in the neutron flux prevented a direct evaluation. However, indirect confirmation of the validity of the calculated value was obtained from rod-drop measurements. The results of the various measurements, which are described below, are summarized in Table 1.2.

1.2.1 Critical Experiment

B. E. Prince J. R. Engel

Analysis of the critical experiment with ^{233}U was of interest as a check on the data and the procedures used

Table 1.1. Some MSRE Operating Statistics

	^{233}U Operation, August 1968–February 1969	Total Through February 1969
Critical time, hr	1821	13,336
Integrated power, Mwhr	5994	78,435
Equivalent full-power hours	747	9753
Salt circulation, hr		
Fuel loop	2238	17,280
Coolant loop	4469	21,375

Table 1.2. MSRE Nuclear Characteristics with ^{233}U

Property	Value	
	Calculated	Observed
Base-line critical concentration,[a] grams of uranium per liter[b]	15.30	15.15
Control rod worth, % $\delta k/k$		
One rod	2.75	2.58
Three rods	7.01	6.9
Temperature coefficient of reactivity, $(\delta k/k)/^{\circ}$F	-8.8×10^{-5}[c]	-8.5×10^{-5}[d] -7.4×10^{-5}[e]
Concentration coefficient of reactivity, $(\delta k/k)/(\delta C/C)$[b]	0.389	0.369
Change in β_{eff} due to fuel circulation	-1.005×10^{-3}	

[a] At 1200°F with fuel stationary and all control rods withdrawn to their upper limits.

[b] Uranium of the isotopic composition of the material added during the critical experiment (91% ^{233}U).

[c] Assumes no gas in the fuel and the operating uranium concentration. The predicted temperature coefficient at the initial critical concentration was -9.4×10^{-5}.

[d] With very little gas.

[e] With about 0.5 vol % gas circulating.

to predict the critical loading. This comparison was complicated and rendered more uncertain because the fuel carrier salt had been used for the ^{235}U operation and contained many of the products formed during the first 72,000 Mwhr of reactor operation. The processing to recover the ^{235}U removed the uranium and those fission products that form volatile fluorides, but practically all the plutonium and the rare-earth fission products remained in the salt. In addition a heel of fuel salt was unavoidably left in the drain tanks when the main charge was transferred to the fuel storage tank to be processed for uranium recovery. All of these factors contribute to the uncertainty in predicting the critical loading.

The original theoretical calculations to predict the ^{233}U critical loading were performed in the summer of 1967.[2] A major application of the results was the specification of the amount of ^{233}U feed material that had to be prepared[3] for the actual experiment. Although we were aware of many of the factors listed above, the reactor was still operating with ^{235}U, so we could only estimate their effects on the critical loading. These calculations led to a predicted critical concentration of 15.82 g/liter (uranium of the isotopic composition of the feed material). While this result provided an adequate basis for specifying material requirements, it could not be regarded as a "best effort" at predicting the critical concentration for the conditions that actually prevailed at the time of the experiment.

Some of the factors that affected the critical uranium concentration were not fully evaluated until after the critical experiment had been completed. When these data became available, we attempted to evaluate the corrections to the original calculations that we knew were required to make the conditions for the computational model conform to the actual conditions at the time of the experiment. The most important of the necessary changes and updating were as follows:

1. In the original calculations, we had assumed that the operation with ^{235}U would be terminated at approximately 60,000 Mwhr exposure. At the time of shutdown from MSRE run 14, the actual exposure was 72,440 Mwhr.
2. In connection with item 1, the residues of plutonium and samarium remaining in the fuel salt had to be reevaluated.
3. For the earlier calculations the concentrations of the most important neutron-poisoning impurities, ^{6}Li in the salt and ^{10}B in the graphite, were assumed equal to the concentrations at the start of operation with ^{235}U. Hence corrections had to be introduced for the burnout of these nuclides.
4. The calculations had been based on the assumption that no residue, or heel, of uranium would remain in the reactor system after the transfer and processing of the fuel salt. From isotopic dilution measurements made in the course of the uranium additions, we concluded that 1.935 kg of uranium (isotopic assay: 32.97% ^{235}U, 66.23% ^{238}U) from the first loading had been left in the drain tanks. This became a part of the fuel salt when the uranium-free salt was returned from the storage tank for the start of the ^{233}U operation.
5. A special addition of 0.89 kg of depleted uranium was made in order to obtain the isotopic abundances necessary for the planned experiment to measure the capture-to-absorption cross-section ratio in ^{233}U. This addition had not been considered in the earlier calculations.
6. Certain changes had been made in the evaluated library of cross-section data for the fissile isotopes since the earlier calculations were performed.

The above modifications were introduced into the theoretical model, and the associated changes in the multiplication constant, as well as the changes in uranium required to compensate for the multiplication changes, were evaluated. The results are summarized in Table 1.3. It is apparent that the largest single correction is that associated with the uranium heel, but all the corrections are significant. Application of these corrections to the originally predicted value led to a revised prediction of 15.30 g/liter. (Note that this value is applicable to stagnant salt at 1200°F with all three control rods withdrawn to their upper limits.) The observed loading was 15.15 g/liter, a discrepancy of only 1% in concentration or 0.4% in k_{eff}.

In addition to the effects listed in Table 1.3, there are two other reactivity effects that were not explicitly included in either the original calculation or the revised prediction. One of these is the negative reactivity contribution of the low-cross-section fission products remaining from the first fuel loading. The magnitude of this reactivity effect depends on the extent to which various fission products left the salt during the ^{235}U

[2] *MSR Program Semiann. Progr. Rept. Aug. 31, 1967*, ORNL-4191, p. 54.

[3] J. M. Chandler and S. E. Bolt, *Preparation of Enriching Salt ^{7}LiF-$^{233}UF_4$ for Refueling the Molten Salt Reactor*, ORNL-4371 (March 1969).

Table 1.3. Changes in Theoretical Calculation of ^{233}U Critical Loading

Correction	Reactivity Effect (% $\Delta k/k$)	Uranium Equivalent[a] (% $\Delta U/U$)
Isotopic changes at 72, 440 Mwhr		
^{239}Pu[b]	+0.095	−0.243
^{10}B	+0.379	−0.973
$^{149}Sm + ^{151}Sm$[c]	+0.061	−0.156
^{6}Li	+0.217	−0.558
Uranium heel		
^{235}U	+0.554	−1.424
^{238}U	−0.147	+0.376
Depleted uranium addition	−0.102	+0.262
Cross-section changes	+0.212	−0.545
Net	+1.269	−3.261

[a]Uranium with isotopic composition of enriching salt (91% ^{233}U).

[b]Assumes no removal during chemical processing.

[c]Net change is positive since effect of dilution by the drain tank salt heel was not accounted for in original calculations.

operation and also on any separation which may have occurred during fluorination to remove the uranium. The effect could be as large as −0.5% $\delta k/k$ if all these fission products remained in the salt. Since it is impossible to estimate the degree of retention realistically with currently available information, we did not include any poisoning for this class of fission products.

The second reactivity effect is that associated with the distortion of the moderator graphite due to neutron irradiation. Results of a detailed analysis of this phenomenon in the MSRE indicate that the reactivity effect at the time of the ^{233}U loading was probably between −0.04 and +0.07% $\delta k/k$. The spread in probable values results from variations in the observed distortion of individual specimens of grade CGB graphite (the material in the MSRE core) as a function of neutron exposure. Although the variations are small compared with the total dimensional change which occurs at high exposures, they represent a substantial fraction of the change associated with the neutron exposures experienced in the MSRE. Since the reactivity effect of this distortion is very small, it was neglected in the evaluation of the critical experiment.

1.2.2 Control Rod Calibration

J. R. Engel

After the achievement of criticality, more uranium was added to the fuel loop to build up the excess reactivity required for routine power operation of the reactor. Measurements were made after the addition of each capsule of fuel to provide data on the reactivity worth of the control rods. We planned to add enough excess reactivity to the loop to permit calibration of one control rod over its entire range of travel. The scheduled loop drain at the end of the calibration (to homogenize the entire fuel charge) would then produce a fissile concentration with the desired reactivity worth – just sufficient for the proposed ^{233}U burnup experiment. The unscheduled drain after the addition of the 18th enriching capsule produced some enhancement of the uranium concentration in the drain tank prior to the scheduled event. Consequently, the calibration was stopped before the control rod was fully inserted in order to limit the final concentration to the prescribed value.

The differential worth of one control rod was measured as a function of its position and the positions of the other two rods using the classic rod-bump–period technique. These measurements were made both with the fuel salt stagnant and with the normal circulation rate. In addition, two series of rod-drop experiments were performed during the uranium loading to obtain integral-worth values. Each series consisted in dropping the rods singly, in pairs, and as a group, also with the salt stagnant and circulating.

In contrast to the original measurements with the ^{235}U fuel, the differential worth measurements produced relatively scattered results. A potentially strong contributor to this scatter is the increasing uncertainty in the exact control rod position as a result of wear in the drive mechanism (a problem similar to that en-

countered in the dynamics tests). Since the rod travel required to establish a given stable reactor period was much smaller with ^{233}U than with ^{235}U, this uncertainty has a greater effect on the results. Another potential source of scatter is minor variations in the core void fraction during individual period runs. In several cases abrupt changes in the "stable" period were observed, but the cause could not be identified. As a consequence of the general scatter in the period measurements, the rod-drop measurements were relied upon for most of the calibration data. A detailed discussion of the evaluation of the control rod calibration is presented in Sect. 4 of this report. The final results are included in Table 1.2.

1.2.3 Temperature Coefficient of Reactivity

C. H. Gabbard

A temperature coefficient of reactivity was measured three times with ^{233}U fuel, each time by slowly changing the temperature of the entire system and observing the control rod position required for criticality at several points from 1175 to 1225°F. There was considerable variation among the values found in these experiments, and they were generally smaller than the theoretical value. These differences can be attributed to the presence of gas in the core, whose steady-state volume depends on temperature and circulation rate.

The first measurements were made in November, near the end of the initial low-power run. The fuel pump was operated to circulate the salt while the salt and graphite temperatures were being changed and leveled off. Then the pump was turned off to allow gas bubbles that were circulating with the salt to agglomerate and float up out of the core. Data on critical rod position and temperatures were logged on the computer and manually, both with the pump running and after it had been off for 15 min, at each of nine temperatures. Temperature coefficients were computed by plotting rod effects vs temperature. The points with the pump off fell very close to a straight line with a slope of -7.75×10^{-5} $(\delta k/k)/°F$. The points with the fuel circulating were more scattered but gave a distinctly different slope: -6.9×10^{-5} $(\delta k/k)/°F$. The difference was not unexpected, since we knew there was an appreciable amount of entrained cover gas circulating with the salt, and past experience had shown the circulating void fraction increasing with decreasing temperature.[4] Thus the fluid density change due to the dependence of gas entrainment on temperature would tend to offset the salt density change with temperature, reducing the magnitude of the reactivity effect of slowly varying temperature. But even the value with the pump off was significantly less than that predicted on the basis of no gas in the salt. Therefore the series of measurements was repeated with great care in January, immediately after the start of run 17. The results with the pump off were practically the same as before, but with circulation the measured value was -7.4×10^{-5} $(\delta k/k)/°F$. The inference was that the variation of the void effect (bubble fraction) with temperature had changed.

After the variable-frequency power supply was put in service and the loop bubble fraction was observed to be very low at reduced fuel circulation rates, the temperature-coefficient measurement was repeated. With the pump running at reduced speed and practically no bubbles circulating with the salt, the data gave a value of -8.5×10^{-5} $(\delta k/k)/°F$. This higher value suggests that the effects of gas had not been completely eliminated in the earlier experiment by simply stopping the pump. That is, a varying amount of gas remained in the core long after the pump was turned off. Direct evidence of gas remaining in the core was an observed effect of pressure on reactivity after 12½ hr of natural-convection circulation and an observation made when the fuel pump was first started at reduced speed. Prior to the latter observation the fuel had been circulating at the normal rate with a void fraction of about 0.5 vol %. The pump was stopped for 1.5 hr while the power supply was changed. Although the salt level showed that most of the bubbles floated out of the loop while the pump was off, when it was restarted at half speed there was a level decrease, indicating further densification of the loop fluid.

The predicted value of isothermal temperature coefficient of reactivity was -8.8×10^{-5} $(\delta k/k)/°F$ at operating fuel concentration (-9.4×10^{-5} at critical concentration). The only directly comparable observed value is the one measured with no circulating gas, and it is only 3.4% smaller. This value, -8.5×10^{-5} $(\delta k/k)/°F$, is used in the reactivity balance to compute effects of overall temperature shifts when the reactor is being operated with a very low void fraction. When the pump is operated at full speed, with a void fraction around 0.5 vol %, the reactivity balance uses -7.4×10^{-5} $(\delta k/k)/°F$.

The individual contributions of the fuel and the graphite to the overall temperature coefficient were not measured experimentally, but separate values are needed in analyses of rapid transients. In view of the

[4] *MSR Program Semiann. Progr. Rept. Feb. 29, 1968*, ORNL-4254, p. 5.

close agreement between the overall coefficient observed with no gas and the predicted isothermal coefficient, the predicted graphite temperature coefficient, 3.2×10^{-5} $(\delta k/k)/°F$, is presumed to be accurate enough. For rapid changes in temperature, where the number of moles of gas circulating with the salt has no time to change, the calculated effect of the gas on the fuel temperature coefficient is very slight, about -0.05×10^{-5} $(\delta k/k)/°F$ change for 0.5 vol % gas.[5] Therefore the fuel coefficient for dynamic analyses is taken to be $-(8.5 - 3.2) \times 10^{-5}$ $(\delta k/k)/°F$.

1.2.4 Concentration Coefficient of Reactivity

J. R. Engel

Data were collected on the variation of the critical control rod configuration with uranium concentration throughout the addition of excess uranium for the control rod calibration. These data were reduced, with the aid of the final rod calibration, to a concentration coefficient of reactivity for uranium of the isotopic composition of the enriching material (91% ^{233}U). The value observed near the initial critical concentration was 0.369 $(\delta k/k)/(\delta C/C)$.

1.3 OPERATIONS ANALYSIS

Startup of the MSRE with ^{233}U fuel did not require modification of the equipment and operating procedures that had been used throughout the years of operation with ^{235}U. Because of the different nuclear characteristics and critical loading of the new fissile material, however, the dynamic characteristics of the reactor system were expected to be different. Considerable effort was devoted, therefore, to testing and analyzing this aspect of the operation. There was also keen interest in the radiation heating and reactivity behavior, since the fission product yields and neutron fluxes were changed. In addition, there were the possible aftereffects of the salt processing to be watched for. It turned out that there were in fact some changes, notably the behavior of gas in the fuel system. Analyses of these subjects are described in this section.

1.3.1 System Dynamics

R. C. Steffy

One of the most obvious differences between operation with ^{233}U and with ^{235}U is the smaller fraction of delayed neutrons with the ^{233}U. In fact, when the fuel is circulating, the effective fraction is only 0.0019, about a third of what it had been with ^{235}U and the smallest of any reactor. But the transient response and the stability of the system are affected by many other parameters as well, and the lighter fuel loading with ^{233}U produced a larger temperature coefficient of reactivity and a longer neutron lifetime. The combined effect of the changes was calculated, and the system was predicted to be stable and not difficult to control.[6] During the very-low-power operation with ^{233}U, dynamics tests designed to determine the neutron level to reactivity transfer function were performed both with the fuel circulating and stationary. Then during the approach to full power, tests were performed at 1, 5, and 8 Mw. The results of these tests showed that the dynamic behavior of the ^{233}U-fueled MSRE was in good agreement with the theoretical predictions.

Tests were performed using pulse, step, pseudorandom binary, and pseudorandom ternary test patterns. However, the small signal strength inherent in the aperiodic signals (pulse and step) was masked by the high level of neutron noise induced by the circulating bubbles (see Sect. 1.3.3) and made results of these tests unusable. Analysis of the data from the pseudorandom ternary tests was not completed by the end of this report period, but the pseudorandom binary tests gave good results.

The initial testing technique which we employed to implement the pseudorandom test patterns was the flux-demand technique, a method whereby the flux is forced to follow the test pattern, as opposed to the conventional method of forcing the control rod to follow the test pattern. Although this technique appeared to offer some advantages,[7] it did not work very well because of an equipment limitation. The natural fluctuations of the flux signal caused the servo to have to move the control rod continually in trying to force the flux to follow a particular test pattern. During this rapid movement the gear-driven indicators were not capable of reporting the exact position of the end of the chain-driven flexible hose on which the poison elements are strung. This loose coupling between indicated and actual control rod position introduced a significant amount of error in the calculation of the input reactivity. An example of results obtained from one of these tests is shown in Fig. 1.2. The scatter in the data is obviously excessive, although it falls around the theoretical predictions.

---

[5] P. N. Haubenreich *et al.*, *MSRE Design and Operations Report. Part III. Nuclear Analysis*, ORNL-TM-730, p. 189 (February 1964).

[6] *MSR Program Semiann. Progr. Rept. Aug. 31, 1968*, ORNL-4344, pp. 46–52.

[7] *Ibid.*, pp. 14–18.

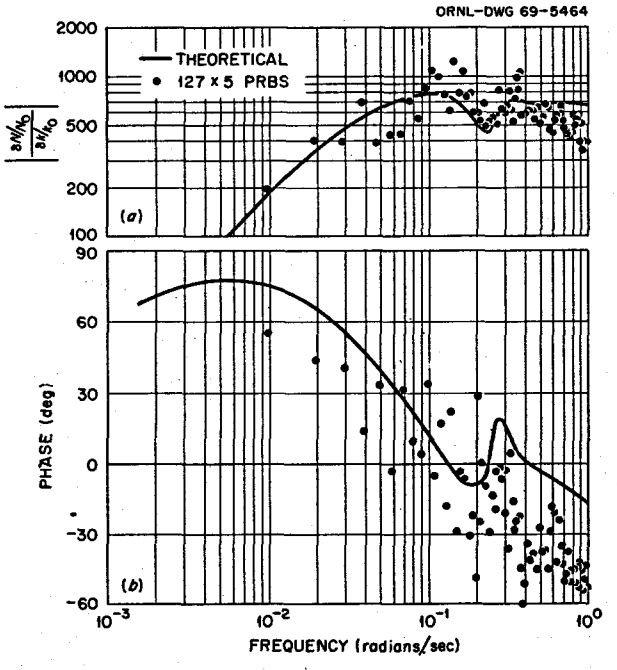

Fig. 1.2. Frequency-Response Plots for the ^{233}U-Fueled MSRE at 8 Mw – Comparison of Theoretical Prediction with Experimental Results Obtained Using Flux-Demand Technique. (*a*) Magnitude ratio, (*b*) phase angle.

To circumvent this error from the control rod indicators, it was necessary to revert to a form of the more conventional method of direct control rod manipulation. In order to get repeatable rod positioning, which is necessary for a pseudorandom binary or ternary test, the flux signal going to the control rod servo system was disconnected, and a voltage proportional to the rod position was inserted. The normal demand part of the servo circuit was also disconnected and fed with a voltage equivalent in magnitude but opposite in sign to the steady-state rod signal. Superimposed on the steady-state demand signal was a voltage which followed the desired test pattern. This improved the quality of the indicated control rod position for two reasons. First, the rod was typically moved about 0.3 in. and then was not disturbed again until the next pulse was due (pulse width varied between 3 and 5 sec, depending upon the particular test). This eliminated both the small jerks and the continuous rod movement. Second, for a pseudorandom binary test, a withdrawal was always followed by an equal-in-magnitude insert and vice versa. This tended to eliminate the accumulation of uncorrectable errors which occcur when the inserts and withdraws are random with respect to each other. When an insert always follows a withdraw and a withdraw always follows an insert, the indicated rod position still may not be the same as the actual rod position, but the discrepancy is a constant, and the error thus induced in the final results may be corrected by applying a constant scale factor.

Results of tests performed at 8 Mw using this "rod-demand" technique are shown in Fig. 1.3. The experimentally determined magnitude ratio, $|(\delta N/N_0)/(\delta k/k_0)|$, has been normalized to agree with the theoretical curves at 0.45 radian/sec. Scatter in the results is obviously much less than was present in the flux-demand tests.

The dip in the theoretical prediction of the magnitude ratio at ~0.25 radian/sec is an effect of the loop circulation, which has a transit time of about 25 sec. The dip shows up in the experimental results, but it is not as pronounced as predicted. This implies that the theoretical model does not allow for enough mixing of the salt in the external loop. Work was started on improving the model so as to give a better approximation to the physical conditions. This should also improve the relation between the experimental and the theoretical phase angle at the higher frequencies.

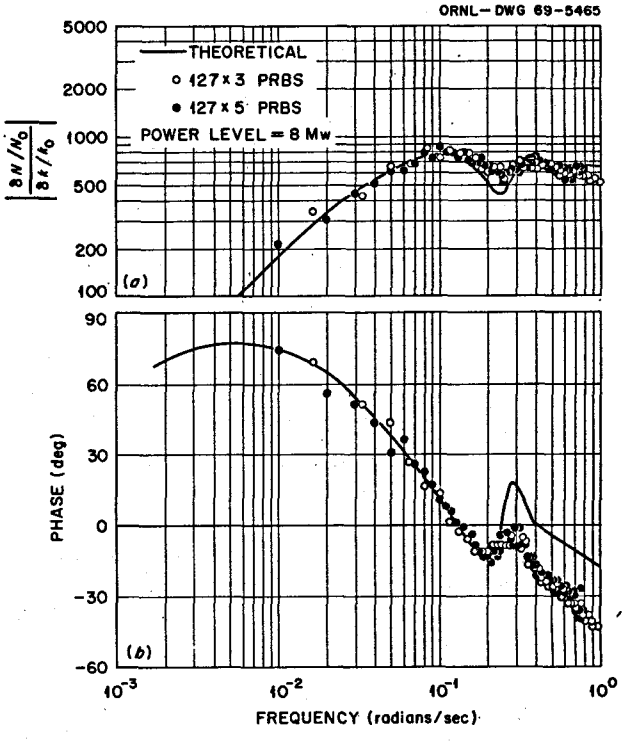

Fig. 1.3. Frequency-Response Plots for the ^{233}U-Fueled MSRE at 8 Mw – Comparison of Theoretical Prediction with Experimental Results Obtained Using Rod-Demand Technique. (*a*) Magnitude ratio (normalized to agree with theory at 0.45 rad/sec), (*b*) phase angle.

In summary, the results of the dynamic testing of the ^{233}U-fueled MSRE showed that the dynamic response of the reactor is very close to the theoretical predictions. Equipment limitations required that the test results be normalized, but testing methods were being improved, with the goal of eliminating this step.

1.3.2 Gas in the Fuel Salt

A. Houtzeel J. R. Engel

One of the most prominent differences between the operation in this report period and earlier operation is the change in the volume fraction of helium bubbles circulating with the fuel salt. Throughout nearly all of the operation up to September 1969, the circulating void fraction was much less than 0.1 vol % (ref. 8). Void fractions as high as ~0.2 vol % were achieved, but only for short times during special tests to study the effects of voids on other reactor parameters. Beginning 16 hr after the start of fuel circulation during the ^{233}U critical experiment, the void fraction has been 0.5 to 0.7 vol % whenever the fuel is circulating at the normal rate. The basic reason for the change has not yet been positively identified, although the characteristics and effects of the change have been examined in considerable detail.

The existence of circulating voids is reflected in many of the reactor operating parameters, some of which provide a quantitative measure of the total voids in the fuel loop while others are only relative or qualitative indicators. The most direct indication of voids in the circulating loop is the inventory of salt in the pump bowl, as indicated by the bubbler level elements. If the reactor is critical, another indication is obtained from the reactivity effect of the voids in the core, provided the indication is not obscured by other reactivity changes. Cross correlation of the noise in the neutron-flux and pressure signals can also be translated into an absolute void fraction. However, the absolute calibration required for this approach was not completed during this report period, so only relative changes in void fraction can be reported at present. The salt level in the annulus of the reactor access nozzle, as indicated by the temperature distribution, is a qualitative indicator of circulating voids. This level decreases when circulating voids transport helium to the annulus and rises when bubble-free salt dissolves gas and carries it out.[9] The xenon poisoning in the reactor also provides some information on circulating voids, but the interpretation is complicated by the reactivity effect of the voids themselves and by the nature of the dependence of xenon poisoning on voids. So far, in the ^{233}U operation, we have used only the pump-bowl level elements for absolute evaluation of the circulating void fractions.

Description of Bubbler Level Elements. – The level indicators in the fuel pump measure the pressure differentials between a reference line and bubbler tubes submerged in the salt. There are two bubbler tubes, one extending 1.626 in. below the center line of the volute and the other 1.874 in. deeper. The gas flow is 0.15 liter/min STP through the reference line and 0.37 liter/min STP through each of the bubblers. The differential pressures are converted into equivalent depths of salt assuming a salt density of 140 lb/ft^3. The range of the indicators is 10 in. of salt of this density, and readout is in percent (1% = 0.1 in.). In addition, the output of the differential pressure cell on the higher bubbler is biased by 19%; so if there were no deviation of the salt density from the assumed value, the two level indicators should read the same.

Measured Void Fractions. – The best measure of circulating void fraction is obtained by observing the changes in pump-bowl level when the fuel pump is first started after a loop fill, when the salt is free of bubbles. When fuel circulation was first started in run 15 (September 14), the level changes in the fuel-pump bowl were very similar to starts in earlier runs when there were almost no circulating voids; that is, the level dropped about 8% as soon as the pump was started and remained there. (This 8% level drop is due to the accumulation of salt in the central part of the pump housing and the spray ring.) The pump was stopped and restarted twice in the first 14 hr, with identical results. Then the beryllium rod was exposed in the pump bowl. All normal-speed pump starts thereafter were different. Each time after the start the level dropped 10 to 15% but then gradually rose. This gradual level rise (in general between 8 and 12% within 30 min) reflected a gradual buildup of gas in the salt loop. A level rise of 8 to 12% is equivalent to displacement of 0.35 to 0.50 ft^3 of salt from the circulating loop by gas, corresponding to a circulating void fraction of 0.5 to 0.7 vol %.

The operation of the fuel pump with a variable-frequency power supply near the end of the report period allowed us to make a preliminary evaluation of the circulating void fraction as a function of pump speed. (Salt flow rates, both in the main loop and through the pump bowl, are directly proportional to pump speed.) With the fuel pump operating at speeds below about 1000 rpm, all evidence indicated that the

[8] *MSR Program Semiann. Progr. Rept. Aug. 31, 1968,* ORNL-4344, pp. 18–19.

[9] *MSR Program Semiann. Progr. Rept. Feb. 29, 1968,* ORNL-4254, pp. 7–9.

circulating void fraction was practically zero. In fact, when the pump was first started at around 530 rpm (nominal 30-Hz power supply), the fuel-pump level decreased about 2% after the initial starting transient. This indicated removal, from the loop, of voids that had not floated out during the 1.3-hr period while the pump was off to connect it to the variable-frequency generator. Figure 1.4 shows the sharp dependence of circulating void fraction on the pump speed above 1000 rpm. The probable reason for the rather sharp threshold will be discussed later. (The points are actually calculated relative to the condition at 530 rpm, where the void fraction was assumed to be zero.)

Prior to the pump-speed experiment, we had attempted to determine the variation of the circulating void fraction with other system parameters. With the fuel pump running at full speed and the reactor power at 5 Mw, we varied the fuel-system temperature and pressure and the pump-bowl salt level over ranges that had changed the void fraction by a factor of 7 during operation with the ^{235}U fuel salt.[10] Some changes were noted, but cross correlation of noise data from the neutron-flux and system-pressure signals indicated that the void fraction changed by no more than a factor of 2. The fact that the void fraction started around 0.5 to 0.7 vol %, compared with around 0.1 vol % in the earlier experiments, may account for the smaller fractional change.

Changes During Beryllium Additions. – Between the start of the ^{233}U operation and the end of this reporting period, five beryllium additions were made to the fuel salt by exposing a beryllium rod in a nickel cage in the pump bowl. Each time there were observable effects on the circulating void fraction, but the behavior was not the same in each case.

As mentioned before, the fuel had been circulating normally with practically no bubbles for 14 hr when the first beryllium rod was lowered into the pump bowl. After about 2 hr the level in the pump started to rise, and from later observations it is evident that the rise was due to a buildup of gas bubbles in the loop, something we had never observed before. The increased void fraction persisted after the beryllium rod was removed. (Another effect was that the transfer rate of salt to the overflow tank increased drastically; see Sect. 1.3.5.)

The exposure of the second beryllium rod was made on October 13, four weeks after the first addition, with

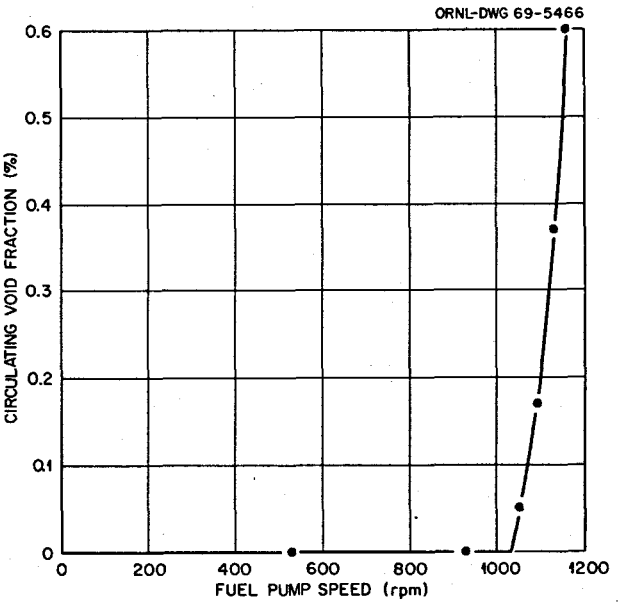

Fig. 1.4. Effect of Fuel Pump Speed on Circulating Void Fraction.

the reactor critical at low power and on flux servo control. The mentioned effects of the first beryllium addition still persisted to some degree. The insertion of this second rod caused some very erratic and unexpected level changes in the pump bowl (see Fig. 1.5), which started almost immediately after the beryllium was lowered into the pump bowl. The spontaneous level changes in the fuel-pump bowl were as large as 1 in. (or 10% on the level indicators), which represents about 0.42 ft^3 of salt (0.6 vol % in the loop). Obviously this salt moved from the salt loop into the fuel-pump bowl and back. Once started, the time required for a level change was 20 to 30 min. At the same times that the level changed, the control rod was moved by the servo control to compensate for spontaneous changes in reactivity of the reactor. The level decreases occurred simultaneously with insertions of the control rod and, conversely, level increases with rod withdrawals. It was concluded that these level fluctuations reflected a varying gas-bubble fraction in the circulating salt, because all other system variables appeared to be constant.

For the third beryllium addition, on November 15, it was decided to operate the fuel pump at a lower-than-normal level to minimize the risk of plugging the off-gas line with foam if the level oscillations occurred again. In contrast to the second beryllium addition, this time it took approximately 2½ hr after the capsule was inserted before anything happened. Then, very slowly, the level decreased about 7%. Simultaneously the

[10] D. N. Fry, R. C. Kryter, and J. C. Robinson, *Measurement of Helium Void Fraction in the MSRE Fuel Salt Using Neutron-Noise Analysis*, ORNL-TM-2315 (Aug. 27, 1968).

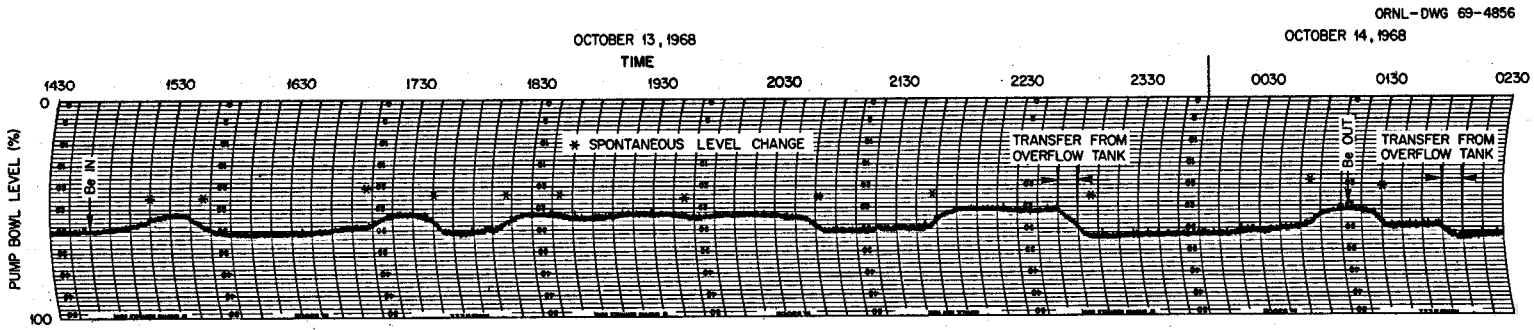

Fig. 1.5. Indicated Salt Level in Fuel Pump During Beryllium Exposure on October 13, 1968.

reactor servo control inserted the control rod 0.9 in. Before the spontaneous level decrease stabilized, the beryllium capsule was taken out temporarily because of concern over operation at this abnormally low level. The reactor system responded almost immediately to the withdrawal. Within 15 min the level came back to its original value, and the control rod was withdrawn to its old position. (The time for these level changes was only 15 to 20 min, remarkably short since it takes about 9 min to process one loop volume through the pump bowl. This implies that the mechanism which governs the removal of introduction of gas bubbles operates with a very high efficiency.) After due consideration the beryllium capsule was inserted for the second time; both the reactivity and the pump level again responded as before. After about 1 hr the level was down 8%, and the control rod had been inserted 1.7 in. Since the effects had not yet leveled out and the level in the fuel-pump bowl was uncomfortably low, it was decided to remove the beryllium capsule again and raise the pump level about 5% by transferring salt from the overflow tank into the pump bowl. Then, for the third time, the same beryllium capsule was lowered into the pump bowl; again the level and control rod came down. This time the system was allowed to level off; the control rod was inserted 2.0 in. by the servo control, and the salt level in the pump bowl stabilized after a drop of 8.5%. (At the same time the difference between the readings of the level indicators also decreased. The significance of this change is discussed later.) When the capsule was finally taken out, the level came up 6%, and the control rod was withdrawn about 2.0 in.

The fourth beryllium addition was different in that there was less beryllium, and it was in the form of short cylinders between short high-temperature magnets. The effects of this addition were detectable but were very mild in comparison with earlier additions.

The fifth beryllium addition took place on January 24 with the reactor at 5 Mw. The power resulted in some "secondary" effects which actually strengthened the idea that the presence of bubbles in the system is strongly related to some of the unexpected events during and after the beryllium additions. As is described in Sect. 1.3.4, power blips were occurring during this time. These blips ceased once the beryllium capsule was lowered into the pump; the linear power trace became smooth. The blips came back after the beryllium was removed. All other effects, such as level and control rod position changes, were similar to those in previous beryllium additions.

Related Pump-Bowl Observations. – Aside from the direct evaluation of the circulating void fraction, we used the indications of the fuel-pump bubblers to extract information about the void fraction and the apparent physical salt level in the pump bowl itself.

We observed that after the first beryllium addition the difference between the readings of the two bubbler level indicators became much larger whenever the salt was being circulated. When the pump was stopped, the readings of the two bubblers came together. Using the difference of submersion of the two bubblers and the difference of the readings of the two level indicators, it is possible to compute a value for the apparent density of the fluid in the zone between the lower points of the bubbler lines. Fluid densities were calculated this way under a variety of conditions with the fuel salt circulating at full flow and stagnant. Although the accuracy of this calculation is limited by uncertainty in the separation distance of the two bubblers, it showed quite clearly that densities for circulating salt were much lower than those for stagnant salt or for circulating salt prior to the first beryllium addition in run 15. It also showed that the apparent salt density between the bubblers was to some extent related to the measured salt level in the fuel pump; a higher calculated salt density (i.e., smaller difference in level readings) generally occurred when the indicated salt level was high. Figure 1.6 shows at least this general trend despite the scatter of the data.

One hypothesis to explain this phenomenon is the following. About 50 gpm of salt are ejected at a velocity of 60 fps from the spray ring onto the surface

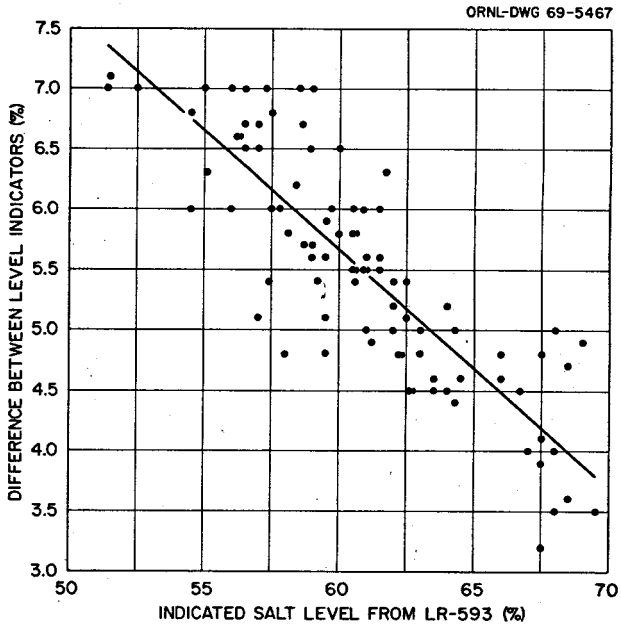

Fig. 1.6. Effect of Salt Level on Difference in Bubbler Readings.

of the salt in the pump bowl. Because of their high velocity the jets easily carry gas under the surface of the salt. The bulk of this entrained gas penetrates to a certain depth in the salt and then rises to the surface. It is obvious that the salt to this depth contains a high void fraction. If the zone containing this large void fraction does not extend down below the upper bubbler, then the two bubbler readings would not be affected much, because basically the level indicators measure a weight of salt. These voids would, of course, increase the real level of the salt in the pump bowl by an amount equivalent to the volume of the voids. If, however, the level of the salt is lowered sufficiently (by transfer to the overflow tank), it is easy to imagine the high-void-fraction region extending below the lower points of one or both of the bubbler lines. In that case, the two level indicators would be differently affected, and the difference in readings would reflect the apparent salt density change in the area between the bubblers. This would explain the tendency for the difference in bubbler readings to increase (i.e., density to decrease) with decreasing level.

Near the end of this report period the pump-speed experiment did much to substantiate this picture. In this experiment the fuel-pump speed was varied over a range from half to full speed. The velocity of the spray ring jets and the flow through the pump bowl vary directly with the speed. The relation between pump speed and the apparent void fraction in the salt between the bubblers is shown in Fig. 1.7. This clearly shows that the void fraction increases as the flow rate through the pump bowl increases and that the void fraction in the pump bowl is at least an order of magnitude higher than that in the loop (cf. Fig. 1.4). Comparison of Figs. 1.4 and 1.7 also shows that a substantial void fraction exists in the zone of the pump bowl between the bubblers before the relatively sharp threshold speed is reached at which bubbles are ingested into the loop. This suggests that the depth to which bubbles penetrate in the pump bowl increases with increasing jet velocity until some of the bubbles are finally drawn into the loop.

Since the indicated bubble fractions in the pump are so high, it is evident that the actual level of the salt-bubble mixture can be substantially higher than the indicated level. This actual fluid level is significant in regard to the transfer of salt to the overflow tank and the possibility of plugging the pump off-gas line with salt. The relevant facts regarding the actual fluid level are as follows:

1. The salt density in the area between the bubbler outlets is more or less known in relation to the weight of salt located above the bubblers from Fig. 1.6.
2. The indicated level of the salt is known when there is a drastic change in the transfer rate to the overflow tank, which presumably means that the real salt level is approximately even with the inlet of the overflow pipe (see Sect. 1.3.5).
3. From Fig. 1.6, we can determine, by extrapolation to zero difference, the level at which the first bubbles get below the outlet of the highest bubbler.

From this information it was possible to estimate approximately the density of the fluid in relation to its depth and the relation between the real and indicated salt levels (see Fig. 1.8). We estimate that the "bubble

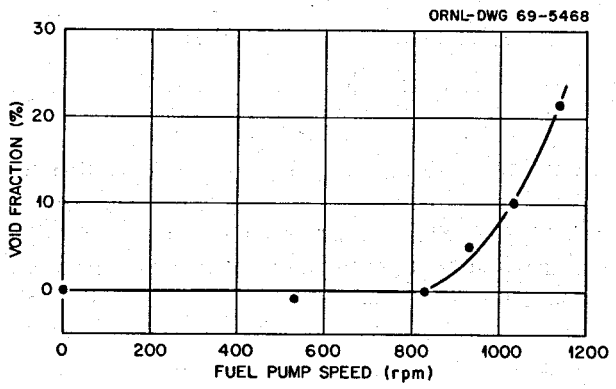

Fig. 1.7. Effect of Fuel Pump Speed on Void Fraction in Pump Bowl Between Bubblers.

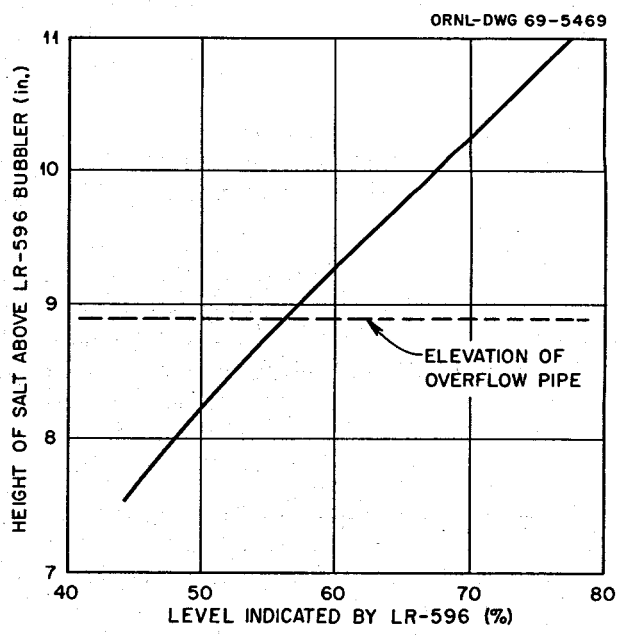

Fig. 1.8. Relation Between Real Level and Indicated Level in Fuel Pump Bowl.

head" has a thickness of approximately 8.8 in. at full flow. However, this thickness is probably variable and depends, among other things, on fuel-pump speed and the level of the top of the salt relative to the spray ring and, possibly, on the elapsed time since the last beryllium addition. The first two factors affect the degree of agitation in the pump bowl, while the last appears to affect the stability of bubbles in the salt. It appears that the bubble head has its maximum thickness just after beryllium additions. Because of the sharp threshold for gas ingestion into the loop, a difference in the thickness of the bubble head of only about 1½ in. could account for the differences in the observed circulating void fraction prior to and after September 1968.

1.3.3 Neutron and Pressure Noise Measurements

R. C. Kryter D. N. Fry J. C. Robinson[11]

As a follow-up on previous studies of the ^{235}U-fueled reactor,[12] analyses were made of the natural fluctuations in cover-gas pressure and neutron density of the ^{233}U-fueled MSRE during normal operation at power. The objectives were (1) to determine if the frequency structure and absolute level of the neutron (NPSD) and pressure (PPSD) power spectral densities had been significantly altered by the refueling, (2) to substantiate the other indications that the loop circulating void fraction had greatly increased, and (3) to see if the NPSD in the vicinity of 1 Hz (identified before as a region sensitive to the void fraction) exhibited its previous strong dependence on certain reactor parameters[13] (notably fuel temperature).

The observed neutron and pressure noise characteristics of the refueled reactor (operating under normal conditions at power) were, relative to the ^{235}U-fueled reactor, as follows:

1. The frequency composition of the *neutron* noise is only slightly different, but the level of the NPSD in the vicinity of 1 Hz is increased by a factor of ~2000 to 6000. (Of this increase, only a factor of 2.2 can be accounted for by the increase in reactor gain associated with the decreased β_e for ^{233}U.)
2. The frequency composition of the *pressure* noise is noticeably different, and the level near 1 Hz is increased by a factor of 10 to 40. (Because of the restriction in the off-gas line, the pressure drops and flow paths of the gas leaving the pump bowl were different for the two series of tests. The significance of this difference has not yet been evaluated.)
3. The average volumetric void fraction of fuel passing through the reactor core, derived from measurements and a model[14] of the system that interrelates NPSD, PPSD, and void fraction, is increased by a factor of ~5.
4. The circulating void fraction, NPSD, and PPSD are all very nearly independent of changes in fuel temperature, cover-gas pressure, and fuel-pump bowl level, in marked contrast to the earlier experience.[13]
5. The void fraction is independent of reactor power level but decreases by a factor of ~13 when the circulating pump is stopped and the fuel is allowed to circulate by natural convection at about 4% of full power.

Detailed explanations of all the above observations have not been attained yet, but all facts indicate that marked changes occurred between the tests with ^{235}U and those with ^{233}U, either in the physical properties of the fuel salt or in the fluid-flow characteristics of the reactor. This tentative explanation may be further illuminated by the results of a series of tests under way at the end of the report period, the goal of which is the isolation of the main sources of primary-loop pressure fluctuations. In any event the studies indicated that it is feasible to use NPSD and PPSD measurements for providing an on-line, continuous estimate of the circulating void fraction, and plans were made to automate the entire calculational procedure, either with an analog computer or the BR-340 digital computer.

1.3.4 Perturbations in Nuclear Power

R. H. Guymon J. L. Crowley
P. N. Haubenreich

With the beginning of high-power operation in January, we observed a phenomenon not seen before: occasional small disturbances in the fuel-salt system that involved brief perturbations of the nuclear power. These came to be called "blips." Although the blips

[11] Consultant from Department of Nuclear Engineering, University of Tennessee, Knoxville.

[12] *MSR Program Semiann. Progr. Rept. Aug. 31, 1968*, ORNL-4344, p. 18.

[13] D. N. Fry, R. C. Kryter, and J. C. Robinson, *Measurement of Helium Void Fraction in the MSRE Fuel Salt Using Neutron-Noise Analysis*, ORNL-TM-2315 (Aug. 27, 1968).

[14] J. C. Robinson and D. N. Fry, *Determination of the Void Fraction in the MSRE Using Small Induced Pressure Perturbations*, ORNL-TM-2318 (Feb. 6, 1969).

were too small to have direct consequences (the nuclear power generally increased by about 10% for a few seconds), intensive efforts were made to arrive at their explanation. These efforts included reviews to see when they had begun, experiments on the effects of system conditions on blip size and frequency, and detailed analysis of observable behavior for clues to the mechanism. It became clear rather early that the blips were not related to the change in fissile material per se or to any chemical instability, but to the unusual amount of gas in the fuel system, discussed in earlier sections.

Characteristic Behavior During Blips. – Blips were first noted as small, fairly sharp spikes on the neutron level record, but it was soon discovered that disturbances occurred almost simultaneously in several other signals from the fuel system. Figure 1.9 is a chart from a multichannel recorder showing behavior of some significant parameters during three typical blips.

The disturbances in fuel-pump level and pressure, although quite small, are highly significant, for they are a clue to the mechanism. Examination of hundreds of blips at various chart speeds and signal amplifications showed that within the second that the neutron flux started up, both salt level and cover-gas pressure signals always started down. The dips, though small, were definitely outside the distribution of normal fluctuations. The direction of the level and pressure changes proved that they were not the result of the excess power, which would tend to make level and pressure go up. Since both decreased, it meant that some salt entered the fuel loop to replace gas that had been compressed somehow other than by the overpressure in the pump bowl.

The bottom trace in Fig. 1.9 is the temperature of a thermocouple in a well in the core specimen access plug at the top of the reactor vessel. Its significance will be discussed later.

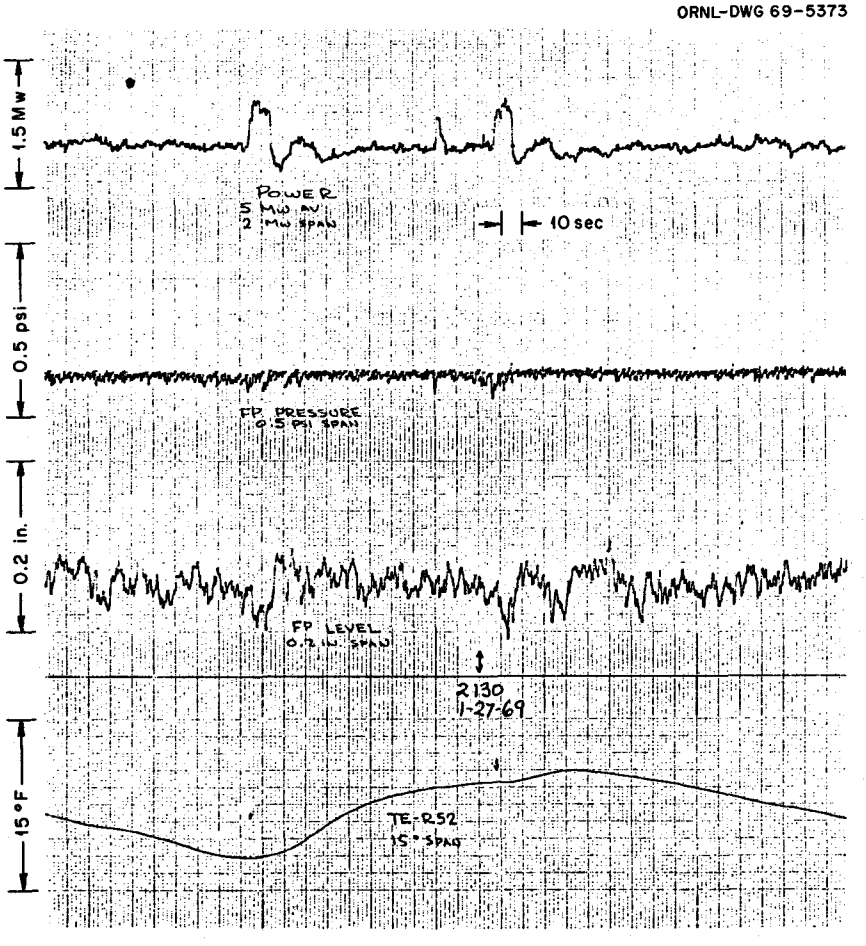

Fig. 1.9. Recorder Chart Showing Nuclear Power, Fuel Pump Pressure, Indicated Fuel Pump Level, and Thermocouple at Bottom of Access Plug During Blips.

It was found that the characteristic disturbances in pump-bowl pressure and level and access plug temperature occurred regardless of the power level, even occurring when the reactor was subcritical. Conversely, power perturbations like those in the blips could be induced by briefly withdrawing a control rod (between 0.01 and 0.02% $\delta k/k$ for a few seconds) without causing the disturbances in level, pressure, or temperature. Such an experiment is shown in Fig. 1.10. The conclusion was that the power blips are but one manifestation of an event which independently affects the other variables.

The nuclear power increase involved in the blips fell in a fairly well-defined range; the largest blip raised the power less than 15%, with the most probable increase being around 10% or less. The duration of the blips, that is, the time that the power remained significantly above the average, ranged from 1 to 40 sec. Size distributions and frequency of occurrence will be discussed in detail below.

Effect of System Conditions on Blips. – Blips were found to occur over the operating range of pressures, fuel-salt temperatures, and pump-bowl levels and at all power levels. What did matter was the amount of gas circulating with the fuel salt: blips were observed only when the circulating gas was on the order of 0.5 vol % or greater.

Large amounts of gas first appeared in the fuel salt on September 15, 2 hr after a beryllium rod was immersed in the pump bowl and weeks before the reactor was critical on ^{233}U. A multipoint recorder chart showed that at the same time that the gas appeared, the access plug thermocouple first began to fluctuate in a fashion similar to that observed later during blips. There was no record of pump pressure or level perturbations, since the normal recorders are not sensitive enough to show

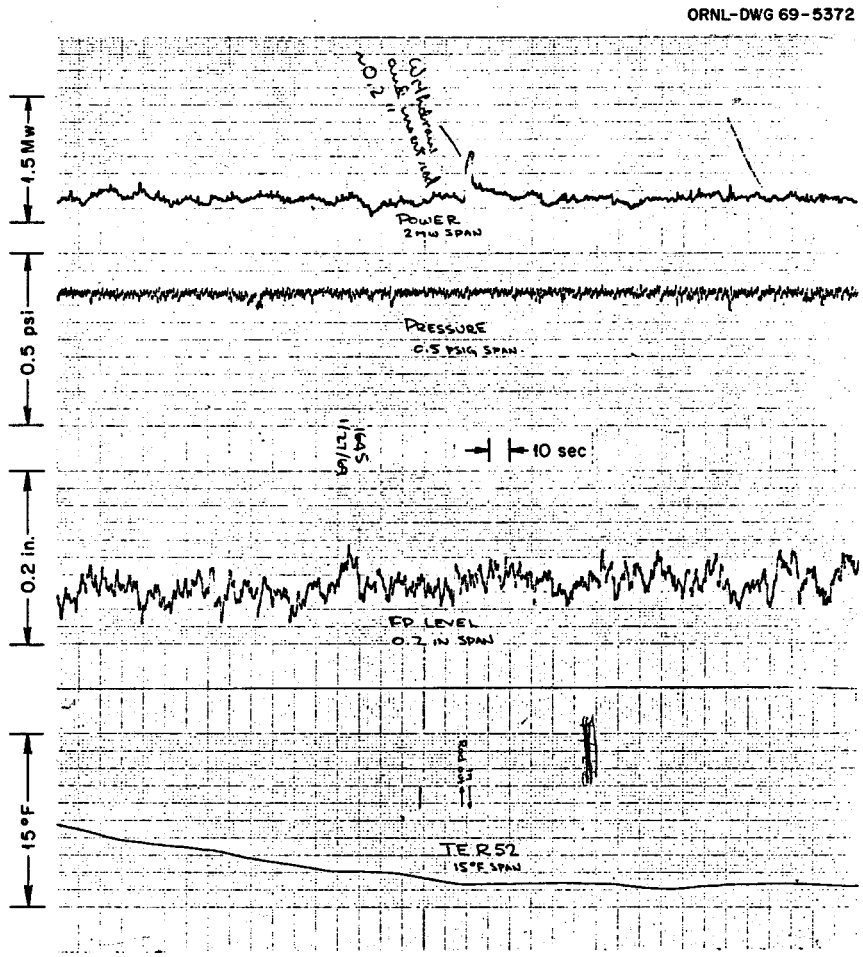

Fig. 1.10. Recorder Chart Showing Nuclear Power, Fuel Pump Pressure, Indicated Fuel Pump Level, and Thermocouple at Bottom of Access Plug During Deliberate Reactivity Perturbations by Control Rod.

such small dips. Search of neutron flux records during early nuclear operation disclosed some blips. Most of the time they could not be seen because the noise at low power and the action of the flux servo system masked them. Blips were tentatively identified on a chart of operation at 50 to 100 w on October 26. One blip of 300 kw occurred during the 30 min on manual rod control on November 27. None occurred during a similar period at 1 Mw the day before. Thus blips seemed to have started with the onset of gas entrainment, but by the time the power was raised, after some eight weeks of fuel circulation, they were not very frequent.

After the shutdown, when fuel circulation was resumed and the power was raised, blips were found to be occurring at a rate of 10 to 20 per hour.

Figure 1.11 shows strips cut from the nuclear power recorder chart for operation at similar conditions on various dates from January 23 to February 17. (The power scale is in percent of 15 Mw, so one division is 150 kw. The time scale is as indicated.) Although the frequency and size of blips varied from hour to hour, the traces shown are fairly typical for the day.

The first trace was recorded 11 days after the beginning of fuel circulation, when the frequency was around 10 to 20 per hour. The second was taken on January 27, three days after a beryllium addition. The

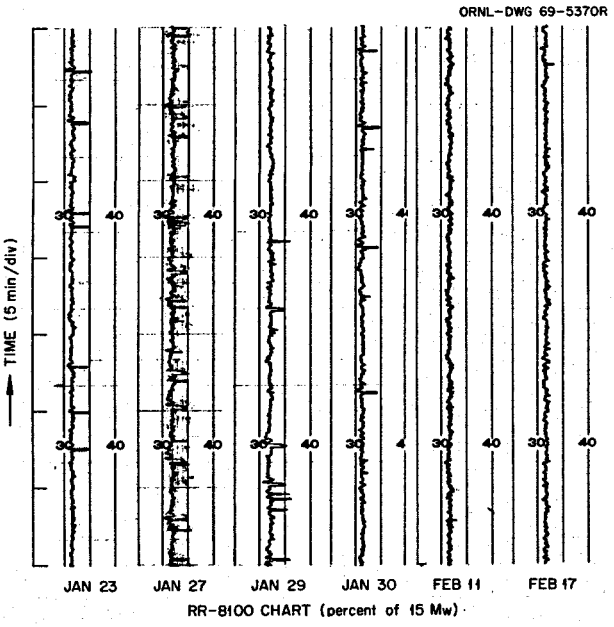

Fig. 1.11. Typical Sections of Nuclear Power Recorder Chart Taken During January and February 1969. Conditions in each case: 5 Mw, 1210°F, 4–5 psig, 51–52% fuel pump level, full flow.

frequency and the average duration of the blips were noticeably greater. Thereafter the blip frequency and average size gradually diminished, as suggested by the other charts; until near the end of February only one or two occurred per 8-hr shift.

Between February 7 and 11, the fuel temperature was varied from 1180 to 1225°F and the pressure from 3 to 9 psig, with little or no significant effect on the blips. The amount of gas in the loop also did not appear to be affected very much by these changes (see Sect. 1.3.3).

There appeared to have been some decrease in the circulating void fraction during the period when the blip frequency was gradually decreasing, but the voids by no means disappeared. Although the fraction could not be measured very accurately, it certainly remained fairly high (0.5 to 0.7 vol %) during the entire period covered by Fig. 1.11. One exception was during the heat-removal test, when the fuel circulated by natural convection at powers up to 354 kw. The power trace on the recorder chart, like those in Fig. 1.11, was absolutely smooth, and no blip occurred in the 7 hr that the reactor was at power during this test. Another exception was a brief period while the beryllium rod was in the salt on January 24. The pump-bowl level showed that the bubble fraction decreased to perhaps 0.3 vol %. The blips, which had been occurring at about 10 per hour, practically stopped. (There were none for 2 hr 20 min.) As soon as the beryllium was removed the bubble fraction rose, and in the next hour there were 17 blips. When a much milder reducing agent, a chromium rod, was exposed to the salt on January 29, there was no clear effect on gas or blips.

The variable-frequency power supply for the fuel pump was set up especially to see what effect reduced circulation rate would have on the entrained gas and the blips. By the time it was ready the blips were not as frequent or as large as they had been, but the experiment was still very convincing. Figure 1.12 shows how reducing the pump speed smoothed out the nuclear power until the chart record appeared the same as it had in the operation with ^{235}U. Reference to Fig. 1.4 shows that the bubble fraction decreased from about 0.4% to 0.2% to less than 0.1% in the three ^{233}U cases. Operation at the lowest speed was continued for five days, during which time there was no blip. When the speed was returned to 1140 rpm, the trace became rough again and blips began to occur.

Size-Frequency Distributions. – Cursory examination of the nuclear power traces when there are blips, as in Fig. 1.9 or 1.11, suggests that there are two kinds of events – the continuous small, random fluctuations and the larger occasional blips, which look like a different kind of event. This impression is confirmed by a

size-frequency plot such as Fig. 1.13. The small fluctuations form the distribution at the left. The blips are the distribution centered at about 500 kw. Figure 1.13 is fairly typical of the first few weeks of power operation. As time went on, the peak in the blip distribution became lower and moved to the left; that is, the blips became less frequent and smaller. Eventually the distribution was submerged in that of the small fluctuations. This was the case by February 17, when the last strip on Fig. 1.11 was recorded. As seen from this figure, however, an occasional blip could still be distinguished, mainly because of its different shape.

Possible Mechanisms. – The small fluctuations in nuclear power are caused by very small fluctuations in system pressure which are translated, through the compressible voids in the core, into reactivity fluctuations.[15]

The mechanism for the blips has not been resolved in detail. It is almost certain, however, that it involves sporadic changes in the amount of gas held up in the core.

There is convincing evidence that the blip mechanism is not movement of separated uranium. In the first place, analyses of the salt showed conditions far removed from any precipitation of uranium or uranium oxide. The absence of any uranium-bearing precipitate is also indicated by the temperatures in the lower head of the reactor, which did not show any abnormal heating there (Sect. 1.3.7). More direct is the evidence of the pump-bowl level and pressure: if a power blip were caused by movement of excess uranium up through the core, the resulting temperature rise would tend to push the salt level up. Such changes in level as occur are in the opposite direction. Furthermore, blips with all the symptoms except the power perturbation occur with the reactor subcritical, when uranium movement would have no effect.

The clue that blips are related to gas in the core is the fact that they occur only when the circulating void fraction is more than about 0.5 vol %. Blips appeared when the gas fraction first increased, and they disappeared when the fraction was reduced by either of two distinctly different mechanisms: reduction of fuel pump speed and exposure of beryllium to the salt.

An intermittent obstruction in the fuel flow between the core and the pump suction would increase the pressure and compress the gas in the core, changing reactivity and pump-bowl level in the observed directions. Consideration of the necessary implications made

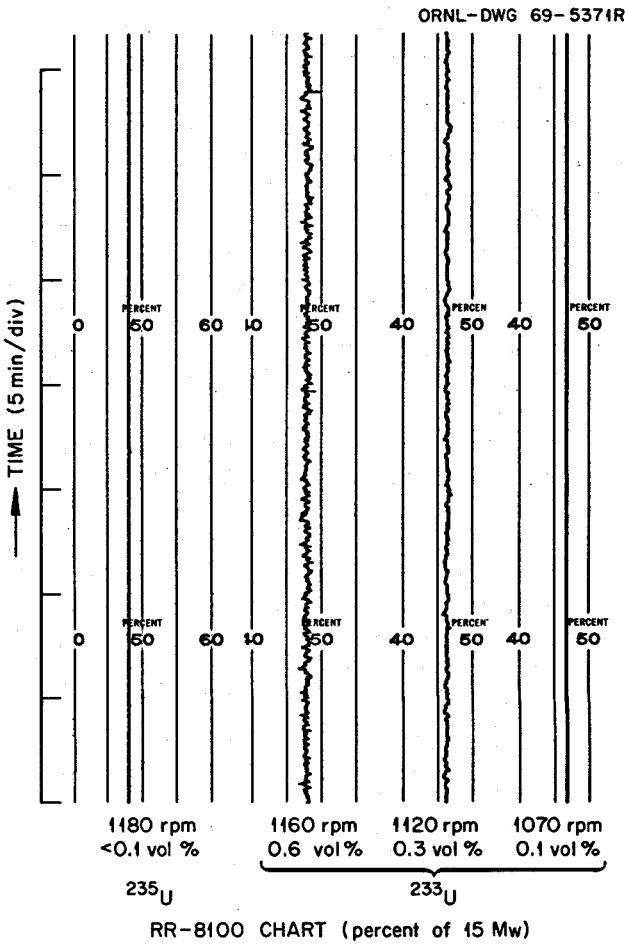

Fig. 1.12. Sections of Nuclear Power Recorder Chart Contrasting ^{235}U Fuel, Full Flow and Few Bubbles, with ^{233}U Fuel, Varying Flow and Bubble Fraction.

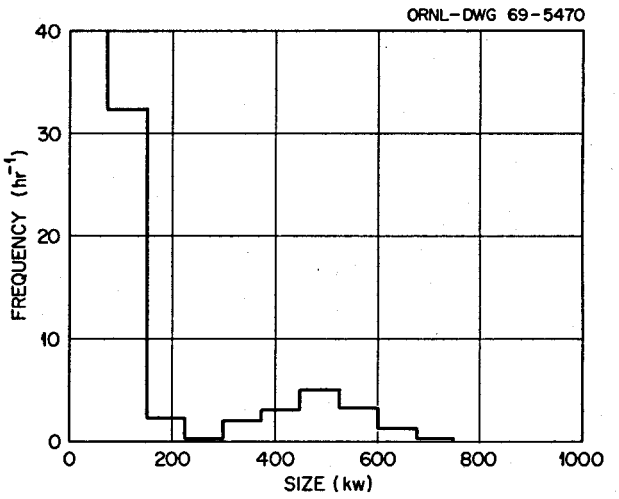

Fig. 1.13. Size-Frequency Distribution of Variations in Nuclear Power, January 21–23, 1969.

[15] *MSR Program Semiann. Progr. Rept. Aug. 31, 1968,* ORNL-4344, pp. 18–19.

this hypothesis seem quite improbable, however. As shown in Sect. 4.3, reactivity increases of about 0.15% $\delta k/k$ in 1 to 2 sec were fairly typical. This corresponds to an increase in fuel density, averaged over the core, of 0.034%. Starting with an average void fraction in the core of 0.6 vol % and an average pressure in the core of 35 psia, a pressure change in the core of 2.0 psi would be required to give the observed reactivity effect. It does not appear that an intermittent flow blockage could occur anywhere between the core and the pump suction, with the possible exception of the perforated metal screen below the outlet from the top of the reactor vessel. The normal pressure drop across this screen is only 0.5 psi, and to cause a pressure change of 2.0 psi in the core, half of the 195-in.^{2} conical screen would have to be covered and then uncovered. This is hardly credible.

What seems much more probable is that a blip is caused by a small quantity of gas which has collected at some point in the core suddenly breaking loose and being swept up and out of the reactor vessel. As little as 2.0 in.^{3} of gas from channels near the center of the core would be enough to produce a 0.015% $\delta k/k$ reactivity increase. There is evidence that some gas does cling in the core, at least under low-flow conditions. (The temperature coefficient measurements implied that all gas did not leave the core when the pump stopped, and a clear indication of a compressible volume in the core was obtained when a slight pressure change after 6 hr of natural convection circulation produced a detectable reactivity change.) The triggering mechanism for release of gas clinging in the core is presumably a very small perturbation in flow or pressure. A possible cause of such perturbations is the occasional release of a burst of gas from the reactor access nozzle which is suddenly compressed as it passes through the pump.

The reasons for suspecting that gas from the access nozzle triggers the blips are: (1) When the circulating bubble fraction is greater than about 0.5%, gas fills the plug annuli all the way down to the juncture with the flowing salt stream; (2) coincidentally with blips, changes are observed in a thermocouple at the bottom of the nozzle which indicate temporary increases in the salt level; and (3) the blip frequency increased while the temperature of the gas trapped in the annuli was being allowed to rise (pushing some gas out into the flowing stream) and temporarily decreased by a factor of 4 when cooling of the annuli was resumed. The thermocouple indication lags the start of the blip, but this is due, at least in part, to heat transfer time constants.

Although there are hypotheses, no theory has been developed that satisfactorily explains all observed aspects of the blips. In particular, there is as yet no explanation of why the higher reactivity (or lower void volume) persists for a variable length of time and then rather quickly returns to the original level.

1.3.5 Salt Transfer to Overflow Tank

A. Houtzeel

Except for a relatively brief period early in the operation of the MSRE (prior to April 1966), salt has consistently transferred from the fuel loop to the overflow tank whenever the fuel pump is running.[16] Although there were variations in the rate of transfer that could not be explained, the rates were generally less than 1.5 lb/hr. During the six-month run with ^{235}U fuel (run 14) the transfer rate consistently averaged about 0.5 lb/hr. The operation with ^{233}U has been marked by very wide variations in the transfer rate, with occasional values as high as 72 lb/hr.

The flush-salt operation in preparation for the ^{233}U runs and the first few hours of operation with ^{233}U fuel (prior to the first beryllium addition) showed transfer rates that were consistent with past experience. The observed rates were in the range of 0.1 to 0.4 lb/hr. After the first beryllium addition in run 15, these rates increased to 4 lb/hr and even much higher. The very high transfer rates occurred after the beryllium capsules had been removed from the pump bowl and gradually diminished to about 4 lb/hr during the next 100 to 150 hr of fuel-salt circulation after the beryllium addition. *During* the beryllium additions, when the salt level was low, the transfer rates were generally much lower, in the order of 1 to 2 lb/hr. The salt transfer rate jumped to 29 lb/hr just after the second beryllium addition and 72 lb/hr after the third addition. Figure 1.14 shows the variation of the transfer rate with time after the third beryllium addition. Generally speaking, it was observed that the higher the indicated fuel-pump level, the higher the transfer rate. However, this was not a linear relation. As shown in Fig. 1.15, there was a drastic decrease in transfer rate once the salt level dropped below a certain threshold value. This change can be explained if the actual level of the salt-gas mixture (foam) in the pump bowl is significantly higher than the level indicated by the bubblers. Then, when the real level of salt with bubbles (say "bubble head") extends beyond the inlet of the overflow pipe, high transfer rates would occur; conversely, if the real level in the

[16] *MSR Program Semiann. Progr. Rept. Aug. 31, 1966*, ORNL-4037, p. 24.

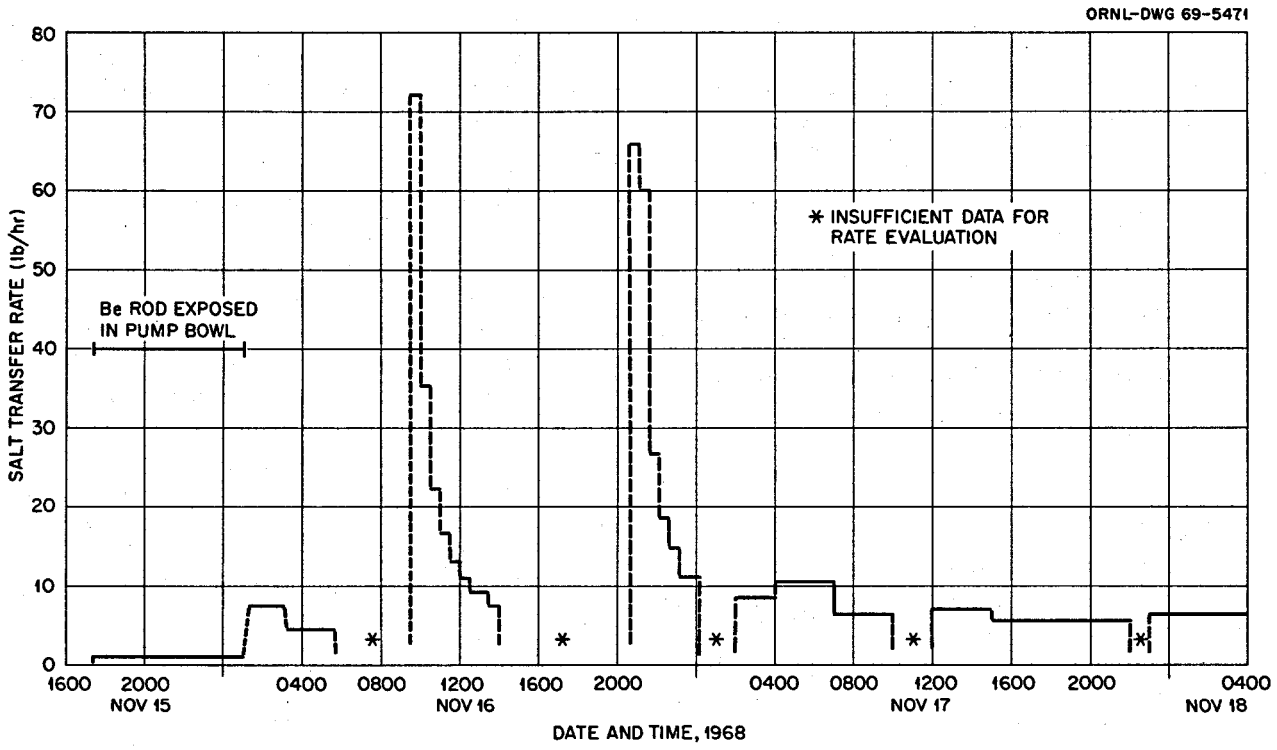

Fig. 1.14. Salt Transfer Rates Following Beryllium Addition on November 15-16, 1968.

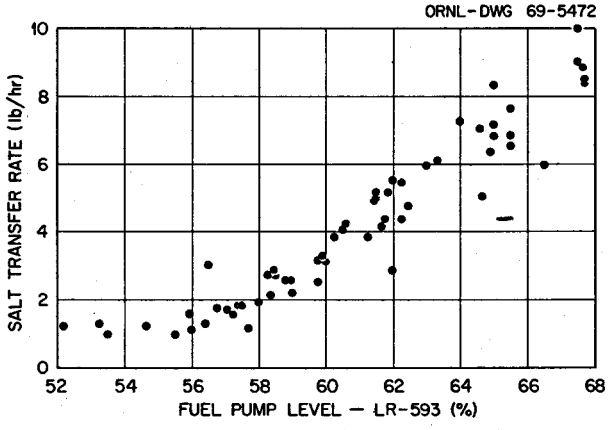

Fig. 1.15. Variation of Salt Transfer Rate with Indicated Salt Level in Fuel Pump Bowl, October 1968.

pump bowl is lower than the overflow pipe (because less salt is in the pump bowl or the salt is less agitated), much lower transfer rates could be expected. All this is consistent with the conclusions that were drawn in Sect. 1.3.2 regarding the salt level.

1.3.6 Thermal-Convection Heat-Removal Test

C. H. Gabbard

A test was conducted to determine the characteristics of heat removal from the MSRE fuel system by natural-convection flow of the fuel salt. Forced circulation was maintained in the coolant system during the test. The experiment was run by increasing the heat-removal rate at the radiator in steps, with the reactor critical, and allowing the system to approach equilibrium prior to the next radiator adjustment. The reactor was in manual control throughout the experiment, and no adjustments were made to the control rods; so the nuclear power was controlled entirely by the inherent feedback of the system. Figure 1.16 shows that the reactor power followed the radiator load smoothly and with little or no tendency to oscillate. For this experiment it had been decided that the temperature difference across the reactor vessel should not exceed about 75°F. With this limitation the maximum power attained, corrected for the afterheat from previous power operation and for changes in electric heater power, was 354 kw. The measured reactor vessel ΔT at this power level was 76°F, and the fuel flow rate was estimated to be 31 gpm.

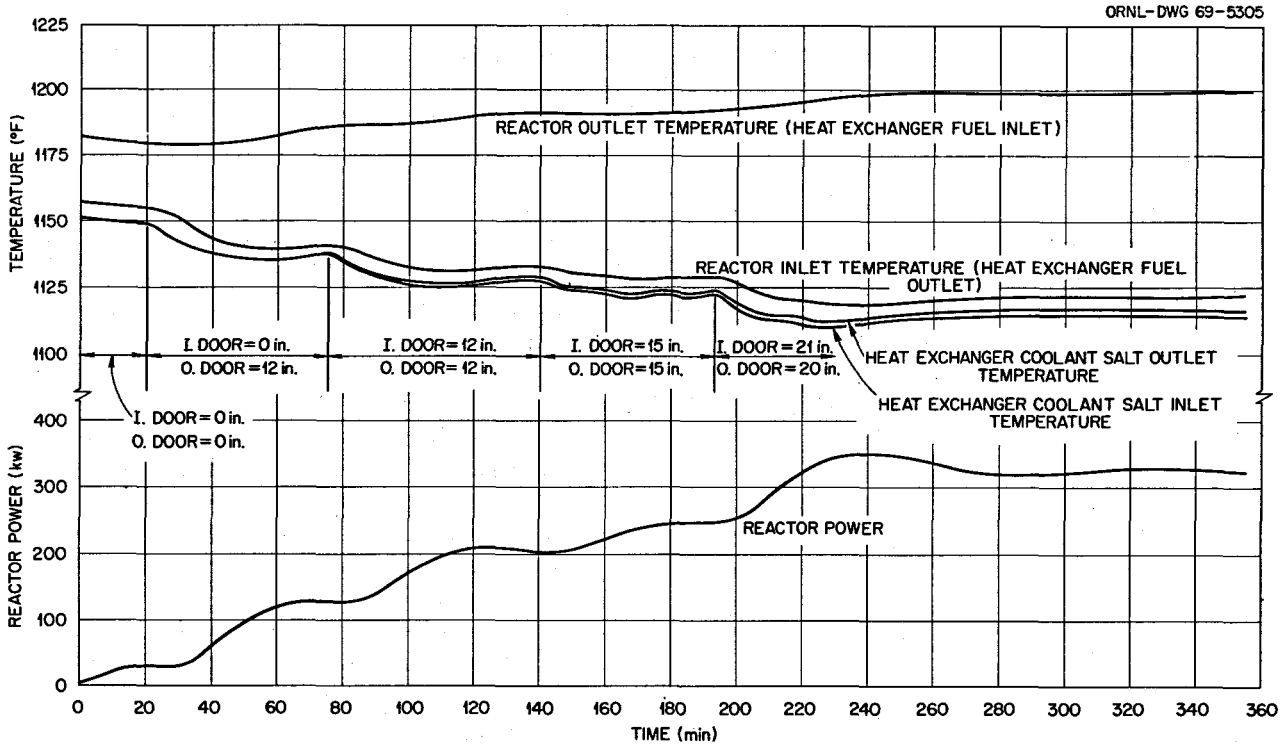

Fig. 1.16. Nuclear Power and Salt Temperatures During Thermal-Convection Heat-Removal Test.

1.3.7 Radiation Heating

C. H. Gabbard

Reactor Vessel. – The temperature differences between the reactor inlet and the lower head and between the inlet and the core support flange during power operation with ^{233}U were examined for any indication of sedimentation buildup within the reactor vessel. The values observed previously[17] (revised to correspond to the reactor power level based on the latest value of coolant salt specific heat) are shown in Table 1.4 along with the data from run 17. The temperature differences were slightly greater with the ^{233}U fuel, presumably as a result of the greater neutron leakage, which results in more fissioning in the peripheral regions of the reactor vessel.

Fuel Pump Tank. – The temperatures on the upper surface of the fuel-pump tank were somewhat lower during run 17 than had been previously observed. Decreases in these temperatures have been observed previously,[18] but no satisfactory explanation of these decreases has been found. When operation of the fuel pump was started on the variable-frequency supply, the pump-tank temperatures at low reactor power were found to increase with increasing pump speed. The temperatures also increased when the restriction in the 522 line at the pump tank cleared following the power increase to 7 Mw at a pump speed of 1000 rpm. However, the full-power temperatures at normal pump speed (1200 rpm) still appear to be slightly less than were observed during run 14.

1.3.8 Thermal Cycle History

C. H. Gabbard

The accumulated thermal cycle history of the various components sensitive to thermal cycle damage is shown in Table 1.5. Approximately 86% of the design thermal

[17] *MSR Program Semiann. Progr. Rept. Feb. 29, 1968,* ORNL-4254, p. 9.

[18] *MSR Program Semiann. Progr. Rept. Aug. 31, 1967,* ORNL-4191, p. 22.

cycle life of the fuel system freeze flanges had been used by the end of February. This compares with a value of 73% at the end of the previous semiannual report period. This relatively large increase is due to the five fills during the ^{233}U fuel loading.

1.4 EQUIPMENT

1.4.1 ^{233}U Loading Equipment

B. H. Webster

Loading the ^{233}U into the MSRE was complicated by radiation, both from the enriching salt and the stripped carrier salt into which it was to be loaded. The quantity of enriching salt to be added (about 14,000 cm^3) made it impractical to use the sampler-enricher, which is limited to about 25 cm^3 per addition. Therefore equipment was designed to load salt into a drain tank containing the radioactive carrier salt. The equipment is shown in Fig. 1.17. Cans of salt containing up to 7 kg of uranium were brought from the TURF, where it had been prepared,[19] in a heavily shielded carrier, one at a time. Each can was lowered from the carrier into the standpipe as shown in Fig. 1.18. After the shield was sealed, the valve leading to the drain tank was opened, and the can, attached to a long rod, was lowered into the upper part of the half-full drain tank. After a few minutes in the 1200°F tank, the enriching salt began to melt; within an hour all had drained into the pool of carrier salt below. After a strain gage device supporting the rod indicated that the can was empty, it was drawn up into the standpipe and the isolation valve closed below it. The empty, but still radioactive, can was then cleaned of gross contamination by rotating it in front of the exhaust line. It was weighed precisely before being stored in the turntable. Only then was another can

Table 1.4. Power-Dependent Temperature Differences Between Fuel Salt Entering, and Points on, the Reactor Vessel

Run No.	Date	Temperature Difference (°F/Mw)	
		Core Support Flange	Lower Head
6	4/66–5/66	1.90	1.39
7	1/67–5/67	1.93	1.35
12	6/67–8/67	1.98	1.40
14	9/67–2/68	2.03	1.28
17[a]	1/69–2/69	2.29	1.54

[a]Fuel in this run was ^{233}U. In other runs it was ^{235}U.

[19]*MSR Program Semiann. Progr. Rept. Aug. 31, 1968,* ORNL-4344, pp. 311–15.

Table 1.5. MSRE Cumulative Thermal Cycle History Through February 1969

Component	Number of Cycles					
	Heat and Cool	Fill and Drain	Power	On and Off	Thaw	Thaw and Transfer
Fuel system	11	49	75			
Coolant system	9	15	70			
Fuel pump	14	44	74	664		
Coolant pump	10	16	70	142		
Freeze flanges 100, 101, 102	11	45	75			
Freeze flanges 200, 201	10	15	70			
Penetrations 200, 201	10	15	70			
Freeze valve						
103	9				29	53
104	18				11	31
105	19				19	55
106	21				31	40
107	14				14	22
108	15				17	27
109	14				23	29
110	8				4	10
111	6				4	6
112	2				1	2
204	10				15	35
206	10				13	34

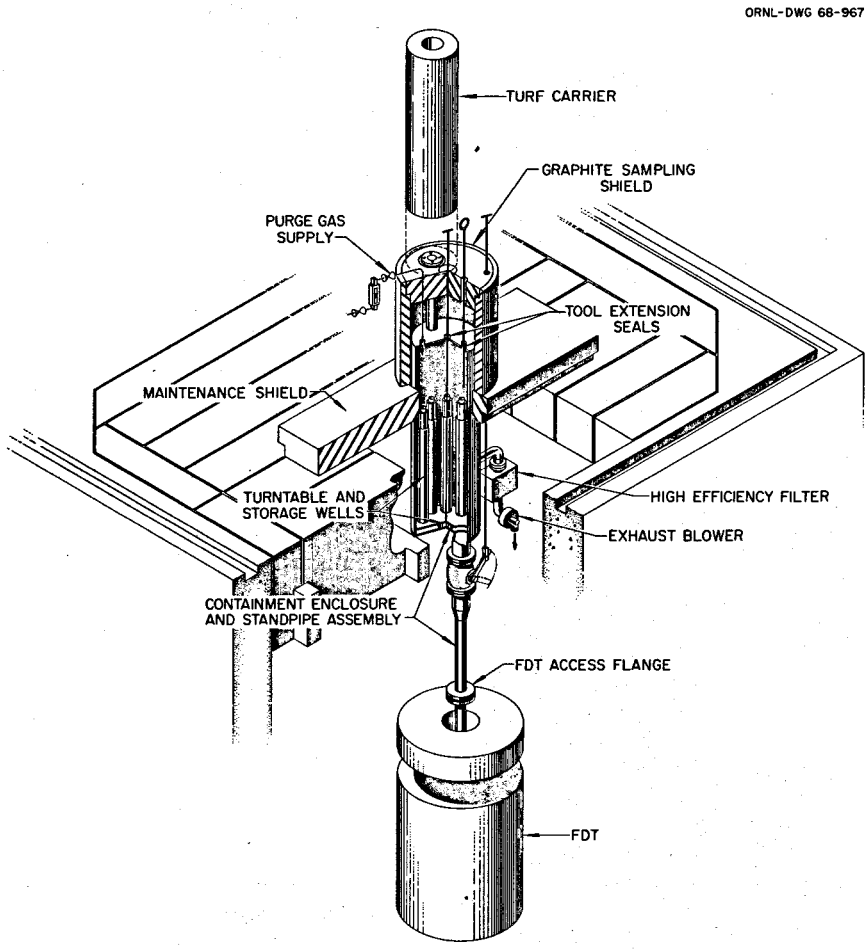

Fig. 1.17. Arrangement for Adding ^{233}U Enriching Salt to Fuel Drain Tank.

brought in. (To eliminate any chance of accidental criticality, only one loaded can was in the equipment at any time.) Six cans of ^{233}U-bearing salt were added in this way, with no release of activity and very low radiation doses to the operator. The efficiency was quite high: less than 0.2% of the salt failed to run out of the cans.

The salt-addition equipment was also used for sampling the salt immediately after processing. A long-handled tool was used to immerse a capsule in the salt, and then lift it up and place it in a transport container in the standpipe. No difficulties were encountered in this operation.

1.4.2 Salt Samplers

M. Richardson R. H. Guymon

Fuel Sampler-Enricher. – During the ^{233}U zero-power experiments (run 15), the fuel sampler-enricher was used to add 27 capsules of enriching salt, to take 28 samples of the fuel salt and fuel-pump cover gas, to expose four rods of beryllium for periods from $3\frac{1}{2}$ to $11\frac{1}{2}$ hr, and to dip six magnets into the salt to retrieve magnetic powder in or on the salt. These operations were carried out with no unusual difficulties or mechanical problems. Although sample capsules would not go all the way to the bottom of the cage in the pump bowl, presumably because of the capsules that had been abandoned there earlier,[20] regular 10-g sample ladles were immersed, and even the longest capsules retrieved salt when the pump level was high.

During the December startup of what was to be the approach to full power, a failure occurred in the sampler-enricher mechanism whose repair entailed some two weeks delay. During an attempt to remove a

[20] *MSR Program Semiann. Progr. Rept. Aug. 31, 1968,* ORNL-4344, pp. 26–29.

capsule from the latch, it was found that the cable could be pulled off the reel without the motor turning. The tentative diagnosis was that one of the pair of drive gears was slipping on its shaft. In order to gain access to the sampler drive unit, it was necessary to remove the shield blocks over the reactor cell. This, in turn, required that the fuel be drained. After a temporary containment enclosure and necessary shielding had been set up around the sampler, the sampler drive assembly was disconnected and lifted, and a 3-in. hole was sawed in the side of the containment box adjacent to the gears. One gear was loose on the shaft because its two setscrews had come loose. We repositioned this gear and tack-welded it on the shaft. The other gear we fastened securely with jam screws on top of the setscrews. A patch was then welded on the box, and the drive was reinstalled. This work was done quickly and without excessive exposure of personnel despite the high radiation levels (10 r/hr at 12 in. from the box) by the use of shielding and extended tools designed especially for this job. Before operation was resumed the manipulator hand was repaired, the illuminator port and viewing window lens were replaced because they had been discolored by radiation, and an imperfect seal in the removal valve was replaced.

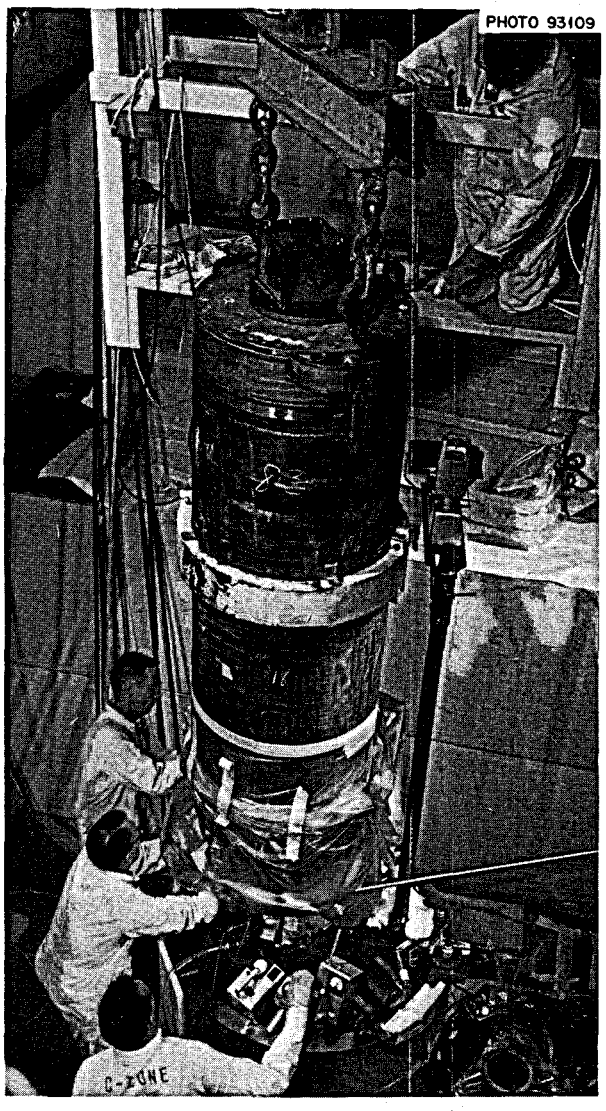

Fig. 1.18. Team Lowering a Can of ^{233}U Enriching Salt into Loading Equipment.

After operations were resumed, the sampler performed acceptably through the end of the report period. Minor difficulty was encountered with the mechanical closure device on the inner containment door, but changing the timing of actions which occur during the closing was effective. In January, while a chromium rod was being exposed in the pump bowl, radioactivity in a sampler exhaust line indicated some release of gas in the sampler. The fuel-pump overpressure was reduced in an effort to stop the release. This was not effective, and it was necessary to withdraw the chromium rod and close the operational valve, thus terminating the chromium addition after 6 hr exposure. The amount of activity released to the stack was inconsequential (<0.08 mc), and after repairs were made, no further releases occurred. The release was apparently not due to, but coincidental with, the chromium addition.

Further checks at the sampler-enricher revealed a leak around the shaft of vacuum pump 1 due to low oil level.

By the end of the report period the sampler-enricher had been used for a total of 141 uranium additions and 426 sampling operations (including beryllium and chromium additions and magnet insertions).

During the report period the coolant-salt sampler was used to take three 10-g samples, bringing the total to 69. No operating difficulties were encountered.

1.4.3 Control Rods and Drives

M. Richardson

Drop times for the MSRE control rods, measured from the initiation of the scram signal with the rod fully withdrawn until it reaches the lower limit, normally are between 0.75 and 1.00 sec. Records showed the drop time on rod 3 gradually increasing over the months from a low of 0.85 sec shortly after it was installed in the fall of 1966. During November 1968 the drop time exceeded 1.00 sec for the first time. Analysis of position vs time during drops showed a

fairly uniform drag or friction over the entire travel. While the reactor was down for the sampler repairs in December, the drive for rod 3 was removed and found to be in good condition except for slight galling on the air tube. The air tube was replaced, but there was no improvement in drop time. The drive from rod 2 was moved to rod 3, and similar slow drop times were observed (1.1 to 1.2 sec). The highly radioactive rod was then lifted from its thimble and inspected using an omniscope. There were only very minor scratches on the poison elements and nothing on the upper hose to indicate any binding in the thimble. It was concluded that the increasing drop time was most likely due to gradually increasing internal friction in the flexible rod. Because of the design of the mechanism, the driving force during a free drop is less than half the weight of the parts that are accelerated. Therefore this force was increased by fitting a 1.5-lb sleeve around the cylinder of the shock absorber in the drive. The drop time then was 0.91 sec, and it decreased slightly after high-temperature operation resumed. At the end of the report period the drop times were averaging 0.84, 0.76, and 0.87 sec for rods 1, 2, and 3 respectively.

1.4.4 Off-Gas Systems

A. I. Krakoviak

The off-gas piping of both the coolant and fuel pumps experienced gradual plugging at the gas outlet pipes of both pumps and also farther downstream.

The restriction in the fuel system off-gas pipe at the pump bowl reported earlier[21,22] reappeared after approximately one month of operation with the new fuel. The restriction was blown clear once during pressure-drop measurements, but reappeared a week later and could not be dislodged by back blowing helium from the drain tank to the pump bowl. The pressure drop across the restriction had increased to 4 psi by the last week in November, when the fuel and coolant systems were drained to clean out the off-gas lines of both systems and also to mix the fuel before the start of full-power operation.

The flange at the fuel-pump bowl was removed, and a flexible cable assembly, connected to a filter and a vacuum pump, was used to ream out the off-gas line to the fuel pump and also to collect a sample of the restricting material (reported in Sect. 11.1).

The reactor was then refilled; after about three weeks of operation, the restriction reappeared in mid-January and gradually increased to a ΔP of 5.5 psi. Because the rapid recurrence of the restriction at the pump-bowl exit threatened to become a serious nuisance, a compact 2-kw heater unit was designed for this section of line. Development tests on a mockup showed that it could be maneuvered into position through the pump support structure using long-handled tools through the maintenance shield. A unit was prepared in case it should be needed. In the last week in February, during a routine transfer of fuel from the overflow tank to the fuel pump, the restriction was blown clear, resulting in a complete transfer of fuel from the overflow tank to the pump bowl. The pressure drop in this section of line was then below the limit of detection (about 0.1 psi).

On two occasions (the latter part of January and the latter part of February) a restriction developed in the fuel system off-gas line downstream of the 4-in. holdup pipe and upstream of the line to the auxiliary charcoal bed. This restriction was blown clear by venting the fuel pump through the drain tanks and then pressurizing the downstream side of the restriction.

During the last week in January a buildup of some material (presumably hydrocarbons from the fuel-pump lubricating oil) at the entrance to all four main charcoal beds resulted in an unacceptable flow restriction through the beds. The water level in the pit was lowered, and about a foot of the inlet sections of all four beds was heated with electrical heaters installed previously for this purpose.[23] Although two of the three heater elements installed on beds 1A and 1B and one element on bed 2B failed, all four charcoal beds were restored to their original flow capacity.

A restriction periodically developed in the vicinity of the safety block valves in the inlet to the off-gas sampler. (The block valves have $^3/_{32}$-in.-diam ports, and the piping is 0.083-in.-ID autoclave tubing.) This line tees off the main off-gas line upstream of the main charcoal beds. The restriction was successfully cleared each time by back blowing with helium. Thermal conductivity measurements upstream and downstream of a hot copper oxide bed showed that about 1 to 2 g of hydrocarbons per day were flowing with the off-gas past the sample point. (See Sect. 11.1.) This is not inconsistent with the indicated losses of oil in the fuel pump.

The coolant off-gas system also experienced gradual plugging at the pump bowl and in the porous metal

[21] *MSR Program Semiann. Progr. Rept. Feb. 28, 1967*, ORNL-4119, pp. 27–29.

[22] *MSR Program Semiann. Progr. Rept. Feb. 28, 1968*, ORNL-4254, pp. 13–14.

[23] *MSR Program Semiann. Progr. Rept. Feb. 28, 1967*, ORNL-4119, pp. 30–31.

filter upstream of PCV-528.[24] Replacement of the filter restored this portion of the system to normal flow; the application of heat with a torch during the November shutdown cleared the restriction at the pump bowl. During the heatup a brown vapor (hydrocarbons) was driven out of the off-gas line, and a cleanout tool inserted toward the pump bowl came out covered with black, heavy grease. The restriction was not cleared, however, until the junction of the off-gas line and the pump bowl was gotten quite hot. There was practically no evolution of vapors from the line at this time, indicating that the restriction was, at least to some extent, salt. Also during the November shutdown, all the coolant off-gas valves were dismantled and cleaned. The valves and interconnecting lines were found to have a light layer of oil on the inner surface, and approximately 10 to 20 cc of liquid oil was cleaned from low pockets in the interconnecting lines. A trap for condensed oil vapors was installed in the line near the pump, and heaters were installed on the line at the exit from the pump bowl. Approximately six weeks after the resumption of operations, the coolant off-gas line at the pump bowl again showed evidence of a restriction, and the heater was energized. The pipe under the heater had been running at 900°F (due to heat conduction from the pump bowl), and the restriction cleared when the temperature increased to 1150°F.

1.4.5 Component Cooling System

P. H. Harley

Component cooling pumps 1 and 2 operated for 3478 and 474 hr, respectively, during the six-month report period. CCP-1 had indicated a slight loss of capacity but was operating satisfactorily at the end of the period.

In December, CCP-2 was shut down by low oil pressure resulting from oil loss through a leaking shaft seal and a sticking oil bypass valve. Both items were replaced. The internal surfaces of the relief valve were coated with a lacquer, which indicated overheating of the oil. An unsuccessful attempt was made to improve cooling of the oil by putting the water to the oil coolers in series instead of parallel. This increased the water flow to the oil cooler of the operating blower from 5 to about 7 gpm but did not have a significant effect on the oil temperature.

1.4.6 Containment and Ventilation

P. H. Harley

In September the annual containment testing was completed with a cell-pressure test at 20 psig. The cell outleakage was 57 scf/day (about 25% of permissible rate). The rest of the containment check was reported previously.[25]

The indicated inleakage (at −2 psig) has been <20 scf/day since the cell was evacuated, with the exception of the first six days. During the initial six days the apparent inleakage started at 78 scf/day and decreased to 22 scf/day. This is typical behavior that occurs as the vapor content of the cell atmosphere increases to an equilibrium value. After the cell comes to an equilibrium vapor pressure, about ½ gal of condensate is removed daily through a condensate collection system. The source of these in-cell water vapors is believed to be a leaking space cooler.

In September the west bank of the ventilation stack roughing filters was replaced because the pressure drop had built up. A standard DOP test of all three banks of absolute filters at that time showed efficiencies between 99.994 and 99.996%. The acceptable efficiency is 99.95%.

The drive belts on stack fan No. 1 failed on February 23, 1968, and ventilation was switched to SF No. 2. As an extra precautionary measure the reactor was taken from 8 Mw to 10 kw while maintenance personnel were called and stack fan No. 1 was repaired and returned to service.

The release of activity to the environment was very low during this report period, being only 0.35 mc of beta-gamma and <0.25 mc of particulate matter. The largest single release was 0.08 mc of beta-gamma activity from a leak which developed at the fuel sampler.

1.4.7 Electrical System

T. L. Hudson

The automatic voltage control system for motor generator set No. 1 failed two times during this report period. Both times the unit was operated on manual control until the vacuum tubes in the automatic controls could be replaced.

There were two automatic transfers of the 50-kva dc-ac inverter load to TVA supply. The first was caused

[24] *MSR Program Semiann. Progr. Rept. Feb. 28, 1968,* ORNL-4254, p. 14.

[25] *MSR Program Semiann. Progr. Rept. Aug. 31, 1968,* ORNL-4344, p. 32.

by a failure of a thyrister in the inverter logic circuit. The other was caused by a momentary ground during maintenance on the computer.

When a transfer occurs, many alarms are received in the control room. Some are caused by loss of operating equipment, and others are due to the momentary loss of control voltage to certain monitors. These have to be reset to stop the alarm and control action. After the first inverter failure, all operating equipment was restarted, but an emergency fuel drain occurred before the reactor-cell air activity monitors were reset. The fuel salt was drained to both drain tanks (FD-1 and FD-2). No drain or other serious condition resulted from the second inverter failure.

1.4.8 Heaters

T. L. Hudson

The operation of the heaters continued with only minor difficulties during this report period. Heater HX-1, located on the south end of the heat exchanger, developed a partial ground in the latter part of October. In order to clear the ground detector lights on bus 5, the heater was taken out of service. This was possible because tests had been performed after run 11 which determined that this heater was not essential for preheating the system from a cold condition.[26] After run 14 this heater had been removed from the reactor cell and lead wire failures in the junction box repaired.[27] The heater functioned satisfactorily during subsequent heatup and until the partial ground developed. The cause of the ground was suspected to be a broken ceramic bead on the lead wire between a heater element and the junction box mounted on top of the unit.

About a 30% drop in current on one heater on the fuel line between the reactor and the fuel pump occurred late in September. After a resistance check indicated a side heater element had failed, the spare heater elements were placed in service.

1.4.9 Other

The fuel- and coolant-salt pumps continued to operate with no sign of trouble. By the end of the report period the fuel pump had run for 23,748 hr and the coolant pump for 25,141 hr. Oil leakage past the lower shaft seal collects in an external tank. The average accumulation rate was 13.5 cc/day for the fuel pump and 14.7 cc/day for the coolant pump. Based on inventories, during the report period 1.5 ± 1 liters of oil was lost from the oil system supplying the fuel pump[28] and 2.2 ± 1 liters from the oil system supplying the coolant pump.

---

[26] *MSR Program Semiann. Progr. Rept. Aug. 31, 1967,* ORNL-4191, p. 31.

[27] *MSR Program Semiann. Progr. Rept. Aug. 31, 1968,* ORNL-4344, p. 31.

[28] Note: 1.5 liters is equivalent to 6.5 g/day. It was estimated that 1 to 2 g/day is entrained in the off-gas stream (see Sect. 1.4.4).

2. Component Development

Dunlap Scott

2.1 FREEZE-FLANGE THERMAL-CYCLE TEST

F. E. Lynch

Thermal cycling of the prototype freeze flange was resumed after the shutdown for inspection at the end of cycle 268.[1] Operation of the flange was continued through cycle 321, when it was again shut down for inspection of the flange and minor repairs to the operation equipment. Very few operation problems were experienced during this period of operation.

A complete dye-penetrant inspection of the inner face and the bore of both flanges was made at the end of cycle 321. The female flange was still free of cracks or

[1] *MSR Program Semiann. Progr. Rept. Aug. 31, 1968,* ORNL-4344, pp. 33–36.

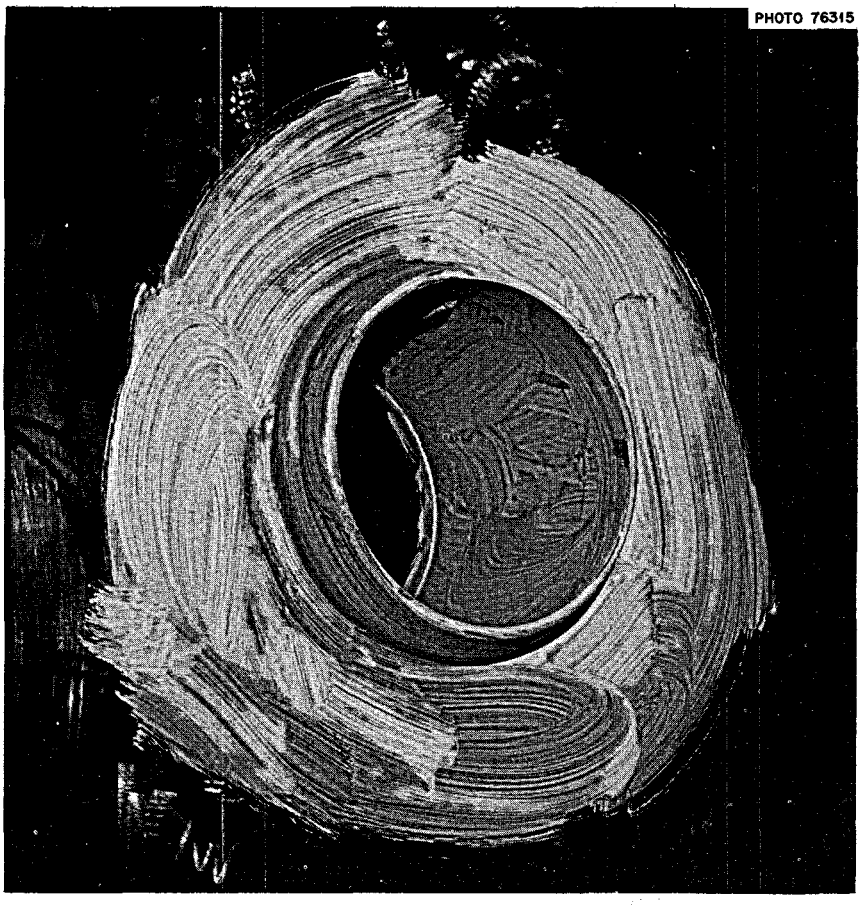

Fig. 2.1. Photograph of Test Freeze Flange Showing Dye-Penetrant Indication of a Crack on the Right Side of Bore.

Fig. 2.2. Photograph of Test Freeze Flange Showing Dye-Penetrant Indication of a Porosity-Type Crack on the Left Side of Bore.

indication of a defect. Penetrant inspection of the male flange inner face and the neck revealed no indication of a crack. The penetrant did indicate the crack observed previously[1] in the bore of the male flange where the alignment stub was welded to the flange face. The crack had lengthened slightly during the 53 cycles, and the porosity in and around the alignment stub weld was more extensive. Figure 2.1 shows the crack, which now extended approximately 120° clockwise from the upper bore thermocouple. A porosity band continued from this point to about 150 to 155°. From this circumferential crack there were porosity bands which propagated ½ to ⅝ in. farther into the bore, being more pronounced at approximately 50, 90, 120, and 150°. A porosity band extended about 155° counterclockwise from the upper bore thermocouple, as shown in Fig. 2.2. The penetrant also indicated a porosity band extending about ½ in. farther into the bore at 90, 120, and 135°.

As reported above, the female flange suffered no crack detectable by the dye-penetrant method of inspection. Therefore it appears that the service life of a flange pair would be greater if two female flanges with an insert to aid in the remote assembly of the flanges were used in place of the present design.

Thermal cycling of the freeze flange was resumed after reassembly. By the end of February the flange had been subjected to a total of 350 thermal cycles. At the end of cycle 371 the inner face and bore of the flanges will again be inspected by the dye-penetrant method and the results checked with a fluorescent penetrant.

2.2 PUMPS

P. G. Smith A. G. Grindell

2.2.1 Mark 2 Fuel Pump

The mark 2 fuel salt pump, which features a larger gas surge space than the pump in the MSRE,[2] underwent initial testing with salt during this report period. By the end of the period it has circulated the molten salt $LiF\text{-}BeF_2\text{-}ZrF_4\text{-}ThF_4\text{-}UF_4$ (68-25-5-1-1 mole %) for

[2] *MSR Program Semiann. Progr. Rept. Feb. 28, 1967,* ORNL-4119, p. 64.

approximately 4000 hr at flows to 1350 gpm and temperatures between 1020 and 1225°F.

Because the unsupported length of shaft is longer in the mark 2 pump, careful measurements of vibration were made during this operation. The maximum axial displacement was approximately 1 mil and the maximum radial displacement was 0.1 mil at 1165 rpm and 1350 gpm, essentially identical to the displacements on the mark 1 pumps in the same facility. The oil leakage rate past the lower shaft seal and into the catch tank was less than 10 cc/day.

From the beginning of salt operation, periodic plugging was experienced in the pump-tank off-gas line. Plug material was found as far as 40 ft downstream from the pump tank collected in valves and other naturally restricted flow areas, where it caused problems in maintaining the purge gas flow of 4 liters/min. After a commercial filter was installed in the line approximately 15 ft from the pump tank, there were no further problems downstream. Plugging occurred later, however, in the off-gas nozzle at the pump tank. About once per week the plugging was cleared by torch heating the nozzle and about 18 in. of the adjacent line or by rapping the nozzle with a hammer. Petrographic examination of a small sample of the plug material showed that it was salt, in nearly spherical droplets of 15 μ diameter and smaller. A possible solution to this problem was suggested, namely, a heated reflux trap at the pump-bowl outlet. The liquid salt aerosols would be impacted on baffle surfaces in tortuous passages in the trap, allowing liquid salt to accumulate into droplets sufficiently large to fall back into the pump tank against the very small drag force of the gas flow. Design and installation of the reflux trap were held up by insufficient funds.

Measurements were started with the radiation densitometer to determine the void fraction of gas circulating around the loop with the salt. Observations were made while the pump was operated at two different liquid levels in the pump tank: 0.3 in. above the normal operating level and 2.4 in. below the normal level. The differences between densitometer measurements taken at zero flow and 1350 gpm at each of the levels indicated that the gas content of the circulating salt was not detectable at or near the normal level, while at the lower level it was 0.1% by volume. The corresponding value at the normal level with the mark 1 pump design in the prototype facility was 0.1%.[3] No information was obtained at the lower level with the mark 1 design.

At the end of the period, operation was continuing for the observation of the shaft seal leakage performance and the plugging in the pump-tank off-gas nozzle. Additional void-fraction measurements were planned at pump-tank liquid levels considerably above normal.

2.2.2 Oil Pump Endurance Test

The oil pump endurance test[2] was continued. By the end of this report period the pump had run for 48,794 hr circulating oil at 160°F and 20 gpm.

---

[3] *MSR Program Semiann. Progr. Rept. Aug. 31, 1966,* ORNL-4037, p. 81.

3. Instrumentation and Controls

S. J. Ditto

3.1 MSRE OPERATING EXPERIENCE

J. L. Redford

Extensive tests were performed on the relays in the rod-scram circuits to ensure that no further relay failures would be experienced. No failures occurred either during the tests or in subsequent operation. These relays are now tested once each 24 hr to detect single failures should they occur. Noise suppressors (RC and diode) were installed across some of the nonsafety contacts of these relays to alleviate the noise which had sometimes caused difficulty during in-service tests of the scram relays.

Both fission chambers were replaced once during this report period. These chambers had been in operation nine months and one year, which is a great improvement over the previously reported three-month average life.[1] The improvement is attributed primarily to changes in the method of sealing the chamber connections and cables against intrusion of water. Several components in the pulse amplifier for the No. 1 wide-range counting channel failed due to overload when the fission chamber in that channel failed. No damage was found in any other components of the channel.

The rod-control servo was modified to allow an increase in the servo dead band to compensate for the more rapid flux response of the reactor with ^{233}U fuel. A further modification was made to allow the rod servo to be used as a rod-position demand, rather than a flux/outlet-temperature demand controller, to give more consistent rod-position variations for some of the dynamics experiments.

An eight-channel Sanborn recorder was installed to monitor several reactor parameters to assist in analysis of the power "blips" which were observed after the beryllium additions were made to the ^{233}U fuel.

A fission chamber and a BF_3 chamber were installed in the drain-tank cell near drain tank No. 2 to monitor the neutron counting rates during the large ^{233}U additions. (Data from these chambers on the multiplication of the internal neutron source also confirmed the conclusion reached from calculations that the drain tanks would provide safe subcritical storage of the ^{233}U fuel.) The chambers were removed before the cells were sealed for the final approach to criticality with ^{233}U.

3.2 CONTROLS SYSTEM DESIGN

P. G. Herndon

Further additions and modifications were made to the instrumentation and controls systems as experience revealed the need or desirability of more information for the operators, improved performance, or increased protection. The number of such changes was considerably less than in the previous period.[1] Twenty-three requests for changes in the design of the reactor system were reviewed. Of these, 2 resulted in minor changes in instrumentation and controls, 8 required only changes in process switch operating setpoints, 11 did not require changes in process instruments or controls, and on the remaining 2, design revisions were pending at the end of the report period.

The major design effort was on the documentation of the instrumentation and controls. Criteria drawings of the reactor system were brought up to date, and recent revisions[1] were added to the drawings of the fuel processing system.

3.3 MSRE COMPUTER SYSTEM

C. D. Martin J. D. Burke C. W. Kunselman

The computer system, which is used mainly for data acquisition, was originally leased from the Bunker-Ramo Corporation with the full-time services of a

[1] *MSR Program Semiann. Progr. Rept. Aug. 31, 1968,* ORNL-4344, p. 43.

maintenance engineer included in the lease agreement. When the computer system was purchased by ORNL in February 1968, the Instrumentation and Controls Division assumed the maintenance responsibility, with emergency maintenance assistance available on call from a Bunker-Ramo representative in Chattanooga. Two ORNL men attended a four-week accelerated maintenance course at the manufacturer's plant in June 1968 and have been maintaining the system since that time.

Modification to the computer-room air-conditioning system to maintain the relative humidity between 40 and 60% required increasing the room temperature from 65 to 70°F. The 5° increase caused overheat problems in three of the nine computer cabinets. This problem was remedied by installing an additional fan in the top of each cabinet to improve internal air circulation.

During the reporting period there were a nominal number of small electronic problems with the computer. These included power supply failures, high-frequency noise on the time-of-day clock signal, and the usual sporadic failures of transistors or diodes. One rather bothersome analog-input-system problem which held up the reactor test program for several days was finally traced to a loose connection in the analog-input cabinet. Time began to take its toll in the mercury-wetted analog input relays, but this was not unexpected, since many of them had more than 25,000,000 operations.

A large effort was started to consolidate certain documentation on the hardware and to compile working logic diagrams of complete systems. In several areas the MSRE computer has specially designed or modified sections not fully covered by the manufacturer's standard system documentation. The analog-input subsystem is a good example. This is the subsystem that has caused the most maintenance problems in the past, and adequate documentation is essential to timely maintenance.

Approximately five man-months of programming were provided for many software system changes that were made almost routinely. (The failure of a single thermocouple sometimes required changes to as many as six different programs. Operation on ^{233}U required changes to the reactivity-balance calculation, and the results of the experiments being conducted on the reactor frequently dictated computer program changes.) The neutron-noise-analysis program was modified to use the computer plotter to plot the power spectral density in addition to typing results.

A significant programming accomplishment during the reporting period was the adaptation of the Digital Equipment Corporation's conversational-mode calculation language FOCAL to the MSRE computer to run in background time. This allowed MSRE personnel not previously familiar with computer programming to program engineering calculations on the computer in the FORTRAN-like language and run them in the computer's "spare time." This time is available in very frequent, short increments, so that a calculation can be interspersed between reactor monitoring functions and can cause a continuous typewriter printout that makes the user feel that he has all of the computer's time rather than just a part of it.

4. MSRE Reactor Analysis

4.1 LONG-TERM ISOTOPIC CHANGES AND REACTIVITY EFFECTS DURING OPERATION WITH ^{233}U

B. E. Prince

Theoretical studies of the MSRE neutronic characteristics with ^{233}U were extended to include the nuclide changes and reactivity effects associated with an extended period of power operation. In particular, the changes in inventories of the various isotopes of uranium and plutonium were calculated, and all changes having a significant effect on the core reactivity were estimated as a function of the time-integrated fission rate. These estimates were based on a revised and updated set of reaction cross sections (ENDF compilation), which were averaged over the energy spectrum of the reactor and the volume of the fuel salt. Table 4.1 is a list of the averaged cross sections entering into the calculation of long-term changes. These are "effective" thermal cross sections, which can be multiplied by the thermal flux magnitude to obtain the average reaction rates per atom per unit volume of salt, that is,

$$\sigma = \frac{\int_0^\infty \int_{V_s} \chi(E)\, \phi(\mathbf{r}, E)\, dE\, dV}{\int_0^{E_c} \int_{V_s} \phi(\mathbf{r}, E)\, dE\, dV},$$

where V_s is the volume of the fuel salt and E_c is the cutoff energy defining the "thermal" component of the flux. The method of approximating the neutron flux distribution, $\phi(\mathbf{r}, E)$, was similar to that described in earlier studies.[1]

The nuclide chain equations for the uranium and plutonium isotopes present in significant quantities in the fuel salts were integrated using the reaction cross sections listed in Table 4.1. The time-integrated fission energy deposition was the independent variable of interest, and in these calculations we assumed that the effective heat energy deposited per fission was 197 Mev for all three fissile nuclides (^{233}U, ^{235}U, and ^{239}Pu) in the fuel salt.

The results of these calculations are summarized in Figs. 4.1 to 4.3. The relative distribution of the fission rate between the various fissile nuclides is indicated in

Table 4.1. Effective Reaction Cross Sections in MSRE Thermal Flux with ^{233}U Fuel

Nuclide	Effective Cross Section (barns)
^{6}Li	476.30
^{10}B	1921.4
^{233}U (absorption)	364.74
^{233}U (fission)	325.67
^{234}U	114.17
^{235}U (absorption)	334.74
^{235}U (fission)	272.54
^{236}U	39.67
^{238}U	34.05
^{239}Pu (absorption)	1426.99
^{239}Pu (fission)	887.43
^{240}Pu	933.99

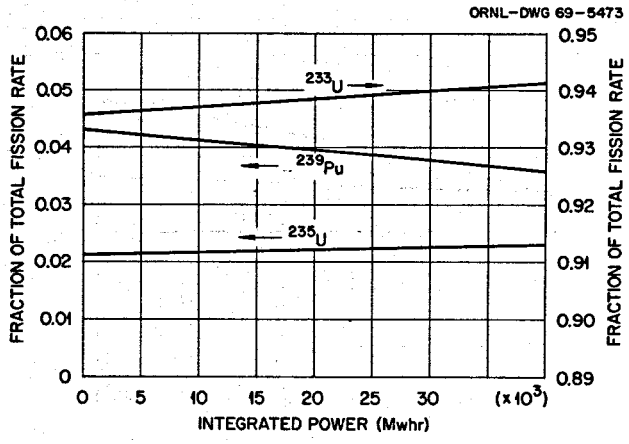

Fig. 4.1. Relative Distribution of Fissions Among Fissile Isotopes in Fuel Salt, for ^{233}U Loading.

[1] *MSR Program Semiann. Progr. Rept. Aug. 31, 1967*, ORNL-4191, pp. 50–58.

Fig. 4.1. These calculations were based on the best evaluation currently available of the heel of ^{235}U which remained from the first loading of the MSRE. The initial plutonium inventories are estimated quantities determined from the cumulative irradiation of the first fuel loading. Figures 4.2 and 4.3 show the changes in total isotopic inventories of uranium and plutonium in circulation which are expected to occur during the planned operation with ^{233}U. In the calculations represented by these figures, we assumed that no readditions of uranium or dilutions caused by draining and mixing with the residue of fuel salt in the drain tank would occur. Any such changes will be accounted for, however, in routine nuclear operations analysis.

The calculated long-term effects of the important nuclide changes on the core reactivity are shown in Fig. 4.4. In this figure the ^{10}B and ^{6}Li burnout effects are the additional changes to be expected, relative to the

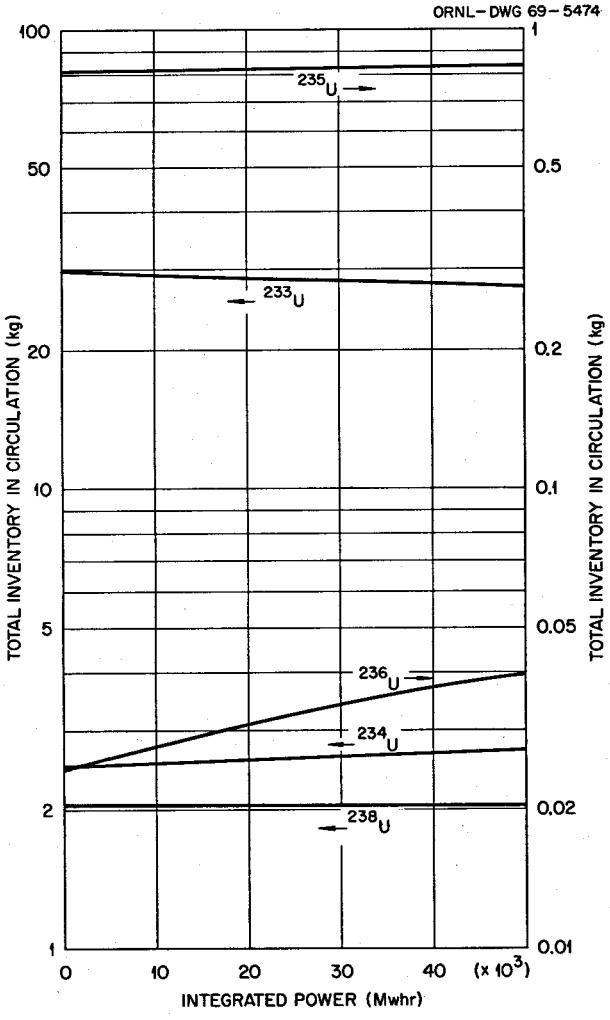

Fig. 4.2. Expected Long-Term Changes in Inventories of Uranium Isotopes During Operation with ^{233}U.

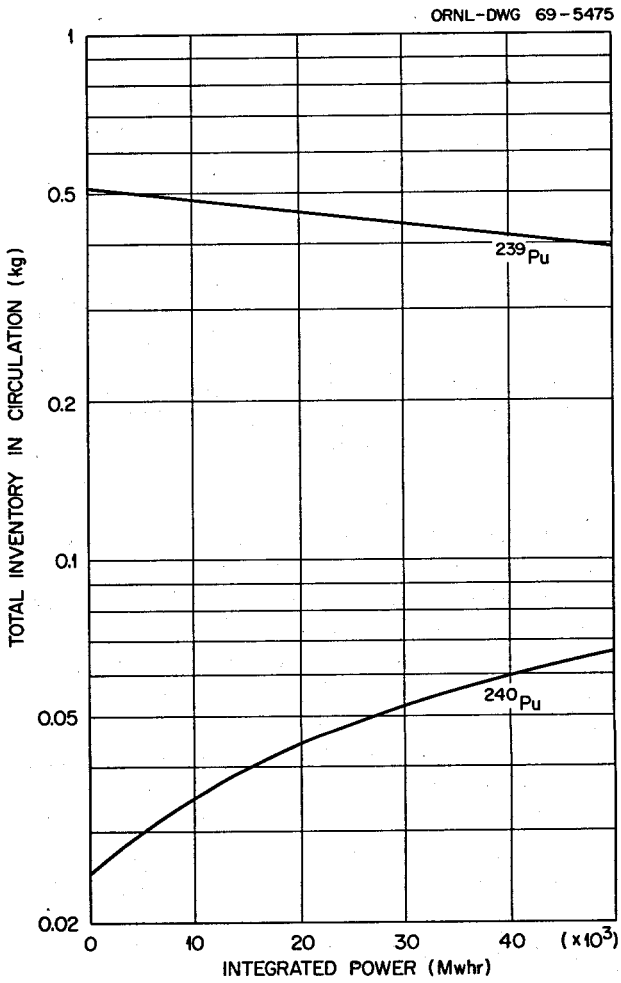

Fig. 4.3. Expected Long-Term Changes in Inventories of Plutonium Isotopes During Operation with ^{233}U.

burnout that had already been estimated during the total exposure with the ^{235}U fuel loading. The ^{235}U reactivity change appearing in this figure actually represents only one component of the net change in ^{235}U, namely, the production of ^{235}U from ^{234}U. The depletion of ^{235}U is presently being accounted for separately in the fissile uranium burnup term in the on-line reactivity balance computations. As evidenced by the curve in Fig. 4.2, these two effects very nearly cancel one another, leaving the net inventory of ^{235}U approximately constant.

The nonsaturating fission product reactivity effect shown in Fig. 4.4 was estimated in a manner similar to that used in some previous studies for the ^{235}U loading.[2] In both cases the fission product yields for

[2] *MSR Program Semiann. Progr. Rept. Aug. 31, 1968,* ORNL-4344, pp. 12–14.

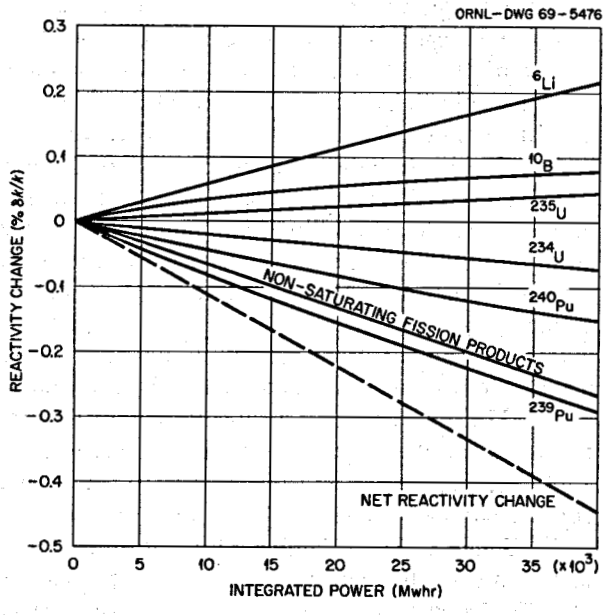

Fig. 4.4. Expected Long-Term Reactivity Effects Due to Various Isotopic Changes During Operation with ^{233}U.

the various fissile isotopes and also the fission product cross-section normalizations were those compiled in ref. 3. Similar to the studies for the ^{235}U loading, we assumed, for calculation of the reactivity effects, that all the noble gases and none of the noble metals would be removed during operation.

The net long-term reactivity change (algebraic sum of the curves shown in Fig. 4.4) is given by the dashed curve of this figure. To a close approximation, this net change is a linear function of the time-integrated power. This curve is currently being used in the on-line reactivity balance calculations.

4.2 ANALYSIS OF ZERO-POWER ROD-CALIBRATION EXPERIMENTS

B. E. Prince

Recalibration of the control rods was necessary for operation with ^{233}U, because of the increased importance of neutron leakage effects and the more "thermalized" energy spectrum relative to the ^{235}U loading. For the earlier loading we had performed both period–differential-worth experiments and rod-drop–integral-worth experiments on the regulating rod.[4] The former measurement determined the slope of the reactivity vs rod position curve at a fixed uranium concentration and an initially critical condition. By adding excess uranium and varying the initial critical rod positions for these experiments, we were able to calibrate the rod over its entire length of travel. In the rod-drop experiments, we determined the total negative reactivity corresponding to the scram of the rod from its initial critical position at some specified uranium concentration. However, because the rod-drop experiment required a more elaborate recording technique and analysis, it was convenient to perform it only a few times during the course of the uranium enrichments. Hence, in the earlier experiments with ^{235}U, we used the results of integrated period–differential-worth data as the basis of our final evaluation of the rod worths. The drop experiments were used mainly to cross check the integrated period data, as well as to test the technique of the rod-drop experiment itself.

When we attempted to apply this same general approach to the ^{233}U calibration experiments, we encountered some obstacles, however. In brief, after the data from the differential-worth measurements were collected and analyzed, the precision of the results proved to be too poor for application in the manner described above. Although we have not been able to pinpoint exactly where all this "scatter" originated, there are reasons to believe that error in the determination of rod position may have caused much of the problem this time (see Sect. 1.2.2).

Because of the poor precision of the differential-worth experiments, it became necessary to rely more heavily on the results of the rod-drop measurements to obtain the information required to calibrate the rods. In the course of the zero-power experiments with ^{233}U, we had performed two sets of drop experiments, one near the start of the excess uranium additions and one when the critical position of the regulating rod was near the position of maximum differential worth. The results of analysis of some of these experiments are described below. Unlike the period–differential-worth measurement, the reactivity determined from the rod-drop experiment is quite insensitive to small errors in the initial and scram positions of the rods. The principal new problem we had to consider was how to interpolate the information from these two sets of experiments to other values of the initial critical rod position and ^{233}U concentration to obtain the shape of the rod worth curves. Although we have not yet completed analysis of all the rod-drop experiments that were performed, the

[3] L. L. Bennett, *Recommended Fission Product Chains for Use in Reactor Evaluation Studies*, ORNL-TM-1658 (Sept. 26, 1966).

[4] B. E. Prince *et al.*, *Zero-Power Physics Experiments on the Molten-Salt Reactor Experiment*, ORNL-4233 (February 1968).

results of the latter should only be to provide certain cross checks on, and information of secondary interest to, the results set forth below.

4.2.1 Rod-Drop Experiments

The first set of experiments were performed after the addition of capsule No. 23. This corresponded to very nearly 30.78 kg of added uranium contained in the fuel loop, or 33.50 kg of total uranium added to the salt (including the drain tank residue). At these conditions the critical position of the regulating rod at 1200°F was approximately 41.8 in. with the pump off and 47.3 in. with the pump on. In the ensuing description the regulating rod will be designated as rod 1 and the shim rods as rods 2 and 3.

As described in ref. 4, in these experiments the integral count is measured starting with the reactor critical a few seconds before the scram and ending about 30 sec after the scram. The fission chamber is positioned so that the initial count rate at the critical condition is about 30,000 counts/sec. The attempt was made to start each experiment at a neutron level equivalent to about 50 w. Since it was impractical, however, to try to obtain exactly the same count rate at the time of rod scram in each experiment, for convenience in analysis we first renormalized the measured counts for each case to correspond to an initial rate of 3×10^4 counts/sec. This should not introduce any error since the system is linear in this range.

The results of the measurements and analyses for the first set of experiments (designated as series A) are shown in the bottom curve in Fig. 4.5 and in all curves in Fig. 4.6. Figure 4.5, bottom curve, corresponds to the scram of rod 1 from its initial critical position of 41.8 in. with the pump off. The circled points are the normalized integral count data, and the curve is the result of numerically integrating the reactor kinetics equations in the manner described in ref. 4. The magnitude of the negative reactivity inserted is used as an adjustable parameter to obtain a close fit to the measured count data. The average accelerations of rods 1 and 2 used for these analyses were 150 and 190 in./sec^2, calculated from average drop-time measurements made subsequent to termination of operation with ^{235}U. In addition, all analyses were normalized to the values of the delayed neutron fractions given in Table 4.2. These are effective values, which include approximate evaluations of (1) the relative abundance of ^{235}U and ^{239}Pu in the fuel salt (source of data for measured delay fractions for all fissile isotopes was ref. 5), (2) the relative energy effectiveness of delayed neutrons in the reactor spectrum, [6] and (3) calculated importance-weighted reductions in delay fractions for the conditions of steady fuel circulation.[7]

The data points for the top curves in Fig. 4.6 correspond to the normalized integral counts for shim

[5] G. R. Keepin, *Physics of Nuclear Kinetics*, p. 90, Addison-Wesley, Reading, Mass., 1965.

[6] *MSR Program Semiann. Progr. Rept. Aug. 31, 1968*, ORNL-4344, pp. 45–46.

[7] *MSR Program Semiann. Progr. Rept. Aug. 31, 1967*, ORNL-4191, p. 59.

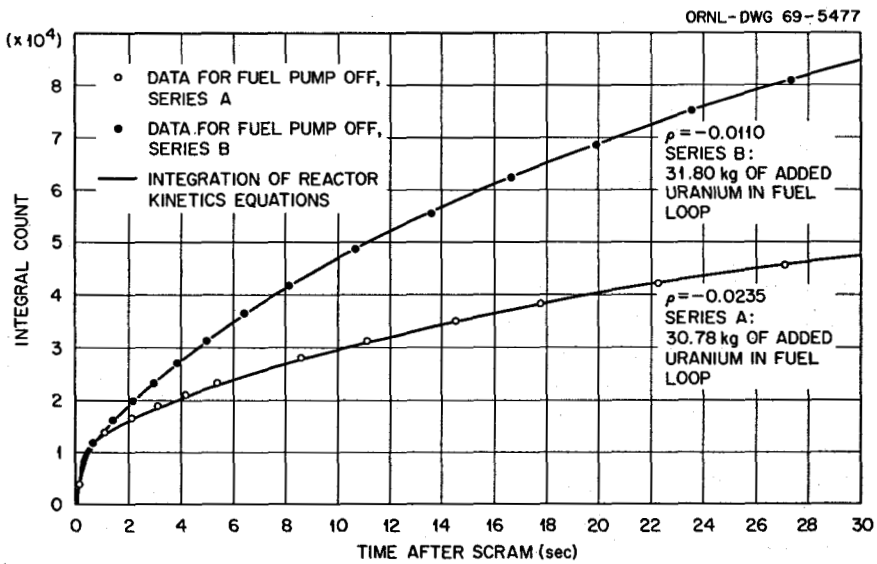

Fig. 4.5. Results of Rod-Drop Experiments for Regulating Rod (Rod 1).

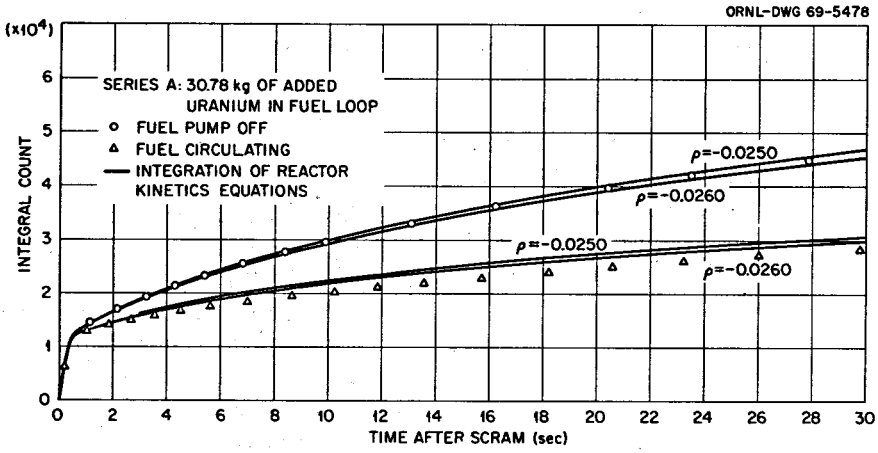

Fig. 4.6. Results of Rod-Drop Experiments for Shim Rod 2.

Table 4.2. Effective Delayed Neutron Fractions for the ^{233}U Loading Used in Analysis of Rod-Calibration Experiments

Group	Stationary Fuel (neutrons per 10^4 fission neutrons)	Circulating Fuel (neutrons per 10^4 fission neutrons)
1	2.376	1.137
2	8.576	4.188
3	7.190	4.370
4	8.214	6.654
5	1.579	1.544
6	1.003	0.998
Total	28.938	18.891

rod 2, scrammed from its upper limit of travel. The pump was off, rod 3 remained set at 51 in., and rod 1 remained at 41.35 in., its initial critical position for this experiment. This case is of particular interest because, except for the slight "shadowing" effect caused by the 9.65-in. insertion of the regulating rod, it is a direct measurement of the total worth of a single shim rod. (In addition, the shim and regulating rods were found to have the same poisoning effect by comparison of their critical positions.)

In order to better illustrate the sensitivity of this measurement to the magnitude of the reactivity insertion, in Fig. 4.6 we have shown two calculated curves corresponding to -2.50 and $-2.60\%\ \delta k/k$. These curves closely bracket the count data, and we can assign a reactivity insertion of $-2.55 \pm 0.05\%\ \delta k/k$ as the "measured" reactivity. Therefore the relative sensitivity or fractional uncertainty in this method should be better than 2%.

The effect of the slight shadowing perturbation caused by rod 1 during the first 10 in. of fall of rod 2 can be estimated from results of rod-shadowing measurements, to be described later in this section. This correction is quite small and should increase the measured reactivity magnitude by about 1%. Thus we can assign $2.58 \pm 0.05\%\ \delta k/k$ as the total worth of a single rod at the concentration of ^{233}U obtaining in this first set of experiments.

The bottom curves of Fig. 4.6 represent the data and results of analysis for the same shim rod, taken with the fuel circulating. As in the experiment with the pump off, rod 2 was scrammed from its upper limit of travel. Rod 3 remained set at its upper limit, and rod 1 remained at its critical position with the pump running, 47.32 in. The solid curves are the results of integrating the kinetics equations for the *same* reactivity magnitudes shown in the top curves of Fig. 4.6, but with the delayed neutron fractions for each precursor group replaced by effective fractions calculated with the theoretical model used previously for MSRE analysis (Table 4.2). These results suggest that the calculated losses in delayed neutron fraction due to circulation may be slightly underestimated by the theoretical model. The observed difference is rather small in comparison with the total effect, however, and we concluded that the calculated delayed-neutron losses are within 15% of the actual losses in the MSRE. (Note that the presence of any entrained gas in the circulating fuel salt should not be significant in interpreting this experiment, since these conditions would have remained essentially constant throughout the experiment.)

The second set of experiments (series B) was performed after 31.80 kg of uranium had been added to

the fuel loop. In this series we have completed only the analysis of the experiment where rod 1 was dropped from its new critical position at this loading (22.25 in. with the pump stopped). These results are shown as the top curve in Fig. 4.5. The negative reactivity obtained from the analysis of this experiment was $-1.10\%\ \delta k/k$. As will be shown below, the results in Fig. 4.5, together with the total measured worth of one rod, provide information sufficient for normalizing and interpolating the rod-calibration measurements.

4.2.2 Reactivity Effect of Excess Uranium

Another calibration curve of special interest which is derived from the zero-power experiments is the variation of excess reactivity with the uranium concentration. Each point on this curve corresponds to the excess reactivity of the system if the rod were withdrawn from its critical position to the upper limit of travel, at a fixed uranium loading. This information is directly applicable to the on-line reactivity balance calculations, since the uranium is depleted and readded in the course of operation. The curve is also of theoretical interest, however, because the uranium additions without compensating rod insertions represent a uniform variation in nuclear properties over the volume of the fuel salt. Of the characteristics calculated in core physics studies, this effect should be one of the most reliable, whereas quantities depending directly on the calculation of the rod poisoning effect are probably the least reliable. Therefore for this problem we have made use of theoretical results concerning the *shape* of the excess-uranium–reactivity curve to aid in interpolating the experimental data described above.

By means of theoretical derivations and arguments based on perturbation theory, one can arrive at the following conclusions:

1. The variation in the excess reactivity ρ with ^{233}U loading for a fixed rod position is closely approximated by the formula

$$\rho \cong \frac{K(C - C_0)}{C} = \frac{K(M - M_0)}{M}, \qquad (1)$$

where K is a constant, C and M are the concentration and mass of ^{233}U in the salt, and subscript 0 refers to the values at the minimum critical loading.

2. If a reactivity measurement is made which involves the motion of the control rod away from its initial critical position at some fixed uranium loading and we wish to interpolate this measurement to another uranium concentration, the factor expressing this relation is approximately proportional to the uranium concentration:

$$\frac{\Delta\rho(C_0)}{\Delta\rho(C)} \cong \frac{C}{C_0}. \qquad (2)$$

We first tested the accuracy of approximation (1) by applying it in the case where an experimental curve was attainable from independent measurements. This was the ^{235}U mass-vs-reactivity data determined by integration of period measurements and reported as Fig. 7 of ref. 4. We found that fitting the data by a theoretical curve of the form (1) required only a very slight change from the "empirical" curve reported in ref. 4.

Approximations (1) and (2) provide all the necessary relationships to interpolate the rod calibration data for the ^{233}U loading. The value of M_0, the loading of the fuel loop at the reference conditions for the initial critical experiment, was 30.59 kg of uranium with isotopic composition of the enriching salt. (Note: The heel of ^{235}U and ^{239}Pu remaining in the salt from the ^{235}U loading constitutes a base-line effect in all these measurements and can be shown to have negligible influence on the analysis following.) The approximations were applied as follows. From Eq. (2) the total reactivity effect of one rod at a loading of 31.80 kg of uranium is approximately

$$2.58(30.78/31.80) = 2.497\%\ \delta k/k.$$

Subtracting the rod-drop reactivity from the total rod effect gives the excess uranium reactivity at 31.80 kg of uranium:

$$\text{excess U reactivity} = 2.497 - 1.10 = 1.397\%\ \delta k/k.$$

This result was then applied to generate the reactivity curve corresponding to Eq. (1),

$$K = \frac{\rho M}{M - M_0} = \frac{(0.01397)(31.80)}{31.80 - 30.59} = 0.369.$$

The curve of Eq. (1) based on these values of the parameters K and M_0 is shown in Fig. 4.7.

These results may be cross-checked for consistency with the rod-drop measurement given by the bottom curve in Fig. 4.5. In this case the reactivity effect of dropping the regulating rod from its critical position at 30.78 kg of uranium was $2.35\%\ \delta k/k$. Then

$$\text{excess U reactivity} = 2.58 - 2.35 = 0.23\%\ \delta k/k.$$

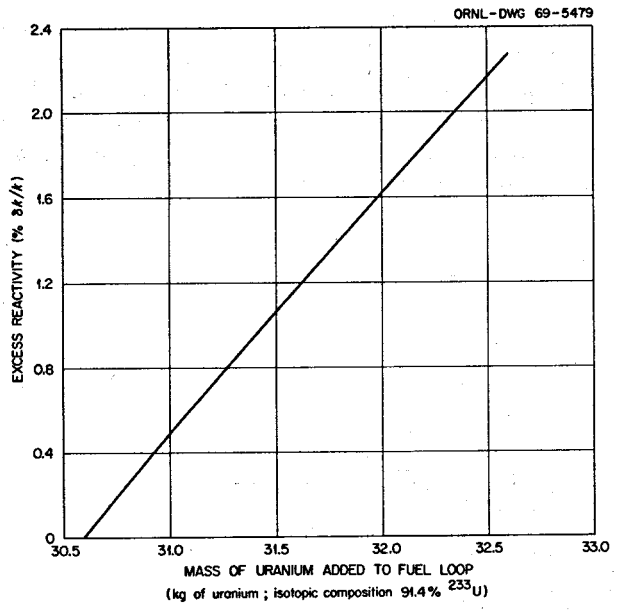

Fig. 4.7. Effect of Uranium Mass on Reactivity in ^{233}U Loading; Theoretical Curve, Normalized to Results from Rod-Drop Experiments.

This is observed to be in close agreement with the value obtained from the interpolated curve in Fig. 4.7.

The results inferred from the above analysis may also be compared with the excess-uranium reactivity effect obtained from theoretical analysis. Differentiation of Eq. (1) shows that K is also equal to the concentration coefficient of reactivity at the minimum critical loading; that is,

$$\left(C\frac{d\rho}{dC}\right)_{C=C_0} = K = 0.369 . \qquad (3)$$

This value of the coefficient compares quite favorably with the value of 0.389 obtained from theoretical calculations.[8]

4.2.3 Summary of Rod-Calibration Information

To synthesize the results of the preceding sections, we used the simple procedure of combining (1) experi-

[8] *MSR Program Semiann. Progr. Rept. Aug. 31, 1967*, ORNL-4191, pp. 50–58.

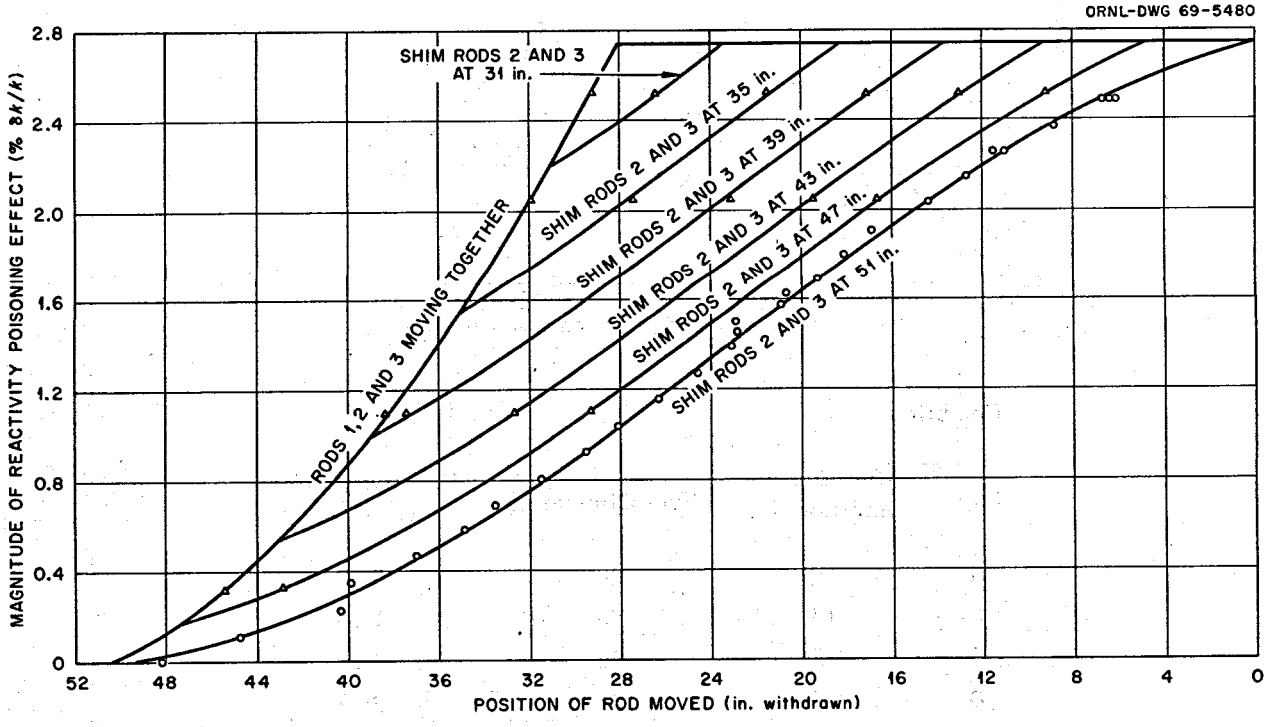

Fig. 4.8. Results of Fit of Rod Calibration Data by Least Squares Formula. ○ Data obtained from measurement of critical rod positions and use of Fig. 4.7. △ Data interpolated from rod-shadowing measurements (Fig. 4.9). Reactivity effects normalized to initial critical loading of 30.59 kg of uranium in fuel loop.

mental measurements of the variation in critical rod position with uranium loading and (2) the information given in Fig. 4.7 to obtain the reactivity effect corresponding to arbitrary insertions of the regulating rod. The results of this procedure are shown as the circled data points in Fig. 4.8. (The small amount of statistical variation in these data probably corresponds to slight uncertainities in the temperature and the rod position.) For convenience in the way we apply this information in the on-line reactivity balance, using Eq. (2) we have put all numerical values of the reactivity in Fig. 4.8 on the basis of one uranium concentration, arbitrarily chosen as the initial critical concentration.

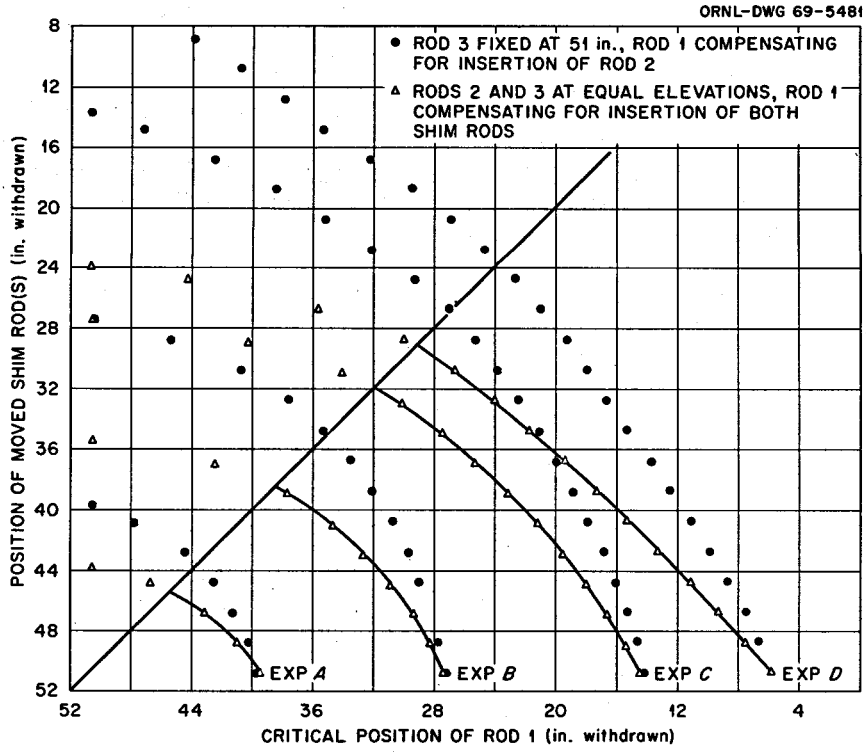

Conditions:

Exp.	After Capsule Addition No.	Fuel Circulating	Reactivity Effect (% $\delta k/k$)*
A	9	Yes	0.32
B	13	No	1.10
C	23	No	2.05
D	27	Yes	2.52

*Normalized to initial critical uranium loading.

Fig. 4.9. Change in Critical Position of Rod 1 as Rods 2 and 3 Are Inserted into Core.

The complete results shown in Fig. 4.8 constitute a summary of the rod-calibration information, which includes the effects of partial insertions of the shim rods. These additional results were obtained by the following procedure. During the course of the uranium additions, we performed several rod-shadowing experiments, in which the change in critical position of the regulating rod was measured as one shim rod and then two banked shim rods were inserted. The procedure was exactly the same as used in the ^{235}U experiments reported in ref. 4. Results of measurements carried out at four different uranium concentrations are plotted in Fig. 4.9. Here the ordinate and abscissa are the shim- and regulating-rod positions, and each plotted point represents a critical configuration of the rods. The particular conditions for each experiment are also indicated in the figure. A sequence of critical positions taken at a fixed uranium concentration and temperature would represent a contour line of constant reactivity relative to the reference condition if the reactivity were being plotted in the dimension perpendicular to the plane of Fig. 4.9.

The data taken from the experiments in which the two shim rods were moved in a bank is of special interest in application to the on-line reactivity-balance calculations because this is the configuration used in the operating reactor. This interest is emphasized in Fig. 4.9 by the smooth curves drawn through these data points. The curves are terminated on the line of equal insertion of the shim and regulating rods because the area to the right of that line is the region in which the rods are operated in the MSRE. From the earlier work with the ^{235}U loading, we developed an analytical formula for the rod reactivity variation with shim- and regulating-rod insertion.[9] This formula contained adjustable parameters which were fitted by least-squares analysis to the measured data in the region of interest. The analysis procedure described in ref. 9 was applied without modification to the ^{233}U experiments, with the resulting least-squares curve fit shown in Fig. 4.8. The triangled points in this figure are check points for the least-squares formula, interpolated from the smooth curves in Fig. 4.9. The least-squares formula provides a good fit to the measured data of Fig. 4.8 for most of the range of rod travel but deviates somewhat from expected values near the upper and lower limits of the range. The total regulating rod reactivity determined from the formula is too large, and the curves probably meet to "bend" more near these limits. (This same situation was encountered earlier in the ^{235}U measurements.) These deviations should not constitute a problem, however, for normal operating procedures keep the tips of the rods well away from these extremes.

In sum, the essential information obtained from the rod-calibration experiments is encompassed in Figs. 4.7 and 4.8 of the preceding description. This information is currently being used in the on-line reactivity-balance calculations, subject to possible future refinements when the final analysis and evaluation of all the zero-power physics experiments with ^{233}U have been completed.

4.3 CALCULATIONS OF REACTIVITY VARIATIONS FROM POWER-TIME RECORDS

B. E. Prince

In the most common problems involving theoretical analysis of reactor dynamics, the time dependence of the neutron population or fission rate is determined, corresponding to a specific perturbation in the reactor properties or geometry. The inverse type of problem arises, however, whenever one wishes to estimate the nature of the original perturbation corresponding to an observed transient in the neutron level. Recently, observation of some small ripples, or "blips," in the power level recorded by the MSRE nuclear instruments provided occasion for some computations of this type. These blips were evidenced by temporary increases of about 10% in the neutron level for various durations of the order of several seconds, followed by a return to the original level. They have lately been shown to disappear when the flow is reduced slightly, and it is believed that they are associated with the movement of gas in the core (see Sect. 1.3.4). However, some calculations were performed (1) to estimate the magnitude and time dependence of the input-reactivity perturbations during these blips, (2) to determine if transients recorded during well-separated intervals of time had any similar features, and (3) to help identify the mechanism producing the reactivity changes. At this date these calculations have been performed for only a few of the blips, recorded during operation of the reactor at 5 Mw. The results have indicated that only a small amount of "input" reactivity (about 0.01 to 0.02% $\delta k/k$) was involved in the production of these transients. However, there do not appear to be any significant conclusions which can be obtained from the time variation of the reactivity, at least from the few cases we have analyzed.

As a basis for mathematical description of this problem, we have used an integrodifferential equation

[9] *MSR Program Semiann. Progr. Rept. Feb. 28, 1966*, ORNL-3936, pp. 82–87.

formulation of the neutron kinetics. This equation has the form

$$\frac{dP}{dt}=\frac{\rho-\beta_T^c}{\Lambda}P+\sum_{i=1}^{6}\left[\frac{\beta_i^c P_0}{\Lambda}+\frac{\beta_i}{\Lambda}\int_0^t e^{-\lambda_i(t-\xi)}H(t-\xi)\,\Delta P(\xi)\,d\xi\right], \quad (1)$$

where

$P(t)$ = reactor power (Mw),

P_0 = power at time zero,

$\Delta P = P - P_0$,

$\rho(t)$ = net reactivity (input + temperature feedback reactivity),

β_i = delay fraction for precursors of ith group of delayed neutrons (neutrons per fission neutron), $i = 1, 2, ..., 6$,

β_i^c = effective delay fraction for the ith group calculated for steady circulation and steady-state neutron level (neutrons per fission neutron),

$$\beta_T^c = \sum_{i=1}^{6}\beta_i^c ,$$

λ_i = decay constant for ith group (sec^{-1}),

Λ = prompt-neutron generation time (sec),

$H(\tau)$ = a kernel function representing the "weight" given to new precursors at time τ after their birth from fission, with radioactive decay factor removed ($\tau = t - \xi$).

The net reactivity is also written as an integral form governing the temperature feedback effects:

$$\rho(t) = \rho_{in}(t) + \alpha_f A\int_0^t G_f(t-\xi)\,\Delta P(\xi)\,d\xi + \alpha_g B\int_0^t G_g(t-\xi)\,\Delta P(\xi)\,d\xi , \quad (2)$$

with

$\rho_{in}(t)$ = input reactivity from "external" perturbation,

$\alpha_{f,g}$ = temperature coefficients of reactivity for fuel salt and graphite respectively,

$G_{f,g}(\tau)$ = kernel functions representing importance-weighted temperature changes in fuel and graphite at time τ caused by a unit change in the heat production at time zero,

A, B = constants containing the heat capacities of the fuel salt and graphite together with spatial weighting factors.

The chief advantage of using the above formulation of the kinetics equations in this problem is that it reduces the approximations required to treat the transport-lag effects between the production of new precursors or heated salt and their influence on the chain reaction at later times. A basic assumption in the present approach is that the neutron population or fission rate can be written as the product of an amplitude function $P(t)$ and a normalized time-independent function distributed like the fundamental mode of the flux. One obtains the kernel functions $H(\tau)$ and $G(\tau)$ by first integrating the distributed-parameter kinetics equations for the precursor concentrations and temperatures and then by importance-weighting the solutions over the reactor core.

A study of some of the computational aspects of this general approach is still in progress and will be reported at a later date. However, in the present application it was possible to make several simplifying assumptions while still retaining the main advantages of the method. First, for the type of transients and time intervals we were interested in, the temperature-reactivity feedback due to graphite heating could be neglected. (Only a small fraction of the heat is deposited directly in the graphite, and the time constants for heat transfer are large compared with the intervals of interest.) Second, we approximated the flux and adjoint, or importance, distributions in the MSRE by a product of a sinusoidal function in the axial direction and a Bessel function in the radial direction. In this way the spatial integrations described above could be carried out analytically. Finally, we restricted the time interval for the calculation to an upper limit of one fuel-loop transit time (~25 sec) so that the core inlet temperature of the salt could be assumed essentially constant and the details of the thermal dynamics of the heat exchanger could be neglected.

The resulting kernel functions used in the inverse calculations of reactivity are shown in Fig. 4.10. The functional dependence of $H(\tau)$ is clearly in accord with that suggested by intuition; at time zero a "pulse" of new precursors is produced in the distribution of the fundamental mode throughout the core, and the importance-weighted value of this pulse is unity. As the fluid containing these precursors leaves the core region, their relative weight decreases to nearly zero after one

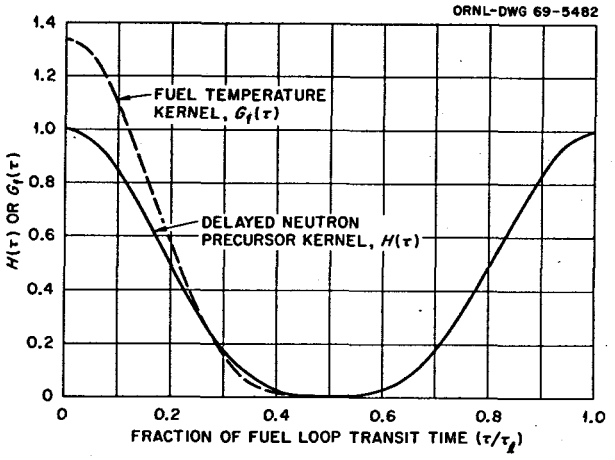

Fig. 4.10. Kernel Functions Used for Calculation of Reactivity from Power-Time Records.

core transit time. (The approximate residence time in the MSRE neutron flux, including weighted contributions of the upper and lower plenums, is about half the loop transit time.) The weight function then rises again as these precursors return to the core after traversing the external circuit. Superimposed on this weight function is the effect of radioactive decay of the precursors, as shown in the last term on the right-hand side of Eq. (1).

The approximate temperature kernel function $G_f(\tau)$, shown as the dashed curve in Fig. 4.10, also exhibits qualitative features similar to those of $H(\tau)$ during the first half of the circulation cycle. Here, however, one can show that it is appropriate to weight the spatial variation with the product of the flux and adjoint functions (the *square* of the flux in the present approximation). This gives rise to a relative weight of 1.33 rather than unity at time zero, and, in addition, there is a radial weighting factor of 1.67 included in the constant A of Eq. (2).

The records of the time dependence of the power level during the blips were obtained from digitized values of the compensated-ion-chamber currents, recorded every quarter-second by the BR-340 data logger. For the purposes of this calculation the power level was assumed to vary linearly with time during these quarter-second intervals. The resulting transients corresponding to several blips recorded while the reactor was operating at 5 Mw are shown in Fig. 4.11. In these observations the reactor control was set on manual so that there would be no compensating motion of the regulating rod during the transient. The solid curves consisting of broken-straight-line segments represent the reactor power level, and the circled points are the associated input-reactivity variations, calculated by use of Eqs. (1) and (2), together with the functions shown in Fig. 4.10. In each case the starting point for the calculation was chosen at the end of an interval where the flux signal appeared relatively quiet, so that the net reactivity at time zero was essentially nil.

As stated at the beginning of this section, no significant conclusions concerning original "causes" can be drawn from details of the time dependence of the perturbations. The total magnitude of the reactivity variation is quite small and within the magnitude which could correspond to temporary pressure fluctuations and movements of entrained gas in the fuel salt. (Note that the reactivity in Fig. 4.11 is plotted in units of the delay fraction corresponding to steady fuel circulation.) The time intervals involved in the "rise" and "fall" portions of the transients do not appear to be significantly different. However, there are also smaller variations in the flux signal which have about the same slope and could also be associated with gas-entrainment effects.

Because it has lately been shown that this entire phenomenon is sensitive to the fuel flow rate and can be removed by slight reductions in the flow, and also because of the very small amount of reactivity variation involved, we have temporarily discontinued further calculations of the type shown in Fig. 4.11. These studies will be resumed if future observations suggest that it would be profitable to extend the analysis further.

4.4 THEORETICAL ANALYSIS OF DYNAMICS WITH ^{233}U FUEL

R. C. Steffy

In the previous semiannual progress report,[10] the stability of the ^{233}U-fueled MSRE was discussed. One of the criteria by which the system was judged to be inherently stable was the determination that the real parts of the eigenvalues of the matrix of the mathematical model[11] of the system were all negative. The previously presented results only included a few eigenvalues nearest the origin for various power levels. A continuation of this investigation has resulted in determining the power dependence of all the eigenvalues. Figure 4.12 is a plot of the more important

[10] *MSR Program Semiann. Progr. Rept. Aug. 31, 1968*, ORNL-4344, pp. 48–52.

[11] A set of 78 coupled linear differential equations which, taken together, characterize the power and temperature response of the MSRE with ^{233}U fuel.

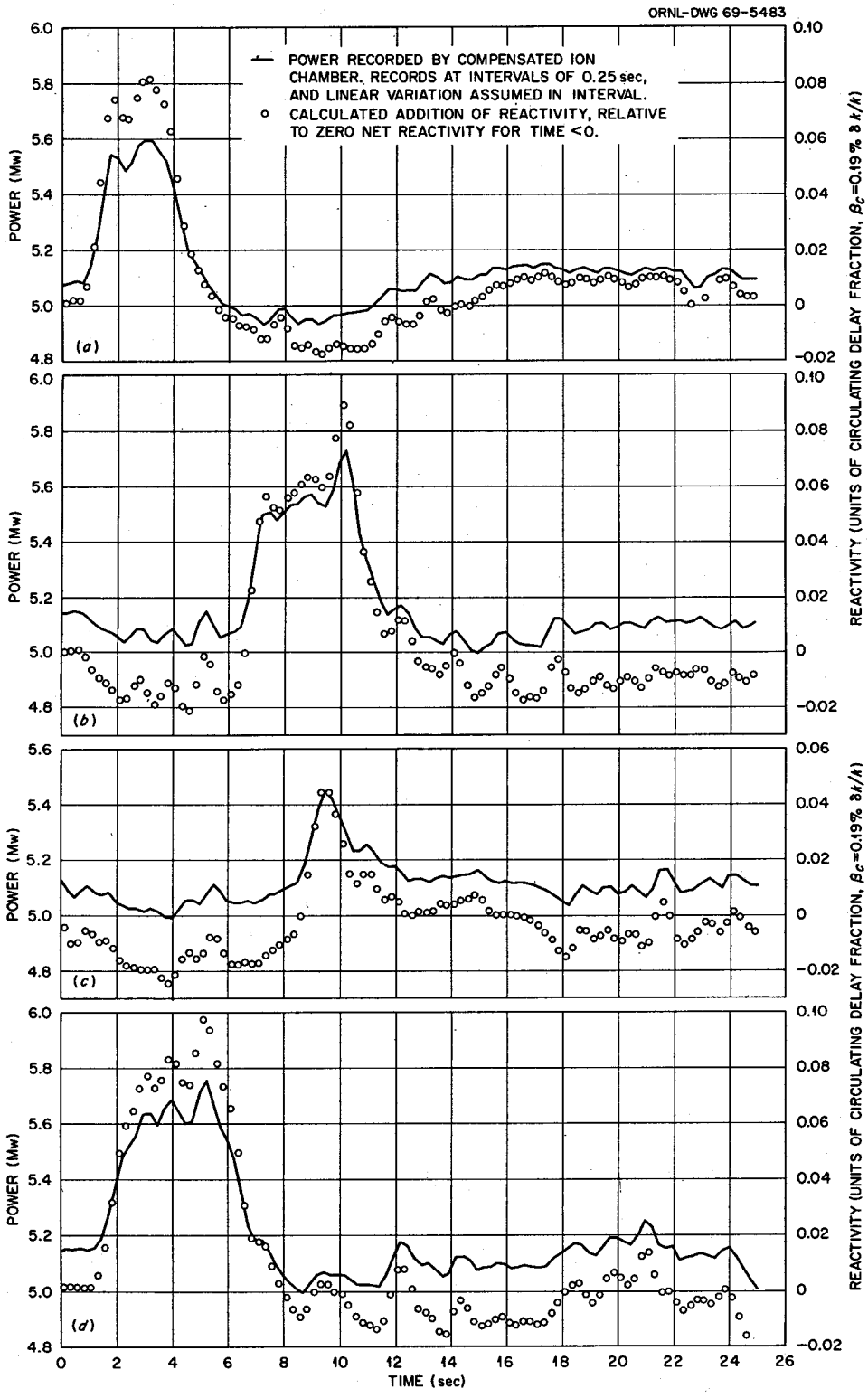

Fig. 4.11. Input-Reactivity Variations Calculated from Power-Time Records.

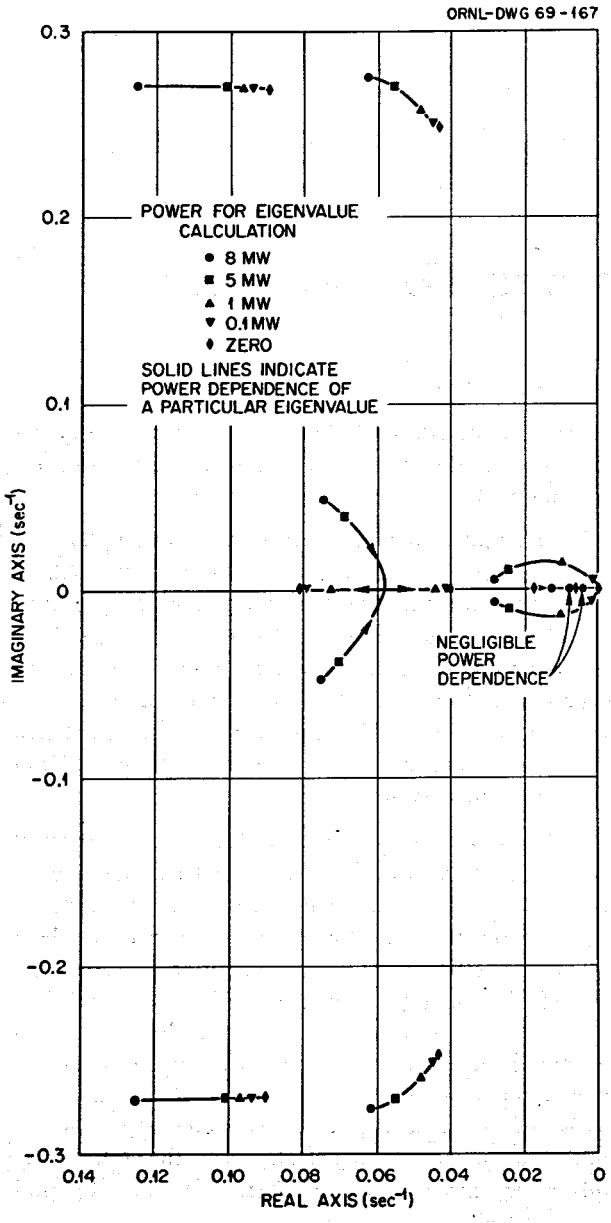

eigenvalues and graphically shows their power dependence. The tendency of the eigenvalues toward the right-hand plane as power is reduced indicates that after a power perturbation the MSRE will be more sluggish in returning to its original state at lower power levels.

At zero power the eigenvalues of the nuclear kinetics equations are all on the real axis, with the most dominant eigenvalue being at the intersection of the real and imaginary axes. This is typical for a zero-power reactor. Also observed in Fig. 4.12 is a set of eigenvalues which do not approach the real axis as power level is increased. These imply that any temperature disturbance in the loop would tend to "ring" around the loop as it decayed. The dependence of these eigenvalues on power is due to the power dependence of the heat transfer coefficient of the radiator.

Fig. 4.12. Power Dependence of the Dominant System Eigenvalues for the ^{233}U-Fueled MSRE.

Part 2. MSBR Design and Development

R. B. Briggs

The purpose of the MSBR design and development activities is to prepare a reference design for a 1000 Mw (electrical) one-fluid MSBR plant; to design a molten-salt breeder experiment (MSBE), operation of which will provide the data and experience necessary to build large MSBR's; and to develop the components and systems for the MSBE.

Work on the reference design for the one-fluid MSBR was begun in October 1967 and has taken most of the effort. Prior progress is reported in our semiannual reports for the periods ending in February and August 1968. The studies have converged on the design of reactor core and vessel described in this report, and we are now investigating some of the more important details of the design. The flow and temperature distributions in the reactor are being calculated, and features required to attain the desired distributions are being incorporated in the design. The distribution of fission products in the reactor systems is being estimated, and the results are being used to provide for adequate removal of the decay heat.

One of the important features of the reactor is the system for rapidly removing krypton and xenon by contacting the circulating fuel salt with helium. Decay of radioactive gases and their daughters results in a large heat load in the off-gas system. Design of this system to meet special requirements imposed by the distribution of heating has also been started.

With the general design of the reference MSBR reasonably well established, we have begun to look at the MSBE. Calculations indicate that a reactor with a power level of 100 to 200 Mw (thermal) can satisfy the requirements that have been proposed to date. An early concept of the reactor is described here.

The amount of the experimental work in the development program is small and is being limited to the most important problems. Work is being done on methods for dispersing bubbles of gas in and separating them from circulating liquids. Preparations continue on experiments to measure the coefficients for transfer of dissolved gases to bubbles in circulating liquids. These experiments are in support of the gaseous fission product removal system.

Better values are being obtained for the thermal conductivities of salts for use in heat transfer calculations. Experiments are in progress to confirm or improve on the relationships used to calculate heat transfer coefficients for molten fluoride salts. The sodium fluoroborate–sodium fluoride eutectic salt has, because of its low melting point and low cost, been proposed for use in the intermediate coolant systems of large molten-salt reactors. Since this is a new salt to the MSR program, a forced convection loop is being operated in engineering tests with the salt. Early difficulties have been overcome, and the loop now operates well.

The equipment for the MSBE is to be designed and built by industrial companies. We are presently proceeding with a plan for obtaining pumps and are preparing a plan for obtaining steam generators from industry.

5. Design

E. S. Bettis

5.1 GENERAL

E. S. Bettis R. C. Robertson

Design study of a 1000 Mw (electrical) MSBR power station is continuing. The basic design described in the last semiannual progress report[1] remains unchanged, but we have made several revisions as a result of more detailed calculations having been completed in such areas as the nuclear physics, stresses, temperatures, and fluid flow. The design modifications have largely been in the reactor internals, in the primary heat exchanger, and in the containment cell wall structure.

Afterheat removal has been more fully investigated. A listing of the design criteria has been made, and the cost estimate has been revised to reflect the design changes and escalation of costs.

The fuel and coolant salt physical properties used in the design study have been previously reported[1] and remain unchanged except that the thermal conductivity of the fuel salt is now established to be more nearly 0.75 Btu hr^{-1} ft^{-1} $(°F)^{-1}$.

5.2 PLANT LAYOUT

E. S. Bettis J. R. McWherter
C. W. Collins H. M. Poly
H. L. Watts

The general layout of the plant, described previously,[1] remains essentially unchanged (Figs. 5.1 and 5.2). As before, the reactor cell contains the reactor, four fuel-salt circulating pumps, and four primary heat exchangers. We have, however, increased the diameter of the reactor cell from 60 ft to 66 ft to accommodate a larger reactor vessel and additional thickness of thermal insulation.

We have reviewed the reactor cell wall construction in some detail. The design must take into account that the wall furnishes biological shielding, insulates against heat losses, provides double containment for the radioactive systems, and is the support structure for all major equipment in the reactor primary system. The cell is being designed for a pressure of about 50 psia; leak-tightness and other characteristics must satisfy the requirements for class B vessels,[2] concrete temperatures must be limited to less than 150°F, and dimensional changes due to thermal expansions must be accommodated. As a result of the review we have made some minor changes in the cell wall construction.

The reinforced concrete biological shielding is a minimum of 8 ft thick. Its maximum temperature is limited to less than 150°F by thermal insulation, gamma shielding, and a circulating-gas heat-removal system. The shielding is provided by the walls of inner and outer carbon steel vessels, which also furnish double containment for the fuel-salt system. Both vessels are designed for 50 psia, and about a 6-in.-wide annular space separates the 2-in.-thick walls. Nitrogen gas at essentially atmospheric pressure will flow through this space in a closed circulating system to remove a total of 0.5 Mw (thermal) of heat. The annular space will also be used for leak detection.

A 9-in. thickness of insulating firebrick is used inside the inner vessel as thermal insulation. Expansion joints are provided in the insulation to allow it to move with the vessel during temperature changes. A thin liner of stainless steel covers the inside of the firebrick to reflect radiant heat, to protect the insulation from damage, and to provide a smooth surface for the cell interior.

The reactor cell atmosphere will probably be nitrogen, normally operated at slightly below atmospheric

[1] M. W. Rosenthal *et al., MSR Program Semiann. Progr. Rept. Aug. 31, 1968,* ORNL-4344.

[2] American Society of Mechanical Engineers, Boiler and Pressure Vessel Code, Nuclear Vessels, sect. III, 1968.

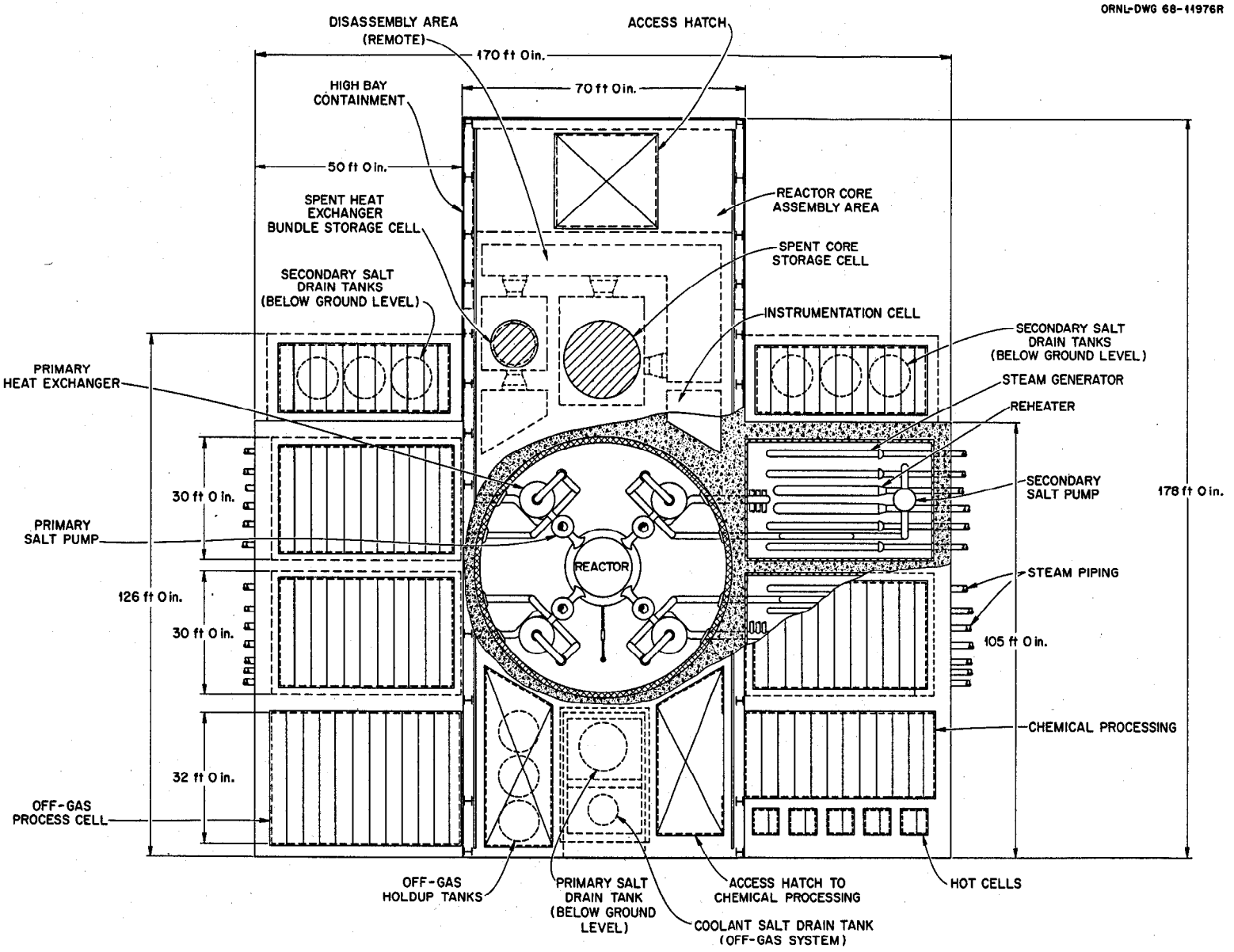

Fig. 5.1. Plan View of Reactor Building.

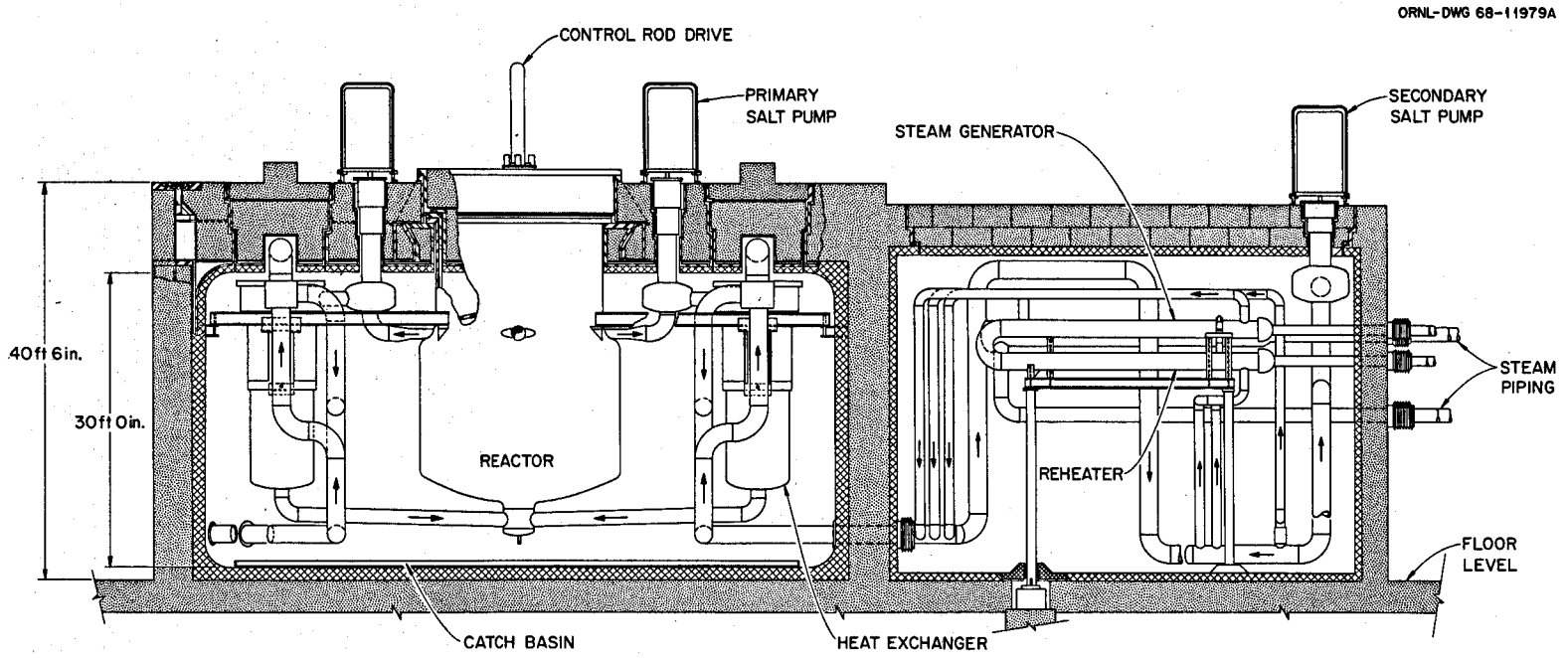

Fig. 5.2. Elevation of Reactor and Steam Cells.

pressure and at a cell temperature of about 1000°F. The ambient temperature in the cell is maintained by energizing electric heaters when required. The heaters are arranged in thimbles around the periphery of the reactor cell and can be maintained without violating the sealed containment. We expect that about 1 Mw of heating capacity will be required.

As the cell is heated to operating temperature, the inner vessel is allowed to expand downward and outward against spring supports. All penetrations of the cell will be provided with double bellows seals to accommodate relative piping movements. These joints will be arranged for periodic testing and replacement if required.

The biological shielding and double containment protection is continued across the top of the cell. Removable roof plugs are provided over all equipment that might require maintenance. The plugs are arranged in two layers, each 4 ft thick, and in such a manner that they can be replaced with a work shield for performing remote maintenance or, for replacement of core graphite, with a track-mounted transport cask and integral crane.

As shown in Fig. 5.1 the four steam-generating cells, the fuel processing cell, and the cell for storage of a spent reactor core are arranged around the centrally located reactor cell. The building housing the reactor cell complex is a sealed structure with a controlled ventilating system. This confinement provides an additional barrier to the escape of airborne activity. This barrier is particularly needed during maintenance operations.

We have also made some minor revisions to the flowsheet for the plant (see Fig. 5.3). The most important change is that the off-gas holdup tank is now cooled by a water system rather than a circulating salt loop. Design of the off-gas system is discussed in Sect. 7.1.

5.3 REACTOR

H. F. Bauman
E. S. Bettis
R. Blumberg
C. W. Collins
W. K. Furlong
E. C. Hise
H. A. McLain
J. R. McWherter
H. M. Poly
H. L. Watts

As the physical size of a molten-salt reactor of a given thermal output is increased over an optimum size, the nuclear performance decreases and the useful life of the graphite moderator and reflector is lengthened. Heretofore, optimum nuclear performance was a basic design requirement for the MSBR, and as a result the life of the core graphite in an optimized 1000 Mw (electrical) reactor was shown in the last semiannual report[1] to be only 1.8 years. We have now studied the possibilities for some tradeoffs in this regard. The details of the studies of the effects of reactor core size on nuclear performance are reported in Sect. 6.1 and are discussed here only with regard to changes in the mechanical design of the 1000 Mw (electrical) MSBR.

We found that if the size of the central region of the reactor core were increased from about 11 ft diam X 11 ft high, as previously reported,[1] to 14 ft diam X 13 ft high and axial reflector regions were added, the fuel conservation coefficient would be decreased by only a few percent but the estimated life of the core graphite would be doubled. In addition, increasing the thickness of the undermoderated outer zone of the core to slightly more than optimum would reduce the damage neutron flux incident on the inner face of the reflector graphite to a maximum of 4×10^{13} neutrons cm^{-2} sec^{-1} and thus assure that the reflector would normally last the lifetime of the plant (30 years) without requiring replacement. This would simplify the reactor design in that the reflector graphite need not be arranged with an ease of replacement similar to that provided for routine maintenance of the core.

When the computer input parameters were adjusted to provide a configuration with a 4-year life for the core graphite and a 30-year life for the reflector graphite, the results suggested that changes in some of the internals would improve the design of the reactor. The tradeoff studies indicated the importance of keeping the volume fraction of salt in the reflector low. They also showed that absorption of neutrons in the ^{135}Xe that could diffuse into graphite of high gas permeability in the reflector region would be too small to have much effect on the reactor performance. Allowing the gas permeability to be high considerably increases the size of graphite piece that can be manufactured, so this finding opened the way to use of large graphite pieces in the reflector. On the basis of these studies the design of the reactor was changed in several respects. The performance values and principal data based on the new reactor dimensions are given in Table 5.1, and the design changes are discussed below.

The central core region, designated zone I, is assembled from 15-ft-long graphite elements 4 X 4 in. in cross section as before. A hole through the center of each element and ridges on each side separate the pieces to furnish flow passages for the salt and provide 13 vol % of salt in the most active portion of the core. The elements are maintained in a compact octagonal array, as shown in Figs. 5.4 and 5.5.

Outside the more active core region there is an undermoderated region containing 37% by volume of salt and designated as zone II. This region reduces the fissioning, and therefore the neutron leakage from the core, by increasing the fraction of absorptions in the thorium. We reduced the thickness of the undermoderated portion to 15 in., and rather than using graphite spheres, we now provide 2-in. by 10-in. by 14-ft-long graphite slabs with flow passages between them to provide the specified salt volume and for cooling.

Between the undermoderated region and the reflector graphite there is a 2-in.-wide annular space filled entirely with fuel salt which accommodates relative dimensional changes, provides clearance for removing and replacing the reactor core assembly, and further reduces the neutron leakage. The width of this space is a compromise with the fuel-salt inventory.

The reflector region consists of 12- by 30- by 48-in.-high graphite blocks stacked around the removable core assembly. As with the core elements, the buoyant force of this graphite in the fuel salt is normally restrained by the top head structure. When the reactor is empty of salt, the weight is carried by the lower head. There is a $\frac{1}{4}$-in. annular clearance between the reflector graphite and the vessel wall to permit an upward flow of fuel salt to cool the wall and maintain it below the design temperature of 1300°F. Hastelloy N

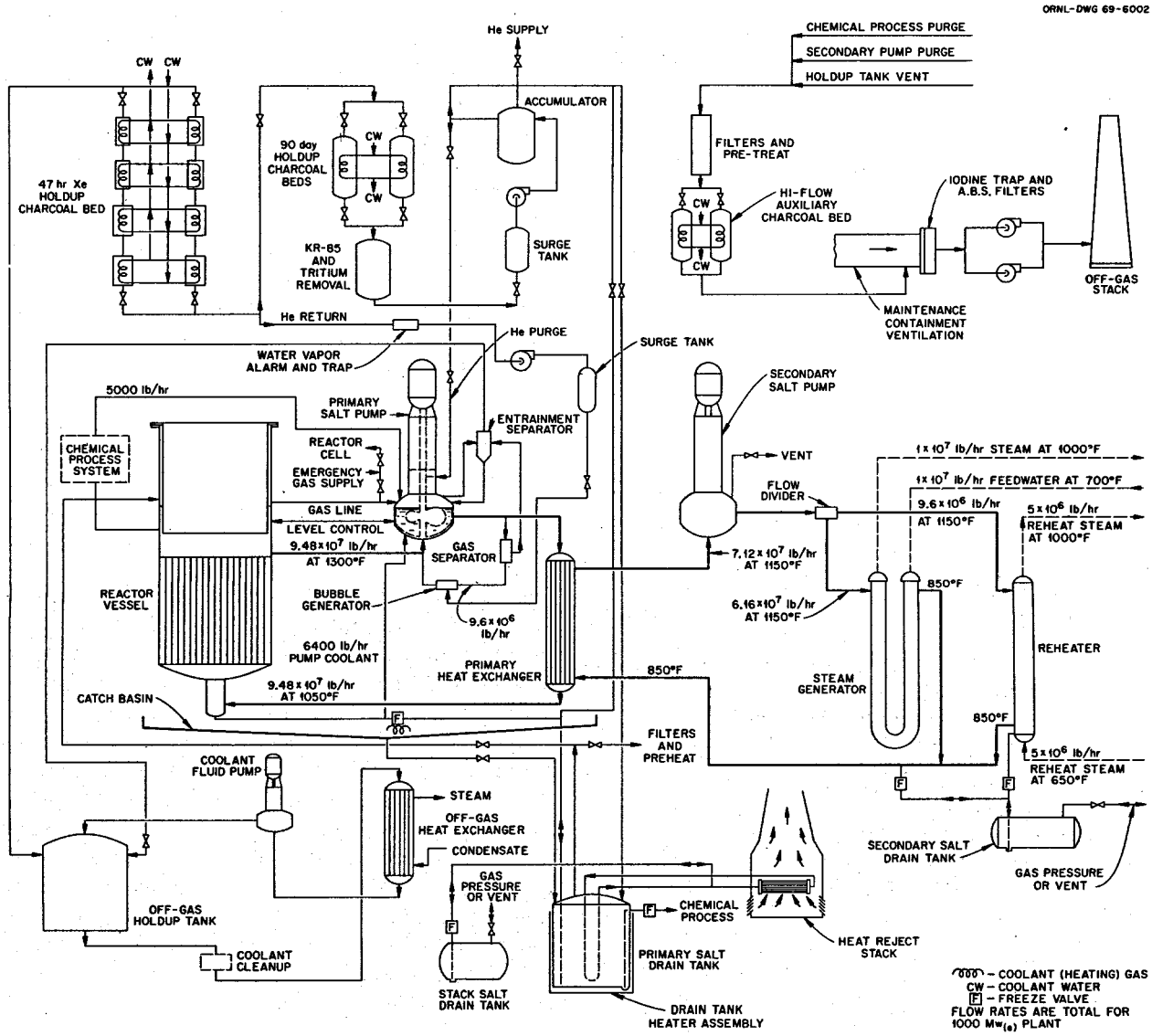

Fig. 5.3. Flow Diagram of 1000-Mw (Electrical) Reactor Plant.

rings mounted in grooves in the blocks, as shown in Fig. 5.5, expand with temperature and cause the graphite to move outward and maintain its relative position with the wall as the system is heated to operating temperature.

The graphite reflector blocks at the bottom of the vessel are slotted to fit over radial Hastelloy N webs in the bed plate which supports the reflector. Although the space between the blocks will increase from about 0.05 in. to 0.1 in. as the system is heated, this arrangement will assure essentially uniform spacing. Hastelloy N rods also run vertically from top to bottom of each stack of graphite reflector blocks to provide vertical alignment. These rods are not secured to the vessel, however.

Table 5.1. Principal Data for 1000 Mw (Electrical) MSBR Station

Plant	
Thermal capacity of reactor, Mw	2250
Gross electrical generation, Mw	1035
Net electrical output of plant, Mw	1000
Overall thermal efficiency, %	44.4
Reactor	
Reactor vessel inside diameter, ft	22
Vessel height at center, ft	20
Vessel wall thickness, in.	2
Vessel head thickness, in.	3
Vessel design pressure, psi	75
Core height, ft	13
Number of core elements	1412
Length of zone I portion of core elements, ft	13
Overall length of core elements, ft	~15
Distance across (octagonal) flats, core zone I, ft	14
Thickness of undermoderated region, zone II, radial, in.	15
Thickness of undermoderated region, zone II, axial, in.	9
Thickness of annulus between reflector and core zone II, in.	2
Reflector thickness, radial, in.	30
Average axial reflector thickness, in.	~22
Volume fraction of salt in core zone I	0.13
Volume fraction of salt in undermoderated region, zone II	0.37
Average core power density, kw/liter	22.2
Maximum thermal neutron flux, neutrons cm^{-2} sec^{-1}	7.9×10^{14}
Maximum graphite damage flux (>50 kev), neutrons cm^{-2} sec^{-1}	3.2×10^{14}
Graphite temperature at maximum flux region, °F	1284
Estimated useful life of graphite in core, years	4
Total weight of graphite in reactor, lb	650,000
Weight of removable core assembly, lb	480,000
Maximum flow velocity in core, fps	8.5
Pressure drop due to salt flow through reactor, psi	18
Total salt volume in primary system, ft^3	1720
Fissile fuel inventory of reactor and processing plant, kg	1470
Thorium inventory, kg	68,000
Breeding ratio	1.06
Yield, %/year	3.3
Doubling time, compounded continuously, years	21

There is an undermoderated region at both the top and bottom of the reactor core. The regions are formed by molded extensions on each end of the core elements that provide a salt-to-graphite volume ratio of about 0.37. The extensions also allow orificing to obtain the desired flow distribution through the core. By varying the salt velocity from about 8.5 fps at the center to about 2 fps near the periphery, a temperature rise of about 250°F can be attained in all flow channels.

The nuclear calculations indicated that axial reflectors would improve the reactor performance sufficiently to warrant including them in the design. The reflectors would also provide thermal shields to protect the Hastelloy N heads from radiation damage. The axial reflector graphite pieces are molded in the form of wedges. They are supported at each end and spaced so that at operating temperature there is about 0.1 in. between them. Holes are provided in the bottom support plate for salt circulation through the bottom axial reflector. The top reflector is cooled by a salt stream that flows upward through the eight 3-in.-diam holes that are provided in the undermoderated region (zone II) for insertion of lifting rods when the core graphite is to be replaced. The fuel salt flows between the top graphite reflector wedges and the head of the vessel and then exits with the bulk of the fuel salt leaving the reactor.

The above-mentioned lifting rods are different from the permanently installed rods shown in previous concepts. Eight seal-welded ports are now provided in the top head of the reactor vessel through which the temporary lifting rods can be inserted prior to the lifting operation. The $2\frac{1}{2}$-in.-diam rods engage the bottom lifting plate by a ball latch which is actuated by a push rod passing upward through each lifting rod. After the rods are engaged they are also attached to the top head so that the entire core can be removed as an assembly. The new arrangement removes Hastelloy N from the periphery of zone II of the core region during reactor operation, where it acted as a nuclear poison, and also eliminates the possibility of radiation embrittlement of the lifting rods.

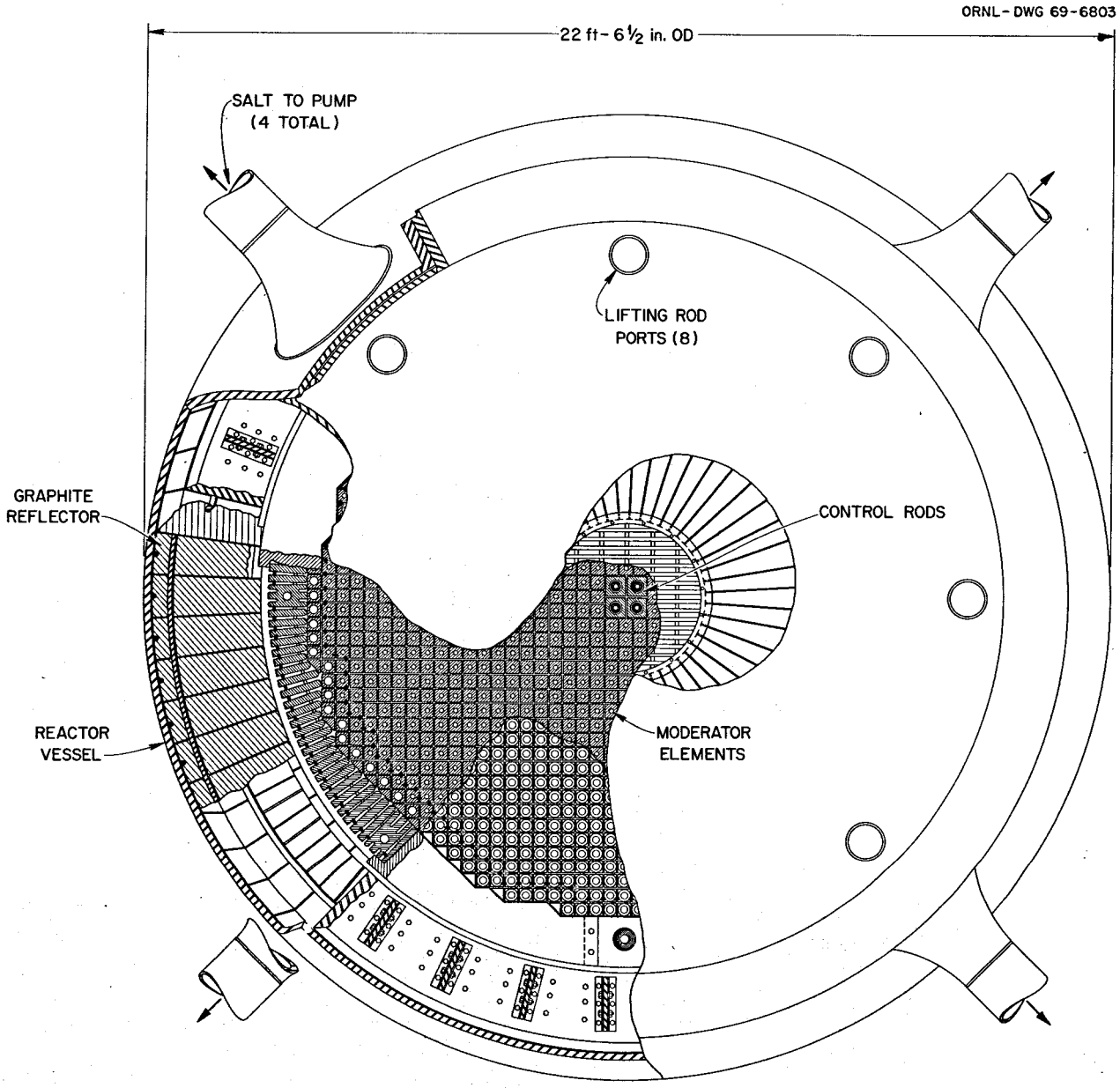

Fig. 5.4. Plan View of MSBR Vessel.

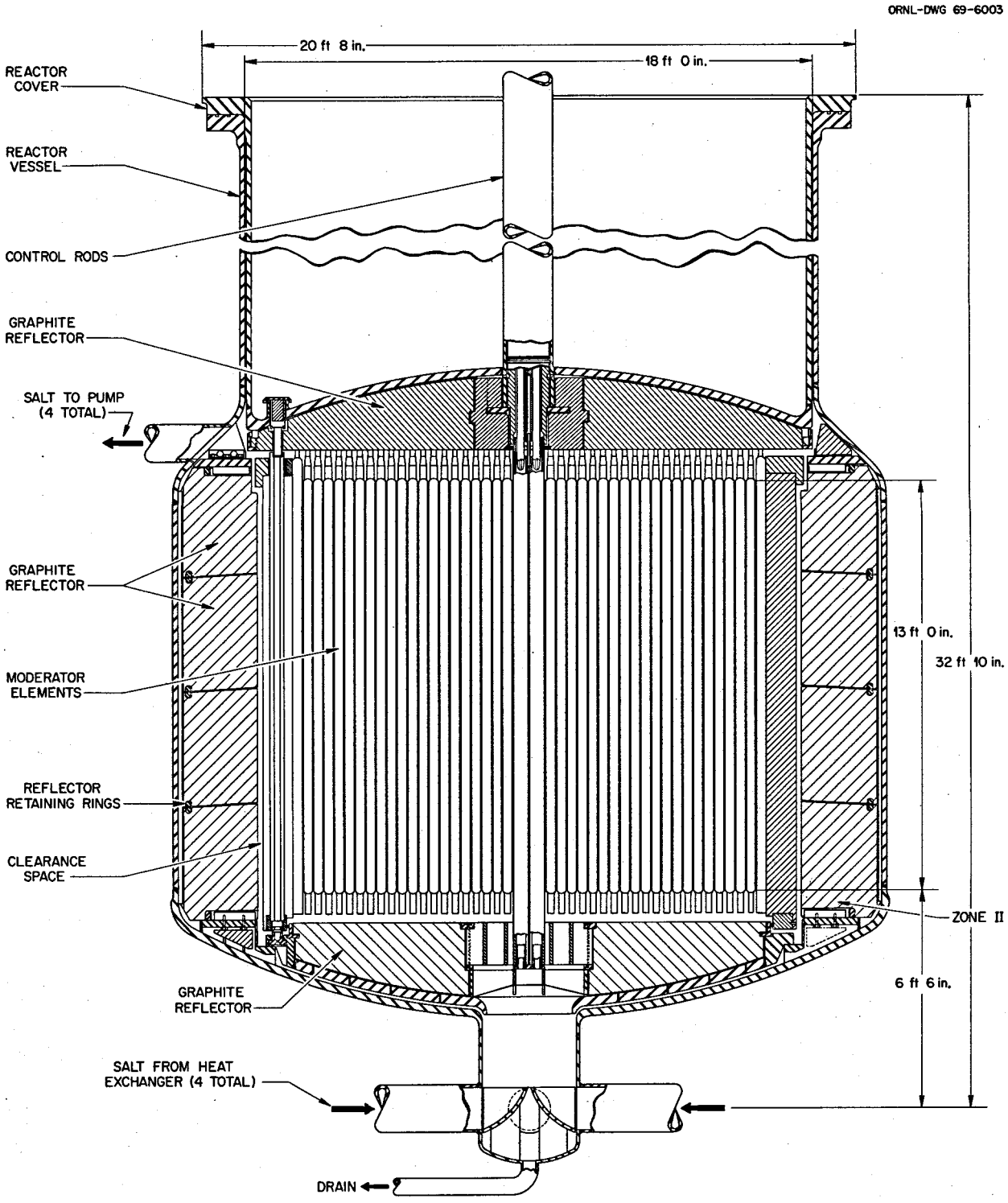

Fig. 5.5. Sectional Elevation of MSBR Vessel.

5.4 PRIMARY HEAT EXCHANGERS

C. E. Bettis H. A. Nelms
H. A. McLain H. L. Watts

The basic design concept for the primary heat exchangers remains unchanged since the last semiannual report.[1] Completion of stress calculations and consideration of problems associated with the baffles, however, led us to revise the upper tube-sheet arrangement. This led to changes in the configuration of the upper head.

A cross section of the revised heat exchanger design is shown in Fig. 5.6, and principal data are given in Table 5.2.

The $\frac{3}{8}$-in.-OD by 22-ft-long tubes are assumed to have spiral grooving to improve the heat transfer and thus reduce the tube-side volume of fuel salt inventory in the exchanger. To reduce tubing stresses, the revised design has shallow sine-wave bends in the upper portion of the tubes, which are bent 90° at the top into an L shape. Rather than the horizontal tube sheet previously used, the tubes are now welded into a cylindrical vertical tube sheet at the top of the exchanger. This arrangement permits a thinner tube sheet than if a flat head were used and also allows the top head seal weld to be located in a cooler region and be more readily accessible at the top of the exchanger.

The upper portion of the tubing containing the bends is not grooved. Since baffling is also not employed in the bent-tube region, the top 5.5 ft of the bundle experiences parallel flow, and the overall heat transfer performance is not as good as previously reported. An 0.8 baffle leakage factor was applied to the heat transfer in the cross-flow region; a leakage factor of 0.5 was used in the pressure drop estimates. As in the previous heat transfer studies, the spiral grooving on the tubes was assumed to enhance the heat transfer coefficient by a factor of 2 on the inside of the tubes and by a factor of 1.3 on the outside. Corresponding pressure drops were increased by these same factors. In revising the design the same number of tubes and the same shell diameter were assumed. This may require some small adjustment when the circumferential and radial pitches for the tube layout are studied more closely.

As with the past straight-tube design, the tube bundle is arranged for removal and replacement in the unlikely event of tube leakage. The concentric cooling salt piping U at the top can be removed, the top clamp on the shell loosened and set aside, the seal weld ground away, and the bundle withdrawn. All these operations must be performed with remotely operated tooling.

Table 5.2. Principal Data for Primary Heat Exchanger

For each of four units

Thermal capacity, Mw (thermal)	563
Tube-side conditions	
Fluid	Fuel salt
Tube size, OD, in.	$\frac{3}{8}$
Approximate length, ft	22
Number of tubes	5920
Inlet-outlet temperatures, °F	1300–1050
Mass flow rate, lb/hr	23.7×10^6
Volume of fuel salt in tubes, ft^3	64
Pressure drop due to flow, psi	129
Shell-side conditions	
Fluid	Coolant salt
Shell ID, ft	5.4
Central tube diameter, ft	1.7
Baffle spacing, ft	1.1
Baffle cut, %	40
Inlet-outlet temperatures, °F	850–1160
Mass flow rate, lb/hr	17.8×10^6
Pressure drop due to flow, psi	74
Approximate overall heat transfer coefficient, Btu hr^{-1} ft^{-2} $(°F)^{-1}$	~950

The shell of the exchanger has been designed for a maximum temperature of 1300°F and an allowable primary stress of 3500 psi.

A computer program was written to optimize the straight-tube heat exchanger design to obtain the minimum tube-side (fuel salt) volume within the pressure drop limitation of 130 psi prescribed by the hydraulic head delivered by the primary-salt pump. After adoption of the bent-tube design, hand calculations have been used, with the machine calculations as a reference, until the computer program can be revised to accommodate the new design.

5.5 STEAM GENERATOR AND SUPERHEATER

C. E. Bettis W. C. Stoddard
H. A. McLain H. L. Watts

The U-tube, U-shell horizontal steam generator pictured in the last semiannual report[1] remains unchanged in appearance, but the data have been slightly revised due to use of more recent values of the physical properties for the coolant salt and a change in the baffle spacing. The revised data are given in Table 5.3.

The revised concept of the steam generator uses constant baffle spacing throughout. There should be little tendency for shell-side stratification. The need for wire lacing or some other form of tube support to minimize vibrations has not yet been fully explored.

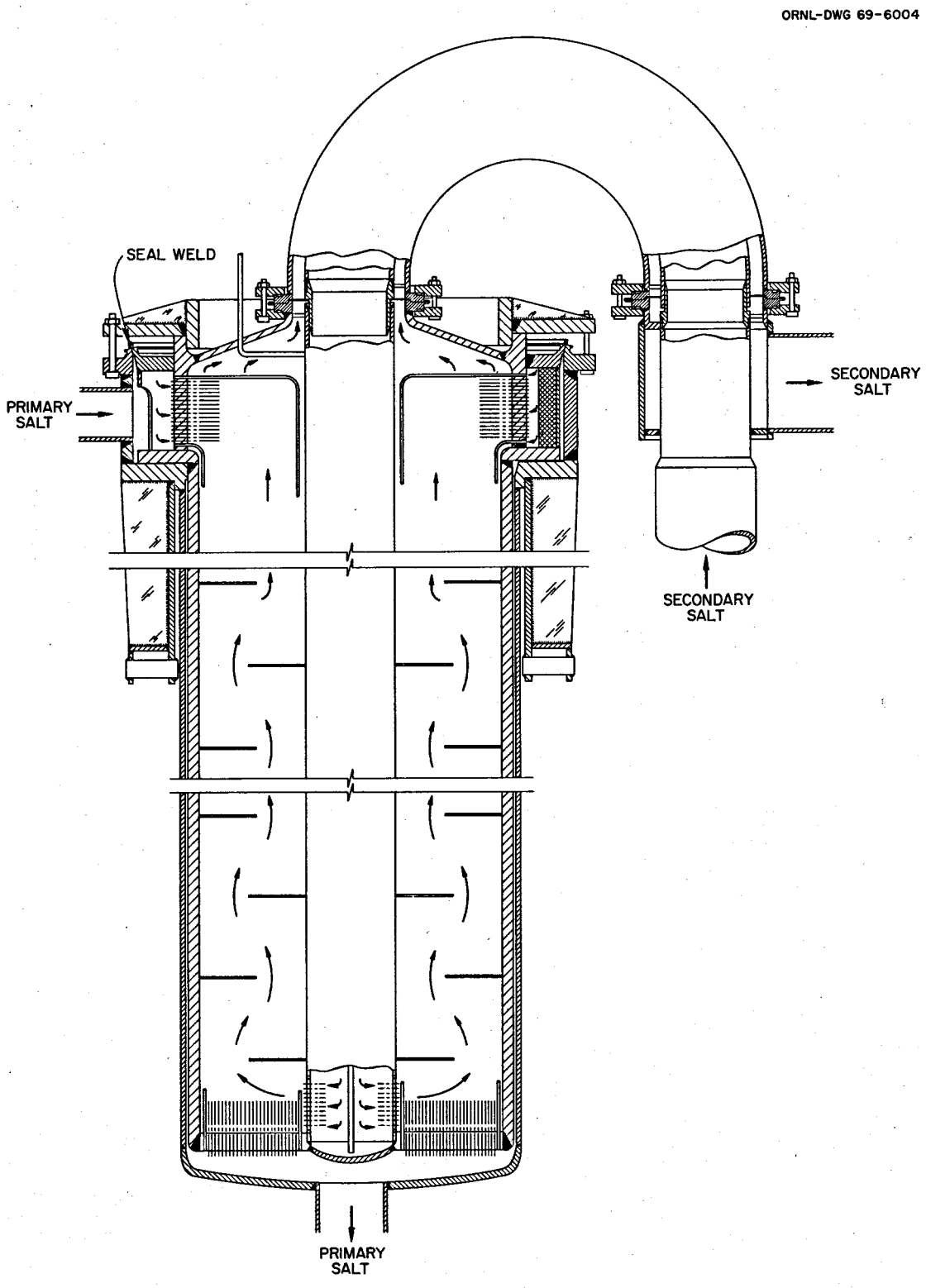

Fig. 5.6. Sectional Elevation of MSBR Primary Heat Exchanger.

Table 5.3. Steam-Generator and Superheater Data

For each of 16 units

Thermal capacity, Mw (thermal)	120.7
Tube-side conditions	
Fluid	Steam at 3600 psia
Tube size, OD, in.	1/2
Approximate length, ft	73
Number of tubes	384
Inlet-outlet temperatures, °F	700–1000
Mass flow rate, lb/hr	630,000
Total heat transfer surface, ft^2	3628
Pressure drop due to flow, psi	150
Shell-side conditions	
Fluid	Coolant salt
Shell ID, ft	1.5
Baffle spacing, ft	4
Inlet-outlet temperatures, °F	1150–850
Mass flow rate, lb/hr	3.85×10^6
Pressure drop due to flow, psi	60
Approximate overall heat transfer coefficient, Btu hr^{-1} ft^{-2} $(°F)^{-1}$	764

5.6 STEAM REHEATER

C. E. Bettis M. Siman-Tov
H. A. McLain H. L. Watts

The steam reheater is a horizontal, counterflow, single-pass shell-and-tube exchanger with disk-and-doughnut baffles which transfers heat from coolant salt in the shell side to steam in the tubes. The design concept previously reported[1] has not been changed, but the heat transfer and pressure drop estimates have been revised to make use of more recent values of the physical properties of the coolant salt. The revised data are listed in Table 5.4.

Table 5.4. Principal Data for Steam Reheater

For each of eight units

Thermal capacity, Mw (thermal)	36.6
Tube-side conditions	
Fluid	Steam at 550 psia
Tube size, OD, in.	5/8
Approximate length, ft	21.5
Number of tubes	580
Inlet-outlet temperatures, °F	650–1000
Mass flow rate, lb/hr	642,000
Pressure drop due to flow, psi	30
Total heat transfer surface, ft^2	2035
Shell-side conditions	
Fluid	Coolant salt
Shell ID, in.	22.4
Baffle spacing, in.	6.6
Inlet-outlet temperatures, °F	1150–850
Mass flow rate, lb/hr	1.2×10^6
Pressure drop due to flow, psi	60
Approximate overall heat transfer coefficient, Btu hr^{-1} ft^{-2} $(°F)^{-1}$	355

This heat exchanger will probably not encounter vibration problems, because the velocities are less than 6.5 fps and the tubes are supported by baffles on a relatively close spacing.

5.7 REMOVAL OF REACTOR AFTERHEAT

W. K. Furlong

5.7.1 Introduction

The normal method of removing reactor afterheat is to transfer it to the steam system by continuing circulation of both the primary and secondary salts. In the event of power failure, battery-operated pony motors on the salt pumps will provide the required circulation. Several abnormal situations would require alternate means of afterheat removal, however. Examples are (1) major rupture of the primary system, with subsequent rapid draining of the salt to the catch basin; (2) a leak in the primary system such that circulation by the pumps will eventually cease; (3) loss of flow in more than one secondary loop; (4) mechanical failure of all primary-salt pumps; and (5) failure of the steam system. This section briefly discusses alternate means of afterheat removal.

5.7.2 Sources of Afterheat

We identify the following five heat sources which remain in the primary system after shutdown:

1. fission due to decay of flux at shutdown, including the effect of delayed neutron precursor transport by the salt,
2. decay of fission products (and daughters) dispersed in the primary salt,
3. decay of noble-metal fission products (and daughters) deposited on graphite and Hastelloy N surfaces,
4. decay of gaseous krypton and xenon (and daughters) diffused into the graphite,
5. heat stored in moderator and reflector graphite.

The contribution from fission, aggravated by pump coastdown, is shown in Fig. 5.7 for ^{235}U fuel and in Fig. 8.3 for ^{233}U fuel. The detailed analysis has been

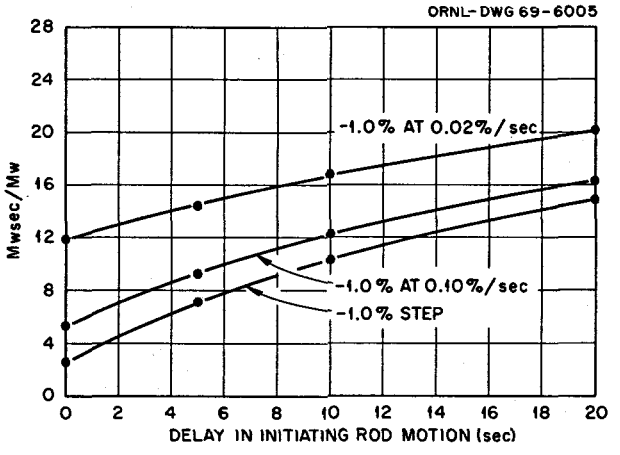

Fig. 5.7. Integral of Reactor Power at 300 sec After Start of Primary Pump Coastdown vs Delay Between Initiation of Coastdown and Insertion of Reactivity for ^{235}U.

made by Sides.[1,3,4] Various combinations of magnitude and rate of reactivity insertion, salt flow change, and delay prior to reactivity insertion have been considered. As an example, the case of flow coastdown with 1% negative reactivity inserted at 0.1%/sec after a 1.0-sec delay, with ^{235}U fuel, would result in 3.75 Mwhr of energy production in the salt. Using only the heat capacity of the salt, this would result in a 113°F rise in salt temperature. In practice, the core heat capacity, which is twice that of the salt, would become available after the salt reached 1200°F (average initial temperature is 1175°F for salt and 1200°F for core graphite). The net effect would be a rise to 1250°F, at 5 min after shutdown, for the salt-graphite system due to the effect of fission heat production alone.

The distribution of fission products in the primary system has been estimated by Briggs[5,6] and Kedl[7] and is discussed in Sects. 5.8 and 7.2. Heat-generation rates and total heat production based on this distribution have been presented by Tallackson.[8] Figure 5.8 shows the heat generation from sources 2, 3, and 4 above.

5.7.3 Heat-Removal Systems

Three heat-removal systems are presently proposed: (1) a drain tank cooling system (for sources 1 and 2

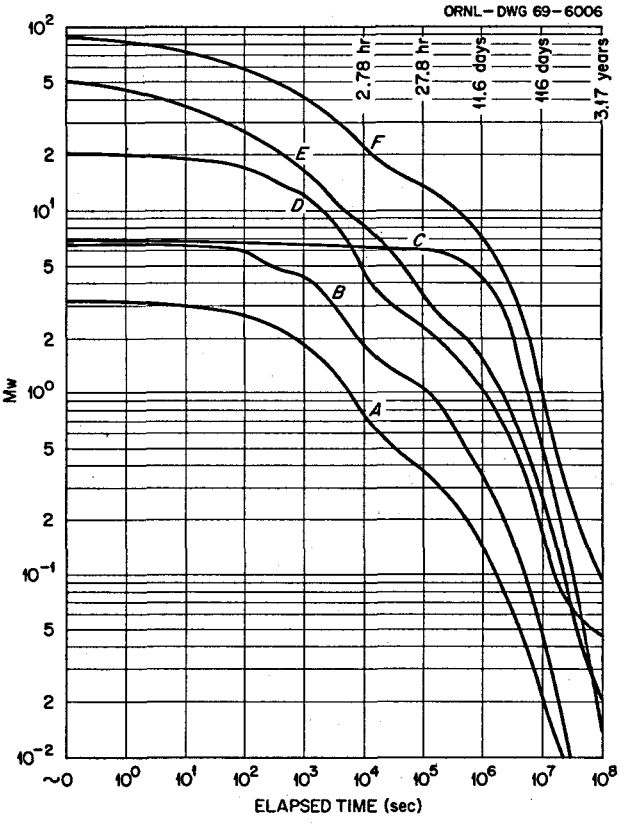

Fig. 5.8. Afterheat Distribution with Saturation Concentrations of Fission Products in a 1000-Mw (Electrical) Single-Fluid MSBR Fueled with ^{235}U. Curve *A* – Afterheat in core region produced by Kr and Xe diffused into the graphite plus heating by 10% of the total noble metal fission products assumed to be plated on surfaces. Curve *B* – Afterheat in the four heat exchangers produced by 40% of total noble metal fission products plated on metal surfaces. Curve *C* – Afterheat in the chemical processing system produced by decay of protactinium and long-lived fission products. Curve *D* – Afterheat in the off-gas system produced by Kr and Xe plus heating by 50% of the total noble metal fission products. Curve *E* – Afterheat produced by fission products which remain dispersed in the primary salt. In curve *A* the concentration of Kr + Xe is that which produces 0.0065 $\delta k/k$ and is obtained by gas sparging on a 30-sec removal cycle. Curves *A*, *B*, and *D* are based on the assumption that the noble metals are either deposited immediately on metal and graphite surfaces or enter the off-gas system immediately. In curves *A*, *B*, and *D* the afterheat includes that from decay of the daughter products of the noble metals and gases.

[3]Internal memorandum from W. H. Sides, "Calculations of Neutron Density Following Primary Salt Pump Coastdown and Insertion of Negative Reactivity," February 1969.

[4]Internal memorandum from W. H. Sides, "Calculations of Neutron Density After Negative Step Insertion of Reactivity," September 1968.

[5]Internal memorandum from R. B. Briggs, "Distribution of Heat Production in a 1000-Mw(e) MSBR," October 25, 1968.

[6]Internal memorandum from R. B. Briggs, "Estimate of the Afterheat by Decay of Noble Metals in MSBR and Comparison with Data from the MSRE," November 1968.

[7]*MSR Program Semiann. Progr. Rept. Aug. 31, 1967*, ORNL-4191.

[8]Internal memorandum from J. R. Tallackson, "Revised Estimates of Maximum Afterheat Deposition in MSBR by Noble Metals," October 1968.

listed above), (2) a core and vessel cooling system (for sources 3 and 4), and (3) an off-gas cooling system. The latter is discussed in Sect. 7.1 of this report.

The general concept of the drain tank and associated cooling system has been previously reported.[9] A stack 150 ft high and 30 ft in diameter was mentioned, but further analysis now indicates that a stack height of about 50 ft with a 45-ft diameter is preferable. In addition, the natural-circulation fluoroborate system will now be made to be independent of the off-gas coolant system because the latter may operate at much lower temperatures. An independent study[10] has recently corroborated the feasibility of our proposed natural-circulation system. A maximum drain tank wall temperature of 1466°F was also previously reported. Although a detailed analysis of transient temperature and flow conditions remains to be completed, we are confident that a temperature somewhat lower than this value will result. Several alternative coolants, including Hitec[11] and water, have been suggested. Hitec has the disadvantage of instability at temperatures on the order of those expected. Water, in a two-phase system, has some advantages, and it is planned to look further at the use of this coolant. With the use of water, it would be possible to unify the off-gas and drain tank cooling systems.

Sources 3 and 4, listed in Sect. 5.7.2 above, affect the reactor and the heat exchangers. The heat from the noble metals deposited on the heat exchanger tubes would be transferred to the steam system, using either forced or natural circulation in the coolant loops. Several means of removing the heat from the reactor have been considered. One would be to maintain the outer vessel surfaces at a relatively low temperature (~1100°F) and transfer the energy by radiation through the graphite region to the vessel. A rough estimate of the resulting peak temperature has been made by Tallackson,[12] and a revised version of those results is shown in Fig. 5.9. The method used to maintain the 1100°F surface temperature has not been specified, but some suggestions include the use of a

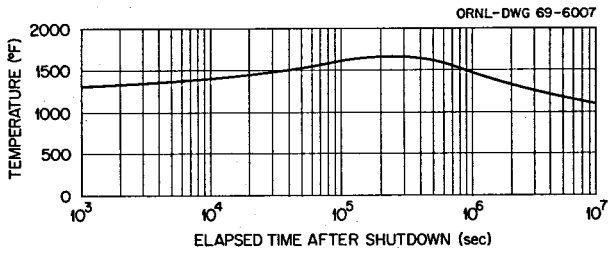

Fig. 5.9. Estimated Maximum Temperature of Graphite in Core After Shutdown of MSBR.

gas-cooled shroud around the vessel, the use of cooled-plate coils in the cell, and movable sections of cell wall insulation to allow radiation and convection heat transfer to the thermal shield cooling system.

A second method of reactor afterheat removal, and the one which has received the greatest attention in the past six months, is to circulate a heavy gas (argon or nitrogen at about 50 psia) with the primary-salt pumps operated at 1200 rpm. The heat would be transferred via the secondary system to the steam system. If any of the coolant-salt pumps are not operable, natural circulation will provide adequate flow. If the steam system is not operable, the heat capacity of the secondary system would be adequate for several hours. The speed of 1200 rpm is above the normal primary pump operating speed but below the critical speed. The pumps would have a separate set of windings for this purpose. To prevent loss of circulating gas in the event of a crack in the primary system and to reduce the stress on the vessel, the reactor cell would be pressurized up to 50 psia. Approximately 25,000 scf of either argon or nitrogen would be required and could be stored in cylinders outside the cell. A helium supply is provided for the off-gas system, and it would have been desirable to also use this for removal of afterheat. However, with the gases in laminar flow, the low Reynolds number of the light gas gives such a high friction factor that the resulting system characteristic intersects the pump characteristics at an intolerably low flow. With argon or nitrogen, however, a flow rate of 17,000 gpm per pump is attained at 1200 rpm. With three of the four primary pumps operating at this speed, 7.7 lb of gas per second can be circulated through the reactor internals.

Using the method of Dusinberre,[13] a program was written to analyze the transient temperatures of the moderator elements (where most of the heat source is

[9] *MSR Program Semiann. Progr. Rept. Feb. 29, 1968*, ORNL-4254.

[10] H. A. Bailey and M. Mondlak, *Design Study of a Natural Convection Cooling System for the Primary Salt Drain Tank of the MSBR*, ORNL-MIT-60 (to be published).

[11] A Du Pont trade name for a eutectic mixture of KNO_3, $NaNO_2$, and $NaNO_3$.

[12] Internal memorandum from J. R. Tallackson, "Revised Estimate of MSBR Core Temperatures Developed After Shutdown," November 1968.

[13] G. M. Dusinberre, *Heat Transfer Calculations by Finite Differences*, International Textbook Company, Scranton, Pa., 1961.

concentrated). Results indicate that the temperature rise can be held to about 100°F above the initial temperature. The temperature-time history is shown in Fig. 5.10. The initial conditions depend on a number of factors, particularly those affecting fissions due to delayed neutrons, source No. 1. Of specific importance are the amount and rate of shutdown reactivity insertion, the delay prior to reactivity insertion, whether or not primary-salt flow is maintained during shutdown, and, if flow is not maintained, the rate of coastdown. In addition to the temperature of the reactor internals when the gas is introduced and the time allowance for thawing the drain valve, draining the salt, introducing the gas, and possibly pressurizing the cell, another important initial condition is the amount of energy stored in the graphite reflector. Besides considerations of graphite life, a major incentive to reduce the reflector temperatures is thus to minimize this stored energy. In present estimates the reflector peak temperatures are on the order of those in the moderator elements, thus minimizing this aspect of the problem, and most reflector sections will now contribute their heat capacity to that available inside the reactor. Allowing 300 sec to thaw the freeze valve and another 700 to completely drain the salt, and assuming a shutdown such that energy is produced as shown in Fig. 5.7 (with 1% reactivity at 0.1%/sec and a 1-sec delay), the average initial graphite temperature inside the reactor will be about 1300°F. The vessel and head, not in contact with large masses of hot salt, will normally be somewhat cooler than the graphite. In summary, on the basis of the initial temperature and temperature rise estimates, the hottest part of the reactor when pressurized gas is used for cooling should not exceed 1400°F under conditions where it is necessary to rapidly drain the primary salt. Analysis of the peak transient temperature in the vessel is still in progress.

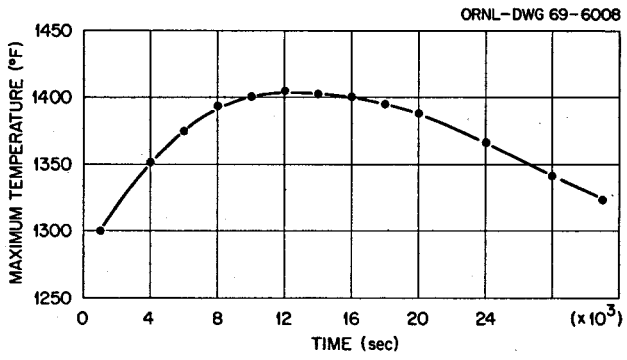

Fig. 5.10. Temperature-Time History of Maximum Graphite Temperature Using Nitrogen Coolant Circulated at 50 psia by Three Pumps at 1200 rpm.

5.8 DISTRIBUTION OF NOBLE-METAL FISSION PRODUCTS AND THEIR DECAY HEAT

R. B. Briggs J. R. Tallackson

Data obtained from operation of the MSRE have indicated that the fission products ranging from element No. 41, niobium, through element 52, tellurium, are reduced to the metallic state in the fuel salt. The metal particles then deposit on metal and graphite surfaces in the reactor and also appear in the off-gas. The mechanism for transporting the particles to the surfaces of metal, graphite, and bubbles of gas circulating in the fuel has not been established, but the particles are believed to be sufficiently small for the transport to be similar to that of molecular species.[14] On the basis of this assumption, the mass transfer coefficients for the metal particles would be proportional to those that have already been calculated for xenon and krypton.

The mass transfer coefficient for xenon, the fluid velocity, and the surface area in each region of the MSBR are shown in Table 5.5. The mass transfer coefficient for metal particles is assumed to be the mass transfer coefficient for xenon multiplied by a constant that has a value less than 1. Under steady-state

[14] S. K. Beal, *Transport of Particles in Turbulent Flow to Channel or Pipe Walls*, WAPD-TM-765 (April 1968).

Table 5.5. Estimates of Mass Transfer Coefficients for Xenon, Surface Area, and Fluid Velocity in MSBR

	Fluid Velocity (fps)	Mass Transfer Coefficient for Xenon (ft/hr)	Surface Area (ft^2)
Graphite			
Core center	14	1.5	4,000[a]
Core outer			
Core average	6	0.8	27,700
Blanket	0.7	0.06	1,700
Metal			
Heat exchanger	9	2.4	40,000
Piping	26	1.2	1,100
Reactor vessel	?	0.5	2,400
Gas bubbles		2	52,000[b]

[a] Assumed to be 15% of core.
[b] Bubble fraction = 0.01 with 0.020-in.-diam bubbles.

Table 5.6. Heat Generated by Decay of Saturation Levels of Noble-Metal Fission Products Produced in a 2250 Mw (Thermal) MSBR Fueled with ^{235}U[a]

Element	0 sec			10^2 sec			3×10^2 sec, 0.0833 hr			10^3 sec, 0.278 hr			3×10^3 sec, 0.833 hr			10^4 sec, 2.78 hr			3×10^4 sec, 8.33 hr		
	β^-	γ	Total	β^-	γ	Total	β^-	γ	Total	β^-	γ	Total	β^-	γ	Total	β^-	γ	Total	β^-	γ	Total
Nb	1665	2,550	4,215	1397	1913	3,310	728	364	1,092	808	1044	1,852	545	860	1405	160	587	747	36	476	512
Mo	870	870	1,740	706	845	1,551	611	755	1,366	440	498	938	273	218	491	233	143	376	220	135	355
Tc	1052	1,465	2,517	1000	1425	2,425	882	1308	2,190	539	836	1,375	129	226	355	1	75	76	0	71	71
Ru	94	227	321	86	226	312	76	226	302	64	224	288	59	219	278	50	202	252	35	173	208
Rh	65	43	108	59	43	102	58	42	100	55	40	95	51	36	87	49	31	80	48	26	74
Te	1233	2,056	3,289	1201	2008	3,209	1137	1922	3,049	944	1643	2,587	566	1070	1636	140	328	468	57	144	201
Subtotal	4979	7,211	12,190	4449	6460	10,909	3492	4617	8,109	2850	4285	7,135	1623	2629	4252	633	1366	1999	396	1025	1421
I	1154	3,002	4,156	1151	3000	4,151	1147	2988	4,135	1126	2935	4,061	1031	2712	3743	719	1965	2684	505	1471	1976
Total	6133	10,213	16,346	5600	9460	15,060	4639	7605	12,244	3976	7220	11,196	2654	5341	7995	1352	3331	4683	901	2496	3397

Element	10^5 sec, 27.8 hr			3×10^5 sec, 83.3 hr			10^6 sec, 278 hr			3×10^6 sec, 833 hr			10^7 sec, 2780 hr			3×10^7 sec, 8333 hr			10^8 sec, 27,778 hr		
	β^-	γ	Total	β^-	γ	Total	β^-	γ	Total	β^-	γ	Total	β^-	γ	Total	β^-	γ	Total	β^-	γ	Total
Nb	32	464	496	31	443	474	26.4	376.2	402.6	16.7	237.8	254.5	3.4	47.8	51.2	0	0.5	0.5	0	0	0
Mo	180	110	290	101	62	163	13.5	8.3	21.8	0	0	0	0	0	0	0	0	0	0	0	0
Tc	0	60	60	0	34	34	0	4.5	4.5	0	0	0	0	0	0	0	0	0	0	0	0
Ru	25	152	177	23	145	168	19.8	126.0	145.8	13.5	84.1	97.6	3.6	20.7	24.3	0.25	0.38	0.63	0	0	0
Rh	44	20	64	37	16	53	33.0	13.0	46.0	31.5	9.5	41.0	27.0	3.9	30.9	17.4	1.5	18.9	3.74	0.31	4.05
Te	47	107	154	30	54	84	12.2	12.7	24.9	6.5	4.1	10.6	2.4	1.3	3.7	0.4	0.2	0.6	0	0	0
Subtotal	328	913	1241	222	754	976	104.9	540.7	645.6	68.2	335.5	403.7	36.4	73.7	110.1	18.05	2.58	20.63	3.8	0.3	4.1
I	351	1137	1488	169	641	810	41.7	140.5	182.2	3.3	7.4	10.7	~0	0	0	0	0	0	0	0	0
Total	679	2050	2729	391	1395	1786	146.6	681.2	827.8	71.5	342.9	414.4	36.4	73.7	110.1	18.0	2.6	20.6	3.8	0.3	4.1

[a]Heat rates are in kilowatts at the indicated times after shutdown. This tabulation is from a FOULBALL-CALDRON computation in which it was assumed that the saturation levels of the noble metals are not reduced by chemical processing. These afterheat rates do not include the afterheat developed by noble metals that are born after shutdown and are the daughters of nonnoble parents.

conditions the metal particles in the primary system are distributed between the surfaces of graphite, metal, and bubbles in proportion to the products of the mass transfer coefficients and the surface areas.

Particle transport to metal, graphite, and bubbles by means of the assumed diffusion mechanism proceeds much faster than particle removal by the chemical processing system; therefore it was assumed that the chemical processing system effects no reduction in surface deposition. Assuming that once a particle reaches a surface it remains there, we find that 10% of the particles will deposit on graphite surfaces, 40% will deposit on metal surfaces, and 50% will be discharged with bubbles to the off-gas system.[7]

Use of this method to estimate the distribution of metallic fission products in the MSRE gives results that are reasonably consistent with the distribution based on analysis of specimens from the core. Direct extrapolation of data from the MSRE would lead to the conclusion that less than 10% of the metallic particles would deposit on the graphite in an MSBR and that the distribution would be different for each of the metallic elements. However, the MSRE data scatter considerably, so it seems reasonable to use the estimates above for MSBR design purposes. The results reported here are for the design as it existed in November 1968 and have not yet been adjusted to the current design.

The distributions shown above were used to estimate afterheating[8] by noble-metal fission products in the primary system. The distribution of, and heat produced in the graphite by, fission product krypton and xenon is discussed by Kedl in Sect. 7.2. In estimating heat production after shutdown, it was assumed that the iodine born in surface deposits after the salt has been drained remains there. For safety analyses it should be assumed that iodine born on surfaces escapes and must be contained.

Table 5.6 lists the principal noble-metal heat producers and their heat productions as a function of elapsed time after shutdown. Figure 5.8 includes curves of afterheat generation in the primary system vs time based on the distribution discussed above.

5.9 REACTOR TEMPERATURES, FLOWS, AND HEAT TRANSFER

W. K. Furlong H. A. McLain

5.9.1 Reactor Core

The basic approach in designing the MSBR core is to regulate the fuel-salt flow through each flow channel to achieve the desired 250°F temperature rise. Other objectives that must be considered in using this approach are that the fuel-salt inventory within the reactor, the pressure drop due to flow, and the vessel wall temperatures must all be kept to a minimum or within allowable limits. Since radiation-induced damage to the graphite is very sensitive to temperature, it is particularly desirable that the graphite temperatures be low in the regions of high damage neutron flux in order to assure at least a four-year useful life for the core moderator elements. The relationships between graphite life, damage flux, and temperature are shown in Fig. 5.11. It is also important that the radial reflector graphite have a sufficiently low temperature to allow a 30-year estimated life, as explained in Sect. 5.3.

The radial distribution of the fission power densities averaged over the total height of the core and axial reflectors in the present MSBR concept is shown in Fig. 5.12. The discontinuity in the curve is between zone I, having 13.2% salt volume, and zone II, having 37% salt volume. The axial distribution of the fission power density in zone I can be approximated closely by a cosine having an extrapolated length of 8.1 ft.

Heat is also generated in the graphite by the gammas produced in the core and by moderation of the neutrons. Heat deposition rates for a core configuration essentially the same as that of the present MSBR concept are shown in Fig. 6.3. To adjust the heat deposition rates of zones I and II of the reactor for the different peak and average core power densities in the two concepts, we assumed that five-sixths of the gamma

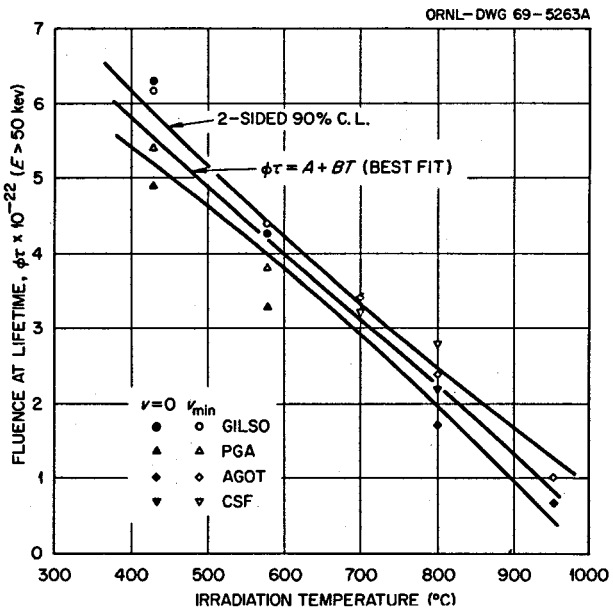

Fig. 5.11. Lifetime vs Temperature, MSBR Core Graphite.

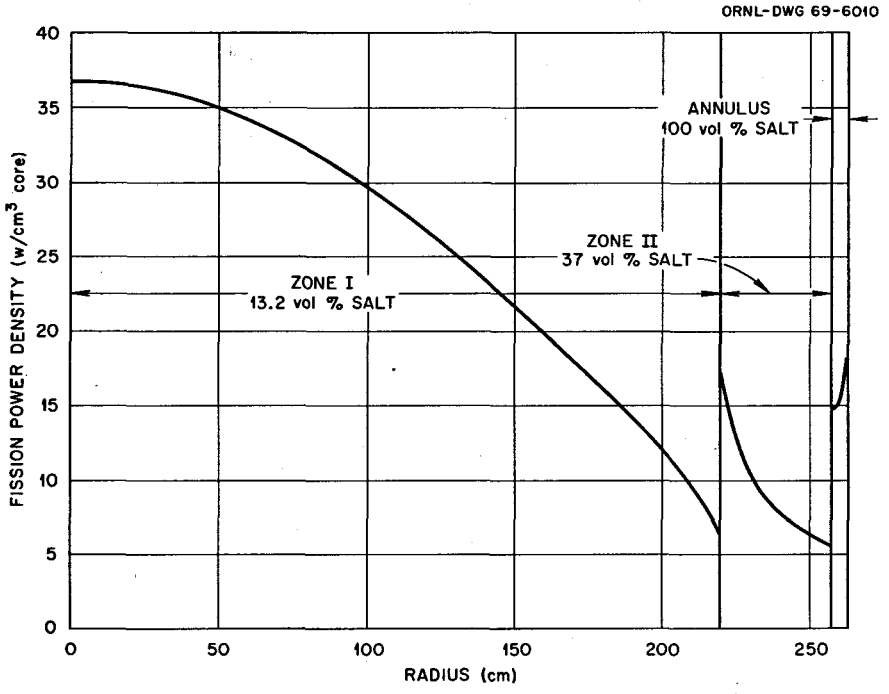

Fig. 5.12. Radial Distribution of Fission Power Density Averaged Over Length of MSBR Core and Both Axial Reflectors.

heating and all of the neutron slowing-down energy is proportional to the local power density and that the remaining one-sixth of the gamma heating is proportional to the average power density in the core.

Several factors influence the shape of the core moderator elements. Preliminary calculations indicated that the elements should be on a 4-in.-square pitch. The most recent physics calculations indicate that they should be designed so that the volume fraction of salt in zone I is 0.132 and in zone II is 0.37. To achieve the relatively low cost of fabrication of the elements by extrusion, the geometry should contain no radii of less than ¼ in. The central hole through the sticks should not be less than 0.6 in. in diameter to assure successful deposition of the pyrolytic graphite coating used to reduce the permeability to salt and xenon gas. Cognizance must be taken of the movement of the elements relative to each other with temperature- and radiation-induced dimensional changes.

As is evident in Fig. 5.12, the highest mass velocity of fuel-salt flow is required at the center of the reactor. If all the flow channels could have equal hydraulic diameters, the pressure drop due to flow through the core could be minimized, but the restriction on the minimum size of the central hole in the elements, mentioned above, dictates that the flow channels between the adjacent elements have smaller hydraulic diameters than the hole. The salt flow through the central hole must then be restricted by orificing. On this basis, the pressure drop of the salt flowing along the center line of the reactor has been determined to be about 18 psi. It can also be seen from Fig. 5.12 that the farther an element is from the center line, the lower the mass velocity of the salt must be to obtain the desired 250°F temperature rise in the salt moving upward through the core.

Two typical cross sections for the graphite moderator elements are shown in Fig. 5.13. The central part of the core, zone IA, will be made up of elements of the type shown in Fig. 5.13*a*, and those farther from the center, zone IB, will have the cross section shown in Fig. 5.13*b*. The hydraulic diameters of the channels between adjacent elements in zone IB are smaller than in zone IA. Since it would not be practical to size the flow passages between the elements at each radial distance from the center of the core to achieve an exact 250°F temperature rise, the central holes will be orificed so that the salt streams discharging from all these flow channels associated with each element will combine into a mixture of the desired temperature. The cross sections of the moderator elements for zone IIA of the reactor are identical to those shown in Fig. 5.13*b* except that the central hole diameter is 2.581 in. instead of 1.347 in.

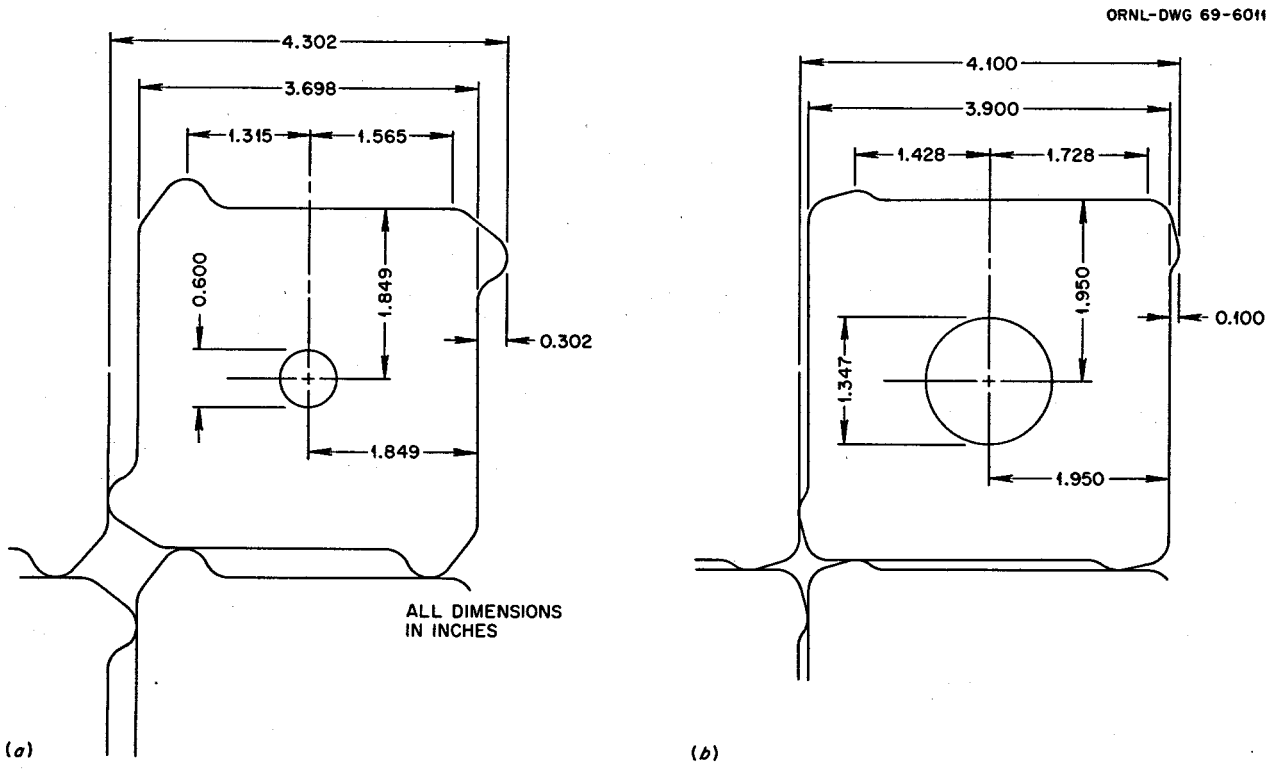

Fig. 5.13. MSBR Graphite Moderator Element for (*a*) Core Zone I-A, (*b*) Core Zone I-B.

Experiments have been reported in which the flow through channels formed by closely packed rods on a triangular pitch is greater than that predicted by the equivalent hydraulic diameter theory.[15] Use of this concept for calculating the salt flow rates through the MSBR core will therefore require verification and further study, particularly in the passages formed by the corners of four adjacent elements.

As would be expected, the highest steady-state graphite temperatures and the greatest irradiation to the moderator graphite would occur at the reactor center line. Calculations were made of the temperature distribution through an element along the center line, both at midheight of the core, where the salt is at an average temperature of 1175°F, and in a plane about 1 ft higher, where the salt is at 1200°F. The results are shown in Fig. 5.14. They show that at midheight the maximum temperature is 1284°F and at 1 ft above midelevation the temperature is 1307°F. Figure 5.14 also illustrates the importance of the central hole in the moderator elements in maintaining the temperatures within acceptable limits.

In making the calculations described above we assumed that the heat transfer coefficient between the graphite and the fuel salt could be predicted by the Dittus-Boelter relationship, that the effect of volumetric heat sources on heat transfer between the graphite and salt were negligible, and that there was no transfer of heat between the graphite and the salt for a distance of 0.1 in. on each side of the apex of the rib on the outer edge of the moderator element. The latter assumption is a first approximation of the fact that the flow in this area is restricted. It also illustrates why the ribs should be kept as narrow as possible. Calculations were made by use of the Astra HEATING code, which is a relaxation heat conduction code that assumes constant thermal conductivity of the materials. The parameters used in these particular calculations are listed in Table 5.7.

Preliminary calculations indicate that vibration of the moderator elements should not be a problem. The magnitude of the vibrations was determined by extrapo-

[15] W. Eifler and R. Nijsing, *Fundamental Studies of Fluid Flow and Heat Transfer in Fuel Element Geometries. II. Experimental Investigation of Velocity Distributions in a Triangular Array of Parallel Rods,* EURATOM report No. EUR 2193.6, Joint Nuclear Research Center, Ispra Establishment, Italy, 1965.

ORNL-DWG 69-6012

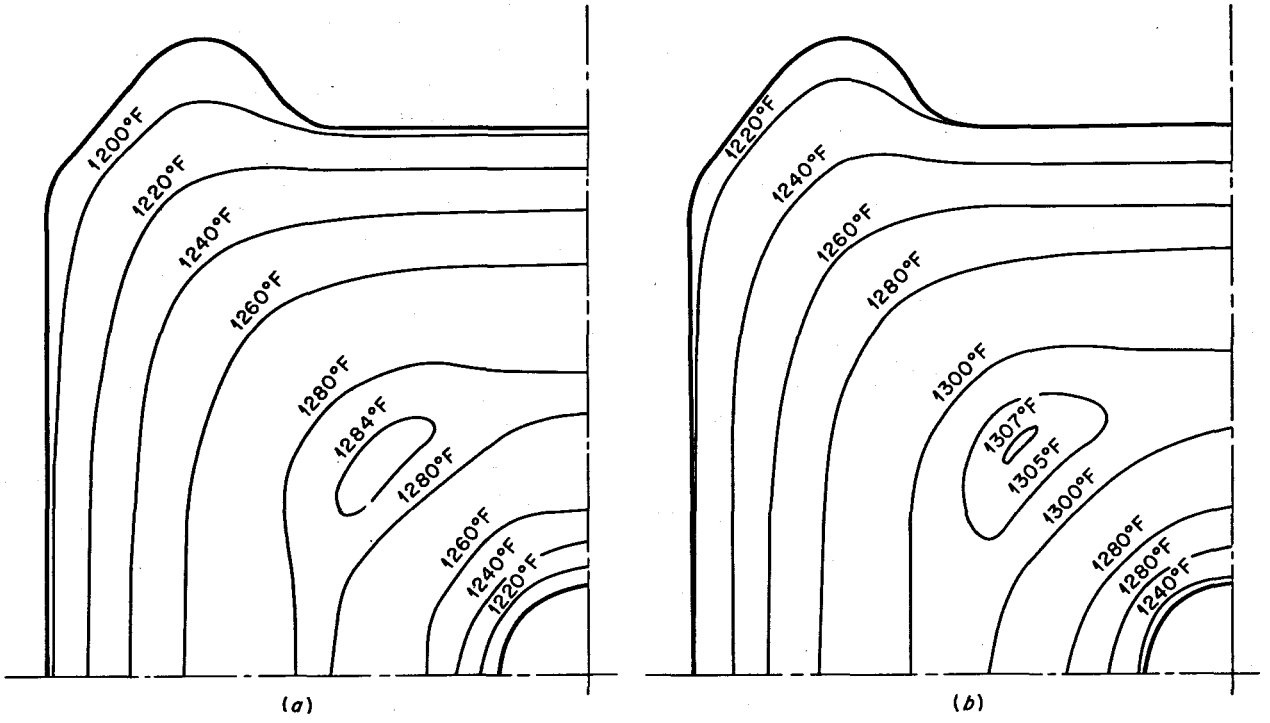

Fig. 5.14. Temperature Distribution in MSBR Moderator Element at (*a*) Mid-Height of Core, (*b*) 1 ft Above Midplane.

lating known information about the amplitude of vibrations with parallel flow[16] and adding to this the rod deflection due to cross flow of salt between the channels. Assuming the velocity of the salt between adjacent channels to be ¼ fps and extrapolating information on vibration due to cross-flow vortex shedding,[17] the sum of the two effects gives a total calculated amplitude of vibration at the center line of less than 0.002 in. Model tests will be required for substantiation, but on this basis we believe that core vibrations will not limit the design.

In connection with the studies mentioned above, it may be noted that a 12- by 12-in. area has been assigned for control rods in the center of the reactor. The salt flow in this region may be in excess of that needed to cool the rods in order to help bring sufficient cool salt to the top axial reflector. Orificing of the flow in this central region will also be required, to minimize variations in the flow with control rod position. Studies are continuing, and efforts will be made to determine if there are any vibration problems associated with the control rods.

[16]D. Burgreen *et al.*, "Vibration of Rod Induced by Water in Parallel Flow," *Trans. ASME* (July 1958).

[17]Y. N. Chen, *Flow-Induced Vibration and Noise in Tube-Bank Heat Exchanger Due to von Karman Streets*, ASME paper 67-VIBR-48 (January 1967).

Table 5.7. Input Parameters for Calculating MSBR Moderator Element Temperatures Using the Astra HEATING Code

Salt temperature, °F	1175	1200
Heat generation rate, Btu hr^{-1} $in.^{-3}$	290.8	286.1
Graphite thermal conductivity, Btu hr^{-1} $in.^{-1}$ $(°F)^{-1}$	1.415	1.415
Heat transfer coefficient for center hole, Btu hr^{-1} $in.^{-2}$ $(°F)^{-1}$	12.26	12.63
Heat transfer coefficient for outer surface, Btu hr^{-1} $in.^{-2}$ $(°F)^{-1}$	12.85	13.22

5.9.2 Flow and Temperatures in Radial Reflector

Determination of reflector temperatures is important because of their relationship to graphite life, amount and temperature of coolant required, and stored energy during afterheat removal. The relationship between life, damage flux, and temperature is shown in Fig. 5.11. For a given nuclear design there is a maximum allowable temperature for any reflector section which is intended to remain fixed in position for the design life of the reactor. Conversely, a temperature distribution calculated for given reflector geometry and coolant

conditions may dictate a reduction in the incident damage flux, even though this entails a departure from optimum nuclear conditions. (This compromise was necessary in the present design, as discussed in Sect. 5.3.) The amount and temperature of coolant are interdependent. The major part of the coolant temperature rise is due to its own internal fission heating, and it is desirable to have each unit volume of salt experience the same plenum-to-plenum temperature rise. On the other hand, the need for improved heat transfer coefficients or lower sink temperatures may dictate a higher flow rate than that required to attain this rise.

A reflector design using graphite blocks averaging about 1 ft^3 in size was rejected when analysis indicated excessive temperatures. The principal cause was fission heat from trapped interstitial salt. This heat had to be transferred to a cooled surface by conduction, which required large temperature gradients. A conclusion was that regions of static salt must be avoided everywhere within the reactor vessel. With the elimination of internal fission heat, the sources in the reflectors would consist only of photons leaking from adjacent blanket regions and from neutron slowing down, as indicated in Fig. 5.15.

The present radial reflector design, shown in Figs. 5.4 and 5.5, has been analyzed using the Astra HEATING code, employing a three-dimensional relaxation technique with constant thermal conductivity. Boundary temperatures were based on the fluid temperature required at a given location for an overall 250°F rise plus an increase in wall temperature from the volumetric heat source in the fluid. In most analyses performed, the fission heating in the salt far exceeds the heat transferred into it from the graphite. Hence the conduction problems have been treated with fixed boundary conditions rather than having to couple the salt and graphite by an energy balance. Heat transfer coefficients were based on laminar flow between graphite segments and between reflector and vessel, but on turbulent flow at the reflector-blanket boundary in the 2-in.-wide annular space between the reflector and the removable core assembly. Results at the axial midplane are shown in Fig. 5.16. This is the location of the peak damage flux, which has been constrained to about 4×10^{13} to achieve design life with the calculated 1250°F surface temperature. The effect of damage flux decrease with distance into the reflector overrides the effect of increasing temperature on the graphite life. Similarly, the axial decrease in damage flux is sufficient to counteract the increasing surface temperature, which reaches a peak several feet above the midplane.

Our studies indicate that to meet the heat-removal requirements and the other objectives discussed above, the flow of salt through the reflector graphite must be in the radial direction rather than vertically upward, as it is in the core. In large part this is due to the fact that the thermal coefficient of expansion of Hastelloy N is greater than that of the graphite. The reflector graphite could be restrained into essentially its room-temperature geometry with little change in the flow channel geometry, but the expanding vessel would draw away from the reflector and increase the salt volume in the annulus between the vessel wall and the graphite. This would result in an undesirable increase in the primary-salt inventory. We therefore decided to restrain the reflector graphite to maintain its position relative to the wall and let the flow passages in the graphite open up as the system is brought up to temperature. With an increase in the width of the flow channels in the reflector graphite, axial flow passages for the reflector

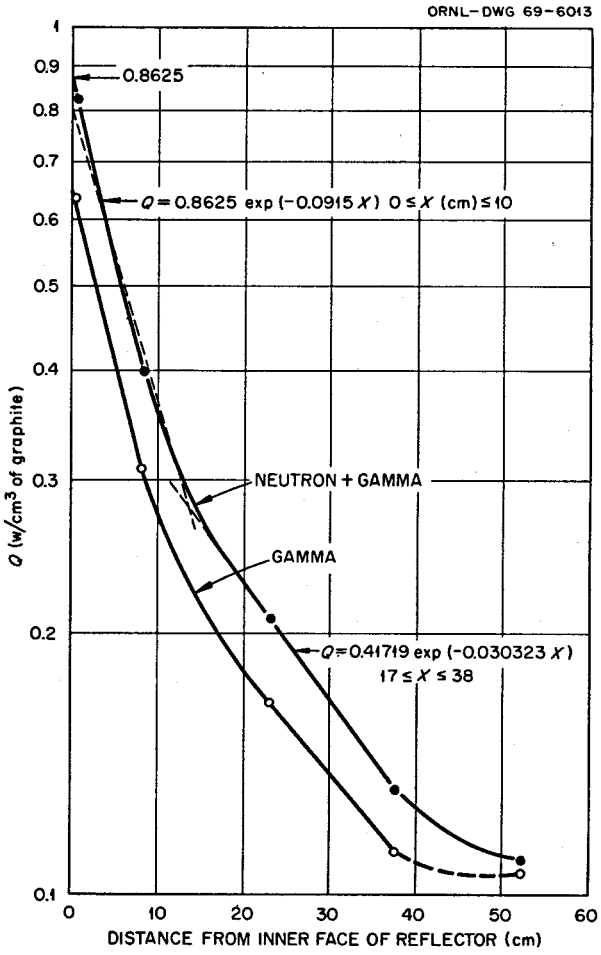

Fig. 5.15. Heating in MSBR Radial Reflector at Mid-Height.

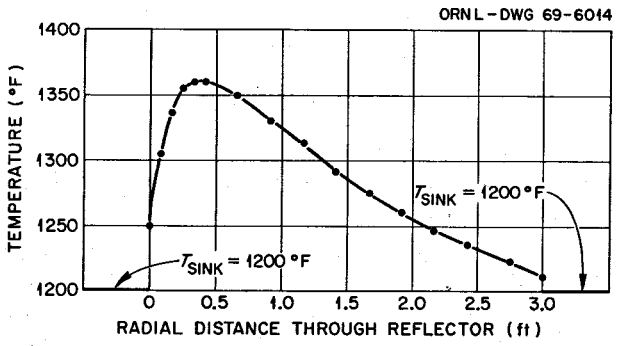

Fig. 5.16. Temperature Distribution in MSBR Radial Reflector at Mid-Height.

cannot be defined. Connecting the reflector flow passages, the annular space at the vessel wall, and the annular space between the reflector and the removable core to common plenums located at the upper and lower ends of the reflector is not satisfactory. There would be inadequate axial flow through the reflector if the pressure difference was limited to the amount necessary to get the desired temperature rise for the salt flow through the annular space. On the other hand, there would be excessive salt flow through the annular spaces if this pressure difference was increased to get the necessary flow through the reflector region. The use of radial flow circumvented this design difficulty.

We decided to have the salt in the reflector flow inward toward the core in order to minimize the vessel wall temperature and because of orificing considerations. The annulus between the core and reflector is orificed at the bottom because of mechanical assembly considerations and because this annulus serves as the collection plenum for the radial flow through the reflector. Salt flow from the undermoderated region of the core into the annulus is restricted by graphite rib seals located between the graphite slabs in the undermoderated region, zone II. Axial distribution of the radial flow through the reflector is controlled by orifices located at the inlets of the radial flow passages. Analysis of flow in this region of the reactor is continuing.

5.9.3 Flow and Temperatures in Axial Reflectors

The axial reflectors are subjected to a 66% higher peak damage flux than the radial reflector. However, the lower one is replaced with the moderator, and the upper one must last only half of design life due to the alternate use of two heads. Hence temperature and damage flux considerations are not as stringent as in the radial reflector. The upper reflector was analyzed using the Astra HEATING code. The axial behavior of the source is shown in Fig. 5.17. The radial variation was described by a cosine. The inner face is subjected to 1300°F salt. The other faces are in contact with somewhat cooler salt which is transported from the reactor inlet, via the control region and lifting rod tubes, to provide a low-temperature sink for the vessel head. On the above basis, the peak temperature was found to be 1363°F, and the surface temperature in the region of peak damage flux is 1265°F. This corresponds to a 20-year graphite life. The lower reflector graphite is cooled on all faces by salt at a temperature only slightly above inlet conditions. This results in a peak temperature in the lower reflector of 1165°F.

A flow of fuel salt is provided for cooling the axial reflectors in much the same manner as for the radial reflector graphite. The flow through the lower axial reflector will be upward, while that through the upper axial reflector will be downward. The salt for the lower reflector is taken from the reactor inlet flow, and it is used to cool the lower head of the vessel and the graphite support plate as well as the axial reflector graphite. The fuel salt for cooling the top head and graphite is brought upward through the control rod region at the center and through the core lifting rod holes in zone II, previously mentioned. This relatively

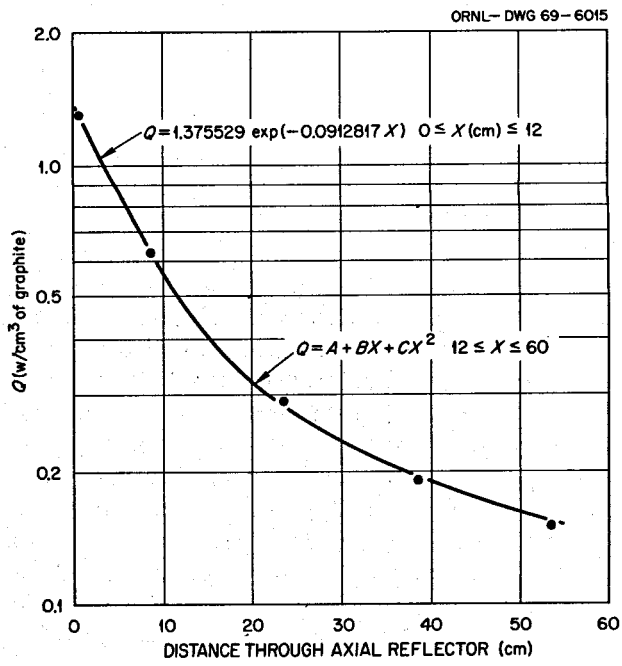

Fig. 5.17. Gamma and Neutron Heating in MSBR Axial Reflectors.

cool salt is used to remove the heat deposited in the upper head and in the upper axial reflector graphite.

5.9.4 Vessel Temperatures

Analysis of the 2-in.-thick vessel wall indicates a peak temperature of 1154°F, occurring at the outer surface at the axial midplane. No credit was taken for heat transfer from the outer vessel surface to the primary cell. A constant salt temperature of 1100°F was used in the vessel wall coolant passage. The basis for this is the very low fission density in the passage. Hence, with radial flow in the reflector and with the flow rate sized to give an overall 250°F rise, most of the salt temperature rise will occur over the inner few inches of the reflector and in the annulus between the reflector and core zone II. The effect of gamma radiation from the heat exchangers on vessel temperature has not been included. Locally hot areas of the vessel and heads, such as the region around the outlet nozzles and other areas bathed by 1300°F salt, have not been analyzed. Temperatures within a few degrees of the salt temperatures are to be expected in these regions. If the calculated stress intensities are too high, a method of shielding the surfaces from the hot salt may be required.

Analysis of the 3-in.-thick upper head indicates that temperatures are on the order of 1120 to 1180°F along the outer surface. This is based on an 1100°F salt temperature on the inner face. At the junction of the hemispherical and cylindrical sections, there is a small region where temperatures approach 1300°F due to the contact with hot salt on the inner surface. This region also coincides with the location of maximum stress intensity and is therefore of concern. Analyses of modified head designs which will result in lower stress values are presently in progress.

The lower head has a reduced incident gamma flux due to the shielding provided by the lifting plate and other structure. It is cooled by salt at inlet conditions, and the combination of these two factors yields maximum temperatures less than 1100°F. Because it is larger in diameter than the upper head, is of different geometry, and must withstand a higher pressure, the lower head has a maximum stress intensity about twice that of the upper head. This occurs at the junction with the cylindrical wall section. Present stress analysis indicates that, with the temperatures calculated, this maximum is allowable by a small margin. Stress analysis is continuing, and additional results will be reported in the future.

5.10 ESTIMATED COSTS OF 1000 Mw (ELECTRICAL) MSBR POWER STATION

R. C. Robertson

The last published cost estimate for a 1000 Mw (electrical) MSBR power station was in the fall of 1968.[18] We have revised this estimate to more nearly represent early 1969 conditions. The total estimated construction cost is given in Table 5.8 and the power generation cost in Table 5.9. The cost of the chemical processing plant is not included in the capital costs given in Table 5.8; it is added into the fuel cycle cost in Table 5.9.

The estimated construction costs are now higher because of an average escalation of costs of about 5% since the late 1968 estimate and because the conceptual

[18]Internal memorandum from Roy C. Robertson, "Comparative Costs of PWR and Single-Fluid MSBR 1000-Mw(e) Power Stations," Nov. 19, 1968.

Table 5.8. Estimated Construction Cost of 1000 Mw (Electrical) MSBR Power Station

	Cost (millions of dollars)	
	MSBR	PWR
Structures and improvements	11.5	15.9
Reactor		
Vessel	5.9	8.0
Graphite	6.0	
Shielding and containment	3.1	*a*
Heating and cooling systems	1.3	4.1
Control rods	1.0	2.0
Cranes	0.2	0.2
Heat transfer systems	22.2	20.4
Drain tanks and fuel handling	4.3	2.0
Waste treatment and disposal	0.5	0.5
Instrumentation and controls	4.1	4.1
Feedwater supply and treatment	5.2	3.9
Steam piping	5.6	5.7
Remote maintenance equipment and other	6.6	1.0
Turbine-generator plant equipment	25.0	36.9
Accessory electrical equipment	5.2	5.2
Miscellaneous	1.4	1.3
	109.1	110.7
Total plus 6% allowance for 54-hr week	115.6	117.3
Total plus 3% local sales tax	119.1	120.9
Total plus 33.5% indirect costs	159.0	161.3

[a]PWR shielding costs are included in the structures account.

Table 5.9. Estimated Power Production Cost in 1000 Mw (Electrical) MSBR Station

	Mills per Kilowatt-Hour
Plant capital cost[a]	3.1
Graphite replacement cost[b]	0.1
Fuel cycle cost[c]	0.5
Operating cost	0.3
Total	4.0

[a]Based on fixed charges of 13.7% and on 80% plant factor.

[b]Based on four-year graphite life and a graphite cost of $10.00 per pound.

[c]Includes fixed charges and operating costs of the chemical processing plant.

design of the reactor also increased in size. The combined effect is for the reactor (plus associated indirect costs) to cost about $5 million more than in the previous estimate.

Other important cost increases are due to the inclusion of the effect of a 54-hr work week and adding a 3% sales tax charge. The first of these increased the construction cost by about $6.5 million and the latter by about $3.5 million.

The estimated costs given here are based on the 1969 value of the dollar and therefore do not include a factor for escalation of prices during a construction period. This is a very substantial expense item that must be added to the construction cost of a plant. It can amount to about 14.5% additional cost, or around $20 million for an MSBR, for a five-year construction period, if escalation continues at the present rate of more than 4%/year.

An important assumption in making MSBR cost estimates is that the costs apply to an established molten-salt reactor industry. This is to say that there is a proven design, development costs have largely been absorbed, and the manufacture of materials, plant construction, and licensing have become routine.

About one-half of the total cost is for more conventional parts of the plant, such as structures, turbine-generators, and associated equipment, and these costs are relatively well established. The reactor costs are less certain because of the preliminary nature of the conceptual design and use of Hastelloy N and special graphite for which there is limited experience in large-scale production.

We feel that the estimated MSBR costs have more relevancy if they are used on a comparative basis rather than as absolute values. Table 5.8 therefore includes the costs of a PWR station[19] estimated under the same set of ground rules used for the MSBR. Whereas the molten-salt reactor included relatively large allowances for the drain tanks and maintenance equipment, this is offset by savings of about $17 million over the light-water reactors for the heat-power system equipment as a result of using high-pressure, high-temperature steam. On the basis of these estimates we believe that the construction costs of an MSBR station and a light-water reactor station would not be greatly different.

The estimated power production costs given in Table 5.9 assume a fixed charge for capital for a privately owned plant of 13.7%. The cost of replacing the graphite every four years is included as a production expense, as is the interest on the cost of the capital set aside to cover future replacements. As shown, the favorable power cost of an MSBR is largely due to the low fuel cycle cost.

5.11 MSBE DESIGN

J. R. McWherter C. W. Collins W. Terry

5.11.1 Introduction

Some conceptual design studies were initiated on the Molten-Salt Breeder Experiment (MSBE). Some of the objectives follow:

1. The plant shall be a facility for testing materials, components, systems, and methods at conditions as near those of the MSBR as practical.
2. The reactor shall have the capability for exposing segments of proposed full-size MSBR core graphite elements at a fast (>50 kev) neutron flux of 5×10^{14} neutrons cm^{-2} sec^{-1} in primary salt at temperatures up to 1300°F.
3. The primary- and secondary-salt compositions shall be essentially the same as proposed for the single-fluid MSBR. Differences should be limited to those which would not significantly alter the chemical or physical properties of the salts.
4. The design power level for the reactor shall be in the range of 100 to 200 Mw (thermal). A conversion ratio near 1.0 is desirable but not essential.
5. The design of the plant should be similar to that proposed for the MSBR. Where practical, the MSBE primary system components shall be similar in design to

[19]Internal communication to J. A. Lane from R. C. Olson, Feb. 18, 1969, based on: J. A. Lane, M. L. Myers, and R. C. Olson, *Power Plant Capital Cost Normalization,* ORNL-TM-2385 (to be published).

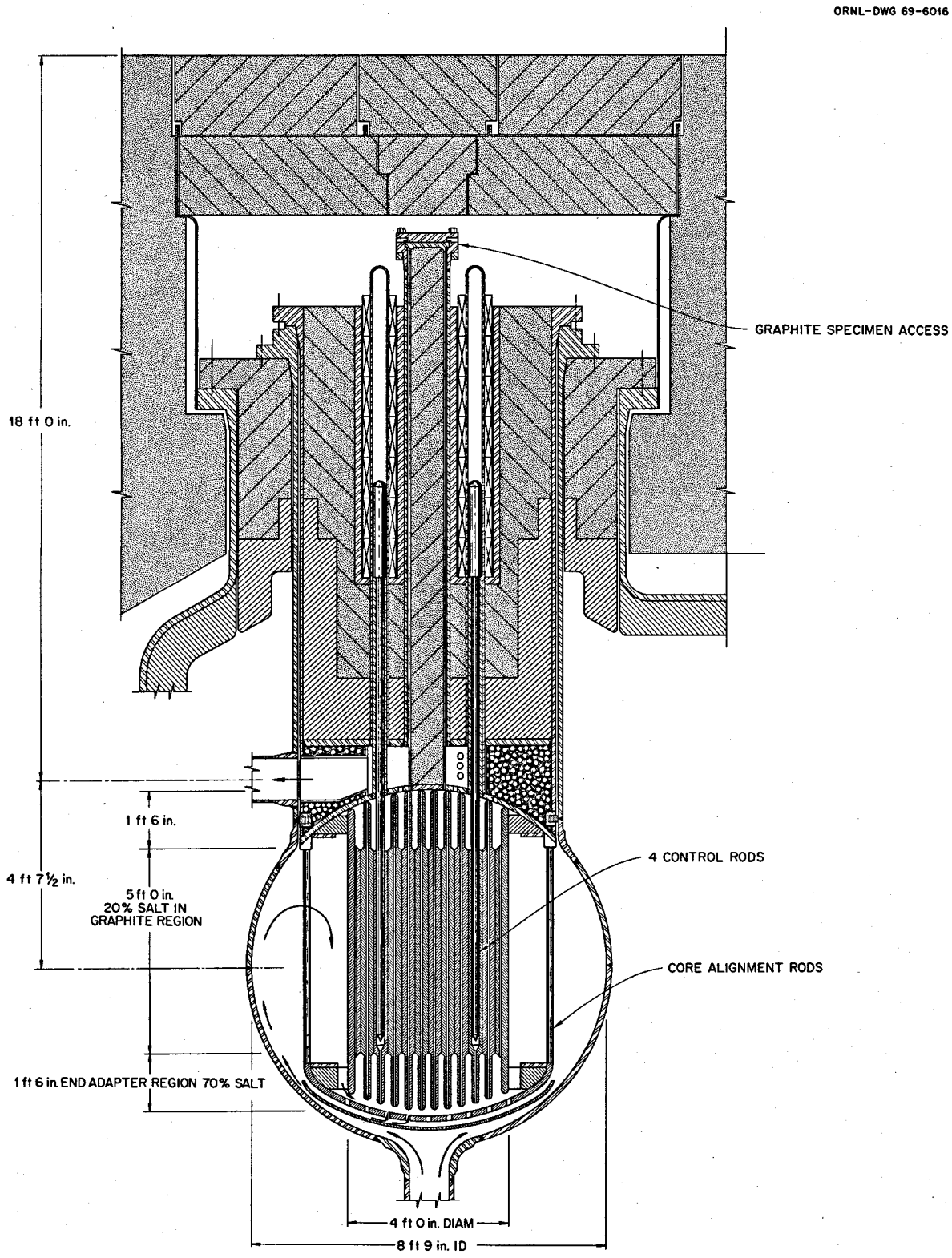

Fig. 5.18. Vertical Section Through MSBE Reactor Vessel.

those proposed for the MSBR and of a size that can be scaled up for use in demonstration plants. The chemical processing of the primary salt shall be done by processes proposed for the MSBR and with equipment of a size which can be scaled up to that for the MSBR.

6. The maximum operating temperatures and, where practical, the temperature differences in the MSBE shall be the same as those of the MSBR. Thermal energy shall be transferred from the primary salt to a secondary salt, from which it will be removed by steam generation at proposed MSBR conditions. Generation of electricity with the steam is not required.

7. Maintenance techniques and procedures proposed for the MSBR shall be used where practicable in the

ORNL-DWG 69-6017

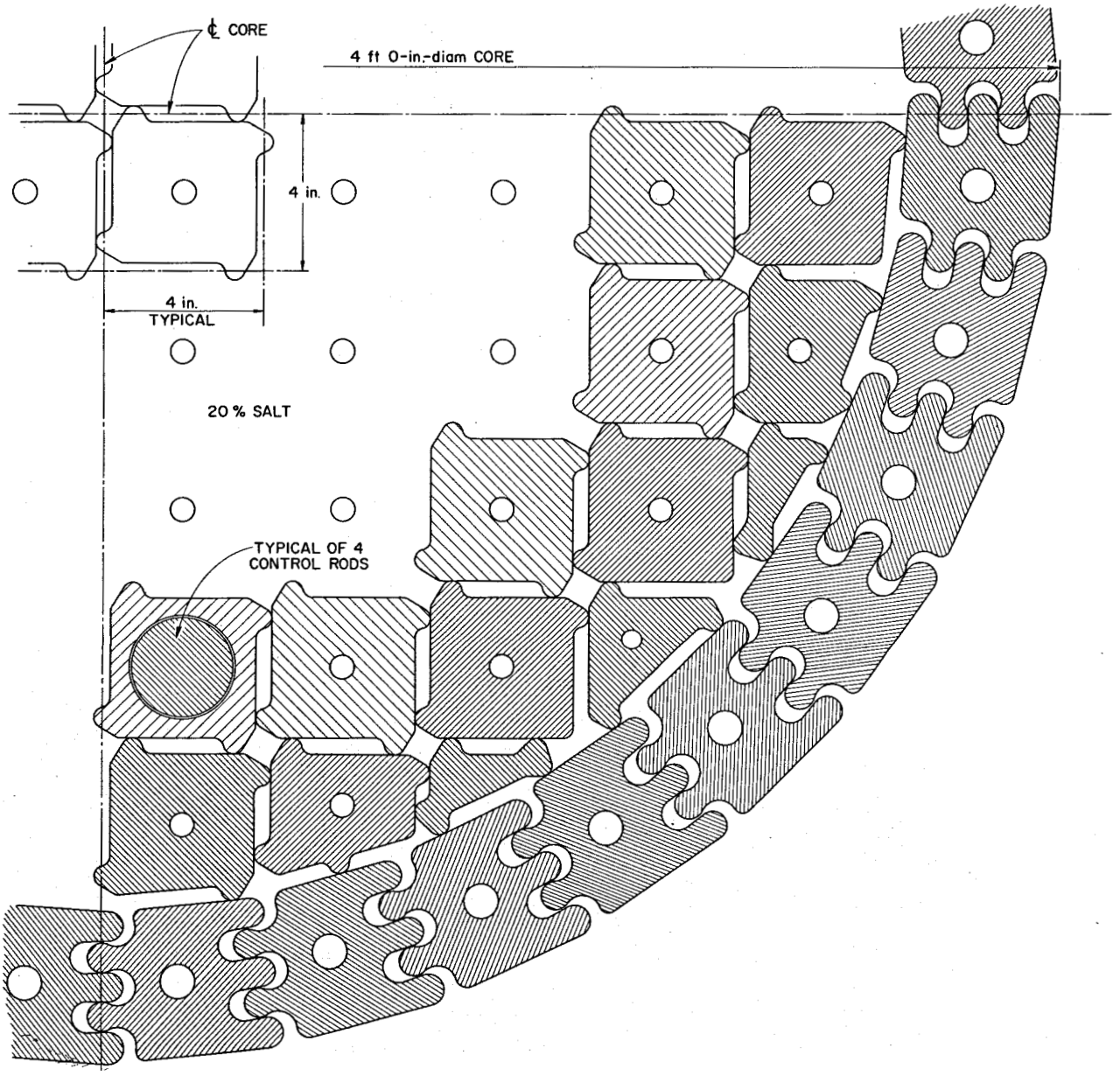

Fig. 5.19. Horizontal Section Through Core of MSBE.

MSBE. Facilities shall be provided for examining components that are removed from the MSBE.

5.11.2 Description of Reactor Plant

The core configuration under study will meet the above requirements at a power level of 170 Mw (thermal) (see Sect. 6.2 for physics analysis). It consists of a large number of 4-in.-square graphite bars arranged vertically in a 4-ft-diam assembly. The middle section of the bars is 5 ft long and has 20% of its nominal cross sectional area open for salt flow. There are $1\frac{1}{2}$-ft-long axial extensions at each end with the cross section reduced so that the salt occupies 70% of the end regions. This assembly is contained in an $8\frac{3}{4}$-ft-diam spherical vessel with the radial region between the 4-ft cylindrical array and the vessel completely filled with salt.

A vertical section through the reactor core is shown in Fig. 5.18. Primary salt (71.5 mole % LiF, 16 mole % BeF_2, 12 mole % ThF_4, 0.5 mole % UF_4) enters the bottom of the reactor vessel and flows through the core as indicated schematically in the figure. No hydraulic analyses of the core have been made. Four control rods with magnetic drives are indicated, although the control rod requirements have not been determined. A $6\frac{1}{4}$-ft-diam extension at the top of the vessel with a removable vessel top head is proposed. This arrangement would permit removal of all the graphite, which is positioned by a lower structure supported by rods attached to the vessel top head. The four central graphite bars can also be removed independently through a central access opening in the top head.

The graphite arrangement is shown in Fig. 5.19, a horizontal section of the core. The outer elements will be fixed in position at top and bottom, but the tongue-and-groove joints in the outer elements will permit some circumferential movement without excessive cross flow through the gap.

A conceptual floor plan of the reactor building is shown in Fig. 5.20. There are separate cells for the primary-salt components, the secondary-salt steam generators, the off-gas processing system, and chemical processing plant. A hot cell for dismantling and evaluation of radioactive components will be provided. All of these cells will be housed in a concrete building with an overhead crane.

Maintenance procedures are incomplete, but it is assumed that a shielded carrier on rails with a closed

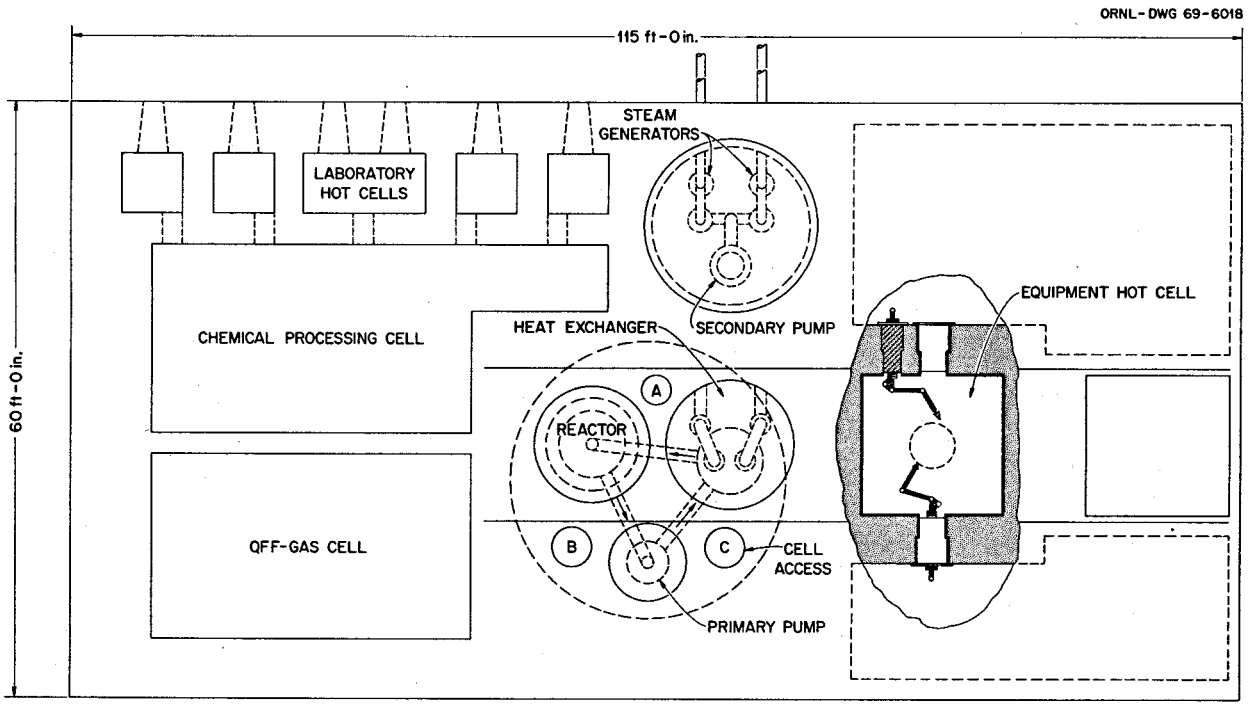

Fig. 5.20. Plan of MSBE Reactor Building.

atmosphere can be used to move the graphite specimens or the entire top-head-and-graphite assembly to the hot cell.

Figure 5.21 is a schematic vertical section through the reactor cell and the steam generator cell.

The primary salt enters the heat exchanger at 1300°F and leaves at 1050°F. The secondary salt enters the heat exchanger at 850°F and leaves through a concentric outlet at 1150°F. The secondary salt is used to generate steam at 1000°F and 3600 psia.

ORNL-DWG 69-6019

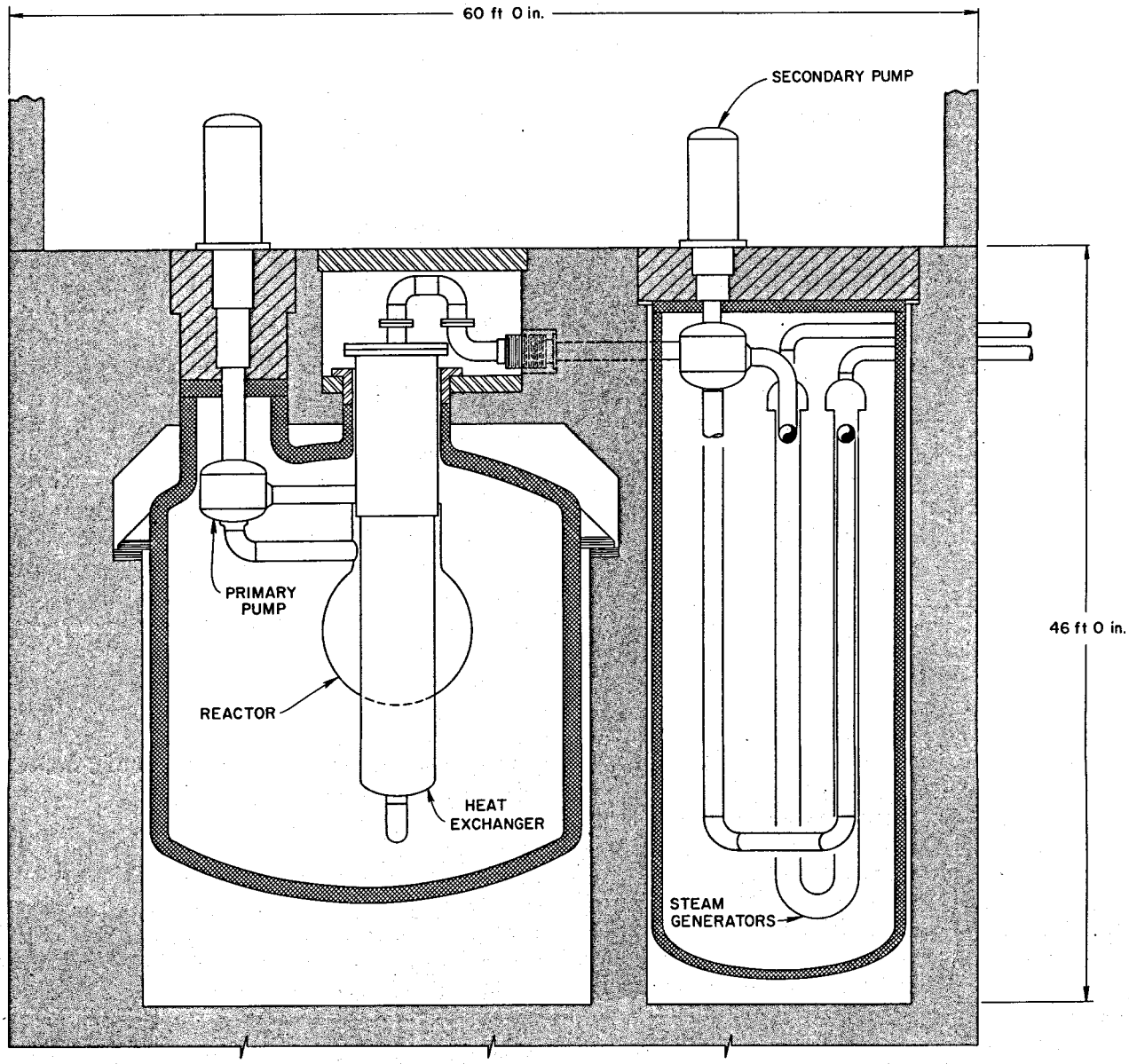

Fig. 5.21. Elevation Section Through Reactor and Coolant Cells.

6. Reactor Physics

A. M. Perry

6.1 PHYSICS ANALYSIS OF MSBR

6.1.1 Optimization of the MSBR

H. F. Bauman

The main factors considered in the optimization of MSBR nuclear designs have been, for some years, the fuel-cycle cost and the annual yield (fractional increase) of bred fuel. However, it has been recognized for some time that the fuel yield (or its inverse, the doubling time) does not fully take into account the influence of fuel specific power in determining the overall amount of natural uranium that will be required to supply an expanding nuclear power economy. It can easily be shown, for a linearly increasing power demand, that the required cumulative input of fissile material into the system, up to the time when the system becomes self-sustaining, varies inversely as GS^2, where G is the breeding gain (breeding ratio minus 1) and S is the specific power in terms of the entire fuel inventory chargeable to the system.

No responsible projections of nuclear power capacity, of course, indicate a linear increase at any time within the next few decades. We observe, however, in comparing the resource requirements for various postulated reactor characteristics (i.e., inventory and doubling time) that the product GS^2 gives a better indication of the fuel input requirements than does the doubling time or yield (which is proportional to GS). The quantity $100GS^2$, [Mw (thermal)/kg]^2, we have called the fuel "conservation coefficient."

In view of these considerations we have modified the figure of merit used in optimizing MSBR designs to allow, optionally, the achievement of maximum conservation coefficient rather than maximum yield or maximum breeding ratio; we have used this option in all of our recent calculations. Indeed, the breeding ratio that results from optimizing an MSBR with respect to the conservation coefficient is typically about 0.01 lower than results from optimizing for yield, but the fuel inventory is also lower. That is, if a reactor optimized for yield has a breeding ratio of 1.07, the modified reactor, reoptimized for the conservation coefficient, would have a breeding ratio closer to 1.06 but would still be judged the better reactor in terms of the objectives of breeding.

The objective function of the ROD[1] optimization is in the form of a polynomial. This allows great flexibility in the selection of factors which will influence the optimum; new terms can be added easily, while terms that are no longer being used can be given zero coefficients. Two terms are employed in the current optimizations: the conservation coefficient, already defined, with a weighting factor of 10, and the damage flux factor, with a weighting of 1. The damage flux factor is computed by ROD as follows. The maximum group 1 (fast) flux is selected by scanning the core. If this flux does not exceed a preselected input flux, the flux factor is 0. If the input flux is exceeded, the difference is divided by 10^{14}, then squared, and multiplied by -1. This gives a term which subtracts from the objective function when the damage flux exceeds the desired value. The use of the flux factor not only permits the user to investigate designs with a predetermined core life, but also tends to drive the optimization toward designs with a low peak fast flux.

The convergence requirement on the ROD calculation is particularly stringent when ROD is used for optimization. The "derivative" calculations, which determine the direction in which the optimization proceeds, are based on a pair of ROD cases which differ by a small increment in the value of the variable considered. Small convergence errors which would be negligible in individual cases can cause serious errors in the derivatives. The convergence of the diffusion calculation in ROD has been particularly slow and difficult since multiple

[1] *Reactor Optimization Design* program; see ORNL-4344, p. 68.

thermal groups with slow-neutron upscatter have been introduced. An upscatter convergence acceleration technique has been adapted for use in ROD and has helped to obtain adequate convergence in a reasonable time. There are still ROD cases that run for several hundred iterations, however, and other convergence acceleration methods are being investigated.

6.1.2 The One-Fluid MSBR Reference Design

H. F. Bauman

The nuclear design studies of the one-fluid MSBR are continuing; however, enough has been learned about the characteristics of the one-fluid system to permit the selection of a reference design which will be the basis of a forthcoming design report. The important data for the reference design are given in Table 6.1. Some of the studies which led to the selection of the reference design are presented in the following section. The performance figures are somewhat higher in the preliminary studies than in the reference design, mainly because the studies were based on an assumed value for the fuel salt inventory, external to the regions being optimized, that proved to be somewhat low.

The reference design has been modified slightly from the optimum design based solely on the conservation coefficient. The conservation coefficient could, in fact, be about 10% higher than that of the reference design. The benefits of the following three modifications were considered to balance this decrease in performance.

The first modification is the extension of the core life. The core was made larger and with a flatter flux, increasing the nominal graphite life from the optimum of 2.4 years to about 4 years. As will be shown in the following section, this costs very little in nuclear performance and should have significant economic advantages.

Second, the reflector thicknesses are less than optimum by about a foot, to reduce the size and capital cost of the reactor vessel.

Third, the thickness of radial core zone 2 was increased by about 6 in. to reduce the fast flux at the face of the reflector. This gives a nominal reflector life of 30 years and eliminates the need for scheduled replacement of the reflector.

6.1.3 Nuclear Design Studies

H. F. Bauman

The reflector has two important effects in the one-fluid MSBR design, namely, the reduction in neutron leakage and the flattening of the power distribution. The power-flattening effect is particularly important since it can extend the core graphite life without any sacrifice in average power density or specific inventory.

The effect of the radial reflector thickness on the MSBR performance is shown in Fig. 6.1. (The effect of axial reflector thickness is similar but, as would be expected from the geometry, about half as great.) The reactor design was similar to the reference MSBR

Table 6.1. Characteristics of the One-Fluid MSBR Reference Design

A. Description	
Identification	CC58
Power, Mw (electrical)	1000
Power, Mw (thermal)	2250
Plant factor	0.8
Dimensions, ft	
Core zone 1	
Height	13.0
Diameter	14.4
Region thicknesses	
Axial: Core zone 2	0.75
Plenum	0.25
Reflector	2.0
Radial: Core zone 2	1.25
Annulus	0.167
Reflector	2.5
Salt fractions	
Core zone 1	0.132
Core zone 2	0.37
Plena	0.85
Annulus	1.0
Reflector	0.01
Salt composition, mole %	
UF_4	0.228
ThF_4	12
BeF_2	16
LiF	72
Processing cycle times for removal of poisons	
1. Kr and Xe, sec	20
2. Se, Zr,[a] Nb, Mo, Tc, Ru, Rh, Pd, Ag, Sb, and Te, sec	20
3. Pa, Cd,[a] In,[a] and Sn,[a] days	3
4. Y, La, Ce, Pr, Nd, Pm, Sm, Eu, and Gd, days	50
5. Cs and Ba, years	5
6. Br[a] and I,[a] days	5

Table 6.1 (continued)

B. Performance

Conservation coefficient, [Mw (thermal)/kg]^2	15.1
Breeding ratio	1.064
Yield, % per annum	3.34
Inventory, fissile, kg	1470
Specific power, Mw (thermal)/kg	1.53
Doubling time, system, years	20.7
Peak damage flux, neutrons cm^{-2} sec^{-1}	
Core zone 1 ($E > 50$ kev)	3.2×10^{14}
Reflector ($E > 50$ kev)	4.2×10^{13}
Vessel ($E > 0.8$ Mev)	1.3×10^{11}
Power density, w/cm^3	
Average	22.2
Peak	65.2
Ratio	2.94
Fission power fractions by zone	
Core zone 1	0.765
Core zone 2	0.167
Annulus and plena	0.056
Reflector	0.012

C. Neutron Balance

	Density (atoms barn^{-1}-cm^{-1})	Neutron Absorptions	Neutron Captures	Fissions (Including $n, 2n$)
Fuel salt (core volume fraction 0.132)				
^{232}Th	3.72 E −3	0.9889	0.9859	0.0031
^{233}Pa	3.91 E −7	0.0017	0.0017	
^{233}U	6.49 E −5	0.9248	0.1001	0.8247
^{234}U	2.29 E −5	0.0809	0.0805	0.0004
^{235}U	5.88 E −6	0.0752	0.0140	0.0612
^{236}U	6.05 E −6	0.0085	0.0084	
^{237}Np	6.51 E −7	0.0059	0.0059	
^{9}Be	4.96 E −3	0.0071	0.0025	0.0046
^{7}Li	2.22 E −2	0.0160	0.0160	
^{6}Li	1.25 E −7	0.0023	0.0023	
F	4.74 E −2	0.0206	0.0206	
Moderator (core volume fraction 0.868)				
Graphite	9.53 E −2	0.0522	0.0522	
Fission products		0.0196	0.0196	
Delayed neutrons lost		0.0032	0.0032	
Leakage		0.0244	0.0244	
Sum ($\eta\epsilon$)		2.2316		

[a]According to our present flowsheet Zr, Cd, In, and Sn are removed on a 200-day cycle and Br and I are removed on a 50-day cycle. The effect on the longer cycle time on the breeding gain is negligible.

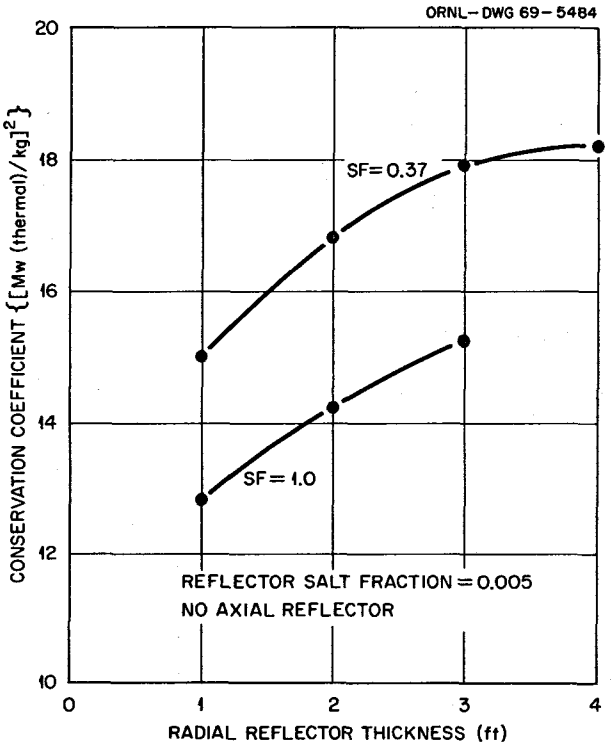

Fig. 6.1. Effect of Radial Reflector Thickness and Salt Fraction in Core Zone 2 on MSBR Performance.

except that a peak power density corresponding to a 2.25-year core life and a somewhat smaller external inventory of salt were assumed. The reactor performance improves markedly with reflector thickness out to about 3 ft and then begins to level off.

Figure 6.1 also shows the effect of the salt fraction in core zone 2 for two cases: all salt and 37% salt, which is the salt fraction corresponding to a random-packed bed of spheres. The zone thickness was allowed to optimize in each case. The 37% salt case is clearly superior, although the effect is rather small considering the large difference in salt fraction.

The effect of the reflector salt fraction on the reactor performance was investigated in the series of cases given in Table 6.2. These cases are very similar to the reference design except that a lower external inventory of salt was assumed. A case with no reflector is included for comparison.

The effect of salt in the reflector is to increase the neutron leakage and the fissile inventory, both of which decrease the performance. The reactor performance is most sensitive at very low reflector salt fraction, rising sharply as zero salt fraction is approached. For the designer this implies that the more successful he is in reducing the reflector salt fraction, the greater the incentive becomes for further reduction. Notice, however, that even in the case with as much as 4% salt in the reflector, the performance was much better than in the no-reflector case. Power peaking was particularly severe in the no-reflector case.

The reflected reactor has the disadvantage of a secondary power peak at the core-reflector interface. An analysis of the temperature and damage flux in this region for an optimum case indicated that the expected life of the graphite near this interface might be about half the desired 30 years. While it is possible to design the reflector so that the graphite could be replaced at infrequent intervals, it seemed desirable to avoid such a major remote maintenance requirement. It was noted that the flux at the reflector face was quite sensitive to the thickness of zone 2 (and the annulus). The thickness of zone 2 was increased to 1.25 ft in the reference design in order to achieve a nominal reflector life of 30 years.

The effect of xenon in a typical reflector was also studied. It was shown that xenon at an atom density of 9×10^{-12} atoms $barn^{-1}$ cm^{-1}, the estimated reflector concentration in a graphite with no resistance to xenon diffusion, had a negligible effect on the performance of the reactor (i.e., about a 1% decrease in the conservation coefficient). The effect on the damage flux in the reflector was also negligible. It was shown that about half the neutrons absorbed in xenon in the reflector would have been lost as increased leakage had the xenon not been present.

The absence of a significant effect of xenon in the reflector may have an appreciable indirect effect on the reactor performance. Since the reflector graphite need not be impermeable to gases, it can be manufactured in larger blocks, permitting a lower salt fraction in the reflector.

The possible effects of flux shaping on the performance of the MSBR were also studied. The flux-factor technique described in Sect. 6.1.1 was used to restrain the peak flux in the ROD optimization in the series of cases given in Table 6.3. In these three cases in spherical geometry, the first was run with no restraint on the damage flux and the next two with increasing restraint on the damage flux. The results showed that a considerable improvement in the graphite life could be obtained with only a minor decrease in the reactor performance.

These results were so encouraging that a similar peak flux restraint was applied to subsequent cases in cylindrical geometry, including the reference design and the cases in Table 6.2. The reactor fissile inventory is

Table 6.2. Effect of Reflector Salt Fraction on MSBR Performance

Fixed parameters:		Salt fraction:	
Core height, ft	13	Core zone 2	0.37
Thickness of plena, ft	0.33	Plena	0.85
Power, Mw (electrical)	1000	Annulus	1.0
Power, Mw (thermal)	2250		
Mole % thorium	12		
Plant factor	0.8		

	Case 1, CC40-44	Case 2, CC41-42	Case 3, CC42-42	Case 4, CC44-45	No Reflector, CC46-39
Reflector salt fraction	0.00	0.01	0.02	0.04	
Conservation coefficient, [Mw (thermal)/kg]^2	18.95	16.42	15.41	14.08	11.36
Breeding gain, %	5.85	5.40	5.47	5.50	6.15
Yield, % per annum	3.56	3.18	3.11	2.98	2.83
Inventory, fissile, kg	1250	1290	1340	1406	1656
Specific power, Mw (thermal)/kg	1.80	1.74	1.68	1.60	1.36
Neutron leakage, %/fissile abs.	1.29	2.26	2.74	3.26	3.48
Dimensions, ft					
Core zone 1, radius[a]	7.14	7.17	7.14	7.38	8.07
Thickness, core zone 2					
axial	1.0	1.0	1.0	1.0	1.33[a]
radial[a]	0.92	0.82	0.89	0.90	1.58
Thickness, annulus[a]	0.083[b]	0.131	0.142	0.100	0.083[b]
Thickness, axial reflector[a]	4.0[b]	2.46	2.58	2.41	0.0
Thickness, radial reflector[a]	4.0[b]	3.28	2.59	2.13	0.0
Salt fraction, core 1[a]	0.134	0.131	0.131	0.134	0.137
Salt volumes, ft^3					
Core 1	279	275	273	297	364
Axial zone 2 + plena	235	234	234	250	372
Radial zone 2 + annulus	308	317	343	324	591
Reflectors	0	52	86	146	0
Total internal	821	877	936	1017	1326
Total system	1398	1454	1513	1594	1903
Power density, w/cm^3					
Average	24.4	24.5	24.2	23.0	16.3
Peak	64.0	63.0	63.6	60.2	64.3
Ratio	2.63	2.57	2.63	2.62	3.94
Graphite life,[c] years	3.7	3.7	3.7	3.9	3.75

[a]Optimized.
[b]Limit.
[c]Allowable fluence 3×10^{22} *nvt*, $E > 50$ kev.

increased by about 5% in extending the core life to about 4 years from the optimum of 2.4 years.

6.1.4 Optimum Thorium Concentration in MSBR

W. R. Cobb

Calculations to determine the optimum ThF_4 mole fraction in the fuel salt of a single-fluid MSBR were previously reported.[2] Changes in the reactor design, in the BeF_2 mole fraction in the salt, and improvements in the computational methods have prompted a reexamination of the question. The previously reported results were suspect because of the known limitations of the code OPTIMERC[3] and because the same cross sections were used for every salt considered.

In the series of calculations described below, the code ROD, an improved version of OPTIMERC, was used to

[2]O. L. Smith, W. R. Cobb, and H. T. Kerr, *MSR Program Semiann. Progr. Rept. Feb. 29, 1968*, ORNL-4254, p. 68.

[3]O. L. Smith, W. R. Cobb, and H. T. Kerr, *MSR Program Semiann. Progr. Rept. Aug. 31, 1968*, ORNL-4344, p. 68.

Table 6.3. MSBR Performance vs Graphite Life (Spherical Geometry)

Fixed parameters:

Reflector thickness, ft	3.0
Mole % thorium	12
Power, Mw (electrical)	1000
Power, Mw (thermal)	2250
Plant factor	0.8

Salt fractions:

Core zone 2	0.37
Reflector	0.005

	Case 1, CF10A-7	Case 2, CF13-27	Case 3, CF16-14
Graphite life,[a] years	2.4[b]	3.9	5.2
Damage flux, 10^{14} neutrons cm^{-2} sec^{-1}	4.8	2.9	2.2
Conservation coefficient, [Mw (thermal)/kg]^2	18.9	18.0	16.6
Breeding gain, %	5.60	5.70	5.66
Yield, % per annum	3.49	3.43	3.28
Inventory, fissile, kg	1224	1266	1314
Specific power, Mw (thermal)/kg	1.84	1.78	1.71
Dimensions, radial, ft			
Core zone 1[c]	6.50	8.14	9.14
Core zone 2[c]	2.04	1.43	1.10
Total core (1 + 2)	8.54	9.57	10.24
Salt fraction, core 1[c]	0.130	0.129	0.131
Peak power density, w/cm^3	98.2	59.8	44.7

[a]Allowable fluence 3×10^{22} *nvt*, $E > 50$ kev.

[b]Optimum with no restraint on damage flux.

[c]Parameter optimized.

determine the optimum design for the three reactors having salt compositions 74-16-10, 72-16-12, 70-16-14 (mole % LiF-BeF_2-ThF_4). The starting point for these three optimizations was an MSBR configuration very similar to the present reference design, but with a two-year graphite life. Each reactor was optimized with respect to five variables: core height, core radius, axial blanket thickness, radial blanket thickness, and core salt volume fraction. The optimum core salt volume fractions and the corresponding equilibrium nuclide concentrations for each reactor were then used to generate new cross sections appropriate for each case. For each reactor considered, three sets of cross sections were used, one each for the core, blanket, and plenum regions. The three reactors were then reoptimized using their respective cross sections, the starting estimates for the five variables being the results of the previous optimization. This procedure was continued until the differences between values of the optimized variables in two successive optimizations were less than 2%.

Characteristics of the three optimum designs are summarized in Table 6.4. Some quantities of interest are shown in Fig. 6.2. The breeding gain increases with

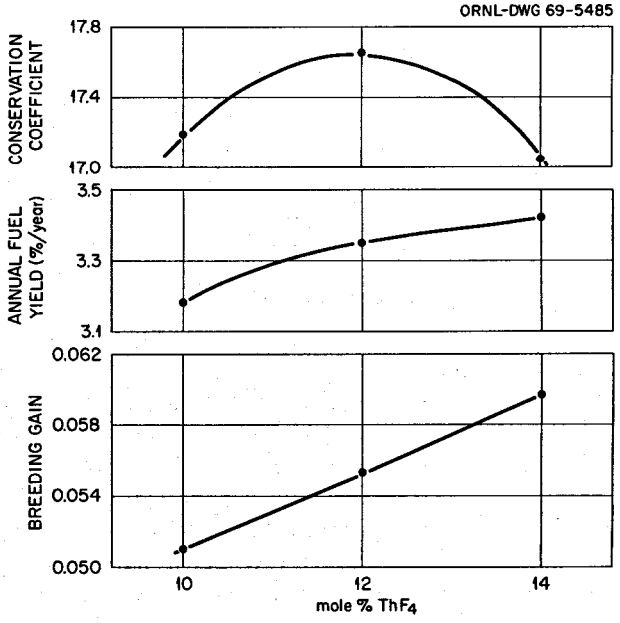

Fig. 6.2. MSBR Performance vs ThF_4 Mole % for Optimum Reactors.

Table 6.4. Optimum Reactor Designs with Different Salt Compositions

Fuel salt, mole % $LiF-BeF_2-ThF_4$	74-16-10	72-16-12	70-16-14
Core height, ft[a]	9.75	9.8	11.7
Core diameter, ft[a]	11.2	11.1	11.5
Radial blanket thickness, ft[a]	2.52	2.20	1.89
Axial blanket thickness, ft[a]	1.45	1.19	0.91
Radial reflector thickness, ft	3.0	3.0	3.0
Axial reflector thickness, ft	2.0	2.0	2.0
Core salt fraction[a]	0.137	0.121	0.114
Radial blanket salt fraction	0.37	0.37	0.37
Axial blanket salt fraction	0.37	0.37	0.37
Reactor power, Mw (thermal)	2250	2250	2250
Average power density, w/cm^3	29.4	33.14	33.5
Maximum power density, w/cm^3	97.3	106.3	101.6
Graphite replacement life, years	2.1	1.9	2.0
Specific fuel inventory, kg/Mw (electrical)	1.23	1.26	1.33
Breeding ratio	1.051	1.055	1.060
Annual fuel yield, % per year	3.18	3.35	3.42
Conservation coefficient	17.19	17.65	17.05

[a]Variables allowed to optimize.

increasing thorium (and hence fuel) concentration, over the range shown, primarily because of reduced parasitic neutron captures in the salt and in the moderator. This increase is achieved, of course, at the expense of a larger fuel inventory. The yield also increases, but more slowly than the breeding gain, because of the increase in fuel inventory.

The conservation coefficient[4] first increases because the breeding gain increases faster than the square of the specific power decreases. Above 12 mole % ThF_4 the inventory rises so rapidly that the decreasing specific power dominates and causes the conservation coefficient to decrease.

From these results it is seen that, with the conservation coefficient as the figure of merit, the best salt composition is at or near 12 mole % ThF_4.

It is interesting to compare this conclusion with that previously obtained using the annual fuel yield as the figure of merit. Those results indicated that the yield continued to increase as the ThF_4 concentration was increased above 12%. The 12 mole % salt was chosen primarily because salts with higher thorium concentrations had poorer heat transfer properties and because separation coefficients in the reductive extraction of rare-earth fission products appear to be somewhat better with the lower thorium concentration. With the figure of merit in which the square of the specific power appears there is a definite nuclear optimum at 12 mole % ThF_4.

6.1.5 Improvements in Computational Tools

W. R. Cobb

Two recent code developments have contributed to increased accuracy and decreased cost of routine design calculations for the MSBR.

The preparation of group constants formerly done by the code TONG on the IBM 7090 is now accomplished by the code XSDRN[5] on the IBM 360/75 (or 360/65). XSDRN is a one-dimensional discrete-ordinates (S_n) code combined with the code NIT, which calculates fine-group constants from resonance parameters by the Nordheim integral treatment. XSDRN cell calculations employ 93 fast groups and 30 thermal groups. From the XSDRN fluxes and 123-group data library, broad-group constants for 5 fast and 4 thermal groups are prepared for use in CITATION and ROD (reactor optimization) calculations.

Multigroup two-dimensional diffusion calculations for MSBR and MSBE design, formerly done with the code EXTERMINATOR-2,[6] are now being done with the

[4]Breeding gain times square of specific power.

[5]N. M. Greene, W. W. Engle, and C. W. Craven, Jr., *XSDRN: A Discrete Ordinates Spectral Averaging Code,* ORNL-TM-2500 (to be published).

[6]T. B. Fowler, M. L. Tobias, and D. R. Vondy, *EXTERMINATOR-2: A Fortran IV Code for Solving Multigroup Neutron Diffusion Equations in Two Dimensions,* ORNL-4078 (April 1967).

recently developed code CITATION.[7] Refinements in mesh representation and convergence accelerating techniques in CITATION make typical nine-energy-group, two-dimensional calculations run three to four times as fast as with EXTERMINATOR.

Also, because of differences in input format as compared with EXTERMINATOR, CITATION more conveniently allows use of multiple sets of cross sections for a particular nuclide. It is especially important to use ^{233}U and thorium cross sections which are appropriate to the energy spectra in the core and blanket respectively.

[7]T. B. Fowler and D. R. Vondy, *Nuclear Reactor Depletion and Dynamics Code: CITATION,* ORNL-TM-2496 (to be published).

6.1.6 Gamma and Neutron Heating in MSBR

O. L. Smith J. T. Ward

Gamma and neutron heat sources in the one-fluid reactor, vessel, and thermal and biological shields were calculated using gamma and neutron transport techniques based on the ANISN transport code. In these calculations the standard handbook recipes were specifically avoided, thereby eliminating the approximations and uncertainties involved in using buildup factors in complicated geometries.

Results are given here for one axial and two radial traverses of the reactor and shields. The region thicknesses and compositions are shown with the results in Figs. 6.3 through 6.8. For the radial traverses, two one-dimensional infinite-cylinder calculations were per-

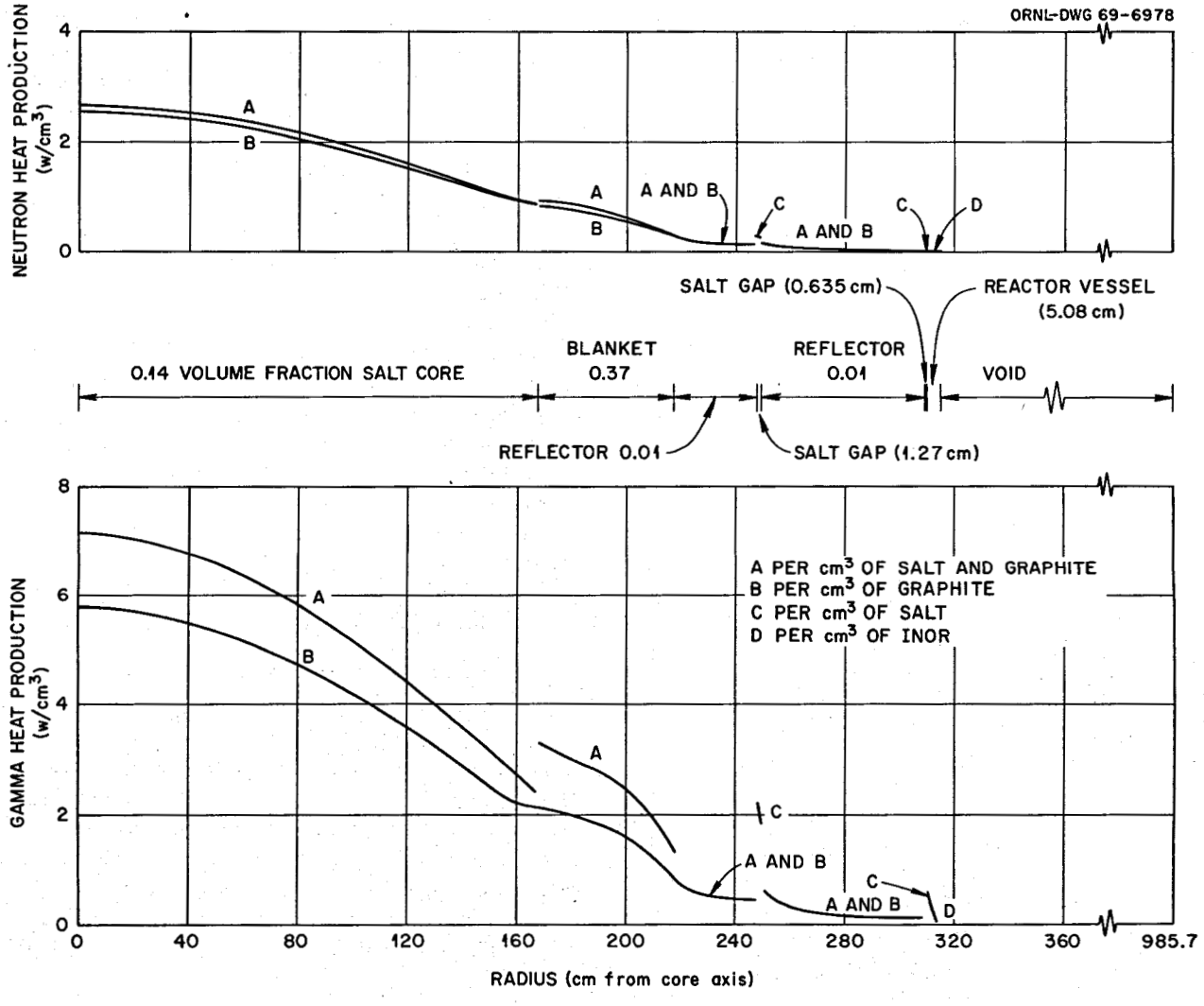

Fig. 6.3. Gamma and Neutron Heating in Core Midplane of 1000 Mw (Electrical) MSBR.

formed, the first at the core midplane, the second in a plane two-thirds of the distance from the midplane to the top of the core. In each case the neutron (and gamma) flux was normalized to the value of the actual center-line core flux at that elevation. No allowance was made for axial buckling. Thus, particularly in the shields, the calculated heat sources should be considered as upper limits to the actual heat sources. It is estimated that the calculated sources inside the reactor vessel are only a few percent high. But because of the large air gap between the vessel and shields, the calculated heat sources in the thermal shield and concrete should be reduced by about 50% to account for the actual finite height of the reactor.

In the axial center-line calculation, the system was represented in slab geometry, infinite in the radial dimension. Again, transverse buckling effects inside the vessel are small. The results for the thermal and biological shields are upper limits, but the overestimation is lower in the axial direction since the air gap is only a few feet.

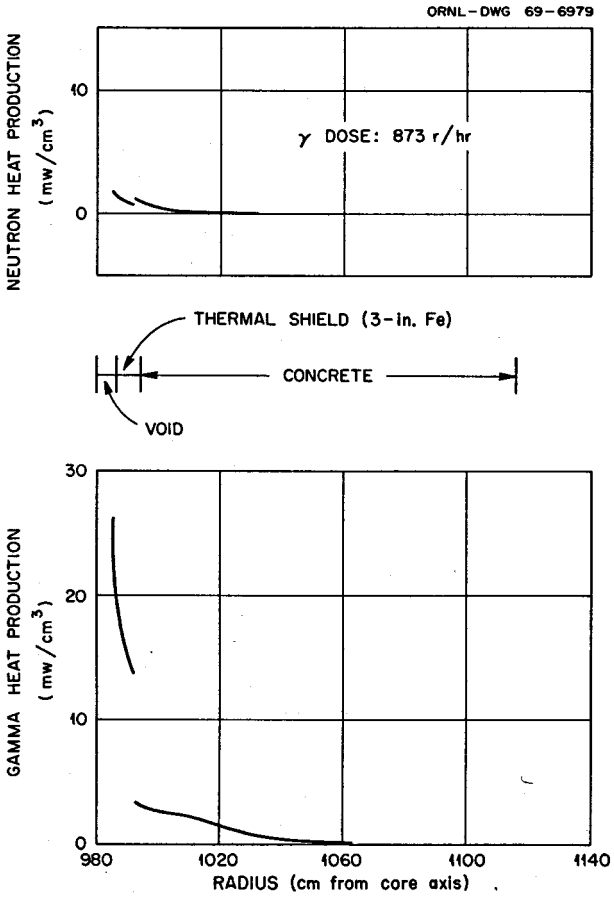

Fig. 6.4. Gamma and Neutron Heating in Core Midplane of 1000 Mw (Electrical) MSBR.

The calculations were performed in several linked stages starting with a one-dimensional ANISN transport calculation of the neutron space and energy distribution in the reactor and shields. From neutron fluxes and scattering cross sections, the neutron heat distribution was determined. The neutron heating in the reactor is shown in Figs. 6.3, 6.5, and 6.7 for the two radial traverses and one axial traverse. In each figure curve *A* shows the heat source per unit volume of *homogenized* core, blanket, reflector, or plenum. Curves *B* and *C* show, respectively, the heat source per unit volume of graphite and salt separately in those regions. Curve *D* shows the heating in the INOR vessel.

Figures 6.4, 6.6, and 6.8 show the neutron heating in the thermal and biological shields. The thermal shield is treated as pure iron. The concrete is a standard grade.

The gamma heat distribution is similarly presented in the figures. Three sources of gammas were calculated from the neutron flux distribution: prompt fission, delayed (fission product), and capture gammas. The first and last of these had the spatial distribution of the neutron flux. The delayed source was assumed uniform in the circulating salt. Since the salt spends approximately half its time in the reactor, approximately half of the delayed gammas are emitted inside the vessel.

These three sources of gammas were combined in a fixed-source ANISN gamma transport calculation using seven gamma energy groups. From the gamma fluxes the gamma heat sources were then calculated.

Also shown in Figs. 6.4, 6.6, and 6.8 are the gamma doses at the external surfaces of the biological shield.

From the results it should be particularly noted that neutron thermalization is a major heat source in the graphite.

6.2 PHYSICS ANALYSIS OF MSBE

6.2.1 MSBE Design Studies

O. S. Smith W. R. Cobb

Additional calculations were performed in the series of conceptual MSBE reactor configurations previously reported.[8] Results of the new calculations are summarized in Table 6.5. There were two objectives for the cases described here: first, to determine the maximum breeding ratio achievable in a reactor having a peak fast damage flux of 5×10^{14} neutrons cm^{-2} sec^{-1}, a core

[8] O. L. Smith and W. R. Cobb, *MSR Program Semiann. Progr. Rept. Aug. 31, 1968*, ORNL-4344, p. 71.

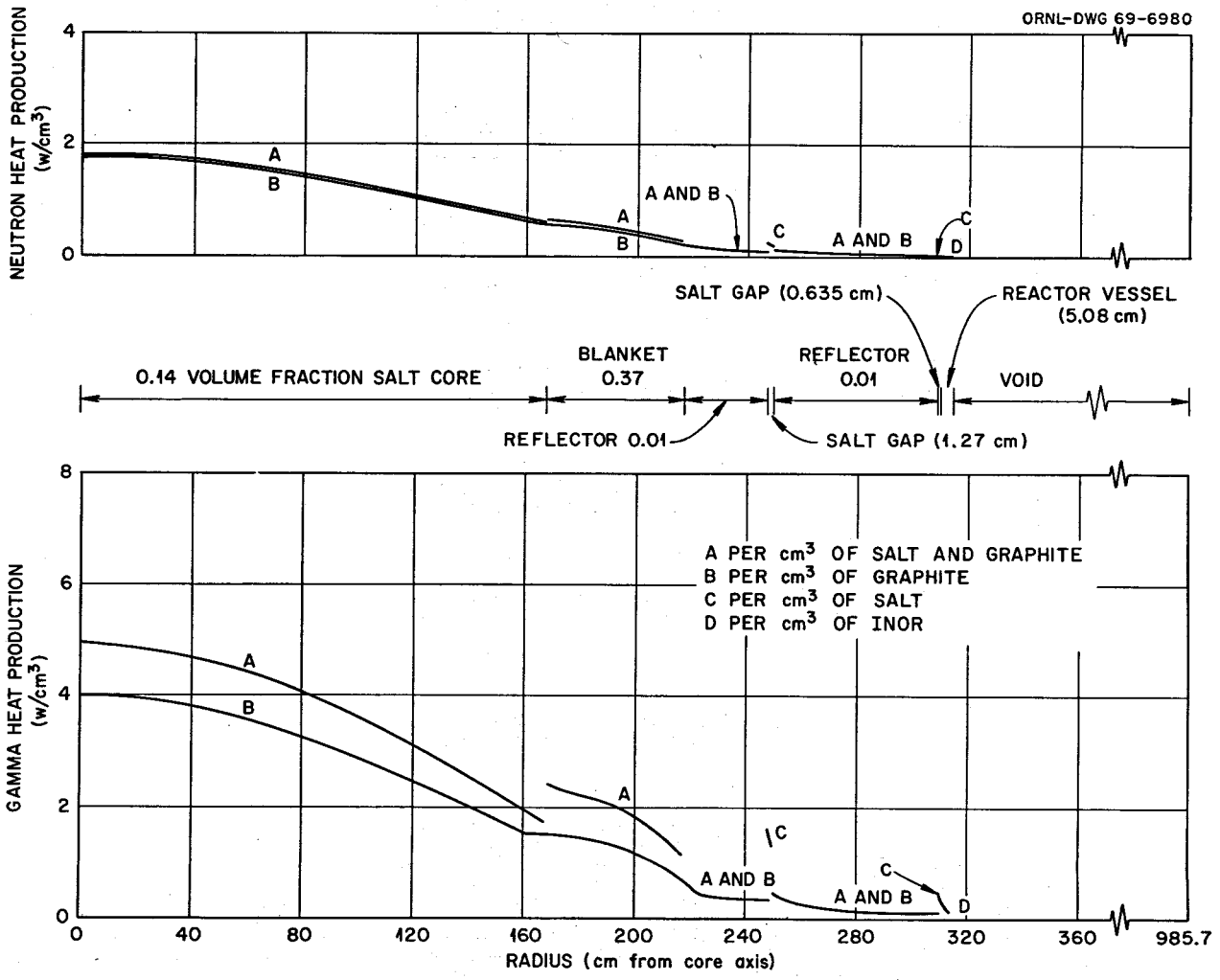

Fig. 6.5. Gamma and Neutron Heating in a Radial Plane Two-Thirds of Distance from Midplane to Top of Core of 1000 Mw (Electrical) MSBR.

Table 6.5. Nuclear Characteristics of Several Conceptual MSBE Reactor Configurations

Case	Core			Axial Blanket		Axial Plena Thickness[a] (ft)	Radial Blanket Thickness (ft)	Mole Fraction of ThF_4	Breeding Ratio[b]	Peak Damage Flux[c] (neutrons cm^{-2} sec^{-1})	Peak Power Density[c] (w/cm^3)	Fraction of Power in Core	Required Power[d] [Mw (thermal)]
	Diameter (ft)	Height (ft)	Salt Fraction	Thickness (ft)	Salt Fraction								
										$\times 10^{14}$			
21	4	6	0.2	2.5	0.5	0.5	3.75	0.14	1.112	1.94	39.5	0.46	258
22	4	6	0.2	2.0	0.5	0.5	3.0	0.14	1.111	2.28	46.8	0.52	219
23	4	6	0.2	1.0	0.5	0.5	2.0	0.14	1.061	2.51	51.2	0.55	199
24	4	6	0.2	2.0	0.5	0.5	2.0	0.14	1.077	2.34	48.1	0.52	214
25	4	5	0.2	1.5	0.5	0.5	2.0	0.14	1.063	2.66	54.7	0.51	188
26	4	5	0.2	1.5	0.5	0.5	2.0	0.12	1.051	2.53	52.8	0.49	198
27	4	5	0.15	1.5	0.5	0.5	2.0	0.12	1.047	2.48	50.6	0.46	202
28	4	5	0.2	1.07	0.7	0.357	2.0	0.14	1.062	2.96	65.3	0.57	169
29[e]	4	5	0.2	1.07	0.7	0.357	2.0	0.14	1.069	3.04	69.0	0.59	164
30	4	5	0.2	1.07	0.7	0.357	2.0	0.12	1.051	2.95	66.5	0.57	169
31	3.5	4.5	0.2	1.07	0.7	0.357	2.0	0.14	1.049	3.67	84.8	0.52	136
32	3	4	0.2	1.07	0.7	0.357	2.0	0.14	1.020	4.29	101.3	0.43	117
33	3	4	0.2	1.0	0.7	0.25	1.75	0.14	0.993	4.45	105.1	0.44	112
34	3	4	0.2	0.75	0.7	0.25	1.5	0.14	0.956	4.70	111.2	0.46	106
35	3	4	0.2	1.0	0.7	0.25	1.0	0.14	0.893	5.02	119.0	0.49	100
36	3	4	0.2	1.0	0.7	0.25	1.75	0.12	0.972	4.34	102.2	0.43	115

[a]Contains 6% INOR.
[b]At start of life with ^{233}U fuel.
[c]At reactor power of 100 Mw (thermal).
[d]Reactor power required to achieve a peak damage flux of 5×10^{14} neutrons cm^{-2} sec^{-1}.
[e]New core cross sections introduced.

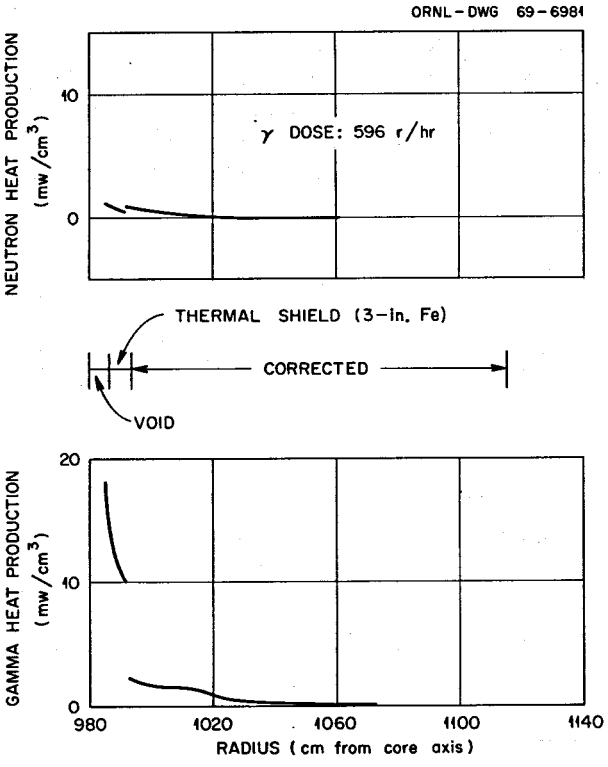

Fig. 6.6. Gamma and Neutron Heating in a Radial Plane Two-Thirds of Distance from Midplane to Top of Core of 1000 Mw (Electrical) MSBR.

power fraction greater than 0.33, and a reactor power in the range of 200 Mw (thermal); second, to determine the minimum reactor power which would produce a peak damage flux of 5×10^{14} neutrons cm^{-2} sec^{-1}, a core power fraction greater than 0.33, and a breeding ratio near unity (i.e., 1.0 ± 0.05). Cases 21–30 were performed to achieve the first objective, cases 31–35 to achieve the second. An axial blanket is shown here to have an important influence on the reactor performance. Previous cases had only a few inches of blanket material in the axial direction. In particular, comparison of case 25 with the previously published case 18 (which had only a few inches of axial blanket) shows that the effect of reducing the core length by 1 ft and adding 1.5 ft of axial blanket at either end of the core improves the breeding ratio without compromising other aspects of the performance. Comparison of cases 26 and 27 shows that the desired core salt fraction is 0.2. Comparison of cases 25 and 28 shows that the axial (and, of course, radial) salt fraction should be made as large as possible in order to harden the blanket spectrum and peak the power production in the core.

During the course of these calculations two new codes, CITATION (an improved version of EXTERMINATOR) and XSDRN (a cross section code which replaces TONG), were introduced into the calculational procedures for the MSBE design studies. CITATION was available and used for all of the cases in Table 6.5, but XSDRN was not available until case 29. Hence the slight difference between cases 28 and 29 reflects the difference between the old and new cross sections.

Case 30 includes all the improvements established in cases 21 through 29 and has 12 mole % ThF_4 (as currently specified in the MSBR fuel salt). This case demonstrates that a reactor operating at 169 Mw (thermal) will produce a damage flux of 5×10^{14}, a core power fraction of 0.57, and a start-of-life breeding ratio of 1.051. This appears to be the most attractive reactor configuration in the 200 Mw (thermal) range.

Cases 31–36 are largely self-explanatory. The desired damage flux can be achieved at lower power levels by decreasing the blanket thickness and sacrificing the breeding ratio. Case 36 shows that a reactor operating at 115 Mw (thermal) with 12 mole % ThF_4 would have a damage flux of 5×10^{14} neutrons cm^{-2} sec^{-1}, a breeding ratio of 0.97, and a core power fraction of 0.43. This appears to be the most attractive reactor configuration in the 100 Mw (thermal) range.

6.3 MSBR EXPERIMENTAL PHYSICS

6.3.1 Initial Results of the Experiment to Measure $\alpha(^{235}U)$ in the MSRE

G. L. Ragan

Samples of the circulating fuel salt were taken during the final run of the MSRE with ^{235}U fuel for use in the measurement of $\alpha(^{235}U)$; $\alpha = \bar{\sigma}_c/\bar{\sigma}_f$. The method relies, as outlined in an earlier report,[9] on precise measurements of the concentrations of ^{235}U and ^{236}U relative to that of ^{238}U.

The isotopic ratios are being measured by Lester A. Smith and co-workers of the Isotopic Analysis Department at the Oak Ridge Gaseous Diffusion Plant. Some of their early measurements have been analyzed, but the results must be considered as preliminary until additional measurements have been made and analyzed and a comprehensive study of errors has been made.

The results presently available appear to agree very well with the spectrum-average value of α that was

[9] *MSR Program Semiann. Progr. Rept. Feb. 29, 1968*, ORNL-4254, p. 72.

calculated on the basis of the ENDF/B cross sections for ^{235}U. The calculated average α was 0.264, while the mass spectrometer measurements, with provisional corrections for burnout of ^{238}U and ^{236}U, indicate a value of 0.255. The errors have not yet been fully determined. While additional mass spectrometer measurements are to be made, and further analysis, both of the values and of the errors, will be required, it appears that the technique will indeed provide valuable integral checks on the differential cross-section measurements.

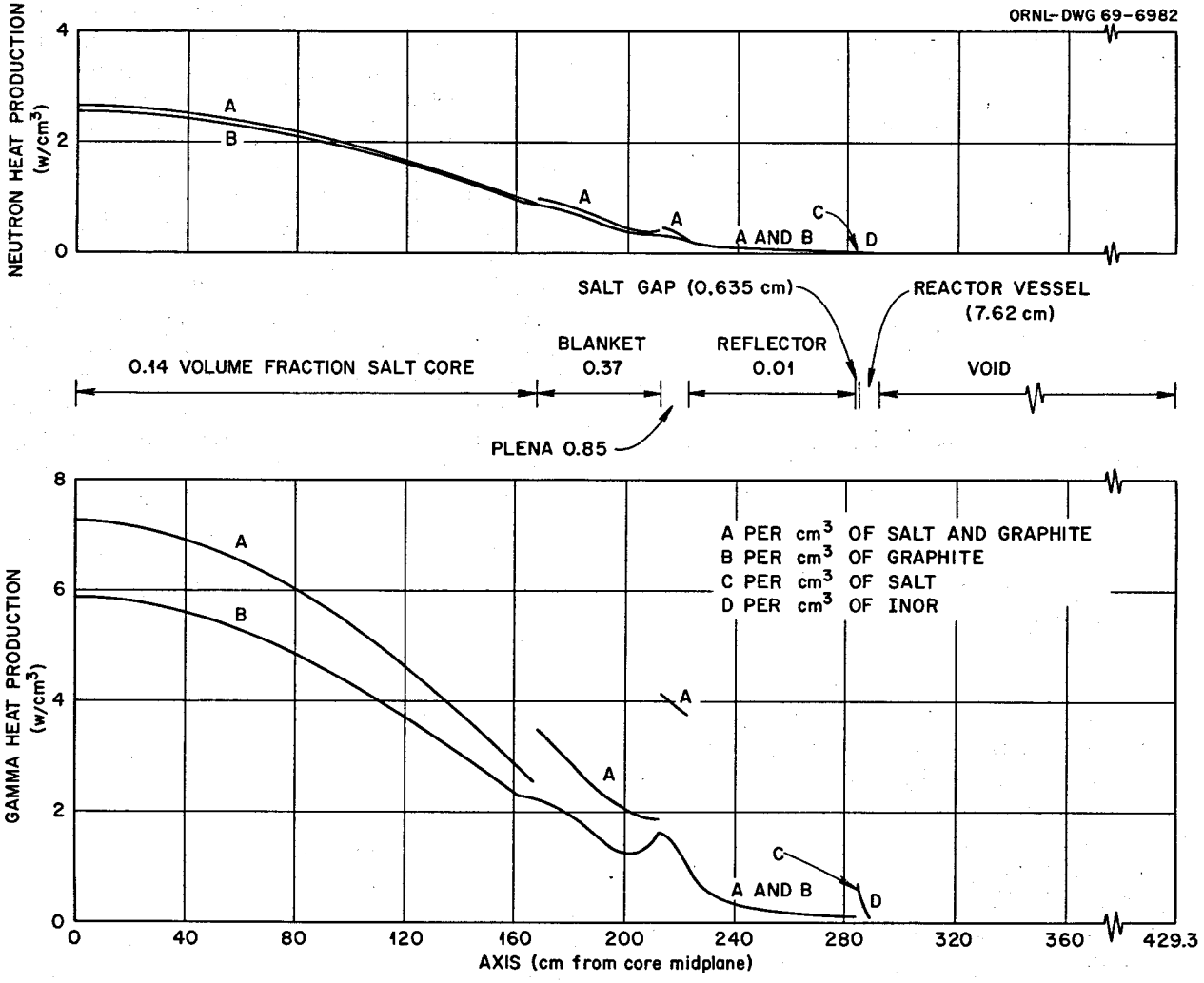

Fig. 6.7. Gamma and Neutron Heating near Core Axis of 1000 Mw (Electrical) MSBR.

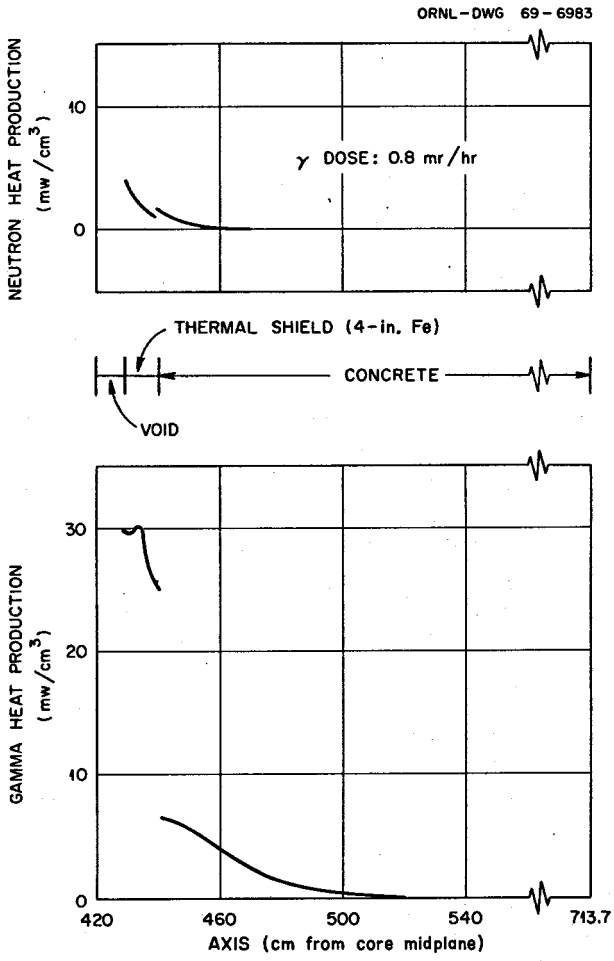

Fig. 6.8. Gamma and Neutron Heating near Core Axis of 1000 Mw (Electrical) MSBR.

7. Systems and Components Development

Dunlap Scott

7.1 OFF-GAS SYSTEM

A. N. Smith R. B. Gallaher Dunlap Scott

The general flow diagram for the off-gas system is shown in Fig. 5.3 and is still essentially as has been described previously.[1] Current estimates indicate that the gas flow from the reactor primary system to the volume holdup in the off-gas system will be about 11 scfm, of which 9 scfm will come from the gas separators and the balance from the purge streams for the pump shafts and miscellaneous instruments. A liquid-metal coolant operated at temperatures below 500°F is being considered for removing heat from the volume holdup tank. If this method is accepted, the system for cooling the liquid metal would have to be set up separately from the primary-salt drain tank coolant system, since the latter would require a much higher minimum operating temperature. The preliminary design concept for the volume holdup tank is described below.

7.1.1 Volume Holdup Tank

The function of the volume holdup tank is to delay the off-gas stream for about 1 hr to permit decay of a large fraction of the short-lived fission products and dissipation of the accompanying heat. The cooling system must be capable of handling a maximum of 18 Mw of decay heat. Provision must be made for the collection and disposal of 1 to 2 lb of solid fission products per day. Although the incoming gas will be 99+% helium, it will contain trace quantities of a variety of other elements, including: tritium (^{3}H); stable Kr and Xe; radioactive Kr and Xe and associated daughters such as Ba, Cs, La, Rb, Sr, Y, and Zr; and a "smoke" of the so-called noble metals, Mo, Ru, Tc, and Te. In addition, there will probably be small amounts of the fuel salt in the form of a mist. Such mist particles will be microspheres and will contain all the ingredients of the fuel stream. In the volume holdup region the noble metals and the daughters of Kr and Xe will be in either the liquid or the solid state, and particles suspended in the gas will probably range in size from about 20 μ down to single atoms.

For the initial approach to the problem, we have assumed that settling or impaction will be used to transfer the particles directly into a coolant stream. The coolant will be recirculated through external equipment for continuous removal of the solids and the associated decay heat. The primary task is the selection of a coolant which will satisfy our tentative requirements for the system. Such a coolant must safely accept and hold the "noble" metals, the daughters of the noble metals, and the daughters of the noble gases and then must release these fission products by treatment only in the proper areas. It must have a vapor pressure low enough to minimize carry-over to the 47-hr holdup system, must be compatible with its container and with fuel salt, and should have an existing technology for use as a heat transfer agent. The eutectic of lead and bismuth appears to offer sufficient attractiveness to merit first place on the list of candidates. It is compatible with the fuel salt, it has high density which should minimize settling out of entrained noble metals, and its low melting point (275°F) may permit operation at low temperature and the use of relatively low-cost alloys as materials of construction.

Figure 7.1 shows a conceptual design of a volume holdup tank utilizing the impaction mechanism for transfer of the solids to a recirculating coolant stream. Performance of the device has been calculated by use of an equation developed for a low-pressure cascade impactor.[2] The results indicate that it should be possible to design a system of reasonable geometry for

[1] *MSR Program Semiann. Progr. Rept. Aug. 31, 1968,* ORNL-4344, pp. 56 ff. and 72 ff.

[2] G. W. Parker and H. Buchholz, *Size Classification of Submicron Particles by a Low Pressure Cascade Impactor,* ORNL-4226 (June 1968).

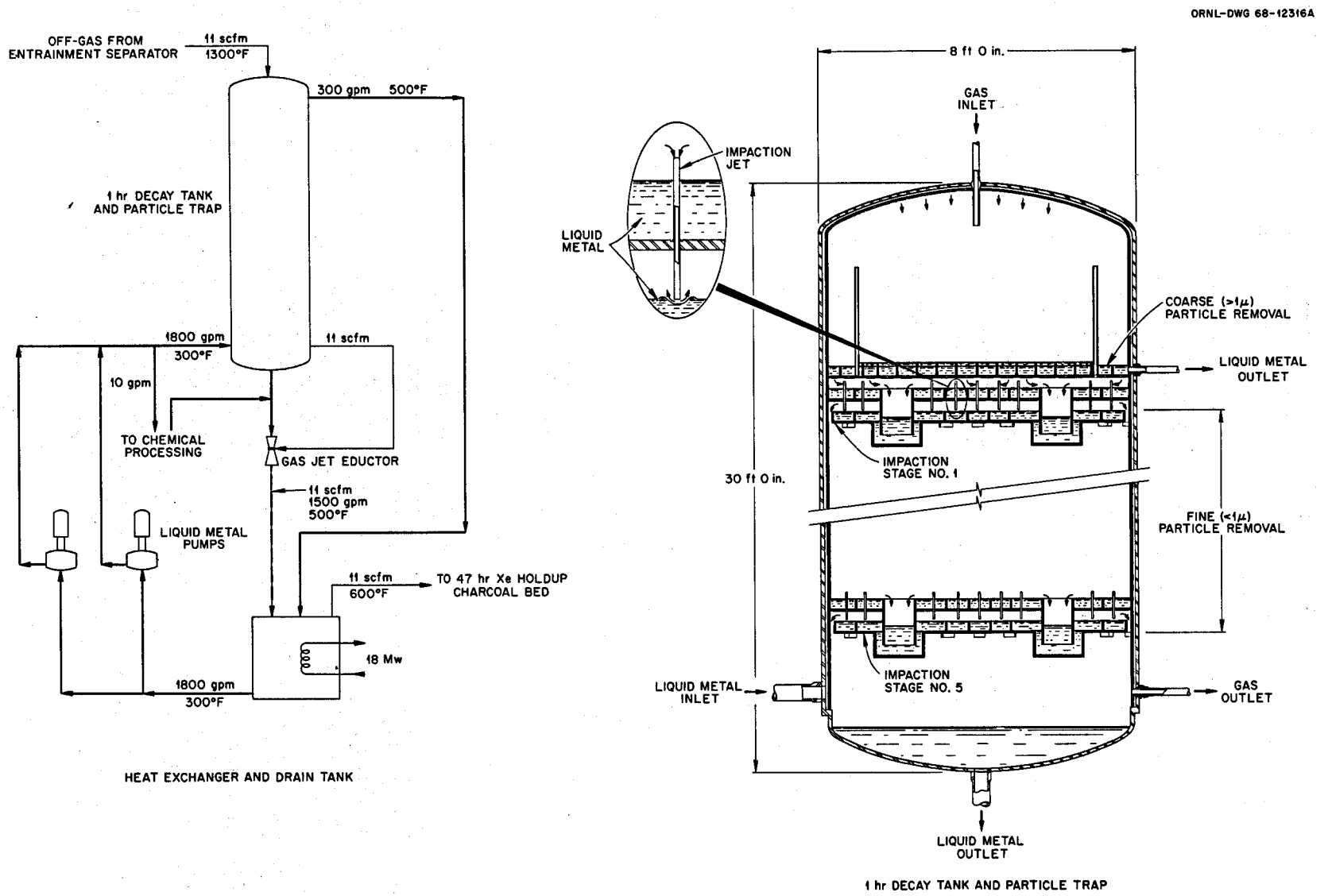

Fig. 7.1. Particle Trap and 1-hr Decay System for MSBR Off-Gas.

removal of particles in the 0.1-to-1.0-μ range. Thus, for removal of 0.15-μ particles at 50% efficiency, forty-two 0.080-in.-diam jets would be required for one stage to handle the gas flow. A number of stages of relatively low efficiency and operated in series will be used to distribute the heat load and to minimize short-circuiting of the gas into the charcoal beds, which are next in the gas system. The volume holdup tank proper will be 8 ft in diameter by 30 ft high. Coolant flow is from top to bottom, and the coolant is also circulated through a jacket to provide cooling for the walls of the vessel and to absorb the gamma energy which is released as part of the fission product decay.

7.2 NOBLE-GAS MIGRATION IN THE MSBR

R. J. Kedl

In the last semiannual progress report,[3] results of ^{135}Xe poisoning calculations were presented for a 1000 Mw (electrical) single-fluid MSBR having a blanket and reflector. The xenon stripping mechanism uses recirculating helium bubbles 0.020 in. in diameter, where the clean helium bubbles are added to the fuel and ^{135}Xe-rich bubbles are stripped out of the fuel in a bypass around the pump. In the calculational model the fuel loop is treated as a well-stripped pot. These computations were repeated for all other noble-gas fission products, of which there are over 30 kryptons and xenons. The results are shown in Table 7.1. Some of the more significant gas-migration parameters are listed below, and the cases are characterized in the table by the ^{135}Xe poison fraction. The tabulated fluxes are about the same for any reasonable combination of these parameters that yield the same ^{135}Xe poison fraction.

^{135}Xe poison fraction, %	1.27	0.56
Volume fraction bubbles in fuel salt	0.002	0.006
Fraction bubbles replaced per loop circuit	0.1	0.1
Xenon diffusion coefficient in bulk graphite, ft^2/hr	10^{-5}	10^{-5}
Xenon diffusion coefficient in graphite coating, ft^2/hr	10^{-7}	10^{-7}
Available void fraction in graphite coating, %	1	1
Graphite coating thickness, in.	0.010	0.010
Mass transfer coefficient to bubbles, ft/hr	2.0	2.0
Graphite surface area in core, ft^2	25,500	25,500

[3] *MSR Program Semiann. Progr. Rept. Aug. 31, 1968*, ORNL-4344.

The flow diagram that forms the basis for the calculations in Table 7.1 is shown in Fig. 7.2. Note that the flux into the bubbles is not necessarily equal to the flux out of the reactor. Some longer-lived noble gases are recycled from the 48-hr holdup system back into the reactor with the helium, and for those gases the flux to the bubbles is less than the flux out of the reactor. For the short-lived gases the flux to the bubbles is greater, because some decay and burnup take place between the time the noble gas enters a bubble and the time the bubble leaves the salt. For very short-lived isotopes, where the half-life is a small part of the loop circuit time, one would question the applicability of the well-stirred pot model. Nevertheless, these computations are adequate for the preliminary designs.

7.2.1 Contribution of the Noble Gases to Afterheat in the Graphite

With the use of the noble-gas flux into graphite, described above, we can compute their contribution to

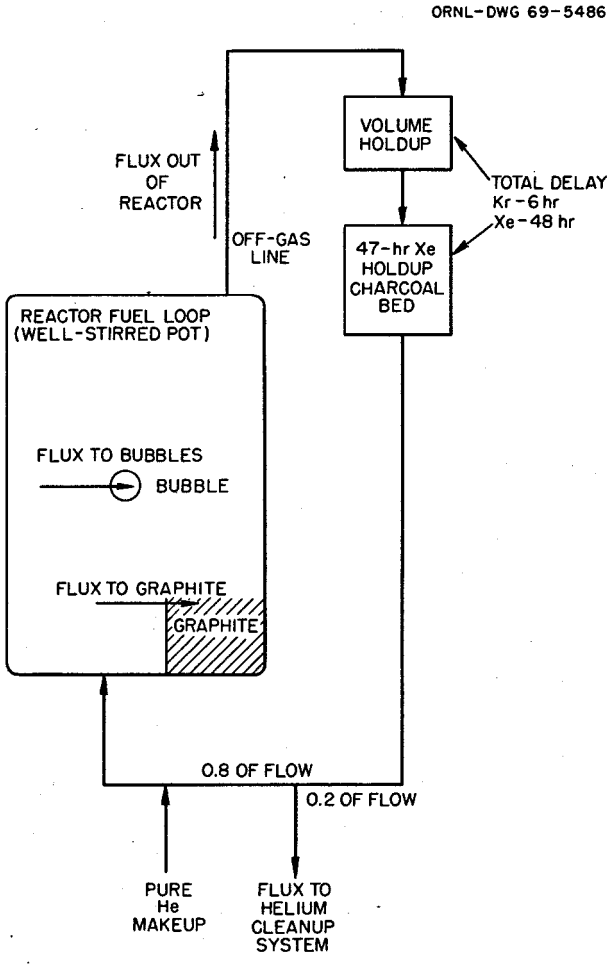

Fig. 7.2. Flow Diagram to Define Terms Used in Table 7.1.

Table 7.1. Noble-Gas Migration in the MSBR

Noble-Gas Isotope	Decay Constant Used in Calculation (hr^{-1})	Cumulative Yield from ^{233}U (fraction)	Thermal Cross Section (barns)	^{135}Xe Poison Fraction = 1.27%				^{135}Xe Poison Fraction = 0.56%			
				Noble-Gas Flux to Graphite (atoms/hr)	Noble-Gas Flux to Bubbles (atoms/hr)	Noble-Gas Flux Out of Reactor (atoms/hr)	Noble-Gas Flux to Helium Cleanup System (atoms/hr)	Noble-Gas Flux to Graphite (atoms/hr)	Noble-Gas Flux to Bubbles (atoms/hr)	Noble-Gas Flux Out of Reactor (atoms/hr)	Noble-Gas Flux to Helium Cleanup System (atoms/hr)
^{82}Kr	1.0×10^{-5}	0.003	45.0	3.71×10^{18}	2.10×10^{21}	1.05×10^{22}	2.10×10^{21}	1.24×10^{18}	2.11×10^{21}	1.05×10^{22}	2.11×10^{21}
^{83}Kr	1.0×10^{-5}	0.0114	0	8.56×10^{17}	3.00×10^{21}	1.50×10^{22}	3.00×10^{21}	2.85×10^{17}	3.00×10^{21}	1.50×10^{22}	3.00×10^{21}
^{84}Kr	1.0×10^{-5}	0.0110	0.160	8.42×10^{17}	2.90×10^{21}	1.45×10^{22}	2.90×10^{21}	2.81×10^{17}	2.90×10^{21}	1.45×10^{22}	2.90×10^{21}
^{85}Kr	7.35×10^{-6}	0.0249	0.096	1.40×10^{18}	6.56×10^{21}	3.28×10^{22}	6.56×10^{21}	4.67×10^{17}	6.56×10^{21}	3.28×10^{22}	6.56×10^{21}
^{86}Kr	1.0×10^{-5}	0.0328	0.060	2.48×10^{18}	8.64×10^{21}	4.32×10^{22}	8.64×10^{21}	8.27×10^{17}	8.64×10^{21}	4.32×10^{22}	8.64×10^{21}
^{87}Kr	0.547	0.0450	500.0	1.87×10^{21}	9.55×10^{21}	9.67×10^{21}	7.27×10^{19}	7.15×10^{19}	1.10×10^{22}	1.11×10^{22}	8.35×10^{19}
^{88}Kr	0.247	0.0570	0	2.34×10^{21}	1.24×10^{21}	1.50×10^{22}	6.87×10^{20}	8.81×10^{20}	1.40×10^{22}	1.70×10^{22}	7.72×10^{20}
^{89}Kr	13.0	0.0623	0	1.77×10^{21}	7.08×10^{21}	5.07×10^{21}	0	9.49×10^{20}	1.14×10^{22}	8.16×10^{21}	0
^{90}Kr	75.6	0.0555	0	7.22×10^{20}	2.01×10^{21}	6.08×10^{20}	0	5.66×10^{20}	4.74×10^{21}	1.43×10^{21}	0
^{91}Kr	249.0	0.0410	0	2.51×10^{20}	5.28×10^{20}	6.13×10^{19}	0	2.28×10^{20}	1.44×10^{21}	1.67×10^{20}	0
^{92}Kr	832.0	0.0296	0	7.17×10^{19}	1.21×10^{20}	4.58×10^{18}	0	6.96×10^{19}	3.53×10^{20}	1.33×10^{19}	0
^{93}Kr	1230.0	0.0142	0	2.48×10^{19}	3.97×10^{19}	1.03×10^{18}	0	2.43×10^{19}	1.17×10^{20}	3.02×10^{18}	0
^{94}Kr	2496.0	0.0062	0	5.88×10^{18}	8.65×10^{18}	1.12×10^{17}	0	5.82×10^{18}	2.57×10^{19}	3.32×10^{17}	0
^{95}Kr	2490.0	0.0019	0	1.80×10^{18}	2.65×10^{18}	3.43×10^{16}	0	1.78×10^{18}	7.87×10^{18}	1.02×10^{17}	0
^{126}Xe	1.0×10^{-5}	0.0020	1.50	3.90×10^{17}	5.27×10^{20}	2.63×10^{21}	5.25×10^{17}	1.30×10^{17}	5.27×10^{20}	2.63×10^{21}	5.26×10^{20}
^{128}Xe	1.0×10^{-5}	0.0002	2.50	4.08×10^{16}	5.00×10^{19}	2.50×10^{20}	4.99×10^{19}	1.36×10^{16}	5.00×10^{19}	2.50×10^{20}	4.99×10^{19}
^{129}Xe	1.0×10^{-5}	0.0210	0	3.48×10^{18}	5.53×10^{21}	2.76×10^{22}	5.52×10^{21}	1.16×10^{18}	5.53×10^{21}	2.76×10^{22}	5.52×10^{21}
^{130}Xe	1.0×10^{-5}	0.0010	2.50	2.21×10^{17}	2.71×10^{20}	1.35×10^{21}	2.71×10^{20}	7.38×10^{20}	2.71×10^{20}	1.35×10^{21}	2.71×10^{20}
^{131}Xe	1.0×10^{-5}	0.0385	120.0	9.42×10^{19}	1.00×10^{22}	5.02×10^{22}	1.00×10^{22}	3.16×10^{19}	1.01×10^{22}	5.05×10^{22}	1.01×10^{22}
^{132}Xe	1.0×10^{-5}	0.0548	0.20	9.30×10^{18}	1.44×10^{22}	7.20×10^{22}	1.44×10^{22}	3.10×10^{18}	1.44×10^{22}	7.20×10^{22}	1.44×10^{22}
^{133}Xe	5.48×10^{-3}	0.0648	190.0	2.36×10^{21}	1.47×10^{22}	3.82×10^{22}	5.87×10^{21}	8.68×10^{20}	1.62×10^{22}	4.21×10^{22}	6.47×10^{21}
^{134}Xe	1.0×10^{-5}	0.0683	0.20	1.16×10^{19}	1.80×10^{22}	8.97×10^{22}	1.79×10^{22}	3.87×10^{18}	1.80×10^{22}	8.98×10^{22}	1.79×10^{22}
^{135}Xe	0.0753	0.0616	1.05×10^{6}	4.61×10^{21}	1.12×10^{22}	1.13×10^{22}	6.11×10^{19}	1.93×10^{21}	1.41×10^{22}	1.43×10^{22}	7.68×10^{19}
^{136}Xe	1.0×10^{-5}	0.0700	0.15	1.18×10^{19}	1.84×10^{22}	9.20×10^{22}	1.84×10^{22}	3.94×10^{18}	1.84×10^{22}	9.20×10^{22}	1.84×10^{22}
^{137}Xe	9.90	0.0716	0	3.87×10^{21}	8.49×10^{21}	6.51×10^{21}	0	2.04×10^{21}	1.34×10^{22}	1.03×10^{22}	0
^{138}Xe	2.446	0.0663	0	4.53×10^{21}	1.09×10^{22}	1.01×10^{22}	0	2.02×10^{21}	1.45×10^{22}	1.35×10^{22}	0
^{139}Xe	60.85	0.0493	0	1.19×10^{21}	2.09×10^{21}	7.31×10^{20}	0	9.01×10^{20}	4.75×10^{21}	1.66×10^{21}	0
^{140}Xe	156.0	0.0352	0	4.45×10^{20}	6.90×10^{20}	1.19×10^{20}	0	3.87×10^{20}	1.80×10^{21}	3.12×10^{20}	0
^{141}Xe	1250.0	0.0180	0	3.80×10^{19}	4.96×10^{19}	1.26×10^{18}	0	3.73×10^{19}	1.46×10^{20}	3.71×10^{18}	0
^{142}Xe	1660.0	0.0163	0	2.64×10^{19}	3.40×10^{19}	6.55×10^{17}	0	2.60×10^{19}	1.00×10^{20}	1.94×10^{18}	0
^{143}Xe	2490.0	0.0017	0	1.86×10^{18}	2.34×10^{18}	3.04×10^{16}	0	1.84×10^{18}	6.96×10^{18}	9.01×10^{16}	0
^{144}Xe	2490.0	0.0001	0	7.74×10^{16}	9.77×10^{16}	1.27×10^{15}	0	7.66×10^{16}	2.90×10^{17}	3.76×10^{15}	0

afterheat. Figure 7.3 shows the results for the case where ^{135}Xe poison fraction is 0.56%. It is assumed that the noble-gas flux into the graphite is constant and continuous for two years with the reactor at power. The amount of noble gases and their daughters can then be computed after this period of time. This computation is based on straight-chain decay and no side decay loops.

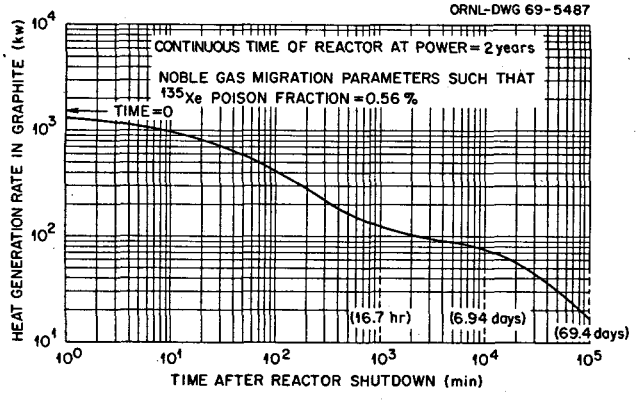

Fig. 7.3. Afterheat Contribution by Noble Gases and Their Daughters Adsorbed by the Graphite in the MSBR Core [1000 Mw (Electrical)]. The residence time for krypton in the charcoal beds is about one-twelfth of that for xenon. The flux of atoms into the off-gas line was calculated by R. J. Kedl using 0.56% poison fraction. Decay heat calculations were made by M. Bell using computer code.

7.2.2 Distribution of Decay Heat in the MSBR Off-Gas System

A. N. Smith M. Bell

An estimate has been made of the distribution of fission product decay heat in the 1000 Mw (electrical) MSBR off-gas system. The calculations were based on the following model:

1. The flux of krypton and xenon into the off-gas line will be as calculated by R. J. Kedl for 0.56% poison fraction (see Table 7.1). Solid daughters of krypton and xenon are assumed to plate out at the point of formation, which gives a high heating value for the pipe sections.
2. The flux to the off-gas will include 50% of the noble-metal fission products. Of these, 100% will be retained in the 1-hr volume holdup.
3. Krypton delay in the charcoal beds will be $^1/_{12}$ xenon delay.
4. The off-gas system will be divided into 20 regions, as shown in Fig. 7.4. The unstable noble gases will decay exponentially in accordance with an assigned delay or residence time. The 1-hr volume holdup and the 47-hr xenon delay charcoal bed were divided into compartments with various delay times in an attempt to obtain approximately equal heat loads. The delay times for the pipe sections were arbitrarily set at 18 sec each.

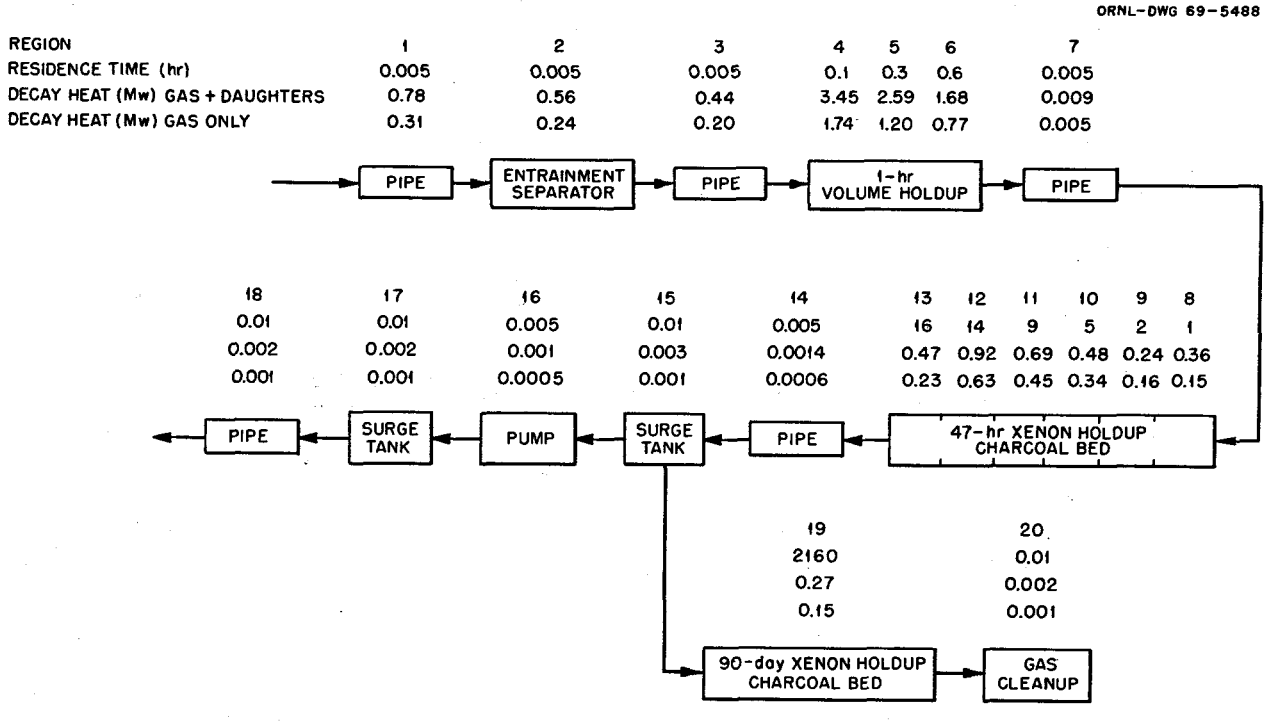

Fig. 7.4. Distribution of Decay Heat in MSBR Off-Gas System.

The results, which are shown in Fig. 7.4, indicate that the total heat load will be about 21 Mw, distributed as follows:

	Heat Released (Mw)	Percent of Heat Load
Entrainment separator and adjacent pipes	1.8	9
1-hr volume holdup	16.5[a]	78
47-hr xenon delay charcoal beds	2.7	13
Remainder, including 90-day xenon delay beds	0.3	0.1
	21.3	

[a]Includes 9 Mw of decay heat from noble metals.

7.3 BUBBLE GENERATOR

R. J. Kedl

After considering several concepts for bubble generators, both fluid and mechanically powered, we have settled on one. It can be thought of as an inverted venturi and consists of a teardrop inside a straight section of pipe. A plastic model has been built and tested with water and air as shown in Fig. 7.5. Air is injected into the throat through forty-eight $\frac{1}{64}$-in.-diam holes in the teardrop. It could just as easily have been injected through holes in the pipe wall or possibly through a porous material. Four teardrop shapes have been tested. The variable parameter in three of them was the throat gap thickness, and in the fourth it was the angle of the diffuser region. The generator has been tested over the following ranges of variables:

Water flow rate, gpm	20–38
Water velocity in 1-in.-ID pipe, fps	8.2–15.5
Air flow rate, scfh	0–2.5
Void fraction, %	0–1.5
Throat gap thickness, in.	0.062, 0.094, 0.125

Many high-speed photographs have been taken of this device, and the following have been observed:

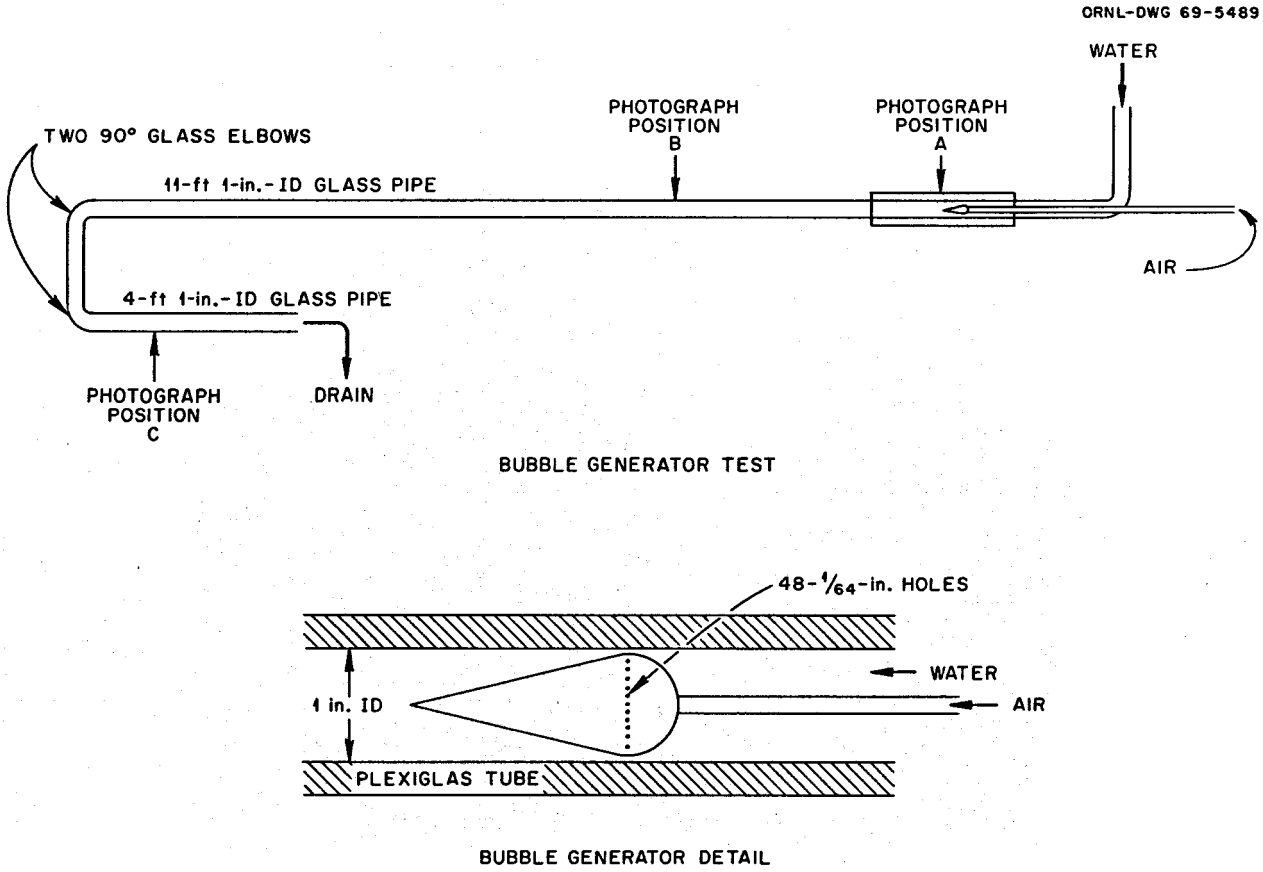

Fig. 7.5. Bubble-Generator Test Flow Diagram.

1. A continuous gas plume develops for each hole in the teardrop and extends into the diffuser region of the teardrop, as shown in Fig. 7.6. The plume is broken up into bubbles by the turbulence developed in the diffuser.
2. The bubble size is independent of the gas flow rate over the range tested.
3. The bubble size is a mild inverse function of the water flow rate.
4. The bubble size is approximately proportional to the throat gap thickness over the range tested and can be approximated by:

   Bubble diameter $\approx$ 0.25 X throat thickness.

5. The bubble size is probably not a strong function of the hole size used for air injection.

Recalling that the target bubble size for the MSBR is 20 mils, a throat gap thickness of about 80 mils would be required.

The principal problem does not involve the bubble generator but rather involves bubble coalescence downstream of the generator. Coalescence of bubbles in this diameter range seems to be a rather strong function of void fraction in the range of 0.1 to 0.5%. This is illustrated by the two series of pictures in Fig. 7.7. In both series the water flow rate is 38 gpm, giving a fluid velocity of 15.5 fps in the glass pipe. The throat gap thickness is 0.094 in. The difference between the series is that in one the void fraction is about 0.5% and in the other the void fraction is about 0.09%. The black line that appears is a paper clip wire 0.036 in. in diameter. Location of the pictures is defined in Fig. 7.5. Location *A* is at the bubble generator. Note that the bubbles are about 20 mils in diameter in both series. Location *B* is about 3½ ft downstream of the generator. Location *C* is 10 ft downstream from *B* and follows two 90° elbows. In the case of the higher void fraction, the bubbles have coalesced to an average diameter of about 40 mils at location *C*. In the case of the lower void fraction there seems to be very little coalescence. Indications from other pictures are that higher fluid velocities will inhibit coalescence, but this must be checked further. The pipe velocities in the MSBR will be over 20 fps, whereas in Fig. 7.7 the fluid velocities are 15.5 fps.

7.4 BUBBLE SEPARATOR

R. J. Kedl

In the previous semiannual report[4] we described experience with a vortex type of in-line bubble sepa-

[4] *MSR Program Semiann. Progr. Rept. Aug. 31, 1968,* ORNL-4344.

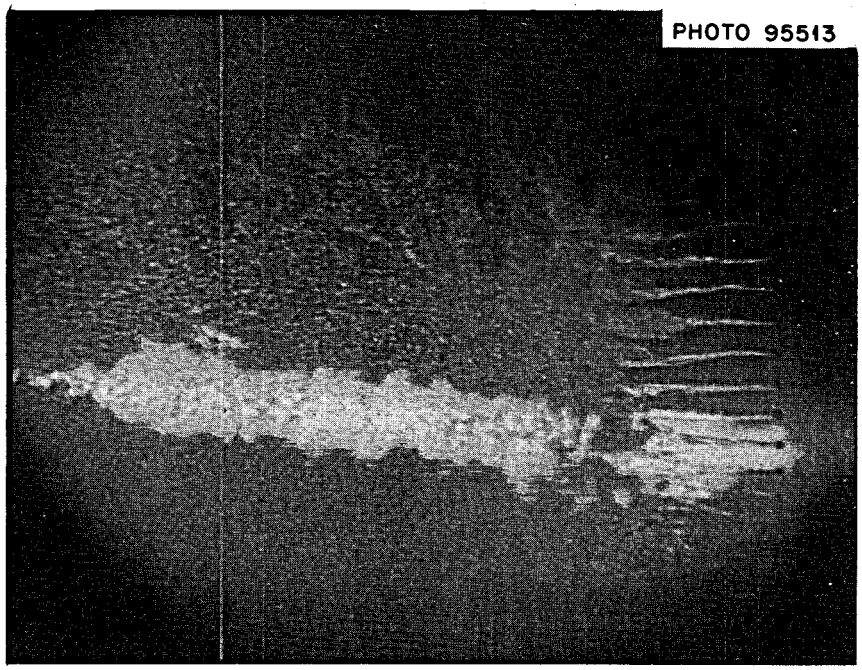

Fig. 7.6. Photograph of Bubbles Formed by Bubble Generator.

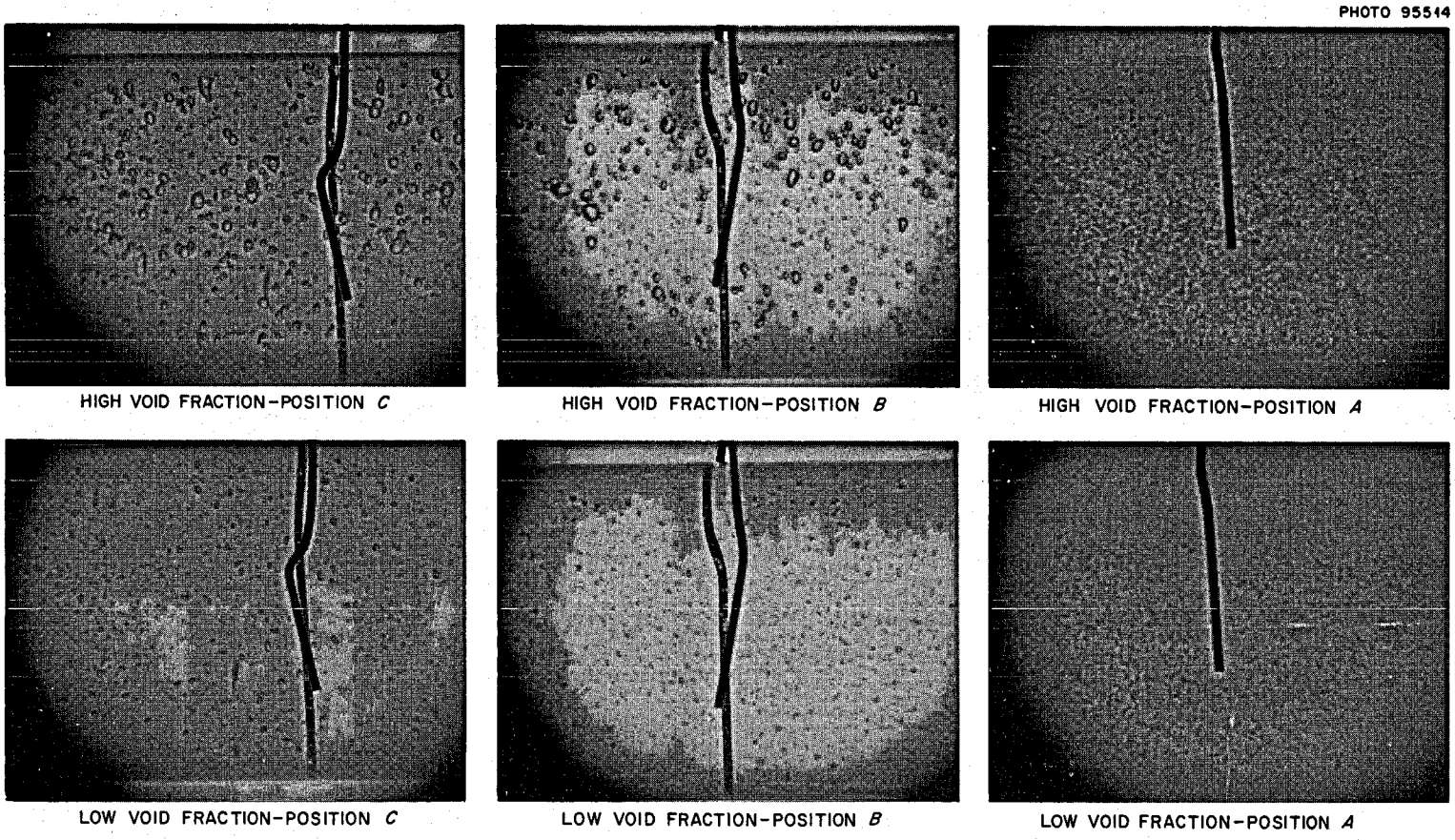

Fig. 7.7. Coalescence of Entrained Bubbles in the Bubble Generator Test. Locations of positions are shown in Fig. 7.5.

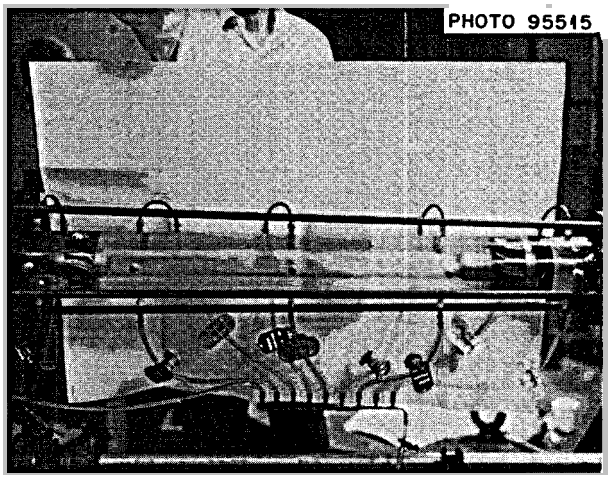

Fig. 7.8. Photograph of Vortex in the Bubble Separator.

rator that was not completely satisfactory because the gas core would not attach to the hub of the recovery vanes. It was postulated that the trouble was associated with the small hub diameter. A new set of vanes was made with a much larger hub, but the problem persisted. A third set of vanes was then made up identical to those used in the HRT but scaled up for our test section diameter. With this newest set of vanes, the gas core does attach to the hub of the recovery vanes much better than before. There is some splashing as the water hits the hub, and consequently some gas bypasses the takeoff line, but almost all the gas can be made to leave through the takeoff line in the hub of the recovery vanes. Note in Fig. 7.8 how the gas core seems to hold onto the hub, as opposed to the photograph in ORNL-4344 (Fig. 7.3, p. 75), where the gas core disintegrates as it approaches the hub. Since these vanes have only recently been installed, no quantitative data are available.

7.5 MOLTEN-SALT STEAM GENERATOR TEST STAND

R. E. Helms

A request for directive, Preliminary Proposal Number 450, Molten-Salt Steam Generator Test Stand, has been sent to the AEC for approval and authorization of expenditures.

The test stand will have a capacity of 3 Mw, necessary to test one or more full-size tubes for large steam generators. It will consist of a molten-salt loop with a gas furnace as a heat source and a water-steam loop capable of operation at subcritical and supercritical pressures. The flow diagram for the proposed installation is shown in Fig. 7.9. This test stand will be operated at salt and steam conditions representative of the MSBR and will have all necessary controls and instrumentation to permit steady-state and transient operation, including simulation of plant startup. The test stand will be used to gain fundamental engineering data and to investigate ideas for generating steam with molten salt. Some of the principal objectives of the development program are as follows:

1. To confirm the salt heat transfer and fluid flow characteristics that were used in steam generator design studies and to confirm the adequacy of a computer code to be used for the design and analysis of full-size molten-salt steam generators.
2. To verify thermal and mechanical design features of a small section of a full-scale molten-salt steam generator.
3. To study the stability and operational performance of a molten-salt-heated steam system.
4. To assure the absence of supercritical whistle in an appropriate simulation of the boiler heat transfer tubes under typical operating conditions.
5. To develop a startup system for the molten-salt steam-generating plant and to demonstrate experimentally the procedures to be used for startup.
6. To investigate the degree of corrosion and scale buildup in a once-through system of this type and to verify the chemical control of the water necessary for acceptable performance. Information on the compatibility of Hastelloy N with steam and salt will supplement the data being obtained from a separate materials testing program.
7. To gain further experience in fabricating components of Hastelloy N.

A conceptual system design description (CSDD) is now being prepared. As part of the design description effort, we are completing the flow diagrams for all the systems of the test stand prior to making the physical layout drawings.

7.6 SODIUM FLUOROBORATE CIRCULATING TEST LOOP

A. N. Smith P. G. Smith R. B. Gallaher

Except for momentary interruptions, the loop operated continuously from August 19, 1968, to November 4, 1968, with the clean charge of sodium fluoroborate–sodium fluoride eutectic salt. During this period

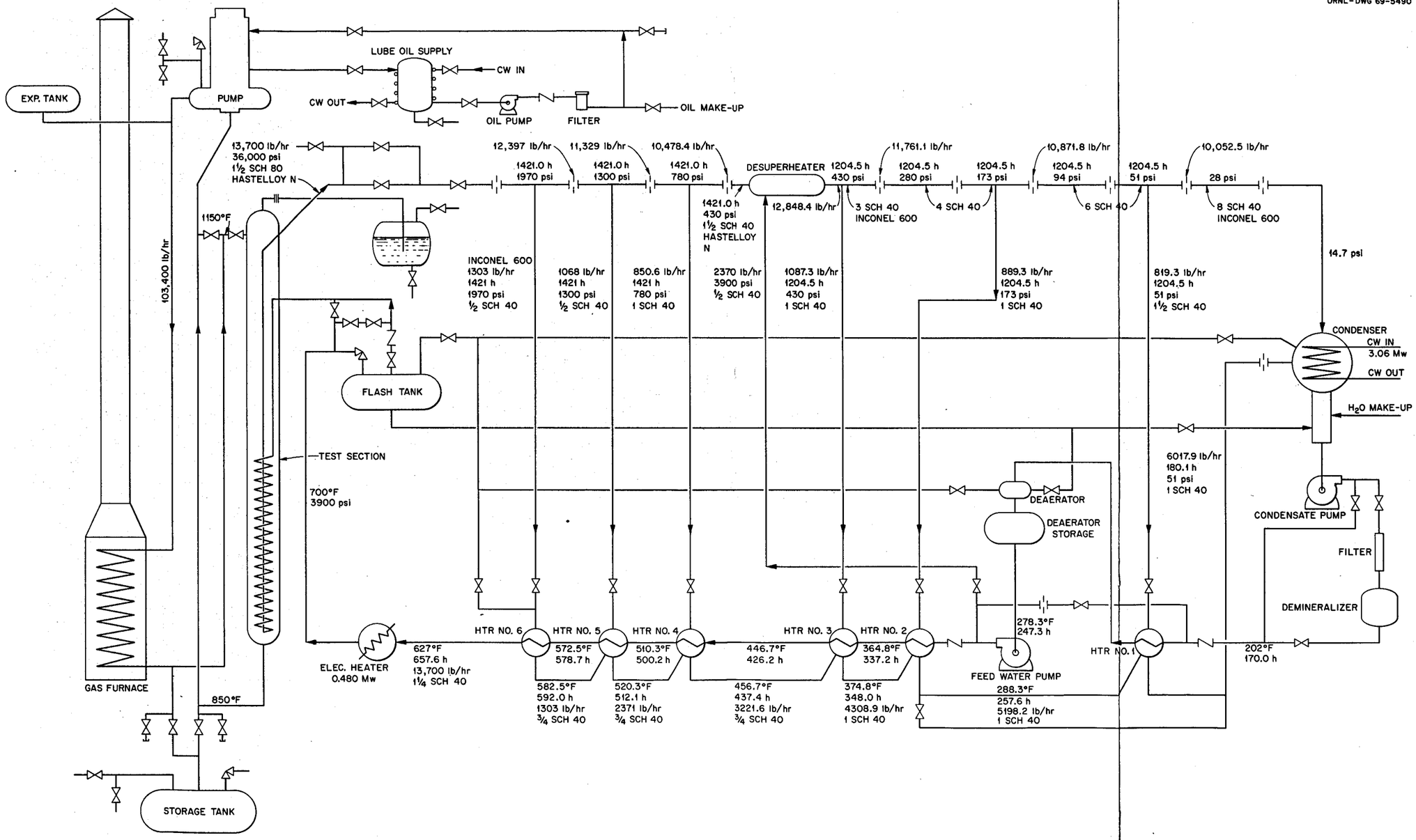

Fig. 7.9. Steam Generator Test Stand – Schematic Flow Diagram.

work was completed on pump cavitation tests,[5] studies were continued on methods of controlling salt composition and on factors which affect formation of restrictions in the gas system, and initial tests were made with a cold finger to investigate cold-zone deposition of corrosion products. The primary reason for shutdown on November 4 was a severe flow restriction in the off-gas line at the pump bowl outlet nozzle. During November and December a test section was installed at the pump bowl outlet to provide pressure and temperature profile data and to permit installation of various traps and filters. The loop was restarted on December 19, 1968, and circulation was continued without interruption through February 1969. Cumulative circulating time is 4600 hr, of which 3600 hr have been with the clean batch of salt. In general, the test work has produced no evidence of any engineering problem which would preclude the use of $NaBF_4$-NaF eutectic as a reactor coolant.

7.6.1 Pumping Characteristics of Sodium Fluoroborate Salt

Results of cavitation tests with the clean charge of sodium fluoroborate and those obtained with the flush charge of salt are compared in Table 7.2. The vapor pressure of the fluoroborate salt and the pump tank gas pressure at the inception of cavitation are shown. A comparison of the changes in vapor pressure and cavitation inception pressure with temperature using the 900°F values as reference is also given. For a particular change in temperature, the change in pump tank pressure at the inception of cavitation should equal the change in vapor pressure.

For the flush charge of fluoroborate the table indicates relatively large differences of from 10 to 50% between theory and test. The results with the clean charge appear consistent with the notion that inception of cavitation in the PK-P pump operating with sodium fluoroborate can be correlated on the basis of net positive suction head and vapor pressure; the differences range from zero to 20%. The available test information does not provide an unequivocal reason for the discrepancies observed with the flush charge of fluoroborate; however, the effect of the impurities on the BF_3 partial pressure is the most likely reason.

The results of the hydraulic performance and cavitation inception tests were reported in an internal memorandum from P. G. Smith dated January 10, 1969.

7.6.2 Control of Salt Composition

In a reactor coolant system, failure to control the salt composition within acceptable limits could result in precipitation of NaF on cold surfaces (decrease in $NaBF_4$ content with resultant increase in liquidus

[5] *MSR Program Semiann. Progr. Rept. Aug. 31, 1968,* ORNL-4344, pp. 75–78.

Table 7.2. Results of Cavitation Inception Tests with Sodium Fluoroborate in PK-P Pump

Salt	Temperature (°F)	Vapor Pressure[a] (psia)	Accumulated Change in Vapor Pressure with Temperature (psi)	Pump Tank Pressure at Inception of Cavitation (psia)	Accumulated Change in Pump Tank Pressure with Temperature (psi)	Difference Between Change in Vapor Pressure and Pump Tank Pressure (psi)	Difference plus Accumulated Change in Vapor Pressure (%)
Flush	900	0.3		18.7			
	1025	1.3	1.0	20.2	1.5	0.5	50
	1150	4.8	4.5	25.7	7.0	2.5	55
	1200	7.7	7.4	29.7	11.0	3.6	50
	1275	14.5	14.2	34.7	16.0	1.8	12
Clean	900	0.3	0	17.5	0		
	1025	1.3	1.0	18.7	1.2	0.2	20
	1150	4.8	4.5	22.0	4.5	0.0	~0
	1275	14.5	14.2	31.7	14.2	0.0	~0

[a] Based on experimental data of S. Cantor, *MSR Program Semiann. Progr. Rept. Feb. 29, 1968,* ORNL-4254, p. 170. This is the measured vapor pressure of the pure eutectic mixture of $NaBF_4$ and NaF and is not necessarily the same as the vapor pressure of the salt in the pump loop.

temperature) or boiling on hot surfaces (increase in $NaBF_4$ content with resultant increase in BF_3 pressure). Control of the salt composition is effected by controlling the BF_3 content of the cover gas over the free surface of the salt in the pump bowl.

Under normal conditions a change in composition results only from transport of BF_3 to the off-gas system by the flow of purge gas through the pump, and this effect is counteracted by feeding BF_3 to the system at a rate equal to the loss rate. The gas flows are so small, compared with the total quantity of BF_3 present in the salt, that rapid changes in salt composition by this mechanism are impossible. For example, in the MSRE coolant system at 1200°F and 24 psig, removal of BF_3 at the maximum rate (zero BF_3 feed) for eight days would reduce the $NaBF_4$ content by only 1%. The composition therefore can be controlled by occasional adjustments in BF_3 feed rate, provided a suitable method can be established for monitoring the salt composition. Following is a brief description and a summary of observations to date on several proposed monitoring methods.

1. *Chemical Analysis of Salt Samples.* The ratio of fluorine to boron or boron to sodium is used to estimate the mole fractions. A preliminary mathematical analysis indicated that the limit of error of the chemical analysis is too great to permit use of this method. A plot of the mole fraction as calculated from analyses of a large number of salt samples from the test loop (Fig. 7.10) tends to verify this conclusion.

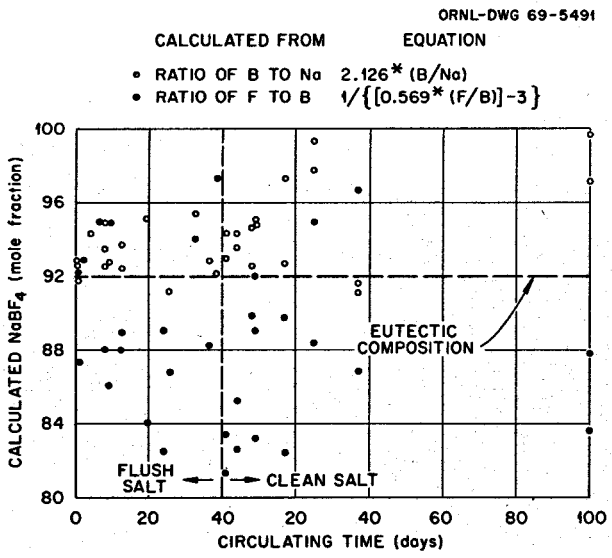

Fig. 7.10. Mole Fraction $NaBF_4$ Calculated from Salt Sample Analyses.

2. *Change in Heat Transfer Coefficient Due to a Salt Deposit.* A heat transfer surface in the salt stream is controlled at a temperature slightly above the normal liquidus temperature. A change in composition would result in a deposit on the cool surface which could be detected by a change in heat transfer coefficient. Evaluation has not been completed, but preferential deposition of corrosion products will probably prevent use of this method.

3. *Differential Thermal Analysis.* The composition is inferred from analysis of temperature profiles obtained by moving a salt sample through carefully controlled freeze and thaw cycles. It appears that some work will be necessary to develop suitable sampling techniques.

4. *Thermal Conductivity of Cover Gas.* The off-gas is assumed to contain the equilibrium concentration of BF_3 for the given salt temperature and composition. The off-gas stream is monitored continuously by a thermal conductivity cell which is calibrated in percent BF_3. The partial pressure of BF_3 is then calculated, and this value is related to the composition by an equation of the following form:

$$\ln P = \ln\left(\frac{f}{1-f}\right) + (A - B/T) ,$$

where

P = partial pressure BF_3, mm Hg,

f = mole fraction $NaBF_4$,

T = temperature, °R,

A, B = constants.

The success of this method depends on the validity of the above equation and on the ability to measure the salt temperature and the BF_3 concentration in the gas with sufficient accuracy. Recent physical property data indicate the following derivative values for the above equation:

$$A = 18.67$$
$$B = 2.5 \times 10^4$$
$$T = 1025°F$$
$$f = 0.92$$
$$dp/dT = 0.75 \text{ mm Hg/°F}$$
$$dp/df = 6.5 \text{ mm Hg/1 mole \%}$$

Experience with the test loop indicates that this method should be feasible for tracking the salt composition. In order for the analysis of the off-gas stream to provide an accurate indication of the composition of

the salt, the gas must leave the pump bowl in equilibrium with the salt in the pump bowl. That this condition is attained in the test loop was indicated by two types of experiments. In one the helium flow to the pump bowl was varied, and this produced no change in the composition of the exit gas. In the second the BF_3 content of the gas that is introduced under the salt through the bubbler tube of the level indicator was varied over a wide range for short periods of time. This also had no effect on the composition of the gas leaving the pump bowl. The thermal conductivity cell used to measure the partial pressure of the BF_3 in the off-gas showed excellent linearity and appeared to hold its calibration adequately. A reactor-grade system would require a built-in calibration system and, as noted above, fairly precise and accurate methods for measuring the operating variables.

7.6.3 Corrosion Product Deposition

We are studying the use of a cold trap in a reactor coolant system to induce preferential deposition of corrosion products and thus minimize scaling of the heat exchanger tubes. Tests are being conducted with the test loop to develop information on corrosion product solubility and on the nature of the deposits which are formed on a cold finger (Fig. 7.11) inserted in the salt in the pump bowl. Operation of this unit for 3 hr at a wall temperature of about 750°F produced a deposit of green crystals of the following composition:

	Na	B	F	Fe	Cr	Ni	O_2
Wt %	21.4	5.91	58.2	3.50	6.61	0.04	0.27

The atomic ratios correspond roughly to a mixture containing 2 moles of Na_3CrF_6 to 9 moles of $NaBF_4$. Further studies will be made to determine whether keeping the wall temperature definitely above the liquidus reduces the $NaBF_4$ concentration.

7.6.4 Gas System Studies

Our experience when operating the test loop with the clean batch of salt from August 19, 1968, to November 4, 1968, was similar to our previous experience with the flush salt in the following respects:

1. Initially, relatively large quantities of a dark-brown liquid accumulated in a mist filter in the off-gas line from the pump bowl. As operation continued, the rate of collection of liquid decreased essentially to zero, and an accumulation of solids became evident, as seen in Fig. 7.12.
2. There was frequent evidence of fouling of the pump bowl pressure control valve. The valve would gradually assume an 80% open position as compared with a position of 20% open when clean. On several occasions the valve stuck in the closed position. Figure 7.13 shows the accumulation of solids on the valve stem.
3. A restriction developed in the off-gas line at the pump bowl outlet nozzle. At first, it could be cleared by blowing with gas or by applying moderate amounts of heat, but the restriction gradually became more intractable and ultimately refused to yield to torching to red heat.

Following the shutdown on November 4, 1968, the off-gas lines were opened for inspection. The restriction at the pump bowl nozzle was found to be a dirty white

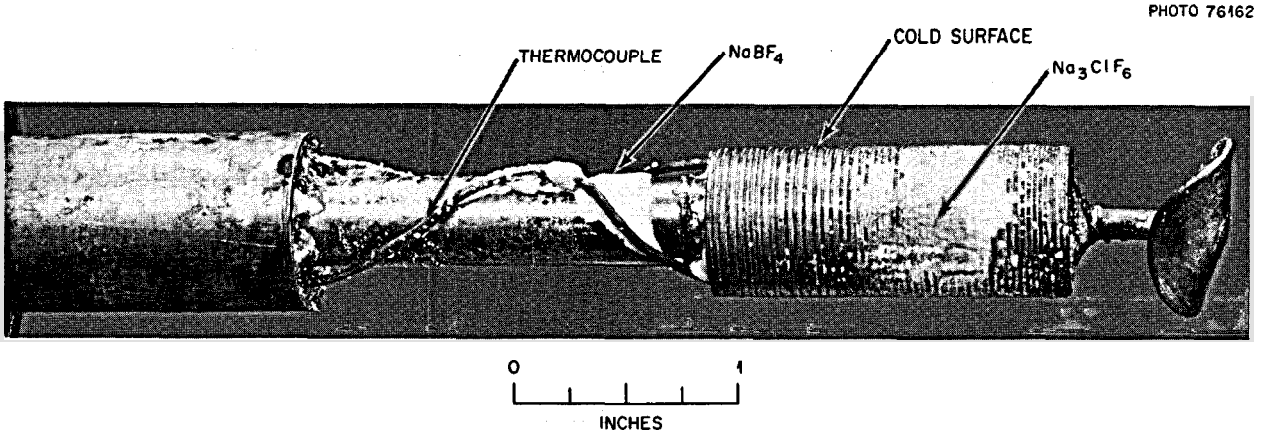

Fig. 7.11. Cold Finger Used for Corrosion Product Deposition Tests – $NaBF_4$ Circulation Test.

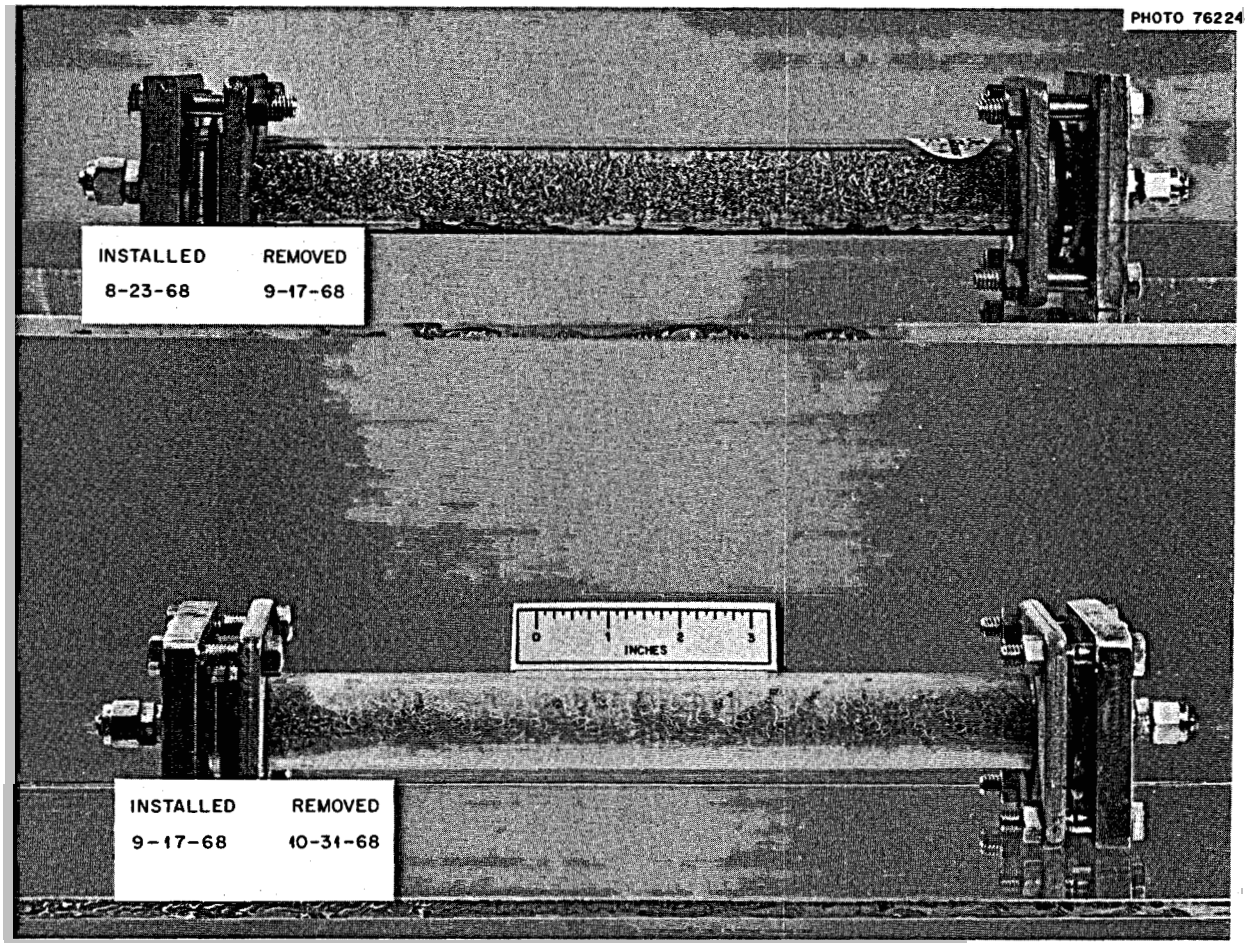

Fig. 7.12. Off-Gas Mist Filter – $NaBF_4$ Circulation Test.

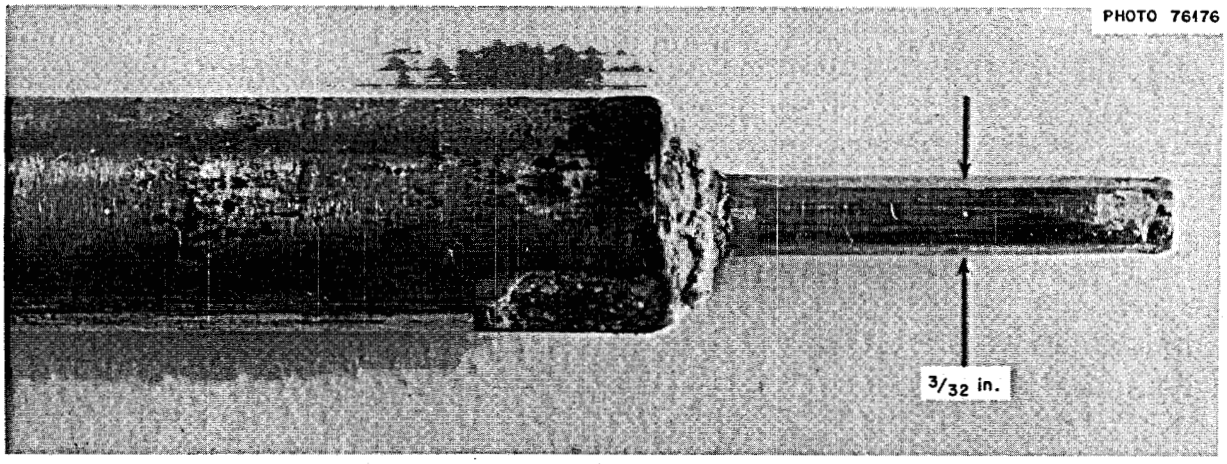

Fig. 7.13. Accumulation of Solids on End of Stem of Pressure Control Valve – $NaBF_4$ Circulation Test.

solid, and quantities of off-white solid were found in the pipeline and in the control valve downstream of the nozzle. Samples were submitted for chemical analysis, results of which are reported as sample III in Table 7.3. Representative analyses of other material removed from the off-gas line since startup of the loop in March 1968 are also shown in the table.

A Calrod heater and thermocouples were installed on the ½-in.-IPS by 6-in.-long vertically oriented off-gas nozzle, and the line immediately downstream was modified to permit pressure profile data to be obtained and to provide for the installation of experimental traps and filters. When operation was resumed on December 19, 1968, the test section contained, in order, a settling tank, a wet-ice cold trap, and a high-efficiency porous metal filter. The settling tank and cold trap were subsequently replaced by an experimental impactor unit, and currently the system is operating with only a porous metal filter.

The normal mode of operation has been with no power to the heater on the off-gas nozzle. Under this condition the pipe wall temperature drops below the salt liquidus, 720°F, at a point just past the nozzle inlet. Heat has been applied on two occasions to relieve flow restrictions. The first time, at 670 hr, heating the nozzle to 950°F resulted in only temporary relief. The second time, at 1000 hr, heating to 1025°F reduced the pressure drop to zero. By the end of February, or 1700 hr cumulative total, the restriction had not reappeared. During this period of operation, solids accumulated in the settling tank, impactor unit, and filter, and a small quantity of dark-brown liquid collected in the cold trap. In all cases the solids were white or light tan; in the flush salt run, the solids removed from the off-gas system were mostly black with some green. The light-tan material is probably a mixture of the white solid and dark-brown liquid. Periodic weighings were made in an attempt to determine collection rates, and samples were submitted for chemical analysis.

Accumulations in the off-gas lines, traps, and control valve have been mixtures of materials. The basic ingredients of the mixtures are a white solid (sample IV) and a viscous liquid (sample I). The solid is primarily $NaBF_4$-NaF eutectic, which is introduced into the vapor space as a salt mist (probably generated by the fountain flow in the pump bowl) and then transported into the off-gas line. In cooling from liquid droplets at 1025°F to solid particles at 720°F, the large surface area of the droplets and the presence of BF_3 at a partial pressure corresponding to the 1025°F temperature make conditions very favorable for absorption of BF_3 by the salt. The solidified particles should also tend to absorb BF_3, but at a much slower rate. As a result, samples of salt removed from the off-gas line contain an excess of BF_3 as compared with the eutectic composition. The viscous liquid is thought to be a hydroxyfluoroboric acid which is present as a low-level impurity in the original charge of salt. This material is transferred to the vapor space by the combined action of the fountain flow and the liquid level bubbler and thence to the off-gas line.

Solids accumulated in the traps have an estimated bulk density of about 0.3 g/cm^3, and they appear to be agglomerates of particles about 1 μ in size. The fact that the particles could be transported to the control valve, which is separated from the pump bowl by 30 ft of tubing having many right-angle bends, also implies particle sizes of 1 μ or less. Solids which were found in the settling tank and the impactor unit were tan in color and had a caked appearance, factors which were

Table 7.3. Analyses of Materials from Off-Gas Line

$NaBF_4$ circulation test, PK-P loop, 9201-3

All results in weight percent

Sample	Date	Na	B	F	Fe	Cr	Ni	O_2	C
I. Brown liquid, PK-S8 off-gas vent[a]	4-11-68		10	51	10				
II. Black powder	5-30-68	9.3	2.9	35.1	15.0	3.0	4.4		24.6
III. White powder	11-5-68	19.3	9.5	66.0	1.0	0.26	0.29	0.67	
IV. White powder from filter	1-13-69	20.4	9.6	68.6	0.05				
Composition of $NaBF_4$-NaF (92-8) eutectic mixture		22.0	9.53	68.44					

[a]Balance of material in liquid, PK-S8, was assumed to be water.

attributed to absorption of the dark-brown liquid. Figure 7.14 shows material collected in the settling tank. The black appearance of solids (sample II) collected in the trap at the pump bowl outlet during the flush salt run is attributed to debris (mostly compounds of Fe and C) left in the loop from previous operations. Similarly, the green appearance was due to residual BULT–4 salt.[6] Deposits on the surface of the porous metal filter were initially snow white but eventually changed to tan as more material accumulated and possibly as a small amount of brown liquid collected on the solid. The deposit had remained white throughout the period in which the cold trap was in operation.

The rate of emission of the salt mist appears to be 0.1 to 0.3 g per 1000 liters of gas. Periodic weighings indicate that the rate of accumulation of material in the filter is somewhat higher when the off-gas nozzle at the pump bowl is clean than during subsequent operation. When the restriction to flow is high at the nozzle, the accumulation rate with the same flow of gas appears to be essentially zero. This effect is attributed to an increase in removal efficiency in the nozzle area as deposits build up and the gas velocity increases.

The rate of emission of the liquid is initially high and then decreases and appears to approach zero, which tends to support the theory of an impurity that is gradually stripped out of the salt. Operation for 600 hr in December 1968 and January 1969 produced an accumulation of about 2 cm^3 in the wet-ice cold trap. This compares with an estimated 30 cm^3 of liquid collected over the same period of time at the beginning of the clean salt operation. Estimates of the total quantity of liquid emitted are equivalent to removal of about 500 ppm of impurity from the salt.

After 1600 hr of operation following the installation of traps and filters, the off-gas pressure control valve is still controlling in its "clean" position of 20% open. This fact, plus visual examination of the filter, indicates that the porous metal has been quite effective in

[6] *MSR Program Semiann. Progr. Rept. Aug. 31, 1968,* ORNL-4344, p. 78.

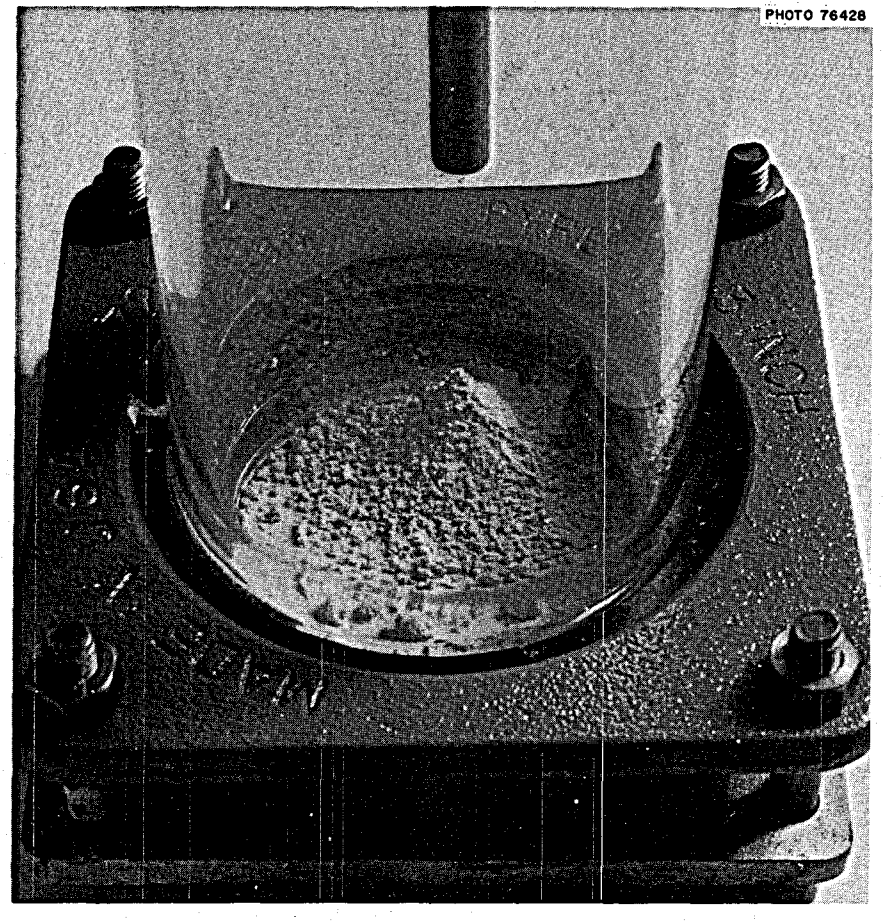

Fig. 7.14. Accumulation of Solids in 3-in.-ID Settling Tank – $NaBF_4$ Circulation Test.

removing the particulate matter from the gas stream. The filter now in use contains three elements in series: NEVA-CLOG, a patented form of perforated metal by Multi-Metal Wire Cloth, Inc., and two layers of porous metal, FM-225 and FM-204, by Huyck, Inc. Each element has a cross-sectional flow area of 3 $in.^2$, and the overall clean pressure drop for the normal loop conditions of 1 cfm/ft^2 is less than 0.1 psi. After 1200 hr of service the total loading was about 5 g, and the pressure drop had not increased appreciably.

The prevention of off-gas restrictions involves a threefold approach: (1) pretreatment of the salt to remove excessive quantities of the brown liquid impurities, (2) development of a trap or entrainment separator which will prevent the formation of plugs in the critical transition region where the salt droplets are cooling and solidifying, and (3) use of a porous metal filter to remove any subcooled particles which are carried past the trap. The inlet section of the trap should be a hot zone where the salt mist is efficiently deentrained and allowed to drain to the pump bowl. The outlet section should be designed to chill the unretained fraction of the mist so that the subcooled particles will remain gas borne and will be carried into the filter section. Several trap designs are under consideration, and selected models will be tested in the loop system.

7.7 MSBR PUMPS

A. G. Grindell P. G. Smith
C. K. McGlothlan L. V. Wilson
H. C. Young

7.7.1 MSBR Primary-Salt Pump

The study concept of the primary-salt pump for the 1000 Mw (electrical) Molten-Salt Breeder Reactor (MSBR) has not changed significantly from that shown and described previously.[7,8] The conceptual layout has been modified, as shown in Fig. 7.15, to reflect approaches to resolving some of the interface problems between the salt pumps and the remainder of the primary pump system. The pump is based on a flow of 16,000 gpm, a head of 150 ft, and a speed of 890 rpm. The required horsepower will be about 2500 for each pump.

Since the reactor is the fixed component in the system, the primary-salt pumps are subjected to thermal expansion displacements of about 2 in. horizontally and about 1 in. vertically at the pump tank. The design effects of these displacements on the pump show in the shield configuration, method of pump support, cell and/or pump containment, and, depending on the method of mounting the drive motor, the coupling between the motor and the pump. The shielding around the concept pump is of the disk-and-doughnut type and will permit the unhindered displacement of the pump and also provide adequate shielding of the lubricant and coolant in the region of the lower bearing and seal. Additional shielding may be provided above the pump tank to reduce nuclear radiation intensity at the crane bay floor to an acceptable biological level.

In our present concept the motor is mounted directly on the crane bay floor, and the pump is suspended on spring-mounted support rods that are free to pivot at both ends. The spring constant of the springs will be sufficiently low that the forces on the pump tank nozzles will not be excessive. The coupling between the motor and the pump is a floating shaft gear which will be installed in the maximum horizontal displacement position. During system heatup the pump will move into a position where the pump shaft will be nominally aligned with the motor shaft for normal pump operating conditions. An alternative concept would have the motor mounted directly on the pump bearing housing. This would eliminate relative thermal displacement between the pump and motor and relieve the coupling from having to accommodate the displacements. However, the spring-support rods would need to accommodate the added weight of the drive motor.

The concept has a large seal leakage containment volume to accept the oil from a gross failure of the lower seal. In addition, a Visco seal, adjacent to the lower seal, will prevent oil from entering the salt system when the shaft is rotating. When the pump is stopped a static shutdown seal can be actuated by gas pressure to prevent the flow of oil down the shaft annulus. The primary purpose of the static shutdown seal is to permit the removal of the bearing housing assembly without removing the shield plug, shaft, and impeller from the pump tank.

Means for cooling the pump tank, its internal structural elements, the pump shaft, and the lower end of the shield plug have been included in the modified concept. The nuclear heat generation in these components will be removed in primary salt (at about 1050°F) from the fill and drain line of the reactor system. The salt enters a plenum around the inner periphery of the pump tank and flows upward in an annular liner. At the junction of the pump tank and

[7] *MSR Program Semiann. Progr. Rept. Feb. 29, 1968,* ORNL-4254, pp. 76–78.

[8] *MSR Program Semiann. Progr. Rept. Aug. 31, 1968,* ORNL-4344, pp. 80–81.

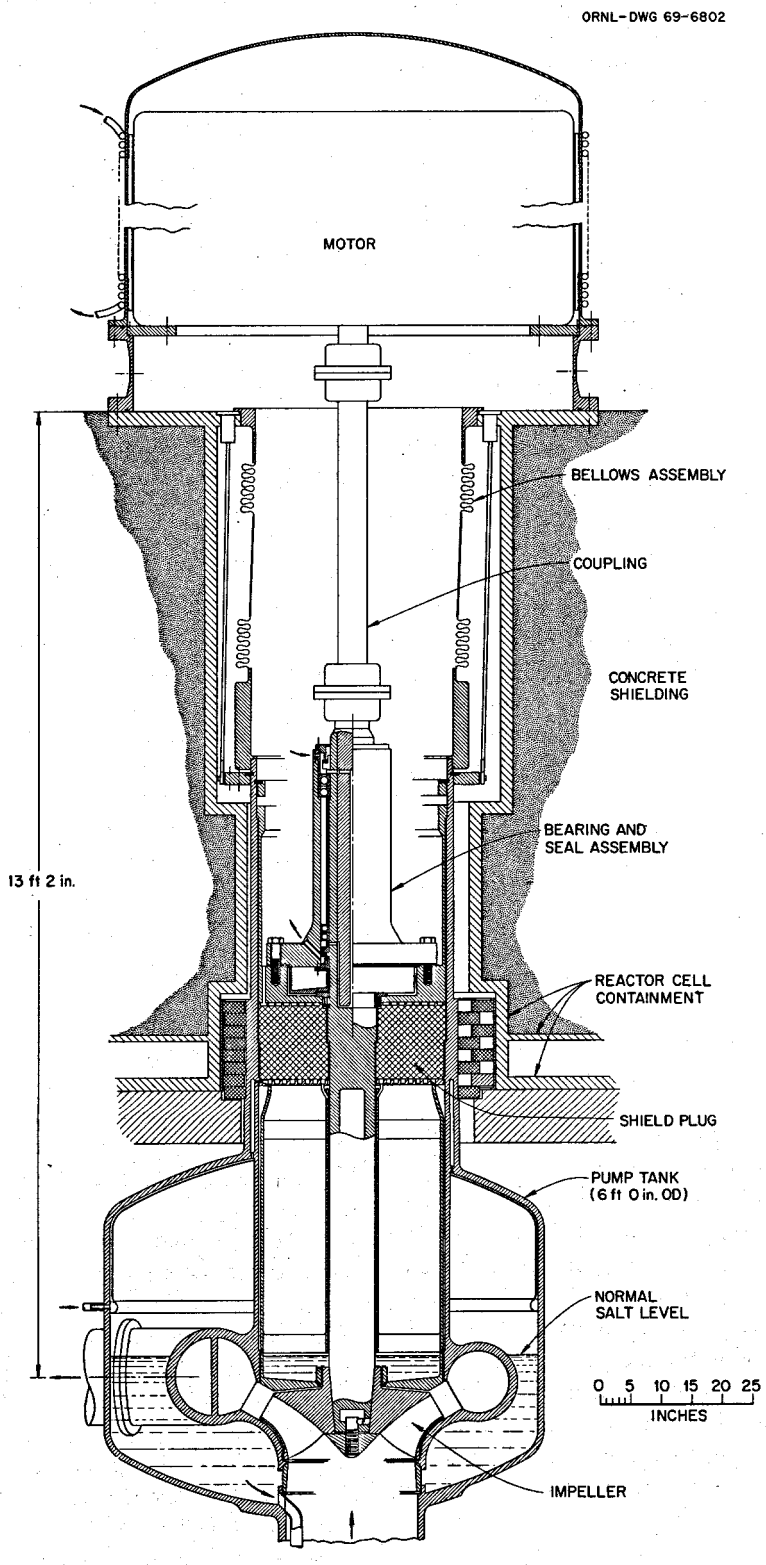

Fig. 7.15. MSBR Primary Salt Pump, Conceptual Layout.

outer pump casing the flow splits, with part of the flow passing downward between the inner and outer pump casings and part of the flow passing across the lower end of the shield plug and into the annulus between the shaft and the shaft sleeve. In the pump tank these flows combine with the fountain flow from the labyrinth seal behind the impeller, the return flow from the chemical processing system, and the return flow from the entrainment separator. All these flows are returned to the main stream of the reactor system through a drain line connecting the bottom of the pump tank to a low-velocity point inside the reactor. Block or spherical fillers will be placed appropriately in the pump tank to reduce the parasitic volume of primary salt.

At each pump the primary cell containment is extended through the concrete shielding above the reactor cell to contain the pump drive motor. The drive motor heat sink is provided by cooling water circulated through cooling coils attached to the outside of the motor containment vessel. Internally a blower attached to the motor shaft will circulate helium through the motor and over cooling fins attached to the inside of the motor containment vessel. The motor is mounted on a ring through which all electrical, instrument, gas, coolant, and lubricant lines are connected to the pump.

7.7.2 Pump Program for the Molten-Salt Breeder Experiment

The plans[9,10] outlined previously to obtain the primary- and secondary-salt pumps for the Molten-Salt Breeder Experiment (MSBE) are progressing. A second draft of the specification for the MSBE primary-salt pump was prepared to include the comments generated in an internal review of the first draft. An evaluation team consisting of personnel from the Purchasing Division, the Reactor Division, and the Inspection Engineering Department was selected. The team developed a rating system for pre- and postproposal evaluation of potential salt pump manufacturers. Also it selected 12 United States pump manufacturers and contacted each by letter to determine his interest in participating in the program and in reviewing a draft copy of the specifications for the primary salt pump. Each of the six pump manufacturers who evinced interest in the program was visited by the team. The purpose of the visit was to receive and discuss the manufacturer's comments about the pump specification, to view his fabrication and test facilities, to discuss his quality assurance organization, and to attempt to gage his interest in the salt pump program. The primary-salt pump specification is being revised to reflect manufacturer comments. An evaluation of the visits is being made to select pump manufacturers to receive a Request for Proposal to participate in the pump program. The Scope of Work portion of the Request for Proposal is being prepared. The specification for the secondary-salt pump, generally patterned after the primary-pump specification, is being prepared.

The scope of the phase I portion[10] was revised to obtain the maximum pump manufacturer participation that can be achieved with the funds available for fiscal year 1970. As now conceived, phase I will be based principally on the following items:

1. Prepare design concepts and layout drawings that meet the general intent of the specifications. It is intended that the primary- and secondary-salt pump designs have sufficient similarity to permit a high degree of interchangeability of parts and to avoid, as much as possible, two parallel design and development efforts.
2. Investigate the limitations of using the same impeller and pump casing design for the primary- and secondary-salt pumps and obtaining the specified hydraulic characteristics by operating at two different speeds and by changing the impeller diameter.
3. Make a parametric study, for the primary-salt pump only, of the relationship between pump speed, pump efficiency, salt volume within the pump, and required net positive suction head. A pump speed and a design concept that are mutually agreeable to both the seller and the Company can then be chosen.
4. Make a study to show that the selected MSBE pump concept can be scaled up satisfactorily to a pump size having a flow capacity of at least 20,000 gpm and a head of 150 ft, and indicate the probable amount of developmental effort required beyond the MSBE program.
5. Make preliminary calculations that will provide approximate component dimensions and show that the concept meets the general intent of the specifications. This can be considered to be the minimal analytical effort required to prove a concept.
6. Make the necessary calculations and analyses to show that the pump design completely meets the requirements of the specifications.
7. Make a detailed layout drawing of the pump concept showing all features needed to meet the specific requirements of the specifications.
8. Revise the phase II and phase III programs submitted by the seller in his proposal, giving more detail on the schedule, manpower requirements, specific

[9] *MSR Program Semiann. Progr. Rept. Feb. 29, 1968,* ORNL-4254, p. 76.

[10] *MSR Program Semiann. Progr. Rept. Aug. 31, 1968,* ORNL-4344, p. 79.

manpower assignments, material requirements, developmental effort, facility modifications and requirements, cost estimates, and the fabrication and testing plans, including location and ownership of facilities.

9. Prepare and submit a phase I report, including all analyses, studies, and layout drawings, that will permit the Company to evaluate the concept and the program plans proposed by the seller.

10. Revise the specifications for the primary and secondary salt pumps as the phase I effort indicates necessary, and prepare new specifications or use Company specifications where applicable.

7.7.3 MSBE Salt Pump Test Stand

The pump test stand[11] will be capable of accommodating full-size MSBE primary and secondary salt pumps and will be located in Building 9201-3, Y-12. We plan to utilize capital funds for its design and construction, which have been estimated to cost $625,000. The detailed design of the stand and the procurement of the requisite Hastelloy N raw materials are scheduled to begin in fiscal year 1969 (if the necessary approvals are obtained in time). Completion of construction is scheduled for early in fiscal year 1972.

Several activities have been completed or broached during the report period. The preliminary design and cost estimates were completed. Project and Laboratory management approvals for the capital fund request were obtained. The safety review was made. The request for directive was prepared, approved by UCCND management, and submitted to the Oak Ridge Operations Office of the AEC. A draft of the system design description for the stand was prepared and is being reviewed internally.

7.7.4 ALPHA Pump

Design work has been started on a small molten-salt or liquid-metal pump to be called the ALPHA pump. It is for laboratory use in corrosion and heat transfer studies. We will attempt to design a versatile pump for flows in the range up to 30 gpm, a head capability up to 300 ft, and a maximum operating temperature of 1400°F. None of the pumps presently in use at the Laboratory meet all these criteria. Additional criteria include (1) a minimum liquid volume within the pump, (2) a minimum salt-wetted surface area within the pump, and (3) a continuous operating capability of 10,000 hr. A small tank will be located adjacent to the pump to provide access to the salt surface for auxiliary equipment and developmental needs.

[11] *Ibid.*, pp. 81–83.

7.8 REMOTE WELDING

P. P. Holz

During this period, we completed the fabrication and started the testing of the automated cutting and welding equipment based on the design developed by the Air Force and the North American Rockwell Corporation. This equipment, referred to in previous reports as "orbital" pipe cutting and welding equipment, employs a drive carriage which fits a range of pipe sizes and provides the mounting base for the pipe cutting and welding heads. Initial tests of the ORNL equipment were performed with a welding programmer loaned to us by the Air Force, after being used by them for automated control of welding process variables during tests of their equipment at Edwards Air Force Base.

Figure 7.16 shows the welding programmer and, in front of it, the remote operation pendant which is used in conjunction with the programmer for emergency shutdown or manual checkout and cutting operations. To the right of the programmer is the welding head, with the electrode and the nozzle of the wire feeding device in the foreground. The large horseshoe-shaped piece is the orbital drive assembly, which fits a limited range of pipe sizes and drives the cutting and welding heads around the pipe. Next is the cutting head, with the blade visible in the foreground. The cutting and welding heads are designed to fit in the open space at the top of the horseshoe-shaped orbital drive mechanism.

Figure 7.17 shows the welding head mounted on the orbital drive mechanism but opened to show the inner parts. The remote control pendant is placed next to the orbital drive mechanism, and the whole assembly is mounted on a 6-in. pipe.

Figure 7.18 shows the orbital carriage with the cutting head in place. The teeth of the cutting head can be seen through the slot in the end of the carriage. The line of the initial cut being made is visible on the top side of the pipe near the edge of the orbital carriage.

The automatic voltage control compares and corrects arc voltage with respect to a standard polarity and a preset voltage. The resultant signal controls the input to the wire feed amplifier, which in turn varies the wire feed rate in a way that reduces weld bead irregularities as the torch traverses the pipe. The welding control programmer lent to us by the Air Force is designed to control and/or sequence each of the following welding variables or functions:

1. welding current vs time,
2. maximum welding current,
3. welding current pulse amperes and pulse time,
4. upslope time,
5. welding time,
6. downslope time,
7. welding voltage,
8. welding tool speed, start time,
9. wire feed speed, start-and-stop time, AVC voltage,
10. oscillator frequency.

The *welding head* performs the following operations: (1) locates the electrode accurately with respect to the weld joint, (2) feeds filler wire at the desired rate to the weld joint, (3) provides space to store sufficient welding wire on a spool for multiple filler weld passes, (4) provides the required flow of inert welding gas to the torch cup, (5) provides power and cooling water flow to the torch head, and (6) provides cross-seam oscillation of the electrode.

The *cutter head* performs the following operations: (1) cuts the pipe, (2) mills the pipe ends square, and (3) mills the required weld joint configuration at the pipe ends.

The complete cutting, welding, and automated control assembly became available just at the close of the reporting period, and only a few operational tests were performed; but these tests, without benefit of operating experience or equipment debugging, gave very encouraging results. The 6-in. stainless steel pipe shown in Figs. 7.16 and 7.17 was successfully cut and welded. The carriage tracked perfectly in cutting and welding through a number of trial sawcuts, bevel cuts, and test welds. The weld beads, including the root paths, looked promising for stainless materials; no other materials were tested. The evenness and consistent quality of the weld bead were especially promising, although no formal weld inspection tests were performed.

A detailed "Proposal for the Development of a Remote Control System for Cutting and Welding Radioactive Pipe and Vessels" was submitted to the Director, Division of Reactor Development and Technology. The proposal covers a five-year, $3,000,000 development program to adapt the orbital equipment to fully remote operation in high radiation fields. The proposed program is planned to yield a complete system, with two prototype working units for fully

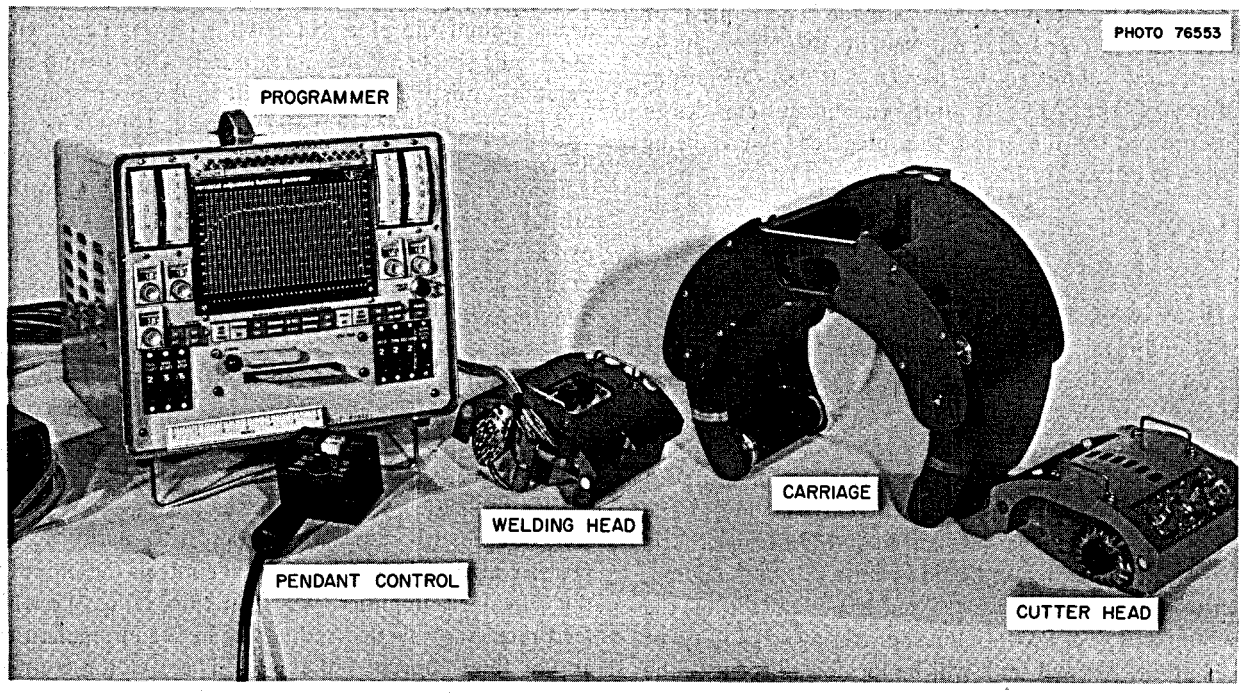

Fig. 7.16. Equipment for "Orbital" Weld System. A commercial TIG welding power supply used with the equipment is not shown.

automated and remotely controlled pipe cutting, welding, and inspection and for seal welding of flanges on reactors and other radioactive systems. Because a remote cutting, welding, and inspection system would be valuable for maintenance of every operating reactor, the proposed development program was recommended for General Reactor Technology funding rather than support within the MSR program.

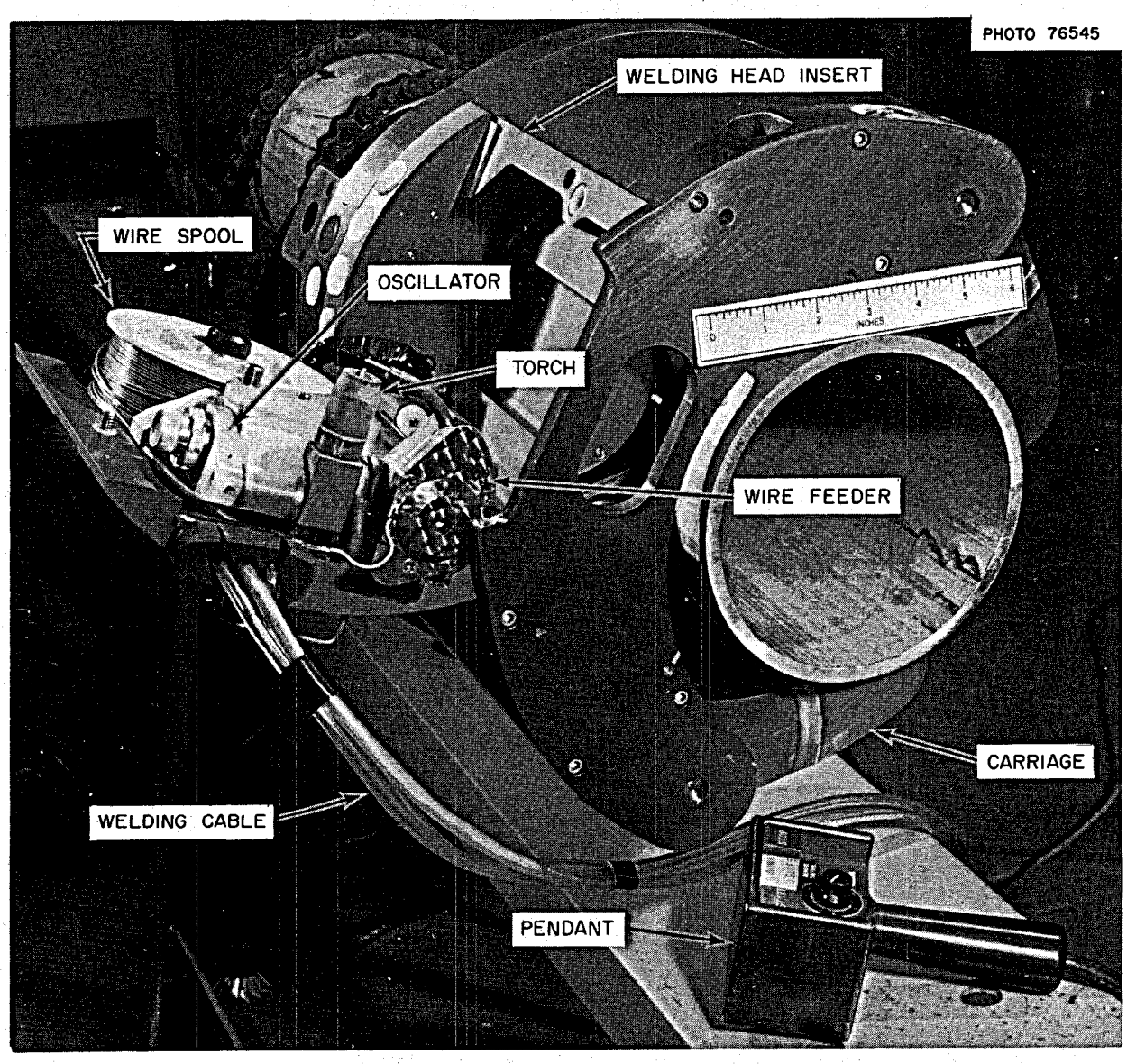

Fig. 7.17. Orbital Welder.

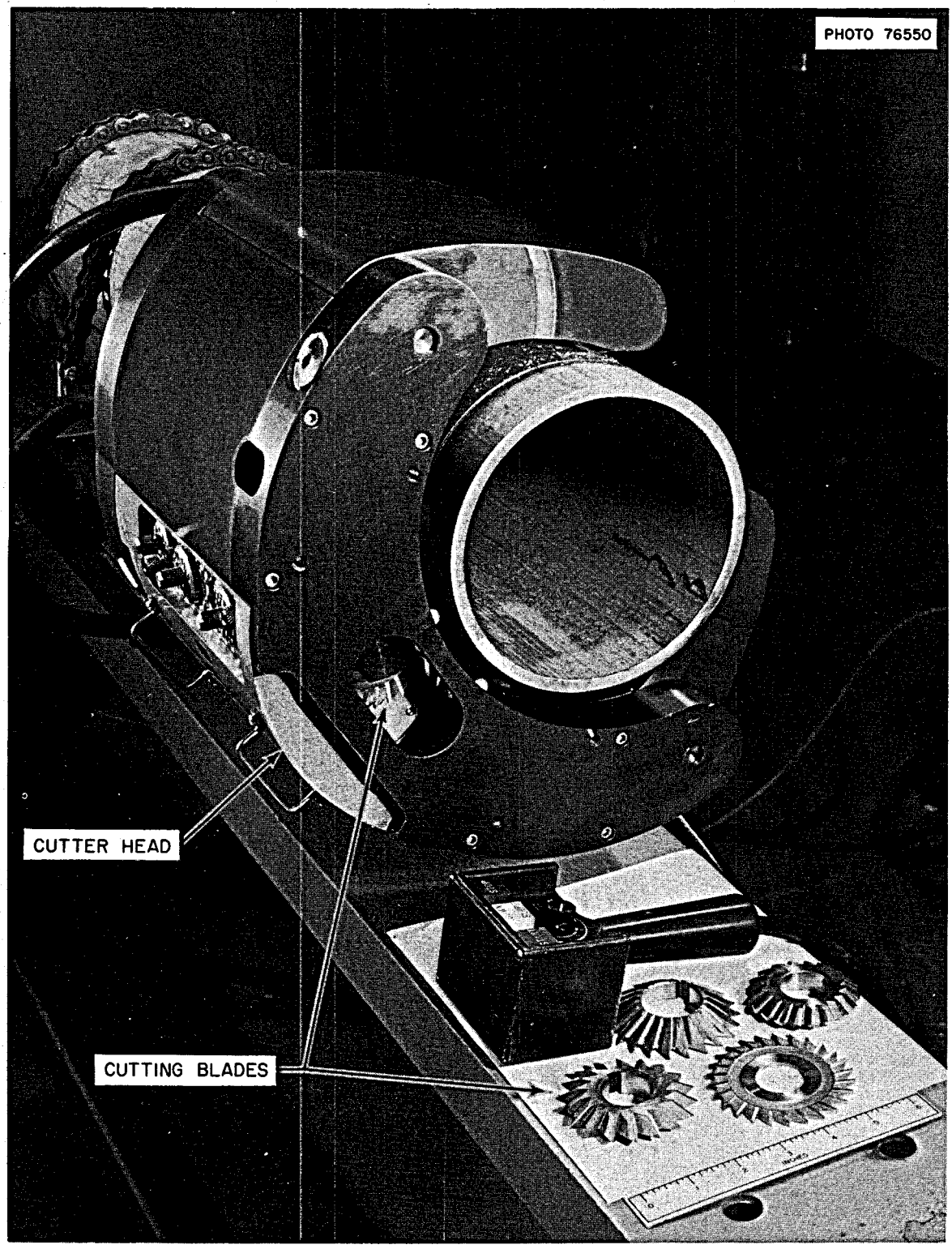

Fig. 7.18. Orbital Cutter.

8. MSBR Instrumentation and Controls

8.1 CONTROL SYSTEM ANALYSIS

W. H. Sides, Jr.

The simulation of the single-fluid 1000 Mw (electrical) MSBR for the preliminary investigation of the overall plant control problems was completed. To the model previously reported,[1] which included a lumped model of the primary heat exchanger and steam generator, was added a lumped model of the reactor heat transfer, a two-group approximation of the core nuclear kinetics equations, and a reactivity control system. The completed lumped model is shown in Fig. 8.1. As in previous calculations, the heat transfer coefficient on the tube side of the exchangers was taken to be proportional to the 0.8 power of the tube-side flow rate and on the shell side proportional to the 0.6 power of the shell-side flow rate. The temperature of the feedwater entering the steam generator was held constant at 700°F, and system pressures were assumed constant.

The nuclear kinetics equations used in the simulation were a two-group form of those from McPhee.[2] The transport lag introduced into the delayed-neutron precursor equations by the circulation of the fuel was approximated by a first-order lag, that is,

$$C_i(t-\tau) \approx C_i(t) - \tau_L \frac{d}{dt} C_i(t) .$$

The temperature coefficients of reactivity for the primary salt and graphite were also included in the simulation.

The conceptual control system for controlling system flows, temperatures, and reactivity is indicated in Fig. 8.1. As in previous studies,[1] the objective of the control system was to maintain the steam temperature within a few degrees of the design value of 1000°F during a transient condition. The previous studies indicated that a variable secondary-salt flow rate was necessary for sufficiently rapid steam temperature control. Therefore, the secondary-salt flow rate was altered at a rate proportional to the error in steam temperature, as indicated in the figure. Previous studies also showed that an acceptable steady-state system temperature profile could be obtained for partial plant load conditions if the secondary-salt flow rate were returned to its 100% power level value following a transient. Therefore the error in secondary-salt flow rate generated by the steam temperature control action produces a rate of change of the reactor outlet temperature set point. This outlet temperature is compared with the reactor inlet temperature, and this reactor ΔT yields the reactor power level set point. This power level set point is compared with the actual reactor power level, and the error signal operates a servo controller which produces appropriate control rod motion with the maximum reactivity insertion rate limited to 0.1%/sec. Thus the secondary-salt flow rate is returned to its 100% power level by altering the reactor temperature level through the reactor outlet temperature set point.

Several transient cases were run with this model, including decreases in power demand from 100% by steps of 10, 30, 50, and 60% and by ramp changes of 30 and 70% each at 5 and 10%/min; changes in reactivity of steps of ±0.05, ±0.1, and −0.5% and, with the reactivity controller disconnected, reactivity steps of ±0.05, +0.01, and −0.1% and ramp changes in reactivity of +0.05 and −0.1% each at 0.1%/min. Also the step loss of one secondary-salt coolant loop was simulated. The system transfer function between control rod reactivity as an input and reactor power was also measured.

The results of load demand perturbations are summarized in Table 8.1. The maximum steam temperature deviations from 1000°F are given, as well as the maximum required rates of change of the secondary-salt flow rate and the control reactivity. The highest reactivity rate is seen to be well below the 0.1%/sec

[1] *MSR Program Semiann. Progr. Rept. Aug. 31, 1968*, ORNL-4344, p. 88.

[2] J. McPhee, *Nucl. Sci. Eng.* 4, 588–97 (1958).

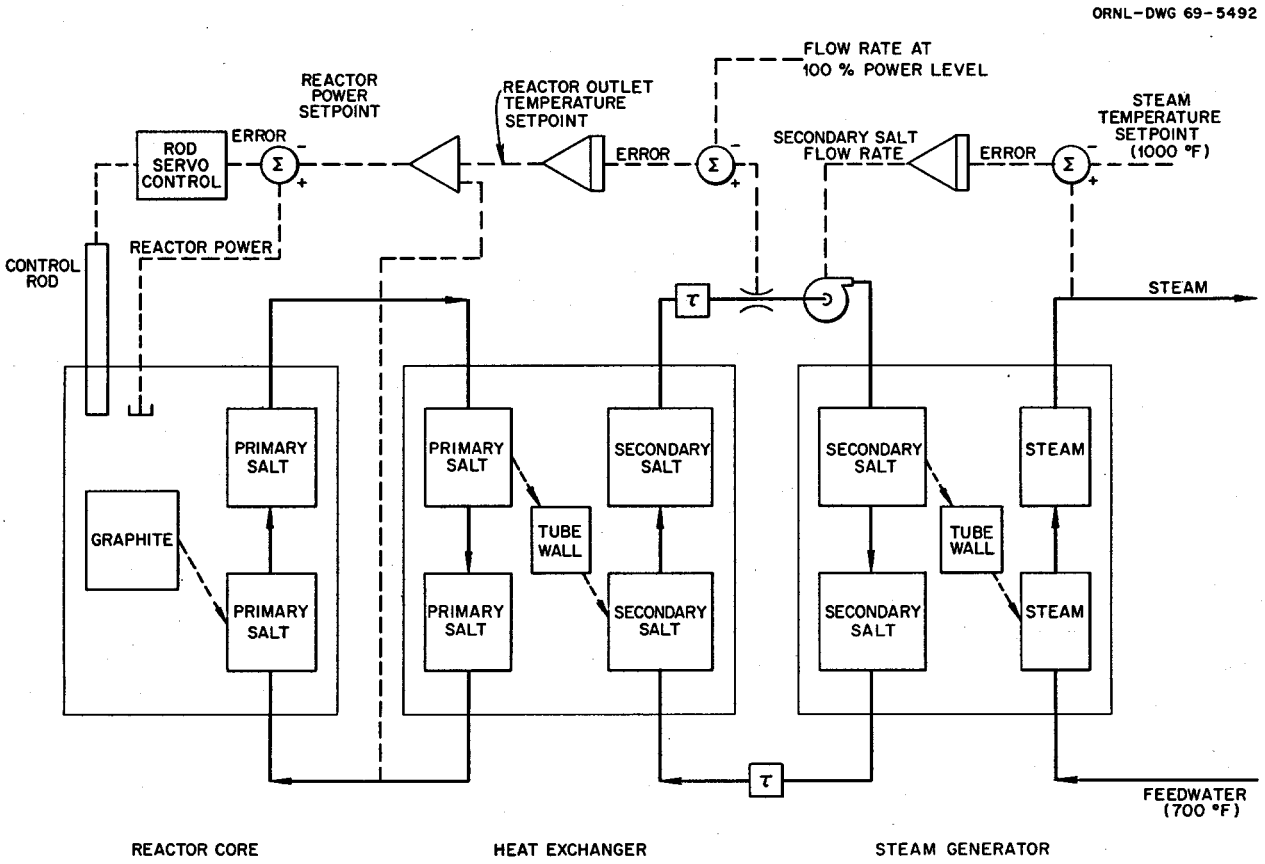

Fig. 8.1. Lumped Model of MSBR for Plant Simulation.

Table 8.1. Results of Load Demand Perturbations

A. Step Losses of Load Demand (from 100%)

Magnitude of Step (%)	Final Steady-State Temperature (°F)				Maximum Steam Temperature Error (°F)	Maximum Rate of Change of Secondary-Salt Flow Rate (%/sec)	Maximum Rate of Change of Reactivity (%/sec)	Maximum Value of Control Reactivity Required (%)
	Reactor Inlet	Reactor Outlet	Secondary Salt Cold Leg	Secondary Salt Hot Leg				
10					13	−0.74	−0.00035	−0.014
30	1009	1183	867	1077	44	−2.3	−0.00106	−0.045
50	976	1098	875	1025	147	−4.3	−0.0030	−0.075

B. 30% Ramp Loss of Load Demand from 100% to 70%

Ramp Rate (%/min)	Maximum Steam Temperature Error (°F)	Maximum Rate of Change of Secondary-Salt Flow Rate (%/sec)	Maximum Rate of Change of Reactivity (%/sec)	Maximum Value of Control Reactivity Required (%)
10	9	−0.41	−0.000175	−0.045
5	5	−0.26	−0.00015	−0.045

maximum allowed by the controller. The maximum value of control reactivity required during a transient is also shown.

The results of the simulation of the loss of one secondary-salt coolant pump indicated that the plant cannot deliver 100% of full load with the temperature and flow limits which were placed on the system in this model, namely, a limit of 110% of full flow per loop on the secondary salt and a limit of 1400°F on the reactor outlet temperature set point.

A complete report on the methods and results of this study is in preparation.[3]

It is apparent from the results of this study that the rather narrow bands within which the temperatures of the two salts must be maintained will produce a necessity for careful control. Such plant maneuvers as increasing and decreasing the load demand on the plant and certain reactivity excursions may allow these temperatures to decrease below the freezing points. However, the models used in these simulations and calculations are abbreviated, and the results are intended only to indicate possible trends in future more detailed investigations. Such investigations are not possible with the analog equipment available at present without either linearizing the simulation equations (reducing the dynamic range) or simulating only a part of the plant at a time or both. Even then the modeling of such a unit as a supercritical steam generator is a difficult task on the analog computer. A more detailed simulation than is attempted here should be attempted by employing more powerful simulation techniques, for example, hybrid computation.

8.2 CALCULATIONS OF NEUTRON DECAY AFTER SHUTDOWN

W. H. Sides, Jr.

The calculation reported previously[4] of the decay of the neutron density in the MSBR core was extended to investigate the effects of (1) the contribution of the photoneutron reaction from beryllium and (2) the loss of all primary-salt flow rate.

8.2.1 Calculation of the Effect of the Beryllium Photoneutron Reaction on Neutron Density After Shutdown

A calculation was made of the neutron source resulting from the $^{9}Be(\gamma,n)2^{4}He$ reaction, based on an estimation of the total gamma-ray flux above 1.67 Mev in the 1000 Mw (electrical) MSBR core. This source was treated as a seventh delayed-neutron group in the circulating fuel kinetics equations of Meghreblian and Holmes.[5] The total gamma-ray flux in the MSBR core of an energy above 1.67 Mev, the threshold for the reaction, and from isotopes having a half-life of between 2 and 35 min was estimated to be approximately 1.3×10^{13} photons cm^{-2} sec^{-1} or less. With a BeF_2 concentration in the primary salt of 16 mole %, the total photoneutron source was calculated to be no greater than 4.22×10^{6} neutrons cm^{-3} sec^{-1}. Treating this source as a seventh delayed-neutron group yielded a value for the delayed-neutron fraction, β, for this group of 1.2×10^{-6} with a mean decay constant of 7.6×10^{-4}/sec. A subsequent seven-group calculation compared with a previous six-group calculation indicated that the contribution of this neutron source to the decay of the neutron density after a -1% step in reactivity was negligible.

8.2.2 Calculation of Neutron Density Following Loss of Primary Flow

The behavior of the neutron density as a function of time after the loss of all primary-salt flow was investigated by a simulation on the Reactor Controls Analog Computer. The steady-state full power for the core was 2250 Mw (thermal). The calculations were carried out for both ^{233}U and ^{235}U.

The event analyzed was one in which all primary-salt pumps coast down from full flow to zero following loss of power to the pumps. Negative control reactivity of up to 1% was inserted into the core either simultaneously with the initiation of pump coastdown or following pump coastdown by some specified delay time. An abbreviated heat transfer model was included to approximate the effect of the temperature coefficients of reactivity. A two-delayed-group model for the kinetics equations was used.[2] The calculation was carried out for times up to 300 sec after the initiation of pump coastdown.

A summary of the results for ^{233}U is shown in Figs. 8.2 and 8.3. Figure 8.2 shows the effects of various amounts and rates of reactivity insertion on the integrated power in the core 300 sec after the initiation of primary flow coastdown and simultaneous insertion of reactivity. The ordinate is given in units of mega-

---

[3] W. H. Sides, *MSBR Control Studies*, ORNL-TM-2489 (to be issued).

[4] *MSR Program Semiann. Progr. Rept. Aug. 31, 1968*, ORNL-4344.

[5] R. V. Meghreblian and D. K. Holmes, *Reactor Analysis*, pp. 590–601, McGraw-Hill, New York, 1960.

watt-seconds of energy generated in the core per initial steady-state megawatt for that fraction of the thermal power which is directly proportional to the neutron density. The insertion of the reactivity as a step is, of course, the upper limit on speed of insertion of reactivity. Figure 8.2 shows, for example, that if −1% in reactivity is inserted at a rate of 0.1%/sec rather than as a step, the amount of energy generated in the core 300 sec after shutdown increases from 1.17 Mwsec/Mw to 2.75 Mwsec/Mw. If the ramp rate is decreased by a factor of 5 to 0.02%/sec, this number increases to 6.08 Mwsec/Mw. The flattening of the curves for the larger amounts of inserted reactivity indicates the diminishing value of increments above 1% in reactivity magnitude.

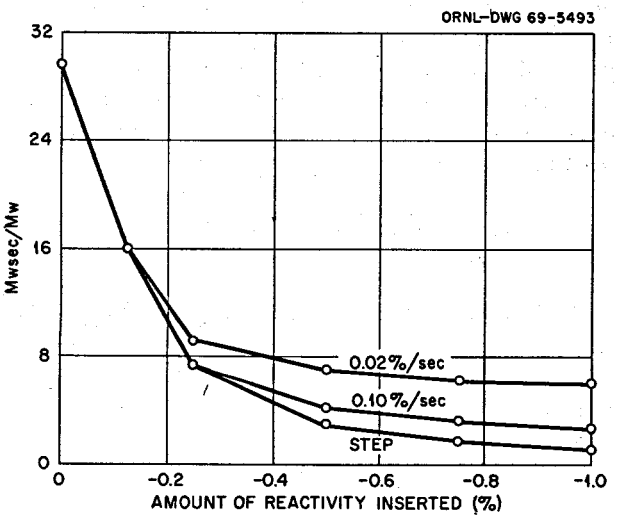

Fig. 8.2. Integral of Reactor Power at 300 sec After Start of Primary Pump Coastdown vs Amount of Reactivity Inserted as a Ramp or Step Initiated Simultaneously with Pump Coastdown for ^{233}U.

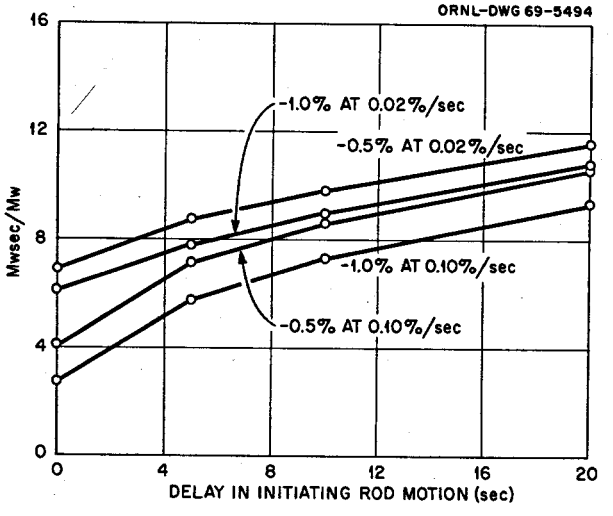

Fig. 8.3. Integral of Reactor Power at 300 sec After Start of Primary Pump Coastdown vs Delay Between Initiation of Flow Coastdown and Insertion of Reactivity for ^{233}U.

If there is a delay between the initiation of pump coastdown and the insertion of reactivity into the core, for example, due to the time required for sensing and evaluating an event, the integrated power generated in the core may be increased. Figure 8.3 shows this effect for delay times of 5, 10, and 20 sec. Reactivity magnitudes of −0.5 and −1.0% at rates of 0.02 and 0.1%/sec were used in accordance with the previous figure. It may be seen from the previous figure that these curves will approach 29.6 Mwsec/Mw as the delay time approaches 300 sec, since this approaches the case of no control action taken after pump coastdown.

8.3 DYNAMIC ANALYSIS OF MSBR STEAM GENERATOR

F. H. Clark O. W. Burke

Work performed at Oak Ridge on the dynamic analysis of the MSBR steam generator has been reported in ORNL-TM-2405, issued January 1969.

A more extensive analysis of the steam generator is being carried on under subcontract with the University of Illinois at the university's hybrid computation facility. Preliminary setup of the problem is complete, and troubles are now being experienced in attaining convergence of the pressure. Such difficulties are not uncommon in dynamic water analyses and are related to the near incompressibility of water. In the supercritical water domain it would not be justified to make the simplifying assumption of incompressibility.

8.4 HIGH-TEMPERATURE RESISTANCE THERMOMETER EVALUATION

R. L. Moore T. M. Cate

Investigation of the feasibility of measuring high temperatures in molten-salt systems with resistance thermometers was continued.[6] Phase I tests of two sets of thermometers (one matched and one unmatched) have been completed. The purpose of these tests was to determine whether gross shifts in calibration would occur during prolonged operation at high temperature with occasional wide variations in operating temperature, including return to room temperature.

[6] *MSR Program Semiann. Progr. Rept. Aug. 31, 1968*, ORNL-4344, pp. 94–95.

The tests were performed by heating the elements from room temperature to a preselected temperature, operating at this temperature for varying periods of time, and then cooling to room temperature. The bridge output voltage was observed during the cycle to detect calibration shifts and to determine the degree of mismatch of the calibration of the two thermometers. Before and after each cycle the ice-bath (32°F) resistance of each element was measured to determine the magnitude of any shift which occurred.

The unmatched (off-the-shelf) set of thermometers was tested first. Results of these tests are shown in Fig. 8.4. No change in calibration was observed after initial successive cycles to 800 and 1200°F; however, when the thermometers were heated to 1400°F there was indication of a calibration shift, and when the thermometers were cooled to room temperature it was noted that a 14-mv shift (equivalent to 5°F) had occurred in the output signal. Subsequent checks showed that the 32°F resistance of one element, 1*A*, had increased from 100.12 to 101.52 ohms and that the resistance of the other element, 1*B*, had increased from 100.2 to 100.32 ohms. During five succeeding cycles to 1200°F no further shift occurred; however, during subsequent cycles of various durations to 1300, 1400, and 1500°F, the resistance of element 1*A* decreased part of the way and that of 1*B* decreased all the way to initial resistance. This suggested that the initial shift was due to induced stresses which were relieved by subsequent operation at high temperature.

Further testing of these thermometers was then deferred to do testing of the second (matched) set and to determine whether the calibration of the first set would continue to shift at room temperature. As shown in Fig. 8.5, the performance of the matched set was similar to that of the unmatched set.

Testing of the first set was resumed and showed that the resistance of the thermometers had not changed during a month at room temperature. This indicated that the thermometers could not be expected to recover their initial calibration in any reasonable time at room temperature. During the subsequent operation, we attempted to determine whether extended operation at 1500°F, the maximum rated temperature, would result in stable operation at all lower temperatures. After several weeks of testing, it appeared that the 32°F resistance of both elements had stabilized, with 1*A* 0.4 ohm above the as-received value and 1*B* at its initial value. No provisions were made for checking the accuracy of the thermometers at high temperature in phase 1 tests, so we do not know at this time whether the 0.4-ohm shift is a zero or span shift.

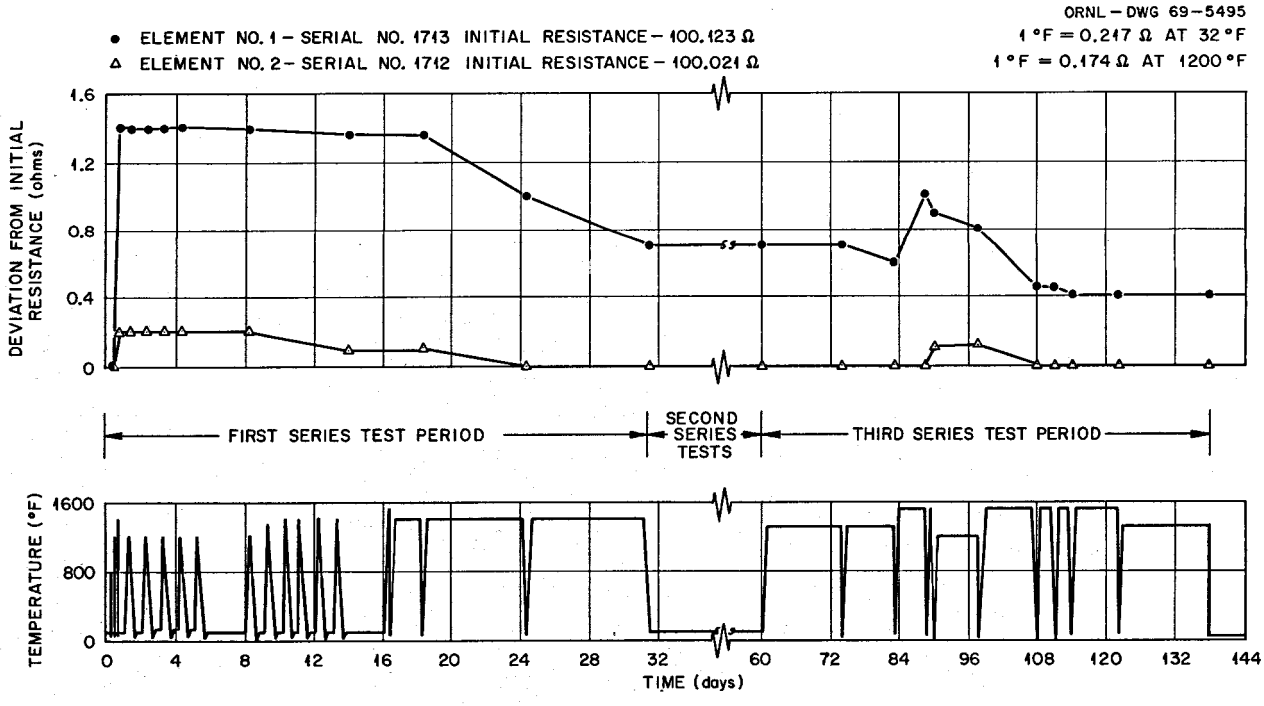

Fig. 8.4. Effect of Temperature Cycling and Extended High-Temperature Operation on the Ice-Bath (32°F) Resistance of an Unmatched Set of Platinum Resistance Thermometers.

The matched set of thermometers was also subjected to extended operation at 1500°F with similar results, as shown in Fig. 8.5. This completed the phase 1 tests. Phase 2 tests are planned in which a more accurate determination will be made of the calibration and rate of shift of calibration of one or more sets of thermometers.

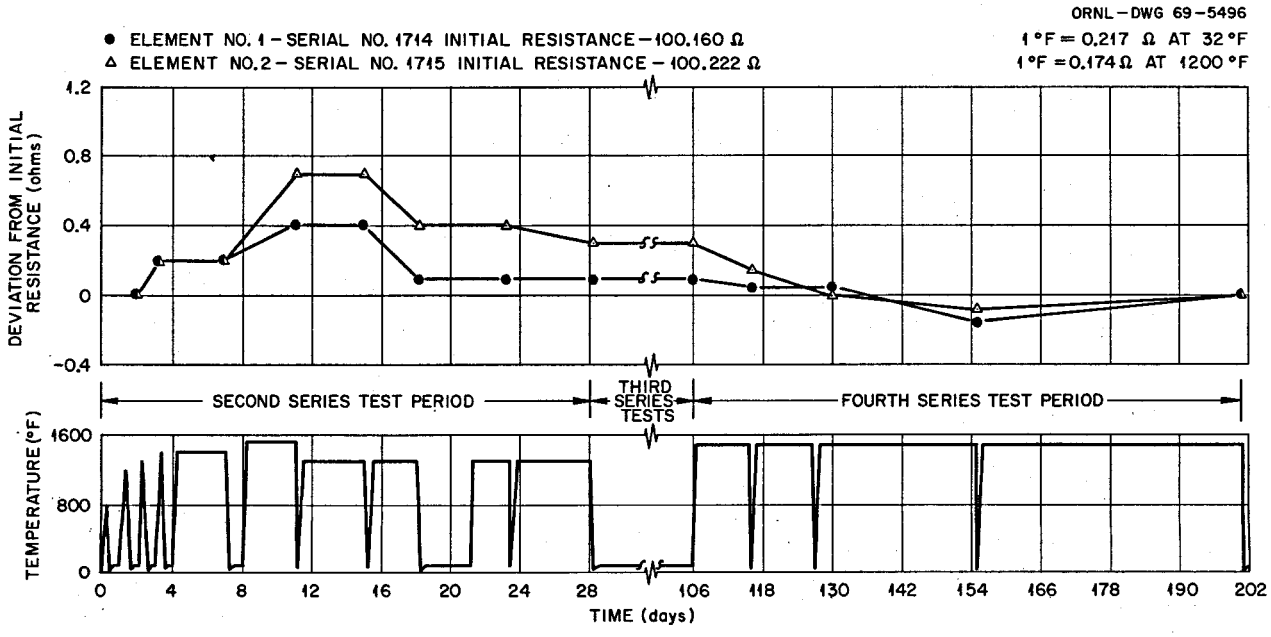

Fig. 8.5. Effect of Temperature Cycling and Extended High-Temperature Operation on the Ice-Bath (32°F) Resistance of a Matched Set of Platinum Resistance Thermometers.

9. Heat Transfer and Thermophysical Properties

9.1 HEAT TRANSFER

B. Cox H. W. Hoffman J. J. Keyes, Jr.

In the previous semiannual report[1] the experimental procedure was described in detail, and a schematic diagram of the system for determining the heat transfer coefficients with molten salts flowing in metal tubes was depicted. Experiments were discussed in which a proposed single-region MSBR fuel salt (LiF-BeF_2-ThF_4-UF_4, 67.5-20-12-0.5 mole %) was employed. The test section was a 24.5-in.-long, 0.25-in.-OD, 0.035-in.-wall Hastelloy N tube, resistance heated. In particular, it was noted that, while the temperature data in the low laminar regime (Reynolds modulus $N_{Re} \cong 800$) were consistent with the pattern expected for fully developed flow beyond a reasonably well-defined entrance length, the data in the low turbulent regime ($N_{Re} \geq 10{,}000$) showed irregular wall temperature variations along the tube which were inconsistent with expected behavior for developed turbulent flow.

During the current report period, a detailed study was made of possible sources of error which could lead to the observed temperature irregularities. It was concluded, for example, that effects of volumetric heat generation in the salt were negligible. Also eliminated as sources of error were effects due to non-steady-state operation, nonuniform heat loss, and spurious emf's induced in the thermocouples by the 60-Hz heating current. Thermocouples which were suspected of being subjected to aging or work hardening were replaced, as were a few faulty channels in the scanning-type readout instrument.

The only uncertainty which could not be eliminated was the influence of a small hole which had been burned in the test section near one end and then repaired by welding. The length of test section downstream from this point (about 120 diameters for flow entering the near end) should be sufficient, it was believed, to minimize the effect of any disturbance produced in the repair zone. However, for some of the runs at moderate and high values of the Reynolds modulus, a more abrupt decrease in wall temperature was observed at a distance about 6 in. from the inlet when the flow entered the end of the tube nearest the repair (located about 3 in. from the inlet) than was observed at a comparable distance for flow entering the opposite end. The amplitude of the disturbance in the wall temperature was about the same for flow in either direction.

Heat transfer experiments employing the modified apparatus with the proposed MSBR fuel salt revealed essentially the same irregularities in axial temperature profile in turbulent flow as had been observed in the initial experiments. The new results covered a range of N_{Re} from 375 to 6570. Table 9.1 is an updated summary of operating conditions for all experiments with the MSBR fuel salt. In one group of runs (55, 61, and 71) the Reynolds modulus was held constant at about 6000 and the inlet liquid temperature at about 1100°F, while the heat flux (based on the liquid enthalpy rise) was varied from 0.66×10^5 to 6.02×10^5 Btu hr^{-1} ft^{-2}. If the abnormalities in the axial temperature profile were due to influence of natural convection or variation in physical properties (possibly changing the radial velocity and temperature profiles sufficiently to delay establishment of fully developed hydrodynamic and thermal conditions), then it would be expected that variations in heat flux would alter the basic shape of the profile. That this is not the case is seen in Fig. 9.1, in which temperatures measured on the outside wall of the test section are plotted as a function of distance along the test section for three different heat flux levels. The corresponding liquid temperature lines are also indicated. Note that, while increasing the heat flux exaggerated the peak in the temperature near the inlet, the rise near the exit, and the irregularities over the middle portion of the test section, the general shape of the three profiles is the same. Thus the heat transfer coefficients calculated from the ratio

[1] *MSR Program Semiann. Progr. Rept. Aug. 31, 1968*, ORNL-4344, pp. 96–100.

Table 9.1. Summary of Operating Conditions for Heat Transfer Studies with an $LiF\text{-}BeF_2\text{-}ThF_4\text{-}UF_4$ (67.5-20-12-0.5 Mole %) Mixture Flowing in a Long Small-Diameter Hastelloy N Tube

Run No.	Liquid Temperature (°F)			W (lb_m/hr)	N_{Re} (exit)	N_{Pr} (exit)	q_f/A (Btu hr^{-1} ft^{-2})	Heat Balance[a]
	T_{in}	T_{out}	ΔT					
							$\times 10^5$	
26	1201.6	1264.9	63.3	850.8	3,770	13.2	1.85	1.18
27	1230.1	1284.0	53.9	1305.6	6,098	12.5	2.41	1.24
28	1256.1	1311.1	55.0	1945.8	9,749	11.7	3.67	1.20
29	1281.3	1340.9	59.6	2325.0	12,543	10.8	4.75	1.12
33	1195.5	1244.1	48.6	1012.2	4,250	13.9	1.69	1.03
34	1219.0	1266.2	47.2	1434.6	6,399	13.1	2.32	1.15
35	1244.5	1290.3	45.8	2203.8	10,483	12.3	3.47	1.10
36	1265.7	1319.7	54.0	2609.4	13,363	11.4	4.83	1.12
37	1188.4	1278.4	90.0	1058.4	4,837	12.8	3.27	1.10
38	1247.7	1331.6	83.9	1524.0	7,999	11.1	4.38	1.10
39	1285.8	1358.0	72.2	2178.0	12,227	10.4	5.40	1.06
40	1316.7	1386.2	69.5	2578.8	15,491	9.72	6.15	1.06
44	1393.8	1440.7	46.9	1715.4	11,713	8.56	2.76	1.13
45	1422.9	1477.9	55.0	1993.2	14,737	7.90	3.76	1.09
46	1452.3	1511.0	58.7	2337.6	18,515	7.37	4.71	1.04
47	1475.4	1545.9	70.5	2434.2	20,658	6.88	5.89	1.07
48	1375.4	1451.2	75.8	115.2	801	8.39	0.30	1.04
49	1104.9	1241.9	137.0	224.4	920	14.2	1.05	1.06
50	1111.9	1215.8	103.9	175.2	672	15.2	0.63	1.13
51	1116.5	1227.6	111.1	94.8	375	14.7	0.36	1.07
52	1113.3	1221.0	107.7	181.2	705	15.0	0.67	1.14
55	1101.7	1199.6	97.9	1792.2	6,568	15.9	6.02	1.05
58	1091.1	1140.2	49.1	1969.8	6,097	18.8	3.32	1.06
61	1092.7	1124.7	32.0	2077.8	6,146	19.8	2.28	1.07
62	1089.7	1157.2	67.5	1909.8	6,204	18.0	4.42	1.07
64	1093.9	1146.0	52.1	622.2	1,959	18.6	1.11	0.94
65	1100.5	1155.4	54.9	622.2	2,016	18.0	1.17	0.94
66	1091.0	1140.6	49.6	507.0	1,571	18.8	0.86	0.94
67	1093.6	1123.6	29.4	999.0	2,946	19.8	1.03	0.90
68	1089.9	1142.0	52.1	851.4	2,648	18.8	1.52	0.98
71	1101.9	1111.3	9.4	2073.6	5,906	20.5	0.66	1.12
72	1098.2	1100.9	2.7	1932.6	5,331	21.1	0.18	0.94
73	1095.7	1111.8	16.3	2076.6	5,916	20.5	1.15	1.01

[a] Heat balance = $\frac{\text{sensible heat gained by fluid + heat loss}}{\text{electrical heat input}}$.

$q_f/A(T_{wall} - T_{liquid})$ all show about the same magnitude of axial variation. These results are suggestive of a laminar-turbulent transition, the effect of which persists to the tube exit.

Because the temperature data suggest that stable hydrodynamic and thermal conditions may be developing near the exit, preliminary estimates have been made of the Nusselt modulus, $N_{Nu} = hD/k$ (where h is the heat transfer coefficient, D the tube inside diameter, and k the salt thermal conductivity) based on test section exit conditions. In Fig. 9.2 the dimensionless heat transfer function $N_{Nu}\,(\mu_s/\mu)^{0.14}/N_{Pr}^{0.33}$ (where N_{Pr} is the Prandtl modulus and μ_s/μ the ratio of fluid absolute viscosity evaluated at the tube surface to that evaluated at the bulk liquid temperature) is plotted against the Reynolds modulus. All physical properties are evaluated near the tube exit and are based on estimates presented in ref. 2. Also plotted are results obtained in the laminar flow regime. In the transition range, $1000 < N_{Re} < 4000$, the tube wall temperatures near the exit were varying too rapidly to permit

[2] S. Cantor (ed.), *Physical Properties of Molten-Salt Reactor Fuel, Coolant, and Flush Salts*, ORNL-TM-2316 (August 1968).

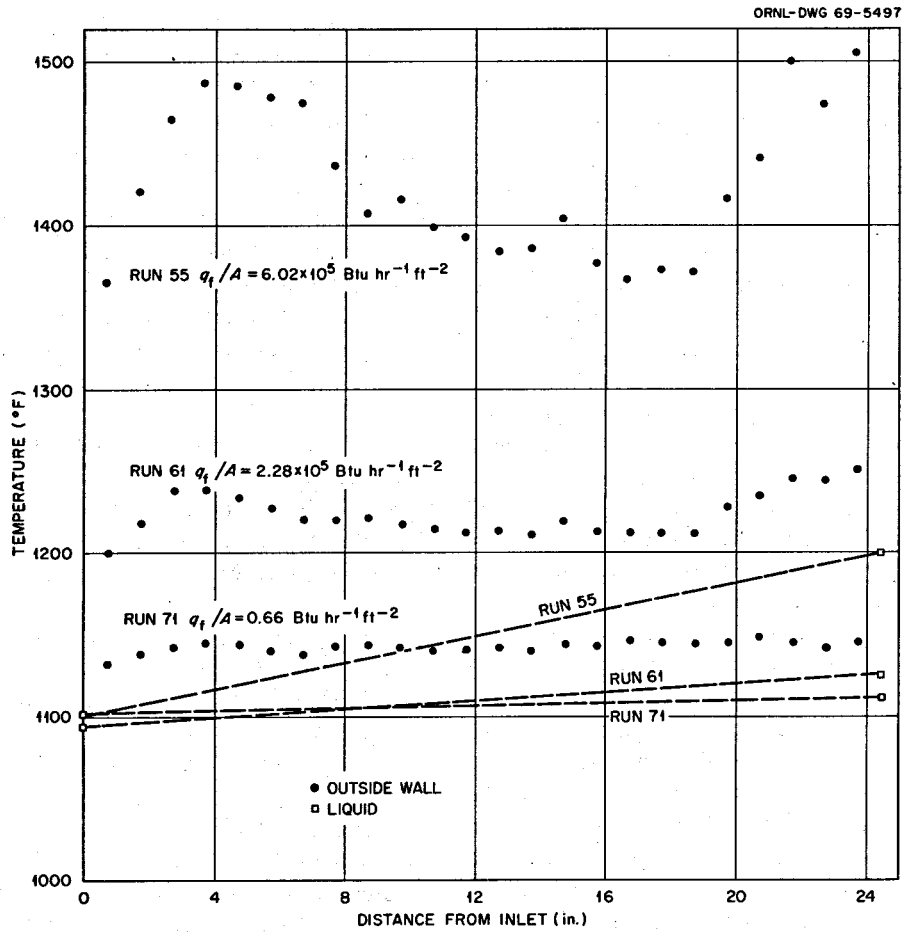

Fig. 9.1. Axial Temperature Profiles for Three Values of Heat Flux with LiF-BeF_2-ThF_4-UF_4 (67.5-20-12-0.5 Mole %) Flowing in an Electrically Heated Tube. $N_{Re} \cong 6000$, $N_{Pr} \cong 19$.

calculation of a consistent h. The empirical correlations of Sieder and Tate[3,4] are shown for comparison. No validity should be attached to the absolute magnitude of the heat transfer results due to the uncertainties in calculation of h. The most significant conclusion from the plot is that, while the laminar data appear to follow the expected dependence on Reynolds modulus, the turbulent data show a greater than expected dependence (i.e., a steeper slope), an observation which is consistent with speculation of a transitional phenomenon persisting to the tube outlet.

By utilizing a theoretical equation suggested by Drew[5] and the laminar heat transfer results, it was possible to estimate the thermal conductivity of the

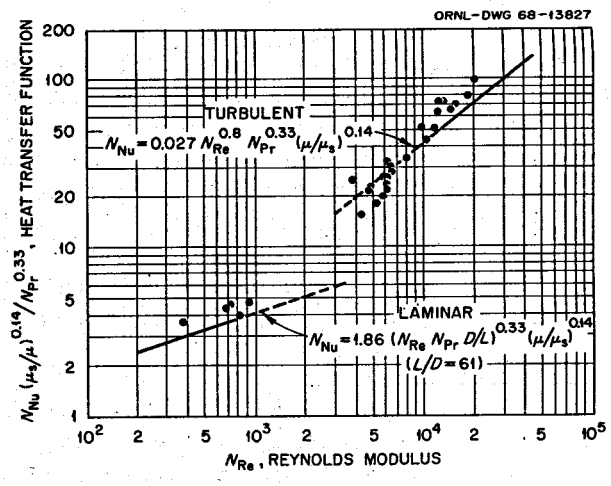

Fig. 9.2. Summary of Preliminary Heat Transfer Measurements near the Test Section Exit with a Proposed MSBR Fuel Salt LiF-BeF_2-ThF_4-UF_4 (67.5-20-12-0.5 Mole %). The lines are the empirical correlations of Sieder and Tate.[3,4]

[3] W. H. McAdams, *Heat Transmission*, 2d ed., p. 168, McGraw-Hill, New York, 1942.

[4] F. Krieth, *Principles of Heat Transfer*, pp. 392–94, International Textbook, Scranton, Pa., 1965.

[5] T. B. Drew *et al.*, *Trans. Am. Inst. Chem. Engrs.* 32, 271 (1936).

fuel salt. At an average bulk salt temperature of 1188°F the average value for the thermal conductivity was found to be 0.68 Btu hr^{-1} ft^{-1} $(°F)^{-1}$ [0.012 w cm^{-1} $(°C)^{-1}$]. Using this value in computing the heat transfer function in Fig. 9.2, the data for laminar flow and for $N_{Re} > 10^4$ fall very close to the Sieder-Tate correlation.

As has been observed, the tube wall temperature patterns near the entrance of the test section suggest the possibility of a laminar-turbulent transition, with approach to developed flow near the outlet. Using correlations for laminar entrance regions[6] and for developed turbulent flow (Dittus-Boelter equation)[3] and physical property data from ref. 2, wall temperatures were predicted and compared with the observations. The measured tube wall temperatures were, in all cases considered, less than those calculated, indicating that the coefficient of heat transfer was abnormally high. The discrepancy was particularly pronounced over the midportion of the test section, suggesting the possibility that irregularities in the inside of the tube could serve for turbulence promotion – these irregularities arising, for example, from deposition of relatively high-melting-point material. However, x rays of the test section indicated no significant deposition. The possibility that excessive test section corrosion could have altered the flow pattern of the salt was also investigated. Portions of the test section were cut out, mounted, etched, and photomicrographed. Figure 9.3 shows both unetched and etched photomicrographs of the tube's inner wall. Because of the high salt temperatures (up to 1550°F) some corrosion is present, but not enough to affect the heat transfer results. The maximum pit depth observed was about ¾ mil. A chemical analysis of the salt showed that no significant composition change occurred during the experiments.

Before proceeding further with MSBR fuel salt experiments, it was decided to evaluate the apparatus and technique by the use of a molten salt having well-known properties and heat transfer behavior. The eutectic mixture known commercially as Hitec, manufactured by Du Pont (KNO_3-$NaNO_2$-$NaNO_3$, 44-49-7 mole %), was chosen because it is known to behave normally with respect to agreement with the standard heat transfer correlations.[7] A new test section, identical in geometry to the original one, was used, and all thermocouples on the test section were replaced. Figures 9.4 and 9.5 are plots of the axial temperature profile for Hitec in turbulent flow. These profiles are in marked contrast to those of Fig. 9.1 for the MSBR salt in that the Hitec data show a region along the midsection of the tube in which the wall and liquid temperature are parallel and hence the heat transfer coefficient is constant, indicative of fully developed flow. A short entrance region is evident in Fig. 9.4, and in both figures slight irregularities in the temperatures near the exit are believed to be due to thermocouple error.

The Hitec runs included three at $N_{Re} \sim 9000$ and three at $N_{Re} \sim 21{,}000$, all with variable heat flux. For nine of the ten turbulent Hitec runs the experimental heat transfer coefficients varied by less than 13% from values predicted by the Dittus-Boelter equation.[3] These results indicate that the experimental apparatus and procedure are reliable and should be applicable to the MSBR fuel salt. The Hitec salt has been removed, the system thoroughly flushed and dried by heating under vacuum, and the MSBR fuel salt has been introduced. No changes in the apparatus will be made.

Should irregular temperature profiles persist when the fuel salt is reexamined, the next step will probably be to lengthen the test section. The addition of a "calming section" upstream of the electrodes would help establish a developed velocity profile in the salt before it is heated, so that only the temperature profile would be developing in the heated section. In the present test section the temperature profile and the velocity profile are developing simultaneously, and associated effects cannot be easily separated and analyzed.

Future plans with the fuel salt call for experiments with spirally corrugated tubes for enhancement of heat transfer. Experiments will also be performed using the proposed MSBR coolant salt (NaF-$NaBF_4$, 8-92 mole %).

9.2 THERMOPHYSICAL PROPERTIES

J. W. Cooke H. W. Hoffman J. J. Keyes, Jr.

9.2.1 Thermal Conductivity

Measurements in both the solid and liquid states have been completed for a proposed MSBR fuel salt mixture (LiF-BeF_2-ThF_4-UF_4, 67.5-20-12-0.5 mole %). A description of the absolute variable-gap apparatus used and its operation has been given previously.[8] The new

[6] W. M. Rohsenow and H. Y. Choi, *Heat, Mass and Momentum Transfer*, p. 166, Prentice-Hall, Englewood Cliffs, N.J., 1961.

[7] H. W. Hoffman and S. I. Cohen, *Fused Salt Heat Transfer. III. Forced-Convection Heat Transfer in Circular Tubes Containing the Salt Mixture $NaNO_2$-$NaNO_3$-KNO_3*, ORNL-2433 (1957).

[8] *MSR Program Semiann. Progr. Rept. Aug. 31, 1968*, ORNL-4344, pp. 100–103.

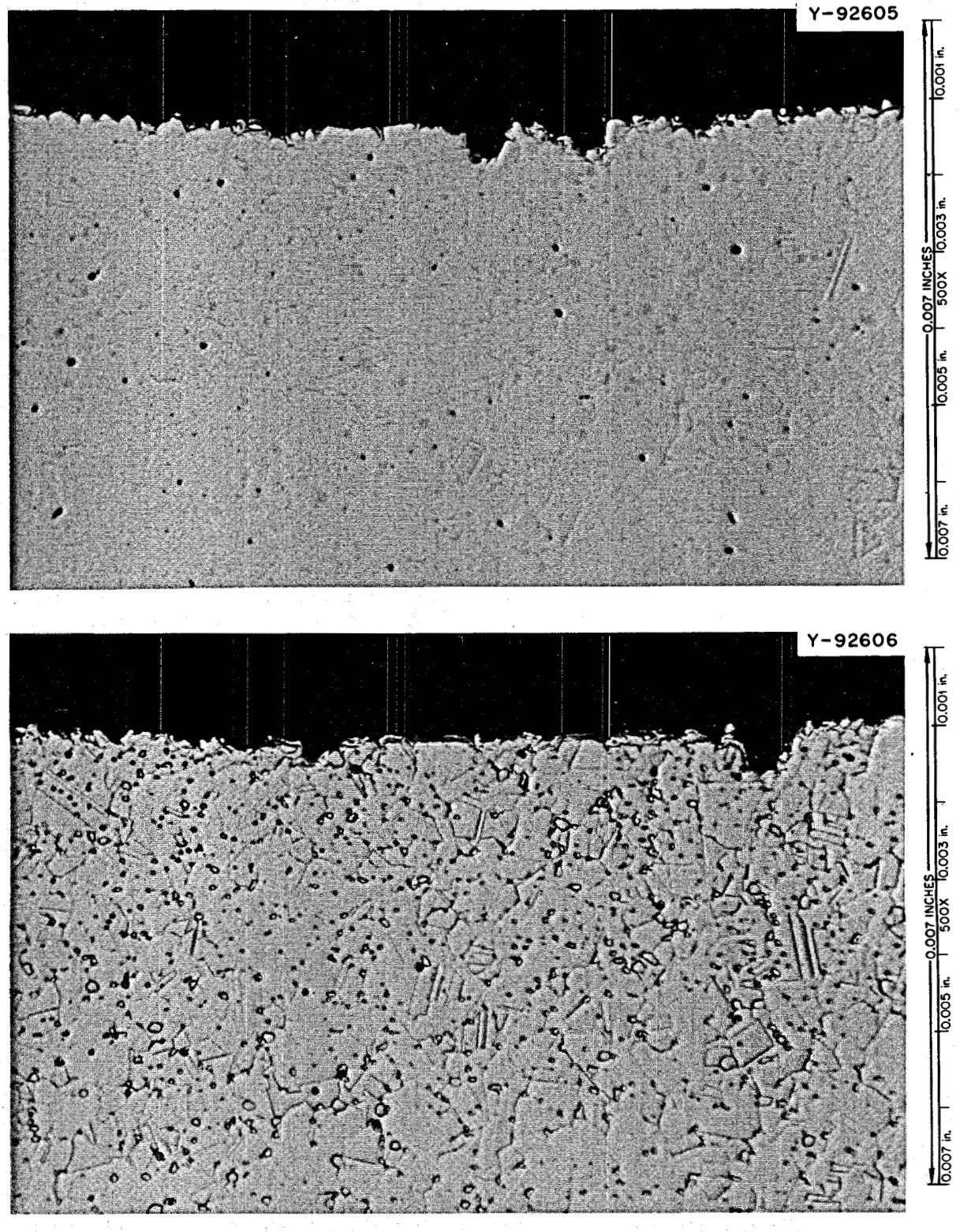

Fig. 9.3. Photomicrographs of Typical Inside Wall of Hastelloy N Test Section Exposed to LiF-BeF_2-ThF_4-UF_4 (67.5-20-12-0.5 Mole %) at a Maximum Temperature of 1550°F. Upper: unetched (500X); lower: etched (500X).

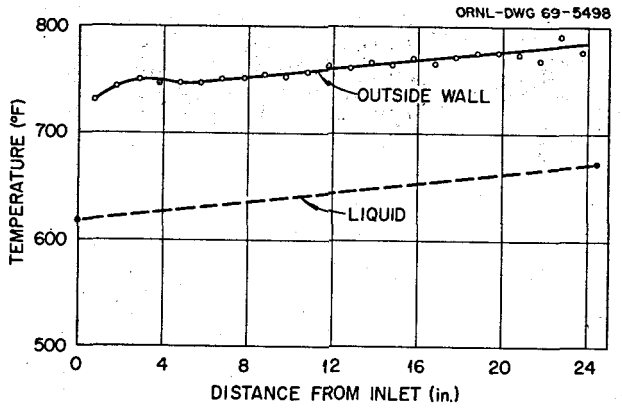

Fig. 9.4. Axial Temperature Profile with Hitec Salt (KNO_3-$NaNO_2$-$NaNO_3$, 44-49-7 Mole %) Flowing in an Electrically Heated Tube. N_{Re} = 8895, N_{Pr} = 6.42, q_f/A = 1.66 X 10^5 Btu hr^{-1} ft^{-2}.

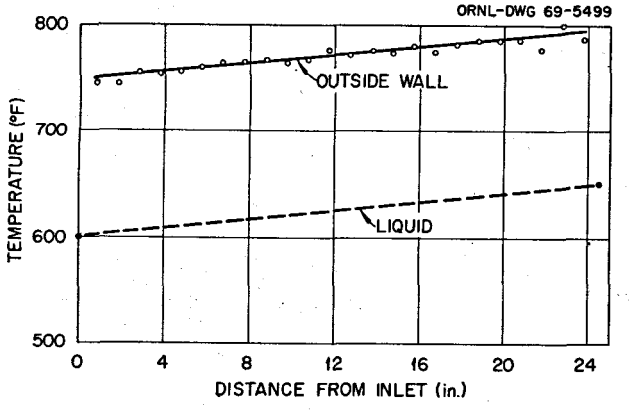

Fig. 9.5. Axial Temperature Profile with Hitec Salt (KNO_3-$NaNO_2$-$NaNO_3$, 44-49-7 Mole %) Flowing in an Electrically Heated Tube. N_{Re} = 21,055, N_{Pr} = 6.83, q_f/A = 3.14 X 10^5 Btu hr^{-1} ft^{-2}.

results, together with previous measurements, are shown plotted vs temperature in Fig. 9.6.

The occurrence of a maximum value of thermal conductivity, which is observed at about 700°C for salt mixtures containing lithium fluoride, has been observed also at lower temperatures by another investigator[9] for KNO_3, $AgNO_3$, KCNS, and $NaHSO_4$. Such a maximum is therefore not unreasonable. The linearly decreasing conductivity of the solid from 300 to 450°C is typical of polycrystalline material. The ratio of the liquid to solid conductivity at the melting point for the MSBR fuel salt was found to be 0.84, which agrees well with the average value of 0.86 ± 0.13 published for a group of salts.[9]

[9]A. G. Turnbull, *Australian J. Appl. Sci.* 12(1), 327 (1961).

Agreement with published data for the solid is gratifying since measurements in the solid state using the variable-gap technique are somewhat more difficult than in the liquid state. The specimen must be melted each time the gap thickness is changed. It is then refrozen, and equilibrium is reestablished at the desired temperature level. The procedure is therefore slow, a full week being required to obtain each value of thermal conductivity. An additional problem relates to the possibility of formation of a void as the specimen contracts while passing from the liquid to the solid phase. However, if the void is small and consistent in shape and location, the measurements will not be affected. On the other hand, if the void is large and inconsistent, its effect on the results will be evident as irregularities in the plot of thermal resistance vs specimen thickness.

A typical plot of thermal resistance vs thickness for the MSBR fuel salt in the solid state at 447°C is shown in Fig. 9.7. Note that the thermal conductivity is derived from the slope of this graph. The data are as consistent as observed for measurement in the liquid state. Furthermore, the resistance extrapolated to zero specimen thickness is essentially the same as that for the liquid measurements, indicating that the fixed resistances (including gas films, surface corrosion films, etc.) were unchanged.

Since the validity of the experimental technique has not been demonstrated, thermal conductivity will be measured for both the solid and liquid states, when possible, for future MSBR salt mixtures. In addition to the MSBR salts, a study will be made of binary salt mixtures (probably LiF-BeF_2) over a wide range of compositions to develop correlations for estimating conductivities of salts, hence reducing the need for tedious and expensive experimental measurements.

9.3 MASS TRANSFER TO CIRCULATING BUBBLES

T. S. Kress J. J. Keyes, Jr.

The initial concept of an experimental facility for investigating mass transfer between a liquid and gas bubbles in cocurrent turbulent flow was presented in the previous semiannual report.[10] This project was commissioned to provide experimental data applicable to a proposed method of removing the fission product poison ^{135}Xe (simulated by oxygen) from the MSBR

[10]*MSR Program Semiann. Progr. Rept. Aug. 31, 1968,* ORNL-4344, p. 106.

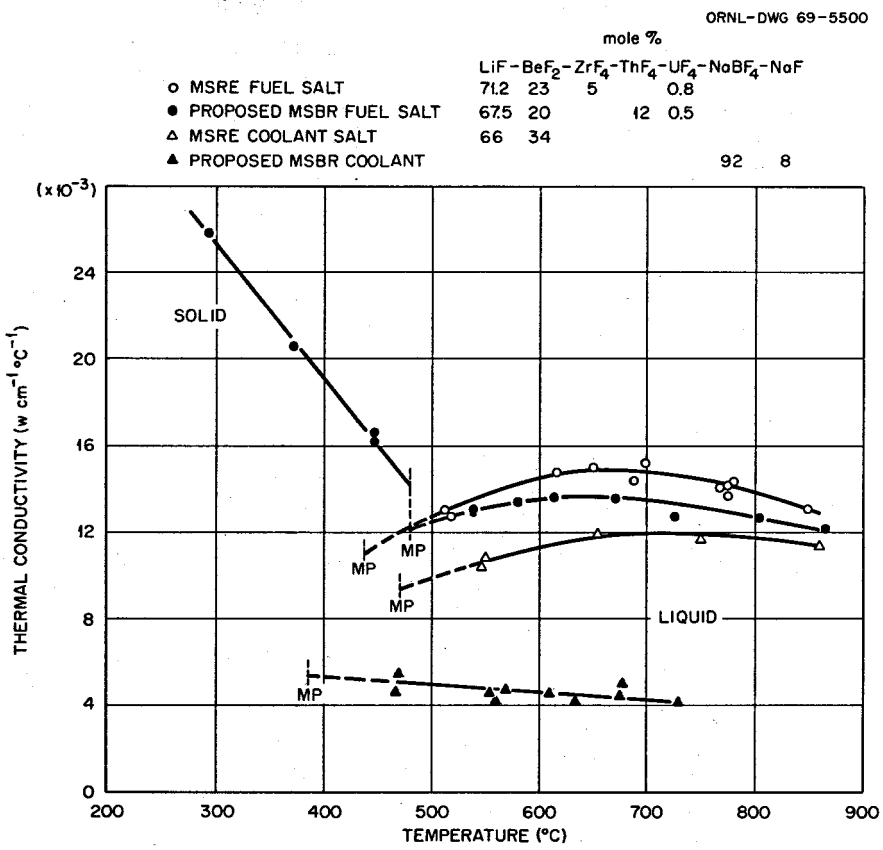

Fig. 9.6. Preliminary Results for the Thermal Conductivity of Several Salt Mixtures of Interest to the MSRE and MSBR Programs.

fuel (simulated by glycerol and water) by transferring it to small circulating helium bubbles continuously injected into and removed from the system.

Detailed design of this facility has now been completed (with the exception of a bubble separating device), and assembly is about 50% complete. The only significant change from the initial concept is the inclusion of provision for operation with the test section either horizontal or vertical. Vertical orientation appears necessary for operation at low and moderate values of the Reynolds modulus to minimize the effect of bubble stratification. The analysis leading to this conclusion is presented in a later section.

Data needed for design of some of the facility components were obtained in several small-scale corollary tests. These included tests on bubble generators and bubble separators utilizing high-speed photographic techniques to observe the bubbles. For example, to generate the many uniform small-diameter bubbles required in the MSBR application, devices were investigated that introduce the gas through fine-mesh screen,

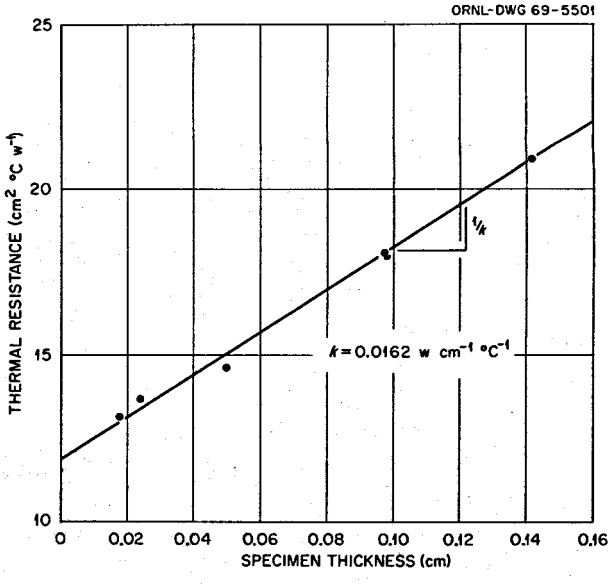

Fig. 9.7. Thermal Resistance as a Function of Specimen Thickness for a Proposed MSBR Fuel Salt (Melting Point ~480°C) at 447°C.

porous metal cylinders, fritted glass disks, and through small holes into various throat positions of a variable-area nozzle. It was determined that the variable-area nozzle method being developed by Kedl[11] provides the most satisfactory performance.

Two types of bubble separators are being considered: a swirl flow centripetal separator being developed by Kedl[11] and fine-mesh conical screens wet by the liquid which act as physical barriers to the bubble. Comparative data for these are still incomplete; conical screens seem to provide good separation if the throughput flow is kept low enough (e.g., about 1 gpm/in.^{2} for a 200-mesh screen). Bubbles smaller than the mesh openings (~0.003 in.) are observed to penetrate the screen, but very few of these small bubbles should be present. While the centripetal separator also appears to give good separation, certain control problems remain to be solved, and such a device may have an undesirable tendency to remove dissolved gases.

To characterize the size and distribution of the bubbles, photographs have been made through a clear, rectangular plastic box filled with a liquid having the same refractive index as the glass conduit inside. A Polaroid camera with diffuse back-lighting from a Strobolume flash unit produced pictures having good resolution for the range of bubble size of interest. Figure 9.8 is an example of such a picture taken during tests on a fritted glass disk bubble generator. The pipe diameter is 1 in., and the speed of the bubbles about 10 fps.

To establish the range of parameters of interest (e.g., Reynolds and Schmidt moduli) over which the mass transfer facility could be operated, the following analysis was made to delineate the conditions controlling dispersion of bubbles in a turbulent liquid.

A basic assumption in the analysis is that bubbles should remain dispersed if the ratio, $\bar{F}_i/\bar{F}_g$, of inertial force to gravity force exerted on the bubble is large. The gravity force is easy to determine, being simply the weight of the displaced fluid,

$$\bar{F}_g = \frac{\rho \pi d^3 g}{6 g_c}, \tag{1}$$

where d is the bubble diameter, ρ is the liquid density, and g and g_c are the local and universal gravitational accelerations respectively.

The inertial forces exerted on a bubble traveling at the local mean velocity in a turbulently flowing liquid are not so easily determined. Consequently, dimensional arguments were applied. In a turbulent fluid the mean variation in velocity, ΔV, over a distance d (greater than the microscale) is (dimensionally) given by

$$\Delta V \sim \left(\frac{\epsilon d g_c}{\rho}\right)^{1/3},$$

where ϵ is the power dissipated per unit volume. Dimensionally, the period T for such velocity variations is given by

$$T \sim \left(\frac{d^2 \rho}{g_c \epsilon}\right)^{1/3}.$$

Therefore it is postulated that the acceleration a undergone by a fluid element of size d is

$$a \cong \frac{\Delta V}{T} \sim \left(\frac{\epsilon d g_c}{\rho}\right)^{1/3} \Big/ \left(\frac{d^2 \rho}{g_c \epsilon}\right)^{1/3} = \left(\frac{\epsilon g_c}{\rho}\right)^{2/3} \Big/ d^{1/3}.$$

A fluid element with this acceleration experiences a "mean" force given by

$$\bar{F}_i = \frac{Ma}{g_c} \sim \frac{\rho \pi d^3}{6 g_c} \left(\frac{\epsilon g_c}{\rho}\right)^{2/3} \Big/ d^{1/3}. \tag{2}$$

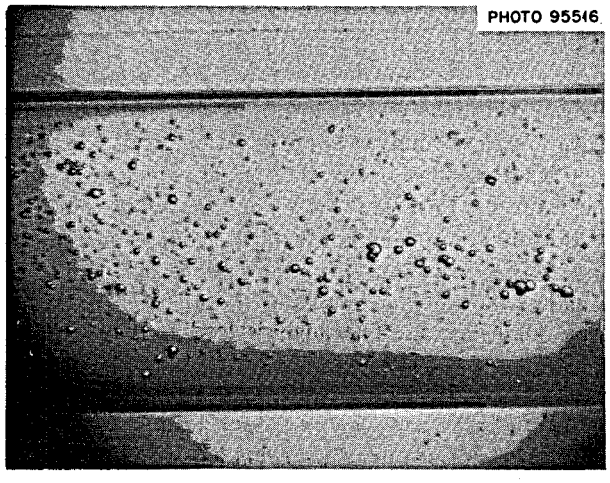

Fig. 9.8. Sample of Photographic Technique for Bubbles Using Polaroid Camera, Strobolume Flash, and Special Photo-Port Around a 1-in.-diam Glass Conduit. Bubble velocity is about 10 fps. The largest bubbles are about 0.035 in. in diameter and most of the very small bubbles about 0.005 in. in diameter.

[11] *Ibid.*, pp. 74–75.

It is postulated that a bubble in the turbulent fluid will experience the same mean forces as those exerted on a fluid element of the same size. Therefore the ratio of inertial to gravity forces after dividing Eq. (2) by Eq. (1) and reducing is

$$\overline{F}_i/\overline{F}_g \sim \left(\frac{\epsilon g_c}{\rho}\right)^{2/3} \Big/ d^{1/3} g \,. \tag{3}$$

It is next assumed that the power dissipation per unit volume is uniform and related to the pressure drop by

$$\epsilon = \overline{V}\frac{\Delta P}{L},$$

where $\overline{V}$ is the mean flow velocity and $\Delta P/L$ is the friction pressure drop per unit length. Using the Blasius equation,

$$\frac{\Delta P}{L} = \frac{f}{D}\frac{\rho D^2}{2g_c},$$

where $f = 0.316/N_{Re}^{1/4}$, ϵ becomes

$$\epsilon = \frac{0.316\mu^3}{2g_c\rho^2 D^4}(N_{Re})^{11/4}, \tag{4}$$

where

D = conduit diameter,

μ = fluid viscosity,

N_{Re} = flow Reynolds modulus,

f = Blasius friction coefficient,

g_c = proportionality constant relating force to the product of mass and acceleration (universal gravitational constant).

Substitution of Eq. (4) into Eq. (3) gives

$$\overline{F}_i/\overline{F}_g \sim \left[\frac{0.316\mu^3 N_{Re}^{11/4}}{2\rho^3 D^4}\right]^{2/3} \Big/ d^{1/3} g \,. \tag{5}$$

Since Eq. (5) was established on dimensional arguments, there will exist a proportionality constant of unknown magnitude (thought to be of order of unity). To establish the value that this ratio should have to serve as a bubble dispersion criterion, use was made of the data of Lamont and Scott,[12] who measured mass transfer coefficients from individual bubbles flowing along with a turbulent liquid both horizontally and vertically and in two conduits of different diameters. The "critical dispersion point" is here taken to occur at conditions for which the mass transfer coefficients for the vertical and horizontal orientations become equal, as given in Table 9.2, based on measurements by Lamont and Scott.

Substitution of the data of case I into Eq. (5) using consistent units gives

$$\overline{F}_i/\overline{F}_g \cong 15,$$

a reasonable value intuitively.

As a check, the data of case II are compared with those of case I:

$$\frac{(F_i/F_g)_I}{(\overline{F}_i/\overline{F}_g)_{II}} = \left(\frac{10^4}{3\times 10^4}\right)^{11/6} \Big/ \left(\frac{5/16}{5/8}\right)^{8/3} = \frac{0.816}{0.831} \cong 1,$$

which is very good agreement.

Therefore the final criterion suggested is that bubbles should remain dispersed if

$$(0.316\mu^3 N_{Re}^{11/4}/2\rho^3 D^4)^{2/3}/d^{1/3}\, g > 15 \tag{6}$$

in any consistent system of units making the ratio dimensionless. Comparison of this criterion with other dispersion data has also shown good agreement.

By applying the dispersion criterion, Eq. (6), to the He-O_2-glycerol mass transfer experiment, the dashed curve shown in Fig. 9.9 was obtained. Since the pump to be used in the experiment has a maximum capacity

[12] J. C. Lamont and D. S. Scott, "An Eddy-Cell Model of Mass Transfer into the Surface of a Turbulent Liquid," presented at the Second Joint Meeting of A.I.Ch.E. and Instituto de Ingenieros Quimicos de Puerto Rico, Tampa, Florida, May 19–22, 1968.

Table 9.2. Conditions at Which Horizontal and Vertical Orientation Mass Transfer Coefficients Become Equal

	Case I	Case II
Conduit diameter, D (in.)	$5/16$	$5/8$
Reynolds modulus, N_{Re}	1.0×10^4	3.0×10^4
Viscosity, μ (centipoises)	0.89	0.89
Density, ρ (g/cm^3)	1.0	1.0
Bubble diameter, d (in.)	$\sim 5/32$	$\sim 5/32$

of 150 gpm (solid line in Fig. 9.9), it is seen that the Reynolds modulus range for fully dispersed operation is somewhat limited. Therefore the facility has been designed so that experiments can be conducted with the test section either vertical or horizontal. This will allow an investigation of bubble dispersion and extend the range over which useful data can be obtained to lower Reynolds moduli.

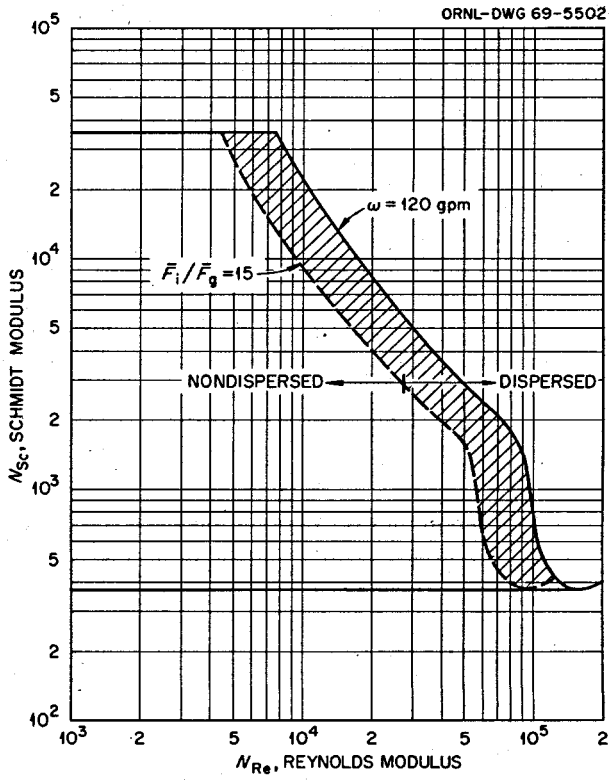

Fig. 9.9. Envelope of Experimental Ranges for the He-O_2-Glycerol Mass Transfer Experiment. Shows the range for which He bubbles should be completely dispersed.

Part 3. Chemistry

W. R. Grimes

The chemical research and development efforts described below provide extensive support to the Molten-Salt Reactor Experiment (MSRE) and to the development of advanced molten-salt reactor systems.

A substantial fraction of these efforts is devoted to the chemistry of the MSRE fuel salt and off-gas streams and to the transport, distribution, and chemistry of fission products in these streams. Operations of the reactor with ^{233}U fuel, as it was reconstituted using the original carrier salt, were initiated in September 1968. Several physicochemical phenomena which had not been noted previously began to appear and have since attracted attention. Principally, these concerned the relation of the redox potential, density, and surface tension of the fuel salt to gas bubble entrainment and distribution of fission products.

Studies of fission product behavior have been continued with specimens removed from the MSRE fuel circuit, with the MSRE off-gas sampler-analyzer, with "synthetic" fuel mixtures, and by investigation of the chemistry of molybdenum, niobium, and ruthenium in molten fluoride mixtures.

The effort to develop chemical separations processes for application to single-fluid molten-salt breeder reactors continues to emphasize methods which employ selective reduction and extraction into molten bismuth containing either lithium or thorium as the reducing agent. The chemical feasibility of ^{233}Pa isolation has been demonstrated by a process which also requires the prior reduction of uranium from the salt mixture and its subsequent oxidation into the salt effluent of a ^{233}Pa column. An alternative process based on selective precipitation of protactinium and uranium oxides continues to show promise and to yield useful information concerning pertinent oxide-fluoride equilibria. Reductive extraction of the lanthanide fission products continues to prove more difficult than the protactinium-uranium extraction but may well lead to useful separations.

A broad program of solution thermodynamics, electrochemistry, spectroscopy, and study of transport processes in molten fluorides continues to supply the basic data for reactor and chemical process design. Investigations of phase equilibria in fluoroborate mixtures continue to yield useful data for evaluation of these materials as secondary coolants.

Advances were made in the development of several analytical chemical methods which suggest their potential application in semiautomated controls for molten-salt reactors. These include electrochemical and spectrophotometric means for determination of the concentration of U^{3+} in fuels and improved methods for the identification of hydrolysis products in molten fluoroborates and for the determination of traces of bismuth in molten-salt breeder reactor fuels.

10. Chemistry of the MSRE

10.1 A MATERIAL BALANCE FOR THE MSRE FUEL SALT

R. E. Thoma

An important feature of MSRE operations with ^{235}U fuel was the excellent agreement between the values of the uranium concentration as determined by standard coulometric methods and from on-site computations of the reactivity balance.[1] It was therefore desirable to continue the application of coulometric methods for

[1] *MSR Program Semiann. Progr. Rept. Feb. 29, 1968,* ORNL-4254, pp. 89–90.

assay of fuels with low uranium concentration, as in MSBR fuels, because of their simplicity and reproducibility. Operation of the MSRE with ^{233}U fuel afforded the first major test of this application. The conditions for the test were less favorable than with the ^{235}U fuel, because, in addition to the fact that the ^{233}U concentration was much lower than with ^{235}U-^{238}U fuel salt, the amounts of carrier salt residues distributed between the chemical reprocessing plant and the fuel system and the amounts of uranium residues which remained in the system after chemical reprocessing were not well known. In an effort to unify the large amount of information concerning the composition, uranium concentration in the fuel, and distribution of fuel salt in the MSRE, a comprehensive material balance was established. The results are summarized in Table 10.1.

The material balance data shown in Table 10.1 comprise the first comprehensive evidence of the fact that the quantities of fuel salt and the concentrations of its constituents are consistent with on-site estimates and with the best estimates of the densities of the salt throughout all MSRE operations. Many of the values contained in Table 10.1 have been cited previously, some in preliminary reports. The origin or significance of other items merits the following explanation or comment.

1. The amounts of fuel transferred to the flush salt were estimated from the results of chemical analyses (fluorometric and delayed neutron activation). From these, results of uranium concentration in the flush salt and weights of salt residues were computed. The masses of flush residues were estimated to be less in proportion to the relative densities of the two salts.

2. The weights of the salt given in items 2 to 5 were measured accurately when the MSRE was initially charged with salt. Items 8 and 10 were also measured accurately.

3. The burnup rate is computed on the basis that the MSRE operates at a full power rating of 8.0 Mw (thermal) and that the total burnup rate of uranium is 1.24 g/Mwd.

4. Items 18 and 19 indicate that the total amount of ^{235}U-^{238}U which is not assignable to operations identified in Table 10.1 is 1.45 kg (0.063%). It is anticipated that this figure will be validated later this year, when uranium is recovered from the NaF absorbers at the Portsmouth Gaseous Diffusion Plant. The current values indicate a low probability that significant amounts of uranium were either transferred to the off-gas system or into the MSRE graphite moderator.

5. The mass of the ^{235}U-^{238}U heel, which was not subjected to chemical reprocessing (item 13), was inferred from isotopic dilution techniques and was estimated from the best fit of analytical values for the isotopic composition of the fuel salt at various stages of preliminary operations of the reactor with ^{233}U fuel with compositions which would result from inclusion of ^{235}U-^{238}U residues (Table 10.2). The isotopic composition of the uranium in the heel was assumed to be identical with the composition of the uranium specimens which were removed from the NaF absorber beds and analyzed.

6. When the MSRE fuel salt was initially constituted from ^{7}LiF-$^{233}UF_4$ and ^{7}LiF-BeF_2-ZrF_4, its nominal concentration was ^{7}LiF-BeF_2-ZrF_4-$^{233}UF_4$ (64.50-30.17-5.19-0.138 mole %) as compared with an average value of its composition during run 14 of ^{7}LiF-BeF_2ZrF_4-$^{235,238}UF_4$ (64.07-29.95-5.15-0.819 mole %). If it is assumed that the quantity of carrier salt to which the ^{233}U concentrate was added was 4724 kg, that the uranium charge was 38.3 kg (including extra ^{238}U added) (item 22), and that the density of the fuel at 650°C is 134 lb/ft^3, the nominal concentration of uranium in the salt is 0.807 wt %. The results of chemical analysis of the fuel salt show that the average concentration has been approximately 1% higher, that is, 0.815 wt %. The weight of the carrier salt reserved for a forthcoming distillation experiment is known only approximately.

Plans are under way to use isotopic dilution methods to determine the quantity of carrier salt left in the fuel processing tank for use in the distillation experiment. The value of 113 kg given in Table 10.1, which is quite uncertain, could be the cause of the difference between the analytical and book concentration of uranium presently in the fuel. If 175 kg were actually in the drain tank, the total fuel charge in the reactor would be nearly 4700 kg, which would make the book value nearly identical with the analytical value. In addition, the density of the fuel salt computed from the volumes measured during drain-fill operations would be 132.3 lb/ft^3, which is the same as that measured in the laboratory and reported in Sect. 12.9 of this report.

10.2 MSRE FUEL CIRCUIT CORROSION CHEMISTRY

R. E. Thoma

Corrosion is minimized in the MSRE fuel circuit by maintaining the fuel salt as slightly reduced with respect to the $Cr^0_{(Hastelloy\ N)} \rightarrow Cr^{2+}$ oxidation potential. This has been accomplished in the past by reduction of ~1% of the uranium inventory to the trivalent state with beryllium metal. Initial experience with the ^{233}U fuel salt showed that the rate of generalized corrosion in the

Table 10.1. Material Balance for MSRE Fuel Salt

Item	Carrier Salt Added[a] (kg)	Total Carrier Salt[a] (kg)	Uranium Added[a] (kg)	$LiF-UF_4$ (73-27 Mole %) Added[a] (kg)	Total Uranium in System[a] (kg)	Total Fuel in System[a] (kg)	Uranium Concentration (wt %)	
							Nominal	Analytical
1. Initial flush salt residue	16.0							
2. Carrier salt charged to drain tank	4558.1	4574.1						
3. $LiF-UF_4$ (depleted) charged to drain tank		4664.1	146.21	236.2	146.21	4810.3	3.04	3.04
4. $LiF-UF_4$ (enriched) charged to drain tank		4699.6	56.98	92.5	203.19	4902.8	4.14	
5. $LiF-UF_4$ (enriched) charged to pump bowl		4715.7	25.79	41.9	228.98	4944.7	4.63	4.61
6. Uranium transferred to flush salt prior to power operation	−17.4	4698.3	−0.74		228.24	4926.6		
7. Flush salt transferred to fuel prior to power operation	16.0	4714.4			228.24	4942.6	4.618	4.611
8. Supplementary $LiF-UF_4$ added during ^{235}U power operation	1.5	4715.9	2.46	4.0	230.70	4946.6		
9. ^{235}U burned during power operation		4715.8	−3.73		226.97	4942.8		
10. Loss by sampling	−5.4	4710.4	−0.256		226.71	4937.2		
11. Net balance at termination of run 14 (including flush-fill transfer effects)		4678.1	−4.48		222.23[b]	4900.3	4.535	4.532
12. Net transfer in final flush			−0.897		221.33	4888.2		
13. Uranium not subject to chemical reprocessing			−1.935 ± 0.035		219.40			
14. Uranium subject to recovery from fuel					219.40			
15. Uranium recovered in chemical processing					217.99 ± 0.5 (99.36%)			
16. Uranium subject to recovery from flush salt					6.12			
17. Uranium recovered from flush salt assuming 99.36% efficiency					6.08			
18. Total uranium recoverable					225.52			
19. Total uranium recovered					224.07			
20. Carrier reserved for distillation experiment	−113.4	4553.5						
21. Supplementary charge for ^{233}U experiment	129.9	4683.5						
22. ^{233}U fuel charge			38.298	62.30		4745.8	0.807	0.815

[a]The number of significant figures used here varies from two to four, depending on their origin; they are used in combination for comparison of nominal and experimental values.

[b]Computed from on-site reactivity balances (4.535% of 4900.3 kg).

fuel circuit was rapid, even though zirconium metal was used previously in chemical reprocessing operations in sufficient amount to allow a small excess of unreacted metal to remain with the reprocessed carrier salt. This treatment was effective in reducing the chromium concentration of the carrier salt from 420 to 34 ppm.[2] Evidently, little or no excess reductant remained in the salt, for during the zero-power experiments in October and November 1968, the concentration of Cr^{2+} in the fuel salt increased continuously until some 28 g (6.2 equivalents) of beryllium metal had been added to the salt.

Generalized corrosion of the MSRE fuel circuitry, as indicated by changes in the Cr^{2+} concentration of the fuel salt, has occurred somewhat more rapidly since the beginning of run 15 than during previous runs. Since salt was first circulated on September 14, 1968, its chromium concentration has risen approximately 36 ppm, that is, from 34 to 70 ppm (Fig. 10.1). The corrosion represented by this increase corresponds to generalized removal of chromium from the walls of the fuel loop to a depth of 0.23 mil.

Beryllium metal rods have been exposed to MSRE fuel salt on four occasions during run 15 in anticipation that a $U^{3+}/\Sigma U$ concentration ratio of 1 to 1.5% would

[2] R. B. Lindauer and C. K. McGlothlan, *Design, Construction, and Testing of a Large Molten Salt Filter*, ORNL-TM-2478, p. 26.

Table 10.2. Isotopic Composition of Uranium in the MSRE Fuel Salt, Run 15

Sample No.	ΣU (kg)	Uranium Isotope/ΣU (%)									
		Estimated					Analytical				
		233	234	235	236	238	233	234	235	236	238
FP14-residue	1.935		0.351	32.979	0.438	66.232	0.006	0.358	32.983	0.412	66.236
FP15-6	23.790	80.404	6.595	3.451	0.210	9.340	80.833	6.692	3.348	0.094	9.116
FP15-9	30.840	82.912	6.793	2.863	0.178	7.254	83.182	6.849	2.850	0.087	7.089
FP15-10	35.720	84.082	6.884	2.584	0.162	6.291	84.214	6.881	2.459	0.081	6.346
FP15-12	35.810	84.099	6.886	2.580	0.162	6.275	84.162	6.906	2.587	0.084	6.260
FP15-18	36.288	84.204	6.895	2.555	0.158	6.188	84.285	6.929	2.557	0.083	6.148
FP15-26	36.867	84.328	6.904	2.526	0.156	6.085	84.569	6.917	2.512	0.083	5.919
FP15-38	37.438	84.449	6.914	2.496	0.153	5.988	84.680	6.920	2.482	0.083	5.480
FP15-55	38.298	84.604	6.927	2.443	0.152	5.874	84.610	6.957	2.482	0.082	5.868
FP15-65	38.298	84.604	6.927	2.443	0.152	5.874	84.641	6.963	2.482	0.082	5.843
FP15-68	38.298	84.604	6.927	2.443	0.152	5.874	84.687	6.948	2.477	0.081	5.808

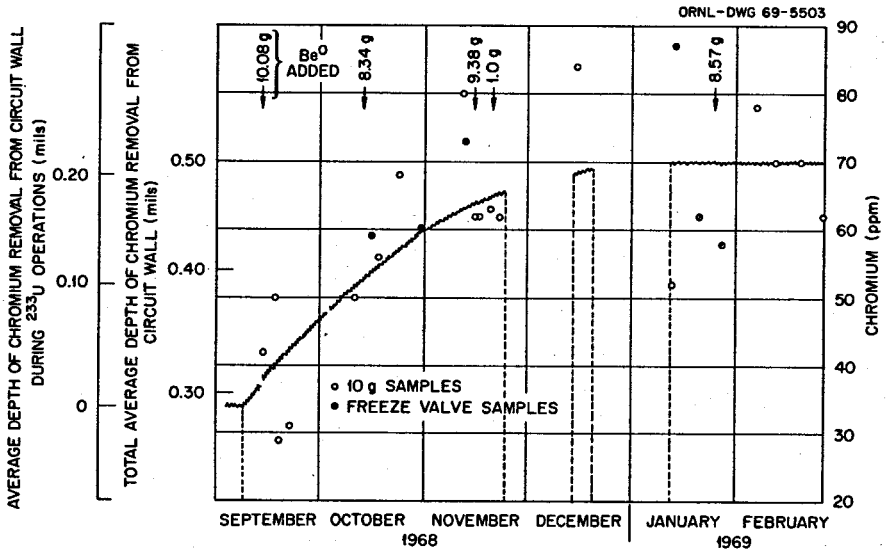

Fig. 10.1. Corrosion of the MSRE Fuel Circuit, Runs 15–17.

be established (see Sect. 10.3). Surprisingly, the residue which was found on and within the first capsule which contained a beryllium rod was preponderantly iron, with lesser amounts of nickel and chromium. The high ratio of iron to chromium in the first residue is regarded as a surprising development, for in reprocessing operations with the fuel carrier salt, concentrations of chromium, iron, and nickel were reduced, respectively, from 460 to 34, 380 to 110, and 180 to <10 ppm.

If chromium was reduced as effectively as is indicated by these analyses, we would have expected no iron to be present, since most of the Fe^{2+} produced by fluorination should have been reduced to the metallic state by the zirconium metal and hydrogen treatments before ionic chromium was reduced. Such a conclusion appears not to be well founded, for not only was the iron-chromium ratio initially high, but corrosion of the fuel circuit continued even after four reduction equivalents (18 g of Be^0) were introduced into the fuel salt. We infer from the high fraction of chromium in the second and third beryllium residues that the concentration of Fe^{2+} in the salt has become negligible and that beryllium has acted to reduce U^{4+} and Cr^{2+} concurrently.

The MSRE fuel circuit was not subjected to comparable corrosion during the zero-power experiments which preceded full-power operations with ^{235}U fuel. We must conclude therefore that the current corrosion behavior is attributable to the current salt charge and to the presence in it initially of some 3 g-atoms of iron as Fe^{2+}.

During the initial stages of operations of the MSRE with ^{233}U fuel, niobium behaved in an unprecedented manner. Previously, little niobium was found in salt samples, but in the early stages of run 15, essentially all of the niobium which was formed remained in the fuel salt. The subsequent changes in niobium concentration clearly reflect variations in the oxidation-reduction potential of the fuel salt; these are described in Sect. 11.1.3 of this report.

It now becomes evident that because the relative free energies of formation of the niobium and chromium fluorides are close (−72.4 kcal per mole of F at 1000°K vs −75.2 kcal for NbF_5 and CrF_2 respectively), the presence of niobium in the fuel signals the possibility that chromium is being oxidized. The presence or absence of niobium in the fuel salt is clearly related to the $U^{3+}/\Sigma U$ concentration ratio. An experimental basis exists therefore for establishing the relationship more exactly, perhaps with sufficient precision that in-line determination of the niobium concentration in such fuels can ultimately be integrated into reactor controls technology.

10.3 ADJUSTMENT OF THE $U^{3+}/\Sigma U$ CONCENTRATION OF THE MSRE FUEL SALT

R. E. Thoma J. M. Dale

On the basis that the oxidation potentials of chromium and niobium differ only slightly in the MSRE fuel salt, we have inferred that the $U^{3+}/\Sigma U$ concentration of the ^{233}U fuel remained essentially nil until after ~6.4 equivalents of Be^0 had been added to the salt and that until then the fuel salt was slightly oxidizing (see Sect. 11.1.3). Since that time an additional 8.57 g (1.90 equivalents) of beryllium has been added to the fuel circuit salt, which contains 35.2 kg of uranium. The $U^{3+}/\Sigma U$ concentration of the fuel salt was thereafter ≤1.26% as power operations began with ^{233}U fuel. Current results of chemical analysis of salt specimens show that the concentration of Cr^{2+} in the fuel salt is now 70 ppm and that corrosion of the fuel circuit has not increased detectably since power operations were initiated. By mid-February 1969, the MSRE had generated ~4000 Mwhr with ^{233}U fuel and had thereby consumed ~200 g of uranium; hence, the U^{3+} fraction at that time was reduced to 0.8%. Adjustment of the $U^{3+}/\Sigma U$ balance will necessarily be more frequent with ^{233}U fuel than with ^{235}U fuel because of the relatively low inventory (38 kg as compared with 225 kg).

Attempts to measure the $U^{3+}/\Sigma U$ concentration are under way. More precise methods than the hydrogen-HF transpiration technique, previously used, are required to analyze this concentration since the overall quantity of UF_3 in the sample is low. For this purpose a voltammetric method has been developed (see Sect. 14) and will be used in the very near future.

Introduction of beryllium metal into the ^{233}U fuel salt apparently caused a major perturbation of salt-gas interactions and resulted in an increase in void fraction in the fuel salt (see Sect. 1, "MSRE Operations"). Initial considerations of this effect called for a review of the probable $U^{3+}/\Sigma U$ concentration during ^{235}U operations for comparison with current behavior and pointed up the fact that previous estimates of $U^{3+}/\Sigma U$ concentrations[3] were slightly lower than originally reported, since they were computed on the basis that the maximum power generated by the MSRE was 7.25 rather than 8.0 Mw (thermal). A revised summary of $U^{3+}/\Sigma U$ concentrations throughout the MSRE power history is shown in Table 10.3 and shows that at the beginning of operations with ^{233}U fuel the concentra-

[3] *MSR Program Semiann. Progr. Rept. Aug. 31, 1967*, ORNL-4191, pp. 110–14.

Table 10.3. Concentration of UF_3 in the MSRE Fuel Salt[a]

Date	Sample No.	Megawatt-Hours	Uranium Consumed (kg)	Uranium Consumed (moles)	Net Equivalents of Oxidation	Total Be^0 Added (g)	Net Equivalents of Reductant Added	Net Equivalents of Reductant	$U^{3+}/\Sigma U$ (%)	
									Calculated	Analytical
		0	0					3.13	0.33	
11/14/66	FP9-14	12,345	0.632	2.67	2.14	0	3.13	0.99	0.10	0.10
1/1/67	FP10-14	14,950	0.766	3.23	2.58	3	3.80	1.22	0.13	
1/3/67	FP10-16	15,050	0.771	3.25	2.60	6	4.46	1.80	0.19	
1/4/67	FP10-18	17,100	0.877	3.70	2.96	7.63	4.82	1.86	0.20	
1/13/67	FP10-23	17,852	0.915	3.86	3.08	18.28	7.19	4.11	0.43	
1/15/67	FP10-25	18,050	0.924	3.90	3.10	18.28	7.19	4.09	0.43	0.66
2/6/67	FP11-5	19,712	1.010	4.26	3.40	18.28	7.19	3.79	0.39	0.60
2/15/67	FP11-10	21,272	1.090	4.60	3.68	29.94	9.77	6.09	0.64	
2/22/67	FP11-13	22,649	1.161	4.90	3.90	29.94	9.77	5.87	0.62	0.69
3/28/67	FP11-32	28,342	1.453	6.13	4.90	29.94	9.77	4.87	0.51	0.45
4/10/67	FP11-40	30,900	1.584	6.68	5.34	38.34	11.64	6.30	0.66	
6/21/67	FP12-6	36,055	1.663	7.01	5.61	38.34	11.64	6.03	0.64	0.71
6/21/67	FP12-8	36,055	1.663	7.01	5.61	46.27	13.40	7.79	0.82	
6/23/67	FP12-9	36,416	1.866	7.87	6.30	56.11	15.58	9.28	0.98	
6/29/67	FP12-11	37,400	1.932	8.15	6.52	56.11	15.58	9.06	0.95	1.30
7/3/67	FP12-13	37,856	1.940	8.19	6.55	64.24	17.38	10.83	1.14	
7/13/67	FP12-15	38,345	1.966	8.30	6.64	76.12	20.02	13.38	1.40	
7/13/67	FP12-21	39,500	2.023	8.54	6.83	76.12	20.02	13.19	1.39	1.0
8/3/67	FP12-56	43,872	2.248	9.49	7.59	85.83	22.18	14.59	1.54	
9/15/67	FP13-5	44,781	2.314	9.76	7.81	85.83	22.18	12.42	1.31	1.60
3/26/68	FP14-(F)	72,454	3.743	15.79	12.63	85.83	22.18	9.55	1.01	
9/15/68	FP15-7	0	0			10.08	2.23	0	0	
10/13/68	FP15-30	0	0			18.42	4.09	0	0	
11/15/68	FP15-62	0	0			27.80	6.17	0	0	
11/20/68	FP15-66	0	0			28.80	6.39	0.22	0.15	
1/22/69	FP17-8	850	0.044	0.19	0.15	37.37	8.29	1.97	1.31	

[a]These numbers assume that the ^{235}U salt originally was 0.16% reduced; that the increase in Cr before initial ^{235}U power operations was real, occurred before 11/14/66, and resulted in reduction of U^{4+} to U^{3+}; that each fission results in oxidation of 0.8 atom of U^{3+}; and that there have been no other losses of U^{3+}.

tions of trivalent uranium were lower than at any time during ^{235}U operations but have been adjusted recently to values which are typical of those present during run 14. Adjustment of the $U^{3+}/\Sigma U$ ratio to its current value of ~1% did not reduce the void fraction of the fuel salt perceptibly. That the concentration of trivalent uranium is intrinsically related to the generation of voids in the salt does not therefore appear to be warranted. The contrast in the appearance of the nickel-beryllium rod assemblies seems to provide a more useful clue to the cause of bubble generation. While none of these cages appeared to be wetted by the salt during ^{235}U operations, each of those removed after treatment of the ^{233}U salt showed evidence that salt had wetted the nickel cage and had adhered to it. A typical example is shown in Fig. 10.2. The presence of bubbles is suggested by the appearance of the upper part of capsule FP17-8 (Fig. 10.3), on which the relic structures of collapsed bubbles seem to be visible. We must conclude that major changes in the salt-metal interfacial tensions were induced as transient behavior and were highly localized. Such behavior apparently had no counterpart in ^{235}U operations.

Numerous causes may be cited in speculation as to the cause of the increased void fraction. For example, the ^{233}U fuel salt density is some 5% less than the ^{235}U salt; the lower density, coupled with a slight reduction in the interfacial tension of this salt, might allow the spray ring jets to generate smaller bubbles which conceivably could be driven sufficiently deep into the pump bowl salt to be entrained in the pump discharge. While the reason for the changes in salt-gas behavior are not known, a variety of plausible models are thus plentiful and are amenable to future tests.

10.4 EXAMINATION OF SIMULATED MSRE FUEL MIXTURE FOR FOAM-PRODUCING PROPERTIES

J. H. Shaffer W. R. Grimes

Following the refueling operations of the MSRE to replace ^{235}U with ^{233}U, the reactor system has experienced some irregularities in its performance.[4] Although the cause of these irregularities has not been identified, the results can be explained by increased foam production at the fuel-gas interface in the pump bowl. The purpose of an experiment now in progress is to examine specific chemical operations performed on the MSRE fuel mixture and their possible contribution to foam production.

[4] A. Houtzeel and J. R. Engel, sect. 1.3.2, this report.

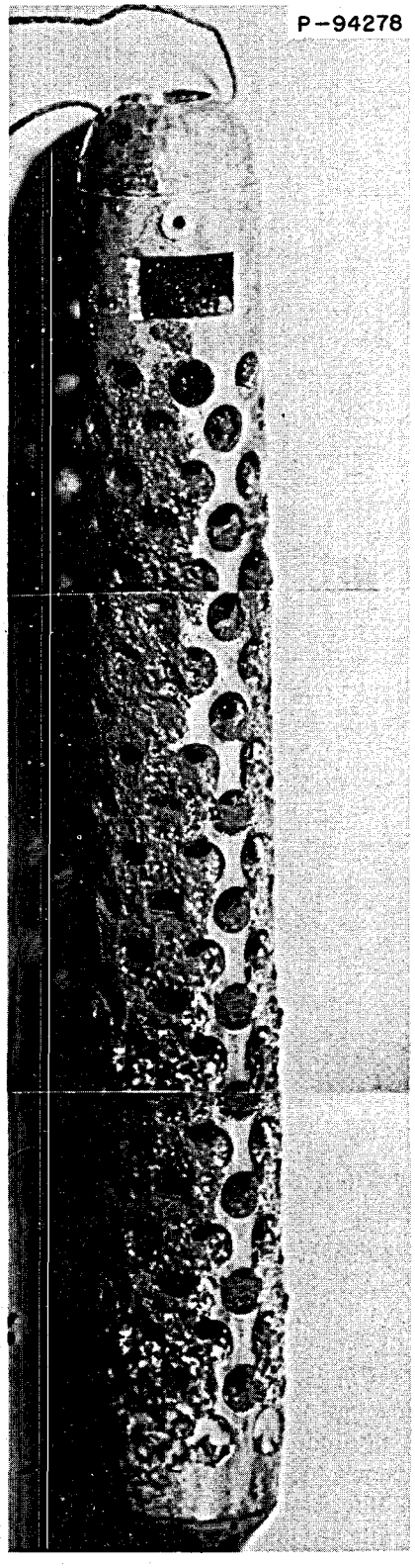

Fig. 10.2. Nickel Cage–Beryllium Rod Assembly No. FP15-30 After Exposure to MSRE Fuel Salt for 10.5 hr.

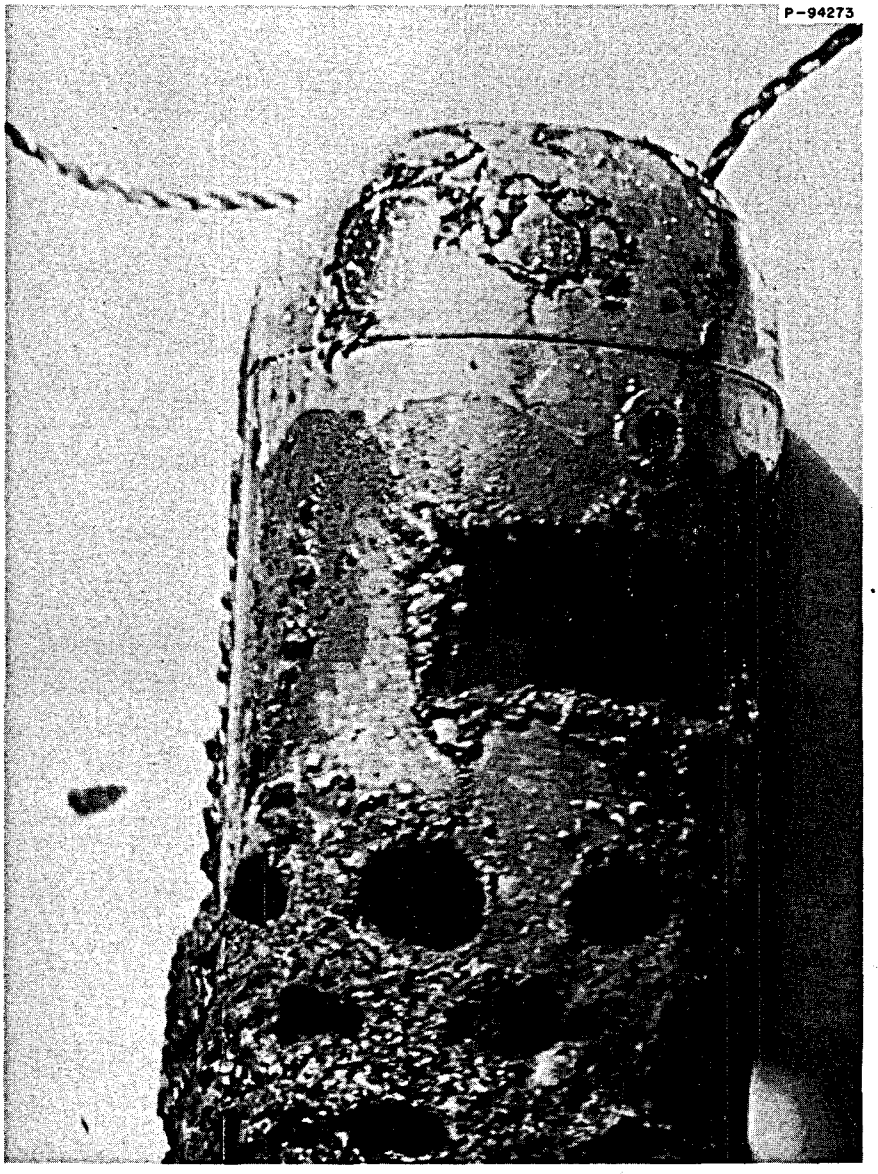

Fig. 10.3. Top of Nickel Cage–Beryllium Rod Assembly No. FP17-8 After Exposure to MSRE Fuel Salt for 12 hr.

This experiment is being conducted with approximately 12.5 kg of $LiF\text{-}BeF_2\text{-}ZrF_4\text{-}UF_4$ (64.8-30.0-5.0-0.25 mole %) contained in a nickel vessel (10 in. diameter by 8 in.) to a depth of about 5 in. Penetrations in the top plate provide for the insertion of a sparge gas tube, two salt level sensing probes, a reference electrode assembly, and a salt sampling port.

The experimental objective has focused on the partial reduction of tetravalent uranium to its trivalent state by reaction with beryllium metal inserted into the pump bowl.

Since this is the principal chemical operation performed in the MSRE pump bowl, its possible contribution to foam production is suspected. The experimental procedure has examined the fluoride mixture at 600°C in the as-prepared condition, at intervals during the reduction of essentially all the uranium to its trivalent state, and after subsequent stepwise oxidation of the mixture with nickel fluoride. Tests for foam production consisted in measurements of the salt level while sparging with argon at flow rates of up to 2 liters/min. Argon was admitted through a $\frac{3}{4}$-in.-diam sintered-nickel disk that closed the end of a nickel tube inserted to within $\frac{1}{2}$ in. of the bottom of the vessel. Melt levels were determined by the abrupt change in electrical resistance noted as the insulated nickel rods

made contact with the salt mixture. Without exception, these tests showed no immediate increase in the salt level ($<1/16$ in.) that would be attributed to the gas sparge operations. Only discontinuous shorting of the probes (at $1/16$ in. above the salt level) by salt splashing was noted.

The insertion of beryllium rods into the salt mixture did result in the reduction of zirconium metal. In earlier development tests, when the reactor fuel mixture contained approximately 0.8 mole % uranium, the rapid reduction of uranium precluded observations of zirconium reduction. While this phenomenon may not exist in the turbulent, high-flow conditions of the reactor pump bowl, the lower uranium concentration of the present fuel mixture appears to have a pronounced effect on its rate of reduction. Subsequent reductions of uranium during this test were achieved by reaction with zirconium metal rods in place of beryllium.

This experiment also provided an opportunity for evaluation of a reference electrode assembly currently being developed for rapid analysis of fluoride melts for trivalent uranium. A nickel–nickel oxide–beryllium oxide reference electrode, currently under development by Hitch and Baes,[5] was inserted into the melt to follow the reduction process. Stable voltages were read at the various reduction intervals. However, their relation to trivalent uranium concentrations could not be accurately established.

Although no confirmation of foam production has been realized to date, the experimental program will examine other techniques for forming salt-gas emulsions and other possible chemical phenomena which may be responsible for the observed behavior of the reactor.

10.5 FOAMING BEHAVIOR IN MOLTEN SALTS

H. W. Kohn F. F. Blankenship

Molten-salt foams were studied in a glass apparatus contained in a special furnace. Purified argon was introduced through a coarse glass frit at the bottom, and visual observations were supplemented, when desirable, with high-speed photography. Our most significant observation throughout these experiments is that we were unable to promote the development of stable foams in clean melts. All of the additives which we might reasonably suspect to be in the pump bowl, that is, carbon dust, graphite powder, beryllium metal, finely divided metallic nickel, and pump oil vapor, were found to be incapable of promoting foams in a vigorously bubbling melt. Melts of lithium fluoroberyllate and of MSRE fuel salt were studied, and their behavior was found to be essentially the same.

Foams were formed only by introducing enough water into the melt, either in the sweep gas or by adding solid hydrates, to give a definite cloudiness. Even so the foam would collapse in less than a minute when the sweep gas was cut off. Simply adding solid oxide as BeO or as Li_2CO_3 ($\rightarrow Li_2O + CO_2$, probably followed by $Li_2O + BeF_2 \rightarrow 2LiF + BeO$) failed to produce foams. This mode of addition fails to produce either the proper state of subdivision or wetting since the particles appear "clumpy" rather than evenly distributed in the melt.

Conditions which cause wetting of the glass container also cause a marked change in the appearance and behavior of the bubbles. An originally wetting melt will produce small, slightly flattened bubbles 2 to 3 mm in diameter. A short treatment with SiF_4 converts this to a nonwetting melt, and the bubbles rapidly change to large disk-shaped objects greater than a centimeter in diameter but less than 2 or 3 mm thick. Adding beryllium metal to such a melt makes it wetting again toward the glass and gives more nearly spherical (but still rather large) bubbles. None of these melts will form a foam.

---

[5] B. F. Hitch and C. F. Baes, Jr., sect. 12.13, this report.

11. Fission Product Behavior

11.1 FISSION PRODUCT BEHAVIOR IN THE MSRE

11.1.1 Examination of Graphite Surveillance Specimens

F. F. Blankenship S. S. Kirslis

Most of the results of the postirradiation examination of the third long-term surveillance assembly, removed from the MSRE on March 25, 1968, have been reported previously.[1] A few additional examinations of the graphite specimens are described below.

Salt-exposed surfaces of five graphite specimens (pyrolytic, Poco, CGB, doubly exposed CGB, and impregnated CGB graphite) were examined by x-ray diffraction. Only graphite lines were observed in the pattern, as was previously observed for electron diffraction, although appreciable quantities of molybdenum were found on the graphite surfaces by spectrographic analysis.

Samples of the same five graphite specimens were mounted and polished for autoradiographic and metallographic examination. The autoradiographs were very similar to those from previously exposed graphite specimens, showing a thin surface region of intense radioactivity with irregular penetrations toward the interior. In the deep interior there was much less activity, with sizable concentration differences between adjacent regions. The pyrolytic graphite specimen showed penetrations of high activity along straight cracks parallel to the graphite planes. These observations are consistent with the previously reported radiochemical results, which indicated considerable variations in concentration profiles between different faces of the same specimens of graphite. These profile variations were confirmed by D. R. Cuneo's results on smaller samples. The previous conclusion is thus confirmed that there are sizable local variations in graphite porosity in all the types of graphite listed except pyrolytic graphite, and that these porosity variations affect significantly the diffusion of activities from the salt interface into the graphite interior.

After rough polishing, metallographic examination of the five graphite specimens yielded results like those on previous surveillance specimens: there was no indication of chemical damage nor of surface films, and the graphite structures showed no changes. Difficulties were experienced in polishing the specimens to the degree required for high-quality metallographs.

11.1.2 Distribution of Fission Products in the MSRE

F. F. Blankenship S. S. Kirslis

In the previously reported material balance[2] for fission products in the MSRE, the values for the percentages of inventory deposited on Hastelloy N surfaces were based on an estimate[3] of 1.2×10^6 cm^2 for the area of metal wetted by the fuel salt. A recent more detailed calculation[4] indicates that the wetted metal area is actually 0.79×10^6 cm^2. Thus the previously reported values for percent deposition on metal should be corrected by the factor 0.79/1.2, or 0.66. It should also be mentioned that no correction was made for the probably sizable effect of fuel turbulence[5] in different regions of the fuel circuit. The measured values of disintegrations per minute per square centimeter of metal remain unchanged.

11.1.3 Fission Product Inventory During ^{233}U Operation

E. L. Compere E. G. Bohlmann

Fission product behavior of many isotopes will be interpreted with reference to the number (or activity)

[1] *MSR Program Semiann. Progr. Rept. Aug. 31, 1968,* ORNL-4344.

[2] *MSR Program Semiann. Progr. Rept. Aug. 31, 1968,* ORNL-4344, p. 136.

[3] W. H. Cook and A. Taboada, personal communication.

[4] J. A. Watts and J. R. Engel, personal communication.

[5] R. B. Briggs, personal communication.

of atoms existing at the time in question which have resulted from the fission history of the reactor. It is convenient to divide the total activity by the mass of salt containing the fission fuel, yielding a nominal activity at the time in question per gram of circulating salt. Mixing with residual salt by transfer to the drain tank is taken into account. Calculations are updated to appropriate reference times, frequently sample time or shutdown time. In general such calculations do not imply any particular fate for given isotopes.

Power operation of MSRE on ^{235}U extended from January 23, 1966, to March 25, 1968. The fuel was subsequently transferred to the drain tanks and there subjected to chemical processing,[6] including fluorine treatment, hydrogen–hydrogen fluoride sparging, and reduction with zirconium metal.

We computed[7] fission product inventories from the power history up to the end of ^{235}U operation in such a way, using one- or two-element decay chains,[8] assuming that it was not necessary to take into consideration the interaction of fission products with neutrons, and that removal of fuel from the system by sampling, etc., was negligible.

Examination of data from salt samples taken after processing, August to September 1968, confirmed that the final zirconium metal reduction treatment had removed all the ^{95}Nb activity, and the activity of ^{95}Nb in the salt was consistent with the ingrowth from ^{95}Zr after this time (see Sect. 11.1.4). Consequently, the inventory of ^{95}Nb was calculated based on this assumption. The inventory of a number of fission product isotopes at the end of runs 14, 15, and 16 and at the beginning of run 15 are shown in Table 11.1. Fission yields were taken from the data assembled by Bell,[9] and half-lives were taken from the current *Table of Isotopes.*[10] Power history, not directly obtainable from the MSRE computer at this time, was read from the nuclear power chart.

Computer programs were developed for the appropriate compression of such data and for the calculation of fission product inventories and decay rates. These were written in Basic-II and were run on the locally available C-A-C time-sharing computer.

Inventory disintegration rates for each isotope as of the time each sample was taken have been computed currently so that data from samples can be promptly compared with inventory values.

11.1.4 Response of ^{95}Nb Activity to Fuel Redox Chemistry

E. L. Compere E. G. Bohlmann

During the ^{235}U operation of the MSRE (through run 14) freeze-valve samples of the fuel salt consistently showed that the ^{95}Nb daughter of ^{95}Zr was not appreciably present in the salt. Data from samples taken during the processing of the carrier salt prior to operation with ^{233}U showed appreciable ^{95}Nb was present after fluorination, but this was removed by the reducing treatment with zirconium metal early in September 1968. During the preparatory and critical operations in run 15, however, the ^{95}Nb formed from ^{95}Zr decay remained dissolved in the salt. That this was due to the salt being in an unexpectedly oxidizing condition was shown by an unusually high corrosion rate, evidenced by increasing Cr^{2+} concentration in the early part of run 15. Additions of Be^0 (6.2 equivalents) designed to inhibit this corrosion accomplished that objective and also resulted in the disappearance of the ^{95}Nb from the salt, as shown in Fig. 11.1.

At this time, other considerations necessitated homogenization of the salt in the circulating loop with an ~8% heel in the drain tank. As shown in the figure, subsequent freeze-valve samples again show that substantial percentages of the niobium inventory (based on power history) are again dissolved in the salt, although the Cr^{2+} concentration appears stabilized. Apparently the oxidant in the heel was just sufficient to reoxidize the Nb (NbF_3), but not to make the melt corrosive. Addition of two more equivalents of Be^0 on January 24, 1969, again caused the niobium to leave the melt.

The niobium percentages were generally lower in runs 16 and 17, compared with run 15. However, the scatter of the data – including that of salt-stable ^{95}Zr – makes the significance of this questionable. Such behavior could be caused by partially irreversible interaction with surfaces – metal, graphite, or gas. The response of the niobium chemistry to the oxidizing state of the melt will be followed carefully in continued MSRE operations in view of possible uses as a redox indicator. After several thousand megawatt-hours of operation sufficient niobium is present (~0.03 mole) to offer a

[6] R. B. Lindauer, *MSR Program Semiann. Progr. Rept. Aug. 31, 1968*, ORNL-4344, pp. 5–11.

[7] E. L. Compere, *MSR Program Semiann. Progr. Rept. Aug. 31, 1968*, ORNL-4344, pp. 208–10.

[8] J. M. West, pp. 7–15 in *Nuclear Engineering Handbook*, ed. by H. Etherington, McGraw-Hill, New York, 1958.

[9] M. J. Bell, sect. 21.4, this report.

[10] C. M. Lederer, J. M. Hollander, and I. Perlman, *Table of Isotopes*, 6th ed., Wiley, New York, 1967.

Table 11.1. Inventory of MSRE Fission Products

(Total atoms existing at given time)/(grams of fuel in circulating system)

Isotope	Yield, ^{233}U Fission[a] (%)	Half-Life[b] (days)	Amount of Fission Product (atoms per gram of circulating salt at time shown)			
			Run 14, Down 3/25/68, 0100	Run 15, Critical 10/2/68, 1400 [0 Mwhr (^{233}U)]	Run 15, Down 11/28/68, 0804 (12.38 Mwhr)	Run 16, Down 12/16/68, 1508[c] (12.47 MMwhr)
^{89}Sr-8	5.86	52	1.16E16	8.23E14	4.05E14	3.16E14
^{90}Sr	5.86	10264	9.68E16	8.69E16	8.66E16	8.65E16
^{91}Sr	5.57	0.403	1.71E14		3.23E12	1.53E10
^{91}Y	5.57	58.8	1.56E16	1.50E15	7.85E14	6.34E14
^{95}Zr	6.05	65	1.85E16	2.18E15	1.21E15	9.92E14
^{95}Nb	6.05	35	9.33E15	5.20E14[d]	7.31E14[d]	6.87E14[d]
^{97}Mo	5.23	0.708	2.37E14		6.22E12	2.7E10
^{99}Mo	4.80	2.79	1.07E15		1.19E13	1.80E11
^{103}Ru	1.80	39.6	5.66E15	1.80E14	7.23E13	5.22E13
^{105}Ru	0.48	0.185	1.21E14		4.2E10	5.3E8
^{106}Ru	0.24	367	3.93E15	2.45E15	2.24E15	2.16E15
^{111}Ag	0.024	7.5	8.20E12	7.3E5	7.0E10	3.2E10
^{125}Sb	0.086	986	2.94E14	2.34E14	2.25E14	2.22E14
^{129m}Te	0.72	34	5.59E14	1.02E13	5.48E12	3.64E12
^{132}Te	4.40	3.25	8.81E14		1.13E13	2.71E11
^{131}I	2.90	8.05	1.33E15	1.6E8	8.46E12	1.64E12
^{140}Ba	5.40	12.8	4.33E15	1.23E11	1.63E13	5.50E12
^{141}Ce	7.09	33	1.00E16	4.64E14	1.63E14	1.04E14
^{143}Ce	5.99	0.138	6.07E13		1.67E11	4.8E9
^{144}Ce	4.61	284	5.14E16	2.93E16	2.55E16	2.44E16
^{137}Cs	6.58	10958	1.03E17	9.29E16	9.25E16	9.24E16
^{147}Nd	1.98	11.1	1.42E15	9.1E9	5.92E12	1.75E12
^{147}Pm	1.98	957	3.18E16	2.63E16	2.52E16	2.49E16
^{155}Eu	0.023	661	4.21E15	3.13E15	2.95E15	2.90E15

[a]Ref. 9.
[b]Ref. 10.
[c]Run 16 critical 12/12/68, 0900.
[d]Assumed removed during fuel processing 9/17/69.

possibility of doing redox titrations in the reactor. Such studies could give information concerning the oxidizing effect of fission, the behavior of noble metal fission products and corrosion products, and the U^{III}-U^{IV} ratio.

11.1.5 MSRE Off-Gas Analyzer-Sampler

E. L. Compere J. L. Rutherford

The MSRE off-gas sampler, which is downstream from the particle trap and ~45 min flow from the pump bowl, was modified[11] prior to run 15. The major change involved replacement of the chemical absorbers for H_2O and CO_2 with a dry molecular sieve (Linde 13X) absorber. This was done because decomposition of the wet magnesium perchlorate absorber material, due to radiation, evolved gases which gave erroneous off-gas impurity measurements. The molecular sieve trap was installed downstream from the heated CuO bed which serves to oxidize hydrocarbon constituents of the gas. The absorber, which may be heated, retains water even at temperatures of 300°C. Carbon dioxide is retained up to about 200°C. Thus hydrocarbon in the gas may be measured by the effect of absorbing its oxidation products.

Adequate reliability and sensitivity of the thermal conductivity cells were demonstrated by conducting

[11]R. B. Gallaher and A. I. Krakoviak, *MSR Program Semiann. Progr. Rept. Aug. 31, 1968*, ORNL-4344, p. 30.

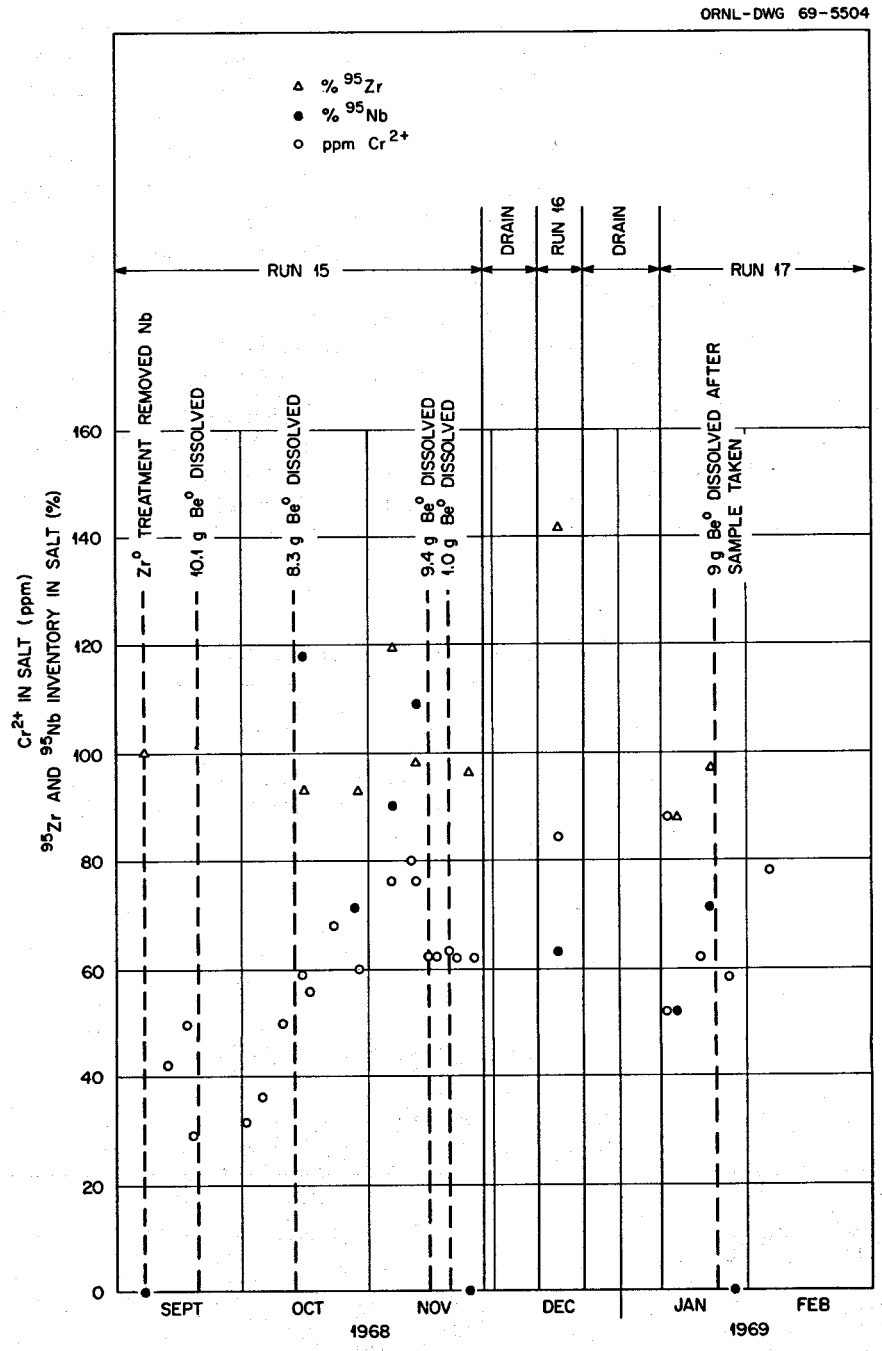

Fig. 11.1. Behavior of Fission Product ^{95}Nb in MSRE.

calibration tests with helium containing ~600 μg of C_4H_{10} per standard liter. A second standard gas was employed containing 120 μg of methane per liter, 240 μg of isobutane per liter, 49 ppm krypton, and 48 ppm xenon; such levels (except for excess methane) are in the range of anticipated off-gas compositions. This gas was used to study the effects of variations in our operating parameters. Variations of test gas flow rates between 25 and 125 cc/min had little effect. Cupric oxide bed temperatures of 1200, 1350, 1400, and 1450°F were employed. Upper temperatures of the CuO are limited by decomposition into Cu_2O and oxygen, which is noticeable at 1350°F and appreciable at 1450°F. However, only isobutane was oxidized at 1200°F, and a temperature of ~1450°F, or possibly higher, is required to oxidize all methane. We chose a CuO operating temperature of 1350°F in order to oxidize all the hydrocarbons (including much of the methane) and to keep the amount of oxygen being evolved from the CuO bed at a tolerable level.

Tests of MSRE off-gas (at operation power >50 w) show hydrocarbon levels ranging between 100 and 300 μg per standard liter (~0.5 to 1.5 g/day). Substantially higher values have been noted after returning from standby to on-line operation; these values declined to the above steady-state range in several hours. Preceding each MSRE run, after transfer of salt from the drain tank to the circulating system, high and slowly declining levels of nonoxidizable impurity in the off-gas were noted. This impurity is believed to be argon, purging from the less accessible regions of the drain tank.

High quantities of impurities were noted in the off-gas during the drain following run 15. These were mostly oxidizable by CuO at 1350°F and were absorbable on the room-temperature molecular sieve absorber, and thereby hydrocarbon. However, about 10% of the impurity was not oxidized. Mass spectrographic analysis (Table 11.2, sample 28) indicated this material to be methane. Methane is a known product of hydrocarbon

Table 11.2. Mass Spectrographic Analysis of MSRE Off-Gas Samples

Sample number	22	23	27	28	29
Date isolated	2/10/68	2/16/68	11/15/68	11/28/68	2/27/69
Date analyzed	11/6/68	11/21/68	11/20/68	12/4/68	3/18/69
MSRE power	5 Mw, 260 hr	5 Mw, 404 hr	50 w	Drain + 6 hr	7–8 Mw, 298 hr
Type sample	Isolation line, sieve	Isolation line, sieve	Direct	CuO bed, sieve	Isolation line, sieve
Substance (vol %)					
He	95.27	90.66	99.75	92.0	87.6
N_2 + CO	2.82	4.39	0.04	2.3	9.94
O_2	0.12	0.59	0.01	0.4	0.46
Ar	0.13	0.06	0.002	0.05	0.13
H_2O	0.08	0.11	0.18	0.03	0.02
CO_2	0.51	2.17	0.002	0.05	1.0
H_2	0.87	0.89	0.007	0.2	0.67
CH_4	0.04	0.22	0.002	4.9	0.03
H-C				0.01	
Kr	0.03	0.12	<0.001	<0.001	0.03
Xe	0.12	0.78	<0.001	0.01	0.12

Isotope	Yield (%)		Isotope/Element (%)				
	^{235}U	^{233}U					
^{83}Kr	0.544	1.17	15.2	14.7			
^{84}Kr	1.00	1.946	26.7	26.7			
^{85}Kr	0.299	0.584	7.6, (8.0[a])	7.3, (7.7[a])			
^{86}Kr	2.02	3.07	50.5	51.3			
^{131}Xe	2.93	2.90	11.4	12.4			12.3
^{132}Xe	4.38	4.54	18.2	19.6			17.3
^{133}Xe	7.61	5.78					2.5 (30.5[b])
^{134}Xe	8.06	5.94	38.8	37.6			32.1
^{136}Xe	6.46	6.64	31.6	30.4			35.8

[a]Corrected for decay; half-life, 10.76 years.
[b]Corrected for decay; half-life, 5.27 days.

cracking and requires CuO temperatures appreciably above 1350°F for complete oxidation.

Hydrocarbon levels of 4 to 10 g/day in the reactor off-gas were observed during the tests using a motor-generator set to vary pump speed. These high levels occurred shortly after the pump was restarted after being off for a short time and did not persist. A parallel increase in unabsorbable products was evident (ranging from 200 to 400 ppm).

During MSRE operations at megawatt power levels, a flow restriction of the lines leading to the off-gas sampler developed regularly, resulting in loss of flow in about a day. Prior operation at the end of run 14 gave similar behavior. During the recent period of operation of the reactor at low power with the pump off for several days (thermal convection operation), no plugging occurred. The restriction, which was found to occur in line 537, can be best relieved by blowing 40 psi helium back and then forward through the line.

A sample of reactor off-gas was taken directly for mass spectrographic analysis during a period of low-power (50 w) operation. This sample (Table 11.2, sample 27) showed 0.18% water, about 0.05% air, and ~0.01% hydrocarbons, which were mostly methane. Most of these impurities, except possibly the hydrocarbons, are believed to have been acquired extraneously, though appropriate preevacuation and flushing techniques were used. A value of 0.01% methane corresponds to 70 μg/liter, or about 0.4 g/day, which is of the same magnitude as values indicated by thermal conductivity analysis reported above.

As the standard gas mixture was first diverted through the absorber after passing through the heated CuO bed, krypton and xenon in the mixture broke through the absorber at different times, which produced "steps" in the thermal conductivity curves, thus offering the possibility of being able to use a frontal analysis technique to examine the reactor off-gas. In addition, krypton and xenon, if present, should appear as an impurity in the helium after passing through the absorber. A steady-state concentration of approximately 75 ppm combined kryptons and xenons should be developed in the reactor off-gas at full power (8 Mw). However, except for some unabsorbable contaminants observed for approximately three days which could have been 50 to 125 ppm krypton and xenon, we have not detected such impurities in the helium using the thermal conductivity cells, though these fission gases have been found by mass spectrographic analysis (Table 11.2, samples 22, 23, 29).

Mass spectrographic analysis has been obtained on several samples of off-gas taken during power operation. Data are given in Table 11.2. Samples 22 and 23 were isolated between valves in line 518 during run 14 and nine months later, after decay of all short-lived isotopes, were collected at liquid-nitrogen temperatures on the molecular sieve, subsequently reheated, and transferred to the sample bottle. A third sample isolated during run 14 was lost due to a leaking nylon valve tip. Sample 29 was isolated between valves in line 518 in late February 1969 (run 17) during a period of full-power operation, subsequently transferred to the low-temperature molecular sieve, and thence to the sample bottle.

The procedure of collecting the sample on a low-temperature molecular sieve permits removal of much of the helium and some of the hydrogen in the sample, while reheating transfers most of the remaining material to the sample bottle. Thus an appreciable concentration effect is obtained.

The samples taken during power operation of the reactor were of interest particularly because of the ratios of isotopes of fission product krypton and xenon. Generally the ratios are consistent with relative fission product yields for the fuel used. Values for ^{131}Xe and ^{132}Xe, which have longer-lived precursors, are below steady-state values indicated by ^{134}Xe and ^{136}Xe.

The ratio $^{136}Xe/^{134}Xe$ is of particular interest because neutron absorption by ^{135}Xe should result in an increase in the proportion of ^{136}Xe. The yield ratio for ^{235}U fission is 0.801,[9] and samples 22 and 23 had ratios of 0.814 and 0.808 respectively. For ^{233}U fission the yield ratio[9] is 1.118, and sample 29 had a ratio of 1.115. The ratios clearly reflect which fuel was in the reactor; closer interpretation will require consideration of the system history when each sample was taken.

Total yields of kryptons were low, doubtless because of the relatively small samples, 500 to 1500 cc, isolated between valves in line 518 in these samples. A more concentrated sample is needed to improve accuracy, and longer periods of steady operation prior to sampling should assist in reaching a steady state. The more concentrated samples can be obtained straightforwardly by passing the off-gas over heated CuO and through the absorber and collecting a suitable amount on the low-temperature molecular sieve.

11.1.6 Examination of Material Recovered from MSRE Off-Gas Line

E. L. Compere

At the end of run 16 a restriction existed in the off-gas line (line 522) near the pump, which had

developed since the line was reamed after run 14.[12] To clear the line and recover some of the material for examination, a reaming tool with a hollow core was attached to flexible metal tubing. This was attached to a "May pack" case and thence to a vacuum pump vented into the off-gas system. The May pack case held several screens of varied aperture and a filter paper. The specialized absorbers normally a part of the May pack assembly were not used.

The tool satisfactorily opened the off-gas line. A small amount of blackish dust was recovered on the filter paper and from the flexible tubing.

Analysis of the residue on the filter paper is shown in Table 11.3. The total amount of each element or isotope was determined and compared with the amount of "inventory" fuel salt that should contain or had produced such a value.

The constituent elements of the fuel salt appear to be present in quantities indicating 4 to 7 mg of fuel salt on the filter paper, as do the isotopes ^{140}Ba, ^{144}Ce, and ^{95}Zr, which usually remain with the salt. It is noteworthy that ^{233}U is in this group, indicating that it was transported only as a salt constituent and that the salt was largely from runs 15 and 16.

The isotopes ^{89}Sr, ^{91}Y, and ^{137}Cs, which have noble-gas precursors, are present in significantly greater proportions, consistent with a mode of transport other than by salt particles.

The "noble metal" isotopes ^{95}Nb, ^{99}Mo, ^{106}Ru, and ^{129m}Te were present in even greater proportions, indicating that they were transported more vigorously than fuel salt. Comparison with inventory is straight-

[12] E. L. Compere, *MSR Program Semiann. Progr. Rept. Aug. 31, 1968*, ORNL-4344, pp. 206–10.

Table 11.3. Material Recovered from MSRE Off-Gas Line After Run 16

Isotope activity corrected to shutdown, 12/16/68

Prior Isotopes in Chain	Isotope or Element	Inventory	Total Found	Total/(Inventory per Milligram of Salt)
	Element	(mg/mg salt)	(mg)	
	Li	0.116	0.80	7
	Be	0.067	0.35	5
	Zr	0.116	0.47	4
	^{233}U	0.0067	0.0396	6
Prior Isotopes in Chain	Isotope	(dis/min per mg salt)	(dis/min)	
16-sec ^{140}Xe → 66-sec ^{140}Cs →	12.8-day ^{140}Ba	4.1E6	1.77E6	8
Short (Xe, Cs, Ba, La) →	284-day ^{144}Ce	4.1E7	1.48E8	4
21-min ^{131}Sb → 25-min ^{131}Te →	8.05-day ^{131}I	9.8E4	1.01E6	10
15% 30-hr ^{131m}Te				
Short (Kr, Rb, Sr) → 10-min ^{95}Y →	65-day ^{95}Zr	7.4E6	3.08E7	4
3.2-min ^{89}Kr → 15-min ^{89}Rb →	52-day ^{89}Sr	2.9E6	3.13E8	110
10-sec ^{91}Kr → 14-min ^{91}Rb → 10-hr ^{91}Sr →	58.8-day ^{91}Y	5.2E6	1.20E8	23
22-sec ^{137}I → 3.9-min ^{137}Xe →	30-year ^{137}Cs	4.1E6	4.31E8	110
Short (Kr, Rb, Sr) → 10-min ^{95}Y → 65-day ^{95}Zr →	35-day ^{95}Nb	9.4E6[a]	1.40E9	150[a]
	2.79-day ^{99}Mo	3.1E4, 3.1E4[a]	2.76E7	900[a]
	367-day ^{106}Ru	2.8E6, 9.8E2[a]	3.51E6	1360[a]
4.6-hr ^{129}Sb →	34-day ^{129m}Te	5.2E4, 2.0E4[a]	9.2E7	1800, 4500[a]

[a] Assumed zero after reprocessing August 1968 before Run 15.

forward in the case of 2.79-day ^{99}Mo and 34-day ^{129m}Te, since much of the inventory was formed in runs 15 and 16. In the case of 367-day ^{106}Ru, although a major part of run 14 material remains (somewhere), salt samples during runs 15 and 16 have shown little to be present in the salt; if only the ^{106}Ru produced by ^{233}U fission is taken into account, the relative sample value is high.

The fuel processing, completed September 7, 1968, appeared to have removed substantially all ^{95}Nb from the salt. Inventory is consequently taken as that produced by decay of ^{95}Zr from run 14 after this time and that produced in runs 15 and 16 (see Sect. 11.1.4 of this report). Thus the "noble metal" elements appear to be present in the material removed from the off-gas line in considerably greater proportion than other materials. It would appear that they had a mode of transport different from the first two groups above, though they may not have been transported all in the same way.

There remains 8.05-day ^{131}I. The examination[12] after run 14 of the jumper section of the off-gas line found appreciable ^{131}I, which may have been transferred as 30-hr ^{131m}Te. In the present case essentially all the ^{131}I inventory came from a short period of high power near the end of run 15. Near-inventory values were found in salt sample FP 16-4, taken just prior to the end of run 16. Thus it appears that the value found here indicates little ^{131}I transferred except as salt.

11.2 FISSION PRODUCT VOLATILIZATION TESTS

S. S. Kirslis F. F. Blankenship

A large number of hot-cell and laboratory tests have been carried out in an effort to characterize more precisely the nature of the process by which fission products "volatilize" from the surface of highly radioactive MSRE fuel salt. This basic information is needed in order to predict with some reliability the behavior to be expected in the MSBR off-gas system.

Results were reported previously[13] from two series of hot-cell tests in which helium was passed slowly over the surface of molten MSRE fuel salt and then through chemical traps or probes which were later sectioned and radiochemically analyzed. Also reported in detail was one of the tests in the fourth series in which particulate matter from the effluent helium was collected on electron microscope screens and identified as fuel salt particles and aggregates varying in diameter from 35 A to several microns. The discussion of the other tests in the third and fourth series will be organized under test type. The third series comprised ten tests carried out one to eight days after installing a fresh 50-g sample of MSRE fuel salt (FP14-62) in the reaction vessel. The series was terminated by a furnace failure which ruined the reaction vessel. The fourth series included 16 tests carried out 5 to 75 days after placing a fresh 50-g sample of MSRE fuel salt in a copper capsule (FP14-69) in the reaction vessel. Failure of a temperature controller caused the melting of the copper capsule after the eighth test (26th day). Fewer radiochemical analyses were obtained on subsequent tests. The top of the reaction vessel for the third and fourth series was of larger size ($\frac{5}{8}$ in. ID) than for the first two series to permit the insertion of the larger test assemblies required for some of the runs.

The results of the third and fourth series of tests are given in detail in Tables 11.4 and 11.5. The main conclusions to be drawn from this mass of data will be given in the following text.

11.2.1 Chemical Probe Tests

In these tests dry helium was passed at 10 cc/min for 50 min over the surface of the molten fuel salt at 600°C, then up through a chemical probe tube whose entrance was $\frac{1}{4}$ to $\frac{1}{2}$ in. above the salt surface. The probe tube contained a 4-μ Felt Metal filter and 1-in.-long sections of NaF and soda lime. In the first two tests of series III, both run one day after salt sampling, the Felt Metal filter appeared to plug, causing a rapid rise in system pressure to 5 psig and a decrease in flow to below 5 cc/min. Correspondingly, the activities found in all sections of the probes were lower by about an order of magnitude than in the similar series II tests. Curiously, the ^{132}Te and ^{129}Te activities were higher than in the series II tests. The third series III test, run eight days after salt sampling, showed normal flow behavior, and the activities behaved as in the series II tests, except that distinctly higher amounts of the tellurium isotopes were found in all probe sections by factors of 100 to 1000.

Three series IV tests were carried out before the temperature controller failed: the first 5 days, the second 17 days, and the third 26 days after the fuel salt sample (FP14-69) was taken. When the activities were calculated back to the fuel sampling time, the results of all three tests were fairly similar and also matched the results of the series II tests. The tellurium isotopes did not behave exceptionally as they did in the series III tests.

[13] S. S. Kirslis and F. F. Blankenship, *MSR Program Semiann. Progr. Rept. Feb. 29, 1968*, ORNL-4254, pp. 100–113.

The observation that the results of the series II tests and the three series IV tests agreed so well (within a rather wide experimental scatter) deserves comment. It should first be realized that if it is assumed that the volatilization behavior varies linearly with the total beta activity of the fuel salt, no large differences would be expected in these experiments. The total beta power of MSRE fuel salt decreases only by a factor of 2 from 1 day after sampling to 12 days after sampling. A decrease of another factor of 2 would require another 100 days of decay. Since the series II tests were performed 1 day after sampling and the series IV tests 5, 17, and 26 days after sampling, the results would be expected to agree within a factor of 2 or 3, which is less than the experimental scatter. It thus appears that the most convenient way to investigate the effect of beta activity on volatilization rate would be to add a large amount of a short-lived beta emitter such as ^{91}Sr to the reaction vessel.

Table 11.4. Results of Third Series of Hot-Cell Tests in Chronological Order

Sample	Age, Days	Conditions	Disintegrations per Minute in Total Sample												Total ^{235}U μg
			^{99}Mo	^{132}Te	^{129}Te	^{103}Ru	^{106}Ru	^{95}Nb	^{95}Zr	^{89}Sr	^{140}Ba	^{141}Ce	^{144}Ce	^{131}I	
1^+	1	7 cc/min, 105 min.	9.7E7	2.01E10	4.8E8	<4.7E5	<1.6E5	1.8E7	7.76E6	6.3E6	7.3E6	6.74E6	5.10E6	3.78E7	2.05
1^-		(Electric charge test)	5.2E8	1.92E10	4.4E8	3.2E6	<3.4E6	1.2E7	3.95E6	7.1E6	8.8E6	6.99E6	5.33E6	2.26E7	1.38
1-0			-	4.9E10	1.05E9	~2.1E7	<1.7E6	5.0E7	~6.1E6	4.0E7	~1.7E7	2.5E7	2.5E7	-	
1-B	1	(Chemical probe test)	~9E6	1.81E9	4.2E7	2.27E5	1.72E4	2.4E6	1.5E6	1.22E6	2.0E6	1.91E6	1.53E6	6.51E7	0.246
1-FM			~3E8	4.36E10	9.9E8	4.69E7	3.0E6	8.27E6	1.2E6	4.67E6	2.3E6	1.74E6	1.31E6	1.21E9	0.22
1-NaF			≤5E6	5.6E7	1.1E6	2.17E5	~1.4E5	<7E4	<2.5E4	<4.2E4	<4.7E4	<9.1E3	<1.5E4	6.23E9	0.01
1-SL			≤5E6	1.98E6	<1.1E5	~1.1E4	≤1.3E4	<5E4	<2.3E4	<2.5E4	<3.9E4	<9.1E3	<1.5E4	8.40E9	0.005
2^+	1	5-cc/min, 40 min.	~3.8E7	1.64E10	4.4E8	4.2E5	<6E4	6.0E6	1.51E6	≤3.3E5	<1.2E5	~7.1E4	<1.6E5	1.23E8	0.109
2^-		(Electric charge test)	2.4E6	1.26E10	3.3E8	8.9E5	<1.1E5	4.7E6	1.42E6	~3.4E5	<2.7E5	~7.3E4	<2.4E5	5.07E7	0.129
2-0			-	~1.2E10	9.4E8	~6.8E6	<2.2E5	7.4E6	~1.4E6	~1.6E6	<9E5	~2.1E4	~2.1E5	-	
2-B	1	(Chemical probe test)	<5E6	4.40E9	1.0E8	1.40E5	≤1.4E4	1.30E7	~3.7E5	<9.2E4	<4E4	<7.5E3	<6E3	6.45E7	≤0.01
2-FM			<2E7	6.74E9	1.7E8	5.72E5	3.9E4	<6.7E5	~6.6E5	<1.1E5	<3E4	<1E4	<8E3	8.58E8	0.03
2-NaF			<2E7	-	-	-	-	-	-	-	-	-	-	8.04E9	≤0.01
2-SL			<3E6	-	-	-	-	-	-	-	-	-	-	4.03E9	0.023
F-1-1(1")	2	15 cc/min, 3¼ hrs.	≤3E8	1.94E10	(~4E8)	~5.6E4	≤8E4	~9.3E5	≤1.8E5	~7.7E5	<2E5	<4E4	<6E4	1.27E9	0.013
F-1-2(2")		(First flow diffusion	≤3.4E6	9.56E9	2.2E8	~4.3E4	≤3E3	2.2E6	<1E5	<1.9E5	<3E5	~6E4	<8E3	2.01E9	0.051
F-1-3(4")		test; sections of Ni	≤9E6	1.09E9	2.4E7	~1.7E4	<4E4	<3.8E5	<2E5	<4.4E5	≤3E5	~6E4	<9E4	1.90E10	0.097
F-1-4(5")		tube before millipore filter)	≤3E7	8.99E7	~1.0E6	~1.6E4	<2E4	6.3E4	<4E4	<3.8E5	≤6E4	~4E4	~4E4	7.34E9	0.026
CTI-B	2	5", 15 cc/min, 2 hrs.	<5E7	3.04E9	7.29E7	3.5E4	1.4E4	5.80E8	1.2E6	<1.0E5	<9E5	~5E4	<6E3	6.23E7	0.03
CTI-NaF		(First closed tube run)	<7E7	1.83E8	4.3E6	~4E3	<4E3	3.3E8	~1.8E5	<1.4E4	<1.5E4	~4.5E3	<4E3	1.40E8	0.09
CTI-Al_2O_3			<3E6	1.28E8	3.0E6	~5E3	<1E4	2.7E6	~6.7E4	<1.2E4	<3.9E4	<9.7E3	<7E3	3.48E9	0.07
CTI-T			<2E7	1.74E8	3.83E6	~1.5E4	<4E3	5.8E5	~2.3E4	1.1E5	<1.8E4	~3E3	<4.0E3	9.76E8	0.68
CTP-1(1")	2-3	15 cc/min, 17¾ hrs.	~9E7	1.3E10	3.02E8	≤3.9E4	≤9.3E4	6.20E8	1.1E7	<1.2E5	<2.8E5	<7E4	<8E4	1.51E10	0.082
CTP-2(2")		(Second flow diffusion	<1.2E7	3.9E9	8.6E7	≤2.5E4	≤3.6E4	2.36E8	1.9E7	<1.4E5	<3.5E5	<8E4	<8E4	2.59E10	0.105
CTP-3(4")		test; sections of Ni	<5E7	-	-	-	-			-	-	-	-	5.02E10	0.133
CTP-4(5")		tube before long Cu tube)	<1E8	-	-		-			-	-	-	-	7.76E10	0.206
CT2-B	3	2", 15 cc/min, 3 hrs.	<2E6	1.01E10	2.32E8	~2.9E4	<1.5E4	6.34E7	2.6E5	<4.5E4	<6E4	~1.6E4	<2E4	1.61E9	0.22
CT2-NaF		(Second closed tube run)	<4E6	6.74E7	1.6E6	~2.1E4	<4E3	~4.8E5	≤1.1E4	<4.4E3	<1.3E4	≤2.6E3	<4E3	1.55E9	0.020
CT2-Al_2O_3			<6E6	5.32E7	1.2E6	~3.4E4	<3.5E3	≤7.2E4	<7E3	<4.4E3	<1.6E4	<3E3	<5E3	4.72E7	0.08
CT2-T			<8.6E5	1.74E8	4.12E6	~5.3E3	<3.8E3	~3.8E4	<7E3	1.8E4	<3E4	<3E3	<3E3	8.93E6	0.098
CT3-B	3	10", 15 cc/min, 4 hrs.	<2E6	3.75E9	8.8E7	-	-	2.25E8	1.1E6	<2.5E4	<4E4	~1.6E4	<1E4	2.49E9	0.266
CT3-NaF		(Third closed tube run)	<2E6	4.0E7	9.24E5	≤3.2E3	<6E3	~6E3	<4E3					1.03E8	0.026
CT3-Al_2O_3			<2E6	2.1E7	4.58E5			~2.5E4	<4E3					7.80E6	0.107
Salt sample dpm/g	5+	7.2296 g, syringe	~1.1E10	<3.5E8	<4E7	~1.05E7	<8E6	0	7.59E10	6.04E10	9.26E10	5.69E10	5.06E10	1.90E10	
3+	8+	8 cc/min, 40 min.	5.6E9	1.00E10	2.5E8	9.95E6	6.9E5	~5.6E6	6.9E6	2.96E7	4.98E7	3.3E7	2.80E7	2.99E7	1.05
3^-		(Electric charge test)	~4.8E9	4.02E9	1.16E8	5.26E6	3.26E5	~2.3E7	4.5E6	4.25E7	9.52E7	3.92E7	3.12E7	2.07E7	2.16
3-0			-	~1.2E10	2.60E8	~3.7E7	~3.3E5	1.7E6	7.93E6	3.4E8	2.95E8	2.1E8	1.6E8	-	
3-B		(Chemical probe test)	<5E7	3.22E10	7.9E8	1.11E7	9.8E5	3.1E7	9.1E6	8.5E7	1.15E8	1.13E8	6.2E7	3.28E7	
3-FM			2.7E8	1.98E10	4.6E8	7.6E6	5.3E5	9.5E6	2.9E6	2.3E7	4.5E6	2.3E6	1.6E6	1.68E8	
3-NaF			6.5E7	1.23E8	1.8E6	2.7E6	4.7E5	7.44E6	3.1E6	6.11E6	1.3E6	5.9E5	4.4E5	1.02E9	
3-SL			<7.9E7	1.40E8	~2.1E6	2.6E6	~3.3E5	≤6E3	≤9E5	6.09E6	1.5E6	8.1E5	6.6E5	2.02E9	
Analysis of Remaining Salt and Liner; values for BS and TS in dpm/g, for BIA and TIA in total dpm in leach.															
BS	8+	Bulk of salt	-	-	<5.5E7	1.86E7	8.50E5	~5.7E10	1.29E11	1.00E11	1.32E11	8.86E10	9.18E10	~2.6E9	
TS		Top 1/4" layer of salt	-	-	~4.75E8	8.96E8	4.20E7	~4.4E10	1.18E11	1.04E11	1.10E11	8.14E10	8.45E10	2.63E10	
BIA		Leach of bottom of liner	-	-	1.25E9	1.76E10	1.03E9	1.11E11	9.2E9	7.10E9	1.11E10	6.46E9	7.80E9	<2E10	
TIA		Leach of top of liner	-	-	1.25E10	1.27E11	6.70E9	5.4E10	4.2E8	2.55E9	2.26E9	5.37E8	6.44E8	<1.0E10	

Second, the agreement between the results for the short-lived (77-hr) ^{132}Te for the series II tests (1-day-old salt) and for the series IV tests (5-, 17-, and 26-day-old salt), when all the activities were calculated back to the time of sampling, implies that the volatilization rate was proportional to the total amount of ^{132}Te in the reaction vessel. The less-reliable results for short-lived ^{99}Mo support a similar conclusion. In future tests, other short-lived nuclides (^{143}Ce, ^{239}Np, ^{111}Ag) will be sought, since it is of practical significance to determine the dependence of volatilization rate on concentration.

Two more chemical probe tests were carried out after the temperature controller failed, causing the reaction vessel temperature to rise above the melting point of the copper capsule (1060°C). The amounts of noble metals volatilized decreased by about a factor of 100. The quantities of most salt-seeking nuclides found in the probes were low by a factor of about 10, but the quantities of ^{235}U were normal. The analysis of a salt sample taken after the temperature rise showed concentrations of all nuclides except ^{95}Nb similar to those in a sample taken 6 days after salt sampling. No ^{95}Nb was found in the 45-day-old sample. Likewise, no ^{95}Nb was found in the last chemical probe. These results suggest that the inadvertent heating of the reaction vessel to about 1060°C caused the noble metals to assume a less volatile form and also interfered with the formation of a fuel salt mist.

The analyses of the remaining salt and the reaction vessel liner after the third hot-cell test have several features of interest. The activities per gram of ^{129}Te, ^{103}Ru, and ^{106}Ru were distinctly higher in the top ¼ in. of the salt than in the remainder, and more of these activities deposited on the liner than remained in the salt. The behavior of ^{95}Nb was apparently different, with a sizable fraction remaining in the salt phase. However, in this case ^{95}Nb was being formed by decay of ^{95}Zr in the frozen salt during the 34 days between the end of the third hot-cell test and the analytical separation of ^{95}Nb. Thus the ^{95}Nb concentration in the salt at the end of the third test was probably low, as

Table 11.5. Results of Fourth Series of Hot-Cell Tests in Chronological Order

Sample	Days Age	Conditions	Disintegrations per Minute in Total Sample												Total ^{235}U μg
			^{99}Mo	^{132}Te	^{129}Te	^{103}Ru	^{106}Ru	^{95}Nb	^{95}Zr	^{89}Sr	^{140}Ba	^{141}Ce	^{144}Ce	^{131}I	
II B	1	10 cc/min, 40 min.	>2E7	>8E7	3E6	1E7	4E6	<4E7	>2E6	>3E6	<7E5	2E6	>4E5	<3E8	<0.2
FM		(Chemical probe test)	<1E9	>3E7	5E6	3E7	<7E6	<6E6	<9E6	1E6	1E6	>5E6	>1E6	<2E10	<0.6
NaF			<2E7	<3E7	<5E6	1E7	~2E7	<3E6	<7E6	<1E7	<1E6	~2E6	3E5	<2E9	<0.44
SL			<3E7	<1E7	1E6	1E7	~1E7	<2E6	1E6	<3E6	3E5	1E6	2E5	<8E8	<0.3
4⁻	5⁺	10 cc/min, 40 min.	<9E7	2.01E9	1.3E7	~2E5	<1.3E5	3.34E7	6.2E5	5.6E5	<2E5	1.3E5	<1.5E5	2.11E8	0.16
4⁺	"	(Electric charge test)	<1.5E8	1.13E9	7.43E6	2.68E5	3.34E5	3.3E7	~1.2E6	1.5E6	<1E6	5.2E5	~9.2E5	9.65E7	0.32
4-0	"		-	4.9E9	2.8E7	~8E6	~6E5	1.6E8	~7.9E5	~5.5E6	≤8E5	≤2.6E5	~5.8E5	6.8E9	(0.22?)
6B	"	(Chemical probe test)	-	1.54E9	1.0E7	6.3E6	6.4E6	1.41E7	3.9E6	2.78E7	-	-	-	4.6E7	0.12
6FM	"		-	9.72E7	7.9E5	~5.4E6	~2.3E6	2.03E6	3.2E6	1.60E7	-	-	-	1.2E9	0.27
6NaF	"		-	<3E6	~2.1E5	1.9E6	4.5E5	2.55E6	8.2E5	8.14E6	-	-	-	1.32E10	≤0.09
6SL	"		-	3.61E7	~5.2E5	5.7E6	2.1E6	5.0E6	5.6E5	1.36E7	-	-	-	2.94E9	0.27
Salt sample dpm/g	6⁺	4.0310g, syringe	<6.4E8	1.66E8	<5.7E6	≤1E7	<1.7E7	~3.2E9	9.13E10	6.67E10	8.68E10	9.60E10	6.67E10	1.40E10	
5⁺	17⁺	10 cc/min, 40 min.	≤1.2E7	2.21E7	1.3E6	3.1E5	~3.3E4	1.03E8	4.3E6	1.85E6	1.17E7	1.06E7	7.96E6	2.6E8	0.515
5⁻	"	(Electric charge test)	≤1.2E7	3.58E7	2.0E6	~5E5	~3E4	7.44E6	4.6E6	9.8E6	5.4E6	4.15E6	3.09E6	4.95E7	0.379
5-0	"		-	~3.0E7	1.3E6	~3.1E5	~3.7E4	-	2.56E6	1.7E6	~3.8E5	2.7E5	~5.5E5	-	0.130
8B	"	(Chemical probe test)	≤1.2E7	3.05E7	1.6E6	1.05E6	3.7E5	1.10E7	2.1E6	1.32E7	6.9E5	-	2.9E7	3.41E7	0.081
8FM	"		<9E6	6.03E6	4.4E5	~4.3E6	~3.2E6	3.90E6	3.8E6	2.85E7	<1.2E6	-	1.4E7	7.60E8	1.86
8NaF	"		-	-	-	-	-	-	-	-	-	-	-	1.75E10	0.011
8SL	"		-	-	-	-	-	-	-	-	-	-	-	1.52E9	1.21
9-B	26⁺	10 cc/min, 40 min.	-	~2.8E7	1.4E6	~3E5	~4E5	6.8E6	1.30E5	1.99E6	4.70E5	1.4E6	4.5E6	1.66E6	0.104
9-FM	"	(Chemical probe test)	-	≤1.6E7	8.7E5	~2E6	~1E6	4.5E6	1.55E6	6.15E6	1.01E6	7.7E5	6E6	6.08E7	0.136
9-NaF	"		-	-	-	-	-	-	-	9.59E6	-	-	-	2.4E9	0.208
9-SL			-	-	-	-	-	-	-	5.77E6	-	-	-	1.8E8	0.136
Salt Sample dpm/g	45⁺	0.2891g, freeze rod			<2.6E7	~3.4E7	<3.1E7	0	1.06E11	8.51E10	1.14E11	8.58E10	8.9E10	~1.4E10	
10-B	46⁺	10 cc/min, 40 min.	-	-	<3.4E4	~2.0E3	<5E3	~2.7E5	2.9E5	<3.3E4	<1.2E5	~5.3E4	~5.3E4	4.9E7	0.125
10-FM	"	(Chemical probe test)	-	-	<3.8E4	<2E4	<5E3	1.18E6	5.5E5	~4.3E4	<1E6	<3E5	<3E5	6.9E8	0.175
10-NaF	"		-	-	<1.5E4	<1.8E4	<5.2E3	~5.2E5	2.5E5	~5.9E4	<3E5	~1.3E6	~1.3E5	1.2E10	0.130
10-SL	"		-	-	<1.5E4	<1.1E5	<8E3	~7.0E4	<1.3E4	<1.4E4	<1.4E5	~3.5E4	~3.5E4	1.3E9	0.224
Salt sample dpm/g	35	6.9221g, syringe			<2.51E7	<1.6E7	<7E6	0	1.50E11	7.40E10	1.10E11	8.78E10	7.76E10	~8.44E10	

in the first salt sample reported in Table 11.4. There was also sizable deposition of ^{95}Nb on the liner walls. The fission products with stable fluorides showed normal concentrations in the fuel and low deposition on the liner walls.

11.2.2 Electric Charge of the Radioactive Aerosols

The particles of most aerosols are electrically charged, with equal numbers of positively and negatively charged particles. One theory of formation of aerosols such as we have observed would require both the metallic and salt particles to be positively charged with respect to the helium environment. It was thus of interest to determine whether our aerosols would collect preferentially on charged electrodes in the gas space above radioactive molten salt. In such experiments voltages in excess of 1000 v are usually applied to the electrodes. This was not easily accomplished in a hot cell, so we compromised by using a voltage of 90 v obtained by connecting four $22\frac{1}{2}$-v batteries in series. The test assembly included the usual chemical probe tube (containing a filter and chemical traps) at ground potential and two $\frac{1}{8}$-in.-diam stainless steel rods as electrodes connected to the batteries. The electrodes and the probe were held in place $\frac{1}{8}$ in. from each other and insulated from each other and from the probe tube by a Lavite spacer 2 in. from the bottom and by a rubber stopper about 6 in. from the bottom of the probe and electrodes. The three chemical probe tests of series III and the first two of series IV were run with electrodes of this type in position.

The activities deposited on the electrodes and on the outside of the chemical probe were leached off with 2 N HNO_3, and the leaches were analyzed radiochemically for 12 isotopes and for ^{235}U by delayed-neutron counting.

The results showed that equal amounts of each activity deposited on both electrodes and that a slightly larger amount (usually) was found on the outside of the grounded probe tube, whose exposed area was twice that of each electrode. While this experiment would have been more definitive if larger voltages had been used, the indication was that the aerosol particles carried no charge of either sign.

11.2.3 Electron Microscope Tests

Attempts were made by two methods to collect aerosol particles which could be examined and identified with the electron microscope. In the first method, helium was passed over the molten fuel-salt surface, then up a $\frac{1}{4}$-in.-diam nickel tube 12 in. long to a Millipore filter which had been coated with a thin evaporated carbon film. Five runs of this type were made with helium flow rates varying from 15 to 100 cc/min and flow durations from 1 to 4 hr. The Millipore filter was dissolved away from the carbon film, which was then picked up on electron microscope screens and examined. Very little particulate matter was found by electron microscope examination of these specimens. Two of the larger particles were identified by electron diffraction as graphite and one large particle as metallic nickel. The bulk of the foreign particles were in the micron size range, were rounded in shape, and tended to form chains. They did not yield a satisfactory diffraction pattern and thus could not be identified. No particles had the appearance of the fuel-salt particles identified by the first run of the second collection method. Apparently most of the latter particles were deposited along the length of the 12-in.-long tube which carried the helium out of the reaction vessel to the Millipore filter holder.

The second collection method, involving direct deposition of aerosol particles on electron microscope screens positioned just above the fuel salt, and the results of its first run were described in detail in the previous report.[13] Four subsequent runs by the same method were carried out but failed to yield satisfactory specimens for examination. Only small fragments of the thin carbon film on the electron microscope screens were found to have survived intact after the exposure, the removal from the screen holder in the hot cell, the packing of the screens into individual bottles provided with miniature desiccators, and the transport of the bottles to the electron microscope. No really satisfactory collections of particles could be found by electron microscopic examinations of the few surviving scraps of carbon film. It is believed that most of the handling problems which destroyed the carbon films may be solved by transferring the screens directly from the screen holder through a small funnel into small plastic pill capsules whose rounded shape will allow only the edges of the flat carbon-coated screens to touch the inner capsule surface. It is clear that the handling problems are not insuperable, since three of the six screens from the first run by this method were recovered in satisfactory condition.

11.2.4 Aerosol Deposition from a Helium Stream

One of the standard methods for determining particle size and its distribution in aerosols is to measure the

deposition gradient along the walls of a tube through which the aerosol flows. If the aerosol contains particles of a uniform size, the diffusion coefficient of the particles can be calculated from the deposition gradient according to the equation:[14]

$$\frac{\Delta \log n_s}{\Delta z} = \frac{5.00D}{Q},$$

where n_s is the number of particles deposited per unit length, z is the distance from the channel entrance, D is the diffusion coefficient of particles in the carrier gas, and Q is the volumetric flow rate. In the derivation of this equation it is assumed that the particles stick to the wall when they collide with it. From the diffusion coefficient the particle size may be estimated.

Two experiments were performed from which values of D could be estimated. In the first, helium was passed at 15 cc/min for 18 hr over the surface of the molten MSRE fuel salt with the gas exiting through a ¼-in.-OD nickel tube 12 in. long. The nickel tube was connected to a coil of ¼-in.-OD copper tubing 100 ft long. The nickel and copper tubes were then disconnected and brought out of the hot cell. The exterior surfaces were decontaminated with a nitric acid wash, the tubes were sectioned, and the interior surface of each length of tubing was leached free of activity. The nickel tube was sectioned into lengths, starting at the inlet end, of 1, 2, 4, and 5 in. Each section was leached with 2 N HNO_3 containing a little HCl. The leaches were analyzed radiochemically for the usual 12 nuclides and for ^{235}U by delayed-neutron counting. The long length of copper tubing was cut into lengths of 1, 3, 6, 10, 15, 25, and 40 ft. It was leached first with NH_4OH, then HCl, and finally with HNO_3. No radiochemical analyses were performed on these leaches, since gamma spectrometer scans showed that all of the activity was ^{131}I. Even after chemically removing 99.9% of the ^{131}I, the gamma scans showed only ^{131}I activity remaining.

The nickel tube leaches also contained predominantly ^{131}I activity, which complicated the accurate measurement of other activities. Most of the latter were on the 1- and 2-in. sections on the inlet end. Reliable analyses of the other two sections could not be made. On the basis of these rather uncertain data, the noble metal activities per inch of tube generally dropped by a factor of about 6 and the salt-seeking species showed no appreciable change in going from a z value of 0.5 in. to one of 2 in. Thus D calculated from the equation given above is about 0.01 for the noble metals and very small for the salt-seeking nuclides. No conclusions regarding aerosol behavior can be drawn from the analytical results for ^{131}I, since it probably traveled as gaseous HI (or possibly CH_3I) produced by the hydrolysis of the molten salt by traces of water in the dried helium stream. It is clear that this gaseous iodine species did not behave as an aerosol particle and in particular that it did not stick to the wall on the first collision with it.

A second similar test was carried out on the ¼-in.-OD nickel tube 12 in. long used as the helium exit tube for the first Millipore filter run. This tube was removed from the reaction vessel after helium had flowed for 3½ hr at 15 cc/min. The tube was put through the same leaching and sectioning procedures used for the nickel tube from the long-copper-tube run. The analyses were again complicated by high ^{131}I activities, but somewhat more satisfactory results were obtained. Again the noble metals showed a decrease in activity per inch of tube from the inlet to the outlet, while the salt-seeking species showed little change. Diffusion coefficients in square centimeters per second calculated from the deposition data were 0.06 for ^{99}Mo, 0.025 for ^{132}Te and ^{129}Te, 0.017 for ^{103}Ru and ^{106}Ru, and 0.021 for ^{95}Nb. These values are probably reliable within a factor of 2 because of the logarithmic way in which the activity ratios enter into the calculation of D. The activity ratios themselves are only reliable within a factor of about 10. From these values of D it is estimated[15] that the diameters of the particles carrying the Te, Ru, and Nb isotopes were in the range 17×10^{-4} to 33×10^{-4} μ, or 17 to 33 A. The ^{99}Mo particles may be somewhat smaller, and the fuel-salt particles carrying the salt-seeking species are indicated to be considerably larger. It is likely that the very small size of the particles carrying noble metals accounts for the fact that they could not be characterized or identified by electron microscope techniques, particularly since their concentrations in the aerosol mixture were low compared with the concentration of fuel-salt particles. The extremely small size of the noble metal particles suggests that the noble metals in the aerosol exist as groups of metal atoms rather than as species sorbed on other very small particles. These interpretations are based on only two rather crude diffusion tube tests and should not be relied upon too heavily until they are confirmed by more refined tests. A

[14] R. L. Bennett, W. C. Hinds, and R. E. Adams, *Development of Iodine Characterization Sampler for Application in Humid Environments*, ORNL-TM-2071, p. 21 (May 1, 1968).

[15] J. W. Thomas, *The Diffusion Battery Method for Aerosal Particle Size Determination*, ORNL-1648, pp.48–51 (Dec. 14, 1953).

significant source of error in the above estimates will be discussed in the next section.

11.2.5 Closed-Tube Diffusion Tests

Before results were available on the flow diffusion tests just described, it was speculated that the aerosol particles might be so large that the deposition gradients could not be estimated. Therefore three closed-tube diffusion tests were carried out to obtain steeper deposition gradients which would indicate qualitative differences in diffusion behavior of the various nuclides. Each diffusion tube was a 12-in. length of ¼-in.-OD nickel tubing welded closed at the upper end. At distances of 2, 5, and 10 in., respectively, from the open bottom ends, the three tubes were provided with chemical traps made by packing 1-in. lengths of the tube with NaF and activated alumina pellets. Each tube was positioned in the reaction vessel with the open end ¼ in. from the surface of the molten MSRE fuel salt, and the gas space above the fuel salt was flushed with a slow flow of 15 cc/min of dried helium. The run durations were 2, 3, and 4 hr, respectively, for the tubes with chemical traps 5, 2, and 10 in. from the open end. After leaching the exterior of each tube free of activity, it was segmented to provide samples of the NaF trap, the alumina trap, and of the tubing below and above the traps. Each sample was dissolved and analyzed radiochemically for 12 nuclides and by delayed-neutron counting for ^{235}U.

The results for the diffusion tubes with the chemical trap 5 in. from the open end were puzzling, since the deposition gradients were hardly steeper than for the flow diffusion tubes, except for ^{95}Nb and ^{95}Zr. The steepest gradients were observed in the tube with the trap 2 in. from the open end. The order of steepness was ^{95}Nb, ^{131}I, ^{132}Te, ^{129}Te, ^{95}Zr, ^{103}Ru, ^{106}Ru, ^{144}Ce, ^{141}Ce, ^{99}Mo, ^{89}Sr, and ^{140}Ba. Compared with the flow diffusion tube results, the ^{95}Nb and ^{95}Zr gradients were much steeper and that for ^{99}Mo much less steep. These discrepancies are not easily explained except as analytical errors. The analyses for the salt-seeking nuclides were particularly difficult since the total leach solutions often contained less than 10^5 dis/min in the presence of 10^9 dis/min of ^{131}I and 10^8 to 10^{10} dis/min of the noble metals. Because of analytical difficulties, complete analyses were obtained on only half the nuclides requested for the third diffusion tube samples. They agreed in general with the results from the second closed tube (trap 2 in. from open end).

The main puzzle in the closed diffusion tube results is why the deposition gradients were not much steeper than observed. It must be concluded that modes of transport other than simple diffusion were operative. Convective currents set up by the considerable thermal gradient up the tube (600°C at the open end, 30°C at the closed end) are a possibility. In any case, these results suggest that the flow diffusion tube results should be corrected for the deposition effects noted in the absence of net flow. This correction would appreciably decrease the deposition gradients and the diffusion coefficients calculated from the flow diffusion tube experiments and thus increase the estimated aerosol particle sizes. The scatter of the data between runs and the lack of correspondence between specimens analyzed are such that it would not be meaningful to attempt to carry out such corrections with the available data. An experiment in which a flow diffusion tube and a closed tube of identical geometry are set up side by side in the reaction vessel appears preferable for obtaining a good closed-tube blank for correcting the flow diffusion tube results.

11.2.6 Volatilization of MSRE Salt in the Absence of Radioactivity

Eight control tests were carried out in the laboratory to test the degree of volatilization of unirradiated MSRE fuel salt under the conditions of the chemical probe tests in the hot cell. A reaction vessel and chemical probe tubes of identical design were used, and the rest of the apparatus was similar to that used in the hot cell. The salt used was of very similar chemical composition to MSRE fuel salt, except that none of the U^{4+} (0.22% ^{235}U) had been reduced to U^{3+}. Runs were made under the same pressure and flow conditions as the hot-cell runs, as well as some at higher pressures and flows. In two runs the helium was bubbled through the salt as it was in some early hot-cell tests.

After each run the chemical probe tube was put through washing, segmenting, and dissolution procedures exactly like those used for the radioactive tubes. The solutions were then analyzed for lithium by flame photometry and for uranium by delayed-neutron counting or by the fluorometric method. It was necessary to concentrate each solution (originally 100 ml) by a factor of 10 by evaporation to detect the elements. A blank on the chemical probe materials and the dissolution reagents was run by carrying out the segmenting, dissolution, and analytical procedures in an identical way on an unexposed chemical probe.

The analyses of the test and blank samples were difficult because the concentrations of uranium and lithium in the solutions were extremely low, of the

order of 0.01 μg/ml in the blanks and in more than half the test solutions. Each sample solution was made up to a standard volume of 100.0 ml. The lithium and uranium analyses approximated the blank values for most of the NaF and soda-lime segments. The uranium contents of the Felt Metal segments also did not exceed the blanks. The bottom empty tube sections contained blank uranium concentrations in three tests, only slight excesses (1 μg) in two other tests, and about 10 μg excesses in the remaining three tests. One of the latter was a bubbling run at 20 cc/min. In general the variations in deposition were not obviously related to the helium flow rate, test duration, or pressure drop across the probe. In the case of lithium, the blank values were consistently exceeded only for the Felt Metal segment. The average excess was about 5 μg of lithium, corresponding to about 50 μg of fuel salt. For the bottom empty tube section, the blanks were usually only slightly exceeded except in the bubbling run at 20 cc/min.

It is difficult to explain the fact that the patterns of deposition of lithium and uranium were different. If both were carried by droplets of fuel salt, the patterns would be identical. Likewise if they traveled as vapors of LiF (or Li_2BeF_4) and UF_4, similar deposition patterns would be expected. Since the deposition patterns for lithium were generally more consistent than for uranium, it may be assumed that the rare high uranium values were due to accidental contamination. In this case the lithium was probably traveling as LiF (or Li_2BeF_4) vapor, and the control test results should be interpreted as indicating no salt aerosol formation over the nonradioactive fuel salt. It is likely that convection and diffusion transferred a large part of the LiF vapor to the probe, since simple transpiration would transport smaller amounts. If the improbable assumption is made that the lithium travels as a component of fuel-salt droplets, the control tests still indicate less than 10% as much aerosol formation as was observed in the hot-cell tests.

11.2.7 Summary and Interpretation of Hot-Cell Test Results

The various hot-cell and laboratory tests described above have confirmed previous information on the nature of the aerosols formed in the gas phase above highly radioactive MSRE fuel and have enlarged on this information. It was determined that neither type of aerosol is highly charged. The deposition behavior of the aerosol flowing through either packed or open tubes indicates that the noble metal aerosols travel independently of each other and their particles are of much smaller diameter (4 to 20 A) than that of the average fuel-salt aerosol particle. The control tests indicated that the molten salt must be radioactive to produce the salt aerosol. It was shown that convection and diffusion effects importantly affected deposition results. These will have to be taken into account or eliminated in future experimental work.

The mechanisms by which the metallic and salt aerosols are formed remain an open question. In the case of the metallic particles, a theory based on the difficulty of nucleation for metal atoms in a molten salt is favored. Individual metal atoms formed by fission or decay might not nucleate as crystals since their concentrations and diffusion coefficients in molten salt are low. The solution would then become highly supersaturated in dissolved metal atoms, which would therefore possess high activity coefficients and correspondingly high escaping tendencies.

11.2.8 Attempt to Sample Foam in Pump Bowl

Fuel density measurements and overflow behavior in the pump bowl during recent MSRE operation indicated that the fuel in the sprayed region of the pump bowl was in a foamy condition. It was of interest to sample the surface salt in the mist-shielded region of the pump bowl to see whether the foam penetrated from the sprayed to the mist-shielded region of the pump bowl and whether the surface salt was chemically or radiochemically different from bulk fuel salt.

A laboratory test indicated that a sample of frozen foam in which about 10% of the smaller bubbles visibly survived could be taken by quickly immersing a cold metal rod in foaming salt and rapidly retrieving it. The same operation was carried out in the MSRE pump bowl with a dog-bone-shaped piece of solid nickel with $\frac{3}{4}$-in.-diam knobs at the end of a 3-in.-long, $\frac{3}{8}$-in.-diam center section. The bottom knob and half of the $\frac{3}{8}$-in.-diam section were covered with a frozen film of fuel salt $\frac{1}{32}$ to $\frac{1}{16}$ in. thick. The knobs protected the brittle film on the center section from cracking off during retrieval up the sampling tube and shipment to the hot cells for examination.

The fuel-salt film was examined under a Kollmorgen periscope and under a 30-power stereomicroscope. It was mostly an opaque milky white with a faint green coloration visible in some regions. The top edge of the film and the region near the bottom of the $\frac{3}{8}$-in.-diam section were a pale transparent green with opaque white dots embedded in it. The exterior surface of the film was quite smooth compared with the jagged surface of

the frozen foam sample taken in the laboratory. However, two small craters about 1 mm in diameter, which looked like the remains of bubbles which burst during freezing, were observed on the outside surface, and two tiny bubbles were found embedded in the transparent salt.

The film was then cracked off the metal sampling device and the interior surface examined. Most of this surface was also smooth and white, but several dozen small hemispherical voids and a number of larger shallow depressions were visible (Fig. 11.2). Those almost surely represented the frozen remains of foam bubbles trapped between the metal and the salt film. Several discrete regions of the inner surface also contained large shallow depressions which were coated with a very thin dark shiny metallic-appearing film (Figs. 11.2 and 11.3). These may have been the remains of a solid-containing foam. It has been speculated that small metal particles might tend to collect at salt-gas interfaces, since the salt does not wet clean metals. A few small flakes of salt actually had the porous appearance of a frozen foam. This salt was also darker in color than other salt flakes (Fig. 11.4).

A sample of white frozen flakes weighing 0.45 g was dissolved and analyzed chemically and radiochemically. The analyses showed normal concentrations of bulk fuel constituents and of fission products with stable fluorides. The concentrations of ^{99}Mo, ^{132}Te, ^{129}Te, ^{103}Ru, and ^{106}Ru were high by about two orders of magnitude compared with fuel-salt samples taken in freeze-valve capsules. This degree of contamination by noble metals may be at least partially explained by the exposure of the unprotected sampler to noble metal aerosols in the pump-bowl cover gas.

A flake of salt film containing some of the dark shiny material on the inner surface was powdered and analyzed by electron diffraction. Only fuel-salt powder patterns were observed. An attempt was also made to identify the dark material on several flakes weighing 66 mg by dissolving away the fuel salt with oxygen-free Verbocit solution (a neutral mixture of sodium Versenate, boric acid, and citric acid) and analyzing the

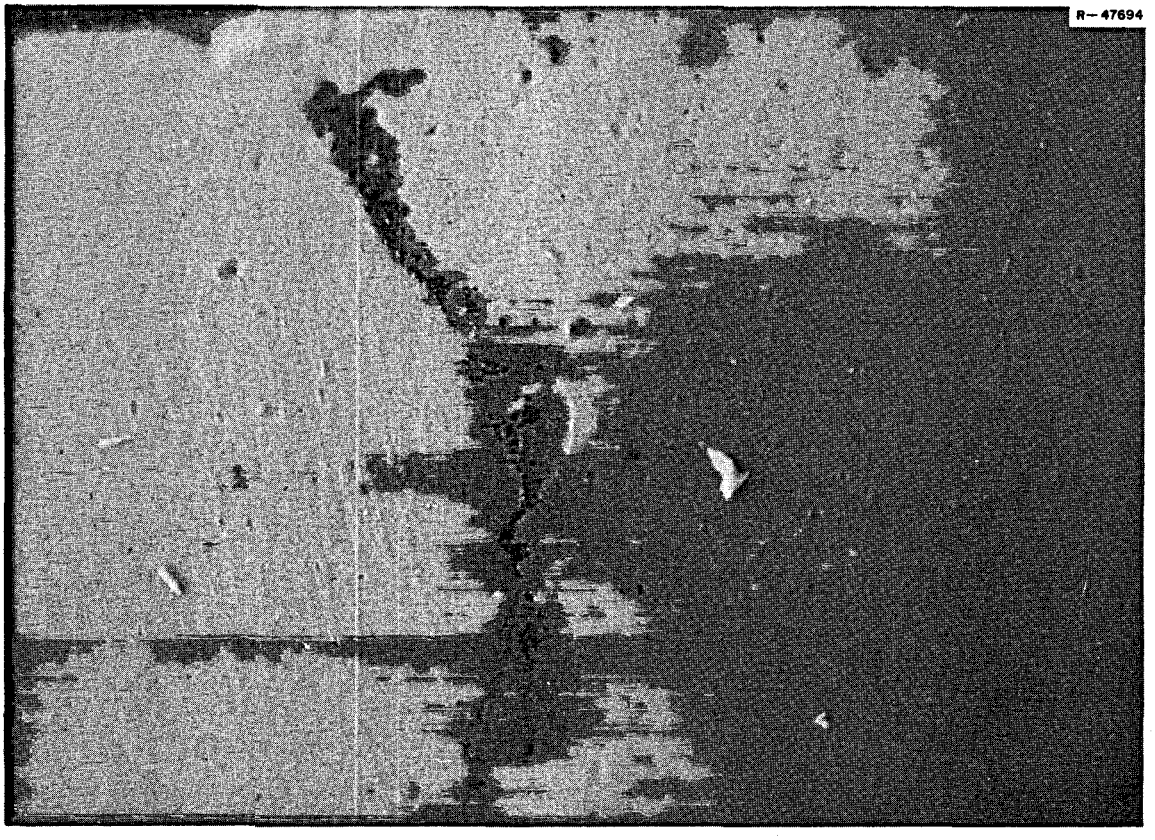

Fig. 11.2. Small Voids and Dark Film, Inner Surface. 30X. Reduced 44%.

residue. The barely visible particles of gray residue (less than 1 mg) were only partially soluble in a mixture of HNO_3 and HCl. Spectrographic analysis of the solution detected only a few micrograms of beryllium and zirconium. A gamma spectrometer scan and radiochemical analyses of the acid solution showed several times more ^{103}Ru and ^{106}Ru than were contained in the Verbocit dissolution of the original 66 mg of salt flakes. A final attempt is being made to identify the dark shiny material more positively by electron-probe examination.

The density of several flakes of the frozen film was measured by observing the density of solutions of $C_2H_2Br_4$ in CCl_4 in which the flakes would just remain suspended. The densities of several flakes ranged from 2.40 to 2.45 g/cc. The density of simulated solid MSRE fuel salt measured by the same method ranged from 2.45 to 2.51 g/cc, with most particles showing a density of 2.49 g/cc. These readings indicate that the frozen flakes contained 2 to 4% voids.

All of the observations listed above indicate that there is probably a small amount of foam, some of which contains insoluble material, on the surface of the fuel salt in the mist-shielded region of the pump bowl. However, it is not a thick foam such as probably exists in the pump bowl outside the mist shield.

11.3 LABORATORY TESTS ON AEROSOL FORMATION OVER MOLTEN SALTS AND TRANSFER OF NIOBIUM FROM SALT TO BISMUTH

H. W. Kohn F. F. Blankenship S. S. Kirslis

Previously described pump-bowl gas analyses and hot-cell tests with MSRE fuel salt[16] have led us to postulate the existence of two types of aerosols over the highly radioactive molten fuel salt: a fume of noble metal fission products and an aerosol of tiny fuel-salt particles. Confirmatory laboratory experiments using tracer levels of radioactivity were begun to investigate

[16]S. S. Kirslis and F. F. Blankenship, *MSR Program Semiann. Progr. Rept. Aug. 31, 1968,* ORNL-4344, pp. 115–41.

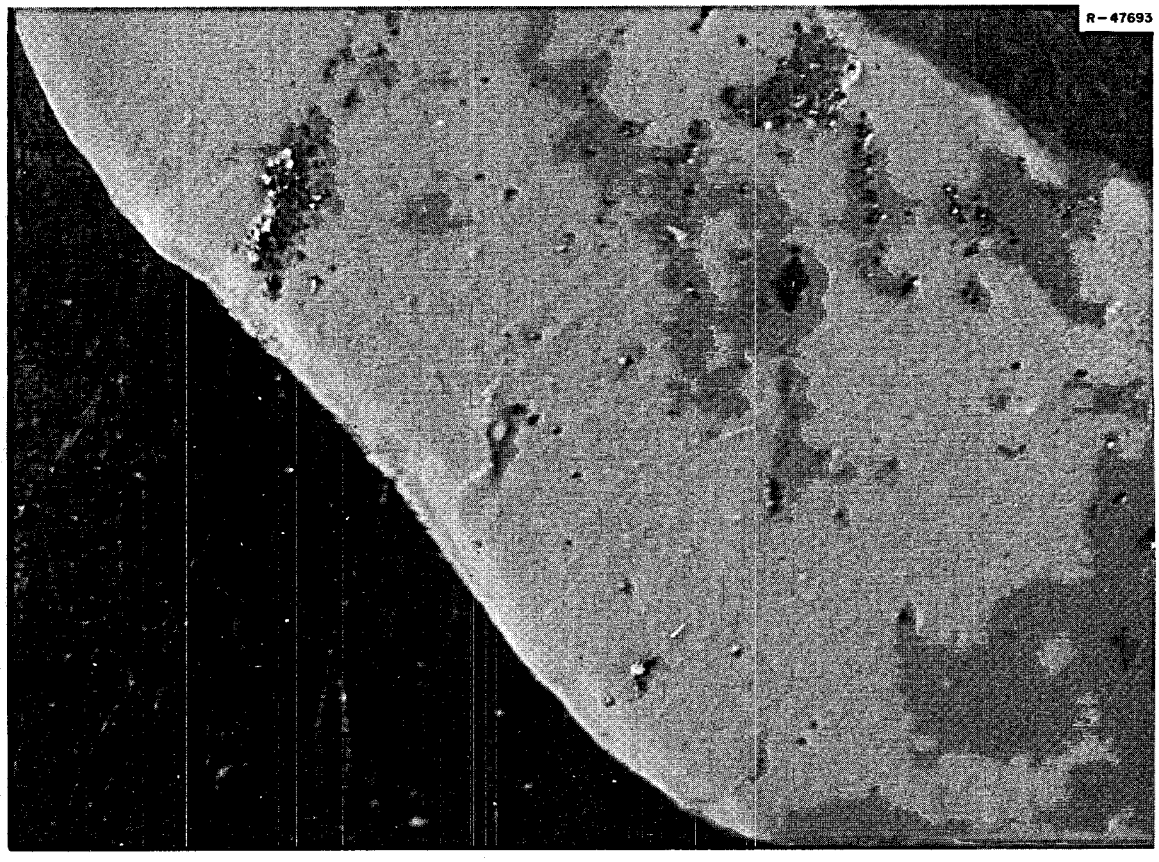

Fig. 11.3. Dark Shiny Film, Inner Surface. 30X. Reduced 43%.

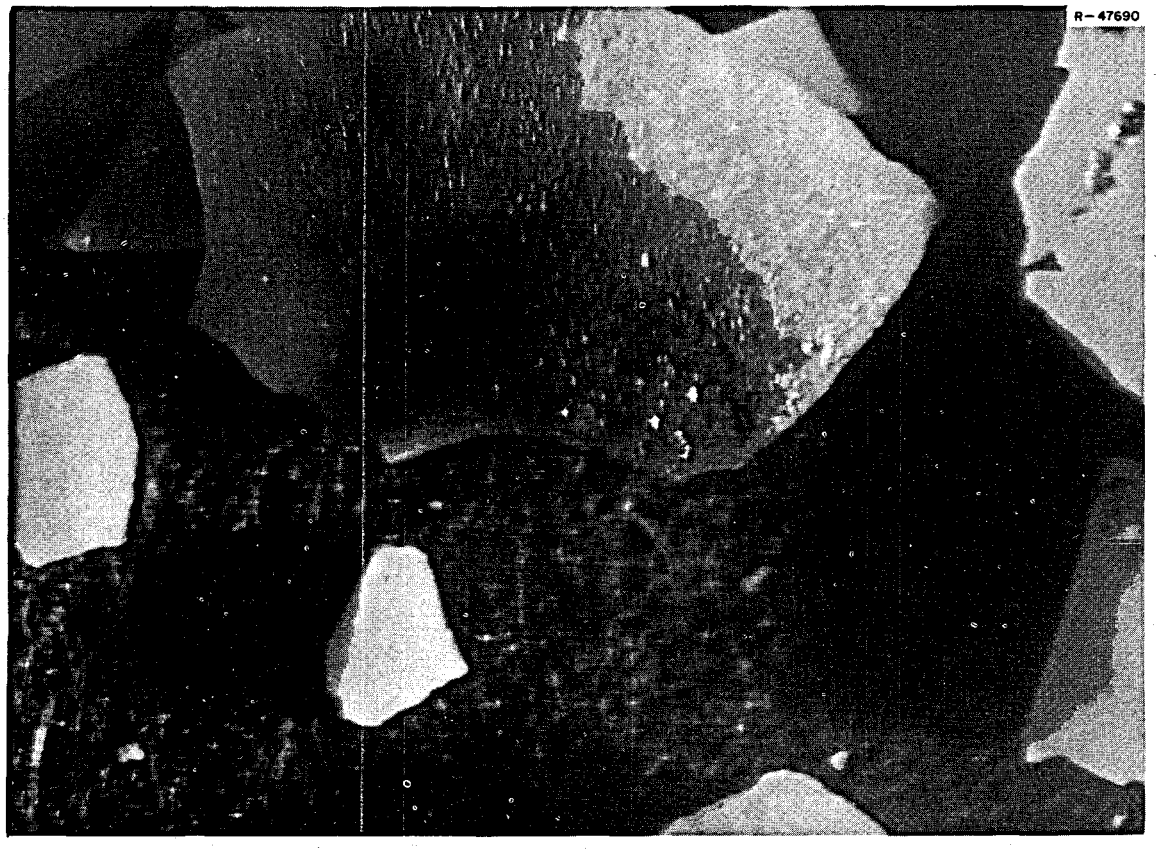

Fig. 11.4. Dark Porous Flake of Frozen Film. 30X. Reduced 44%.

some features of the process of radioaerosol formation over molten salts. In particular, we wished to investigate the hypothesis that noble metals escape from molten salts because of the difficulty of nucleation of individually formed atoms into metal crystals. A convenient isotope for this study was 65-day ^{95}Zr, which could be added to the melt as a soluble fluoride and allowed to decay atom by atom to 35-day ^{95}Nb. In a reduced melt, the reduction of niobium to metal should be zero order in reductant.

In the first tests the simulated fuel salt contained 0.1 mc of freshly separated ^{95}Zr in 40 g of salt.[17] The apparatus that contained the salt and the procedure were similar to those used in the hot-cell probe-tube tests,[18] except that in some tests no flow was passed through the probes and in most cases the activity of the tubes was counted without decontaminating the outside of the probe tubes. These simplifications in procedure interfered with a direct comparison with the hot-cell tests, but the presence or absence of flow or of bubbling had little effect on the amount of tracer collected. The first tracer experiments were also meant to be only of an exploratory nature.

The melt was treated for 1½ hr with a 50-50 mixture of H_2 and HF to convert oxides to fluorides. Then probe tubes, used as gas exit lines from the pot containing the fuel, were exposed at various sweep rates, temperatures, pressures, and degrees of reduction of the fuel salt. Other parameters – the degree of bubbling, flow rate, and distance of the probe tubes from the melt, as well as their geometry – were also varied. At the conclusion of the experiment four salt samples, one from the top of the melt, one from the middle, one from the bottom, and one more representative of the total sample, were taken and counted. The top of the reaction bomb, the inside bomb casing, four pieces of the nickel liner, and the nickel bubbling tube were washed; the washings were analyzed for

[17] J. H. Holloway and F. N. Nelson, *J. Chromatog.* 14, 255 (1964).

[18] S. S. Kirslis and F. F. Blankenship, *MSR Program Semiann. Progr. Rept. Feb. 29, 1968,* ORNL-4254, p. 102.

^{95}Nb and ^{95}Zr as well as for lithium and uranium so that we could check the percent recovery in the washings and the composition of the adhering material. The results of these analyses are presented in Table 11.6. It is noted that the niobium preferentially migrates to the surface of the salt, to the bottom, and to the walls of the container. The bulk salt is somewhat depleted in ^{95}Nb, as expected. It is possible that some of this is due to precipitation of ZrO_2, since the bottom fraction of the salt is enriched also in ^{95}Zr.

It was considered important to make sure that the melt was indeed reducing so that the niobium would be in the elemental form. Otherwise the niobium would have escaped into the gas space as a volatile fluoride. A log of operations and their effects is given in Table 11.7. The first reduction (corresponding to 1% of the U^{4+}) was done by adding a milligram of zirconium metal. This was followed by more severe reducing conditions; further additions of 20 mg of UF_3 and, after some temperature cycling, another addition of 200 mg of UF_3. The degree of reduction had little effect on the amount of total deposition on the probe tubes. The ratio ^{95}Nb/^{95}Zr on the probe tubes was always greater than this ratio in the salt, usually more than ten times greater. The only treatment which increased the deposition greatly was applying a vacuum or sparging the melt with HF after some niobium had grown in. The HF sparge also increased the ratio ^{95}Nb/^{95}Zr on the probes to several hundred times what it was in the melt.

The principal conclusions of the tracer tests were as follows: (1) Small amounts of ^{95}Nb, and to a lesser extent salt as a carrier of ^{95}Zr, escaped to the gas phase, presumably by the same mechanisms as in the hot-cell tests on fuel. (2) The degree of reduction had little influence on the total deposition of ^{95}Nb in the probe tubes. (3) The deposition mechanism is probably controlled by diffusion, since low flow rates and gentle

Table 11.6. Analysis of Final Samples

All samples corrected to time of sampling

A. Salt Samples

Sample	^{95}Zr (dis min^{-1} g^{-1})	^{95}Nb (dis min^{-1} g^{-1})	Enrichment
Surface	3.3E7	2.5E7	1.5
Center	2.3E7	8.4E6	0.73
Bottom	4.5E7	8.1E7	3.6
Bulk	2.1E7	9.3E6	0.88
Standard[a]	1.7E7	6.0E6	0.97

B. Washings

	^{95}Zr (dis/min)	^{95}Nb (dis/min)	Enrichment[b]	Excess ^{95}Nb (cm^{-2})[c]
Bomb casing	1.1E6	7.9E5	1.4	2.5E3
Bomb top	6.4E5	4.3E5	1.3	3.9E5
Container, 5 cm just above salt	3.6E6	1.5E5	0.8	
Container, top 2 cm	2.7E5	3.0E5	2.2	1.2E4
Container contacting salt, top 3 cm	5.3E5	5.4E5	2.0	2.0E4
Container contacting salt, next 4 cm	2.1E5	5.0E5	4.7	1.5E4
Dip tube	9.2E4	1.3E5	2.7	2.5E3

[a]The standard salt sample was removed from the melt at the beginning of the experiment and was counted throughout to check the ^{95}Nb/^{95}Zr ratio and the counting procedures.

[b]Enrichment is the ratio of ^{95}Nb/^{95}Zr in the sample to the ^{95}Nb/^{95}Zr in the standard.

[c]Excess ^{95}Nb is the total ^{95}Nb minus that ^{95}Nb associated with the ^{95}Zr in the adhering salt.

Table 11.7. Deposition of ^{95}Nb and ^{95}Zr from Fuel Salt

Operation	Time Interval (hr)	Rate of Deposition of ^{95}Zr (dis min^{-1} hr^{-1})	Rate of Deposition of ^{95}Nb (dis min^{-1} hr^{-1})	Enrichment Factor, $\frac{^{95}Nb/^{95}Zr \text{ in probe}}{^{95}Nb/^{95}Zr \text{ in melt}}$, Calculated
1 Bubbled He, 560°C	0–44.5	3.3E4	5.0E3	4.1
2 Bubbled He + 5% H_2	44.5–68.5	6.5E3	7.4E3	20
3 Add Zr^0	68.5–139.5	2.3E2	1.9E3	76
4 Same	139.5–164.5	1.1E3	2.6E3	19
5 Sweep, no bubbling	164.5–188	1.2E3	8.1E3	45
6 Add 20 mg UF_3	188–211.5	3.2E3	2.0E4	37
7 T = 605°C	211.5–235.5	2.1E3	1.9E4	49
8 560°C, HF, 200 mg UF_3	235.5–307.5	5.3E3	5.1E4	40
		Total Counts, ^{95}Zr and ^{95}Nb		
9 Stopped flow	333–334	5.2E4		
10 p = 5 psi	335.5–337	4.8E4		
11 High area probe	355.5–356.5	4.6E4		
12 Vacuum	358–360	5.8E5	6.1E5	3.9
13 0.5 mm He + H_2	361.5–363	2.5E6	3.7E6	5.0
14 HF sparge	382.5–384	1.2E4	1.4E6	391
15 He + H_2 sweep	384–386	9.0E2	2.8E6	1130
16 T = 470°C	476–500	5.4E2	5.8E3	29
17 470°C, 200 mg UF_3	500–524	1.0E2	5.3E3	134
18 420°C	530.5–548	1.2E2	1.3E3	26
19 200°C	581–642	4.0E1		
20 420°C	642–658	1.5E2		

bubbling did not give greater total deposition rates than stopped flow, in agreement with the hot-cell tests. (4) In both tracer experiments and hot-cell tests most of the ^{95}Nb remains in the salt, whereas in the reactor only a low percentage remains in the fuel. It should be noted, however, that the tracer and hot-cell tests are run for only short times over a stagnant melt, whereas the reactor is vigorously circulated and sparged and is at a steady state concerning those isotopes. (5) In the tracer experiment about 25% of the ^{95}Nb migrates to the container wall during the total experiment (one month).

The relative rates of escape of ^{95}Nb to the gas phase in the tracer experiment and in the second hot-cell tests (a few hundredths to one percent per hour) are in essential agreement. In the first hot-cell tests, however, the rate of ^{95}Nb escape to the gas phase was much greater. Most of this can be accounted for by a few high results obtained when the melt was vigorously bubbled. In the reactor about 50% of the ^{95}Nb escaped to the gas, and a similar amount migrated to the walls. Our best guess so far is that the differences in the three results (reactor, hot-cell, and tracer experiments) are due to engineering parameters involving stirring and efficiency of mass transfer which are difficult to evaluate with our present experimental arrangement.

The most plausible explanation that we can offer at present is that both salt and niobium are moving by diffusion and that the niobium, under severe reducing conditions, preferentially leaves the melt as unnucleated metal atoms. The calculated nucleation rate in the melt is too low to allow nucleation, and the calculated gaseous nucleation rate is indeed adequate. However, a serious drawback to this picture is that the ^{95}Nb metal atoms should pass across the interface between the melt and the container wall as readily as they escape through the gas-melt interface. One would ordinarily expect the ^{95}Nb to stick to the wall at every collision, yet this is not borne out by the data. The contamination of the wall and the bomb top is far too low. Some of this deficit could be due to a loss of deposited ^{95}Nb as a volatile fluoride during the intermediate HF treatment.

Some further tests were carried out to measure the extractability of reduced niobium from MSRE salt into liquid bismuth. The salt melt containing ^{95}Zr and ^{95}Nb was purified with $HF-H_2$, reduced with zirconium

metal, and contacted with liquid bismuth at 600°C in a molybdenum container. At the same time, coupons of several metals and of Grafoil[19] were exposed to the reduced melt.

Only 2% of the ^{95}Nb in the salt phase transferred to the bismuth phase in three days, possibly because of the lack of adequate mass transfer across the interface. Deposition rates in the liquid for ^{95}Nb on molybdenum, nickel, and stainless steel exposed in the gas in the previous experimental melt were similar to rates on the probe specimens. Especially noteworthy were the much lower deposition rates of ^{95}Nb and ^{95}Zr on the Grafoil specimens.

We attempted to repeat this experiment using a better grade of bismuth, a carbon crucible, and a molybdenum lift pump[20] for stirring. Due to a failure of the circulating pump diaphragm, this experiment was a dismal failure. The salt could not be reduced. The one item of information that we were able to salvage from this experiment was that niobium from an unreduced melt will not migrate into bismuth. Deposition of niobium on the molybdenum surfaces from this oxidized melt was about one and a half orders of magnitude slower than it was in the previous experiment, and deposition on the carbon crucible was about the same as the deposition on the molybdenum crucible in the previous experiment.

11.4 THE CHEMISTRY OF THE NOBLE FISSION PRODUCT FLUORIDES

C. F. Weaver J. W. Gooch, Jr.
H. A. Friedman J. D. Redman

11.4.1 Molybdenum Fluoride Synthesis, Characterization, and Stability

It was previously reported[21,22] that MoF_4 may be synthesized by disproportionating MoF_5 in approximately 1 atm of MoF_6 and that the compound was stable for many days at a temperature of 200°C and pressures in the micron range. It was also found that the compound decomposed at somewhat higher temperatures (<300°C) to MoF_3 and a volatile product. Conclusions about decomposition were only tenuous because the Pyrex container was attacked by the fluorides. Since then two samples of MoF_4 have been decomposed in copper containers under a dynamic vacuum of 25 μ for 14 days at 265 and 352°C. In both cases the MoF_4 decomposed to form MoF_3 and volatile materials, but the reaction was incomplete. The thermal instability of MoF_4 was further investigated using a time-of-flight mass spectrometer and a copper Knudsen cell over a temperature range of 225 to 750°C. The results are described below under mass spectroscopic studies of fluorides.

The solubility of MoF_3 in molten $2LiF \cdot BeF_2$ was determined by investigating the phase equilibria along the join $2LiF \cdot BeF_2$-MoF_3. The results are shown in Fig. 11.5. The binary compound $LiF \cdot MoF_3$ was previously reported[23,24] along with its optical properties and x-ray diffraction pattern. A ternary invariant reaction,

$$\text{liquid} + LiF \cdot MoF_3 \rightleftharpoons 2LiF \cdot BeF_2 + MoF_3 ,$$

was observed at 404 ± 14°C. The large uncertainty in temperature was caused by difficulty in achieving subsolidus equilibria. This number will be refined by experiments now in progress. The invariant reaction

[19]Grafoil is a new type of graphite in the form of a flexible sheet made by Union Carbide.

[20]C. F. Baes and C. E. L. Bamberger, *Reactor Chem. Div. Ann. Progr. Rept. Dec. 31, 1968,* ORNL-4400.

[21]C. F. Weaver, H. A. Friedman, and D. N. Hess, *MSR Program Semiann. Progr. Rept. Aug. 31, 1968,* ORNL-4344, pp. 153–55.

[22]C. F. Weaver, H. A. Friedman, J. W. Gooch, Jr., and D. N. Hess, *Reactor Chem. Div. Ann. Progr. Rept. Dec. 31, 1968,* ORNL-4400.

[23]C. F. Weaver, H. A. Friedman, and D. N. Hess, *Reactor Chem. Div. Ann. Progr. Rept. Dec. 31, 1967,* ORNL-4229, pp. 33–37.

[24]C. F. Weaver, H. A. Friedman, and D. N. Hess, *MSR Program Semiann. Progr. Rept. Feb. 29, 1968,* ORNL-4254, pp. 129–34.

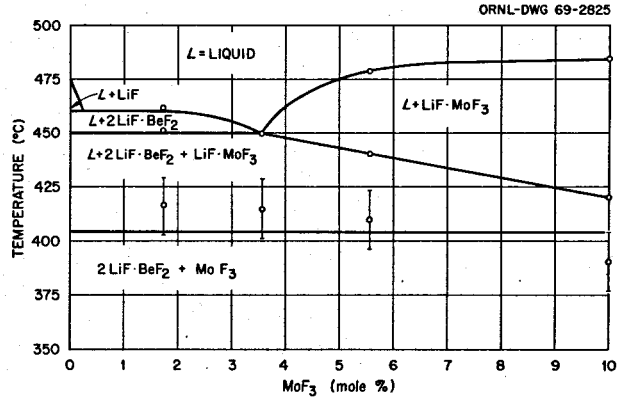

Fig. 11.5. The Join $2LiF \cdot BeF_2$-MoF_3.

implies the existence of the compatibility triangle: $2LiF \cdot BeF_2$-$LiF \cdot MoF_3$-MoF_3.

Recent experiments in the binary system LiF-MoF_3 have shown that the compound $5LiF \cdot 2MoF_3$[23,24] has a lower limit of stability at >525°C, the decomposition reaction being $5LiF \cdot 2MoF_3 \rightleftharpoons 3LiF + 2LiF \cdot MoF_3$.

The studies[21-25] of the rate of removal of Mo^{3+} from molten $2LiF \cdot BeF_2$ have continued. The most stable conditions encountered thus far are at 500°C; neither the flow rate of He nor H_2 firing of the copper container strongly affected either the order or rate constant for the Mo^{3+} removal from the molten $2LiF \cdot BeF_2$. The half-order rate constants associated with Figs. 11.6 and 11.7 are defined as $K = t^{-1/2}(C_0^{1/2} - C^{1/2})$ and are 8.1×10^{-3} $ppm^{1/2}$ hr^{-1} and 7.3×10^{-3} $ppm^{1/2}$ hr^{-1} respectively.

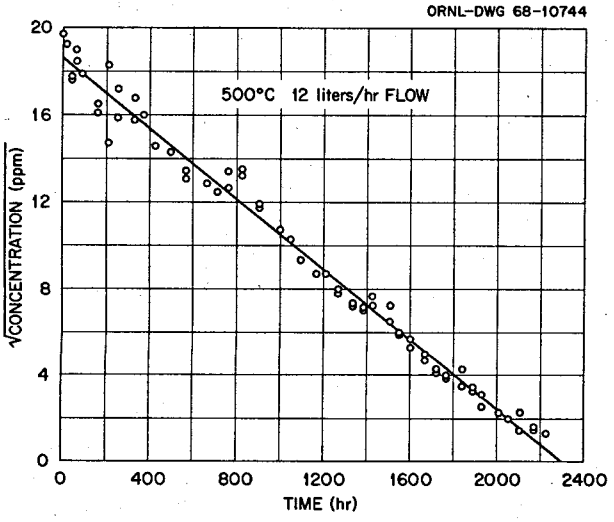

Fig. 11.6. Removal of Mo^{3+} from Molten $2LiF \cdot BeF_2$.

The composition of the gas associated with the disproportionation of MoF_3 dissolved in molten $2LiF \cdot BeF_2$ has been determined by mass spectroscopy and is described below.

Studies of the rate of removal of Mo^{3+} from more complex systems have just been initiated. It was found that the addition of 1–2 mole % of UF_4 to $2LiF \cdot BeF_2$ has no appreciable effect on the behavior of the molybdenum. The addition of UF_3 to the system LiF-BeF_2-UF_4-MoF_3 in the concentration range near 5000 ppm of U^{3+} reduced the Mo^{3+} at least a thousand times faster than the disproportionation. However, concentrations of U^{3+} in the 100 ppm range and in excess of the Mo^{3+} concentration did not appear to reduce the molybdenum. Experiments are now under way to determine if this surprising result is an artifact

[25] C. F. Weaver and H. A. Friedman, *MSR Program Semiann. Progr. Rept. Aug. 31, 1967*, ORNL-4191, pp. 142–44.

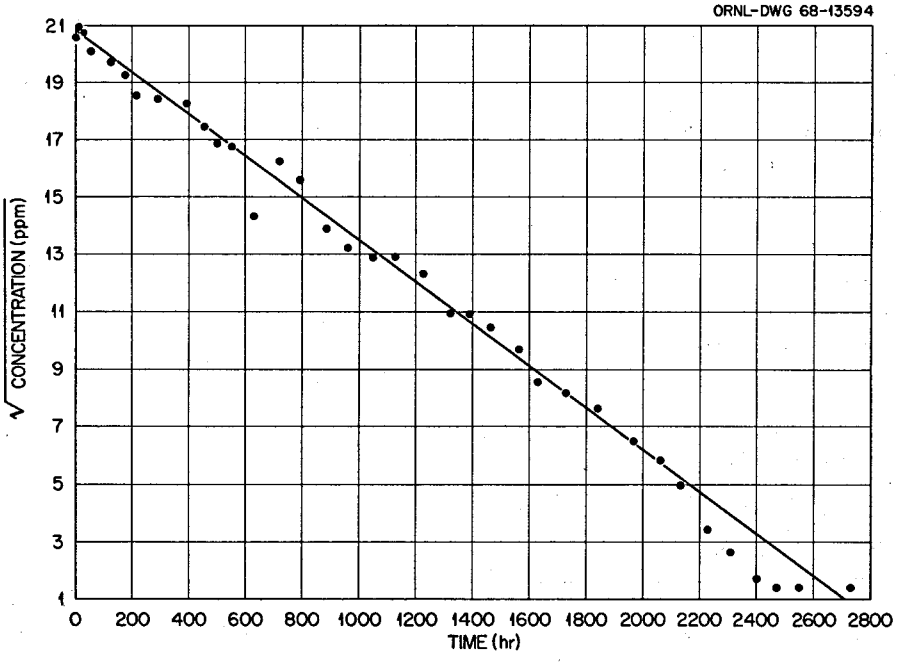

Fig. 11.7. Removal of Mo^{3+} from Molten $2LiF \cdot BeF_2$.

of our experimental procedure or evidence for the equilibrium $3UF_3 + MoF_3 \rightleftharpoons Mo + 3UF_4$.

11.4.2 Mass Spectrometric Studies of Fluorides

Mass spectrometric studies of pure MoF_3 have shown[26] (Fig. 11.8, dashed lines) that the gas escaping from a Knudsen cell in the temperature range 500–700°C was predominantly MoF_5 with lesser amounts of both MoF_6 and MoF_4 and that the ratio of MoF_4 to MoF_5 increased with temperature. Similar studies with LiF-BeF_2-MoF_3 (60-30-10 mole %) in the temperature range 500 to 800°C indicated (Fig. 11.8, solid lines) that the same three materials (MoF_4, MoF_5, and MoF_6) were present but that the amount of MoF_4 was markedly increased at the expense of both MoF_5 and MoF_6, that the ratio of MoF_4 to MoF_5 again increased with temperature, and that the MoF_4 became the more dominant species at ~590°C. The molybdenum fluoride dimer previously observed over pure MoF_3 was not observed with the LiF-BeF_2-MoF_3 mixture. Two groups of fragments with typical molybdenum isotopic ratios were observed at 600°C having 228 and 130 amu (for ^{98}Mo). Neither of these peaks was observed in previous studies involving molybdenum fluorides or oxyfluorides in the absence of molten $2LiF \cdot BeF_2$. It is possible that they represent the trimer fragments $^{7}LiF \cdot {}^{98}MoF_3 \cdot BeF_2{}^{+}$ and

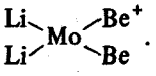

In any event they were a minor portion (~2%) of the effusing vapor. In addition, this study has shown that the molten $2LiF \cdot BeF_2$ solvent tends to stabilize Mo^{3+} and that copper is much superior to nickel as a container material. Both observations are consistent with our experience in synthesis and solution kinetics.

A sample of freshly prepared MoF_4 was completely sublimed in a copper Knudsen cell over the temperature range 225 to 750°C. The residue was found by x-ray

[26] R. A. Strehlow and J. D. Redman, *MSR Program Semiann. Progr. Rept. Feb. 29, 1968*, ORNL-4254, pp. 134–36.

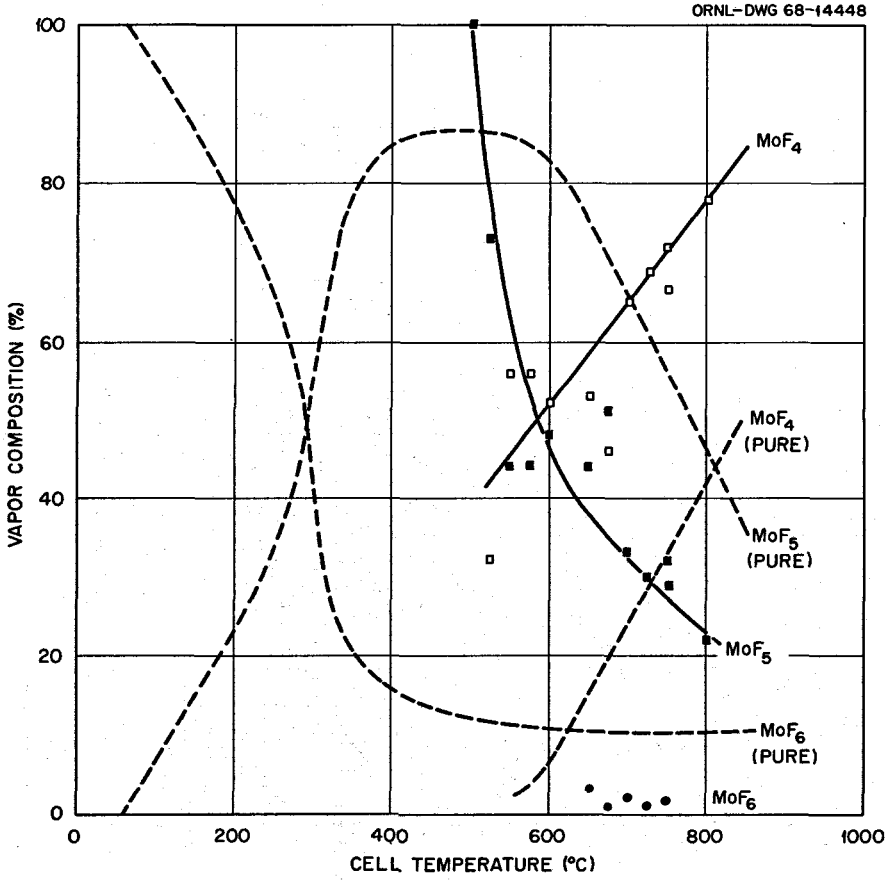

Fig. 11.8. Vapor Composition over MoF_3 in Molten $2LiF \cdot BeF_2$ Compared with That over Pure MoF_3.

diffraction to be molybdenum metal. No gases were observed below 225°C. As has been observed with all previous molybdenum fluorides, the gaseous products were MoF_4, MoF_5, and MoF_6, the relative concentrations of which varied with temperature and with the particular condensed phases involved. The dominant vapor species above solid MoF_4 at temperatures greater than 560°C was MoF_4.

We plan to pursue this and similar studies with other systems employed in MSR technology, since at present mass spectrometry is the only approach which has provided definite information about the composition of the gas phase associated with Mo^{3+} solutions. For this reason the following work with RuF_3 and NbF_5 was done.

The sample of RuF_3, prepared by D. E. LaValle, disproportionated in the Knudsen cell between 600 and 700°C forming ruthenium metal, identified by x-ray diffraction, and either RuF_4 or RuF_5. The total cell pressure at 650°C was estimated to be about 10^{-4} torr. Ionization efficiency curves for the ion fragments at 650°C are shown in Fig. 11.9. The appearance potentials, obtained by the vanishing-current technique, are listed in Table 11.8. The RuF_4^+ ion may be formed either by simple ionization of RuF_4 or by dissociative ionization of RuF_5. The latter method is characteristic of many metal halide systems,[27] including those of molybdenum and niobium.

In Table 11.9 are cracking patterns of the vapor species as a function of temperature (600 to 700°) for 75 ev electron energy and as a function of electron energy (18 to 75 ev) for 650°. Over the 100° temperature range, within which the metal fluoride completely effused, no significant change in the relative abundance of the ions was seen. The temperature

[27]K. F. Zmbov and J. L. Margrave, "Mass Spectrometric Studies of Scandium, Yttrium, Lanthanum, and Rare-Earth Fluorides," pp. 267–89 in *Mass Spectrometry in Inorganic Chemistry*, ed. by R. F. Gould, ACS, Washington, D.C., 1968.

Table 11.8. Appearance Potentials for Ion Fragments from Vapor over RuF_3 at 650°C

Ion	Appearance Potential (ev)[a]
RuF_4^+	15.3
RuF_3^+	15.9
RuF_2^+	18.5
RuF^+	22.0
Ru^+	25.5

[a]Argon reference gas: Ar^+ at 15.75 ev.

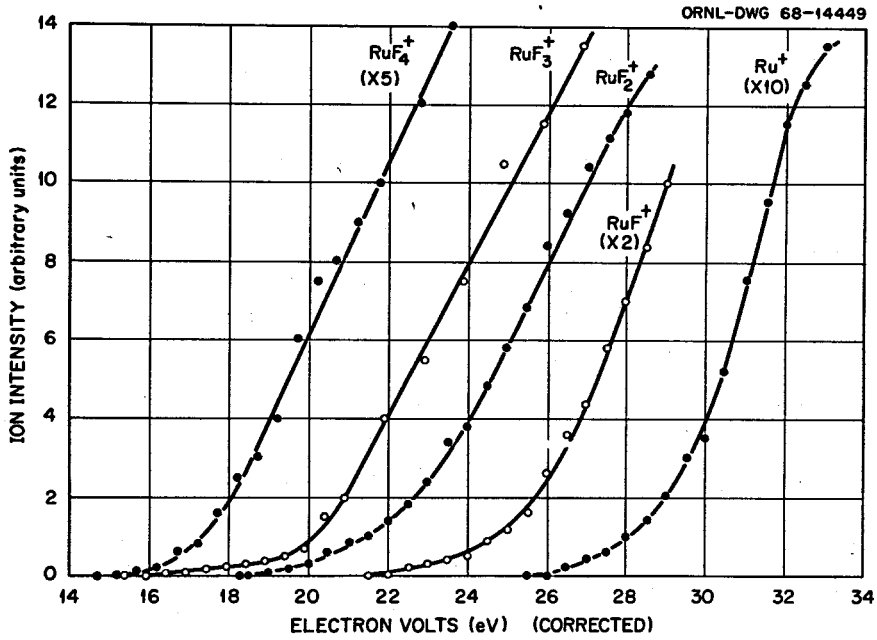

Fig. 11.9. Ionization Efficiency Curves for Vapor over RuF_3.

Table 11.9. Cracking Patterns for the Vapor over RuF_3

Ion	Relative Abundance (75 ev)			Relative Abundance (650°C)					
	600°C	650°C	700°C	18 ev	19 ev	25 ev	30 ev	40 ev	60 ev
RuF_4^+	19	25	17	100	72	44	31	23	31
RuF_3^+	100	100	100	80	100	100	100	100	100
RuF_2^+	32	39	33				26	32	47
RuF^+	18	23	24				12	14	26
Ru^+	31	44	39				15	16	41

stability of the effusing ruthenium fluoride indicates the presence of only one neutral precursor. At lower electron energies (less than 30 ev) the RuF_3^+ to RuF_4^+ ratio decreased. This effect, as seen in the ionization efficiency curves for RuF_3^+ and RuF_4^+ of Fig. 11.9, could be expected for a parent ion, as it undergoes less fragmenting at lower electron energies. It appears, therefore, that RuF_4 undergoes simple ionization, which is unusual, and that the disproportionation reaction is $4RuF_3 \rightarrow Ru^0 + 3RuF_4$.

A sample of NbF_5, synthesized by L. M. Toth and H. A. Friedman, was sublimed in a Knudsen cell at 75°C leaving a residue, containing 1.6 wt % oxygen, which was not volatile at this temperature. The residue gave off $NbOF_3$ in the temperature range 300–575°C and again above 700°C. The cell pressure at 75°C was estimated to be between 10^{-3} and 10^{-2} torr. The cracking patterns for NbF_5 and $NbOF_3$ at 75 ev are shown in Table 11.10. The ionization efficiency curves are given in Fig. 11.10. The appearance potentials obtained from these curves are listed in Table 11.10. Since the NbF_5^+ parent peak is absent, the NbF_5 must undergo dissociative ionization, typical of metal halides.[27] This suggests that the neutral precursors for the $Nb_2F_9^+$ and the $Nb_3F_{14}^+$ ions are the dimer Nb_2F_{10} and the trimer Nb_3F_{15} respectively.

The behavior of the Nb, Mo, and Ru fluorides studied thus far is strikingly different. The niobium forms at least two polymers, Nb_2F_{10} and Nb_3F_{15}; the molybdenum forms Mo_2F_{10}; while ruthenium gave no evidence of polymerization. The strong tendency to form oxyfluorides is shared by all these elements, but the relative volatilities differ. In the case of molybdenum the oxyfluorides are somewhat more volatile than the fluorides but not sufficiently so to provide an easy separation of the species. On the other hand both ruthenium and niobium form oxyfluorides which are much less volatile and allow complete separation of the fluorides. The probability that the ruthenium fluorides undergo simple rather than dissociative ionization, discussed above, distinguishes them from the molybdenum and niobium fluorides.

Table 11.10. Cracking Patterns for NbF_5 at 75°C and $NbOF_3$ at 800°C

Ion	Relative Intensity	Appearance Potential[a] (ev)
	NbF_5	
Nb^+	0.3	
NbF^+	1.0	
NbF_2^+	2.0	
NbF_3^+	14.0	21.2
NbF_4^+	100	14.5
$Nb_2F_6^+$	0.06	
$Nb_2F_7^+$	0.4	
$Nb_2F_8^+$	1.50	
$Nb_2F_9^+$	55.0	16.0
$Nb_3F_{13}^+$	0.06	
$Nb_3F_{14}^+$	2.0	18.7
	$NbOF_3$	
Nb^+	14.0	
NbO^+	8	
NbF^+	8	
$NbOF^+$	13	
NbF_2^+	13	
$NbOF_2^+$	100	
NbF_3^+	1.0	
$NbOF_3^+$	50	
NbF_4^+	<0.1	

[a]Argon reference gas: Ar^+ at 15.75 ev.

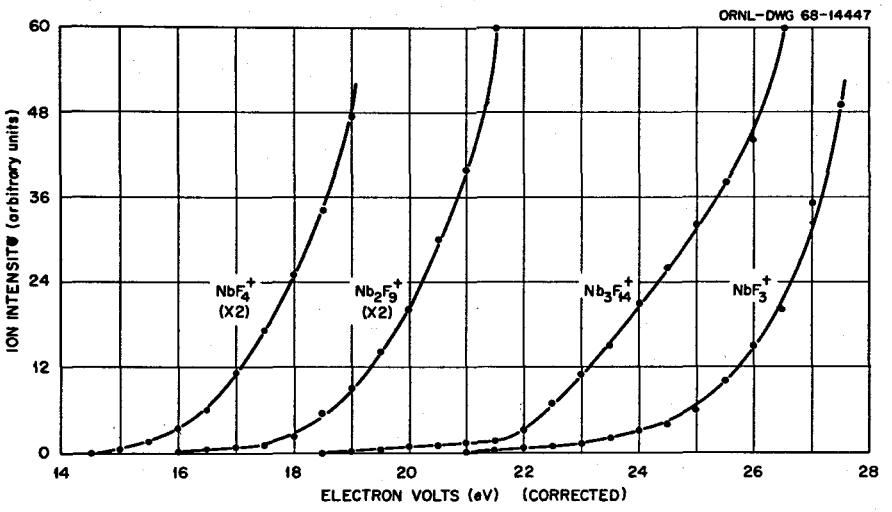

Fig. 11.10. Ionization Efficiency Curves for Vapor over NbF_5.

In addition to the noble metal fission product work, recent interest[28] in the use of aluminum halides to form volatile complexes with actinide or rare-earth fluorides prompted a mass spectrometric study of vapor species over $LiF\text{-}BeF_2\text{-}ThF_4$ (72-16-12 mole %) containing PrF_3 and AlF_3. The barren fuel, spiked with 10 wt % PrF_3 and 11 wt % AlF_3, was loaded in a nickel Knudsen cell crucible. Vapor species effusing from the cell were monitored over the temperature range of 650 to 850°C. The total pressure inside the cell at 850°C was estimated to be near 0.2 μ. The only volatile aluminum complexes observed were $LiAlF_4$ and Li_2AlF_5 (about 8:1). No fragments containing praseodymium or thorium were seen.

The lack of such fragments at the low pressures involved does not imply their absence at higher partial pressures of AlF_3. It has been amply demonstrated with chlorides[29-31] that higher total pressures (1 to 3 atm) produce significant partial pressures (10 to 100 torrs) of the volatile complexes. Even though AlF_3 is much less volatile than $AlCl_3$, pressures a thousand times higher than those used above (0.2 μ) are available below 1000°C. If interest warrants, these studies could be profitably pursued by distillation or transpiration experiments.

---

[28] C. F. Weaver to H. F. McDuffie, personal communication, 1968; A. M. Weinberg to W. R. Grimes, personal communication, 1968; M. A. Bredig to W. R. Grimes, personal communication, 1968.

[29] D. M. Gruen and H. A. Øye, *Inorg. Nucl. Chem. Letters* 3, 453–55 (1967).

[30] D. M. Gruen and R. L. McBeth, *Inorg. Nucl. Chem. Letters* 4, 299–303 (1968).

[31] E. W. Dewing, *Nature* 214, 483 (1967).

12. Physical Chemistry of Molten Salts

12.1 CeF_3 SOLUBILITY IN MOLTEN MIXTURES OF LiF, BeF_2, AND ThF_4

C. J. Barton L. O. Gilpatrick Judy A. Fredricksen[1]

Data on the solubility of CeF_3 in five ternary LiF-BeF_2-ThF_4 mixtures and one LiF-ThF_4 mixture were reported earlier.[2,3] Comparison of these data with the results of previous investigations of the solubility of CeF_3 in LiF-BeF_2 melts[4] and PuF_3 in similar compositions[5] pointed to the conclusion that the solubility of PuF_3 in the ternary mixtures will probably be adequate to fuel a reactor based on PuF_3 as the fissile agent.

We have extended this study by providing data on CeF_3 solubility in three additional ternary solvent compositions and three LiF-ThF_4 mixtures in order to determine the effect of solvent composition on CeF_3 solubility (see the following section). The data obtained, together with calculated heats of solution, are shown in Table 12.1 along with the previously reported data (slightly revised for the composition containing 16.7 mole % ThF_4 by a reexamination of the extrapolation of rather scattered data). The significance of the data in the last two columns of Table 12.1 is discussed in the following section.

As indicated in the 600°C column in Table 12.1, the liquidus temperatures of several solvent compositions listed here appear to be higher than given by the

[1]Summer participant, St. Cloud State College, St. Cloud, Minn.

[2]L. O. Gilpatrick, C. J. Barton, and J. A. Fredricksen, *MSR Program Semiann. Progr. Rept. Aug. 31, 1968*, ORNL-4344, p. 161.

[3]J. A. Fredricksen, L. O. Gilpatrick, and C. J. Barton, *Solubility of Cerium Trifluoride in Molten Mixtures of LiF, BeF_2 and ThF_4*, ORNL-TM-2335 (January 1969).

[4]W. T. Ward *et al.*, *Solubility Relations Among Rare-Earth Fluorides in Selected Molten Fluoride Solvents*, ORNL-2749 (October 1959).

[5]C. J. Barton, *J. Phys. Chem.* 64, 306 (1960).

Table 12.1. Solubility and Heat of Solution of CeF_3 in Mixtures of LiF, BeF_2, and ThF_4

Mixture No.	Salt Composition (mole %)			CeF_3 Solubility (mole %)		Heat of Solution (cal/mole)	$ThF_4/(ThF_4 + BeF_2)$	Free LiF (mole %)
	LiF	BeF_2	ThF_4	600°C	800°C			
1	72	16	12	1.6	5.5	11,600	0.428	+4
2	73	0	27	2.6	9.0	11,560	1.000	−7
3	72.7	4.8	22.5	2.4	7.9	11,100	0.824	−4
4	68	20	12	1.35	6.0	13,890	0.375	−8
5	72.3	11.0	16.7	2.1	7.0	11,200	0.603	0
6	67.8	25.2	7.0	1.05	5.0	14,530	0.217	−4
7	58	30	12	1.1	5.3	14,640	0.286	−38
8	75	17.9	7.1	1.5	6.6	13,800	0.284	+18
9	58.4	20.0	21.6	(1.75)[a]	6.6	12,350	0.519	−46
10	67	0	33	(2.6)[a]	8.4	10,900	1.000	−32
11	80	0	20	(3.1)[a]	10.9	11,700	1.000	+20
12	60	0	40	(2.5)[a]	8.6	11,500	1.000	−60
13	66.7	33.3	0	0.60	(3.7)[b]	17,500	0	0
14	72.7	27.3	0	0.95	(5.7)[b]	16,700	0	+18

[a]Extrapolated value, below liquidus temperature of the solvent.
[b]Extrapolated from values at lower temperatures (see ref. 4).

published phase diagrams for the LiF-BeF_2-ThF_4 (ref. 6) and LiF-ThF_4 systems.[7] Observation of phase changes other than CeF_3 solubility was beyond the scope of this investigation, but there were indications from cooling curves obtained during the course of the investigation that the relatively high solubility of CeF_3 in the melts lowers significantly the crystallization temperature of the primary phase of the solvent composition.

12.2 CORRELATION OF CeF_3 SOLUBILITY WITH SOLVENT COMPOSITION

M. A. Bredig C. J. Barton

Preliminary attempts[3] to relate the solubility of CeF_3 in LiF-BeF_2-ThF_4 mixtures to solvent composition gave unsatisfactory results. We have found the molar ratio of ThF_4 to BeF_2 to be the dominant factor for the binary and ternary mixtures listed in Table 12.1, which includes two LiF-BeF_2 solvents studied earlier.[4] The smooth lines of Fig. 12.1 (where the compositions in Table 12.1 are identified by mixture number) show the nearly linear dependence of the solubility of CeF_3, $s = 100 \times CeF_3/(CeF_3 + LiF + BeF_2 + ThF_4)$, on $u = ThF_4/(ThF_4 + BeF_2)$ in accordance with the equations

$$s(600°C) = 0.50 + 2.60u - 0.40u^2 ,$$

$$s(700°C) = 1.60 + 4.23u - 0.88u^2 ,$$

$$s(800°C) = 3.80 + 5.80u - 0.80u^2 .$$

The only significant deviation among the ternary mixtures, $\Delta s = +0.30, +0.70$, and 1.20 mole % CeF_3 at 600, 700, and 800°C, respectively, occurred for solvent No. 8, LiF-BeF_2-ThF_4 (75.0-17.9-7.1 mole %), with a "free LiF" content, $b = LiF - 2BeF_2 - 3ThF_4$, of 18 mole % LiF. The significance of b as a secondary parameter is further demonstrated by the similarity of the Δs values listed above with $\Delta s = +0.40, +0.80$, and +1.70 mole % CeF_3 at 600, 700, and 800°C for the binary mixture No. 14, LiF-BeF_2 (72.7-27.3 mole %), having the same "free LiF" content, $b = 18$.

The solubility of CeF_3 in LiF-ThF_4 mixtures as a function of ThF_4 content is shown in Fig. 12.2. Some of the CeF_3 solubility data reported[4] for LiF-BeF_2 mixtures are included for comparison. The solubility of CeF_3 in LiF at 700 and 600°C was obtained from the LiF-CeF_3 phase diagram[8] by extrapolating below the eutectic temperature (755°C). The measurements in the range 20 to 33 mole % ThF_4 show the solubility of CeF_3 to increase with decreasing ThF_4 content by 20 to 30%, depending on the temperature. The solubility may be assumed to increase smoothly with increasing "free LiF" concentration along the broken lines of Fig. 12.2. At 800°C the CeF_3 solubility appeared to be higher with 40 mole % ThF_4 than with 33, but the difference is within the scatter of the data. The range of ThF_4 concentrations that could be conveniently investigated was limited by high liquidus temperatures.

In LiF-BeF_2 mixtures the CeF_3 solubility goes through a distinct minimum at approximately 38 mole % BeF_2, its value at 48 mole % being approximately 50% greater than the minimum value.[3,4]

An attempt has been made to rationalize the observed dependence of the CeF_3 solubility in LiF-BeF_2-ThF_4 mixtures on solvent composition. The dependence reflects the significance of the greater availability of F^- ions for interaction with Ce^{3+} in melts richer in LiF. This was indicated by the considerable negative deviation from ideality in the LiF-CeF_3 phase diagram. Values, measured or extrapolated, for the CeF_3 concentrations of the CeF_3 liquidus at 600 to 800° exceed those estimated from the known entropy of fusion of CeF_3 [7.62 cal $(°C)^{-1}$ $mole^{-1}$ at the melting point of CeF_3] by factors of 4 to 2 respectively. In LiF-BeF_2 mixtures containing 25 to 50 mole % BeF_2, the solubility is very much smaller than ideal. This positive deviation from ideality can be attributed to the much weaker interionic forces between the singly charged Li^+ ions and the relatively large BeF_4^{2-} anions (cf. also the low melting points) as compared with the forces between the triply charged Ce^{3+} and the relatively small F^- ions. Although molten Li_3ThF_7 contains even larger complex anions, ThF_7^{3-}, it exhibits a CeF_3 solubility intermediate between that in LiF and Li_2BeF_4. This apparent anomaly is readily attributed to the fact that the Ce^{3+} ions, with a charge-to-size ratio, or "ionic potential," $z/r \cong 3$, compete for F^- ions much more successfully with Th^{4+} ($z/r \cong 4$) than with Be^{2+} ($z/r \cong 6$).

Several ternary compositions have negative values of "free LiF," but they do fit the correlation shown in the bottom part of Fig. 12.1. This may be explained by reference to Fig. 12.2, which shows very little change in CeF_3 solubility in LiF-ThF_4 mixtures in the range 25 to 40 mole % ThF_4.

[6] R. E. Thoma *et al., J. Phys. Chem.* 64, 865 (1960).

[7] R. E. Thoma *et al., J. Phys. Chem.* 63, 1266 (1959).

[8] C. J. Barton *et al.*, in *Phase Diagrams of Nuclear Materials*, R. E. Thoma, ed., ORNL-2548 (November 1959).

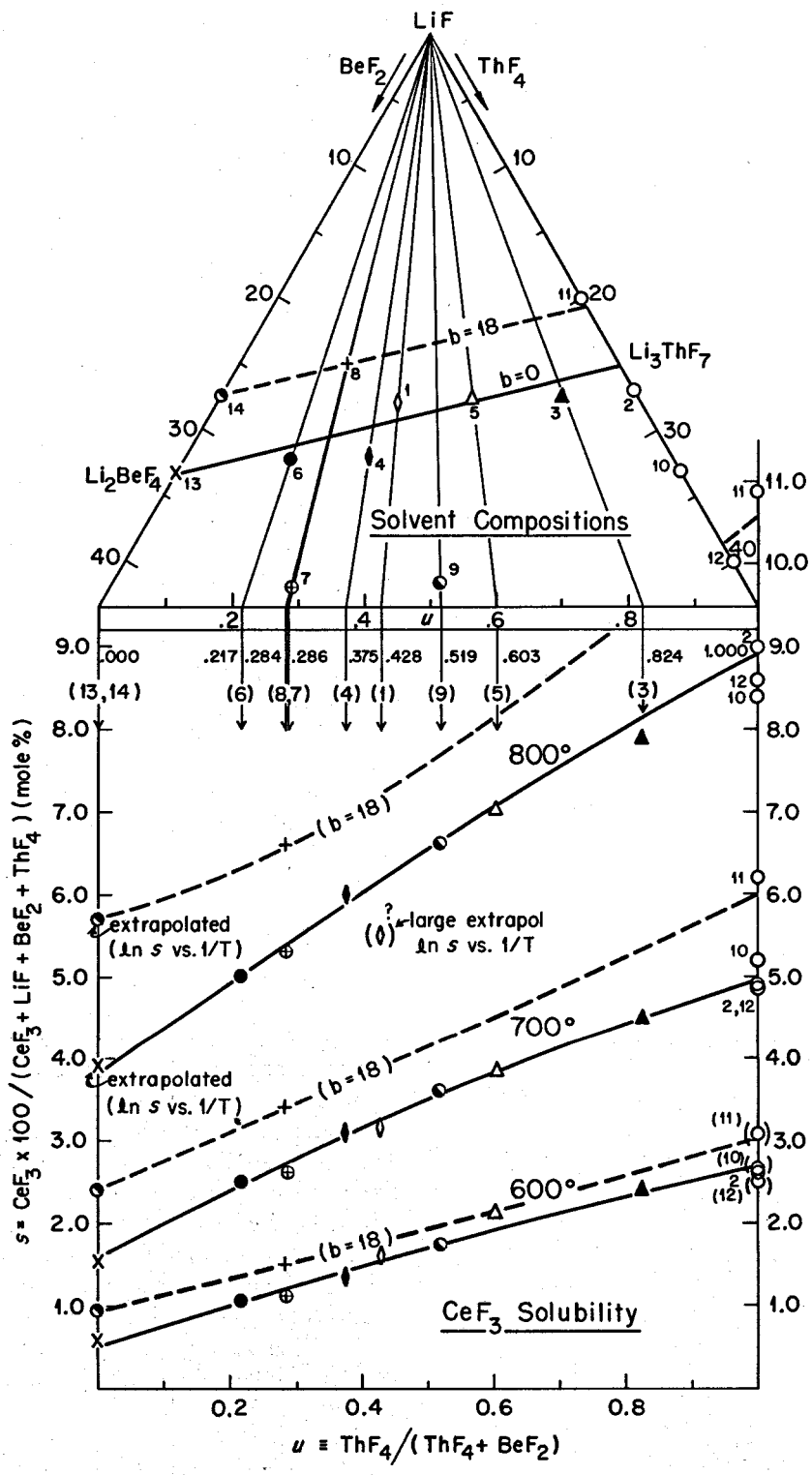

Fig. 12.1. Correlation of CeF_3 Solubility in LiF-BeF_2-ThF_4 Mixtures with Solvent Composition.

Finally, we compare apparent heats of solution of CeF_3, ΔH (soln.), in the various solvents (Table 12.1). Those given for LiF-BeF_2 mixtures, approximately 17 kcal/mole, exceed considerably the heat of fusion of CeF_3, ΔH (fusion), which may be estimated from the value 13.4 kcal at the melting point as 10 to 12 kcal for temperatures of 600 to 800°C. On the other hand, on substitution of ThF_4 for BeF_2 (Fig. 12.3) the heat of solution drops to the vicinity of the heat of fusion, that is, 11 kcal, in line with the considerations of the preceding paragraph on the smaller deviation from ideality.

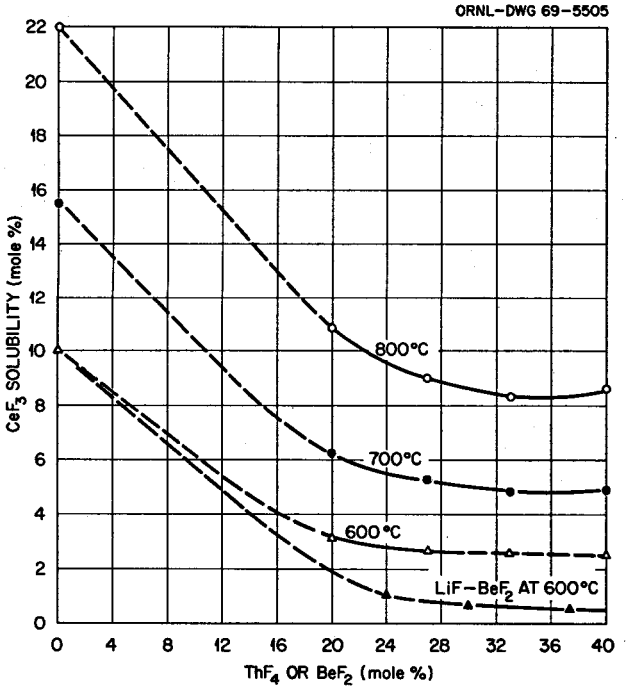

Fig. 12.2. Solubility of CeF_3 in LiF-ThF_4 Mixtures.

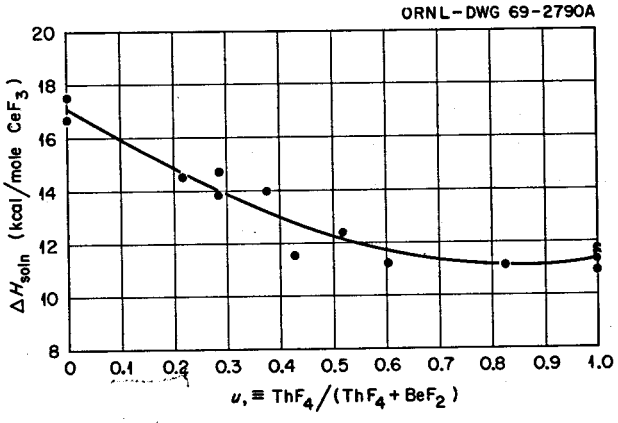

Fig. 12.3. Heat of Solution of CeF_3 in LiF-BeF_4-ThF_4 Mixtures (600–800°C).

The values shown in Fig. 12.3 for the heat of solution of CeF_3 in two LiF-BeF_2 mixtures are somewhat higher than those calculated for other LiF-BeF_2 solvents and are much greater than more recent values[9] for the heat of solution of NdF_3 and SmF_3 in LiF-BeF_2 (66-34 mole %), 11.5 and 10.5 kcal/mole respectively. The shape of the curve in the low-ThF_4 end of Fig. 12.3 is not firmly established, and this fact, coupled with the scatter of the points, indicates that only qualitative significance should be attached to the relationship between heat of solution and solvent composition in this system at the present time.

12.3 ZONE MELTING OF FLUORIDE SALTS

E. L. Compere Terry Dorsett[10]

Zone melting and cyclic slow cooling tests have been conducted on LiF-BeF_2-ThF_4 mixtures (72-16-12 and 57-33-10 mole % with ~0.3 and 0.025 mole % CeF_3 added) to determine the separation of constituents, particularly thorium and cerium, that develops under several schemes of operation. The 72-16-12 salt is a base composition for MSBR single-region fuel. The 57-33-10 salt may represent about the maximum beryllium content that could be employed in a single-region MSBR fuel and in any event, in terms of phase behavior, is situated in a phase field different from the first composition. Cerium trifluoride was used to represent the rare-earth group because it permitted straightforward chemical analysis at low concentration levels.

Two kinds of tests were conducted, zone melting and cyclic slow cooling. In all tests, nickel tubes 0.305 in. in inside diameter by 12 in. long were filled with the powdered salt and capped. After the melting cycles were completed, the salt was recovered from successive 1-in. sections and submitted for chemical analysis for all constituents. In the zone-melting experiments a heater with three 1.8-in. heating zones and two 1.8-in. cooling zones was passed along the tube at 1.5 cm/hr. Temperatures alternated between 650 and 350°C. Experiments were conducted with downward, horizontal, and, in one case, upward moving zones. The upward zone movement resulted in cracking the tube after the first pass because of expansion of entrapped melt.

Horizontal zone-melting tests were checked with a level only in the case of tube 22. Data from several tests are shown in Table 12.2.

---

[9] *MSR Program Semiann. Progr. Rept. Feb. 28, 1967*, ORNL-4119, p. 144.

[10] Summer ORAU student participant from Maryville College, Maryville, Tenn.

Table 12.2. Composition of End Sections in Zone Melting and Cyclic Slow Cooling of $LiF-BeF_2-ThF_4$ Mixtures

Tube No.	Operation	Section	Composition (mole %)			
			LiF	BeF_2	ThF_4	CeF_3
	Original composition, 72-16-12 mole % salt		71.6	16.9	11.5	
16	Six horizontal passes of three-zone heater	Entry	73.9	11.0	15.1	
		Exit	71.1	18.4	10.6	
10	Four downward passes of three-zone heater	Bottom	71.7	13.4	14.9	
		3d	73.1	8.7	18.2	
		10th	68.5	23.0	8.5	
		12th (top)	71.2	21.6	7.2	
	Original composition, 72-16-12 mole % salt + 0.07 wt % CeF_3		71.1	16.4	12.5	0.025
23	Twelve slow 600–350°C cycles with vertical tube	Bottom	70.5	10.3	19.2	0.030
		Top	70.5	24.7	4.8	0.016
22	Four horizontal passes of three-zone heater	Entry	74.0	12.0	14.0	0.044
		Exit	70.6	14.9	14.5	0.031
20	One upward pass of three-zone heater	Entry (bottom)	72.0	14.8	13.2	0.023
		Exit (top)	70.3	19.0	10.7	0.022
	Original composition, 72-16-12 mole % salt + 1.0 wt % CeF_3		71.4	16.8	11.5	0.32
14	Twelve slow 600–350°C cycles with vertical tube	Bottom	73.0	11.7	14.0	0.32
		Top	69.2	21.9	8.7	0.26
11	Four horizontal passes of three-zone heater	Entry	69.7	22.8	7.8	0.22
		Exit	73.0	10.3	16.3	0.38
	Original composition, 57-33-10 mole % salt + 1.0 wt % CeF_3		57.0	32.5	10.2	0.38
17	Twelve slow 600–350°C cycles with vertical tube	Bottom	43.1	16.4	40.0	0.56
		3d of 8 sections	54.9	23.2	21.1	0.84
		Top	59.9	38.0	1.9	0.19

In cyclic slow cooling experiments, suggested by E. G. Bohlmann, the tube was positioned vertically in a furnace, heated to 600°C, and cooled to 350°C over a period of 1 hr. Twelve such cycles were made, and the tube was sectioned for analysis. Data from several tests are shown in Table 12.2.

12.3.1 Phase Behavior

The phase behavior of the $LiF-BeF_2-ThF_4$ is given by Thoma in a published liquidus diagram[11] and in recent unpublished tie-line data. The composition $LiF-BeF_2-ThF_4$ (72-16-12 mole %) lies in the phase field of the compound $3LiF \cdot ThF_4$ (melting point 580°C) and its solid solutions. This phase field, about 3 to 6 mole % wide, extends in a gentle curve from the region of the compound $3LiF \cdot ThF_4$ toward a composition finally at about 60-37-3, liquidus 433°C, with a halt at 444°C at 65-31-4. The tie-line data indicate that the first solid to form from our composition should be a $3LiF \cdot ThF_4$ solid solution $LiF-BeF_2-ThF_4$ (69-7-24 mole %) and that LiF begins to coprecipitate with solid solutions of about this composition, the melt tending toward a final composition of perhaps 67-28-5 (or even 65-31-4). All our consistent data on the 72-16-12 original composition have remained within this phase field and between these limits and appear generally explicable on such a basis.

The original composition $LiF-BeF_2-ThF_4$ (57-33-10 mole %, liquidus 500°C) falls within the phase field of the compound $LiF \cdot 2ThF_4$, which melts incongruently at about 940°C. The adjacent phase field is that of $LiF \cdot 4ThF_4$, and melts should tend toward 63-31-6, 448°C, and then to 60-37-3 mole %.

The data of tube 17 suggest that the cyclic slow cooling process resulted in the precipitation of

[11] R. E. Thoma *et al., J. Phys. Chem.* 64, 865 (1960).

$LiF \cdot 2ThF_4$, which settled to the bottom of the tube. This first precipitate never remelted entirely; tie-line diagrams and chemical analysis of samples imply a possible disproportionation yielding some $LiF \cdot 4ThF_4$, but additional material is not available for the definitive x-ray or petrographic analysis.

The final melt was about 60-38-2 mole % .

Thus for the 57-33-10 mole % composition, the observed data appear essentially consistent with previously established phase diagrams.

12.3.2 *Zone Melting*

Five zone-melting experiments are summarized in Table 12.2, all based on the composition 72-16-12 mole %. The separations attained were modest and did not proceed beyond the phase limits discussed above. Compositions richest in thorium were generally found in the lower regions of the tubes with either upward or downward passes, suggesting sedimentation of heavy precipitates. Horizontal passes generally gave poor separation. Tube 11, which gave highest thorium concentration at the exit end, was indicated by sample volumes possibly to have been tilted slightly downward.

As will be discussed below, little separation of CeF_3 was effected by zone melting.

12.3.3 Cyclic Slow Cooling

Cyclic slow cooling in a slender geometry generally resulted in appreciably higher concentrations of thorium being found nearest the bottom. This behavior is to be expected if precipitates are free to settle, because the phases richest in thorium are heavier and also melt highest and thus are formed first. It is also indicated that the resultant stratification may persist in favorable (tall) geometries.

Behavior is again in accord with known phase relationships.

12.3.4 Cerium

Cerium behavior is best examined with reference to the solubility study of Fredricksen, Gilpatrick, and Barton.[12]

This study shows that the solubility in our 72-16-12 compositions at the liquidus temperature of ~500°C was over 0.5 mole %. However, as the melt approaches a final composition in the vicinity of 67-28-5, the solubility is diminished. The final liquidus temperature is also lower (~450°C) for this composition, so that the final solubility would appear to be about 0.18 mole %. Tubes 11 and 14 appear to fall within this category of loss of cerium, as solubility and the decreasing amount of melt phase caused coprecipitation to occur.

The final melt from our 57-33-10 mole % mixture was not much different, and a comparable final cerium solubility would be expected. Similar but more pronounced coprecipitation is evident. The maximum amount of CeF_3 occurring in this case is somewhat up from the bottom, probably because the precipitated thorium compounds did not remelt, as discussed above.

The zone-melting behavior of cerium trifluoride is shown by tubes 20, 22, and 23, where solubility limits were not exceeded. Because the cerium did not concentrate in the melt but, if anything, appeared to follow thorium, it is possible that it was contained in the solid solutions based on $3LiF \cdot ThF_4$.

In any event no effective separation of thorium from rare earths is shown by these experiments.

12.4 BEHAVIOR OF CeF_3 IN THE FRACTIONAL CRYSTALLIZATION OF ThF_4 FROM LiF-BeF_2-ThF_4 MELTS

C. J. Barton

Because of difficulty experienced in separating rare earths from thorium-rich single-fluid fluoride fuel compositions, the possibility of removing a fraction of the thorium by fractional crystallization was examined. It is necessary, of course, that the rare-earth fluorides remain in the liquid when the thorium is removed. In the experiments reported here CeF_3 was used to typify the rare earths. Compere and Dorsett have also reported crystallization data for the system LiF-BeF_2-ThF_4-CeF_3 (see Sect. 12.3), but the CeF_3 concentrations used in those studies, 0.03 and 0.3 mole %, were considerably higher than in present investigations, 100 ppm CeF_3 by weight = 0.003 mole %, which is presumed to be realistic for breeder reactors.

Examination of the LiF-BeF_2-ThF_4 phase diagrams[13] led to the choice of the composition LiF-BeF_2-ThF_4 (58-30-12 mole %) for the first study. The phase diagram indicates that the primary phase for the composition is $LiF \cdot 2ThF_4$ and that secondary crystallization does not occur until the concentration of ThF_4 in the melt is rather low.

The apparatus and sampling technique used in this study were essentially identical to those used in CeF_3

[12] J. A. Fredricksen, L. O. Gilpatrick, and C. J. Barton, *Solubility of Cerium Trifluoride in Molten Mixtures of LiF, BeF_2, and ThF_4*, ORNL-TM-2335 (January 1969).

[13] R. E. Thoma *et al.*, *J. Phys. Chem.* 64, 865 (1960).

solubility studies.[14] Because of the low cerium concentration, sole reliance on this determination was placed on the radiochemical technique.[14] The melt was prepared by mixing 197 g of prepurified $LiF-BeF_2$ (66-34 mole %), 250 g of ThF_4, 45 mg of CeF_3, and 0.5 mc of ^{144}Ce. The melt was treated with mixed H_2 and HF at 720°C for 45 min followed by hydrogen alone. Filtered samples of the liquid were removed, the apparatus was cooled below the liquidus temperature, another filtered sample was taken, and the process was repeated at still lower temperatures. Three series of samples were obtained on different days, starting above the liquidus temperature each time, and the samples were analyzed by Analytical Chemistry Division personnel for lithium, beryllium, and thorium and by the writer for cerium. The results are displayed in Table 12.3.

The data show that 565°C is below the liquidus temperature, whereas the published phase diagram indicates an approximate liquidus temperature of 525°C. A filtered sample taken at 650°C was used for gradient studies (L. O. Gilpatrick and H. Insley) that showed $LiF \cdot 2ThF_4$ crystallizing at 576 ± 3°C and $LiF \cdot ThF_4$ at 489° or higher. Since the data show that CeF_3 begins to disappear from the melt in the temperature range 520 to 490°C, it seems likely that its removal can be attributed to association with $LiF \cdot ThF_4$ crystals. The above-mentioned quenching study also shows that secondary crystallization occurred at a higher temperature than predicted by the phase diagram.[13]

The data in Table 12.3 show that it is possible to remove about half the ThF_4 from the composition $LiF-BeF_2-ThF_4$ (60-28-12 mole %, average of four analyses) by fractional crystallization and that removal of more than 70% of the ThF_4 is possible with some loss of CeF_3 from the melt. Only qualitative significance can be attached to the CeF_3 losses because of the scatter in the data, which may indicate that equilibrium between dissolved CeF_3 and solid $LiF \cdot ThF_4$ was not achieved. It is not apparent from study of the $LiF-BeF_2-ThF_4$ phase diagram or of Compere and Dorsett's data whether any other composition of practical interest for use in molten-salt breeder reactors will give better performance in regard to ThF_4–rare-earth separation than the one used in this investigation.

12.5 PROPERTIES OF THE ALKALI FLUOROBORATES

C. J. Barton L. O. Gilpatrick H. Insley

12.5.1 Phase Relations in Fluoroborate Systems

Phase diagrams in the ternary and binary systems that include the components $NaF-KF-BF_3$ have continued

[14] J. A. Fredricksen, L. O. Gilpatrick, and C. J. Barton, *Solubility of Cerium Trifluoride in Molten Mixtures of LiF, BeF_2, and ThF_4*, ORNL-TM-2335 (January 1969).

Table 12.3. Analysis of Filtered Samples of $LiF-BeF_2-ThF_4$

Series No.	Sample Temperature (°C)	Sample Composition (mole %)			CeF_3 Concentration (ppm)
		LiF	BeF_2	ThF_4	
1	720	59.6	28.3	12.1	100
1	720	59.3	29.6	11.1	100
1	530	63.2	31.5	5.3	100[a]
1	490	62.7	33.3	4.0	55
2	640	61.1	27.0	11.9	100
2	555	62.0	30.5	7.5	100[a]
2	517	61.9	31.3	6.8	100[a]
2	460	64.0	32.7	3.3	68
3	650	60.2	27.0	12.8	100
3	565	63.2	27.9	8.9	100[a]
3	520	64.0	29.6	6.4	100[a]
3	487	64.6	30.4	5.0	83
3	455	65.0	31.6	3.4	29

[a] Cerium-144 count per milligram of sample higher than that of the original melt because of the lower thorium content (less internal absorption of the soft ^{144}Ce gamma radiation).

to be of interest because of possible use of mixtures of these materials as coolant salts for molten-salt reactors. Additional data have been collected covering regions previously bypassed, and some regions were reexamined using better-quality $NaBF_4$ than was available at the beginning of the study. Efforts were made to prepare pure hydroxyfluoroborate compounds.

12.5.2 The System NaF-KF-BF_3

Gradient quench analysis and differential thermal analysis (DTA) were used to examine 15 new compositions near the expected minimum liquidus temperature for the ternary system; the data are listed in Table 12.4. Uncertainties for the quench and DTA data are about ±3 and ±1°C respectively. It was previously reported that a minimum solidus temperature of 360°C ± 5° existed,[15] but we have been unable to locate a composition with a liquidus temperature below 376°C. Liquidus and solidus are separated by a two-phase region (primary phase and liquid) in a temperature range equal to or greater than 11°C in all compositions near the minimum that have been examined to date. We are continuing the search for the minimum melting composition in this part of the ternary system that theoretically should exist with a very small separation between liquidus and solidus temperatures.

Four compositions were examined by the gradient quench technique with the purpose of better defining the minimum liquidus temperature in the part of the ternary system bounded by the compounds NaF-KF-KBF_4. The data shown in Table 12.5 indicate that the ternary eutectic is at a lower NaF composition than was reported previously[16] (~6 mole %) and must contain less than 3 mole % NaF. Presently available data show that the three solid phases in equilibrium at the ternary eutectic composition are NaF, KF, and $NaBF_4$-KBF_4 solid solution with a melting point of 458°C, 18°C higher than that reported previously.[16] The eutectic temperature reported earlier as 455° for the limiting binary KBF_4-KF was revised upward to 460°.[17] The limits of accuracy for the gradient quench temperature are of the same order as the temperature difference, ±3°C. Additional work is needed to determine the exact composition of the ternary eutectic.

Table 12.4. DTA and Quench Data for the System NaF-KF-BF_3

Composition (mole %)			Primary Phase	Liquidus Temperature (°C)	
NaF	KF	BF_3		DTA	Quench
52.2[a]	0	47.8	Eutectic	384	385
49.5	1.5	49	SS[b]		392
50.5	1.5	48	NaF		392
48	3	49	SS	383	377
49	3	48		379	<382
50	3	47	NaF	376	416
47	4	49	SS	385	376
48	4	48	SS	379	381
46	5	49	SS		382
47	5	48	NaF	381	382
45	6	49	SS	388	383
46	6	48	SS	383	382
45	7	48	NaF	385	399
44	8	48	NaF	388	390
43	8.5	48.5	NaF + SS	392	388
40	11	49	SS	406	398

[a]Data taken from the binary system NaF-$NaBF_4$ at the eutectic composition where liquidus and solidus coincide.

[b]SS = $NaBF_4$-KBF_4 solid solution.

12.5.3 The System KF-KBF_4

The phase diagram for the system KF-KBF_4 reported earlier[18] was based on data for mixtures containing 50 to 95 mole % KBF_4. Four additional compositions were

[15]*Reactor Chem. Div. Ann. Progr. Rept. Dec. 31, 1968,* ORNL-4400, in preparation.

[16]*MSR Program Semiann. Progr. Rept. Feb. 29, 1968,* ORNL-4257, p. 167.

[17]L. O. Gilpatrick, H. Insley, and C. J. Barton, *Reactor Chem. Div. Ann. Progr. Rept. Dec. 31, 1968,* ORNL-4400.

[18]*MSR Program Semiann. Progr. Rept. Aug. 31, 1967,* ORNL-4191, pp. 158–59.

Table 12.5. Quench Data for the System NaF-KF-BF_3

Composition (mole %)			Temperature (°C)	Primary Phases	Temperature (°C)	Secondary Phases	Temperature (°C)	Eutectic Phases
NaF	KF	BF_3						
7	63	30	621	KF	610	KF + NaF	458	KF + NaF + SS
3	61	36	538	KF + NaF	538	KF + NaF	457	KF + NaF + SS
3	57	40	511	NaF	485	KF + NaF	458	KF + NaF + SS
3	52	45	554	NaF	485	NaF + SS	458	KF + NaF + SS

examined in the high-KF composition range of this system. Liquidus temperatures were measured by DTA and gradient quench methods. Results were in agreement with the partial phase diagram presented earlier, and we still find no evidence of the $KF \cdot KBF_4$ and $KF \cdot 2KBF_4$ compounds reported by Pawlenko.[19] Experimental temperatures determined by DTA were from 17 to 36° higher than those determined by the quench technique. We believe the DTA data to be the more reliable, since they represent in each case the results of measurements made during several thermal cycles. Data are shown in Table 12.6.

12.5.4 The System $NaBF_4$-KBF_4

Compositions containing 80, 85, 90, 95 mole % $NaBF_4$ were examined by the gradient quench technique. The data for these compositions made from high-purity materials confirm the DTA results which were reported earlier,[20] showing a minimum liquidus temperature of 396 ± 2°C at a composition of approximately 90 mole % $NaBF_4$ in this solid-solution system. We usually find agreement of this sort for invariant temperature determinations, in contrast to differences in liquidus measurements mentioned in the previous section.

12.5.5 The System NaF-$NaBF_4$

New compositions were made from the better $NaBF_4$ now available to improve the data for this two-component system, which was the first to be studied. DTA was used to measure the liquidus temperatures given in Table 12.7. Results indicate an increase of about 10°C in the liquidus boundary temperature in the region of 30 mole % $NaBF_4$, where the deviation from the previously reported diagram[16] is greatest.

12.6 LIMITS OF MISCIBILITY IN MOLTEN-SALT SYSTEMS: KBF_4-LiF, Li_2BeF_4-KI, AND Li_2BeF_4-KBF_4

A. S. Dworkin M. A. Bredig

12.6.1 The System KBF_4-LiF

The NaF liquidus in the phase diagram of the reciprocal salt system NaF-KBF_4, containing cations and anions all of unit charge but of widely differing sizes, has been interpreted in terms of a large positive deviation from ideality.[21] It was then predicted and has now been confirmed that replacement of NaF by LiF brings about separation into two liquids. In this system the more stable ion pairing is: [Li^+ (charge-radius ratio $z/r \approx 1.7$), F^- (≈0.75)] and [K^+ (≈0.75), $(BF_4)^-$ (≈0.40)].

At 840°C the miscibility of molten LiF and KBF_4 is indeed small, the two conjugate monotectic liquids containing 3 and 99% LiF in equilibrium with solid LiF (Fig. 12.4). The observed slight variance of the mono-

Table 12.6. DTA and Quench Data for the System KF-KBF_4

Composition (mole %)		Primary Phase	Liquidus Temperature (°C)	
KF	KBF_4		DTA	Quench
60	40	KF	715	679
66.7	33.3	KF	745	713
75	25	KF	778	748
90	10	KF	828	811

Table 12.7. DTA Data for the System NaF-$NaBF_4$

Composition (mole %)		Temperatures (°C ± 2°)		
NaF	$NaBF_4$	Liquidus	Solidus	Crystal Transition
17.9	82.1	538		
37.0	62.9	736		
56.7	43.3	858		
77.7	22.3	937	384	247

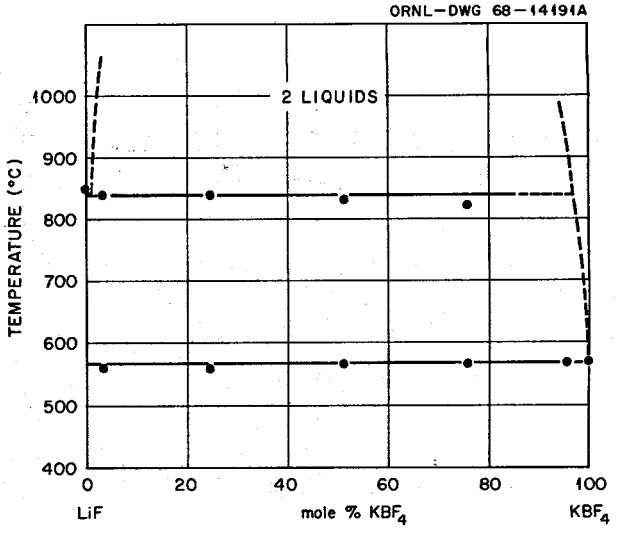

Fig. 12.4. The System LiF-KBF_4.

[19] S. Pawlenko, *Z. Anorg. Allgem. Chem.* 336, 172 (1965).

[20] *MSR Program Semiann. Progr. Rept. Aug. 31, 1968*, ORNL-4344 p. 156.

[21] M. A. Bredig, *MSR Program Semiann. Progr. Rept. Feb. 29, 1968*, ORNL-4254, pp. 167–68.

tectic temperature with composition may be caused by the formation of some KF through dissociation of KBF_4. The eutectic point lies at 564°C and about 0.5% LiF. No attempt was made to determine the predictably high temperature of complete miscibility because of the large BF_3 dissociation pressure involved.

12.6.2 The System Li_2BeF_4-KI

The system contains as the more stable ion pairs [Li^+ ($z/r \approx 1.7$), $(BeF_4)^{2-}$ (≈0.8)] and [K^+ (≈0.75), I^- (≈0.45)]. We have been able roughly to delineate the region of two conjugate liquids as well as the eutectic and monotectic equilibria (Fig. 12.5). At a critical solution (consolute) temperature of 945°C (above which only one liquid phase exists) the critical solution contains 53% KI. At 665°C the two conjugate monotectic liquidus contain 7 and 98% KI in equilibrium with solid KI. The observed large variance of the monotectic temperature, a decline with decreasing KI concentration, may be caused by the presence of excess BeF_2 in the Li_2BeF_4 sample used (LiF-BeF_2, 66-34 mole %). However, it must also be recognized that the system is a reciprocal *pseudo*binary one and that even

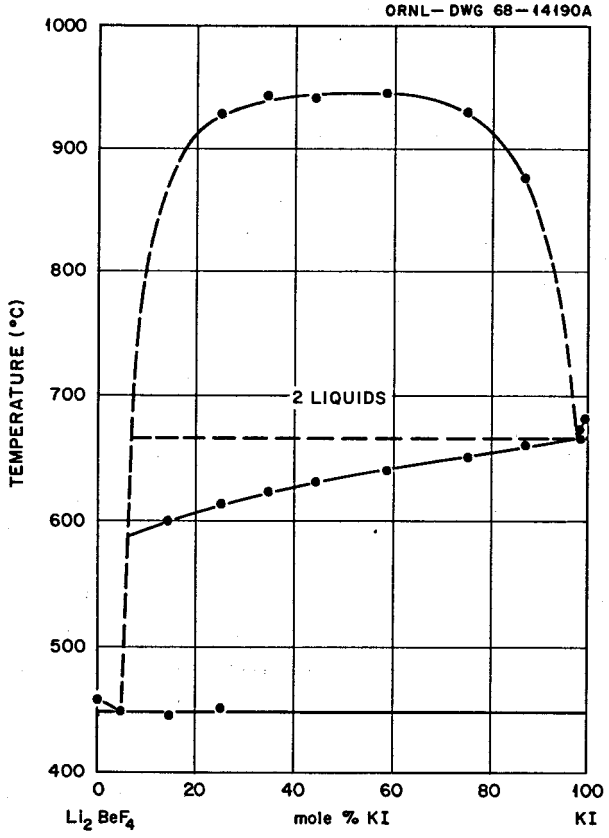

Fig. 12.5. The System Li_2BeF_4-KI.

without excess BeF_2 the compositions of the two liquid phases are likely to be more complicated than shown in Fig. 12.5. The eutectic point lies at about 450° and 4 mole % KI. Large supercooling effects and our observation of what may be a metastable phase of the Li_2BeF_4 with added KI made the establishment of the eutectic approximate at best.

12.6.3 The System Li_2BeF_4-KBF_4

The more stable ion pairs are: [Li^+ ($z/r \approx 1.7$), $(BeF_4)^{2-}$ (≈0.8)] and [K^+ (≈0.75), $(BF_4)^-$ (≈0.4)]. With the similarity in z/r for BF_4^- and I^-, the eutectic and monotectic equilibria in the system were expected, and found, to be very similar to those reported above for the Li_2BeF_4-KI system. At 554°C the two conjugate monotectic liquids contain about 5 and 98% KBF_4 in equilibrium with solid KBF_4. The eutectic point lies at about 450° and 4 mole % KBF_4. Because of expected high BF_3 gas pressure, no attempt was made to determine the consolute temperature, but it is probably close to that found in the Li_2BeF_4-KI system. The difficulties described above in establishing the monotectic and eutectic equilibria for the Li_2BeF_4-KI system were again encountered in almost identical fashion for the Li_2BeF_4-KBF_4 system.

The much greater miscibility in the Li_2BeF_4-$NaBF_4$ system indicated from the liquid-liquid distribution studies of Bamberger *et al.*[22] is due to the smaller size of the sodium ion. Further delineation of the entire two-liquid region may be desirable, possibly by the technique of thermal analysis. In the present study it was the only method thus far employed by us. More detailed knowledge may be gained by the use of additional techniques such as sampling at temperature or quenching with subsequent analysis of the separated phases (high-temperature centrifuge?). More studies of simpler systems such as LiF-KI, LiF-KBr, LiF-CsCl, etc., may also be desirable to further our basic, quantitative understanding of the phenomenon of liquid-phase separation in molten-salt systems.

12.7 SOLUBILITY OF THORIUM METAL IN MOLTEN LITHIUM FLUORIDE–THORIUM FLUORIDE MIXTURES

H. R. Bronstein M. A. Bredig

With an improved analytical technique (R. Apple, Analytical Chemistry Division) involving the mass-

[22] C. E. Bamberger *et al.*, *MSR Program Semiann. Progr. Rept. Feb. 29, 1968*, ORNL-4254, pp. 171–73.

spectroscopic determination of hydrogen produced on dissolution in aqueous acid, the apparent solubility of thorium metal in molten LiF-ThF_4 (73-27 mole %) at 620°C has been firmly established as 0.1 mole %. The particular form in which the thorium metal dissolves in the melt is as yet undetermined. Russian workers, using electrochemical techniques,[23-28] claim to have demonstrated the presence of ionic species of lower valency when the metals beryllium, zirconium, and thorium are equilibrated with alkali halide melts containing the normal chlorides of those metals.

If on dissolving in the LiF-ThF_4 melt the thorium metal forms an ion of lower valency, $Th^{(4-n)+}$, an inert metal electrode such as tantalum should assume the same potential in that melt as a thorium metal electrode, because the potential-determining process occurring at each electrode is the same,

$$Th^{(4-n)+} \rightleftharpoons Th^{4+} + ne^- \,. \qquad (1)$$

However, a dissolution mechanism other than the formation of a thorium species of lower valency might conceivably also yield a zero potential difference. This is the reaction

$$Th^0 + 4LiF \rightleftharpoons ThF_4 + 4(Li^+ + e^-) \,, \qquad (2)$$

where the electron may be considered to have *F*-, or color-, center-like properties. At equilibrium the potential developed will be the same for the thorium electrode and for an inert metal electrode,

$$E^\circ_{Th^0/Th^{4+}} - \frac{RT}{4F} \ln a_{Th^{4+}} + E^\circ_{(Li^+ + e^-)/LiF} - \frac{RT}{F} \ln \frac{a_{LiF}}{a_{(Li^+ - e^-)}} \,.$$

In two experiments the potential developed initially between a thorium electrode and a tantalum electrode placed in an LiF-ThF_4 (73-27 mole %) melt at 620°C was 950 mv. This potential remained constant for approximately 20 min, and then a slow downward drift commenced, terminating after 8 hr in a potential difference of essentially zero. The second solution model does not seem to afford a very satisfactory explanation of the zero potential, since available thermodynamic data for reaction (2) above (ΔG_f° = −435 and −126 kcal/mole ThF_4 and LiF, respectively, at 600°C) would predict a quantity of color centers two orders of magnitude smaller than that found analytically (4 × 0.1 mole % "Th metal"; cf. above). The assumption that a thorium species of lower valency exists seems, at present, to provide a better tentative explanation of the results obtained, even though attempts to confirm this conclusion with spectroscopic techniques (J. P. Young, Analytical Chemistry Division) have not yet proved to be successful.

[23] M. V. Smirnov and L. E. Ivanovskii, *Zh. Fiz. Khim.* 31 802 (1957).

[24] M. V. Smirnov and V. A. Chemezov, *Dokl. Adad. Nauk SSSR* 120, 122 (1958).

[25] M. V. Smirnov and N. Ya. Chukruv, *Russ. J. Inorg. Chem.* 4, 1168 (1959).

[26] N. I. Kornilov and N. G. Ilyushchenko, *Electrochem. Molten Solid Electrolytes* 5, 71 (1967).

[27] V. Ya. Kudyakov *et al.*, *At. Energ.* (USSR) 24, 448 (1969).

[28] M. V. Smirnov and L. D. Yushina, *Izv. Akad. Nauk SSSR, Otd. Khim. Nauk*, No. 2, 1285 (1956) and No. 2, 251 (1959). See, however, R. Srinivasan and S. N. Flengas, *Can. J. Chem.* 42, 1315 (1964).

12.8 THE CRYSTAL STRUCTURE OF KBF_4

G. D. Brunton

Although the low-temperature polymorph of KBF_4 has always been considered to be isostructural with $KClO_4$ and $BaSO_4$, the structure has never been adequately determined, and the lattice parameters which were published were incorrect.[29,30] The structure has been completely determined from three-dimensional x-ray data as a part of an extensive study of complex fluoride compounds, and precise values for the lattice parameters were determined.

The low-temperature polymorph of KBF_4 crystallizes with the orthorhombic space group *Pnma* and with lattice parameters a_0 = 8.6588(5), b_0 = 5.4800(4), and c_0 = 7.0299(8) A. The calculated density is 2.5067 g/cc. The structure is shown in Fig. 12.6.

In the low-temperature form of KBF_4 the K^+ ion is coordinated by eight F^- ions at distances less than 3.0 A and by more F^- ions at 3.075 A. The K^+ polyhedron shares edges with three and corners with four BF_4 tetrahedra. The BF_4 tetrahedra are slightly irregular, with tetrahedral angles of 108.5 to 111.4° and B-F distances 1.378 to 1.391 A. The B-F distances are almost equal to the B-F distances for $NaBF_4$ (1.386 and 1.392 ± 0.002 A) found from a refinement[31] of the

[29] B. Pesce, *Gazz. Chim. Ital.* 60, 936 (1930).

[30] A. Ballanca and F. Sgarlata, *Rend. Soc. Mineral. Ital.* 7, 42 (1951).

[31] G. Brunton, *Acta Cryst.* B24, 1703 (1968).

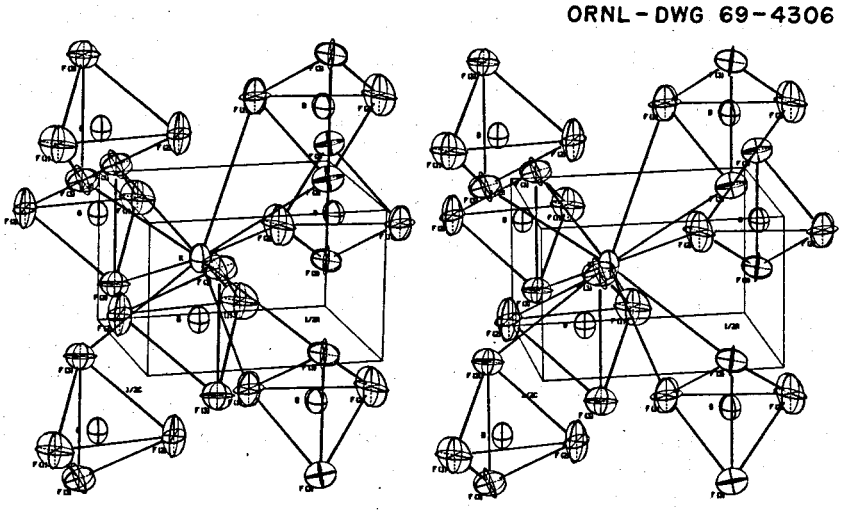

Fig. 12.6. Structure of the Orthorhombic Low Temperature from Percent KBF_4.

$NaBF_4$ structure proposed by Weiss and Zohner.[32] A calculated B-F single-bond distance is 1.37 A.[33]

12.9 DENSITIES OF MOLTEN SALTS

Stanley Cantor

A dilatometric apparatus, previously described,[34] is being used to measure densities of molten salts. Since the last report[34] the accuracy of the measurements has improved, primarily by minimizing the volume occupied by bubbles below the surface of the melt. Apparent bubble volumes as high as 0.8% have been estimated from measurements of melt volume vs pressure. For melts which do not wet the nickel containment vessels, the apparent bubble volume comprises 0.3 to 0.8% of the melt volume; for melts which wet (e.g., $NaNO_3$ and KNO_3), the apparent bubble volume is 0.1% or less.

Three steps are now taken to reduce bubble volume: (1) evacuation of the solid salt for at least 16 hr, (2) evacuation of the apparatus just above the liquidus temperature of the salt (this procedure is not applied to volatile melts such as fluoroborates), and (3) maintenance of an inert-gas pressure of about 70 psig during measurements. By these three procedures apparent bubble volumes are reduced to less than 0.1%.

The reliability of the dilatometric apparatus has been assessed by determining the densities of $NaNO_3$ and KNO_3. Both salts have been measured extensively by the buoyancy method. For our density measurements of $NaNO_3$, in the range 313 to 425°C, the results are given by the equation ρ (g/cm^3) = 2.131 − 7.08 × $10^{-4}t$ (°C); the standard deviation in ρ is 0.001 g/cm^3. These densities are 0.4 to 0.5% greater than those compiled by Janz.[35] Densities of KNO_3 were measured in the temperature range 346 to 612°C; the equation representing the results is $\rho = 2.136 - 7.62 \times 10^{-4}t$. Our densities are 0.1 to 0.3% greater than those measured by Bloom *et al.*[36] Thus the measurements of $NaNO_3$ and KNO_3 indicate that the dilatometric technique is providing densities that are accurate to within 0.5%.

Five other melts have been measured. The results are summarized in Table 12.8. The first salt, $NaBF_4$-NaF (92-8 mole %), is a possible coolant for molten-salt reactors. Densities of this melt were previously measured[34] over a shorter temperature range. The densities given in Table 12.8 are believed to be more reliable and are approximately 0.27% less than the earlier results.

The second salt mixture is very similar in chemical composition to the present MSRE fuel salt. The experimental densities are within 1% of the densities calculated from additive molar volumes;[37] for example,

[32] A. Weiss and K. Zohner, *Phys. Status Solidi* **21**, 257 (1967).

[33] L. Pauling, *Nature of the Chemical Bond*, 3d ed., p. 318, Cornell University Press, Ithaca, N.Y., 1960.

[34] S. Cantor and J. A. Bornmann, *MSR Program Semiann. Progr. Rept. Aug. 31, 1968*, ORNL-4344, pp. 159–60.

[35] G. J. Janz, *Molten Salts Handbook*, p. 42, Academic, New York, 1967.

[36] H. Bloom *et al.*, *Trans. Faraday Soc.* 49, 1458 (1953).

[37] S. Cantor, *Reactor Chem. Div. Ann. Progr. Rept., Dec. 31, 1965*, ORNL-3913, pp. 27–29.

12.8. Density of Molten Salts

Salt Composition (mole %)	Temperature Range Measured (°C)	Density-Temperature Equation (ρ, g/cm^3; t, °C)
92.0 $NaBF_4$ 8.0 NaF	399.5–590.8	$\rho = 2.252 - 7.11 \times 10^{-4}\, t$ Standard error in ρ = 0.0018
64.79 LiF 29.96 BeF_2 4.99 ZrF_4 0.26 UF_4	524.3–761.1	$\rho = 2.553 - 5.62 \times 10^{-4}\, t$ Standard error in ρ = 0.0017
66.0 LiF 34.0 BeF_2	514.5–820.3	$\rho = 2.280 - 4.88 \times 10^{-4}\, t$ Standard error in ρ = 0.000462
$NaBF_4$	410.9–544.6	$\rho = 2.304 - 8.42 \times 10^{-4}\, t$ Standard error in ρ = 0.0027
KBF_4	577.7–673.6	$\rho = 2.178 - 7.65 \times 10^{-4}\, t$ Standard error in ρ = 0.0096

at 600°C the calculated density is 2.198 g/cm^3; the experimental density is 2.216 g/cm^3.

The third mixture listed is the composition of the MSRE coolant. The measured densities are approximately 1% greater than those predicted from additive molar volumes.[37]

The fourth and fifth salts in Table 12.8 are single-component melts. The results listed were obtained before we established suitable methods for reducing bubble volume. More refined measurements of these salts will be made. For the present the densities given may be considered accurate to within 2%.

12.10 SPECTROSCOPY OF FLUORIDE MEDIA

L. M. Toth G. P. Smith

The establishment of a molten-fluoride visible-ultraviolet absorption spectroscopy program has been essentially completed. It includes the development of the diamond-windowed spectrophotometric cell,[38] which is unreactive to molten fluorides, and the production of fluoride solvents and solutes of the purity required for spectroscopy.

12.10.1 The Diamond-Windowed Cell

Operating experience with the diamond-windowed cell has been acquired during this period. With the production of pure solutions (described in the next section), it has been possible to use the automatic data-handling systems presently available on commercial spectrometers.

In particular, we are now able to record spectra on paper tape and either combine them with others or subtract components from composite spectra through the use of the computer. It represents an improvement in molten-fluoride data handling, both with respect to speed and quality of output, which has never before been available.

Continuous usage of the diamonds during the past seven months with a wide variety of molten fluorides has caused some wear on the diamonds. Examination under a microscope reveals a slight etch on one face of one window. It is not known why the wear has been confined to only one surface. Possible causes of etching can be associated with either the reactivity of the fluoride solutions or oxygen contaminants in the helium cover gas surrounding the diamond cell. This wear on the diamonds has not detracted from their usage as molten fluoride windows because it is too slight to be detected by the spectrometer. It is possible, however, that the diamonds will have to be repolished on an annual basis to remove any accumulated damage.

12.10.2 Salt Purification for Fluoride Spectroscopy

L. M. Toth G. P. Smith

Although the production of pure fluoride salts may be viewed as a trivial task for the experienced molten-salt personnel, there is little information on record concerning details of technique or quality of product. It is anticipated that this section might be of use to others who may need salts of the quality described here.

[38] L. M. Toth, J. P. Young, and G. P. Smith, *MSR Program Semiann. Progr. Rept. Aug. 31, 1968*, ORNL-4344, p. 168.

Table 12.9. Purity of ZrF_4, NbF_5, and LiF Single Crystals

Salt	Purification Process			Product Evaluation	
	Method	Temperature (°C)	Process Time	General	$KBrF_4$ Oxide Analysis (ppm)
ZrF_4	Two sublimations	590–600	3 days each	TSC 0.25g[a]	70
NbF_5	Sublimation	100	5 days	TSC 0.50	<50
LiF	HF sparging	900	1 hr	TSC	<50

[a]TSC 0.25 g: "transparent single crystals" followed by average weight of single crystals.

Melts which are both low in oxide content and free of suspended matter are a prerequisite for spectroscopy of dilute species in fluoride solvents. Even small amounts of solutes which react with the soluble oxides and leave solution cause problems either by remaining suspended and scattering light or by precipitating and collecting on the windows of the cell.

The salts are best purified as individual components instead of as the mixed salts. We use the customary approach of subliming volatile fluorides and HF sparging molten nonvolatile fluorides with gaseous HF.

It is usually the practice to sublime volatile fluorides at temperatures where the vapor pressure of the salt is 10 to 100 torrs. These pressures in a system with background pressures of the same magnitude result in sublimation rates yielding approximately 100 g of "purified" salt per day (see, for example, ref. 39). These high sublimation rates cause entrainment of impurities which baffle plates are only partially effective in removing.

We have found that low sublimation rates produced by salt pressures of <0.1 torr in a background pressure of 10^{-4} to 10^{-5} torr eliminate the need of baffles and yield much better results. For some very impure salts it has been necessary to sublime a second time (as in the case of ZrF_4). At these low sublimation rates we have been able to produce up to 50 g of salt in two to three days.

The results on some of these fluoride salts are listed in Table 12.9.

12.11 THE DISTRIBUTION OF U^{4+} BETWEEN MOLTEN LiF-BeF_2-ThF_4-UF_4 AND A (U-Th)O_2 SOLID SOLUTION

C. E. Bamberger C. F. Baes, Jr. A. L. Johnson

We have previously reported studies[40,41] of the distribution of U^{4+} between a molten fluoride phase and a (U-Th)O_2 solid-solution phase by the ion exchange reaction

$$U^{4+}(F) + Th^{4+}(O) \rightleftharpoons U^{4+}(O) + Th^{4+}(F) , \quad (1)$$

for which we may write the quotient

$$Q = \frac{X_{UO_2} X_{ThF_4}}{X_{ThO_2} X_{UF_4}} .$$

The results obtained indicate that in the stirred vessel used at a stirring rate of 150 rpm and a fluoride to oxide phase ratio >1:1 (on a weight basis), several hundred hours were required for equilibrium at 680°C.

In continuing these measurements, we have improved the seal in the stirred vessel,[42] and this has permitted an increase in the stirring rate from 150 to 500 rpm. With this more rapid stirring and an increased ratio of fluoride phase to oxide phase (4:1), exchange equilibrium has been attained in periods less than 70 hr when the oxide phase was <0.8 mole fraction UO_2. This was true whether the previously equilibrated system had been disturbed by the addition of UO_2, ThO_2, or UF_4, or just by a change of temperature (Fig. 12.7). The path followed by the UF_4 concentration of the fluoride phase was unexpectedly complex when UO_2 or ThO_2 was added, showing both a maximum above and a minimum below the final equilibrium value. Considerably more information is needed concerning the effects of a number of variables – such as the stirring rate, the quantities of each phase, and the amounts of material to be exchanged – before the rate of approach to equilibrium can be predicted or perhaps significantly increased. However, it seems clear from the

[39]L. B. Yeatts, Jr., and W. T. Rainey, Jr., *Reactor Chem. Div. Ann. Progr. Rept. Jan. 31, 1965*, ORNL-3789, p. 330.

[40]B. F. Hitch, C. E. Bamberger, and C. F. Baes, Jr., *Reactor Chem. Div. Ann. Progr. Rept. Dec. 1966*, ORNL-4076, p. 18.

[41]C. E. Bamberger and C. F. Baes, Jr., *MSR Program Semiann. Progr. Rept. Aug. 31, 1968*, ORNL-4344, p. 171.

[42]C. E. Bamberger *et al.*, *Reactor Chem. Div. Ann. Progr. Rept. Dec. 31, 1968*, ORNL-4400 (in preparation).

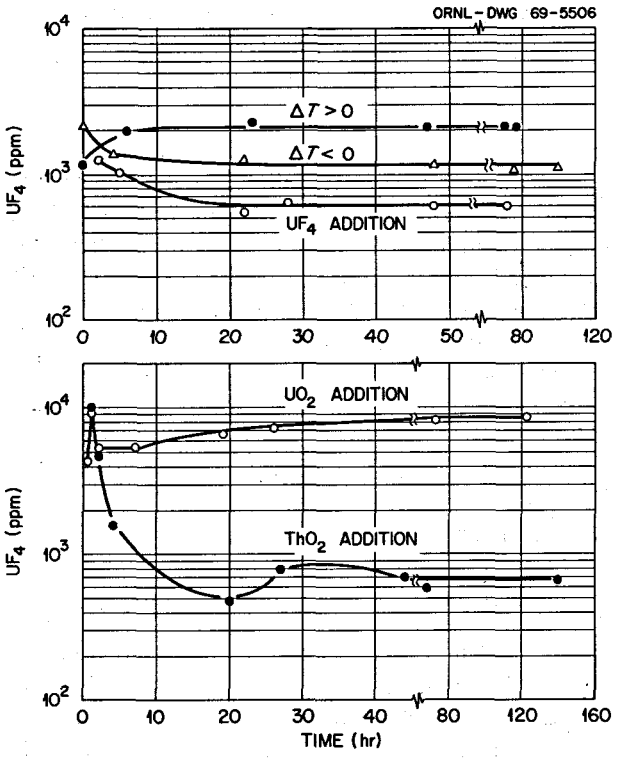

Fig. 12.7. Approach to Equilibrium in the Exchange of U^{4+} and Th^{4+} Between Molten Fluoride and Solid Oxide Solutions After the System Has Been Disturbed.

present results that the exchange process is as rapid and reversible as could be expected in view of the fact that each time the system is disturbed the return to equilibrium requires that the composition of the entire oxide phase must be changed by repeated recrystallization until it is brought to a homogeneous equilibrium composition.

The fluoride phase has been sampled frequently by means of copper filter sticks, and uranium analysis of these samples has been obtained in order to follow the U^{4+}-Th^{4+} exchange. Material balance has been used to determine the concentrations of the other major components of the fluoride phase and the composition of the oxide phase. The oxide phase, sampled less frequently, has been analyzed by x-ray diffraction.[43] This has continued to show that below $X_{UO_2} = 0.8$ a homogeneous (U-Th)O_2 solid solution is the equilibrium oxide phase, as expected. Its composition, based on a determination of the lattice constant, has been within <2% of the material balance value.

[43] Performed by R. L. Sherman, Analytical Chemistry Division.

In some of these equilibrations, hydrogen was added to the argon cover gas used in order to reduce to the tetravalent state any traces of oxidized uranium which might be present in the oxide phase. The equilibrium quotients obtained in such cases agreed well with values obtained in the absence of hydrogen, suggesting that oxidized uranium had not been present in significant amounts in the system.

When the uranium content of the oxide phase was increased above $X_{UO_2} = 0.8$, increasingly long equilibration times were required before the distribution quotient became constant. Furthermore, some x-ray analyses[43] indicated that oxide crystals of more than one composition persisted for long periods in this composition range. At $X_{UO_2} \sim 0.95$, equilibrium results have not yet been obtained. This decreasing exchange rate is probably caused by decreasing solubility of the oxide phase in the fluoride phase as X_{UO_2} is increased. For future measurements in this region, we plan to begin each experiment with prepared oxide solid solutions and fluoride melts of nearly equilibrium compositions.

The results obtained thus far (Fig. 12.8) with $X_{UO_2} < 0.8$, with a salt phase of the composition LiF-BeF_2-ThF_4-UF_4 (72-16-12-≤0.36), and with temperatures in the range 580 to 780°C show that Q varies considerably with the oxide composition and the temperature. The results may be represented by the expression

$$\log Q = \log\left[\frac{X_{UO_2} X_{ThF_4}}{X_{UF_4} X_{ThO_2}}\right] = (2124 + 509X_{UO_2})/T .$$

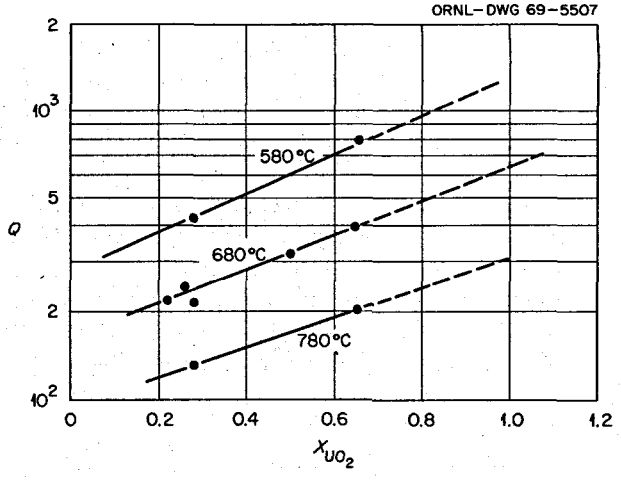

Fig. 12.8. Variation of the Exchange Quotient for Reaction (1) with Composition of the Oxide Phase and the Temperature.

Table 12.10. Values of Q for Reaction (1) at $X_{UO_2} = 0.28$ and 680°

X_{LiF}	X_{ThF_4}	Free Fluoride[a]	Q
0.719	0.120	+3.83	215 ± 16
0.684	0.164	−11.23	222 ± 16
0.751	0.124	+12.82	220 ± 16
0.743	0.110	+12.02	229 ± 17

[a]Free fluoride is defined as $(X_{LiF}-2X_{BeF_2}-3X_{ThF_4}) \times 100$.

It has been found, however, that Q is not significantly changed when the composition of the fluoride phase is varied while holding the composition of the oxide phase constant (Table 12.10).

Since the exchange reaction, Eq. (1), involves two ions of the same charge and nearly the same size, Q might have been expected to be near unity. Actually, however, it has been known for some time that UO_2 is much less soluble than is ThO_2 in these molten fluorides,[44] and hence Q should be considerably above unity, as indeed is the case.

The dependence of Q on the composition of the oxide phase, along with its lack of dependence on the composition of the fluoride phase, shows the oxide phase to be a nonideal regular solution with

$$\log \gamma_{UO_2} = \frac{255}{T} X^2_{ThO_2}$$

and

$$\log \gamma_{ThO_2} = \frac{255}{T} X^2_{UO_2} ,$$

wherein there is a zero excess entropy of mixing but a positive heat of mixing. Finally, the simple two-parameter expression for Q, above, indicates that the entropy of the exchange reaction is also zero.

Upon completion of the measurements at high values of X_{UO_2}, we will investigate the distribution of Pa^{4+} in this system in order to define the behavior to be expected in an MSBR fuel inadvertently contaminated with oxide and also to explore further the potential applicability of this system to fuel reprocessing.

[44]J. H. Shaffer, G. M. Watson, and W. R. Grimes, *Reactor Chem. Div. Ann. Progr. Rept. Jan. 1960*, ORNL-2931, p. 90.

12.12 AN Ni-NiO-BeO ELECTRODE AS A REFERENCE ELECTRODE IN MOLTEN FLUORIDES

B. F. Hitch C. F. Baes, Jr.

We have reported[45] previously that the Ni-NiO-BeO electrode showed promise as a reference electrode in molten fluorides. The potential of this electrode is established by a low (0.002 mole/kg at 600°C)[46] Ni^{2+} concentration produced by saturating $2LiF\text{-}BeF_2$ mixtures with both BeO and NiO.

Studies of the cell

$$Be^0 | LiF\text{-}BeF_2 \| LiF\text{-}BeF_2 , Ni^{2+} | BeO, NiO | Ni^0 , \qquad (1)$$
$$(66\text{-}34) \quad (66\text{-}34) \quad (c) \quad (c)$$

with the assumed cell reaction being

$$Be^0 + NiO(c) \rightleftharpoons BeO(c) + Ni^0 ,$$

were completed. Since all the reactants and products are of fixed activity, the measured cell potential should be the standard cell potential E° and a function only of temperature if the $LiF\text{-}BeF_2$ mixture is the same in both half-cells.

In our early potentiometric measurements of the above cell, the compartment for the nickel electrode was constructed of copper tubing with a copper frit (25 to 40 μ porosity) welded onto the lower end. Excess BeO and NiO were added to this compartment, and the $LiF\text{-}BeF_2$ solution was then forced through the copper frit into the compartment by a small gas pressure. A nickel tube served as the nickel electrode and also permitted gas sparging. Cell potentials were erratic, but on various occasions we were able to achieve stable potentials for as long as 24 hr. The major difficulty encountered was that the cell potential would reach a maximum value and then begin drifting toward a lesser value. In an attempt to improve the performance of the nickel electrode, we modified the compartment described above by using a more dense copper frit (<10 μ pore size), and in another version we used nickel tubing clad in copper. Neither modification resulted in any significant improvement in the behavior of the cell potential.

Since the possibility of electrical shorts between the $Ni^{2+}|Ni$ electrode and the metal electrode compart-

[45]B. F. Hitch and C. F. Baes, Jr., *MSR Program Semiann. Progr. Rept. Aug. 31, 1968*, ORNL-4344, p. 167.

[46]C. F. Baes, Jr., *Thermodynamics*, vol. 1, p. 409, IAEA, Vienna, 1966.

ments could have been responsible for some of the difficulties described above, we fabricated a compartment using silica tubing and a silica frit. The silica served as an electrical insulator for the nickel electrode and contained the oxide-saturated 2LiF-BeF_2 mixture.[47] An improved nickel electrode was also used in the silica compartments. This electrode was fabricated by welding a small ($^3/_{16}$ × $^3/_8$ in.) rectangle of sintered metal to $^1/_8$-in. nickel rod. The sintered nickel was then "painted" with an aqueous slurry of $Ni(OH)_2$ and fired at 1000°C. This provided a larger surface area for the electrode reaction as well as a source of NiO.

Using a silica compartment and the improved nickel electrode, we obtained standard cell potentials (E°) over a temperature range of 525 to 715°C, as shown in Fig. 12.9. The standard cell potential is given by $E^\circ = 1.8872 - 0.000044T$ (v). Potential measurements were made over a period of one week, and although the silica was attacked by the fluoride melt, it did not rupture, nor did the electrode potential show any appreciable variation during this period. The standard cell potential compares well with values calculated using the formation free energies of BeO[48] and NiO.[49]

We are presently using the $Ni^{2+}|Ni$ electrode described above, with the silica clad in nickel tubing, to measure the redox potential of the U^{4+}/U^{3+} couple in the cell

$$\mathrm{Pt}\left|\begin{matrix}\mathrm{UF_4,UF_3,}\\ \mathrm{LiF,}\\ \mathrm{BeF_2}\end{matrix}\right\|\left|\begin{matrix}\mathrm{LiF,}\\ \mathrm{BeF_2,}\\ \mathrm{Ni^{2+}}\end{matrix}\right|\left|\begin{matrix}\mathrm{NiO}(c),\\ \mathrm{BeO}(c)\end{matrix}\right|\mathrm{Ni}\,.$$

If, in the above cell, we assume that the internal transport number of Li^+ is 1, which seems reasonable from the work of Romberger and Braunstein,[50] we may then sum the following processes:

$$F^-(1) + UF_3(1) \rightarrow UF_4(1) + e^-\,,$$

$$Li^+(1) \rightarrow Li^+(2)\,,$$

$$e^- + \tfrac{1}{2}NiO + \tfrac{1}{2}BeF_2(2) \rightarrow \tfrac{1}{2}Ni^0 + \tfrac{1}{2}BeO + F^-(2)\,,$$

where (1) denotes the half-cell containing UF_4, UF_3, LiF, BeF_2 and (2) denotes the nickel reference electrode half-cell.

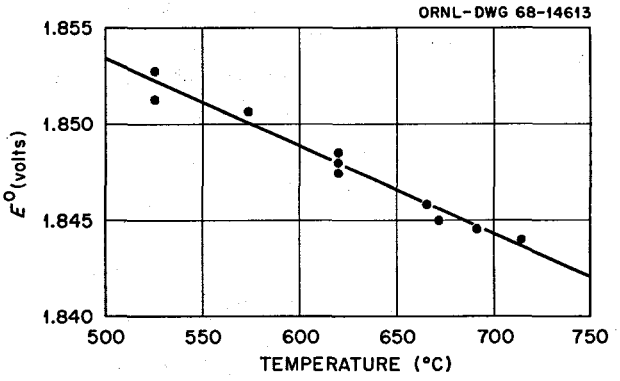

Fig. 12.9. Standard Cell Potential (Cell 1) E° as a Function of Temperature.

The cell reaction is then

$$\tfrac{1}{2}NiO + LiF(1) + UF_3(1) + \tfrac{1}{2}BeF_2(2) \rightleftharpoons UF_4(1) + LiF(2) + \tfrac{1}{2}Ni^0 + \tfrac{1}{2}BeO\,,$$

and the Nernst expression is

$$E = E^\circ - \frac{RT}{F}\ln\left(\frac{a_{UF_4}}{a_{UF_3}}\right)_{(1)} \times \frac{a_{LiF(2)}}{a_{LiF(1)}\,a_{BeF_2(2)}}\,.$$

Measurements so far have been made in an LiF-BeF_2-UF_4 (66-33-1) melt. Uranium trifluoride has been formed by adding beryllium or zirconium metal as the reductant. Results indicate that the first few additions of reductant were consumed by impurities in the melt, and even after careful purification a small amount of impurities existed. From the potential measurements the major impurity seems to be hydroxide ion. Reproducible results have been difficult to obtain using beryllium and zirconium metal as reductants. However, results obtained using NiF_2 to oxidize the UF_3 are reproducible but are not in agreement with cell potentials calculated from available thermochemical data. This inconsistency of about 40 mv will be investigated further.

The $Ni^{2+}|Ni$ electrode shows promise for use as a reference electrode in molten fluorides. We hope to improve the compartment assembly by using porous BeO or ZrO_2 instead of silica. Both of these materials will be investigated in the near future.

---

[47] C. E. L. Bamberger, C. F. Baes, Jr., and J. P. Young, *J. Inorg. Nucl. Chem.* 30, 1979 (1968).

[48] B. F. Hitch and C. F. Baes, Jr., *J. Inorg. Chem.* 8(2), 201 (1969).

[49] J. F. Elliott and M. Gleisen, *Thermochemistry for Steelmaking*, p. 190, Addison-Wesley, Reading, Mass.

[50] K. A. Romberger and J. Braunstein, sect. 12.13, this report.

12.13 EMF MEASUREMENTS WITH CONCENTRATION CELLS WITH TRANSFERENCE IN MOLTEN MIXTURES OF LiF AND BeF_2

K. A. Romberger J. Braunstein

The correlation and interpretation of ionic transport properties in molten fluoride systems, especially BeF_2-containing mixtures, is important in the development of electroanalytical methods for the molten-salt reactor and for electrolytic separation processes.[51] Here we report measurements of the transference numbers of Li^+ and Be^{2+} in LiF-BeF_2 mixtures.

Electromotive force measurements have been made of the concentration cell with transference

$$\mathrm{Be}\left|\begin{array}{c}\mathrm{LiF}\\ \mathrm{BeF_2}\\ \mathrm{I}\end{array}\right\|\left|\begin{array}{c}\mathrm{LiF}\\ \mathrm{BeF_2}\\ \mathrm{II}\end{array}\right|\mathrm{Be}\,. \qquad (1)$$

These measurements have covered the composition range in the indicator half-cell (II) from 0.33 to 0.51 mole fraction BeF_2 at 500°C and from 0.27 to 0.70 mole fraction BeF_2 at 610°C. The reference half-cell (I) contained 0.34 mole fraction BeF_2 at 500°C and 0.70 mole fraction BeF_2 at 610°.

The furnace[52] and cell, the latter shown schematically in Fig. 12.10, were of silica. Spectrophotometric[53] and conductance[54] measurements have demonstrated the compatibility of silica containers with these LiF-BeF_2 mixtures. Beryllium rod electrodes, clamped to nickel rods, were dipped in melt in the bulk compartment (II) and in the small reference half-cells. The liquid junction between the two compartments was made through coarse-grade (150-μ) fritted silica disks. These disks have relatively little surface area and ensure a conduction path through liquid rather than through a silica membrane. Behl and Egan had reported drift of emf with fine-porosity silica frits in emf measurements with molten chlorides and adopted powdered alumina as the diffusion barrier.[55] No such drift was observed with our silica frits.

The smaller reference compartment (I) was filled initially from melt contained in the larger indicator compartment (II). The initial emf's were 0 ± 1.7 mv. The composition of the bulk compartment was changed by stepwise additions of BeF_2 and also LiF at each temperature while measuring the emf, E_t. The emf equilibrated within about 15 min after an addition of BeF_2 or LiF, the approximate time required for salt dissolution and reestablishment of temperature control. Mechanical stirring through a Teflon seal, under a dried helium atmosphere, speeded equilibration.

The emf of cell I is shown as a function of composition in Fig. 12.11. At 500° the composition was first varied from 0.34 to 0.51 mole fraction BeF_2 by additions of BeF_2. It was then lowered to 0.33 mole fraction BeF_2 by additions of LiF. At 610°C the composition was varied from 0.70 to 0.27 and then back to 0.33 mole fraction BeF_2. Values of E_t for both LiF and BeF_2 additions fell on the same line within ±2 mv. Additions of LiF and BeF_2 were made through a ball valve under helium pressure. Lithium fluoride was previously sintered under hydrogen, while BeF_2 was a clear glass which had been vacuum distilled in nickel. The LiF-BeF_2 mixture (0.34 mole fraction BeF_2) was filtered through fritted nickel under hydrogen before use.

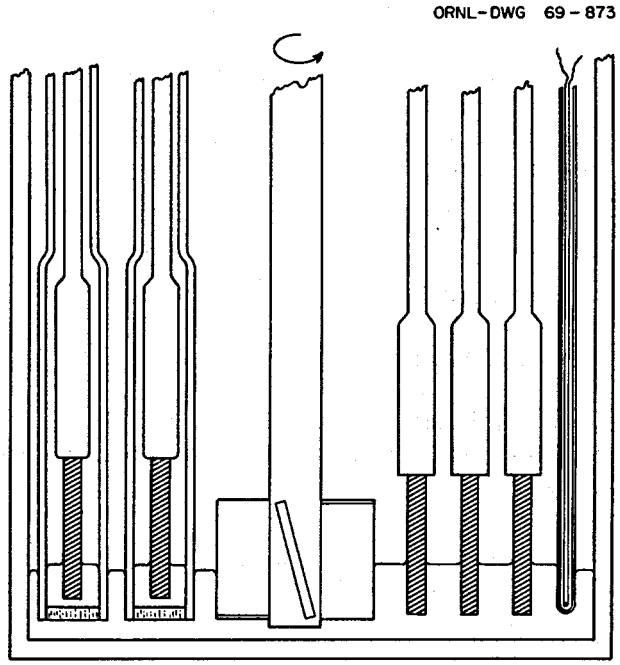

Fig. 12.10. Silica Cell Compartment and Reference Half Cell for Measurement of EMF of Cell with Transference.

[51] K. A. Romberger and J. Braunstein, *Reactor Chem. Div. Ann. Progr. Rept. Dec. 31, 1968,* ORNL-4400 (in preparation).

[52] K. A. Romberger, *MSR Program Semiann. Progr. Rept. Feb. 29, 1968,* ORNL-4254, p. 149.

[53] C. E. Bamberger, C. F. Baes, and J. P. Young, *J. Inorg. Nucl. Chem.* 30, 1979 (1968).

[54] G. D. Robbins and J. Braunstein, in *Symposium on Characterization and Analysis in Molten Salts,* ed. by G. Mamantov, Marcel Dekker, Inc., New York, 1969 (in press).

[55] W. K. Behl and J. Egan, *J. Phys. Chem.* 71, 1764 (1967).

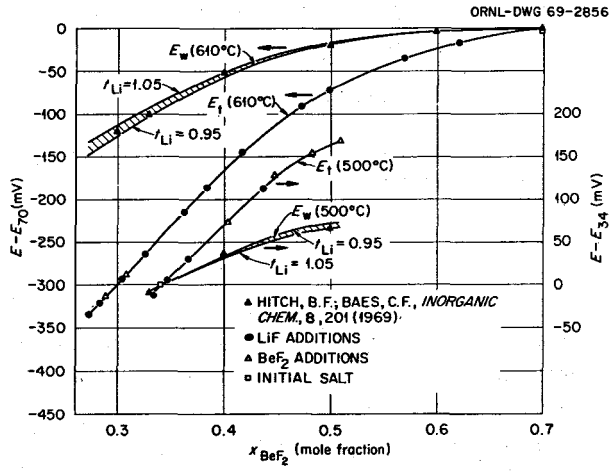

Fig. 12.11. EMF of Concentration Cells With (E_t) and Without[55] (E_w) Transference in the System LiF-BeF_2.

Hitch and Baes[56] measured the emf of the cells

$$\mathrm{Pt,H_2\,HF}\left|\begin{matrix}\mathrm{LiF}\\ \mathrm{BeF_2}\end{matrix}\right|\mathrm{Be} \qquad (2)$$

as a function of temperature for BeF_2 mole fractions of 0.30, 0.33, 0.40, 0.50, 0.60, 0.70, 0.80, and 0.90. The difference of emf of two cells such as (2), with differing melt concentrations, is the emf of a concentration cell without transference, with beryllium electrodes, corresponding to the same electrode reactions as for cell I. These differences, E_w, also are shown in Fig. 12.11. The difference between E_w and E_t over relatively small differences of composition indicates liquid junction potentials of appreciable magnitude.

If the transference numbers of lithium ion and beryllium ion, relative to fluoride ion as the internal reference, are t_{Li} and t_{Be}, with $T_{Li} = 1 - t_{Be}$, consideration of the electrode reactions, transference, and the Gibbs-Duhem equation gives[55,57]

$$dE_t = t_{Li}\left(\frac{1+x}{1-x}\right)dE_w \qquad (3a)$$

or

$$t_{Li} = \left(\frac{1-x}{1+x}\right)\frac{dE_t}{dE_w} = \left(\frac{1-x}{1+x}\right)\frac{dE_t/dx}{dE_w/dx}, \qquad (3b)$$

where x is the mole fraction of beryllium fluoride. The mean transference number over the range of composition between I and II is

$$\bar{t}_{Li} = \frac{E_t^{II} - E_t^{I}}{\int_I^{II}\frac{1+x}{1-x}\,dE_w}. \qquad (4)$$

Equation (4) may be applied to small composition intervals, to determine the composition dependence of t_{Li}, or over a large interval if t_{Li} varies little with composition.

At 610°C, Eqs. (3*b*) and (4) both yield values for t_{Li} of 1.00 ± 0.05 in the composition range $0.30 < x_{BeF_2} < 0.50$. At higher concentrations of BeF_2, the magnitude of the changes in E_t and especially in E_w is considerably smaller than at the lower BeF_2 concentrations (see Fig. 12.11). For the composition range $0.50 < x_{BeF_2} < 0.70$, the error in E_w is approximately 15%, while for the range $0.60 < x_{BeF_2} < 0.70$, the uncertainty in E_w is over 100%; that is, $E_w = 2.9 \pm 3.4$ mv. If the E_w value at 0.60 mole fraction BeF_2 is omitted, then $\bar{t}_{Li}$ is 1.0 ± 0.2 for the composition interval $0.50 < x_{BeF_2} < 0.70$. The large uncertainties in E_w in this composition range render use of the derivative relation (3*b*) imprecise. On a plot of E_t vs E_w the value of E_w at 0.60 mole fraction BeF_2 falls about 2 mv below the smooth curve through the other points, this smooth curve corresponding to $t_{Li} = 1.0 \pm 0.05$. The error is within that quoted by Hitch and Baes.[56] The value of t_{Li} calculated with Eq. (4) from the 500°C data is 1.00 ± 0.05 for the interval $0.33 < x_{BeF_2} < 0.50$. Scatter in the values of E_t for this preliminary experiment is too large and the number of measured values of E_w in this range is too small to apply Eq. (3*b*).

E_w can be calculated as a function of composition as

$$E_w = \int_I^{II}\frac{1}{t_{Li}}\left(\frac{1-x}{1+x}\right)dE_t \qquad (5)$$

from experimental values of E_t if t_{Li} is known. The bands shown in Fig. 12.11 are the calculated limits of E_w when t_{Li} is assumed to be 0.95 and 1.05. Within their listed uncertainties the values of E_w as given by Hitch and Baes fall within these bands. We conclude that $t_{Li} = 1.0 \pm 0.05$ in the range $0.3 <$

[56] B. F. Hitch and C. F. Baes, Jr., *An EMF Study in LiF-BeF_2 Solutions*, ORNL-4257; *Inorg. Chem.* 8, 201 (1969).

[57] C. Wagner in *Electrochemistry and Electrochemical Engineering*, vol. 4, ed. by P. Delahay, p. 11, Interscience, New York, 1966.

$x_{BeF_2} < 0.5$, probably in the range $0.3 < x_{BeF_2} < 0.7$, and possibly over the entire concentration range.

The mobility of lithium ion is given by[55,57]

$$u_{Li} = \frac{t_{Li}\kappa}{Z_{Li}C_{Li}F} = \frac{t_{Li}\kappa\{M_{LiF} + [x/(1-x)]M_{BeF_2}\}}{Z_{Li}F\rho}. \quad (6)$$

In the above expression, κ is the specific conductance of the melt, the M's are the formula weights of the components, Z is the charge ($Z_{Li} = 1$), F is the faraday, and ρ is the density. With $t_{Li} = 1$ and the reported conductance[54] and density[58] of LiF-BeF_2 mixtures, the calculated mobilities of lithium ion (relative to fluoride) in mixtures containing 0.34 and 0.51 mole fraction BeF_2 are, respectively, 4.0×10^{-4} and 2.7×10^{-4} cm^2 sec^{-1} volt^{-1} at 500°C and 6×10^{-4} and 4×10^{-4} cm^2 sec^{-1} volt^{-1} at 610°C. (These values are smaller than those for Li^+ in LiCl-$PbCl_2$ mixtures and for K^+ in KCl-$MgCl_2$ mixtures, but are similar to those for Mg^{2+} in KCl-$MgCl_2$ mixtures.[55]) The mobility of beryllium ion is zero within the experimental error. A negative value of t_{Be}, corresponding to the reported experimental uncertainty ($t_{Be} = 0 \mp 0.05$), seems highly unlikely since it would imply that beryllium ions move toward the anode faster than fluoride ions.

Additional emf measurements are in progress to extend the range of temperatures and BeF_2 concentrations. Measurements will be made in metal (Mo, Ta) systems to verify inertness of the silica apparatus and to permit the use of Li(Bi) alloy electrodes, which react with silica. With both Be and Li(Bi)-alloy reference electrodes, E_w and E_f can both be determined in one experiment. This will provide an independent check of activity data in the LiF-BeF_2 system and extend the results to composition regions where gas electrodes, used in previous measurements, are difficult to employ. Precise determination of the transference numbers should make it possible to use beryllium electrodes in fritted compartments as thermodynamic reference electrodes, for example, for the evaluation of free energies and enthalpies of mixing. High BeF_2 concentrations in the reference compartment retard mixing and increase electrode lifetime.

[58] S. Cantor, W. T. Ward, and C. T. Moynihan, *J. Chem. Phys.* (in press).

12.14 ELECTRICAL CONDUCTANCE OF MOLTEN KNO_3

G. D. Robbins J. Braunstein

Specific conductances κ are obtained from measured resistance R by employing the relation

$$\kappa = (1/R)(l/a), \quad (1)$$

where l/a is the cell constant. The value of l/a usually is obtained by measuring the resistance of a material of known specific conductance, preferably one having properties similar to the system to be investigated.

In the course of investigating electrical conductivities of molten fluoride systems of relevance to the MSRE and MSBR programs, it became necessary to select a reference salt for use in the determination of cell constants. Based on ease of handling, availability, stability to atmospheric conditions, and compatibility with container materials – especially silica – molten potassium nitrate seemed the most reasonable choice among molten salts for such a reference material. However, the results of reported investigations in this system at temperatures up to 100°C above the melting point differ by amounts considerably larger than the claimed experimental uncertainty.

In a recent review of electrical conductance measurements in molten fluorides,[59] errors arising from the use of a Wheatstone-type (or Jones) conductance bridge were discussed. Some possible origins of frequency variation of the measured resistance were also presented.

The object of this work was a careful measurement of specific conductance as a function of temperature for molten potassium nitrate to provide reliable values for use in cell constant determination in our molten-fluoride program. Because of the frequent use of potassium nitrate as a reference point in studies of transport properties of molten salts,[60-63] accurate values of its specific conductance and temperature

[59] G. D. Robbins, *Electrical Conductivity of Molten Fluorides. A Review*, ORNL-TM-2180 (March 1968); *J. Electrochem. Soc.*, in press.

[60] C. A. Angell, *J. Phys. Chem.* 68, 1917 (1964).

[61] *Ibid.*, 70, 2793 (1966).

[62] B. DeNooijer, *The Electrical Conductivity of Molten Nitrates and Binary Nitrates*, thesis, University of Amsterdam, Netherlands, 1965.

[63] J. C. T. Kwak, *Diffusional and Electrical Mobilities of Tracer Ions in Ionic Liquids*, thesis, University of Amsterdam, Netherlands, 1967.

dependence are important quantities in their own right to the physical chemistry of molten salts.

As discussed previously, errors can arise in determining molten-salt conductivities from the use of measuring bridges with a balancing arm having a parallel resistance and capacitance. Accordingly, a specially constructed bridge[64] with series components in the balancing arm was employed in measuring resistances in the molten nitrate. The type of silica conductance cell used here has been previously described.[65] For the determination of the cell constant a 0.1-demal aqueous potassium chloride solution (prepared from single-crystal KCl) was used, for which the specific conductance is well established.[66,67] The resistance of the aqueous electrolyte was determined in a controlled-temperature bath at 25°C employing the Jones bridge because of the large resistances involved.

For measurements in the molten nitrate the maximum peak-to-peak voltage applied to the series-component bridge was 30 to 110 mv, and the measured resistance did not vary with frequency (<0.2 ohm ± 0.2%, random) from 1 to 20 kilohertz. More specific experimental detail may be found in ref. 68.

Table 12.11 shows specific conductance vs temperature data for molten potassium nitrate as determined with the series-component bridge. To check for possible errors in conductance due to nitrite formation, the following procedure was adopted:

Between each resistance determination at successively higher temperatures, the resistance was measured near the melting point (see Fig. 12.12). It was planned to discard the last datum at the elevated temperature when a low-temperature value failed to duplicate the previously determined values. However, no discrepancy appeared up to 541°C, the temperature limit of the furnace. From this one might conclude either that sufficiently little nitrite had formed to be detected or that the specific conductances of KNO_3 and KNO_2 were identical within the limits of measurements, in which case the results remained valid. However, the possibility exists for identical conductivities near 350°C with divergent values appearing at increased temperatures. Accordingly, an addition of 5 mole % KNO_2 was made, which resulted in the datum represented by the triangle in Fig. 12.12 at 359°C, well outside the data scatter.

Table 12.11. Specific Conductance of KNO_3 vs Temperature

Temperature (°C)	κ (ohms^{-1} cm^{-1})
345.4	0.645_9
349.9	0.659_9
351.6	0.664_7
353.5	0.670_5
353.5	0.669_6
354.9	0.675_8
355.4	0.676_4
357.5	0.683_4
358.5	0.686_7
360.6	0.692_1
360.8	0.693_4
363.7	0.704_2
376.6	0.744_4
380.0	0.753_6
386.6	0.774_0
392.0	0.790_8
419.9	0.873_1
445.2	0.946_2
464.4	1.001_4
485.2	1.056_5
485.7	1.055_7
499.5	1.093_7
520.5	1.147_0
541.3	1.198_8

To recheck the KNO_3 specific conductance results, a completely new dip cell was constructed and its cell constant (141.4 cm^{-1}) determined in 0.1-demal KCl as before. A newly calibrated Pt vs Pt–10% Rh thermocouple measured temperature. The squares at 370 and 422°C show these results, which agreed with the previous results within 0.2%.

The curve shown in Fig. 12.12 represents the computer-fitted least-squares equation (σ = 0.0008)

$$\kappa = -0.7098 + 4.6202 \times 10^{-3} t\,(°C) - 2.0221 \times 10^{-6} t^2$$

based on the 24 data in Table 12.11. Of the previous investigations in this system only the limited-temperature-range equation (343–391°C) of Smith and Van Artsdalen[69] agrees well with the results reported

[64] G. D. Robbins and J. Braunstein, *Reactor Chem. Div. Ann. Progr. Rept. Dec. 31, 1967*, ORNL-4229, p. 57.

[65] G. D. Robbins and J. Braunstein, *MSR Program Semiann. Progr. Rept. Aug. 31, 1968*, ORNL-4344, p. 163.

[66] R. A. Robinson and R. H. Stokes, *Electrolyte Solutions*, 2d ed., p. 462, Butterworths, London, 1959.

[67] G. Jones and B. C. Bradshaw, *J. Am. Chem. Soc.* 55, 1780 (1933).

[68] G. D. Robbins and J. Braunstein, *The Specific Conductance of Potassium Nitrate*, ORNL-4375 (March 1969).

[69] D. F. Smith and E. R. Van Artsdalen, *Chem. Div. Semiann. Progr. Rept. June 20, 1956*, ORNL-2171, p. 80.

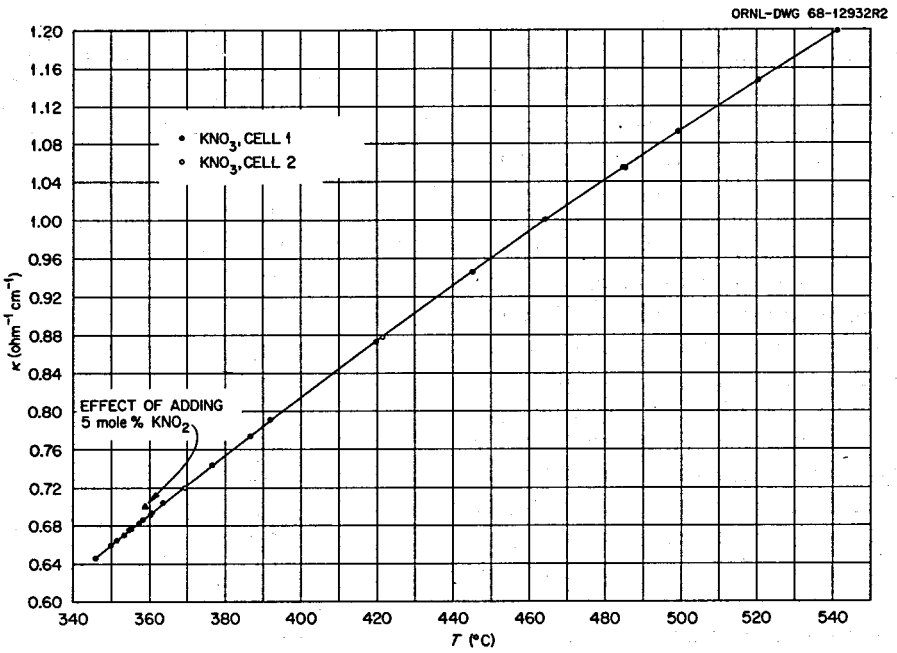

Fig. 12.12. Specific Conductance of Molten KNO_3 vs Temperature.

here (maximum deviation = 0.4%). If all errors are assumed to be random and independent with uncertainties assigned to κ of 0.2% from cell constant determination, 0.1% from resistance measurement, 0.2% from possible nitrite impurity, and 0.2% from temperature measurement, the probable error is 0.3%. We consider these results to have an accuracy of better than ±0.5% and to demonstrate the potential of KNO_3 as a molten-salt conductance standard.

12.15 ELECTRICAL CONDUCTANCE OF MOLTEN BERYLLIUM FLUORIDE

G. D. Robbins J. Braunstein

As part of an investigation of the temperature dependence of electrical conductivities in the molten LiF-BeF_2 system, a preliminary study of the variation of conductance with temperature in pure molten beryllium fluoride has been completed. In addition to its importance as a primary component of fuel and coolant salts for the MSRP, much fundamental interest is centered on the conductance of molten BeF_2 because of its ability to supercool, allowing approach toward the theoretical "glass-transition–zero-mobility" temperature. One might thus expect marked non-Arrhenius behavior in its transport properties (particularly viscosity and electrical conductivity). Yet such behavior was not found for the viscosity over many orders of magnitude.[70]

The extremely high viscosity (>7 X 10^5 poises at 600°C)[70] and the network structure of molten BeF_2 pose special problems in the measurement of specific conductance due to the large resistances involved. Consequently, a different type of electrode configuration from that previously described was employed in this investigation. This consisted of two parallel L-shaped platinized platinum wires (20 gage) immersed directly into the melt to a depth of 7 mm. A silica thermocouple well, dipping into the melt and attached to the electrode assembly, contained a calibrated Pt vs Pt–10% Rh thermocouple for accurate temperature measurement (±0.2°C). The cell constant at 7 mm depth of immersion was determined to be 0.638 ohm^{-1} cm^{-1} (±5%) in 0.01-demal KCl solution,[71] prepared from single-crystal potassium chloride.

Hand-picked glass-clear pieces of distilled beryllium fluoride[72] were loaded, in a dry box, into a silica cell of the type previously described[73] and melted in a helium atmosphere. A silica-Lavite furnace[74] permitted visual

---

[70] S. Cantor, W. T. Ward, and C. T. Moynihan, *J. Chem. Phys.*, in press (1969).

[71] Obtained from A. S. Quist and W. L. Marshall.

[72] Brush Beryllium Co.; distilled by B. F. Hitch.

[73] *MSR Program Semiann. Progr. Rept. Aug. 31, 1968*, ORNL-4344, p. 163.

[74] K. A. Romberger, *MSR Program Semiann. Progr. Rept. Feb. 29, 1968*, ORNL-4254 p. 149.

observation of the melt. On melting, the BeF_2 chunks slowly coalesced, trapping inert-gas bubbles which slowly disappeared with heating during the first day of operation. Small immobile gas bubbles were observed to form and adhere to the silica wall about the third day. (This was probably SiF_4 formed via the reaction $2BeF_2 + SiO_2 \rightarrow SiF_4\uparrow + 2BeO$.) A wisp of particulate matter could also be seen in the bulk; otherwise the melt appeared clear and colorless. Neither bubbles nor particulate matter was observed in the conducting region between the electrodes. No change in appearance occurred during the subsequent 11 weeks the molten fluoride remained in the cell (except an occasional initiation of crystallization during supercooling). At the end of this period, analysis of samples from the interior of the frozen melt (all of which was glass clear) showed the following impurities (in ppm by weight): 3 Fe, 15 K, 50 Li, and 100 Na. Other metals detectable by semiquantitative spectrographic analysis were below the limits of detection. While this impurity level is higher than desirable, it is several orders of magnitude lower than the only previous investigation in this system.[75]

The Jones conductance bridge[76] was tested with dummy components in place of the cell (calibrated resistances and 20 μf capacitance, connected in series) as a function of frequency to ascertain the accuracy which could be expected with the very large experimental resistances (considerably greater than those for which the bridge was designed). For a given level of accuracy the range of frequency over which this accuracy could be maintained decreased as the resistance increased. For 1% accuracy the available frequency range for resistances of 1×10^5 ohms was 0.3 to 10.0 kilohertz, while the range decreased to 0.6–2.0 kilohertz, for resistances of 1×10^6 ohms. (For resistances of the order of 1×10^7 ohms, 3% accuracy was possible only over the frequency range 0.80 to 0.90 kilohertz.) Measured resistances of the cell containing molten BeF_2 ranged from 8×10^4 to 8×10^6 ohms and were invariant with frequency within the accuracy limits of the bridge. This is an indication (although not proof) that the conductance is not by minor electroactive impurities, which would very likely result in frequency-dependent conductance if the impurities were oxidized or reduced at the electrodes. This is especially so due to the large peak-to-peak voltages of 0.1 to 2.0 v which had to be applied (depending on the magnitude of the resistance) to obtain a detectable current of 1 to 5 μa. Even with the large resistances encountered here, the silica appeared to be an electrical insulator, and no parallel conductance through the silica could be detected.

Specific conductances, κ, for molten BeF_2 obtained after two weeks and after three weeks are presented in Fig. 12.13 for the temperature range 685 to 530°C – the latter temperature being 25° below the melting point. Also shown are data (triangles) obtained during the last eight weeks of the experiment which represent long equilibration periods before measurement. These periods ranged from 5 to 75 hr, depending on the temperature, often with repeated monitoring to ensure that true equilibrium had been attained. The absence of long-term drift in the data is an indication that no corrosion sufficient to affect the results occurred. Data obtained during the first several days of the experiment (not shown) varied from day to day, with points falling on both sides of the curve. This behavior is possibly due to the slow migration to the surface and evolution from the melt of inert-gas microbubbles too small to be visible. The extreme viscosity of this material reflects, in slow motion, effects which normally would have terminated before measurement began.

The curve shown in Fig. 12.13 is represented by

$$\ln \kappa = -21.32\,(\pm 2.57) - \frac{7939\,(\pm 1124)}{T} + 0.01855\,(\pm 0.00146)T,$$

where T is in degrees Kelvin and the values in parentheses are standard errors of the parameters. This equation was obtained by a least-squares computer fit to equally weighted values of $\ln \kappa$, which corresponds to assigning constant relative errors to values of κ. The standard deviation of fit was 0.0213 (±2% in κ). The one previous investigation of specific conductance in this system[75] contained one datum near the temperature range encompassed here. It differed by approximately 30% from our extrapolated value. However, viscosities obtained with the same apparatus have been shown to be in error.[77]

Specific conductance data were combined with the density data of Cantor[70] to yield equivalent conductances Λ, shown in Fig. 12.14 ($\Lambda = \kappa \times$ equivalent weight/density). Although the curvature of this plot indicates non-Arrhenius behavior, the curvature is in the wrong direction to correspond to "glass-transition–zero-mobility" concepts. Empirically fitting an equa-

[75] J. D. Mackenzie, *J. Chem. Phys.* 32, 1150 (1960).

[76] P. H. Dike, *Rev. Sci. Instr.* 2, 379 (1931).

[77] C. T. Moynihan and S. Cantor, *J. Chem. Phys.* 48, 115 (1968).

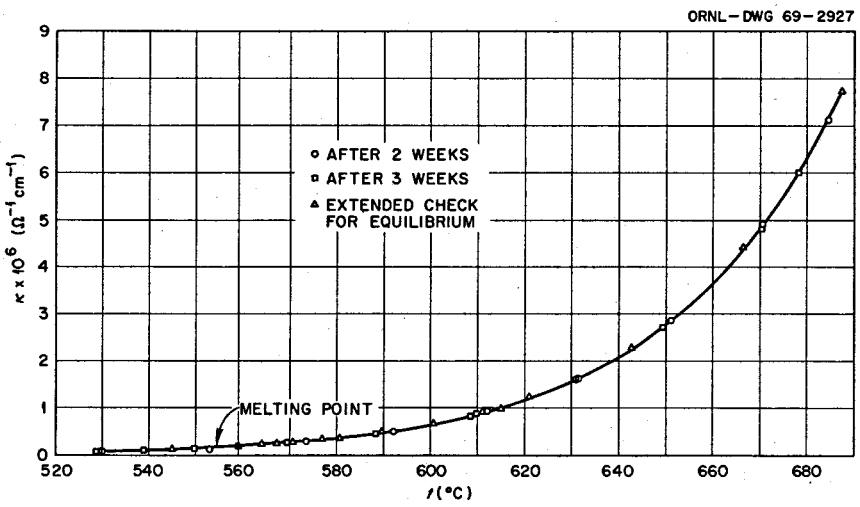

Fig. 12.13. Specific Conductance vs Temperature (°C) for Molten BeF_2.

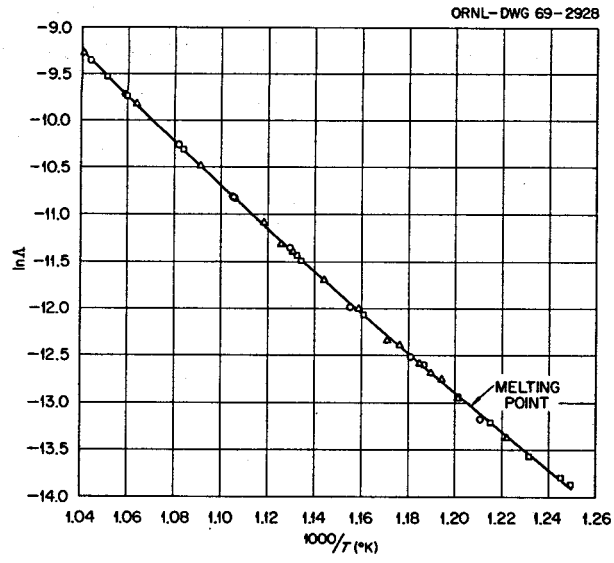

Fig. 12.14. Natural Logarithm of Equivalent Conductance vs Reciprocal Temperature (°K) for Molten BeF_2.

tion of the form employed with the specific conductance data gives (σ = 0.0211)

$$\ln \Lambda = -18.63\,(\pm 2.55) - \frac{8038\,(\pm 1115)}{T} + 0.01846\,(\pm 0.00145)T\,.$$

Constraining a linear Arrhenius-type equation to fit the data results in an "average" energy of activation for equivalent conductance of 44.1 (±0.3) kcal/mole.

Since neither the possibility of conductance by minor impurities nor by more than one mechanism, as has been proposed for molten $BeCl_2$,[78] can be excluded, we await results extending the lower limit of temperature before attempting further interpretation of these data. An electrode configuration consisting of large parallel platinum foils is currently under construction. This assembly will result in considerably lower measured resistances, which will permit investigation further into the supercooled region. In addition, charging the conductance cell with different samples of beryllium fluoride, which will have different levels of trace impurities, should help clarify their possible role in the conduction process.

[78] K. Ohmae and T. Kuroda, *J. Electrochem. Soc. Japan* 36, 163 (1968).

13. Chemistry of Molten-Salt Reactor Fuel Reprocessing Technology

Current design of the two-region, single-fluid MSBR includes provisions for chemically reprocessing the reactor fuel for isolation of ^{233}Pa and for removing rare-earth fission products. Development efforts for these processes have pursued the reductive extraction concept whereby constituents of the fuel salt are selectively extracted into molten bismuth containing either lithium or thorium as the reducing agent. The chemical feasibility of ^{233}Pa isolation has been demonstrated by a process which also requires the prior reduction of uranium from the salt mixture and its subsequent oxidation into the salt effluent of the ^{233}Pa extraction column. Chemical researches are engaged in further evaluation of the supporting equilibrium data and in determination of the chemical behavior of those fission products and salt impurities which will be simultaneously extracted in the ^{233}Pa isolation process.

The rare-earth removal process will likely utilize the barren salt effluent of the ^{233}Pa isolation process. Although the chemical feasibility of the salt-bismuth extraction process for removal of rare earths has been demonstrated, their separation from thorium, a major constituent of the salt phase, may be insufficient for engineering design purposes. Present studies seek other molten-metal systems, metal additives to bismuth, and varied process applications to achieve improved rare-earth separations.

13.1 SIMULTANEOUS EXTRACTION OF ZIRCONIUM AND URANIUM AND OF ZIRCONIUM AND PROTACTINIUM

D. M. Moulton J. H. Shaffer

It is known that the solubility in bismuth of uranium and zirconium together is much less than when they are separate. For example, Weinberg *et al.*[1] report the solubility of uranium at 400°C to be about 1400 ppm, while at 210 ppm zirconium it falls to under 1100. (Zirconium solubility by itself is about 360 ppm.) From these data it is not possible to make an accurate extrapolation to 600°, but the effect of zirconium on uranium solubility seems to rise slightly with higher temperatures. Zirconium is produced in large amounts as a fission product. Earlier work[2] had indicated that it would be extracted from LiF-BeF_2 (66-34 mole %) a little less easily than uranium.

It is important to know where zirconium will extract in a single-fluid reactor salt and also whether there will be any interaction with uranium in the bismuth phase, affecting either the extractability or the solubility. These systems have been investigated in the single-fluid salt LiF-BeF_2-ThF_4 (68-20-12 mole %). Zirconium analyses, which had been a source of trouble earlier, were made by counting the ^{95}Zr on a lithium-drifted germanium diode, which will resolve this peak from that of its daughter, ^{95}Nb. Chemical and spectrochemical analyses for zirconium gave generally good checks with this method. Graphite apparatus was used throughout.

In the first experiment 2.97 kg of salt containing 6.06 g of labeled zirconium as ZrF_4 was extracted with 3.00 kg of bismuth at 600 and 700° using portions of thorium metal as the reductant. About 6.2 g of uranium metal was next added, and the system was hydrofluorinated to oxidize the uranium and the zirconium. The reduction was then repeated as before. In the second experiment, 3.97 kg of salt with 6.05 g of zirconium and about 1 mc of ^{233}Pa was extracted with 3.00 kg of bismuth in the usual fashion at 600 and 700°.

In the first part of the first experiment, the object was to determine the extractability of zirconium alone. The reduction potential difference between lithium and thorium was 0.09 v lower than had been found several times before in this salt. It seemed that abnormally high

---

[1] A. F. Weinberg *et al., Trans. Met. Soc. AIME* **221**, 83 (1961).

[2] *Reactor Chem. Div. Ann. Progr. Rept. Dec. 31, 1967*, ORNL-4229, p. 41, and unreported work from this experiment.

lithium values were responsible, so this voltage has been added to both the Li-Th and Li-Zr potentials. No such anomaly appeared at 700°. Zirconium balance was good throughout the experiment. The potentials found in the first half of this experiment are as follows:

Temperature (°C)	$E'_{0Li} - E'_{0Th}$	$E'_{0Li} - E'_{0Zr}$	$E'_{0Th} - E'_{0Zr}$
600	−0.426 ± 0.060	−0.597 ± 0.077	−0.145 ± 0.047
700	−0.433 ± 0.027	−0.615 ± 0.027	−0.166 ± 0.053

Ferris *et al.*[3] report $E'_{0Th} - E'_{0Zr} = -0.25$ at 600° for a somewhat different salt (69.2-19.4-11.4 mole %) of higher free fluoride content.

The potentials found in the second half of this experiment are listed below:

Temperature (°C)	$E'_{0Li} - E'_{0Th}$	$E'_{0Li} - E'_{0Zr}$	$E'_{0Zr} - E'_{0U}$	$E'_{0Th} - E'_{0Zr}$
600	−0.452 ± 0.053	−0.597 ± 0.080	−0.017 ± 0.009	−0.128 ± 0.049
700	−0.476 ± 0.053	−0.638 ± 0.070	−0.003 ± 0.015	−0.168 ± 0.056

Within the error of the measurements there is no difference in the zirconium behavior with and without uranium. The zirconium and uranium balances were not good, however. The maximum of these found in the metal (when they were essentially gone from the salt) was about 900 and 1400 ppm, respectively, or 45 and 67% of that present and 30 and 10% of saturation at 600°. We had reached 1900 ppm zirconium, or 95% of that added, in the first part of the experiment. Ferris[4] reached 2900 ppm uranium and 2200 ppm zirconium at 600° using filtered samples. He found $E'_{0Th} - E'_{0Zr} = -0.243$ and $E'_{0Zr} - E'_{0U} = -0.002$ in a salt of composition 72-16-12 mole %.

In the zirconium-protactinium extraction the effect of zirconium on protactinium could be observed but not the converse, since only tracer protactinium was used. The potentials are shown in the table. In the last column are shown the potentials obtained in an earlier protactinium-uranium extraction from the same salt.

Here again there is no difference within the accuracy of the measurements. Protactinium balance was good throughout the experiment. The maximum zirconium concentration in the metal (1900 ppm) was not far from the 2020 ppm added originally. From the protactinium-zirconium difference in this experiment and the protactinium-uranium difference in the older one, one can find $E'_{0Zr} - E'_{0U} = -0.018$ at both 600 and 700°; this is derived from experiment where uranium and zirconium were present separately and is about the same as that where they were together.

The error limits on these experiments prevent any positive claims of solute-solute interaction in these experiments. Nevertheless, there is some indication that protactinium is easier to extract in the presence of zirconium and that zirconium and uranium are both harder to extract when together than when separate. Protactinium-zirconium separation should be quite easy; the uranium-zirconium separation may be rather difficult.

13.2 PROTACTINIUM STUDIES IN THE HIGH-ALPHA MOLTEN-SALT LABORATORY

C. J. Barton R. G. Ross

Part of the data obtained from an experiment (8-20-68) in which the single-region fuel salt LiF-BeF_2-ThF_4-UF_4 (72-16-12-0.25 mole %) containing 100 ppm ^{231}Pa was equilibrated with Bi-Th alloy in a molybdenum container was reported previously.[5] The experiment was conducted in two parts (1 and 2). Initially (part 1) sufficient thorium was added to the bismuth to reduce all the UF_4 and PaF_4 to the metals and leave an

Temperature (°C)	$E'_{0Li} - E'_{0Th}$	$E'_{0Th} - E'_{0Pa}$	$E'_{0Th} - E'_{0Zr}$	$E'_{0Pa} - E'_{0Zr}$	$E'_{0Pa} - E'_{0U}$
600	−0.440 ± 0.021	−0.148 ± 0.016	−0.165 ± 0.040	−0.085 ± 0.004	
700	−0.435 ± 0.028	−0.152 ± 0.004	−0.209 ± 0.025	−0.082 ± 0.011	
600	−0.422 ± 0.013	−0.128 ± 0.015			−0.067 ± 0.025
700	−0.434 ± 0.019	−0.138 ± 0.006			−0.064 ± 0.029

[3] Private communication, Dec. 2, 1968.

[4] Private communication, Feb. 3, 1969.

[5] *MSR Program Semiann. Progr. Rept. Aug. 31, 1968*, ORNL-4344, pp. 184–85.

Table 13.1. Separation Factors for Uranium and Protactinium Between LiF-BeF_2-ThF_4 (72-16-12 Mole %) and Bi-Th Alloy

Experiment	Temperature (°C)	Average $X_{Th}(Bi)$	α_{Th}^{U}	α_{Th}^{Pa}	α_{Pa}^{U}
		$\times 10^3$			
Part 1	630	1.26	25,800	1680	15.4
Part 2A	630	1.67	25,300	1275	19.8
Part 2B	805	2.34	6,000	380	15.8

excess of 1700 ppm of thorium. This mixture was held at 630° for about seven days, during which time the only changes involved changing the sparge gas between argon and helium, flowing or static. The protactinium and uranium concentrations were essentially constant regardless of the sparge gas or flow condition. The protactinium and uranium were then returned to the salt phase by oxidation with H_2-HF, and reduction was again effected (part 2) but this time with incremental thorium additions. With the melt temperature at 630°C (part 2A) additions were continued until thorium solubility in bismuth at this temperature was exceeded. The temperature was then increased to 805°C and equilibrium reestablished (part 2B).

Separation factors,

$$\alpha_B^A = \frac{X_A(\text{Bi})\, X_B(\text{salt})}{X_B(\text{Bi})\, X_A(\text{salt})},$$

calculated for this experiment are shown in Table 13.1.

The large separation factors in the table confirm that uranium, protactinium, and thorium can be effectively separated in a fuel processing plant using the reductive extraction method.

13.3 FURTHER STUDIES OF THE REDUCTIVE EXTRACTION OF PROTACTINIUM FROM SINGLE-FLUID MSBR FUEL SALT BY THORIUM IN MOLTEN BISMUTH

R. G. Ross C. E. Bamberger C. F. Baes, Jr.

Successful reductive extraction of ^{231}Pa at the 100-ppm level from a single-region MSBR fuel composition by thorium in liquid bismuth has been demonstrated by Ferris *et al.*[6] and by Barton *et al.* (Sect. 13.2). Additional measurements have since been undertaken by us to help determine accurately the equilibrium quotient for the extraction reaction

$$Pa^{4+}(F) + Th^0(Bi) \rightleftharpoons Pa^0(Bi) + Th^{4+}(F), \qquad (1)$$

$$Q_{Th}^{Pa} = \frac{X_{Pa^0}(\text{Bi})/X_{Pa^{4+}}(\text{F})}{X_{Th^0}(\text{Bi})/X_{Th^{4+}}(\text{F})},$$

and to determine also whether this quotient depends significantly on the concentration of Pa^0 and/or U^0 in the bismuth phase. While the previous studies indicate that reproducible results should be obtained when molybdenum is used as a container material, such data in fact have been difficult to obtain. These additional measurements therefore seemed especially desirable in view of the importance of good equilibrium data to the development of a fuel reprocessing method employing reductive extraction.

The present measurements were performed in a molybdenum-lined nickel vessel (Fig. 13.1) equipped with a gas lift to provide improved mixing of the phases. (Tests in a silica container revealed that gas sparging alone produces negligible mixing of molten bismuth into the molten fluoride.) To avoid the possibility that appreciable amounts of impurities such as water or oxygen might be introduced by a once-through sparging gas system, a recirculating gas system was used. The circuit included a neoprene-diaphragm pump, the gas lift in the extraction vessel, a fritted nickel filter in the gas exit line, an NaF trap (for any trace of HF), and an $Mg(ClO_4)_2$ trap. The experiments were performed at 625°C ± 2° using ~250 g of single-region salt (LiF-BeF_2-ThF_4, 72-16-12 mole %) to which initially ^{231}Pa and ^{233}Pa were added and later 0.25 mole % UF_4 was added. This was hydrofluorinated in situ together with 250 g of bismuth in the molybdenum liner. Hydrogen gas sparging for 4 to 6 hr followed, and then the hydrogen was replaced by argon at 4 to 5 psig before recirculation was started. Crystal bar thorium metal was added as the reducing agent. Stainless steel filter sticks were used for sampling the bismuth phase, and copper filter sticks were used for sampling the salt phase. Molybdenum filter sticks were also fabricated and tested by sampling both phases. These, unlike filter sticks of stainless steel or copper, are fully compatible with both phases. They were mechanically satisfactory, and the surface oxide can be easily reduced with hydrogen at 1000°C.

Thus far, two successful runs have been made in the absence of uranium and one with uranium present. In the first series of measurements it was found, surprisingly, that quite large amounts of thorium could be

[6] L. M. Ferris, *MSR Program Semiann. Progr. Rept. Aug. 31, 1968*, ORNL-4344.

added to the bismuth phase – $X_{Th^0}(Bi)$ calculated to reach 0.0014 – with very little protactinium extraction, and even this small amount decreased slowly with time. It was surmised that the thorium was consumed by an oxidizing impurity present in relatively large amounts. The contents of the vessel were re-treated with HF-H_2 and hydrogen. After this second treatment, thorium metal additions produced protactinium extractions in the absence of uranium (Fig. 13.2) which agree well with results obtained previously by Barton in the presence of 0.26 mole % UF_4. (The cause of the initial thorium consumption without protactinium extraction, we are tempted to speculate, was molybdenum oxide, initially present and not completely reduced in the initial treatment of the salt.) Uranium tetrafluoride was then added to bring its concentration in the salt phase to 0.25 mole %, and the thorium additions were continued. Again the results compare well with those obtained by Barton (Fig. 13.3). The favorable comparison in Fig. 13.2 is based on material balance calculations of the thorium concentration in bismuth (allowing for the consumption of Th^0 by Li and Pa

ORNL-DWG 69-2234

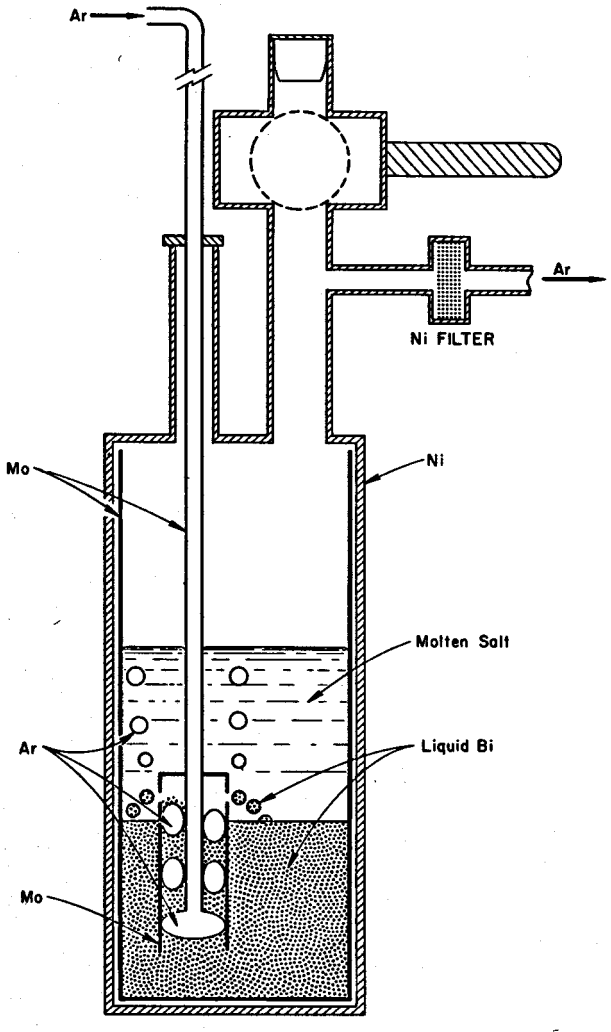

Fig. 13.1. Vessel for Reductive Extraction Experiments.

ORNL-DWG 69-2235R

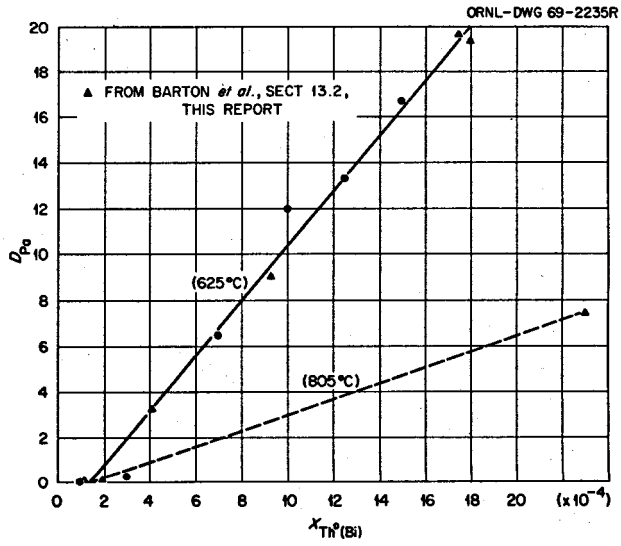

Fig. 13.2. Variation of Pa Distribution Coefficient with Mole Fraction of Thorium in the Bismuth Phase.

ORNL-DWG 69-6654

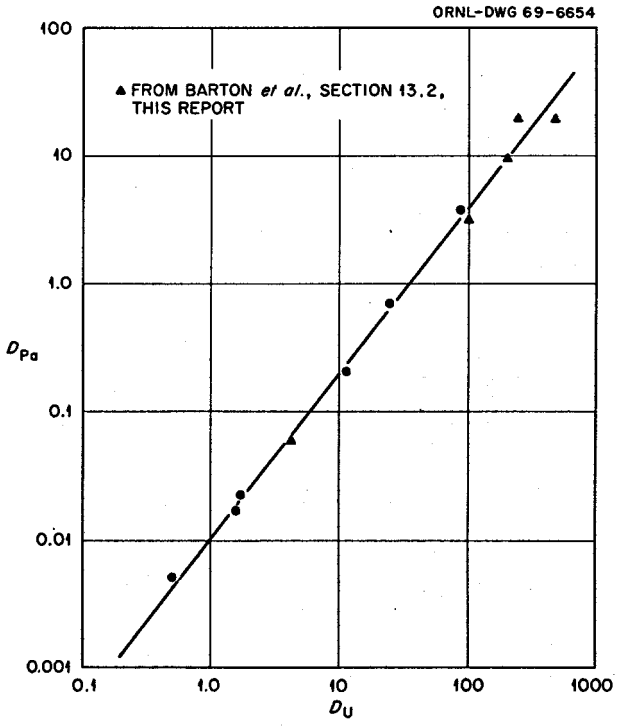

Fig. 13.3. Variation of Pa Distribution Coefficient with U Distribution Coefficient.

reduction) for the present results and on direct thorium analysis for Barton's results.

Interestingly, it appears that in all these measurements, $\sim 10^{-4}$ mole fraction of thorium was ineffective in extracting protactinium. This could have been caused by a small amount of some unknown substance, present in reproducible amounts in the bismuth, which combined with this much thorium, the product remaining in solution. A more likely possibility, we believe, is that this effect is caused by ZrF_4 which was present initially in the salt at ~150 ppm. This should have been extracted by the thorium and could then have been mistaken for thorium in the subsequent colorimetric determinations. It would be included as well in the material balance calculation of the thorium in the bismuth phase.

The correlation of D_{Pa} vs D_U, where $D_M = X_{M(Bi)}/X_{M(F)}$, in Fig. 13.3 is excellent, giving the expected slope of $4/3$, which confirms that protactinium is tetravalent and uranium is trivalent under these extraction conditions. This correlation further indicates that interactions of U^0 and Pa^0 do not occur in the bismuth phase at the concentration levels involved. From the results in Figs. 13.2 and 13.3 we have:

$$Q_{Pa}^{U} = D_U^{4/3}/D_{Pa} = 121\,(625°C)\,,$$

$$Q_{Th}^{Pa} = D_{Pa}/D_{Th} = 1450\,(625°C)\,.$$

One result reported by Barton *et al.* may be used to calculate

$$Q_{Th}^{Pa} = 414\,(805°C)\,.$$

The two results are given within their uncertainty by

$$\log Q_{Th}^{Pa} = 2830/T\,.$$

This would indicate that ΔS for the extraction reaction (1) is zero, a result which could well be general for such reactions which involve ions of similar size and valence in the salt phase and metal of similar character in the bismuth phase. The value of Q_{Th}^{Pa} is unaffected by the presence of up to 7000 ppm uranium in the bismuth phase.

In our future measurements we expect to extend the present study to include the extraction behavior of protactinium and uranium when they are both present at high concentrations (e.g., 1500 ppm each) in the bismuth phase.

13.4 REDUCTIVE EXTRACTION OF RARE EARTHS FROM MOLTEN MIXTURES OF LiF, BeF_2, AND ThF_4 INTO BISMUTH

D. M. Moulton J. H. Shaffer

Studies of the equilibrium distribution of cerium, neodymium, and samarium between the simulated MSBR solvent mixture, LiF-BeF_2-ThF_4 (72-16-12 mole %), and bismuth have been completed. Values for their distribution coefficients, D_{Ln}, and their separation factors, D_{Ln}/D_{Th}, at 600 and 700°C when the bismuth was saturated with thorium are as follows:

Rare Earth	600°C		700°C	
	D_{Ln}	D_{Ln}/D_{Th}	D_{Ln}	D_{Ln}/D_{Th}
Cerium	0.077	3.67	0.157	2.64
Neodymium	0.051	2.43	0.142	2.68
Samarium	0.045	2.14	0.082	1.55

These separation factors are based on $D_{Th} = 0.021$ at 600°C and $D_{Th} = 0.053$ at 700°C.

The investigation of salt composition effects on the reductive extraction of cerium into bismuth was extended to two additional salt compositions.[7] In the mixture LiF-BeF_2-ThF_4 (67-30-3 mole %), the extraction of cerium by thorium can be described by the equation

$$K = D_{Ce}^4/D_{Th}^3 = 8.2 \text{ at } 600°C\,.$$

At the limiting reduction potential of thorium saturation in bismuth, the distribution coefficient for cerium is about 0.26 and the separation factor is about 3.2 at 600°C. The equilibrium distribution of cerium between the salt solvent mixture, LiF-BeF_2-ThF_4 (76.8-6.2-17 mole %), and bismuth yielded a value of about 5.3 for the equilibrium constant K at 600°C. At thorium saturation in bismuth, the distribution coefficient for cerium is about 0.064 and its separation factor is about 4.4 at 600°C. This salt composition was proposed for a reprocessing scheme which would precede the reductive extraction process by a vacuum distillation process. The experimental results obtained for both of these salt mixtures are in fair agreement with the "free fluoride" model of M. A. Bredig for describing salt solvent effects on the extraction equilibrium.

[7] *MSR Program Semiann. Progr. Rept. Aug. 31, 1968,* ORNL-4344, p. 176.

13.5 METAL PHASES OTHER THAN BISMUTH FOR RARE-EARTH EXTRACTION

D. M. Moulton J. H. Shaffer

By now it is well known that the extraction of rare earths from thorium-containing molten fluorides into bismuth requires large bismuth volumes, because of the low solubility of thorium, and gives rather small rare-earth–thorium separations. While it is possible to design a reprocessing facility using this system, there could be practical advantages in changing the metal phase to reduce one or both of these difficulties.

There is not a good theoretical basis for choosing an alternative metal system, though, as discussed presently, our understanding of the nature of these mixtures is growing. We have investigated a number of combinations using a new technique, shown in Fig. 13.4. A 2-g sample of the metal contained in a small graphite cup serves as the cathode for the electrolytic reduction of labeled cerium from a 3.9-kg melt of $LiF\text{-}BeF_2\text{-}ThF_4$ (68-20-12 mole %) at 700°. A beryllium rod is used as a sacrificial anode and also as a reference at zero current. After a few hundred milliampere-hours of electrolysis (the exact time is determined, somewhat intuitively, when the potential levels out), the entire metal sample is removed and analyzed. The amount of material extracted does not affect the salt composition significantly, so it can be reused many times. The pool of bismuth in the bottom of the steel vessel extracts some of the thorium daughters (Pb-Bi-Tl) which might otherwise confuse the radiochemical analysis; it is not sampled or used in any other way.

This method is useful for screening metal combinations because it takes only a few hours per sample, in contrast to the old way where a large metal pool was in the bottom and a new vessel and salt had to be prepared for each combination. So far we have not been able to get very quantitative results because we cannot determine the point of thorium saturation very well and any precipitate is necessarily included with the sample. For this reason the metals are here simply grouped into the three categories listed in Table 13.2: those extracting more, about the same (within a factor of 2), and less cerium than pure bismuth (per weight of solvent metal).

It will be noted that Bi-Au is not a good extractant, in contrast to what had been reported earlier.[8] In the present experiment the solvent contained 30% gold rather than 3% and apparently has rather different

[8] *MSR Program Semiann. Progr. Rept. Aug. 31, 1968,* ORNL-4344, p. 180.

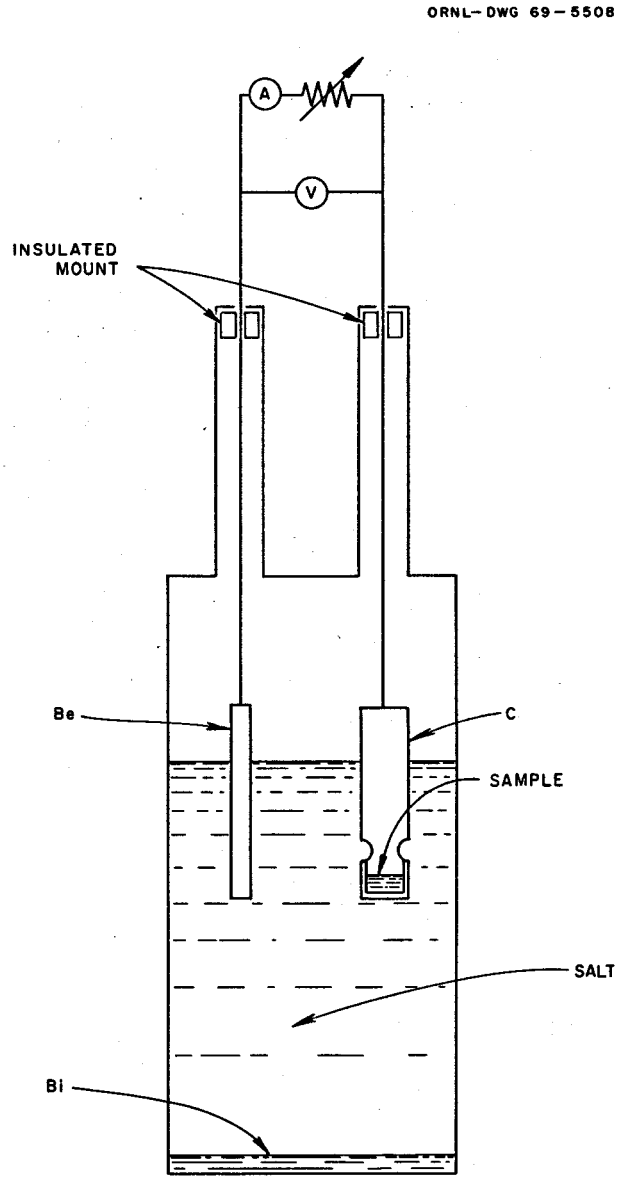

Fig. 13.4. Electrolytic Apparatus for Alloy Testing. Gas lines, valves, furnace, etc., not shown.

Table 13.2. Extraction of Ce from $LiF\text{-}BeF_2\text{-}ThF_4$ (68-20-12 Mole %) at 700° into Various Metals

More than Bismuth	Same	Less
Mg-Ag, Mg-Cu, Al-Ag, Al-Au, Al-Cu	Sn, Bi, In-Au, Sn-Cu	Bi-Ag, Sn-Au, Bi-Sb, Bi-Au, Pb-Au, Zn, Bi-Pt, Ge-Au, Pb, Sn-Ag, Pb-Ag

properties. The Sn and Sn-Cu both contained amounts of Th far in excess of the saturation value for pure Sn. $ThSn_3$ undoubtedly precipitated, and the high cerium count probably is due to a solid solution of $CeSn_3$ in this; the structure is the same (Cu_3Au), and the lattice parameters are practically identical. We did not really expect the tin-, lead-, and zinc-based systems to be very good, but this was based on reasoning too speculative to exclude such easy experiments.

The magnesium- and aluminum-based solvents, especially the former, extracted quite a lot of rare earth. The thorium content of the aluminum was also high (the Mg was not analyzed by this writing). Cerium separation in these systems is probably lower than in bismuth. Thus they may be better suited for removing the thorium and leaving rare earths behind. The investigation of these and other metal combinations is continuing.

In addition to the experimental results, increasing familiarity with liquid-metal systems in general allows us to make certain observations on the possible alternatives to bismuth. Ideally one would like a liquid-metal system which will form strong intermetallics with the rare earths and weak ones or none with thorium. Thorium and the rare earths are similar enough as metals so that this solvent probably does not exist, at least not if it contains one of the low-melting nontransition metals. Starting with bismuth, we can consider what additives might stabilize the rare earths more than thorium. Alkalis and alkaline earths will not help. Metals in the first half of the transition series are likely to be of little use and are scarcely soluble anyway. Those in the second half will form intermetallics with rare earths and thorium, but the thorium compounds will probably be stronger, except perhaps for the coinage metals. Many of these compounds owe their stability to geometric structures which will not persist in dilute solution. Posttransition metals form increasingly strong compounds with partially ionic bonding. Here the stabilization of the rare earths will be somewhat greater, as is seen with bismuth. To be useful, however, the relative stabilities of the rare-earth and thorium intermetallics must be such as to overcome the substantial difference in stability of rare-earth and thorium fluorides. A large enough difference between rare-earth and thorium alloys will probably not be found in the more electropositive metals to the left of bismuth. Of the elements which might form stronger compounds than bismuth, antimony seems to go in the wrong direction, and arsenic, selenium, and tellurium have not been tried. It is very likely that these considerations will apply to extraction systems based on any of the posttransition elements. In all of these the solubility of the thorium intermetallics is a problem, and stronger intermetallics may be less soluble still. The preliminary experimental results with lead, zinc, tin, germanium, and indium are in agreement with these predictions.

It is not likely that there will be any solvents based on the ordinary transition metals with low enough melting points to be useful, though there are some interesting eutectics of cerium with 15 to 30% of the elements from Mn to Cu and also Ag and Au that melt at 400 to 600° and should dissolve Th very well. They will probably be rather strong reducing agents and will pose severe containment problems.

Of the pretransition metals, only Mg and Al are worth considering. These are the only good pure solvents for thorium if Hg and Pu are excluded as impractical. They are both quite active and will reduce the salt to some extent, especially magnesium; thus some alloying to lower their activity may be useful. However, this may also lower the thorium solubility.

In general, then, it looks as though improvements in reductive extraction will be fairly small as long as bismuth is used as the basis for the solvent. Of course, small improvements could be very welcome. The use of entirely different solvent systems containing magnesium, aluminum, or cerium could result in much higher thorium and rare-earth extraction, but there would be some contamination of the salt by these metals.

13.6 SEPARATION OF CERIUM FROM THORIUM IN BISMUTH BY COLD ZONE DEPOSITION OF THORIUM BISMUTHIDE

D. M. Richardson W. R. Grimes J. H. Shaffer

In experiments conducted thus far on the reductive extraction of rare earths from $LiF\text{-}BeF_2\text{-}ThF_4$ mixtures into bismuth, separation factors (D_{Ln}/D_{Th}) of less than 10 have been found under equilibrium conditions and at temperatures from 500 to 800°C. Although these values may be sufficient for reprocessing the MSBR fuel solvent by the reductive extraction process, much higher values could greatly improve the plant efficiency. Accordingly, various parameters of the extraction process principle are being investigated to improve its application to the reprocessing requirements of the MSBR. To this end, an experiment is now in progress to examine the cold zone deposition of thorium from bismuth which also contains a dissolved rare earth. The chemical feasibility of this application will depend on the precipitation of pure $ThBi_2$ rather than a coprecipi-

tation with the metallic rare earth. The experimental procedure embodies the extraction of cerium from a simulated MSBR fuel solvent at 700°C into flowing bismuth and its back extraction by hydrofluorination into a recovery salt mixture, as shown schematically in Fig. 13.5. The recirculating bismuth stream will be contacted with solid thorium bismuthide at 700°C to achieve its saturation with thorium. The exit stream from the extraction vessel will pass through a cold trap (outlet temperature of about 400°C) before flowing to the recovery vessel. Thus the comparative transport of cerium and thorium to the recovery salt will indicate the effectiveness of the cold zone deposition application. At the conclusion of the experiment the cold trap will be drained of bismuth and sacrificed for analyses of its cerium content and possibly the composition of the precipitating phase.

The objectives of this experiment have resulted in the construction of a simple pump loop which utilizes an electromagnetic device to achieve low flow rates of

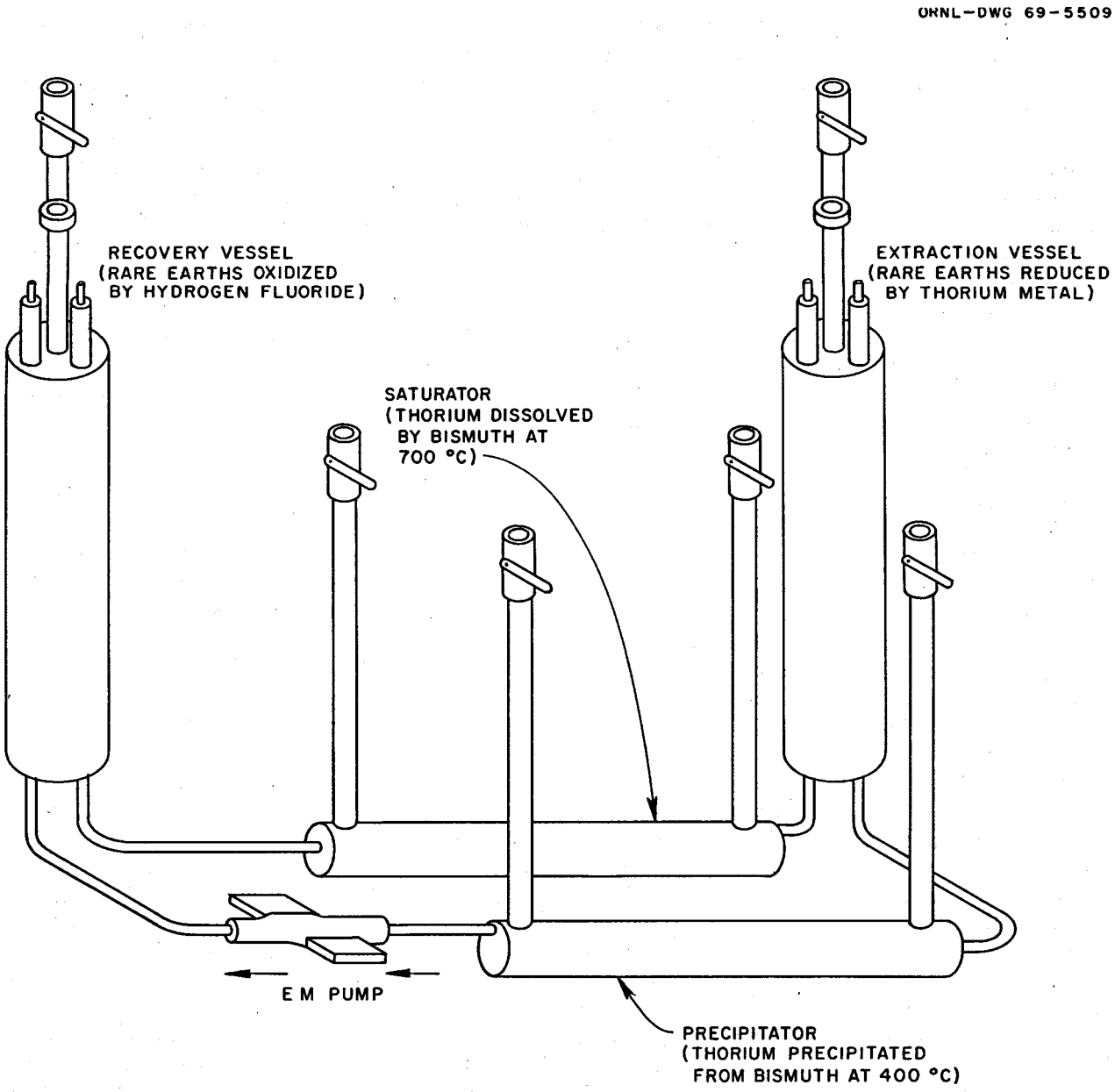

Fig. 13.5. Circulating Bismuth Loop for Separating Thorium from Rare Earths by Cold-Zone Deposition.

bismuth. The hot trap and cold trap are of identical construction and depend upon tightly packed stainless steel demister material (Yorkmesh) for the retention of solids. Each trap is equipped with Calrod heaters and will be cooled by a countercurrent flow of an external air-water stream. The extraction and recovery vessels were fabricated from 4-in. iron pipe size (IPS) 304L stainless steel pipe and are fitted with graphite cylinders of $\frac{1}{8}$-in. wall thickness for primary containment of the salt mixtures. Bottom penetrations provide for the circulation of bismuth through each vessel, while top penetrations provide for loading and sampling procedures.

The experimental assembly contains approximately 35 kg of bismuth, which provides an approximate 1-in. depth of bismuth in each vessel. The fuel solvent mixture will be simulated by approximately 2 kg of LiF-BeF_2-ThF_4 (68-20-12 mole %) which contains 100 ppm cerium and about 5 mc of ^{144}Ce activity. Because of relatively large requirements, thorium will be introduced into the bismuth system by reduction from LiF-BeF_2-ThF_4 (68-20-12 mole %) by added beryllium metal in the recovery section of the apparatus. When thorium reduction is complete, the recovery salt will have a composition of approximately 60 mole % LiF and 40 mole % BeF_2 and a liquidus temperature of about 450°C.

Experimental progress thus far has included the circulation of bismuth in the system with the EM pump at rates of about 50 to 200 cc/min, the addition of the recovery salt mixture, and hydrofluorination of the recovery salt while recirculating bismuth to remove oxides from the metal phase. Beryllium metal is currently being added to the recovery salt mixture incrementally to achieve thorium reduction. Upon ascertainment of near-complete removal of thorium from the recovery salt and its collection in the appropriate trap, the fuel solvent mixture will be loaded into the extraction vessel. The progress of the experiment will be monitored from radiochemical analyses of samples taken periodically from each salt phase and at four locations in the metal phase system. The results of chemical and spectrographic analyses of these samples for thorium, lithium, and beryllium will provide further description of the experimental results.

13.7 EXTRACTION OF THORIUM BY ELECTROLYTIC REDUCTION INTO FLOWING LIQUID LEAD FROM MOLTEN MIXTURES OF LiF, BeF_2, ThF_4, AND RARE-EARTH FLUORIDES

D. M. Richardson J. H. Shaffer

The experimental result of earlier unreported work was that rare earths did not reductively extract into lead from molten LiF-BeF_2 (66-34 mole %). A practical use of this finding may be that the separation of rare earths and thorium can be achieved by the reductive extraction of thorium into lead with the rare-earth fluorides remaining in the barren molten salt. Subsequently the thorium dissolved in lead would be back extracted by hydrofluorination into a clean melt of LiF-BeF_2, and the resulting salt mix would be suitable for the addition of uranium fluoride and recharging as single-region breeder reactor fuel. In the absence of thorium, rare earths can be effectively extracted from the barren salt into molten bismuth.

Since the chemical feasibility of such a procedure appeared promising, a small pump loop has been constructed to test this process in a dynamic, nonequilibrium system in which the reduction of thorium is effected by electrolysis. The entire system was constructed of stainless steel and was assembled by inert arc welding and is shown schematically as Fig. 13.6. The extraction and recovery vessels are vertically mounted 4-in. IPS tanks that are interconnected at the bottoms by two parallel, horizontal $\frac{3}{4}$-in. IPS lines. An ac electromagnetic pump is installed in one of the lines. The vessels are fitted with graphite sleeves of $\frac{1}{8}$-in. wall thickness for primary containment of the salt mixtures. Top penetrations provide for loading and sampling, gas sparging and venting, and insertion of insulated probes for electrolysis and level measurement.

The extraction vessel salt will be hydrogen sparged and will be exposed at its center to a noble-metal anode. A hydrogen-diffusion anode thimble of 75% palladium–25% silver has been constructed for trial in initial operation. The recovery vessel salt will be sparged with a mixture of hydrogen and hydrogen fluoride. In addition to salt, both vessels will contain approximately 2 in. of recirculating liquid lead. Since the vessels are separately sparged and vented, and because the relative

height of the liquid columns is sensitive to small differences in gas phase pressures, a liquid level interlock has been installed. When the liquid level in either vessel is depressed more than a preset amount, a level probe open circuit occurs which opens a fast-acting valve connecting the two gas volumes, turns off the pump, and disconnects power supplied to the anode. Manual reset is required.

The net effect of this process is to transfer the thorium fluoride in one container of salt to another, and the total mass of salt remains constant. In each container, however, there are large changes of salt volume and density from the beginning to the end of the transfer. Provision has been made to follow the progress of the transfer on a periodic basis by measurements of salt density using a bubble-pressure vs liquid-depth probe. Additionally, salt samples will be taken.

If the composition of the simulated MSBR fuel solvent is selected as $LiF\text{-}BeF_2\text{-}ThF_4$ (65-23-12 mole %), the reduction and removal of all thorium electrolytically (i.e., no added metals) would result in the binary mixture $LiF\text{-}BeF_2$ (73.8-26.2 mole %), which melts at about 625°C. However, the lead stream at saturation with thorium (~200 ppm) will contain about 10 ppm lithium. Thus, assuming a constant transport ratio of 1.66 mole of Li per mole of Th, the resulting binary salt mixture should contain about 66 mole % of LiF and the balance of BeF_2 and should melt at less than 500°C. Accordingly, this experiment will be conducted with these salt mixtures. Experimental status at this time is the successful operation of the pumped loop with a charge of hydrogen-fired lead. After additions of the appropriate salt batches, isothermal operation at 600°C will be initiated.

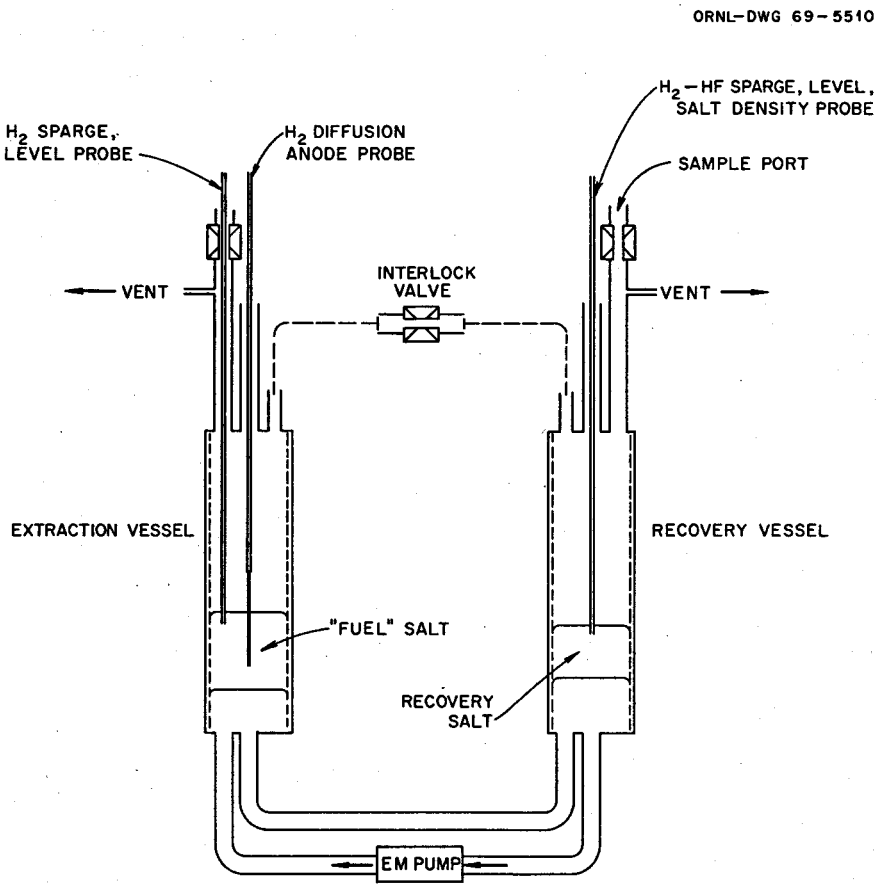

Fig. 13.6. Circulating Lead Loop Thorium Electrolyzer.

14. Development and Evaluation of Analytical Methods for Molten-Salt Reactors

J. C. White

14.1 DETERMINATION OF OXIDE IN MSRE FUEL

R. F. Apple J. M. Dale
A. S. Meyer

The first sample of the ^{233}U fuel (FP 17-5) was analyzed by the hydrofluorination procedure, and a concentration of 61 ppm was determined. A satisfactory recovery of oxide from an SnO_2 standard indicated that the apparatus was functioning reliably. This concentration does not differ significantly from that found through the ^{235}U operation (54 ± 8 ppm).

During the last few analyses a potential failure of the oxide apparatus was noted. Increasingly high pressures are required to maintain the flow of gas through the system during the hydrofluorination step. This increased Δp apparently occurs across the NaF trap that is used to separate HF from water in the effluent gas. It is assumed that during the repeated absorption and regeneration steps the absorbent particles degraded to form a more tightly packed bed, particularly at the entrance end of the trap. As these more closely packed particles swell during HF absorption, the flow is restricted.

The problem has not yet interfered with any analyses; but, on the basis of a rough extrapolation, only a few more analyses can be made before it will be necessary to replace the trap. The shutdown of the MSRE is imminent, and the replacement of the trap would be expensive and involve radiation exposure to personnel. It has been decided, therefore, to defer replacement at this time and to restrict determinations to essential MSRE samples. If the technique is applied to the in-line analysis of MSR salt streams, it will obviously be necessary to provide remotely replaceable traps.

14.2 DETERMINATION OF THE OXIDATION STATE OF CONSTITUENTS OF MSRE FUEL

J. M. Dale R. F. Apple
A. S. Meyer J. E. Caton
C. M. Boyd

The measurement of the redox condition of the ^{233}U fuel is currently the most important analytical development problem remaining for the MSRE. It is believed to influence corrosion rates, it affects the distribution of certain fission products within the reactor system, and it is readily adjustable via the addition of beryllium metal. Accordingly, the main development effort has been directed toward the development of techniques for this measurement. Three diverse approaches have been pursued.

14.2.1 Determination of Total Reducing Power of MSR Salts

A sealed-tube dissolution technique has been applied to the determination of the total reducing power of radioactive MSRE fuel. Preliminary feasibility studies of this approach are described elsewhere.[1] A special apparatus was required for this determination. The requirements were that the apparatus would provide a means of evacuation and sealing of the dissolution tubes and be compact enough to be transferred between hot cells. A photograph of the apparatus is shown in Fig. 14.1. Fragments of salt weighing about 250 mg are placed in a dissolution tube that is fitted with a break seal

[1] R. F. Apple and A. S. Meyer, *MSR Program Semiann. Progr. Rept. Aug. 31, 1968*, ORNL-4344, p. 189.

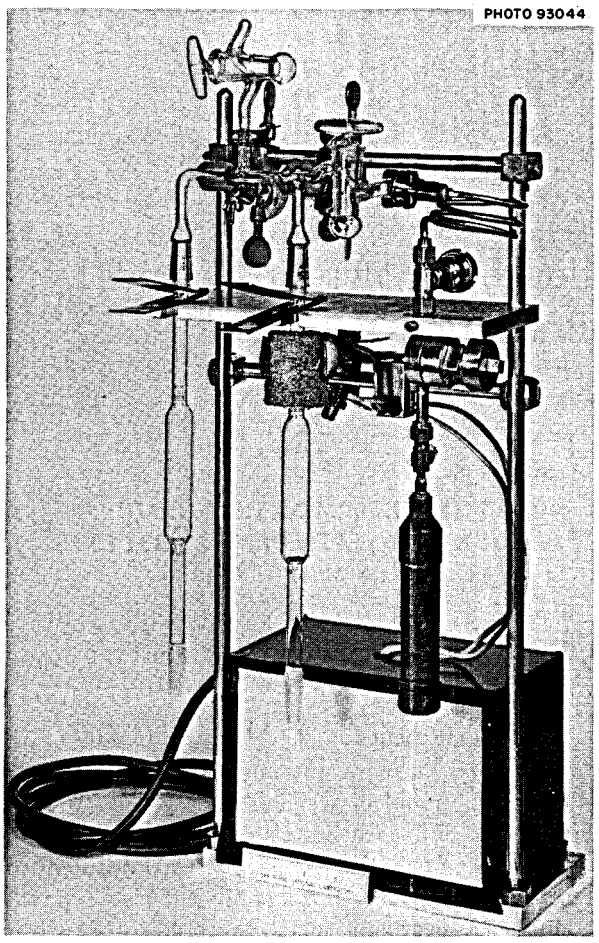

Fig. 14.1. Hot-Cell Apparatus for Total Reducing Power in MSRE Salts.

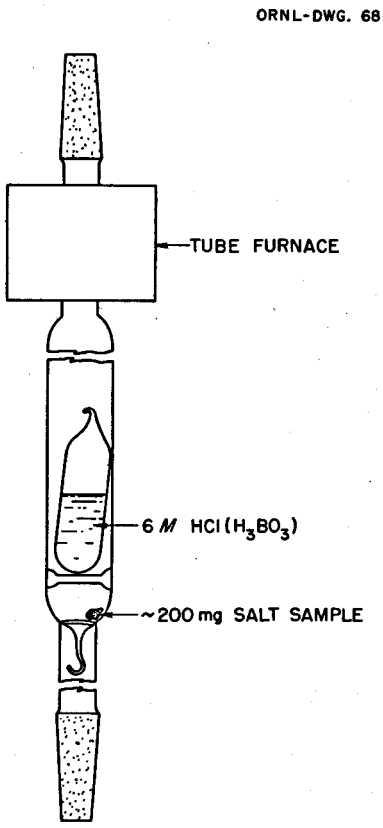

Fig. 14.2. Dissolution Bulb for Total Reducing Power in MSRE Salts.

and contains a thin-walled ampul containing about 6 ml of evacuated 6 *M* $HCl\text{-}H_3BO_3$ dissolver solution (see Fig. 14.2). The neck of the tube is then passed through the platinum-wound furnace and connected to the manifold via a standard taper joint. The dissolution tube is then evacuated with the cryogenic sorption pump (13X molecular sieve at liquid-nitrogen temperatures) and sealed off with the furnace. The ampul is broken by shaking, and the dissolution tube is sealed in a steel bomb and heated to 250°C under a suitable overpressure for 16 hr. When the dissolution is completed, the break-seal end of the tube is connected to the left-hand port of the manifold, and a receiver tube is connected through the furnace and evacuated. After the dissolver solution is frozen in liquid nitrogen, the break seal is broken, and the evolved hydrogen is distributed through the system. The receiver tube is also cooled in liquid nitrogen to minimize thermal diffusion effects, and a standard addition of helium (1 cc at 38 mm pressure) is made through the stopcock at the top of the apparatus. After a 15-min period of equilibration the receiver tube is sealed off and removed from the hot cell for mass spectrographic determination of the H_2/He ratio. The solution is transferred to an empty dissolver tube, which is sealed off and carried through the entire procedure to determine the amount of hydrogen generated by radiolysis.

A modification of the dissolution technique was necessary for hot-cell operations. The conventional technique of adding a weighed amount of dry ice to the bomb provides a suitable overpressure for laboratory dissolutions, but an undetermined quantity of the dry ice evaporates during the longer period required for remote sealing. Simulated tests indicated that approximately 50% of the dissolution tubes would be broken during hot-cell dissolutions. A comparison of the vapor-pressure curves of the common stable organic reagents with extrapolated values of

the pressures reported for 6 *M* HCl[2] revealed that the pressure of the dissolver solution was most closely paralleled by that of methyl alcohol. When 10 ml of methyl alcohol was sealed into the bombs, no breakage occurred.

The method was originally developed to determine free metals in the reprocessed solvent salt. When the apparatus was completed, uranium additions to the fuel had already been started, and an attempt was made to apply it to the determination of U(III). The results of the analyses of two fuel samples are summarized in Table 14.1.

During the period between samplings sufficient beryllium metal was added to the reactor fuel to increase the yield of hydrogen by 0.55 micromole/g. Also, some $LiUF_5$ fuel concentrate was added. The calculated increase in the hydrogen yields was not obtained. It is evident that the method in its present form is not suitable for the determination of U(III) in these samples. The hydrogen is derived predominantly from dispersed metal in the samples; and because a fragment that represents only about 2% of the sample is taken, any inhomogeneities in the distribution of the metals in the frozen salt would yield nonrepresentative samples. Also, the weighing and transfer of the salt fragments in the hot cell is time consuming, and this atmospheric exposure may introduce significant indeterminate oxidation errors.

The technique offers high sensitivity, and a specialized sampling approach will undoubtedly prove of value for reducing-power measurements of other types of MSRP samples. As time permits, studies will be resumed to determine its ultimate sensitivity and precision and to determine its limitations as to sample size and types of salts that can be dissolved.

14.2.2 Determination of U(III) in Radioactive MSRE Fuel by a Hydrogen Reduction Method

The application of this method to the determination of U(III) in the original ^{235}U fuel and the development of a remote method for the measurement of HF generated by the hydrogenation of the current ^{233}U fuel have been described previously.[3,4] When the precision of the remote determination of HF was demonstrated to be adequate for the measurement of HF in the effluent from the hydrogenation of ^{233}U fuel, an apparatus was assembled to simulate the hydrogenation of radioactive salt samples. This apparatus consisted of a copper block furnace fitted with a nickel liner of internal diameter equal to that of a sample ladle, appropriate sparging and exit tubes, and an addition port. The hydrogenator was heated with a precision furnace that maintained a temperature differential of less than 5°C over the region occupied by the sample. Provision was also made to change the depth of the melts to determine whether equilibrium was closely approached during the hydrogen transpirations.

Before salt was added to the hydrogenator, pulses of HF in a stream of hydrogen were passed through the system to determine the time constant of the apparatus. A portion of the HF was delayed in the apparatus. This delay is apparently caused by adsorption on the surface of the hydrogenator, since the effect becomes less pronounced when successive pulses are introduced. The period of delay is on the order of 1 hr and is the result of chemisorption, as the retention period increases with temperature. The adsorption is stronger on nickel than on copper surfaces. By comparison of the shape of the HF pulses with those of an unadsorbed gas, argon, the quantities of HF adsorbed were estimated to be about 2 to 3 micromoles. Adsorption of such quantities of HF would not introduce a significant error in the results of the analysis of the ^{235}U fuels, but a complex correction would be required for the lower yields expected from the ^{233}U fuel. It should be noted that while the adsorption of HF complicates batch analyses of the fuel, it would not interfere with in-line methods. Surfaces would become rapidly saturated, so that the steady-state concentra-

Table 14.1. Total Reducing Power of Fuel Salt

	Sample FP-15-5	Sample FP-15-25
Uranium, ppm	4730	7340
Nickel, ppm	46	51
Iron, ppm	140	140
Chromium, ppm	42	50
Total H_2, micromoles/g	4.07	3.69
Blank corr., micromoles/g	0.22	0.22
Nickel corr., micromoles/g	0.78	0.87
Iron corr., micromoles/g	2.51	2.51
Chromium corr., micromoles/g	0.11	0
U^{3+} equivalent	0.44	0.09
$U^{3+}/\Sigma U$, %	4.3	0.6

[2] Z. I. Simkhovich, *J. Appl. Chem. USSR* 30, 1312 (1957).

[3] J. M. Dale, R. F. Apple, and A. S. Meyer, *MSR Program Semiann. Progr. Rept. Aug. 31, 1967*, ORNL-4191, p. 167.

[4] J. M. Dale *et al.*, *MSR Program Semiann. Progr. Rept. Aug. 31, 1968*, ORNL-4344, p. 188.

tion of HF in the effluent would correspond to its rate of production in the fuel.

Investigation of the method was discontinued temporarily because the voltammetric method, described in the following section, gave promise of more immediate results.

14.2.3 Voltammetric Determination of U(IV)/U(III) Ratios in MSRE Fuel

An apparatus has been designed to permit electrochemical measurements in a sample of radioactive MSRE fuel. The objective of this work is to measure the potential ($E_{3/4}$) of the U(IV) to U(III) reduction wave vs the potential (E) of a platinum reference electrode which is poised by the bulk concentration of U(IV) and U(III) in the melt. The difference between these two potentials gives a measure of the U(IV)/U(III) ratio, as shown in Fig. 14.3. This has been verified in nonradioactive melts, and the experimental results are described in the next section of this report.

The electrochemical cell (Fig. 14.4) was designed so that the measurements could be made directly in the sampling ladle. The ladle is cut at a prescored point below the level of the salt, and the lower portion, which contains the bulk of the salt, is placed in a nickel liner. Both are then placed in the cell. This operation can be completed in about 5 min to minimize atmospheric contamination of the sample. The top of the cell is fitted with a Teflon bushing which is penetrated by three $\frac{1}{8}$-in. metal electrode support rods and a sparging tube. The electrodes (~50-mil platinum-rhodium wire) are sheathed with boron nitride insulators, which define their area and prevent electrical contact between electrodes or with the cell walls.

A cell identical to the one which is to be installed in the hot cell was used in the laboratory to carry out measurements on a sample of simulated MSRE fuel. It was shown that the U(III) in the molten salt was stable in the system and that a 5-min exposure of the surface of the solid salt to the atmosphere did not change the U(III) concentration upon remelting.

The electrochemical cell is being installed in the hot cell, and it is planned to make measurements on a sample of radioactive MSRE salt.

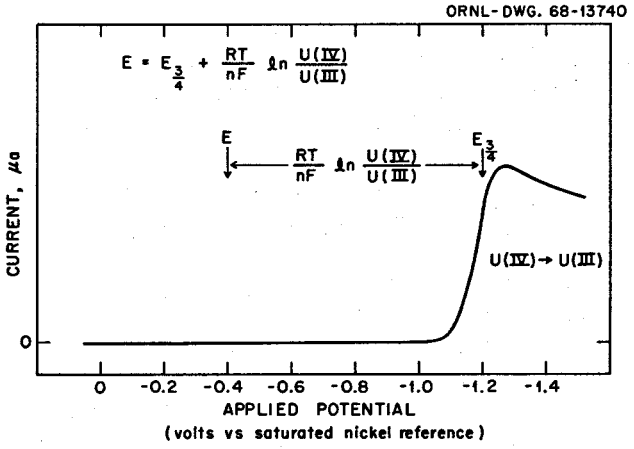

Fig. 14.3. Electrochemical Analysis of U(IV)/U(III).

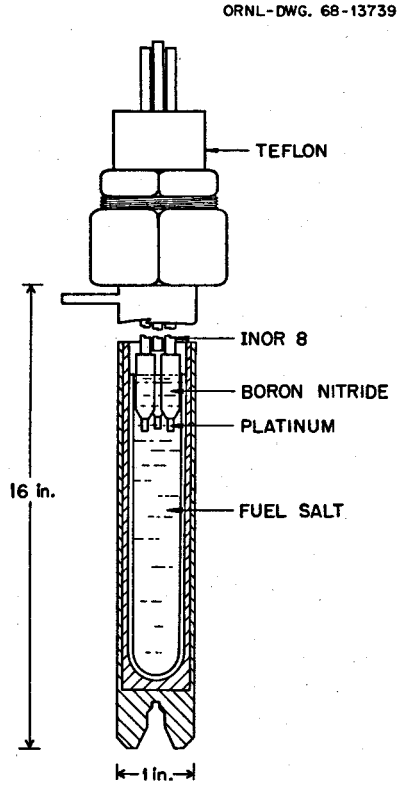

Fig. 14.4. Electrochemical Cell for U(IV)/U(III) Ratio Determination in MSRE Fuel.

14.3 EMF, VOLTAMMETRIC, AND SPECTROPHOTOMETRIC MEASUREMENTS ON THE U(IV)/U(III) COUPLE IN MOLTEN LiF-BeF_2-ZrF_4

H. W. Jenkins[5] D. L. Manning
Gleb Mamantov[6] J. P. Young

When the MSRE fuel is in a reducing condition, the U(IV)/U(III) couple determines the redox condition of the salt. The measurement of the U(IV)/U(III) ratio is therefore essential to a fundamental understanding of fuel chemistry.

Potentiometric determination of this ratio requires the value of the standard electrode potential of the U(IV)/U(III) couple relative to the standard electrode potential of a reference couple. The standard potential of the U(IV)/U(III) couple was calculated with respect to a hypothetical unit mole fraction Ni/Ni(II) electrode (arbitrarily set at 0.0 v) from emf measurements on the galvanic cell Pt|U(IV), U(III)||Ni(II)|Ni. The cell consisted of an Ni/Ni(II) reference electrode contained in a boron nitride compartment and a platinum wire immersed in a melt containing U(III) and U(IV). The cell potential was measured as a function of the U(IV)/U(III) ratio, which was varied by the controlled reduction of U(IV) to U(III) with a zirconium rod immersed in the solution. Measured cell potentials were corrected, using the Nernst equation, to values vs a unit mole fraction Ni/Ni(II) electrode. The corrected potentials were plotted vs log [U(IV)/U(III)]; the slope of a line through these points agreed well with the theoretical slope predicted by the Nernst equation. The standard potential of the U(IV)/U(III) couple, corresponding to a U(IV)/U(III) ratio of 1, was found to be 1.48 ± 0.01 v at 500°C.

A simple voltammetric method was also developed for the determination of the U(IV)/U(III) ratio, when U(IV) > U(III). This method should be generally applicable to the determination of the ratio Ox/Red, where Ox and Red are the oxidized and reduced forms of the reversible soluble couple Ox + ne = Red. The method involves the measurement of the potential difference between the equilibrium potential of the melt, measured by an inert platinum electrode immersed in the melt, and the voltammetric equivalent of the standard potential of the U(IV)/U(III) couple, $E_{1/2}$.

For linear sweep voltammetry at a stationary electrode, the polarographic half-wave potential $E_{1/2}$ corresponds to the potential on a voltammogram at which the current is equal to 85% of the peak current. This assumes a reversible couple with both oxidized and reduced forms being soluble, which is the case for the U(IV)/U(III) couple.

Table 14.2. Determination of U(IV)/U(III) Ratios

U(IV)/U(III) Ratio[a]	U (mole %)	$E_{1/2}$ vs Equilibrium Potential (v)	
		Calculated	Measured
140	~0.3	−0.329	−0.345
29.3	~0.3	−0.225	−0.225
6.7	~0.3	−0.127	−0.130
10	~0.15	−0.153	−0.175

[a]Determined from spectral measurements.

The equilibrium potential of the U(IV)/U(III) couple is given by

$$E_{eq} = E^{\circ} + \frac{2.3RT}{nF} \log \frac{U(IV)}{U(III)},$$

and since $E_{1/2}$ is approximately equal to E°,

$$E_{eq} - E_{1/2} = \frac{2.3RT}{nF} \log \frac{U(IV)}{U(III)}.$$

Simultaneous with the emf and voltammetric measurements on the U(IV)/U(III) couple, samples were withdrawn for a spectrophotometric determination of both U(IV) and U(III) directly in the fused salt. The samples were contained in graphite windowless cells. Each sample was allowed to solidify and was then transferred to a heated spectrophotometric facility. The complete operation was performed without exposing the sample to the atmosphere; such exposure would probably alter the oxidation state of the solute. On remelting the sample in a helium atmosphere, its spectrum was obtained. The absorbance of U(IV) was determined at 640 nm and that of U(III) at 360 or 890 nm, depending on its concentration level.[7]

A comparison of the spectrophotometric and voltammetric results is shown in Table 14.2. Determination of the U(IV)/U(III) ratio yielded results in good agreement with values determined spectrophotometrically over a range of about 140 to 7. This method has several advantages: (1) no other reference elec-

[5]ORAU Fellow, University of Tennessee.

[6]Consultant, Department of Chemistry, University of Tennessee.

[7]J. P. Young, *Inorg. Chem.* 6, 1486 (1967).

trode is required, (2) no standard electrode potentials need be known, and (3) the electrode area need not be known in order to determine the U(IV)/U(III) ratio.

14.4 EMF MEASUREMENTS IN MOLTEN FLUORIDES

H. W. Jenkins[5] D. L. Manning
Gleb Mamantov[6]

The nickel/nickel(II) couple, contained in a boron nitride compartment, was demonstrated to be a useful reference electrode for emf measurements in molten fluorides.[8] Utilizing the nickel/nickel(II) reference, the program of emf measurements was continued on galvanic cells of the type $Ni|NiF_2||M^{n+}|M$ and $Ni|NiF_2||M^{n+}|M^{m+}|Pt$, and the standard electrode potentials evaluated so far are shown in Table 14.3. It is believed that the agreement between the measured values and those calculated by Baes is quite good, even though the solvents were not the same. The standard electrode potentials for Fe(II)/Fe and Fe(III)/Fe(II) relative to nickel were evaluated in both LiF-BeF_2-ZrF_4 and LiF-NaF-KF (FLINAK). FLINAK, having a higher concentration of free fluoride ions than LiF-BeF_2-ZrF_4, did not appreciably change the value of the Fe(II)/Fe couple; however, the Fe(III)/Fe(II) standard potential exhibited a cathodic shift of 366 mv. It is believed that this is attributable, in part, to a greater complexing affinity of fluoride ions toward Fe(III) than Fe(II).

The wetting of the boron nitride reference electrode compartment by the two melts was observed to be quite different. FLINAK wets the boron nitride quite rapidly; the resistance is lowered to <1000 ohms in 24 to 48 hr at 500°C; in LiF-BeF_2-ZrF_4, 10 to 14 days are required to lower the resistance to about 10 kilo-ohms at 500°C. The difference in wetting ability of the two solvents appears to depend on the free oxide content of the melts. In support of this it was observed that LiF-BeF_2 wets the boron nitride at about the same rate as FLINAK. The LiF-BeF_2 differs from LiF-BeF_2-ZrF_4 by the 5 mole % ZrF_4 which is added to precipitate free oxide as insoluble ZrO_2. An alternate explanation is that wetting is a function of the free fluoride concentration and is delayed in melts containing negative free fluoride.

14.5. DEVELOPMENT OF A MOLTEN-SALT SPECTROPHOTOMETRIC FACILITY FOR HOT-CELL USE

J. P. Young

Work on the molten-salt spectrophotometric facility for hot-cell use has continued.[9] The contract for

[8] D. L. Manning, H. W. Jenkins, and Gleb Mamantov, *MSR Program Semiann. Progr. Rept. Feb. 28, 1967*, ORNL-4119, p. 162.

[9] J. P. Young, *MSR Program Semiann. Progr. Rept. Aug. 31, 1968*, ORNL-4344, p. 192.

Table 14.3. Standard Electrode Potentials in Molten Fluorides

Electrode Couple	Measured Electrode Potentials[a] (v)		Calculated,[b] 500°C
	In LiF-BeF_2-ZrF_4 at 500°	In LiF-NaF-KF at 500°	
Be(II)/Be	−2.120		−2.211
Zr(IV)/Zr	−1.742		−1.772
U(IV)/U(III)	−1.480		−1.517
Cr(II)/Cr	−0.701		
Cr(III)/Cr(II)	−0.514		
Fe(II)/Fe	−0.410	−0.390	−0.413
Ni(II)/Ni	0.000	0.000	0.0
Fe(III)/Fe(II)	0.166	−0.200	

[a] Standard state for all solutes except beryllium(II) is the hypothetical unit mole fraction solution. The beryllium(II) standard state is the solvent composition LiF-BeF_2 (66-34 mole %).

[b] C. F. Baes, Jr., *Thermodynamics*, vol. 1, IAEA, Vienna, 1966 (values in LiF-BeF_2, converted to 500°C).

the design and fabrication of the extended optical path has been awarded to Cary Instruments, of Varian Associates; delivery of the completed system, including a Cary 14H spectrophotometer, is scheduled for August 1969. The general arrangement of the spectrophotometer, the extended optical path into and out of the hot cell, and the various components required for handling the radioactive molten fluoride salt samples are shown in Fig. 14.5. A description of the design and function of the pieces of equipment shown in the hot cell was given previously.[9] Fabrication of the optics furnace, top assembly, and transport container has been completed; fabrication of the sample loading furnace is almost complete. The completed pieces of equipment have undergone preliminary testing, and where necessary they have been modified to improve their functional operation. Not shown in the figure are the various service lines, such as water, electrical, vacuum, and helium, or the various traps for vacuum operation or radioactive gas retention, which are necessary for proper performance of the system. Design of these components is presently under way. Decontamination of the hot cell, cell 7 of Building 3019, where the facility will be installed, has been completed. F. L. Hannon (General Engineering Division, ORNL) has assisted in all these operations.

The joint electrochemical-spectrophotometric study of the determination of U(III)/U(IV) mixtures in simulated MSR fuel, described elsewhere in this section, carried out in cooperation with Jenkins, Manning, and Mamantov, was quite helpful. The excellent correlation of analytical results for this ratio by two independent methods, directly in the melt, provide a very firm basis on which to proceed in the development of both methods for use with reactor fuels. The method of sampling for spectral measurements closely parallels the procedure to be used in the transfer of a sample of MSR fuel from the reactor to the optics furnace.[9] The main differences result from the nonradioactive nature of the present case and the fact that the sample was caught and

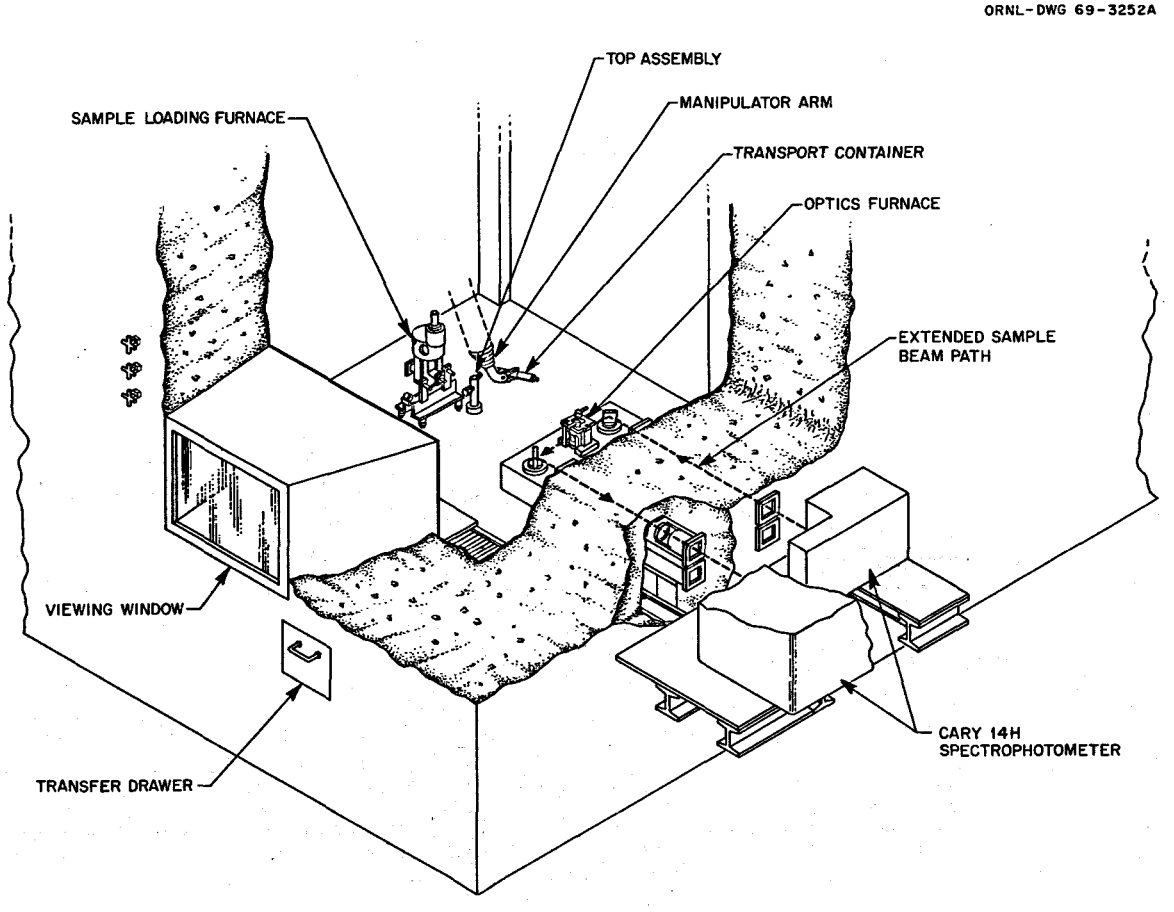

Fig. 14.5. Spectrophotometer Installation.

removed directly in a windowless cell. In the MSR procedure, 5 g of sample will be removed from the reactor and dispensed, without exposure to the atmosphere, into several windowless cells for spectral determination. Path-length determination of liquids confined in windowless cells is generally difficult. With the captive liquid cells we use, the path length of molten fluoride salts contained therein will be approximately 0.7 cm (±10%). One point that became obvious in the electrochemical-spectrochemical study was that the intensity of the U(IV) absorption peaks could be used as an internal standard to check the path lengths of the melts held in the cell. This improves the accuracy of the U(III) measurement. In the MSR samples the total uranium concentration will be known from other analyses, so the path length of MSR melts in windowless containers can be calculated from this knowledge and the intensity of the U(IV) absorption peaks in the sample. If the concentration of U(III) happens to be large, corrections of the U(IV) concentrations will be necessary, of course, and can be applied.

14.6 ABSORPTION SPECTRA OF 3*d* TRANSITION-METAL IONS IN MOLTEN LiF-BeF_2

J. P. Young

Further spectral studies of 3*d* transition-metal ions in molten fluoride salts have been carried out. A summary of the absorption spectra of the ions that have been studied in molten Li_2BeF_4 is presented in Fig. 14.6. The information in the legend describes how to interpret the figure. Horizontal lines show general areas of absorptions, and vertical lines denote peak and shoulder positions. Relatively weak absorptions are noted. The regions where the absorption of these solutions becomes very intense are shown as non-*d*-*d* transitions. The solvent Li_2BeF_4 is trans-

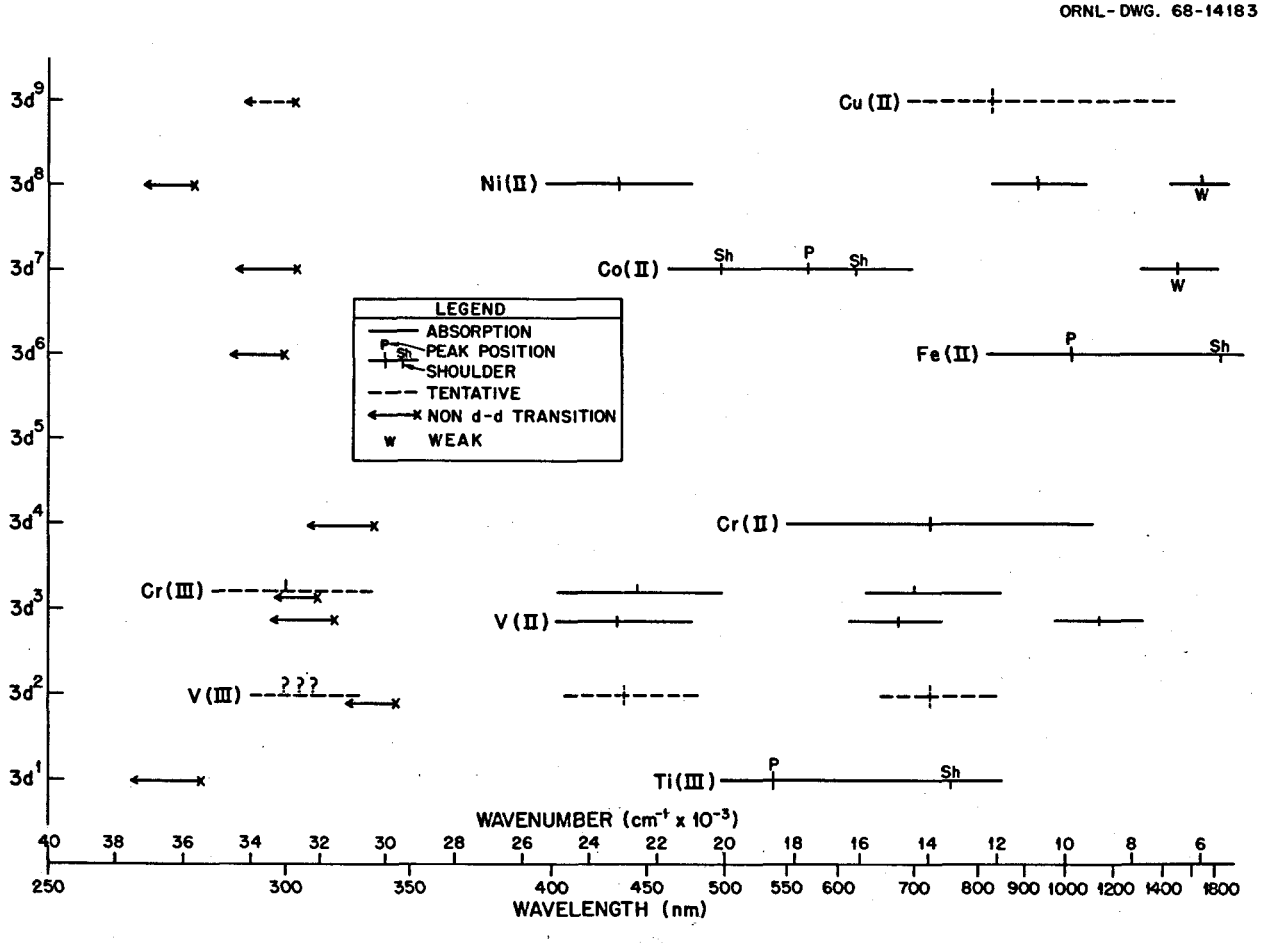

Fig. 14.6. Absorption Peaks of 3*d* Solutions in Molten LiF-BeF_2 at 550°C.

parent over this range of wavelengths. At least one example of each $3d^n$ configuration, except $3d^5$, has been observed. Except for Fe(II), Ni(II), Cr(II), and Cr(III), which were described earlier,[10] the figure is comprised of data that have been collected this period. Molar absorptivities are not known accurately yet but in all cases appear to be less than ~20. From the weak intensity of the spectra, coupled with the position of the spectral peaks, it is reasonable to assume that these solute ions are situated in high symmetry, possibly O_h, in these melts. Exceptions to this generality are Ti(III) and Fe(II), which may be distorted for O_h symmetry by Jahn-Teller effects. Although many of these ionic species are not of direct importance to MSR melts, it is desired to obtain such related spectral data for several reasons:

1. Such data provide a broader basis on which to generalize about the nature of solute species in fluoride melts.
2. They provide background information to apply to new areas of interest and applications as they occur.
3. They demonstrated that the techniques, apparatus, and methods of preparation are adequate to handle and maintain unusual or reactive oxidation states of certain elements. For example, Ti(III) was made from Ti^0 + Ti(IV); V(II) was prepared in the melt by reacting V^0 with Fe(III).

The study of the effect of solvent composition on the coordination and spectrum of solute species in fluoride melts is also continuing.[9] The spectrum of Co(II) is not altered, even in an Li_2BeF_4 melt that is made BeF_2-rich to LiF-BeF_2 (60-40 mole %). Considering stabilization energies for octahedral coordination, it would be expected that the coordination of Co(II) could most readily be changed from octahedral to tetrahedral[9] as the solvent composition is altered. Further studies of coordination behavior are under way.

14.7 EFFECT OF REDUCTANTS ON METAL-FLUORIDE-SALT WETTING BEHAVIOR

J. P. Young K. A. Romberger
J. Braunstein

Because of the practical implications arising from changes in the wetting behavior of molten fluoride salts, particularly LiF-BeF_2-base salts, it is of value to describe our experimental observations of these phenomena. These observations were generally made peripherally after some other experiment. Wetting and nonwetting behavior is summarized in Table 14.4. Most of these observations were made on cooled samples that had been prepared for windowless-cell spectroscopy. It is assumed that no gross change in contact angle occurred on freezing, and, in fact, those solutions which appear wetting as solids were more prone to run out of windowless cells when molten. Evidence to support this comes from visual observations made during filtrations of molten LiF-BeF_2 through sintered-nickel frits. In these experiments an LiF-BeF_2 melt which was in contact with a hydrogen atmosphere and beryllium metal completely wet a sintered-nickel frit during filtration, while a similar melt in the presence of hydrogen but in the absence of beryllium remained completely nonwetting to the frit during filtration. The typical appearance of a wetting and nonwetting layer of LiF-BeF_2 on a nickel frit is shown in Fig. 14.7.

The mechanism for this wetting action is unknown, but certain generalizations can be made. From Table 14.4 it can be noted that all containers are electrical conductors. In all cases when very active metals are in contact with melts containing one or several of their dissolved solute species, wetting occurs. Nickel was not wet by melts that contained dissolved Ni(II); nickel is a relatively noble metal. It is interesting to note that U(IV)/U(III) mixtures which contain no U^0 do not wet, while melts containing only Sm(II) do wet. This may imply that, under the experimental conditions of the test, U(III) did not disproportionate to U^0 where Sm(II) did disproportionate to yield Sm^0. In the Nd(III)-Nd^0 case, no evidence of Nd(II) was seen spectrally, but wetting occurred. LiF-BeF_2 which contained added, and relatively insoluble, oxides did not wet. This is perhaps in line with the generally observed fact that molten LiF-BeF_2 does not initially wet SiO_2 containers. In Table 14.4, salts and metals in parenthesis indicate that these states were present as a result of the container material or as a result of chemical reaction. In the latter case spectral proof of this species was obtained. Further studies are planned to investigate the electrochemical and chemical causes for this behavior.

14.8 DETERMINATION OF CONTAMINANTS IN THE BLANKET GAS OF $NaBF_4$ TESTS

R. F. Apple A. S. Meyer

The off-gas system of the circulating fluoroborate loop has been found to be contaminated with a

[10] J. P. Young, *Inorg. Chem.*, in press.

Table 14.4. Wetting Behavior of Various Fluoride Melts

Molten Solution	Contacting Reductant	Container Material	Wetting
$LiF\text{-}BeF_2$	None	Graphite, copper, nickel	No
$LiF\text{-}BeF_2$	H_2 (1 atm)	Nickel	No
$LiF\text{-}BeF_2$	Beryllium	Graphite, copper, nickel	Yes
$LiF\text{-}BeF_2 + (BeO)_s$	None	Graphite	No
$LiF\text{-}BeF_2 + (ThO_2)_s$	None	Graphite	No
$LiF\text{-}BeF_2\text{-}ZrF_4$	None	Graphite	No
$LiF\text{-}BeF_2\text{-}ZrF_4$	Beryllium or zirconium	Graphite	Yes
$LiF\text{-}BeF_2\text{-}UF_4\text{-}UF_3$, U(IV)/U(III) = >140 to 7	None	Graphite	No
$LiF\text{-}BeF_2\text{-}UF_4\text{-}UF_3$	Uranium or beryllium	Graphite, copper	Yes
$LiF\text{-}BeF_2$-U(IV)-U(V)	None	Graphite	No
$LiF\text{-}BeF_2\text{-}NiF_2$ (1%)	Nickel	Nickel	No
$LiF\text{-}BeF_2\text{-}TiF_4$ (1–2%)	None	Graphite	No
$LiF\text{-}BeF_2\text{-}TiF_4$ (TiF_3)	Titanium	Graphite	Yes
$LiF\text{-}BeF_2\text{-}NdF_3$	Neodymium	Copper	Yes
$LiF\text{-}BeF_2\text{-}SmF_3$ (SmF_2)	Samarium	Graphite	Yes
$LiF\text{-}BeF_2\text{-}EuF_3$ (EuF_2)	Europium	Graphite	Yes
$LiF\text{-}BeF_2\text{-}SmF_2$	None	Copper	Yes
$LiF\text{-}ThF_4$	None	Graphite	No
$LiF\text{-}ThF_4$	Thorium	Graphite	Yes
$LiF\text{-}ThF_4$	(Thorium)	Thorium	Yes

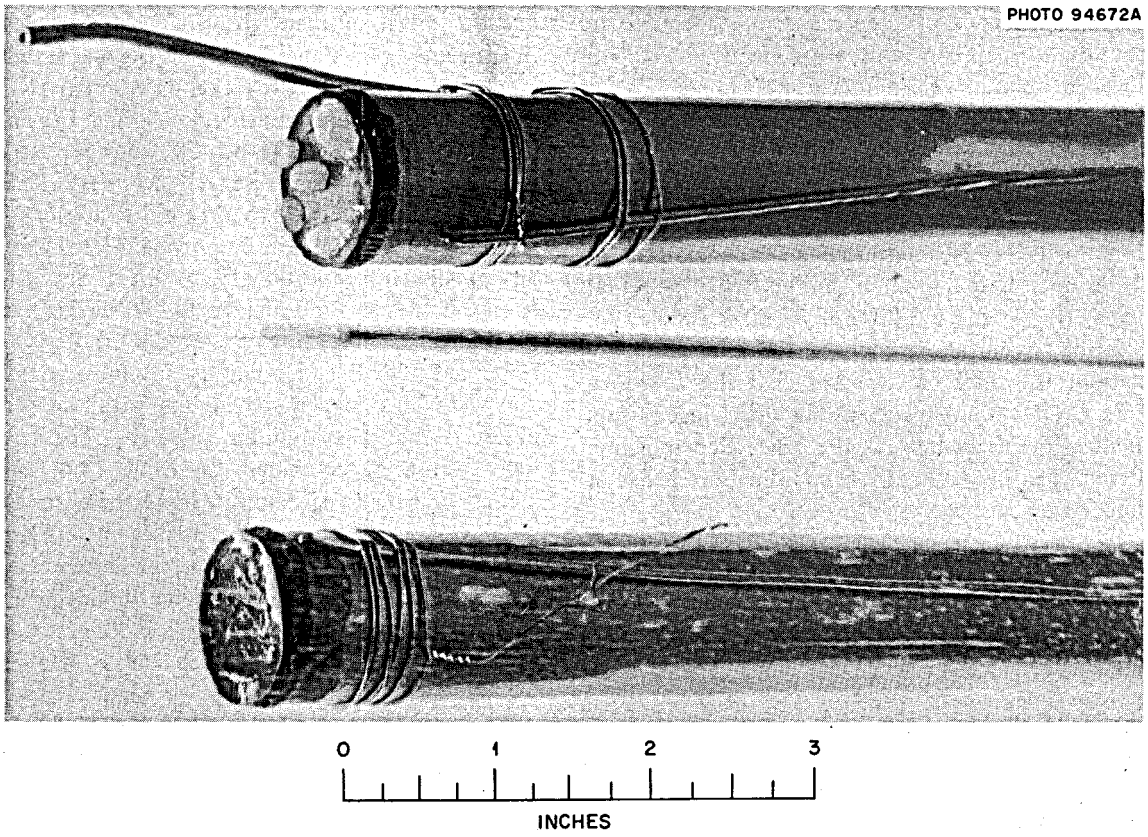

Fig. 14.7. Appearance of $LiF\text{-}BeF_2$ in Contact with a Nickel Frit. Top, nonwetting; bottom, wetting.

dense corrosive liquid and a white solid. Both of these materials are deposited, at least in part, at points remote from the pump bowl and could introduce maintenance problems when $NaBF_4$ is used as an MSR coolant salt. The white deposit was found to consist of agglomerated particles of an $NaBF_4$ aerosol, which can be removed by mechanical means, so the analytical effort is being concentrated on the liquid deposits.

The liquid deposits were originally thought to be associated with pump oil, but their almost complete solubility in water indicates that they are inorganic. Initial samples were dark brown, but one sample was transparent with a greenish-brown tinge. The material appears to be volatile, since in at least one case a deposit was observed to dry up during later operations of the loop. Collection rates decreased during the loop operations. The total quantity collected was not precisely measured but was estimated to correspond to a few hundred parts per million of contaminant in the salt charged to the loop.[11]

A. A. Palko[12] suggested the material was an equilibrium mixture of hydroxyfluoroboric acids, which are almost always formed from the reaction of BF_3 with traces of adsorbed moisture when BF_3 is first introduced into a metal system. It was not possible to confirm this analytically because the samples were not available in a weighable form. The samples were collected in a 1-ft section of 1-in. borosilicate glass pipe fitted with brass end plates and packed with stainless steel mesh. The composition of the original samples was probably altered through loss of BF_3 on attempted transfer. In subsequent samples a visual estimate of the quantity of liquid was made, and the fitting on the end of the trap was then opened under water. Copious fuming was observed, with the formation of an evanescent white scum (presumably boric acid) on the surface of the water. After the initial reaction had subsided, the trap was washed with water to yield a turbid solution. The combined solution was analyzed to determine the total quantity of soluble material present.

Some generalizations can be made for the liquid samples analyzed. The predominant components are fluorine and boron, present in a ratio slightly in excess of 3 to 1 after corrections are made for fluoride combined with cation contaminants. Stainless steel corrosion products are present in ppm to percentage range, with iron and chromium predominating. Varying quantities of silicon and sodium are present, along with traces of copper. Some plating of copper on the stainless steel packing was also observed.

The analyses are consistent with a liquid of average composition of BF_3-H_2O which at room temperature contains a complex equilibrium mixture of fluoroboric and hydroxyfluoroboric acids.[13] L. O. Gilpatrick has found that the oxygen in $NaBF_4$ is not completely removed by the heating and evacuation treatment used to prepare the loop's charge. Approximately 200 ppm remain, probably as $NaBF_3OH$ or its hydrate. He has found that this oxide is removed by sparging with BF_3.

Since the liquid is no longer being collected in the off-gas system, it will not be possible to characterize it unambiguously. In view of the above information we plan to assume that it consists of BF_3 hydrates, to generate such hydrates within a laboratory system, and to study their transfer and develop methods for removing them from off-gas streams. A gas train consisting of fluorothene traps connected by Teflon tubing has been assembled to perform these tests. The first trap was charged with water and sparged with an equimolar mixture of BF_3 and helium. When no further increase in the volume of the solution was noted and BF_3 passed freely through the system, the delivery tube was withdrawn to a point just above the solution, and the effluent gas was passed through two traps cooled in an acetone–dry-ice bath. This temperature is not sufficient to condense BF_3. Liquid was observed to be transferred at a significant rate. After 40 hr sparging at 100 cc/min, approximately 0.5 cc was collected. The trapping was obviously of low efficiency, since comparable quantities were collected in both of the traps. The traps have now been packed with Teflon-6, and the experiment will be repeated to try to obtain valid transfer rates. When a reliable rate has been established, various adsorbents will be interposed between the source and collection traps. We plan first to test molecular sieves because of their high capacity and convenience in handling. A large-pore (13X) sieve will be tested as a total adsorbent of the hydrate. Also a 3A sieve will be evaluated to determine if these compounds can be dehydrated.

[11] A. N. Smith, Reactor Division, personal communication.
[12] Chemistry Division.

[13] Christian A. Wamser, *J. Am. Chem. Soc.* 73, 409 (1961).

14.9 DETERMINATION OF BISMUTH IN MSRP SALTS

W. R. Laing P. F. Thomason
C. Feldman G. Goldberg
T. H. Handley

The use of the liquid-metal extraction system proposed for the reprocessing of molten-salt breeder reactor fuel will generate return streams to the reactor that may be contaminated with bismuth. During the lifetime of a power reactor, trace concentrations will represent a cumulative transfer of substantial quantities of bismuth. More sensitive methods are needed to determine the concentration of bismuth that is introduced to MSRP salts during extraction steps and to evaluate the efficiency of methods for stripping bismuth from salts. A number of groups have carried out development studies by diverse methods. Only a brief summary of this work will be presented at this time; a more detailed report will be made when optimum methods have been selected.

14.9.1 Polarography

The first salt samples were analyzed by derivative polarographic measurements in perchloric acid media. For LiF-BeF_2 and LiF-BeF_2-ZrF_4 samples, detection limits are approximately 20 ppm. Because the uranium and bismuth waves are too close (~0.1 v) for complete resolution, a positive bias is encountered in the analysis of uranium-bearing fuels. The method is not considered to give accurate results for typical fuel compositions containing less than about 100 ppm bismuth. It has been discontinued in favor of the spectrophotometric method described below.

14.9.2 Spectrophotometry

Both potassium iodide and thiourea give selective color reactions of approximately equal sensitivity. The iodide reagent is favored because the solid reagent can be added with little dilution of the sample solutions. By the use of 5-cm optical paths, measurements can be extended to the 10-ppm range for 1-g samples. No interference results from the usual concentrations of corrosion products; up to 200 μg of iron and copper can be tolerated. Uranium interference begins at about the 5-mg level but can be eliminated by the use of a sample blank. This is the method now used for routine analysis. Recent samples have contained undetectable quantities of bismuth.

14.9.3 Emission Spectrography

The detection limits for bismuth in a dc arc are approximately 30 ng, but it is possible to introduce only a few milligrams of the salt to an arc, and the measurement is subject to interference from the complex spectra of uranium and thorium. Preliminary experiments using tracer techniques have demonstrated that it is possible to quantitatively separate the bismuth from the major sample constituents by extracting sulfuric acid solutions with dithizone in chloroform. The extract can then be evaporated onto a graphite electrode so that the bismuth from a substantial sample of salt can be arced. The limits and precision of the method have not yet been established, but on the basis of past experience with similar techniques, measurements at the 1-ppm level appear practical.

14.9.4 Polarographic Stripping

The sensitivity of the polarographic determination of metallic ions can be increased by plating the metal onto an electrode for an extended period and measuring the stripping current generated during an anodic scan. In the technique now being tested, bismuth is plated onto a small (~0.5 mm) suspended drop of mercury. A small drop is used to minimize diffusion periods within the electrode, so that sharp stripping current peaks are obtained. The principal problem in the application of this technique to MSRP samples is that the stripping waves of copper and bismuth almost coincide. In addition to that in the salt samples, traces of copper are present in most analytical reagents. Attempts to separate these waves by complexing have been unsuccessful, and we are now attempting to plate the bismuth selectively. Thiocyanate strongly complexes copper so that its reduction wave becomes cathodic to bismuth, and it appears feasible to separate the bismuth by plating it at a potential intermediate to that of the bismuth and copper waves. Optimum conditions for the determination are now being established. With a 5-min plating period followed by stripping at 1 v/min, detection limits are estimated at 0.1 ppm.

14.9.5 Isotopic Exchange

Isotopic exchange methods are based on the equilibration of a solution of the element with an essentially immiscible phase that contains in fixed concentration a comparable quantity of a radioisotope of the element. When exchange is complete the radio-

isotope will be distributed in proportion to the quantity of the elements in the two phases, and the original concentration can be computed from a measurement of the distribution coefficient by counting. Practical analytical application of this principle can be made through the liquid-liquid extraction of metal ion complexes. This technique has been applied to the determination of ppm concentrations of mercury with a precision of about 1%.[14] For simplest applications the extraction system must rigorously fulfill certain criteria. (1) The complex must be essentially undissociated and strongly distributed to the donor phase; that is, the radioisotope complex must be quantitatively extracted in the absence of excess ligand. (2) Any constituents of the sample that form complexes of comparable or greater strength must be removed before the equilibration.

A two-step procedure for bismuth appears to fulfill the above criteria. The bismuth is first extracted from ammoniacal cyanide solution into a chloroform solution of dithizone. Only Pb^{2+}, Tl^{+}, and Sn^{2+} accompany the bismuth. The organic phase is then equilibrated with an aqueous solution of ^{207}Bi-EDTA complex. Bismuth forms a much stronger EDTA complex than any of the three accompanying ions. The method has the disadvantage of rather slow exchange. Approximately 20 min are required for equilibration. It has not yet been possible to determine the ultimate sensitivity of the method because the radioactive bismuth available is contaminated with normal bismuth. A new preparation (by bombardment of a purified lead target) will be needed to evaluate the method at the ppm level.

[14] T. H. Handley, *Anal. Chem.* 36, 153 (1964).

Part 4. Molten-Salt Irradiation Experiments

E. G. Bohlmann

As indicated in the last report of this series, the in-pile program has been suspended because of budgetary limitations. Additional wetting studies indicated that very stringent gas purification measures will have to be used in future small-scale experiments, such as the in-pile thermal convection autoclave, if wetting by the salt and concomitant confusion of the experimental results are to be avoided. Titanium or uranium metal hot trapping at the points of entry of gas streams into the loop are indicated as minimum requirements.

A reexamination of the ORR Engineering Test Facilities (HN-1 and HS-1) indicated that the maximum power density achievable in an in-pile loop experiment would be ~400 w/cc even with major modifications.

15. Molten-Salt Convection Loop in ORR

E. L. Compere H. C. Savage E. G. Bohlmann

15.1 STUDIES OF SURFACE WETTING OF GRAPHITE BY MOLTEN SALT

Surface wetting of graphite by molten salt at the point of contact with a gas phase has been shown in glove-box experiments to occur at extremely minute concentrations of moisture (<1 ppm) in the helium cover gas; subsequently, salt crawled along graphite that extended into the gas phase. Graphite immersed in molten salt in contact with such atmospheres was not wetted. The results suggest that the graphite in the ORR molten-salt loop experiment became wetted during the multiple sample-withdrawal drain operation in which tank argon containing ~4 ppm moisture was used to manipulate the salt.

The observed importance of the three-phase contact area also suggests that moisture-promoted wetting is lateral only and should not proceed inward from a graphite surface, since salt which has covered the surface will prevent moisture-containing gas from getting to a deeper contact area and furthering the penetration.

Bubbling tank helium (4 ppm H_2O) at ~100 cc/min successively through three containers (30 g each) of molten salt at 600°C was not an effective cleaning procedure, because oxygen analyses of the salt showed equal increase in each bubbler and only about half of the moisture was removed. Graphite was wetted in less than a day by a droplet of salt in a heated quartz tube through which the gas from the bubblers was passed. Reaction rates thus do not appear to be very rapid relative to residence time in a bubbler.

Laboratory experiments were conducted in a vacuum line made up of quartz and stainless steel tubing. The specimen used was a droplet of molten salt (LiF-BeF_2, 66-34 mole %) on a graphite planchet. The graphite had been preheated under vacuum in the quartz tube, and the salt was placed on it in an argon glove box. All gas which entered the system was passed through titanium sponge hot traps and in this experiment also passed over 5 in. of heated titanium sponge in the quartz tube before reaching the salt. The system was evacuated, the droplet melted, and helium flow started. With such stringent precautions it was possible to maintain the salt droplet unchanged, clear and nonwetting, for a week. We then continued the gas flow but ceased to heat the titanium sponge adjacent to the droplet. After five days the droplet showed evidence of beginning to wet the graphite. During this period, only enough moisture entered the system to cover the estimated titanium surface a few times.

Thus it was shown that wetting could be prevented by stringent purification of the gas.

Part 5. Materials Development

W. P. Eatherly H. E. McCoy J. R. Weir, Jr.

Our materials program has emphasized four main problem areas during this reporting period: (1) irradiation damage to graphite, (2) sealing graphite to obtain a low permeability to fission gases, (3) irradiation embrittlement of Hastelloy N, and (4) the compatibility of Hastelloy N with our proposed coolant salt, sodium fluoroborate.

Several graphites were obtained from commercial vendors, and some were fabricated in local facilities for study in our irradiation damage program. Some of these materials have been irradiated to a fast fluence of 2.5×10^{22} neutrons/cm^2 (>50 kev). Experimental techniques are being developed so that we can use transmission electron microscopy, x-ray diffraction, and physical property measurements to characterize these materials before and after irradiation.

Graphite substrates having helium diffusivities in the range of 10^{-2} to 10^{-3} cm^2/sec are being sealed by impregnation with a gaseous hydrocarbon to obtain surface diffusivities of $<10^{-8}$ cm^2/sec. Most of our work to date has been with optimizing process parameters, but some samples have been irradiated.

Hastelloy N is embrittled in a thermal-neutron environment by helium produced by the $^{10}B(n,\alpha)^7Li$ transmutation. This embrittlement can be reduced by alloying with titanium, but good postirradiation properties result only when the irradiation temperature does not exceed 660°C. This temperature sensitivity has been related to the instability of the MC-type carbide, and further alloying additions to stabilize the desired carbide are being sought.

Our proposed coolant, sodium fluoroborate, seems to corrode Hastelloy N more than salts containing lithium and beryllium fluorides. Our results indicate that the corrosion rate in the sodium fluoroborate is sensitive to the water content. Several thermal convection loops and one forced convection loop are being used to study this problem.

16. MSRE Surveillance Program

16.1 EXAMINATION OF PARTICLES REMOVED FROM PUMP BOWL WITH MAGNETS

R. E. Gehlbach H. Mateer
T. J. Henson J. L. Miller, Jr.

Examination of three MSRE pump bowl magnets, FP-15-53, FP-15-67, and FP-16-2, revealed magnetic particles clinging to the magnets and cladding material. In some instances these particles resembled whiskers, but in most cases, closer optical examination showed them to be finely divided metallic particles. We utilized gamma scanning, electron microprobe, x-ray diffraction, spectrochemical analysis, and metallography to identify the particles. The results are summarized in Tables 16.1 to 16.3.

To obtain the sample from the magnet in the hot cells, a camel's-hair brush was used to remove the particles into a receptacle. In this brushing operation a small amount of the hair from the brush was unavoidably mixed with the sample. Removal of the hair was extremely difficult, so the hair was weighed as sample material also. In the spectrographic analysis, this portion of the sample went undetected as carbon along with the fluorine from the MSRE salts. Since the sample weight was in the milligram range, the weight contribution of the hair was considerable. Consequently the spectrographic results were inordinately low. However, by calculating the fluorine salt contribution that is known to accompany the sample and normalizing the

Table 16.1. Summary of Spectrochemical and X-Ray Diffraction Analyses of Batches of Particles Removed from MSRE Pump Bowl Magnets

Magnet	Spectrochemical Composition (%)										X-Ray Diffraction
	Al	Be	Cr	Cu	Fe	Li	Mn	Mo	Ni	Zr	
FP-15-53[a]		FT	M		VS	T	T	T	S	VFT	
FP-15-67	0.12	2.21	1.27		15.1	4.01		0.13	1.80	1.31	Fe (S); Ni (W)
FP-16-2	0.11	3.88	0.7		17.7	7.0		0.095	2.46	1.85	Fe (S); Ni (W)

[a]VS = very strong, S = strong, M = medium, T = trace, W = weak, FT = faint trace, and VFT = very faint trace.

Table 16.2. Normalized Quantitative Spectrochemical Analysis

Magnet	Composition (%)					
	Fluorine Salt	Fe	Ni	Cr	Mo	Al
FP-15-67	59	34	4.0	2.9	0.29	0.27
FP-16-2	68	27	3.7	1.1	0.15	0.17

Table 16.3. Summary of Microprobe Analyses of Individual Particles

Magnet	Particle No.	Composition (%)			
		Fe	Ni	Cr	Mo
FP-15-53	1		>95		
	2[a]	65.0	8.9	20.8	
	3[a]	69.8	7.0	18.1	
	4	97% Al + 1.6 Cu + 1.9 Zn + two phases; phase No. 1[b]: Al + 12Si + 7Cu + 2Zn; phase No. 2[b]: Al + 3Si + 1.7Cu + 22Fe			
FP-16-2	1	>99	T		
	2	91		9	
	3	6	94		
	4	2	98		
	5	6	92		2
	6[b]	75	2	22	
	7[b]	60	4	36	2
	8[c]	VS	T		
	9[c]	VS	W		
	10[c]	VS		M	
	11[c]	W	VS		
	12[c]	W	VS		

[a]Particles identified as stainless steel shavings (see text).
[b]Phases and particles were very small, and extreme caution should be used in interpretation.
[c]VS - very strong, M = medium, W = weak, and T = trace.

results, the percentages to two significant figures were obtained (Table 16.2).

16.1.1 Observations on Particles from Magnet FP-15-53

Four particles from FP-15-53 were mounted and examined with the electron microprobe. One particle was >95% Ni, and neither Mo nor Cr was detected. Two other particles examined by microprobe analysis were Fe with about 18% Cr and 8% Ni, similar to many austenitic stainless steels. These particles appeared metallographically to be primarily single phase. Attempted etching with 2% Nital (iron etchant) did not alter the polished surface, but the structure shown in the insert of Fig. 16.1 resulted from a glyceregia etch, indicating either a very small grain size or severe deformation. Both particles were magnetic, indicating either bcc iron or heavily cold-worked austenitic stainless steel. One particle was removed from the mount and is shown in Fig. 16.1. Debye-Scherrer x-ray patterns revealed that the particle was austenitic, indicating that both were probably stainless steel shavings picked up during removal of "real" MSRE particles from the magnet.

Another particle was primarily aluminum. Metallographic study revealed a typical cast eutectic structure with at least two phases in the matrix. Besides Al, one phase contained Si, Cu, and Zn, and the other Fe, Si, and Cu. The matrix contained very small amounts of Cu and Zn. This particle had a very low level of activity, and gamma spectroscopy was employed to determine the nuclides responsible for the limited activity. Long counting times were used, and only ^{95}Nb, ^{103}Ru, and ^{106}Ru were detected. The nuclides present in highest concentrations in the MSRE salt were not detected, presenting some doubt that the particle was removed from the pump bowl, particularly since the particle was

PHOTO 95517

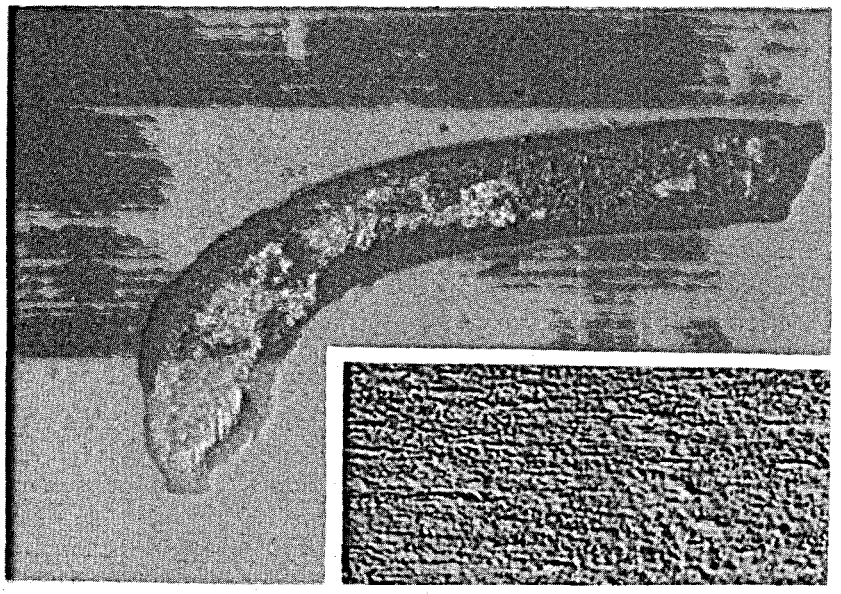

Fig. 16.1. Austenitic Stainless Steel Shaving Introduced to FP-15-57, 100X. Insert shows microstructure of particle after polishing and glyceregia etch. Interference contrast, 1000X.

nonmagnetic. Due to the small quantity of particles, x-ray diffraction analysis of FP-15-53 was not possible.

16.1.2 Observations on Particles from Magnet FP-16-2

A batch of particles from FP-16-2 was mounted for microprobe and metallographic study. These particles were much smaller than the stainless steel shavings, ranging from 30 to $<1\ \mu$ in size. Nearly 50 to 60 particles were apparent, and microprobe x-ray displays indicated that the majority were primarily Fe and several were primarily Ni; Mo and Cr were detected in some very small particles. Semiquantitative analyses were performed on several particles, with the results shown in Table 16.3. Generally the particles were relatively pure Fe, primarily Ni with some Fe, or mixtures of Fe and Cr with some Ni. Small amounts of Mo were present in two particles. Metallographic studies revealed that the iron particles had similar structures after etching with 2% Nital, as shown in Fig. 16.2.

X-ray diffraction analysis of batches of particles from FP-15-67 and FP-16-2 revealed bcc Fe (rather than austenite) as the primary constituent, with Ni as a minor phase.

PHOTO 95518

Fig. 16.2. Microstructure of Typical Iron Particles Removed from FP-16-2. Etchant: 2% Nital, 1500X (1 mil = 1.5 in.). Note small particle size compared with Fig. 16.1.

17. Graphite Studies

17.1 FUNDAMENTAL STUDIES OF RADIATION DAMAGE MECHANISMS IN GRAPHITE

D. K. Holmes J. C. Crump
S. M. Ohr T. S. Noggle
W. E. Atkinson

An effort is being made to contribute to improvement of the characteristics of reactor graphite under conditions of long-exposure, high-temperature irradiation by trying to understand the basic nature of radiation damage in graphite. The years of research effort put into this problem by various groups in the past have not produced any acceptable quantitative model of the accumulation of damage in graphite even under the most ideal conditions. Therefore, in an attempt to establish a clear understanding of the basic processes, it has been considered worth while to take a new look at damage in natural single crystals of graphite and in good pyrolytic material.

The justification for undertaking such a program in the face of the obvious difficulties shown by the lack of progress in the past lies in the hope of using a better experimental approach and in a closely correlated effort between theory and experiment in a group whose past interests have been in the basic nature of radiation damage.

The experimental idea is to use fast electrons or charged particles to produce the damage in simulation of fast-neutron irradiations. In its optimum form the idea is to irradiate graphite specimens in the 200-kev Hitachi electron microscope with the electron beam of the instrument (which is energetic enough to displace carbon atoms from their lattice positions) and to examine them in situ. This would allow for very accurate control of dose rate and total dose along with fair control of the specimen temperature. It is known from previous work of other groups that the damage in graphite is easily observable in the electron microscope in the form of large dislocation loops and defect clusters, the former arising from the clustering of interstitial carbon atoms between the layer planes. A careful study of the formation, growth, and annealing of these clusters should lead to an understanding of the reason why so much damage persists in this form rather than suffering annihilation.

The experimental work is as yet only in a preliminary stage. Some single crystals (provided by G. Hinman of Gulf General Atomic) and some pyrolytic material have been irradiated in the microscope. Observable damage has been produced in the form of defect clusters. For example, in a sample of pyrolytic material exposed to a total of 10^{22} 200-kev electrons per square centimeter at 550°C there were observed clusters having average radii of about 50 A with a density of about 10^{16} clusters per cubic centimeter. In a general way these results are consistent with those obtained by previous investigators using fast neutrons at a roughly equivalent total dose. However, no detailed comparison can be made until many more irradiations have been made under varying conditions. The exact nature of the clusters obtained to date has not been clarified; further study in the electron microscope is needed to determine if the defects being observed are indeed interstitial loops and, if they are not, whether interstitial loops are also present.

The intent of the theoretical program is to attempt to understand the experimental results by a closely correlated study of kinetic equations covering the production, diffusion, annihilation, and clustering of defects. With such a set of equations, various hypotheses can be introduced and tested by comparing the results with the equivalent experimental data. As the initial effort it has been decided to study Mayer's theory, which says that substitutional boron atoms play a vital role in the damage process. The suggestion is that wandering interstitial carbon atoms are trapped near such boron sites and are thus effectively slowed down in their rate of diffusion through the lattice. Further, as the interstitial rests at its trapping position, it is very likely to be joined by a second interstitial which will thus nucleate a stable cluster. Mayer's experimental results indicate that such boron trapping sites are the dominant feature of radiation damage in graphite even down at concentrations as low as 10^{-7} atomic fraction of boron.

A set of coupled kinetic equations has been programmed for the IBM 360 model 75 computer. These equations determine the time variation of the densities of interstitials, vacancies, interstitials trapped at boron atoms, clusters of interstitials at boron atoms, and clusters of interstitials homogeneously nucleated. Such equations present considerable difficulty toward obtaining acceptable accuracy and stability. Most of the research effort to date has been expended in adapting a Gauss-Seidel integration scheme to this particular set of equations in order to integrate with enough efficiency to permit the achievement of the desired total damage level. Mayer himself has not integrated such equations, although he discussed them and deduced what their asymptotic solutions should be. Our very preliminary results tend to confirm the general form of his solution.

17.2 GRAPHITIZATION CHEMISTRY AND BINDER SYSTEM DEVELOPMENT[1]

R. A. Strehlow

Increase of the microstructural strength and density of graphite for MSBR use should improve both gas permeability characteristics and irradiation lifetime. The chemical studies program on carbonization and binder system development is concerned with chemical factors which influence the structural properties of a fabricated graphite. This concern stems principally from two facts: The first is that weight and volume yields of carbon are strong functions of the chemical structure of starting material as well as of carbonizing conditions. The second is that carbon precursor mixtures can yield coke mixtures with significant variability in microstructure and graphitizability.

Economic and technical factors operate together to place coal tar pitch in an eminent position among binder systems for nuclear graphite. However, measured volumetric yields of coal tar pitch were found to range from 20% for the softer grades to only about 40% for the highest-softening-point materials (grade 350). Since some carbon precursor compounds offer volumetric yields of more easily graphitized carbon near 60%, marked improvements in strength and fabricated density are possible. For improvements of this magnitude, overall process costs competitive with those of the coal tar materials may be realized.

Of course, volumetric yield is but one of several essential qualities of a carbon-binder system. Appropriate fluidity, carbonization kinetics, and product carbon structure are all required for the optimal application of a binder system. Appropriate flow properties may be achieved by construction of polycomponent mixtures or by proper use and selection of fugitive material. It is not now known whether a reasonably small number of components will yield a suitable liquid. Studies have been begun of phase relations among carbon precursor materials such as acenaphthylene and isotruxene. However, knowledge of the kinetics of crystallization processes for mixtures is also needed for further development of synthetic binder systems and for altered or modified pitches.

Carbonization reactions proceed with rates and temperature coefficients of rate which vary with the structure of the pyrolyzing species. Mixed coke types can be generated from mixtures of compounds such as biphenyl and anthracene.[2] Since it may be safely presumed that a segregated development of coke types within a carbon body during baking will lead to structural weakness and impaired crystallinity in the product, a study of microstructural development is a necessary accompaniment to the carbonization studies. Model compounds with sufficiently low vapor pressure to prevent facile evaporation generally have a complex structure which may follow more than one route in the carbonization. Since this is so, either high-pressure coking or great restriction in selection of compounds must be employed. Fortunately, there are a few polycyclic aromatic hydrocarbons such as decacyclene, $C_{36}H_{18}$, which are at once symmetric and of high molecular weight so that studies can be made on their carbonization. Work of this type is continuing.

The inference should be drawn from the above discussion that binder system development can proceed from two complementary bases. The first is the use of model compounds primarily to define the carbonization process – rates, catalysis, product quality, and its alteration. The second is to determine the basic phase data needed to construct a useful improved binder system using either precursor mixtures or modifications of coal tar or petroleum pitches.

[1] These comments are based on work performed in the Chemistry Development Department of the Development Division, Y-12 Plant.

[2] Alvin Weintraub, thesis, Pennsylvania State University, Graduate School, Department of Nuclear Engineering, September 1967.

17.3 HOT PRESSING OF GRAPHITE PELLETS USING VARIOUS BINDERS[3]

L. G. Overholser

Graphite pellets were prepared for machining and subsequent irradiation testing in HFIR by hot pressing AXM graphite flour[4] and various binder materials. Variables examined include the type and quantity of binder as well as pressing temperatures and pressures.

AXM graphite flour (−200 mesh), purified by HCl treatment at ~2200°C, was used as filler in all runs. Isotruxene (ITX), acenaphthylene (ACN), decacyclene, and Allied Chemical Company grade 350 coal tar pitch were used as binders. The binders were crushed, where necessary, sieved, and the −70 mesh fraction used in hot pressing. The flour-binder mixture was prepared by superficially dry blending the powders, slurrying with acetone, and evaporating the acetone to yield a dry powder. The graphite sleeve and die used in hot pressing gave a pellet having a nominal diameter of 3 in. Pellets hot pressed at 1400°C were heat treated later at 2800°C without pressure.

[3]Work performed by Chemical Engineering Department, Development Division, Y-12 Plant.

[4]This flour was obtained by milling AXM graphite produced by Poco Graphite, Inc.

Data obtained for the various graphite pellets are given in Table 17.1. The bulk density was calculated from the weight and geometric volume and the residual binder carbon content from the increase in weight of the formed graphite over the weight of contained flour. The carbon yield or coking value represents the ratio of weight of residual carbon obtained after pyrolysis of the binder to the weight of binder originally present. Pellets prepared using ACN as binder are characterized by low bulk carbon densities and low binder carbon contents. These binders also give low carbon yields. All pellets pressed with these binders had at least one large radial crack. The high-melting grade 350 coal tar pitch gives the highest bulk densities, carbon yields, and carbon binder contents. Isotruxene and decacyclene give bulk densities, binder carbon contents, and carbon yields intermediate between the 350 pitch and the ACN binder.

The density of parts cut from one of the pellets prepared with ITX as binder increased from 1.63 to 1.80 g/cm^3 when given a single impregnation with ITX. This technique makes it feasible to prepare graphites of higher density than obtainable by merely varying the conditions of pressing but still using a single binder material. In addition to the variation of densities found for the various binders, the carbons formed by pyrolysis of these binders differ in graphitizability. For example,

Table 17.1. Data for Various Hot-Pressed Graphite Pellets

Grade[a]	AXM Filler (g)	Binder		Pressing Conditions		Pressed Pellet				Carbon Yield (%)
		Type	pph	Temperature (°C)	Pressure (psi)	Length (in.)	Weight (g)	Bulk Density (g/cm^3)	Binder Carbon (%)	
YMI-4[b]	410	ITX	25	1400	1600	2.63	481	1.63	14.8	70
	410	ITX	25	1400	1600	2.59	471	1.62	13.0	62
YMI-3[c]	410	ITX	35	1400	1600	2.60	475	1.63	13.7	48
(YMI-2)	400	ITX	35	1400	2400	2.42	458	1.68	12.7	42
(YMI-5)	410	ITX	25	2800	2400	2.28	475	1.76	13.7	64
YMI-13[c]	410	ITX	25	2800	2400	2.35	478	1.76	14.2	61
	400	ACN	35	1400	1600	2.50	430	1.55	7.0	21
(YMACN-8)	380	ACN	50	1400	1600	2.42	421	1.54	9.7	22
YM350-10[c]	390	350 pitch	35	1400	1600	2.60	490	1.69	20	74
(YM350-12)	390	350 pitch	35	1400	1600	2.65	491	1.67	20	74
(YM350-9)	410	350 pitch	35	1400	1600	2.77	515	1.67	20	73
YM350-11[c]	400	350 pitch	35	2800	2400	2.39	500	1.80	20	72
(YM350-14)	400	350 pitch	35	2800	2400	2.43	501	1.78	20	72
	390	Decacyclene	35	1400	1600	2.48	463	1.65	15.8	54
	390	Decacyclene	35	2800	2400	2.24	463	1.76	15.8	54

[a]Those with grade designations are those supplied to ORNL for evaluation, and those enclosed in parentheses are those that are currently being evaluated.

[b]This grade, which is similar to YMI-3, was impregnated with ITX at 1000 psi and graphitized again at 2800°C; some of the resulting properties are given in Table 17.2.

[c]This material has been selected for the irradiation studies in the High Flux Isotope Reactor (HFIR).

ITX and 350 pitch yield carbons which are more difficult to graphitize than the carbons obtained from ACN and decacyclene.

The original AXM graphite is known to be remarkably stable under irradiation (cf. Sect. 17.9). Hence the flour used in the above samples should also be stable. Since the microstructures of the above binders differ significantly, the irradiation of these materials should clearly delineate the role of the binder in controlling dimensional changes of graphites under irradiation.

17.4 PROCUREMENT AND PHYSICAL PROPERTY MEASUREMENTS ON NEW GRADES OF GRAPHITE

W. H. Cook

The first trial fabrications of new grades of graphite have been received and are in the early stages of examination. The objectives are (1) to develop the most radiation-stable and fabricable grades of graphite for MSBR applications and (2) to determine the fundamental factors that make one grade of graphite resist radiation damage more than others. In many instances, the data from the research toward these objectives are mutually beneficial; however, the research associated with the first is on a more pressing time schedule.

The development programs are of the mutual interest and effort of the Chemical Engineering Development Department (CEDD) of the Y-12 Plant and ORNL.[5] All of the fabrication data reported for these new graphites were supplied by R. L. Hamner and L. G. Overholser. Some of the fabrication details are given in Sect. 17.3.

To develop the most stable and fabricable material, the work is concentrated on the most radiation-resistant materials currently known, the Poco graphites. These materials are not currently being fabricated in large enough sizes for the present MSBE and MSBR designs; so work has been initiated in CEDD to make shapes by the classical extrusion techniques with these and other materials as fillers. Grades Y586 and Y588 shown in Table 17.2 are typical. They are bonded with polymerized furfuryl alcohol, Varcum,[6] which produces a poor-quality, turbostratic graphite for the binder phase. Grade AXF bodies were crushed and sized by the CEDD to supply one filler, and the other, grade 2033, was supplied by the manufacturer already crushed and sized. Little is known about grade 2033 material. Grade AXF has a bulk density ranging from 1.80 to 1.88 g/cm^3 and a typical gas permeability to helium of 4.0×10^{-2} cm^2/sec. As shown in Table 17.2, the grade AXF "reconstituted" as grade Y586 did not sacrifice these starting properties. In fact, the gas permeability was improved (i.e., decreased) by a surprising amount to 3.1×10^{-4} cm^2/sec. Additional properties are being measured, and their irradiation stabilities to fast neutrons will be determined in the HFIR. Should the overall properties of the starting materials not be degraded too much by this process and in the scaleup to MSBR sizes, this well-established technology for fabrication would be suitable for fabricating the shapes required for MSBR's.

The rest of the grades of graphite listed in Table 17.2 are being studied for more special and fundamental purposes. Historically, graphite has been made from natural materials and/or their by-products. Thousands of complex hydrocarbon compounds may be involved in these natural materials, and they are usually typical of their particular source. This presents such problems as (1) maintaining the quantity and quality limits of starting materials required for a product when a certain natural source is depleted and (2) sorting out the complex compounds that may contribute to resitance to radiation damage. One approach that may be helpful toward solving both of these problems is to synthesize part or all of the starting components. Grades YMI-3, YMI-4I, and YMI-13 represent initial work in this direction. Preliminary data suggest that radiation damage may be decreased if the binder component is equal to or greater in quality to the filler material so that in effect they are indistinguishable from each other, that is, the finished product behaves as if it were a monolithic material. A secondary but desirable goal is to find binders and impregnants that produce higher carbon yields during pyrolysis. This would decrease both the initial porosity in the base stock and the number of impregnations required to reduce porosity and pore entrance diameters in the base stock. An attempt to do this has been to synthesize the starting materials, the isotruxene [$C_6H_3(C_6H_5)_3$] binder and impregnant in these studies. The molding technique is used to conserve the limited quantities of the synthesized isotruxene.

Poco grade AXM was used as the filler in these experimental grades because of low cost and availability. It differs from grade AXF in that its bulk density is lower (1.70 to 1.79 g/cm^3). The relatively high resistance to radiation damage of the filler should help emphasize the effects of irradiation on the isotruxene binder and impregnant. Grade YMI-3 is a

[5] The fabrication work is in part done by ORNL personnel on loan to the CEDD, R. L. Hamner, L. G. Overholser, and R. A. Strehlow.

[6] Varcum Chemical, a Division of Reichhold Chemicals, Inc., Niagara Falls, N.Y.

Table 17.2. Initial Fabrication and Properties Data[a] on New Grades of Graphite

Grade	Filler		Binder	Molding Conditions		Graphitizing Temperature (°C)[b]	Density (g/cm³)		Accessible Porosity (%)		Orientation With Grain[c]	Specific Resistance (microhm-cm)	Flexural Strength (psi)[d]	Modulus of Elasticity (psi)[d]	Strain to Fracture (%)[d]	Helium Permeability (cm²/sec)
	Type	Particle Size		psi	°C		Bulk	Real	Total	With Pore Entrances <1 μ						
														× 10⁶		
AXF[e,f]		(<25μ)					1.81		15.0	90		1575	6720	1.40	0.669	4.0×10^{-2}
Y586[g]	AXF[f]	−60 mesh (<250μ)	Varcum[h]			2900	1.84	2.002[i]	6.51	88	∥	1475	4950	1.50	0.456	3.1×10^{-4}
											⊥					2.7×10^{-4}
Y588[g]	2033	−60 mesh (250μ)	Varcum			2900	1.82	1.999[i]	6.87	85	∥	1585	4570		~0.4	7.3×10^{-4}
											⊥					4.7×10^{-4}
YMI-3	AXM[f]	−200 mesh (<75μ)	ITX[j]	1600	1400	2800	1.62				∥	2200				
											⊥	2340				6.0×10^{-2}
YMI-41[k]	AXM	−200 mesh (<75μ)	ITX	1600	1400	2800	1.82				∥	1785				
											⊥	1935				1.1×10^{-2}
YMI-13	AXM	−200 mesh (<75μ)	ITX	2400	2800		1.73				∥	2150				2.7×10^{-2}
											⊥	2790				
YM350-10	AXM	−200 mesh (<75μ)	Pitch 350[l]	1600	1400	2800	1.65				∥	2220				
											⊥	2350				1.6×10^{-2}
YM350-11	AXM	−200 mesh (<75μ)	Pitch 350	2400	2800		1.75				∥	2000				
											⊥	2750				1.6×10^{-2}

[a] These are typical, not statistical.
[b] At temperatures 1–1½ hr. These and all data to the left are from CEDD of Y-12; the fabrication details for some of these are given in Sect. 17.3.
[c] The long dimension of a filler particle and the general orientation of the *a* axes of the grain (filler particle).
[d] Determined by the Mechanical Properties Group.
[e] Grade AXF is included for comparison with the reconstituted material, grade Y586.
[f] Manufactured by Poco Graphite, Inc., Garland, Tex.
[g] These were extruded; the rest were hot pressed.
[h] Polymerized furfuryl alcohol manufactured by Varcum Chemical Co.
[i] Supplied by R. L. Hamner, Y-12 CEDD.
[j] Isotruxene, $C_6H_3(C_6H_5)_3$.
[k] Impregnated with isotruxene at 1000 psi and graphitized again at 2800°C.
[l] Allied 350 hard pitch (mp ~180°C).

body bonded with isotruxene, and YMI-4I is both bonded and then impregnated with isotruxene.

The common commercial coal tar pitch binders usually used in the fabrication of graphites have a carbon yield of approximately 55% (ref. 7). The carbon yield for isotruxene is around 67%, an appreciable increase over that of the coal tar pitch binders. However, the overall results are somewhat disappointing. The bulk density of the YMI-3 is lower than that of the filler material, and that for YMI-13 is not usually high for the forming technique used. The density of YMI-4I was increased substantially by the single impregnation with isotruxene, but the gas permeability was not altered much when compared with that of YMI-3 in Table 17.2.

The YM350 series in Table 17.2 brings us back to more complex binders. However, the 350 pitch used for these is a relatively hard binder that has a good carbon yield of approximately 72%. Again, the bulk densities and gas permeabilities are not outstanding for these first trials.

The specific resistances reported for grades Y586 and Y588 in Table 17.2 are slightly high, as one might expect with furfuryl alcohol binder and the particle size of the filler used. The specific resistances for all the YMI and YM350 series are very high. In a qualitative way, the high resistance suggests that the particles are covered well by the binders, as they should be, and that the binders are not producing good graphitic structures.

It is important when considering the properties of the grades listed in Table 17.2 to recall that these are all the first products produced by these new approaches. The full potential of these materials cannot be assessed until the fabrication parameters are further developed. Other synthesized binders will be introduced as these studies progress. We shall continue to make relatively comprehensive property measurements on these and other grades of these series in order to (1) assist in developing desirable fabrication techniques and (2) to determine the potentials of these new materials.

17.5 PHYSICAL PROPERTIES OF GRAPHITES

R. S. Graves J. P. Moore
D. L. McElroy

We initiated a physical properties study of potential MSBR materials of construction. Initial interest is focused on the thermal conductivity of various grades of graphites and the influence of temperature, anisotropy, and irradiation.

A comparative longitudinal-heat-flow apparatus[8] was used to measure the thermal conductivity (λ) of three types of graphite from 300 to 475°K in the directions perpendicular and parallel to the pressing direction. Some of the properties of these graphites were reported previously.[9] Our measurements of the thermal conductivity and the room-temperature electrical resistivity (ρ) are given in Table 17.3. The thermal conductivity values have a probable accuracy of ±3%. The electrical resistivity results are 25 to 50 microhm-cm lower than those reported previously. This difference is in the correct direction to be caused by a geometric effect of isopotentials at the current leads of short samples. The thermal conductivity of these graphites decreases with increasing temperature and indicates from 5 to 30% anisotropy. This temperature dependence agrees with our previous findings on CGB graphite, which showed an inverse relation between thermal conductivity and the absolute temperature.[10] This indicates three phonon scattering processes are acting, and this scattering limits lattice heat conduction insulators above their Debye temperature. Our previous findings show this relation to hold below the Debye temperature of graphite. The anisotropy ratios $\lambda\perp/\lambda\parallel$ and $\rho\parallel/\rho\perp$ of the various graphites agree to within 5%. In a previous study we noted that the resistivity ratio changed less than 8% from 300 to 1300 K.[10]

Finally, thermal conductivity measurements were obtained on one sample irradiated in the ORR to an approximate fast fluence of 4.8×10^{19} neutrons/cm^2 at 700°C; the results are given in Table 17.3. This 50% reduction in the thermal conductivity agrees with reported findings on the effects of irradiation. Further tests and analysis of this are planned.

17.6 X-RAY STUDIES

O. B. Cavin

The dimensional stability of polycrystalline graphite shapes under neutron irradiation is partially a function

[7] W. P. Eatherly and E. L. Piper, "Manufacture," p. 32 in *Nuclear Graphite*, ed. by R. E. Nightingale, Academic, New York, 1962.

[8] J. P. Moore *et al.*, *Thermal Conductivity Measurements on Solids Between 20 and 150°C Using a Comparative-Longitudinal Apparatus*, ORNL-4121 (June 1967).

[9] W. H. Cook, J. L. Griffith, and O. B. Cavin, *MSR Program Semiann. Progr. Rept. Aug. 31, 1968*, ORNL-4344, pp. 226–27.

[10] J. P. Moore, T. G. Godfrey, and D. L. McElroy, "Thermal Properties of Grade CGB Graphite" in *Proc. Fourth Conf. Thermal Conductivity U.S.N.R.D.L.* (October 1964).

Table 17.3. Physical Properties of Three Graphites

Grade	Direction[a] Measured	Thermal Conductivity (λ) at the Indicated Temperature (w cm^{-1} $°K^{-1}$)					$\lambda_\perp/\lambda_\parallel$	Electrical Resistivity (ρ) at 298°K (microhm-cm)	$\rho_\parallel/\rho_\perp$
		300°K	350°K	400°K	450°K	475°K			
ATJ-S	⊥	1.55	1.51	1.43	1.34	1.30	1.28	841.6	1.33
ATJ-S	∥	1.21	1.18	1.13	1.05	1.01		1122.3	
ATJ-SG	⊥	1.33	1.29	1.23	1.16	1.12	1.10	1011.4	1.13
ATJ-SG	∥	1.21	1.18	1.13	1.05	1.01		1150.6	
H-337	⊥	1.58	1.58	1.51	1.43	1.39	1.05	778.8	1.06
H-337	∥	1.50	1.49	1.42	0.32	1.27		826.5	
ATJ-SG[b]	∥	0.62	0.67	(0.66)					

[a]Direction indicates orientation with respect to pressing direction. ⊥ = perpendicular; ∥ = parallel.
[b]Irradiated at 700°C to 4.8×10^{19} neutrons/cm^2.

of the bulk crystalline anisotropy of the material. Therefore, to characterize and study potential graphites, we are determining by x-ray analysis the anisotropy of the basal plane distribution prior to irradiation. We have shown that there is a linear relationship between the radiation-induced growth rates at constant volume and the bulk anisotropy.[11]

The distribution of basal planes in the graphite is proportional to the x-ray intensity distribution diffracted from those planes. From x-ray intensity data vs angular position, a preferred-orientation parameter can be calculated by the following formula defined by Price and Bokros:[12]

$$R_\parallel = \frac{\int_0^{\pi/2}\int_0^{\pi/2} I(\phi,\beta)\sin^3\phi\, d\phi\, d\beta}{\int_0^{\pi/2}\int_0^{\pi/2} I(\phi,\beta)\sin\phi\, d\phi\, d\beta}, \qquad (1)$$

where

ϕ = angle between normals to sample surface and basal planes,

β = angle of rotation about sample normal,

$I(\phi,\beta)$ = x-ray intensity at angle ϕ and β.

If the material has an axis of symmetry coincident with the forming axis the integration through the angle β is constant, and the above equation reduces to a single integration in ϕ. However, we have found that in many cases the axis of symmetry is not coincident with the forming axis, in which case it is desirable to do the double integration. Since there are two directions in the orthogonal system acting normal to the forming axis, and by assuming an axis of symmetry in the parallel direction, then

$$R_\perp = 1 - R_\parallel/2\,. \qquad (2)$$

We are using a Schulz preferred-orientation attachment mounted onto a North American Philips x-ray diffractometer and vanadium-filtered chromium radiation. The diffracted intensity data from samples whose surface is perpendicular and parallel to the forming axis are recorded onto a computer-compatible perforated paper tape. Eighty data points per 360° β rotation are averaged for each 5° increment of ϕ. Substitution of these values into Eq. (1), with the β integration approximated by the averaging, yields an R value in a direction perpendicular to the sample surface. This procedure can be repeated on a sample oriented perpendicular to the one just discussed.

We have used this technique for determining the preferred orientation parameters of a number of grades of graphite, and the results are shown in Table 17.4. By averaging the data through complete rotations in the angle β and using samples whose surfaces are perpendicular and parallel to the forming axis, we have determined R values independently in the two directions. The validity of this approach is indicated by the small deviation from the theoretical value of 2 for the sum of the R values in the three orthogonal directions. These are the R values relative to the forming axis with no assumption about the position of the symmetry axis.

Isotropic materials will have R values in each of the three orthogonal directions equal to 0.667. Samples

[11]C. R. Kennedy, this report, Sect. 17.9.

[12]R. J. Price and J. C. Bokros, *J. Appl. Phys.* 36, 1897 (1965).

Table 17.4. Anisotropy Values of Various Graphites

Grade	$R_{\parallel}$	$R_{\perp}$	T^a
BY 12	0.588	0.706	2.000
RY 12-00029	0.792	0.600	1.992
RY 12-00031	0.808	0.594	1.996
AXF	0.673	0.663	1.999
AXF-3000	0.667	0.666	1.999
AXF-5QBG	0.667	0.666	1.999
AXF-5QBG (3000°C)	0.656	0.671	1.998
H 364	0.645	0.676	1.997
H 337	0.659	0.670	1.985
ATJ-S	0.617	0.684	1.985
ATJ-SG	0.638	0.680	1.998
BY 12 NF	0.585	0.707	1.999
1425[b] (pipe)	0.783	$R_r = 0.590$ $R_\theta = 0.627$	2.000

[a] $T = R_{\parallel} + 2R_{\perp}$.
[b] Three-dimensional anisotropy.

having $R_{\parallel}$ less than 0.667 indicate a molding texture, while those having $R_{\parallel}$ greater than this have an extrusion texture; the magnitude of this deviation indicates the degree of anisotropy. A single crystal will have $R_{\parallel} = 0$ and $R_{\perp} = 1$. Note that several of the materials studied have R values very close to the predicted 0.667 for complete isotropy (Table 17.4).

These anisotropy values have made it possible to better understand the effects of binder and filler on the radiation growth rates of various graphites (Fig. 17.14, Sect. 17.9). The growth rates at constant volume and the preferred orientation parameter correlate as a straight line, indicating that, even though some have different binders and fabrication procedures, the growth rates are dependent mainly upon the degree of anisotropy.

17.7 ELECTRON MICROSCOPY OF GRAPHITE

C. S. Morgan C. S. Yust

Direct observation of the substructure of polycrystalline graphites by transmission electron microscopy may permit a better understanding of the process of radiation damage in these materials. Although a substantial amount of transmission microscopy has been done on single-crystal graphite, the transmission work on bulk polycrystalline graphite is quite limited. The first requirement in this study was the development of a suitable thinning technique. We found that thinning by mechanical polishing can be used to prepare satisfactory specimens of AXF graphite. The application of this technique to other graphites is being evaluated.

A variety of graphites will be examined in the as-fabricated and the irradiated conditions to determine the substructure change with irradiation. Fig. 17.1 shows a transmission electron micrograph of type AXF graphite as fabricated. The structure is composed of regions about 1 μ in diameter within which exist aligned ribbons of materials. Cracks are sometimes seen between the ribbons, as well as between regions of different alignment. Although numerous spots are usually present, electron diffraction patterns of the smallest possible selected area always yield rings, thus indicating that the crystallite size is quite small. Smaller units which go in and out of contrast with tilting agree in size with the crystallite size determined by x-ray line broadening (250 A). Boundary regions in the AXF graphite are not well defined.

17.8 GAS IMPREGNATION OF GRAPHITE WITH CARBON

R. L. Beatty D. V. Kiplinger

We have been studying a vacuum-pressure pulsing technique to seal graphite for MSBR use as discussed earlier.[13] The current specification on surface tightness of the graphite is a room-temperature permeability to helium not greater than 10^{-8} cm^2/sec. Accordingly, we are studying means to optimize the gas impregnation process.

The effect of process temperature is shown clearly in Fig. 17.2. In this set of experiments we maintained constant the substrate type (Poco AXF graphite) and the vacuum and butadiene exposure periods. The initial slopes of high rates of weight gain shown by the curves in Fig. 17.2 indicate the coating of a very large surface area, namely, the walls of the entire open-pore structure. The sharp changes of slope indicate the closing of most of the pore volume during a relatively small increment of processing time, thus attesting the uniformity of pore size of the AXF graphite substrate. Each specimen was sealed to a low helium permeability after this sharp change in slope, and the leveled-out section of each curve involves essentially coating of only the specimen geometrical surface area. A comparison of the slopes of the latter portion of these curves shows clearly that increasing the temperature increases the rate of deposition. This effect is also shown by the points at which pores are closed at the different temperatures. Lowering temperature results in slowing down the sealing process while increasing the depth of penetration and, eventually, the final amount of impregnant deposited. The 750°C deposition curve leveled out at a specimen weight increase of 7.5%, essentially

[13] *MSR Program Semiann. Progr. Rept. Aug. 31, 1968*, ORNL-4344, pp. 230–31.

Fig. 17.1. Transmission Electron Micrograph of a Thinned Area in the AXF Graphite. The sample has a uniform thickness and the various tones varying from white to black indicate variations in the orientation of different regions. 85,000X.

all internal deposit. Data indicate that a finite, though often immeasurable, amount of surface coating is required to achieve a helium permeability less than 10^{-8} cm^2/sec at room temperature.

We must optimize the gas impregnation process for a given type of substrate. Figure 17.3 shows the effect of varying the vacuum pulse period. For the Poco AXF substrate, a sealing temperature of 850°C, and a butadiene pulse of ½ sec, we found that shortening the vacuum pulse from 60 to 15 sec served to increase the rate and depth of impregnation as well as to accelerate the process. In this case further accelerating the sealing by shortening the vacuum pulse to 7.5 sec resulted in some sacrifice in penetration.

The effect of substrate pore structure on deposition and sealing rates is shown in Fig. 17.4. The fine-pore AXF graphite exposes a very large surface area for coating, so that the deposition rate is high until essentially all the pores are closed. The ATJ-SG graphite, which has about the same open-pore volume but a much larger average pore size, gains weight at a lower rate for the given set of processing conditions. The lack of a sharp change of slope in the ATJ-SG curve attests the wide pore-size distribution of this material. These data indicate that for the processing conditions shown a small, uniform pore size is very desirable for gas impregnation. However, a graphite such as the ATJ-SG can be impregnated fairly efficiently if processing conditions are optimized for it. In this case the temperature of 850°C may be near optimum for the AXF, but higher temperatures improved processing efficiency for the ATJ-SG.

Evaluation of the carbon impregnant seal, of course, must include irradiation testing, and this is in progress. The first group of gas-pulse-impregnated specimens prepared for irradiation in the HFIR was unloaded in December. The eleven specimens had received fast-neutron fluences ranging from 7.6 to 12.7 X 10^{21} neutrons/cm^2 at 705°C. Helium permeabilities before irradiation ranged from 1.2 X 10^{-7} to less than 1.3 X 10^{-10} cm^2/sec. After irradiation ten of the specimens showed helium permeabilities greater than 10^{-6} cm^2/sec, and the eleventh specimen was measured at 1.7 X 10^{-7} cm^2/sec. While these results do not show spectacular success, we are very encouraged that in the first test one specimen came very close to giving the desired performance. Since the permeability of this specimen before irradiation was about 10^{-8} cm^2/sec, the increase due to the test was approximately one order of magnitude, an acceptable damage if the initial permeability were lower.

There were two complicating factors in assessing the irradiation performance relative to helium permeability, both of which brighten the outlook for achieving satisfactory results over that obtained by a cursory glance at the data. First, we were attempting to study

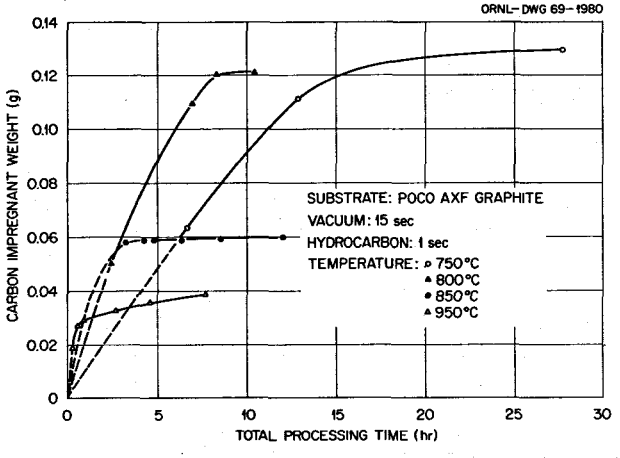

Fig. 17.2. Effect of Temperature on Rate and Final Amount of Carbon Impregnation.

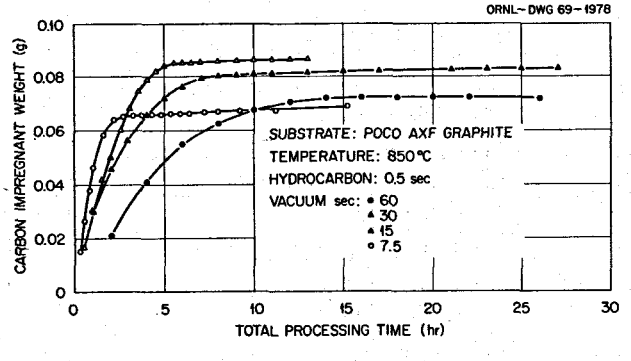

Fig. 17.3. Effect of Vacuum Period on Rate and Final Amount of Carbon Impregnation.

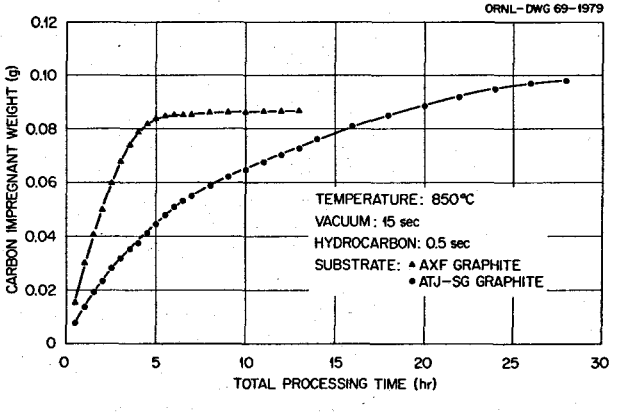

Fig. 17.4. Effect of Substrate Pore Structure on Rate and Final Amount of Carbon Impregnation.

only the seal on the outer surface of the cylindrical specimens, since the inner surface is in contact with a stainless steel spine in the test rig assembly during irradiation. This may cause damage other than that induced by neutrons. Since a coating which tends to form on the inner surface, if undisturbed, can dominate the helium-leak measurements, we reamed out the bore of each specimen after impregnating and before leak checking. However, after the irradiation experiment was assembled we learned that the reaming operation was inadequate. It seems that reaming can serve to smear the graphite and actually make the surface less permeable. To eliminate this problem it is necessary to actually gouge a groove in the bore of the specimen before leak checking, a procedure we employed in fabricating the second set of specimens. The second complication is the problem of how to determine permeability. Since we actually measure a leak rate, some wall thickness must be used to calculate a permeability. We arbitrarily use the total wall thickness of the specimen for this purpose, but we know that the gas-tight section is much thinner. It is interesting to note that if we use one-tenth of the total wall thickness in the permeability calculation, the result for the best specimen after this first test is about 10^{-8} cm^2/sec, the value which is currently specified as the necessary graphite surface permeability for an MSBR.

We have prepared a new group of test specimens, which were inserted in the HFIR in early February. Seven new specimens and three of the first set, including the one having the 10^{-7} cm^2/sec helium permeability, will be irradiated in the HFIR to a peak fast fluence of about 2.5×10^{22} neutrons/cm^2.

17.9 GRAPHITE IRRADIATION IN HFIR

C. R. Kennedy

HFIR graphite irradiation experiments 5 and 6 have been removed from the reactor, the specimens measured, and a number of the samples recycled in experiments 7 and 8. The samples have received exposures up to 2.5×10^{22} neutrons/cm^2 (>50 kev) and will accumulate up to 3.8×10^{22} neutrons/cm^2 when they are removed from HFIR in May 1969.

The materials that have been irradiated and have given significant results are listed in Table 17.5. The linear

Table 17.5. Graphites Irradiated in HFIR Experiments

Grade	Source	Forming Method	Density (g/cm^3)	Remarks
BY-12	Y-12	Molded	1.88	GLCC 1008 graphite flour; pitch binder; two impregnations; 3000°C
RY-12-29	Y-12	Extruded	1.89	85% GLCC 1008 graphite flour; 15% Thermax; Varcum binder; 3000°C
RY-12-31	Y-12	Extruded	1.80	GLCC 1008 graphite flour; Varcum binder; 3000°C
Natural flake	Y-12	Molded	1.83	Madagascar natural flake flour; pitch binder; 3000°C
H364	GLCC	?	1.94	Proprietary materials and forming method; reasonably isotropic; 2800°C; laboratory processed
H337	GLCC	?	2.00	Same as H364; pilot plant processed
1425	UCC	Extruded	1.82	Needle coke graphite; pitch bonded; multiple impregnation; 2800°C
ATJ-S	UCC	Molded	1.91	Needle coke graphite; pitch bonded; multiple impregnation; 2800°C
ATJ-SG	UCC	Molded	1.80	ATJ-S processed using Gilso carbon coke
AXF	Poco	Molded	1.82	Proprietary materials and forming; very isotropic; 2300°C
AXF-3	Poco	Molded	1.82	AXF heat treated 1 hr at 3000°C
AXF-5QBG	Poco	Molded	1.86	AXF material with a single impregnation; heated to 2500°C
AXF-5QBG-3	Poco	Molded	1.85	AXF-5QBG heat treated to 3000°C
AXF-UFG	Poco	Molded		A fine-grained AXF graphite; 2500°C

dimensional changes resulting from the irradiation are given in Figs. 17.5–17.8. The curves drawn in these figures, with the exception of the Poco grade, were obtained from least-squares fitting of the data to a quadratic expression. The volumetric changes were calculated from the linear dimensional change data. The volumetric change curves are given in Figs. 17.9–17.11. The more isotropic grades, H364, H337, and Poco grades, have considerably more scatter in their results than the anisotropic grades. This is undoubtably a result of small sample-to-sample variations in the preferred orientation. Dimensional stability is a result of isotropy where the high growth rates in the *c* and *a* axis directions are balanced. Slight variations in the preferred orientation will result in a much larger fractional variation in growth than for the anisotropic grades having much larger linear dimensional changes.

The analysis of these results is still in progress; however, several significant behavioral characteristics which are important to the development of a more radiation-resistant graphite are apparent. The first is that the maximum densification of the graphite is a linear function of the original density, as shown in Fig. 17.12. One material, grade 1425, is obviously off the curve, and grades ATJ-S and ATJ-SG are on the low side; however, the Poco grades have not densified fully and are not plotted. The 1425 grade is the only material in which the impregnate is apparent in the microstructure and appears to be a distinct second phase. This

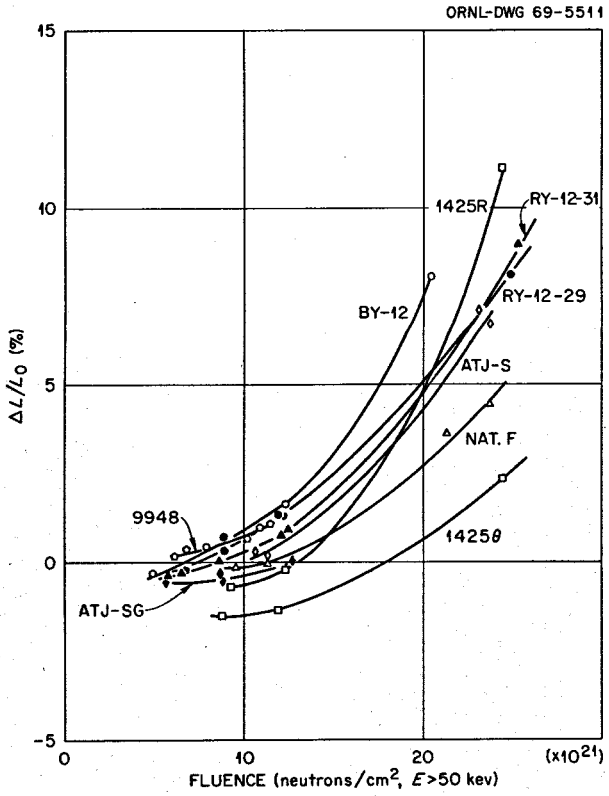

Fig. 17.5. Growth of Graphite Normal to the Extrusion Direction or Parallel to the Molding Direction, 715°C.

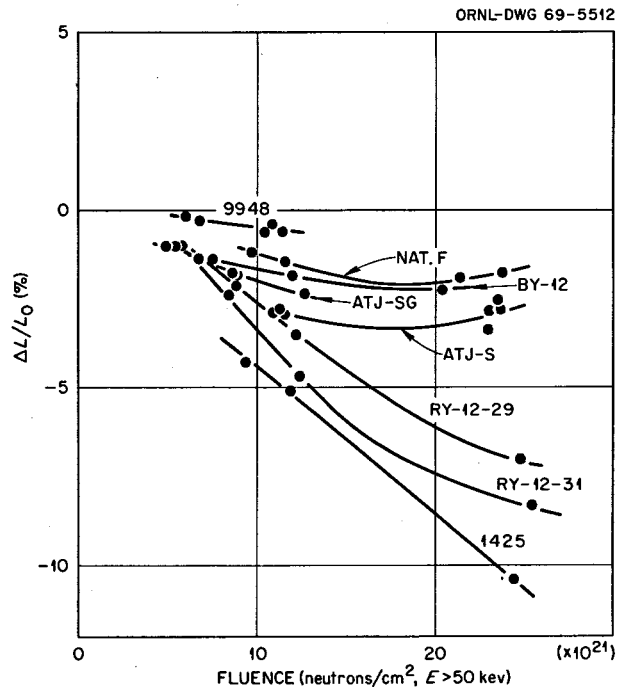

Fig. 17.6. Growth of Graphite in the Extrusion Direction or Normal to the Molding Direction, 715°C.

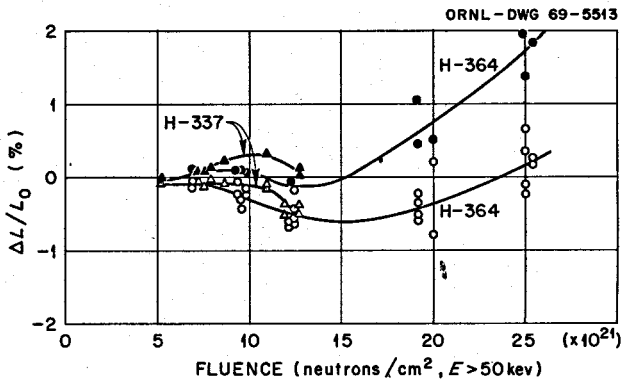

Fig. 17.7. Growth of Graphite Grades H-364 and H-337, 715°C.

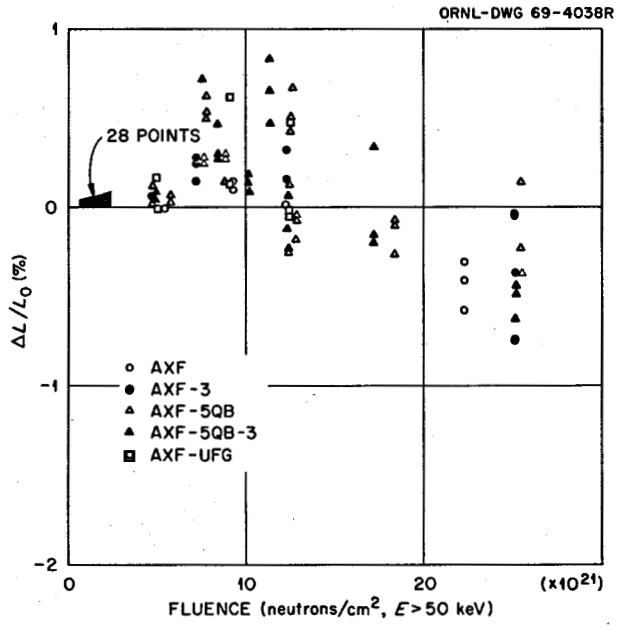

Fig. 17.8. Growth of POCO Graphites at 715°C.

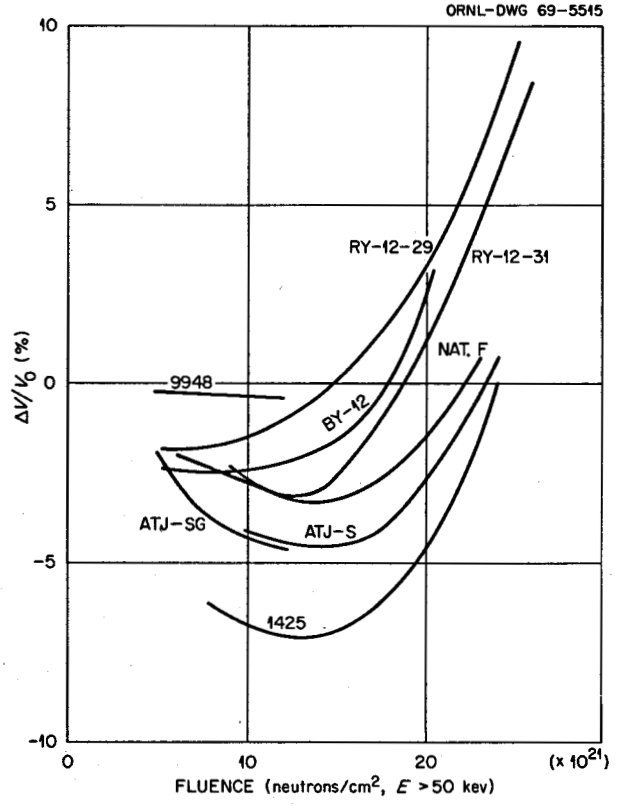

Fig. 17.9. Volume Changes of Graphite Grades at 715°C.

would suggest that the second-phase carbon is not part of the structure and that the true structural density is much lower than 1.83 g/cm^3. The ATJ-S and ATJ-SG are heavily impregnated grades; however, the impregnate has graphitized and cannot be distinguished in the microstructure. It might be that again the impregnate has not completely integrated with the structure and is not completely a part of the true structural density. The major difference in the graphites with different original densities is a reduction of open-pore volume with increasing density. Therefore the relationship shown in Fig. 17.12 is strong evidence that the closure of the open pore volume is the major contribution to the densification of the graphite. The significance of the relationship in Fig. 17.12 is that it demonstrates a serious problem in obtaining an extended life for conventional graphites fabricated to the high density required for the MSBR. The term "conven-

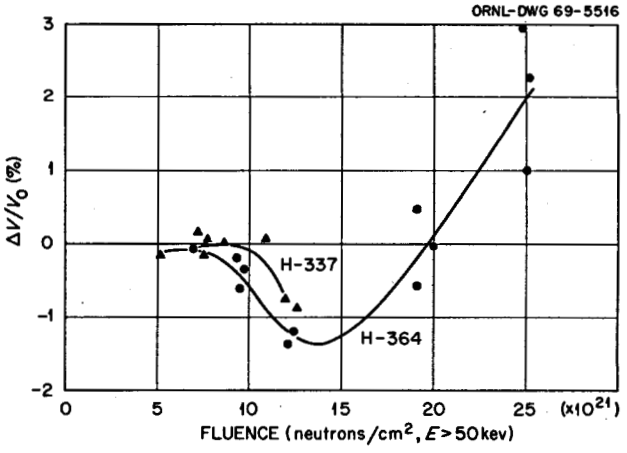

Fig. 17.10. Volume Change of Graphite Grades H-364 and H-337, 715°C.

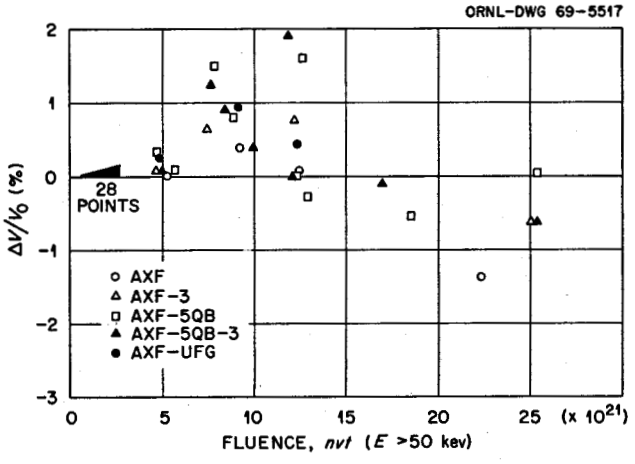

Fig. 17.11. Volume Changes in Poco Graphites at 715°C.

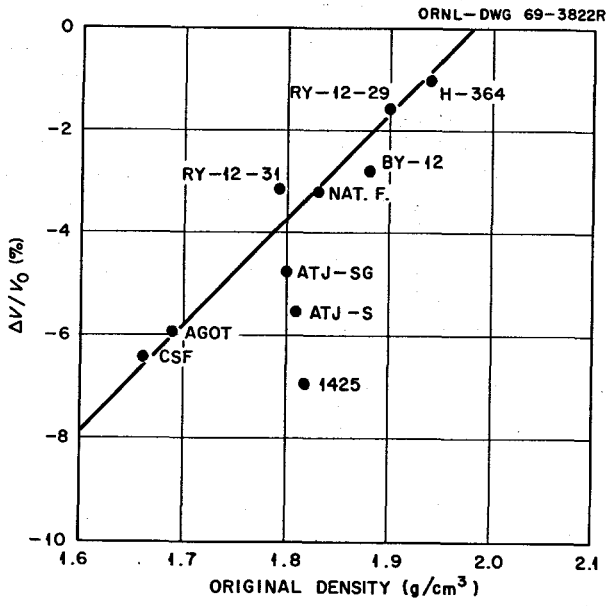

Fig. 17.12. Maximum Densification as a Function of Original Density, 715°C.

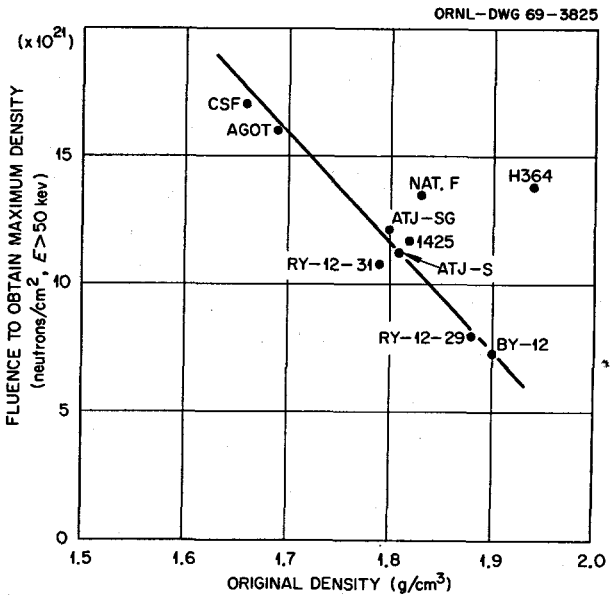

Fig. 17.13. Fluence to Obtain Maximum Density as a Function of Original Density.

tional graphites" excludes grades H364, H337, and the Poco grades in the light of an exceptional behavioral characteristic extending their expected lifetime as described below.

If the densification rate is common for the graphites, then the fluence required to obtain the maximum density will also be a linear function of the original density. This relationship is shown in Fig. 17.13. This means that the more dense conventional materials will achieve their maximum density more quickly, begin to expand, and have a shorter lifetime.[14] There are two materials, H364 and natural flake, that do not fall on the curve, and obviously the unplotted Poco grades would not follow this correlation. The initial structure of the natural flake grade is probably the most highly graphitic of the group. Thus the initial crystallite growth rates and the initial densification rate would be lower, and the fluence required for maximum densification would be extended. The lower crystallite growth rate can only be hypothesized, since it will be shown that the crystallite growth rates at minimum volume are the same for all the grades of graphite tested.

The H364 and the Poco grades do not fall on the curve in Fig. 17.13 because of a delayed densification. This factor is very significant since it results in an extension of the lifetime of the graphite. This delay in densification is undoubtedly a result of the high continuity of *c* axis in the structure. The high continuity of *c* axis is reflected by the very high coefficient of thermal expansion for these materials, 7 to 7.5 X 10^{-6}/°C for the Poco grades and 6 to 7 X 10^{-6} for H337 and H364 grades. Although the Poco and H337 grades have not reached their maximum density and could not be included in Fig. 17.13, they do exhibit an initial delay period (Figs. 17.7 and 17.8) and will very likely fall above the line. A high continuity of *c* axis in the structure is required for the *c*-axis growth to cancel the *a*-axis shrinkage and eliminate linear dimensional changes and densification. The isotropy can be obtained either by randomization of anisotropic coke particles or by randomization of the crystallites within the coke particle to obtain an isotropic coke. If anisotropic coke is used, the coke particle will change dimensions, and differential growth must be absorbed in the boundaries between coke particles. However, if the coke is isotropic, the differential growth will be absorbed in the boundaries between crystallites within the coke particle. The isotropic particles would not change dimensions, and the differential growth between particles

[14] The "lifetime" of the graphite is defined as that exposure where void generation as evidenced by volume expansion is sufficient to increase the open-pore size, allowing excessive fission product and poison accumulation. We have arbitrarily chosen the fluence required to return the material back to its initial volume after some densification. This is a conservative approach and may be particularly conservative for those graphites which only densify 1–2% before expansion. The actual limitation in lifetime will have to be determined by experiment.

would be eliminated. At present, it is not certain how grades H337 and H364 obtain their isotropy, but preliminary observations using electron transmission microscopy[15] of the Poco grades indicate that their isotropy is obtained by using isotropic coke particles.

We do not understand why these graphites begin to densify after a significant period of irradiation. The *c*-axis continuity appears to be reduced, as evidenced by the observation that the coefficient of thermal expansion decreases as the material begins to densify.[16] The internal stresses created by the differential growth should be compressive in the *c*-axis direction, so it is difficult to understand how this could cause separations along the *c* axis. However, these graphites (H364, H337, Poco grades) have begun to densify after an initial delay, and the H364 has already achieved maximum density and experienced some volume expansion.

The Poco and H364 materials are significantly superior in their resistance to both linear and volumetric change during irradiation. The Poco grades have not achieved their maximum densification in the present data. It is fairly evident that if the relationship in Fig. 17.12 holds for the Poco grades (density of about 1.85 g/cm^3) and they densify to the indicated 3–3.5% volume change, the fluence required to achieve maximum density will be greater than 3×10^{22} neutrons/cm^2. The extent that the lifetime will be extended would be conjecture at this time. The Poco material is not available in the necessary shapes and sizes required for an MSBR, and it will be necessary to develop fabrication procedures for this graphite before it can be considered a potential candidate for MSBR applications. The H364 and H337 grades of graphite are reasonably stable and are available in the necessary sizes and shapes. This material is still in the development stages, and further property improvements may be possible. These materials are currently prime candidates for use in early MSBR's.

One final significant result in this study is our analysis of the linear dimensional changes. The linear dimensional changes are largely dependent upon the preferred orientation of the graphite. However, volumetric changes, due to void closure, void production, and lattice parameter changes, are also reflected in the linear dimensional changes. These volumetric changes generally do not have the same anisotropy functions as the crystallographic growth rates, so it is difficult to separate the observed linear growth rates into crystallite and volumetric growth. This must be done to compare the effects of fabrication variables on the growth rates under irradiation. The solution to this problem is to obtain the linear growth rates when the volume change rate is 0, thereby eliminating the volumetric contribution to linear growth. This allows a comparison of the growth rates when they are dependent solely upon the dimensional changes of the crystallites and their preferred orientation. This can be done by using the following equation which describes the growth rates in the *i*, *j*, and *k* directions in a single-phase model:

$$\begin{aligned} \dot{G}_i &= R_i \dot{G}_a + (1 - R_i)\dot{G}_c + F_i(\dot{V}) , \\ \dot{G}_j &= R_j \dot{G}_a + (1 - R_j)\dot{G}_c + F_j(\dot{V}) , \\ \dot{G}_k &= R_k \dot{G}_a + (1 - R_k)\dot{G}_c + F_k(\dot{V}) , \end{aligned} \tag{1}$$

where

$$\dot{G} = \frac{1}{l_0} \frac{dl}{d(\phi t)} ,$$

$$\dot{V} = \frac{1}{V_0} \frac{dv}{d(\phi t)} ,$$

$F(\dot{V})$ = contribution of volumetric changes to linear growth,

R = orientation parameter determined by x-ray diffraction.[17]

The linear growth rate of each material determined when $F(\dot{V}) = 0$ is plotted as a function of its orientation parameter, R, giving a graphical representation of Eq. (1). For the unique condition of $F(\dot{V}) = 0$, the intercept of such a plot at $R = 0$ and $R = 1$ yields the average crystallite growth rates in the *c* and *a* direction respectively. The linear growth rates obtained for all the materials at their respective fluence when $F(\dot{V}) = 0$ are given in Fig. 17.14.

The rather remarkable agreement of ten grades of graphite is surprising. This indicates that all ten materials have essentially the same average crystallite growth rates independent of binder, Thermax additions, impregnations, and filler coke. It is also significant to note that the linear growth rates when $F(\dot{V}) = 0$ were obtained over a range of exposures (7×10^{21} to 17×10^{21} neutrons/cm^2). This implies that the average crystallite growth rates are constant over this exposure range. As mentioned earlier, it has been previously reported[18] that crystallite growth rates decrease with

[15] C. S. Morgan and C. S. Yust, sect. 17.7, this report.

[16] A. L. Pitner, *Irradiation Behavior of Poco Graphites*, BNWL-CC-193 (November 1969).

[17] O. B. Cavin, sect. 17.6, this report.

[18] J. C. Bockros and A. S. Schwartz, *A Model to Describe Neutron-Induced Dimensional Changes in Pyrolytic Carbon*, GA-7700 (March 1967).

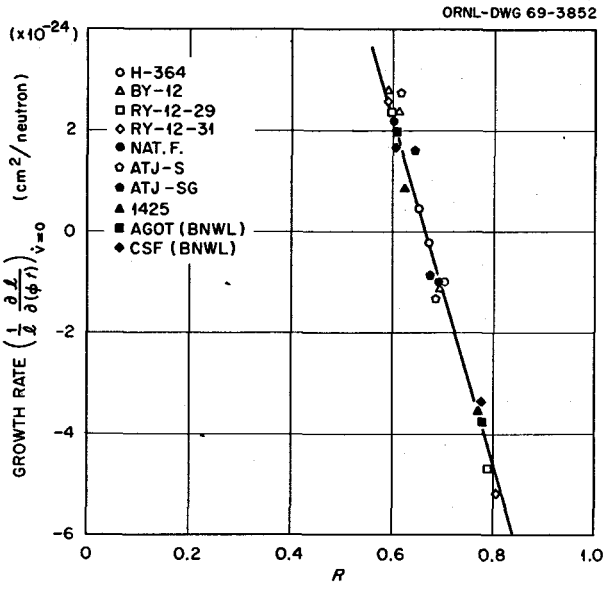

Fig. 17.14. Growth Rate of Graphite as a Function of Preferred Orientation, 715°C.

increasing crystallite size. These differences in crystallite growth rates may be real at low exposures when they were measured. However, crystallite size measurements of irradiated materials indicate that all materials increase or decrease to a common crystallite size of ~150–200 A.[19] This observation indicates that only short-term benefits can be obtained from increased crystallite size in the graphite.

In general, these results and the analysis of the results lead to several conclusions:

1. Linear dimensional stability is obtainable only with isotropic or near-isotropic materials.
2. Volumetric changes also contribute to linear dimensional changes, and the magnitude of their contribution is reduced by increasing the original structural density.
3. The major behavioral characteristic that separates grades H364, H337, and Poco graphites from the conventional graphites is that of a delayed densification. This is the only process observed which appears to extend the useful life of the graphite. The origin of this desirable characteristic is not clear, but we have observed it only in the two types of materials having isotropic structures with very high coefficients of thermal expansion.

[19] J. W. Helm, *The H-3 Irradiation Experiment: Irradiation of EGCR Graphite – Interim Report No. 2,* HW 71500B (September 1964).

17.10 CALCULATION OF LIFETIME AND INDUCED STRESSES IN MSBR CORES

S. J. Chang
W. P. Eatherly
J. W. Prados

To assess the potential effects of fast-neutron damage in the core graphite of a molten-salt reactor, preliminary calculations of induced stress distributions and distortions have been carried out by three different techniques. As a first approximation, the core graphite is assumed to be in the form of long cylindrical tubes, although the actual shape will be more complex.

We start with the basic constitutive equations

$$\dot{\epsilon}_i = \frac{1}{E}\left[\dot{\sigma}_i - \mu(\dot{\sigma}_j + \dot{\sigma}_k)\right] + \frac{1}{E''}\left[\dot{\sigma}_i - \mu''(\dot{\sigma}_j + \dot{\sigma}_k)\right] f(\phi, t) + k\phi\left[\sigma_i - \mu'(\sigma_j + \sigma_k)\right] + g(\phi, t),$$

in which ϵ_i and σ_i are the strain and stress in the ith direction, the first term on the right is the elastic distortion, the second the primary creep, the third the secondary creep, and the last the rate of radiation-induced distortion. Since the primary creep is a rapidly saturating function, one may substitute the asymptotic value of the function f, thereby suppressing its time dependence and combining it with the first term. Hence

$$\dot{\epsilon}_i = \frac{1}{\langle E\rangle}\left[\dot{\sigma}_i - \langle\mu\rangle(\dot{\sigma}_j + \dot{\sigma}_k)\right] + k\phi\left[\sigma_i - \mu'(\sigma_j + \sigma_k)\right] + g(\phi, t),$$

where $\langle E\rangle$ and $\langle\mu\rangle$ are the effective Young's modulus and Poisson's ratio respectively.

A solution to these equations in closed analytic form can be found by using operator algebra. The solution is limited to the requirement that the parameters $\langle E\rangle$, $\langle\mu\rangle$, $k\phi$, and μ' not be functions of radial position in the cylinder. This restriction is not a serious one for the present calculations.

A second solution has been developed by modifying an iterative technique employed in the analysis of stress and distortion in coated-particle fuels.[20] This approach permits $k\phi$ to be a function of radial position, does not

[20] J. W. Prados and T. G. Godfrey, *STRETCH, a Computer Program for Predicting Coated-Particle Irradiation Behavior, Modification IV,* ORNL-TM-2127 (April 1968).

require isotropy in the graphite, and permits the secondary creep to be a more general function of the stresses.

The third solution, using an impulse-type analysis, has also been derived,[21] which further generalizes the solutions to arbitrary boundary shapes providing only that elastic solutions can be found. It is limited, however, to a linear stress dependence in the secondary creep.

All three solutions have been computer programmed, debugged, and shown to give the same numerical results within their region of overlap. In particular, the stresses and distortions have been calculated for the present reactor parameters aimed at a four-year graphite life. The material parameters employed are as follows:

Young's modulus: $E = 1.9 \times 10^6$ psi,

Poisson's ratio: $\mu = 0.27$,

thermal expansion coefficient: $\alpha = (5.52 \times 10^{-6} + 1.00 \times 10^{-9} T)\,(°C)^{-1}$,

thermal conductivity: $K = 37.63(T + 273.1)^{0.7}$ w cm^{-1} $(°C)^{-1}$,

secondary "Poisson's ratio": $\mu'' = 0.50$,

creep coefficient: $k = (5.3 - 1.45 \times 10^{-2}\, T + 1.4 \times 10^{-5} T^2) \times 10^{-27}$ (psi nvt)$^{-1}$.

The induced distortion rate $g(\phi, t)$ was derived primarily from the experimentally determined behavior of British isotropic Gilso graphite:

$$g = \frac{4G_m}{\tau}\left(1 - 2\frac{t}{\tau}\right),$$

where

$G_m = -4.01 + 2.97 \times 10^{-3} T$ percent,

$\phi_\tau = (9.36 - 8.93 \times 10^{-3} T) \times 10^{22}$ (nvt),

τ = lifetime, sec.

In all the above equations T is the graphite temperature in degrees centigrade.

Parameters associated with the reactor were taken as follows:

salt temperature: $T_0 = 625 - 75 \cos\frac{\pi z}{l}$ deg C,

flux: $\phi = (3.2 \times 10^{14}) \sin\frac{\pi z}{l}$ neutrons/cm^2 $(E > 50$ kev),

gamma heating: $q = 0.71 + 4.39 \sin\frac{\pi z}{l}$ w/cm^3,

graphite outer radius: $b = 5.39$ cm,

graphite inner radius: $a = 0.762$ cm,

where z/l is the fractional height along the core center line. The heat transfer coefficient between the salt and graphite was calculated from the Dittus-Boelter equation for turbulent flow with salt properties as follows:

thermal conductivity: 0.75 Btu hr^{-1} ft^{-1} $(°F)^{-1}$,

flow: 6.08×10^6 lb ft^{-2} hr^{-1},

viscosity: 0.193 exp [7816/T (°F)] lb/ft,

specific heat: 0.324 Btu lb^{-1} $(°F)^{-1}$.

Over the temperatures of interest this yields a heat transfer coefficient

$$h = 2.012 \times 10^{-3} T - 0.316 \text{ w cm}^{-2}\,(°C)^{-1}.$$

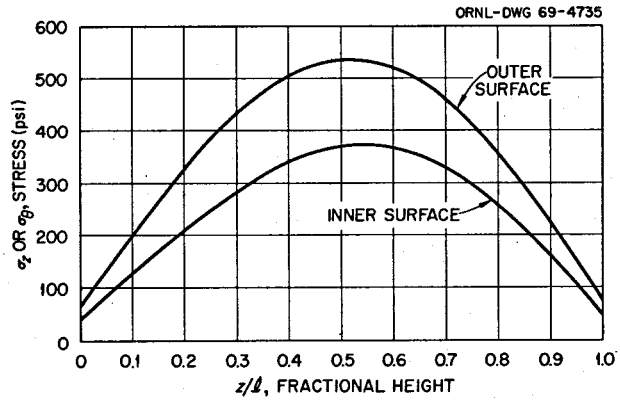

Fig. 17.15. Maximum Thermal Stresses Developed in the Graphite at Reactor Startup.

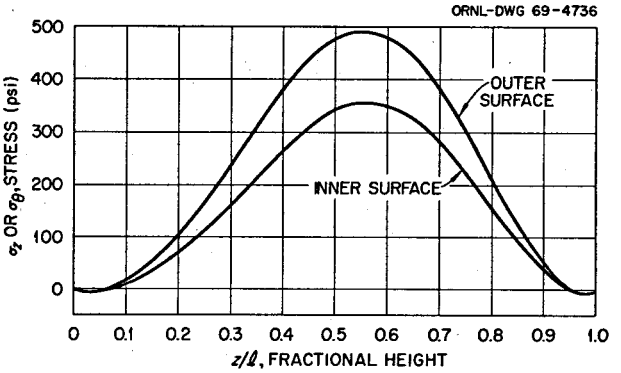

Fig. 17.16. Maximum Radiation-Induced Stresses Developed in the Graphite at the End of Core Life.

[21] S. J. Chang, *Visco-Elastic Analysis of Graphite Under Neutron Irradiation and Temperature Distribution*, ORNL-TM-2407, to be published.

The results of the calculations are as follows: The graphite is under the most severe flux-temperature environment at $z/l = 0.55$ (i.e., slightly over halfway up the core) and at that point has a lifetime[22] of 4.1 years. The maximum thermal stresses are tensile and occur at the surfaces of the graphite (see Fig. 17.15). They anneal out due to creep in a few weeks time and do not exceed 560 psi. The maximum radiation-induced stresses are tensile and occur at the end of the graphite life (see Fig. 17.16). They do not exceed 500 psi. Since the graphite should have an ultimate tensile strength of about 5000 psi, these stresses are not significant.

The dimensional behaviors are shown in Figs. 17.17 and 17.18. These are expressed in terms of the function G_i, representing the percentage distortion of the ith dimension. The cylindrical graphite tubes will show a maximum radial shrinkage of about 2.2% and a maximum axial shrinkage of about 1.6%. These dimensional changes are significant but can be compensated for in the core design.

Recent data on the irradiation of newer graphites given in Sect. 17.9 suggest that materials superior to the British Gilso graphite will be available within the next few years. Hence the above numbers represent an upper limit to the stresses and distortions which can be expected in an actual reactor.

[22] As the definition of lifetime, we take a priori the time at which the most damaged region in the graphite returns to its original volume.

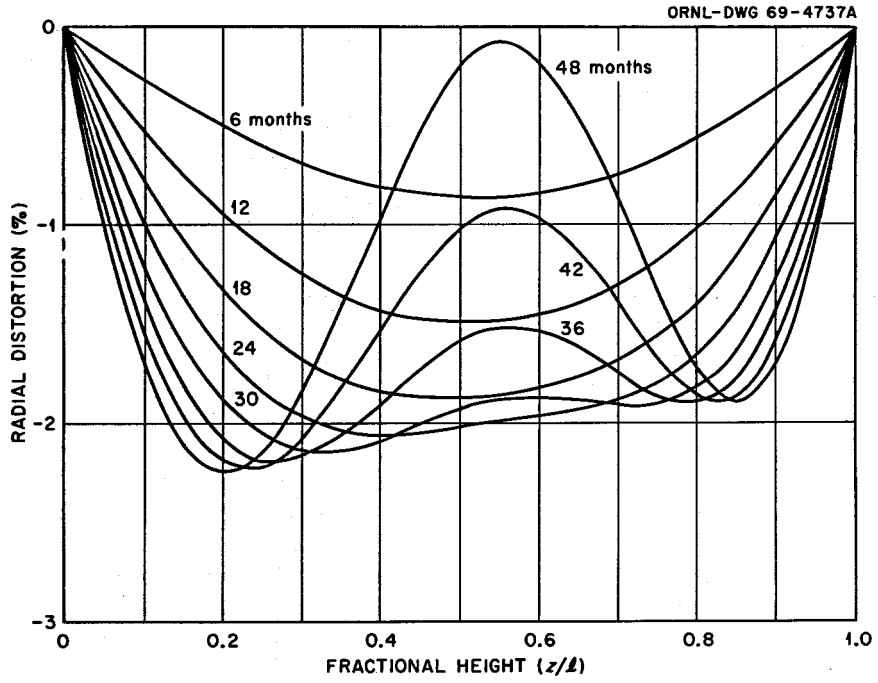

Fig. 17.17. Radially Induced Distortion of Graphite as a Function of Axial Position on the Reactor Core Centerline as a Function of Time.

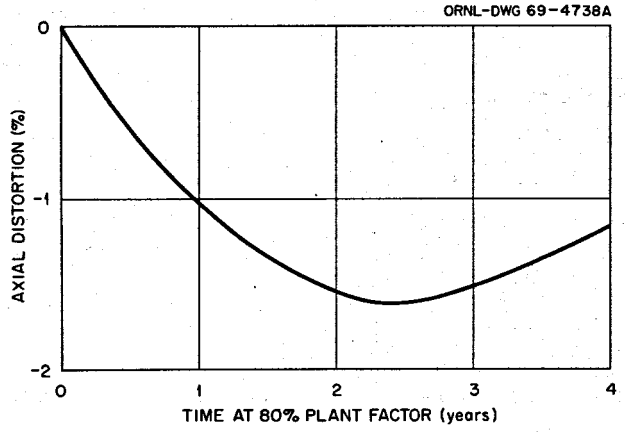

Fig. 17.18. Axially Induced Distortion of Graphite on Reactor Core Centerline as a Function of Time.

18. Hastelloy N

18.1 INFLUENCE OF TITANIUM AND CARBON ON THE MECHANICAL PROPERTIES OF NICKEL-BASE ALLOYS

C. E. Sessions

We have extensively investigated the influence of titanium and carbon interactions on the high-temperature creep-rupture properties of laboratory melts of Ni–12% Mo–7% Cr alloy. The influences of heat treatment, strain rate, and composition were evaluated for creep testing at 650°C in air. Representative results of the heats listed in Table 18.1 will be discussed. The material investigated has a base composition of Ni–12% Mo–7% Cr–0.5% Ti, with the carbon content increasing from 0.003 to 0.32% for heats 193 to 242. We also included heat 198, which contains no titanium and 0.04% C. Thus a comparison of heats 196 and 198 would give the effect of titanium alone, since these two alloys have an equivalent carbon content.

Carbon concentration has a marked effect on the rupture life of this alloy (Fig. 18.1). The rupture life increases by four orders of magnitude for a factor of 100 increase in the carbon level. No added strengthening is found, however, above ~0.1% C. This increase in rupture life is the result of a marked decrease in the rate of secondary creep deformation, as shown in Fig. 18.2. The steady-state creep rate decreases by three orders of magnitude over the carbon levels investigated for each of the three different pretest heat treatments shown in Fig. 18.2. Note that the samples aged 100 hr at 870°C have a higher creep rate than either of the solution-annealed samples. Also, the presence of 0.5% Ti lowers the creep rate at the 0.05% C level by a factor of approximately 10.

A correlation of the creep ductility as a function of carbon content and secondary creep rate is shown in Figs. 18.3 and 18.4 respectively. The total elongation experienced at rupture when tested at 40,000 psi and 650°C shows little variation for the heat treatments investigated over the range of carbon concentration of 0.003 to 0.1%. Above 0.1% C we observed an increase in ductility at 40,000 psi. The heat with no titanium, No. 198, exhibits roughly the same ductility as the heats containing titanium.

Correlating the total elongation with creep rate, as in Fig. 18.4, for the intermediate and high carbon levels, we find lower ductility at a given creep rate for the heat without titanium (No. 198). The corresponding heats containing titanium (heats 195 and 196) show 8 to 10% greater total elongation for a given creep rate at 650°C. For the higher carbon levels (0.27 and 0.32% C) the ductility–strain-rate relationships differ even though the carbon levels of the two heats are nearly the same.

A final comparison of the effect of titanium on the rupture life of this alloy is shown in Fig. 18.5 for three different heat treatments. The presence of 0.5% Ti

Table 18.1. Compositions of Experimental Nickel-Base Alloys

In weight percent

Alloy	Mo	Cr	Ti	C	Fe	Si	Mn	Al	S
193	13.5	7.0	0.48	0.003	0.03	0.01	<0.02	<0.05	<0.002
194	13.4	7.3	0.47	0.007	0.03	0.02	<0.02	<0.05	0.003
195	13.7	7.6	0.54	0.037	0.03	0.01	<0.02	<0.05	<0.002
196	11.5	6.7	0.51	0.053	0.07	0.01	<0.02	<0.05	<0.002
238	12.5	7.2	0.50	0.096	0.22	0.02	0.08	<0.05	0.004
197	11.3	6.6	0.47	0.27	0.07	0.01	<0.02	<0.05	<0.002
242	12.0	7.4	0.53	0.32	0.31	0.02	0.12	<0.05	0.004
198	12.4	7.3	<0.01	0.042	0.13	0.01	<0.02	<0.05	<0.002

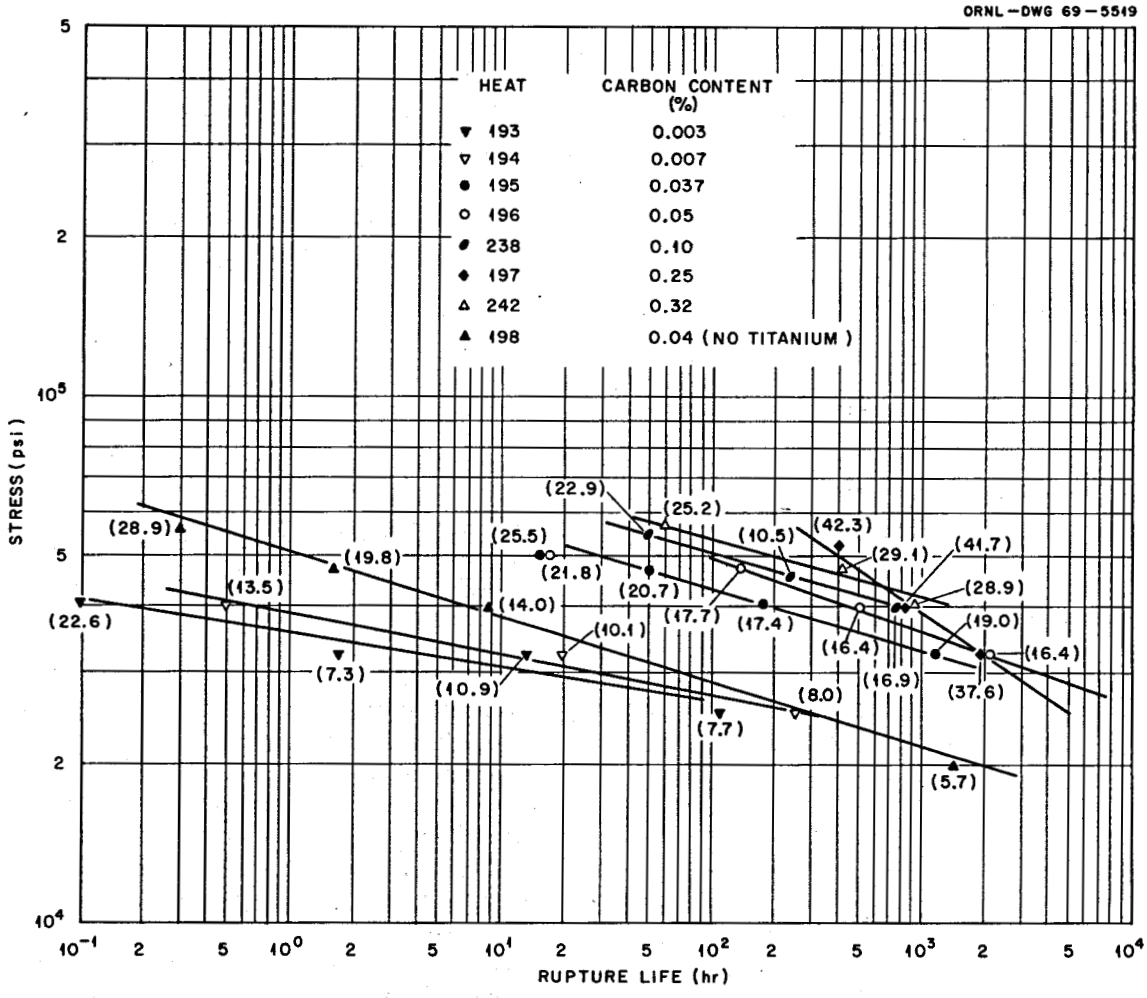

Fig. 18.1. Creep Rupture of Ni–12% Mo–7% Cr–0.5% Ti Alloy at 650°C as a Function of Carbon Content.

increases the rupture life by about 1½ orders of magnitude at a given stress level and increases the ductility to some extent, particularly at the lower stress levels.

The strong influence of carbon and titanium on the creep properties of this alloy indicates that carbide precipitates very likely play an important role in determining the properties. Future work will concentrate on identifying these precipitates.

18.2 AGING OF MODIFIED HASTELLOY N

C. E. Sessions

We are evaluating the tensile and creep properties of four heats of titanium-modified (0.15 to 1.2%) Hastelloy N after aging at temperatures of 650 and 760°C. As reported previously,[1,2] the tensile property changes after 3000 hr of aging at 650 and 760°C indicated that aging did result in a reduction in the high-temperature ductility of the modified alloy and that the change was more significant after the 760°C treatment. This indication of a thermal instability in the alloy system, however, required assessment for longer aging times and for creep conditions to fully characterize the material.

Table 18.2 shows the effects of aging on the properties of the four alloys investigated. The samples were aged for 1500 and 3000 hr at 650 and 760°C, and the tensile properties were measured at 650°C at a

[1] C. E. Sessions, *Fuels and Materials Development Program Quart. Progr. Rept. Sept. 30, 1968*, ORNL-4350, pp. 163–73.

[2] C. E. Sessions, *MSR Program Semiann. Progr. Rept. Aug. 31, 1968*, ORNL-4344, pp. 239–43.

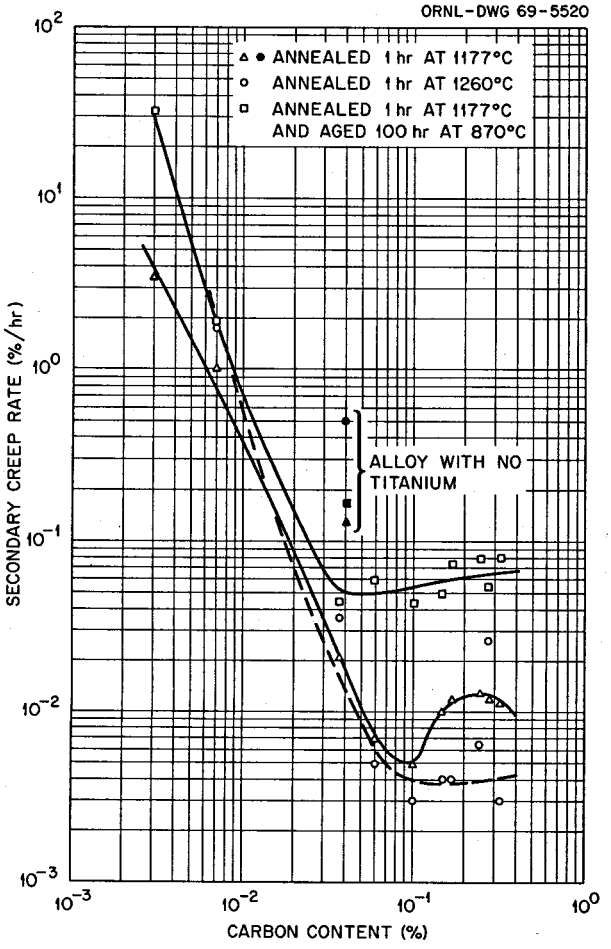

Fig. 18.2. Influence of Carbon on the Secondary Creep Rate of Ni–12% Mo–7% Cr–0.5% Ti Alloy at 650°C and 40,000 psi.

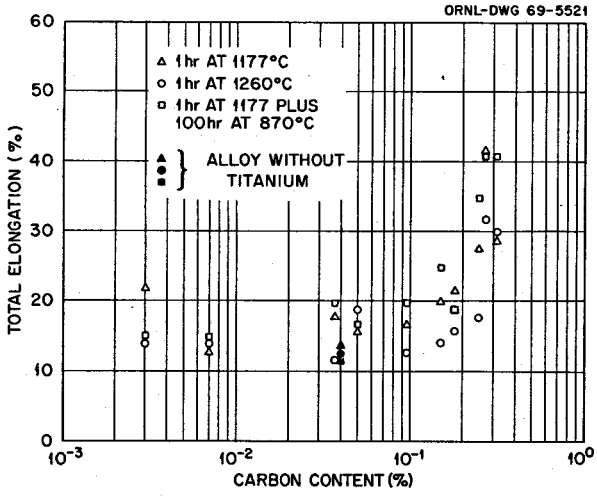

Fig. 18.3. Effect of Carbon and Titanium on the Total Creep Elongation of Ni–12% Mo–7% Cr–0.5% Ti Alloy at 650°C and 40,000 psi.

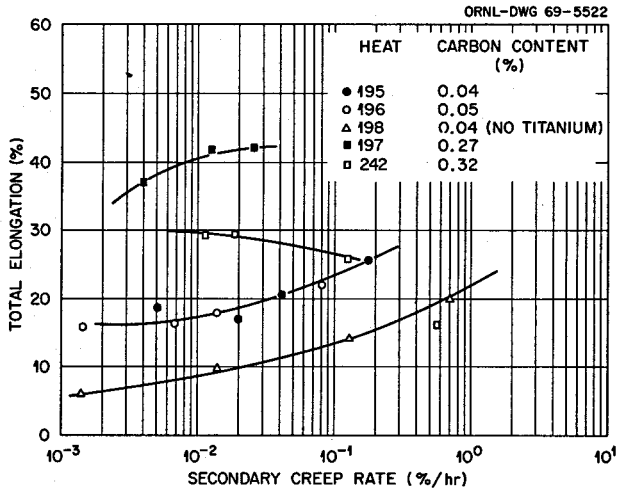

Fig. 18.4. Correlation of Total Creep Elongation with the Secondary Creep Rate at 650°C for Ni–12% Mo–7% Cr–0.5% Ti Alloys with Varying Carbon Contents After a 1-hr Annealing at 1177°C. Solution anneal.

strain rate of 0.002 min^{-1}. The effect of aging at 650°C is to reduce the high-temperature ductility slightly after 1500 hr and significantly after 3000 hr for each heat except 466-548. Aging at 760°C reduces the ductility for all heats a significant amount after both 1500 and 3000 hr. A corresponding increase in the yield and ultimate tensile strengths is found for most aging conditions.

The effect of pretest thermal-mechanical treatment is to influence the overall level of strength and ductility, as shown in Table 18.2; however, the influence of any particular pretest heat treatment differs from heat to heat.

Representative tensile curves showing the effect of prior aging on the 650°C behavior are shown in Fig. 18.6. Each curve is for heat 467-548 (1.2% Ti), with the heat treatments listed in the caption. If we interpret the serrations as being due to the effect of solute-atom–dislocation interactions, then the 760°C aging treatment has eliminated the serrations by precipitation of solutes from solid solution.

Evaluation of the effects of aging on the creep properties of these modified alloys is currently in progress. Table 18.3 lists the results from control and aged samples tested to date. The control tests on unaged samples show the greatest strength and the lowest ductility for the prestrained material. The optimum ductility was obtained from the samples solution annealed at 1260°C prior to creep testing. Tests on the aged samples indicate no deterioration in the creep properties due to aging 1500 hr at either 650

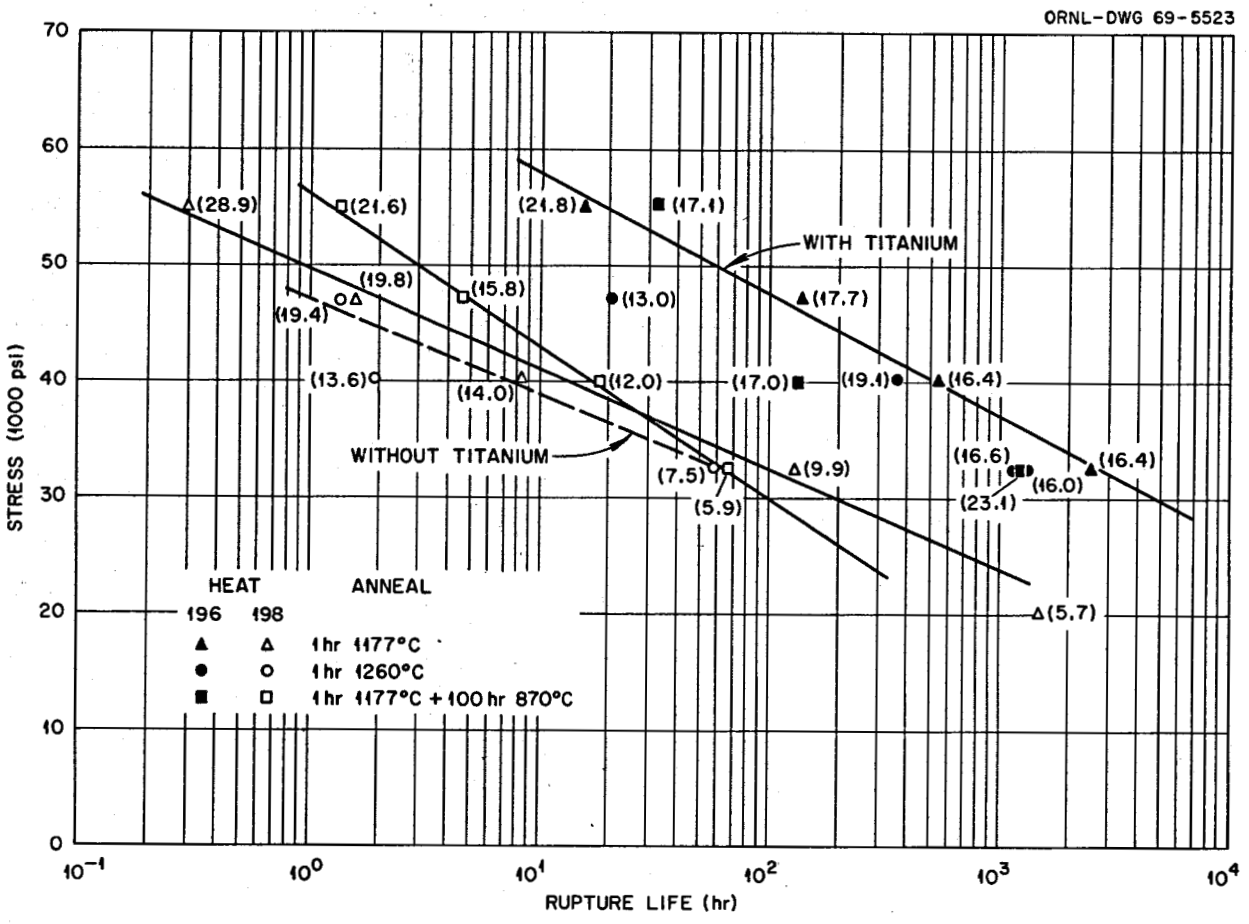

Fig. 18.5. Influence of Heat Treatment on the Stress Rupture Properties of Ni–12% Cr–0.04% C Alloy With and Without 0.5% Titanium.

or 760°C. However, heats 466-535 (0.15% Ti) and 466-541 (0.30% Ti) exhibit a loss of creep strength and ductility after aging 3000 hr at 760°C. In agreement with the tensile results, heat 466-548 (0.45% Ti) actually showed an increase in strength and ductility after 1500 and 3000 hr at the 650°C aging temperature. No conclusions can be drawn from the tests on heat 467-548 (1.2% Ti) except that the as-annealed properties are definitely superior to the creep properties of the three heats containing lesser amounts.

The few tests completed indicate that in some heats a deterioration in high-temperature properties is found after aging, but none of these changes are large enough to account for the gross deterioration in creep strength and ductility that has recently been found for modified Hastelloy N when irradiated at temperatures above 700°C;[3] that is, the effects found under irradiation cannot be accounted for by thermal aging effects alone.

18.3 INFLUENCE OF IRRADIATION TEMPERATURE ON THE CREEP-RUPTURE PROPERTIES OF HASTELLOY N

H. E. McCoy

Our previous studies showed that titanium-modified (0.5%) Hastelloy N had good postirradiation properties when irradiated at temperatures up to 660°C, but that very poor properties resulted for irradiating above 704°C.[4] We also found that a small melt that did not contain titanium exhibited a similar dependence on irradiation temperature; so we suspected that the variation of properties with irradiation temperature

[3] H. E. McCoy, *Fuels and Materials Development Program Quart. Progr. Rept. Sept. 30, 1968*, ORNL-4350, pp. 163–73.

[4] H. E. McCoy, *MSR Program Semiann. Progr. Rept. Aug. 31, 1968*, ORNL-4344, pp. 244–47.

Table 18.2. Comparison of Pre- and Postaging Properties of Modified Hastelloy N Measured at 650°C[a]

Heat	Titanium Content[b] (%)	Heat Treatment	Properties Before Aging		Percent Change in Properties After Aging Indicated Time at 650°C				Percent Change in Properties After Aging Indicated Time at 760°C			
			Uniform Elongation (%)	Yield Strength (ksi)	Uniform Elongation		Yield Strength		Uniform Elongation		Yield Strength	
					1500 hr	3000 hr	1500 hr	3000 hr	1500 hr	3000 hr	1500 hr	3000 hr
466-535	0.15	121[c]	27.4	28.9	−9	−32	34	36	−42	−51	22	13
		123[d]	30.4	25.3	−31	−60	31	39	−55	−53	30	21
		109[e]	18.9	48.5	−20	−43	19	11	−38	−42	2	−8
466-541	0.30											1
		121	31.4	27.0	12	5	30	28	−43	−51	23	16
		123	30.7	21.4	−47	−66	24	40	−50	−56	46	39
		109	22.6	44.9	−4	−20	7	−2	−51	−57	0	−4
466-548	0.45	121	29.3	24.7	38	35	20	21	20	−31	22	22
		123	30.0	20.4	57	48	19	28	8	−17	33	26
		109	20.0	42.8	36	34	5	3	−26	−27	−3	−5
467-548	1.2	121	34.5	36.6	−18	−24	27	18	−25	−29	14	11
		123	41.3	29.1	−41	−58	47	54	−73	−68	61	53
		109	23.1	68.8	−6	−21	−6	−11	−10	−11	−10	−19

[a]Tensile tested at 650°C and 0.002 min^{-1} strain rate.
[b]All alloys have a nominal composition of Ni–12% Mo–7% Cr–0.2% Mn–0.05% C.
[c]1 hr at 1177°C solution anneal.
[d]1 hr at 1260°C solution anneal.
[e]1 hr at 1177°C anneal plus 10% prestrain at room temperature.

might be general for Hastelloy N. However, our work with standard air-melted Hastelloy N showed that this material was insensitive to irradiation temperature. The types of carbide precipitates were found to depend on the alloy composition and the irradiation temperature; in general, MC carbides were associated with good properties, and M_6C and M_2C were found in samples having poor postirradiation properties.[5]

We then irradiated several experimental alloys that contained various amounts of carbide-forming elements such as Hf, Nb, Ti, Zr, and Y. The nominal chemical compositions of the alloys studied are given in Table 18.4, and the results of postirradiation creep-rupture tests are summarized in Fig. 18.7. All the data points shown in Fig. 18.7 are for samples irradiated at 760°C and tested at 650°C. The first number by each point is the heat designation, and the second number is the fracture strain. The lines were determined by previous tests and are labeled, but no data points are shown.

Heat 5911 is standard Hastelloy N that has been vacuum melted. When irradiated at 650°C its properties are represented by the indicated solid line; but after irradiation at 760°C the rupture life is much shorter, and the fracture strains are very low.

Several heats containing 0.5% Ti were included in this study. The data on heat 66-548 used to construct the line on the extreme left of Fig. 18.7 were presented previously.[4] The indicated points for this same heat from the current experiment agree well with the previous observations. The other heats containing 0.5% Ti (21545, 104, 7320, 67-526) were not affected as drastically by irradiation temperature, but their postirradiation properties are not as good as those for standard air-melted Hastelloy N. Alloys 107 (1% Ti) and 67-548 (1.2% Ti) give some indication that alloys with higher titanium concentrations may be stable during irradiation at 760°C.

Alloy 273 was prepared to determine whether a small addition of silicon (0.5%) would help stabilize the desired MC-type carbide in an alloy containing 0.5% Ti during irradiation at 760°C. Comparison of the results

[5]R. E. Gehlbach, this report, sect. 18.4.

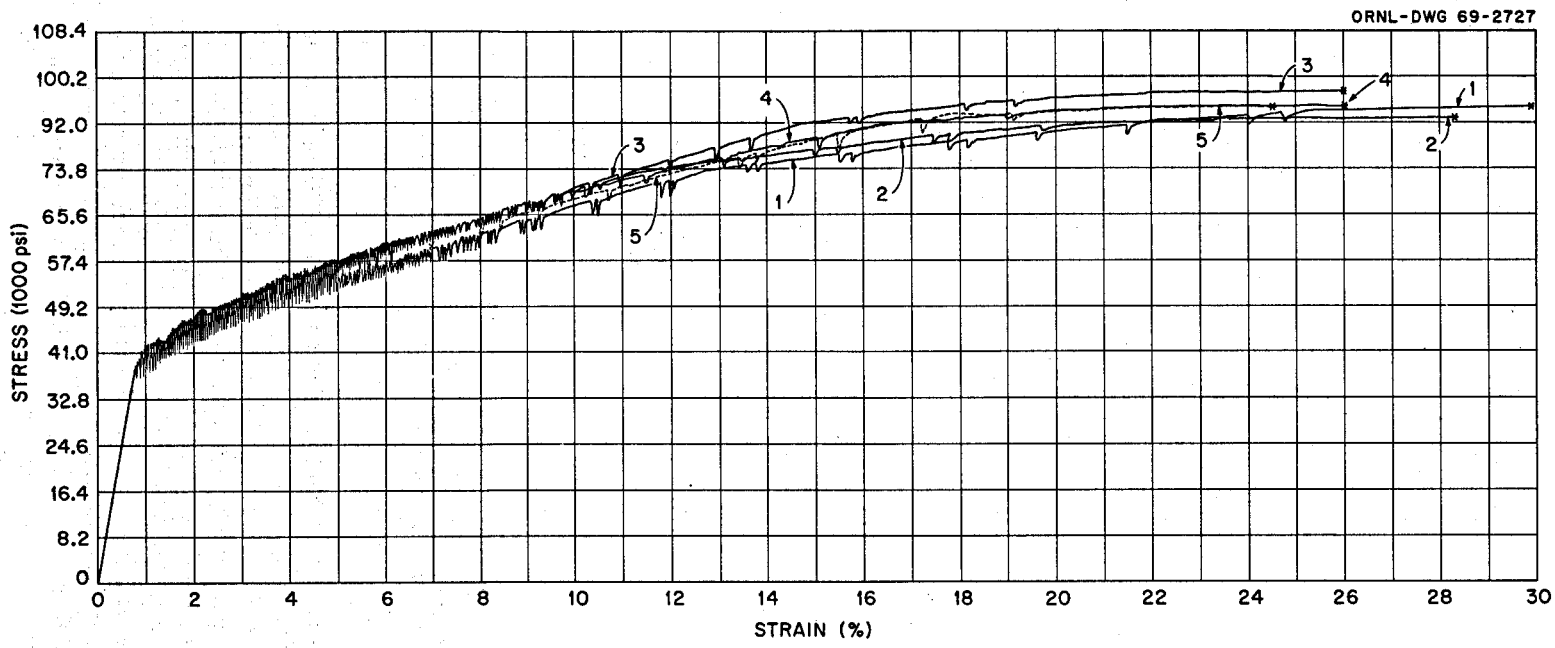

Fig. 18.6. Tensile Curve for Aged and Unaged Samples of Hastelloy N. Heat 467-548 (1.2% Ti). (1) As solution annealed 1 hr at 1177°C; (2) as solution annealed at 1177°C plus aged 3000 hr at 650°C; (3) as solution annealed at 1177°C plus aged 3000 hr at 760°C; (4) as solution annealed at 1177°C plus aged 1500 hr at 760°C; (5) as solution annealed at 1177°C plus aged 1500 hr at 650°C.

Table 18.3. Results of Creep-Rupture Tests on Titanium-Modified Hastelloy N Tested at 40,000 psi and 650°C

Heat	Pretest Anneal	Aging Time (hr)	Aging Temperature (°C)	Rupture Life (hr)	Fracture Strain (%)	Minimum Creep Rate (%/hr)	Reduction in Area (%)
466-535	121[a]	0		166	9.5	0.013	10.6
	123[b]	0		51	13.6	0.012	24.4
	109[c]	0		194	3.6	0.005	6.4
	121	1500	650				
	121	1500	760	136	11.3	0.049	17.4
	123	3000	650	217	13.7	0.035	15.2
	123	3000	760	26	8.3	0.087	9.5
	121	3000	650	138	13.6	0.063	14.3
	121	3000	760	64	9.5	0.007	13.2
466-541	121	0		342	15.2	0.006	17.7
	123	0		189	21.5	0.008	26.6
	109	0		309	5.9	0.004	13.9
	121	1500	650				
	121	1500	760	217	18.9	0.054	19.5
	123	3000	650	50	9.7	0.072	12.9
	123	3000	760	41	9.9	0.084	17.6
	121	3000	650	508	27.6	0.031	26.9
466-548	121	0		358	16.7	0.012	22.3
	123	0		125	19.3	0.011	28.2
	109	0		620	11.7	0.006	17.8
	121	1500	650	670	27.2	0.020	30.1
	121	1500	760	42	7.9	0.120	18.3
		(duplicate)		594	42.1	0.025	34.2
	123	3000	650	345	29.1	0.097	37.3
	123	3000	760	175	24.1	0.066	37.6
	121	3000	760	135	16.7	0.054	21.9
467-548	121	0		1100	41.1		38
	123	0		2472	21.6	0.004	17.6
	109	0		2149	30.5	0.005	29.0
	121	1500	650				
	121	1500	760	1006	32.4	0.019	47.7
	123	3000	650	>850	>5		
	123	3000	760	1454	20.4	0.010	

[a] 1 hr at 1177°C.
[b] 1 hr at 1260°C.
[c] 1 hr at 1177°C plus 10% prestrain.

for heats 104 and 273 indicates that the silicon addition did not lead to improved properties.

Alloys 146 and 147 contain 1% Zr in addition to small amounts of Re. The postirradiation properties of these alloys are quite good, and the improved behavior is probably due to the Zr since alloy 112 (1.2% Zr) also has good properties. However, since the Zr addition causes poor weldability, we plan no further development of alloys with Zr additions.

Heat 67-504 (0.5% Hf) was found to have excellent properties following irradiation at 650°C,[6] but the results shown in Fig. 18.7 for this alloy after irradiation at 760°C are poor. Heat 232 with 1% Hf has improved properties, and heat 184 with 1% Ti and 1% Hf has even better properties.

Heat 237 contains 1% Nb and 0.2% Si, and the postirradiation properties are not very good. Heat 181 contains 2% Nb, 0.5% Ti, and no Si, and the properties are very attractive. The question of whether a sufficient quantity of Nb could be added to give good postirradiation properties is still open.

[6] H. E. McCoy, *MSR Program Semiann. Progr. Rept. Aug. 31, 1968*, ORNL-4344, pp. 211–23.

Table 18.4. Nominal Compositions of Alloys Studied

Alloy	Content (wt %)								
	Ni	Mo	Cr	Fe	Si	Mn	C	Ti	Other
Standard N	Bal	16	7	4	0.5	0.5	0.05	0	
5911	Bal	16	7	0	<0.1	0.2	0.05	0	
66-548	Bal	12	7	0	0	0.2	0.05	0.5	
21545	Bal	12	7	0	0	0.2	0.05	0.5	
104	Bal	12	7	0	0	0.2	0.05	0.5	
7320	Bal	12	7	0.1	0	0.2	0.05	0.5	
67-526	Bal	16	7	0	0	0.2	0.05	0.5	2 W
107	Bal	12	7	0	0	0.2	0.05	1.0	
67-548	Bal	12	7	0	0	0.2	0.05	1.2	
273	Bal	12	7	0	0.5	0.2	0.05	0.5	
146	Bal	12	7	0	0	0.2	0.05	0	1 Zr, 0.1 Re
147	Bal	12	7	0	0	0.2	0.05	0	1 Zr, 1 Re
112	Bal	12	7	0	0	0.2	0.05	0	1.2 Zr
67-504	Bal	12	7	0	0	0.2	0.05	0	0.5 Hf
232	Bal	12	7	4	0.2	0.5	0.05	0	1 Hf
184	Bal	12	7	4	0.2	0.5	0.05	1.0	1 Hf
237	Bal	12	7	4	0.2	0.5	0.05	0	1 Nb
181	Bal	12	7	0	0	0.2	0.05	0.5	2 Nb
1^3	Bal	12	7	4	0.2	0.5	0.05	1	1 Y

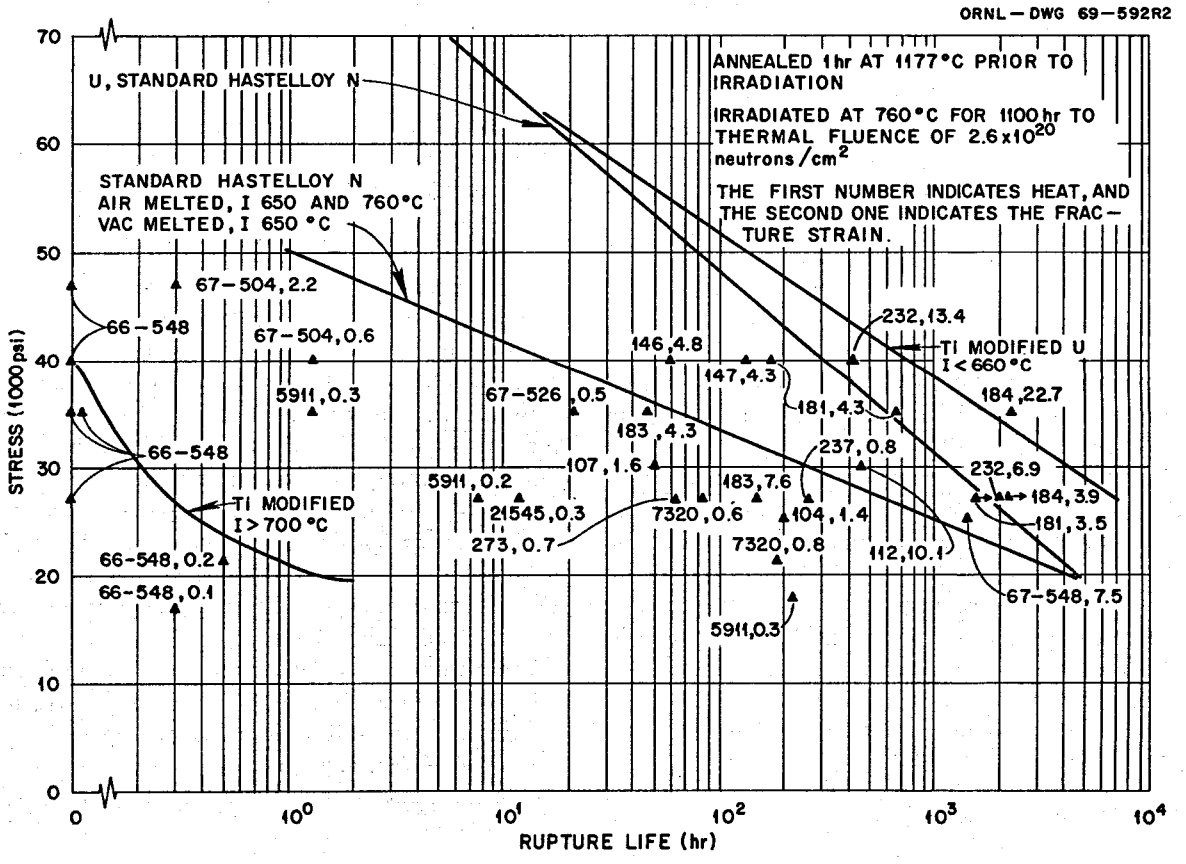

Fig. 18.7. Stress Rupture Properties of Several Modified Hastelloy N Alloys Measured in Postirradiation Creep Tests at 650°C.

The postirradiation rupture life of heat 183 (1% Ti and 1% Y) is not very good, but its fracture strains are attractive. Metallographic examination showed that the grain size was very small, and our previous experience leads us to believe that higher preirradiation anneals (to get a larger grain size) might improve the rupture life.

These observations show that several alloy combinations involving additions of Nb, Hf, Ti, and Y have promise for prolonged use at temperatures above 700°C.

18.4 ELECTRON MICROSCOPY STUDIES

R. E. Gehlbach S. W. Cook

We reported previously that carbide precipitation in Hastelloy N is sensitive to the chemical composition.[7,8] In the air-melted heats of the standard alloy, containing 0.4 to 0.6% Si, only M_6C-type precipitates form. They are enriched in silicon and are stabilized by its presence. Reduction of the silicon to trace levels, as is possible by vacuum melting practice, results in M_2C-type precipitation after exposure to intermediate aging temperatures. This M_2C can be readily put into solid solution at normal solution-annealing temperatures, whereas the M_6C type is not heat treatable.

Precipitation in the modified (12% Mo) versions of the alloy is sensitive to alloying additions of Ti, Nb, Zr, and Hf,[9] and when these elements are present the precipitation processes are temperature dependent. Mechanical properties, particularly after irradiation, are also affected by composition and temperature.[10] We are concentrating our studies on understanding the role of these alloying additions on the types and morphologies of precipitates and evaluating the effects they have in controlling the mechanical behavior of the material after irradiation. The precipitates being studied are those that result from aging at 650 and 760°C (an MSBR will operate at 704°C).

The various carbides have been identified using several techniques. The types and relative amounts of carbides present in a specimen were determined by dissolving the matrix and analyzing the remaining precipitates by x-ray diffraction. Selected-area electron diffraction and electron-microscope–microprobe analysis were used to relate the crystal structure, morphology, and composition of individual precipitates on extraction replicas. The distribution of precipitates was observed by electron microscopy of thinned bulk specimens and extraction replicas.

Since the silicon level in these modified alloys is low, the M_6C formed in the standard material is not present. In the modified alloys without additions of the Ti-group elements, only M_2C precipitates at aging temperatures of 650 and 760°C. The addition of the Ti-group elements promotes the formation and stability of carbides of the MC type, having face-centered cubic structures with lattice parameters ranging from 4.21 to 4.68 A. Higher concentrations of the Ti-group elements are required to stabilize the MC types at 760°C than at 650°C. These trends are shown in Table 18.5.

The M_2C carbides have the Mo_2C structure but contain about 10 to 20% Cr and thus would be more appropriately designated $(Mo,Cr)_2C$. The compositions of the MC types depend on the amount of the particular elements from the Ti group contained in the material. At low Ti concentrations, (Mo,Cr)C is formed. Increasing the concentration of Ti in the alloy results in some Ti substituting for Cr in the carbides, with an increase in lattice parameter. Adding Nb, Hf, or Zr promotes the stability of the carbides of that group (e.g., HfC). In general, the MC carbides are finer than the M_2C type, and their distribution in the bulk material would appear to result in superior postirradiation mechanical properties than would that of the M_2C precipitate.

The distribution of MC, or (Mo,Cr)C, in heat 66-548 (a commercial alloy with 0.45% Ti) after aging at 650°C is shown in Fig. 18.8. Particular importance is given to the fact that many fine precipitates lie adjacent to the grain boundaries and extend into the matrix. In contrast, aging this material at 760°C produces larger precipitates in both the matrix and grain boundaries. Some precipitate also exists in the form of very thin (probably <100 A) continuous films covering extensive areas in the grain boundaries. These thin films and the helium bubbles noted in this material after irradiation[11] would be expected to result in poor postirradiation mechanical properties.

The distributions of precipitates formed during irradiation and formed by aging in the absence of irradiation at similar temperatures are different. Figure 18.9 is a transmission electron micrograph of an unstressed specimen irradiated for 1128 hr at 635°C in the ORR.

---

[7] *MSR Program Semiann. Progr. Rept. Feb. 29, 1968,* ORNL-4254, pp. 206–13.

[8] *MSR Program Semiann. Progr. Rept. Aug. 31, 1968,* ORNL-4344, pp. 247–50.

[9] Hereafter the alloying elements Ti, Zr, Nb, and Hf will be referred to as the Ti-group elements.

[10] H. E. McCoy, this report, sect. 18.3.

[11] *MSR Program Semiann. Progr. Rept. Aug. 31, 1968,* ORNL-4344, pp. 249–50.

Table 18.5. Phases Present in Various Hastelloy-N-Type Alloys After Aging (>1000 hr) at the Indicated Temperature

Alloy	650°C	760°C
Standard Hastelloy N (0.5% Si)	M_6C	M_6C
Standard Hastelloy N(<0.1% Si)	M_2C	M_2C
198 (12% Mo)	M_2C	
66-535 (12% Mo–0.12% Ti)	MC + M_2C	M_2C
196 (12% Mo–0.5% Ti)	MC + $(M_2C)^a$	
66-548 (12% Mo–0.45% Ti)	MC	$(MC)^a$ + M_2C
107 (12% Mo–1.0% Ti)	MC	
67-548 (12% Mo–1.2% Ti)		MC
112 (12% Mo–1.0% Zr)	MC	
181 (12% Mo–0.5% Ti–2% Nb–0.2% Si)	MC	MC
184 (12% Mo–1% Ti–1% Hf)		MC

[a]Phase present in minor amount.

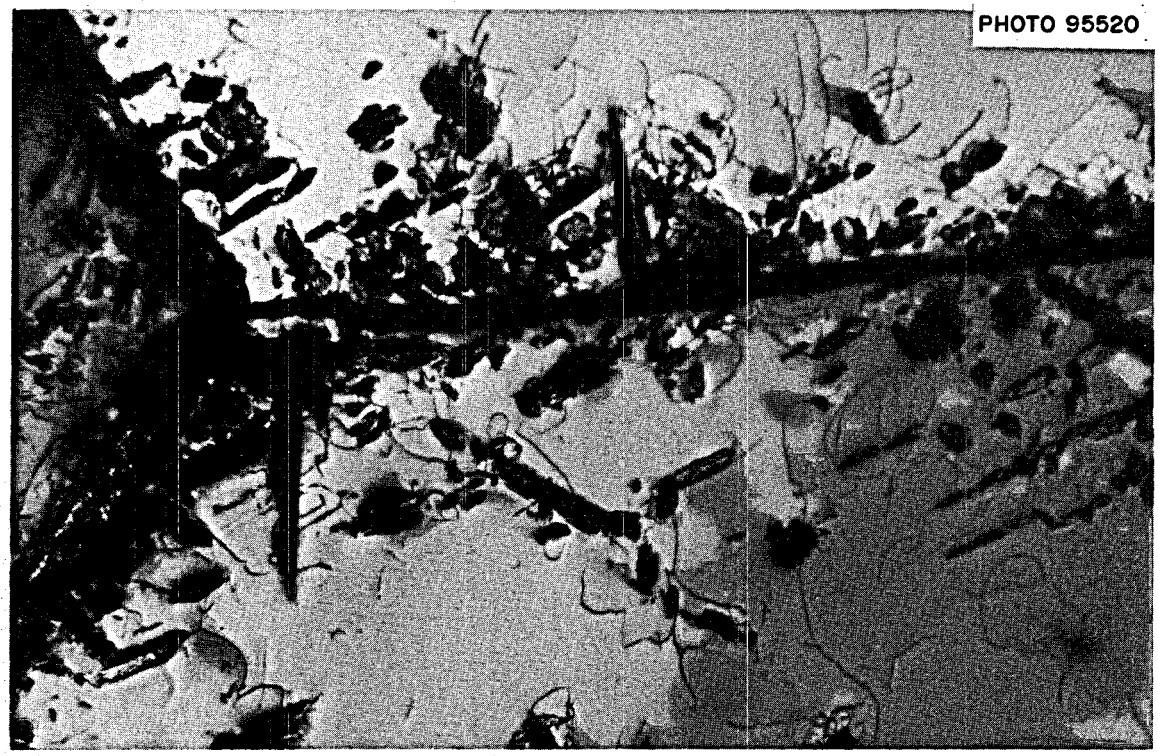

Fig. 18.8. Distribution of MC Carbides in Hastelloy N (Heat 66-548, 0.45% Ti) After Aging 1500 hr at 650°C. 10,000X.

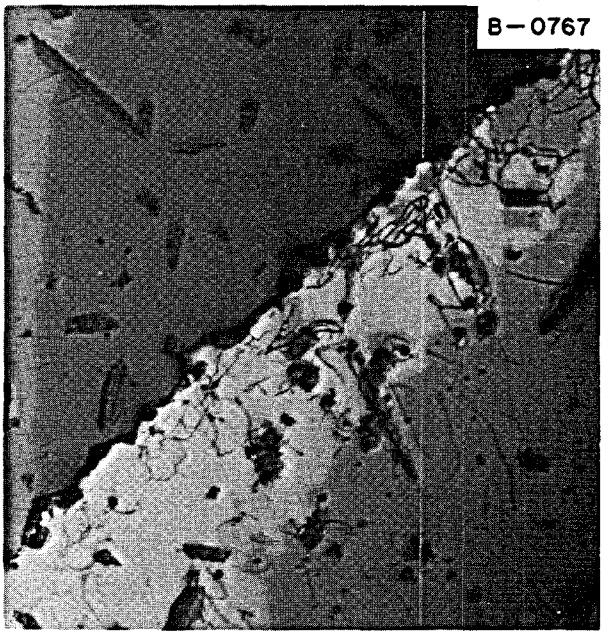

Fig. 18.9. Distribution of Precipitates in Hastelloy N (Heat 66-548, 0.45% Ti) After Irradiating for 1128 hr at 635°C. 10,000X.

Although a considerable amount of precipitate is present in the grain boundaries, the distribution is considerably different from that obtained by aging in the absence of irradiation at 650°C (Fig. 18.8). Essentially no precipitates were present in a specimen irradiated for 1128 hr at 703°C; however, many bubbles were present on the grain boundaries, and fracture occurred in this material with essentially no strain.[12] Bubbles were observed at grain boundaries in the material after irradiation at 635°C, but the irregular precipitates in the grain boundaries probably strengthen the boundaries and prevent the propagation of grain boundary cracks.

It would appear that a structure similar to that shown in Fig. 18.8 would result in good postirradiation properties. The fine precipitates along grain boundaries seem characteristic of the MC-type carbides. As shown in Table 18.5, increasing the amounts of the Ti-group elements promotes the stability of these carbides. The alloys with the higher concentrations of these elements (heats 181, 184, 67-548) exhibit excellent postirradiation properties after irradiation at 760°C.[12] Although we have not examined the phases present in these alloys after irradiation, it appears likely that the MC carbides are present and occur in a favorable distribution.

[12] H. E. McCoy, this report, sect. 18.3.

18.5 MEASUREMENT OF RESIDUAL STRESSES IN HASTELLOY N WELDS

A. G. Cepolina D. A. Canonico

We have been investigating the levels and distribution of residual welding stresses in ½-in.-thick Hastelloy N plate and the effects of various thermal treatments to reduce or eliminate these stresses. The theory and experimental procedures were discussed previously,[13,14] and more recently data were presented[15] relating the as-welded residual stresses to variations in heat input and shielding gas. The effect of stress-relief treatments at 1177, 870, and 650°C on the distribution of the residual stresses was also discussed.[15]

[13] *MSR Program Semiann. Progr. Rept. Aug. 31, 1967,* ORNL-4191, pp. 223–26.

[14] *MSR Program Semiann. Progr. Rept. Feb. 29, 1968,* ORNL-4254, pp. 215–17.

[15] *MSR Program Semiann. Progr. Rept. Aug. 31, 1968,* ORNL-4344, pp. 256–57.

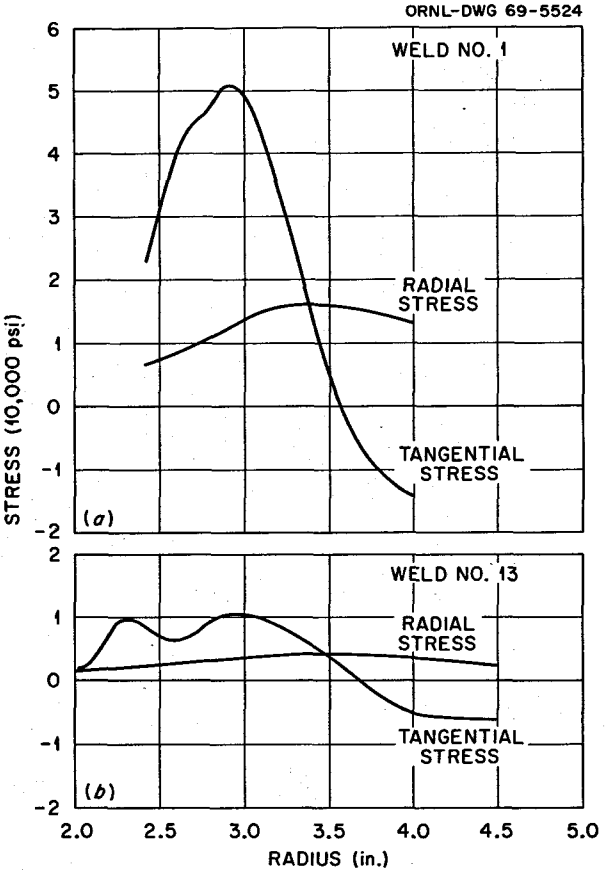

Fig. 18.10. Tangential and Radial Residual Stresses in ½-in.-thick Hastelloy N Plates. The welds were circular and had a radius (*R*) of 3 in. from the center of the plate. (*a*) As-welded plate, (*b*) annealed 6 hr at 760°C after welding.

Recently, we have investigated the effects of a treatment of 6 hr at 760°C on the residual stresses of weldments made at 15,000 j per inch of weld. The results of this treatment on the residual stresses are shown in Fig. 18.10. For comparison, we have included the distribution of the as-welded residual stresses. It can be seen that the 760°C treatment is effective toward reducing the peak tangential and radial residual stresses. Undoubtedly, even lower values can be attained with a longer treatment at 760°C.

18.6 CORROSION STUDIES

J. W. Koger A. P. Litman

We are continuing our study of the compatibility of fused fluoride salts with structural materials of interest to the MSRP. The studies currently are centered around the compatibility of the Hastelloy N alloys with salts appropriate for single-fluid breeder reactors, but some tests begun earlier with salts of interest for two-fluid systems have been continued. Eight natural circulation loops are presently in operation. Table 18.6 details the service parameters of these test units, and Table 18.7 gives the compositions of the standard and titanium-modified Hastelloy N.

18.6.1 Fuel Salts

Loop 1255, constructed of standard Hastelloy N and containing a simulated MSRE fuel salt plus 1 mole % ThF_4, continues to operate without difficulty after 6.9 years.

Loop 1258, constructed of type 304L stainless steel and containing removable specimens in the hot leg, has operated about 5.6 years with the same salt as loop 1255. A plot of the weight change of the insert specimens at various temperatures is given in Fig. 18.11 as a function of operating time. The corrosion rates based on these weight changes range from 1 to 2 mils/year.

Loop NCL-16, constructed of standard Hastelloy N with removable specimens in each leg, has operated with the two-fluid MSBR fuel salt for over 9000 hr. A plot of the weight change of the specimens in the hottest and coldest positions as a function of operating time is given in Fig. 18.12. The average corrosion rate has been <0.05 mil/year in this loop. The hot-leg specimens show that the titanium-modified alloy specimens at 704°C (1300°F) and 676°C (1250°F) have smaller weight changes than the standard specimens at 660°C (1220°F). Figure 18.13 shows the changes in concentration of chromium and iron in the salt as a function of operating time. The chromium has shown a steady increase (linear for the last 4000 hr), while the iron increased initially and now is slowly decreasing as the iron fluoride oxidizes the chromium in the Hastelloy N.

18.6.2 Fertile-Fissile Salts

Loops NCL-18 and NCL-19, constructed of standard Hastelloy N with removable specimens in each leg, have operated for 2900 and 3600 hr, respectively, with the fertile-fissile salt under identical temperature conditions. Loop NCL-19 has a molybdenum hot finger containing bismuth at the bottom of the hot leg (Fig. 18.14). These loops are being operated to obtain data on the compatibility of the fertile-fissile salt with the Hastelloy alloys and to determine if contacting the salt with liquid bismuth will affect the corrosion rate.

The weight changes of specimens from loop NCL-18 were measured after 1465 hr exposure to the salt. The standard Hastelloy N specimen at 699°C lost 0.5 mg/cm^2, while the titanium-modified Hastelloy N specimen at the same temperature lost 0.3 mg/cm^2.

The weight changes of specimens from loop NCL-19 were measured after 2250 hr exposure to the salt. The standard Hastelloy N specimen at 699°C lost 0.6 mg/cm^2, while the titanium-modified Hastelloy N specimen at the same temperature lost 0.2 mg/cm^2. Table 18.8 gives the bismuth concentration in the salt after various operating times.

We are investigating the reason for the large amount of bismuth in the 840-hr salt sample. The lower bismuth content in later salt samples indicates either that the analysis was in error or that bismuth was possibly entrapped in the salt. Work is under way to establish the sensitivity of the bismuth chemical analysis procedure to salts of these types. A study of the analytical procedure for the determination of bismuth in the salt has indicated that at the 100-ppm level, one should not place much confidence in the numerical values. Additional evidence of analytical uncertainty was found in the reported bismuth analyses of the salt from loop NCL-18, <25 ppm at 0 hr, 60 ppm at 672 hr, <20 ppm at 1817 hr (loop NCL-18 does not contain any intentional bismuth addition). In any case no effect of bismuth is apparent in the corrosion rates. Specimens in loops NCL-18 and NCL-19 do not show significantly different weight changes. In 1484 hr of operation the chromium content of the salt increased from <25 to 57 ppm in both loops. No changes in the concentrations of the other constituents have been noted.

Table 18.6. MSRP Natural Circulation Loop Operation Through February 28, 1969

Loop No.	Loop Material	Specimens	Salt Type	Salt Composition (mole %)	Maximum Temperature (°C)	ΔT (°C)	Operating Time (hr)
1255	Hastelloy N	Hastelloy N + 2% Nb[a,b]	Fuel	LiF-BeF_2-ZrF_4-UF_4-ThF_4 (70-23-5-1-1)	704	90	60,600
1258	Type 304L SS	Type 304L stainless steel[b,c]	Fuel	LiF-BeF_2-ZrF_4-UF_4-ThF_4 (70-23-5-1-1)	688	100	49,300
NCL-13	Hastelloy N	Hastelloy N[c,d]	Coolant	$NaBF_4$-NaF (92-8)	607	150	4,700[e]
NCL-13A	Hastelloy N	Hastelloy N; Ti-modified Hastelloy N controls[c,d]	Coolant	$NaBF_4$-NaF (92-8)	607	125	3,100
NCL-14	Hastelloy N	Ti-modified Hastelloy N[c,d]	Coolant	$NaBF_4$-NaF (92-8)	607	150	11,600
NCL-15	Hastelloy N	Ti-modified Hastelloy N; Hastelloy N controls[c,d]	Blanket	LiF-BeF_2-ThF_4 (73-2-25)	677	55	2,000[f]
NCL-15A	Hastelloy N	Ti-modified Hastelloy N; Hastelloy N controls[c,d]	Blanket	LiF-BeF_2-ThF_4 (73-2-25)	677	55	4,700
NCL-16	Hastelloy N	Ti-modified Hastelloy N; Hastelloy N controls[c,d]	Fuel	LiF-BeF_2-UF_4 (65.5-34.0-0.5)	704	170	9,000
NCL-17	Hastelloy N	Ti-modified Hastelloy N; Hastelloy N controls[c,d]	Coolant	$NaBF_4$-NaF (92-8) plus water vapor additions	607	150	Estimated startup 3-1-69
NCL-18	Hastelloy N	Ti-modified Hastelloy N; Hastelloy N controls[c,d]	Fertile-fissile	LiF-BeF_2-ThF_4-UF_4 (68-20-12-0.3)	704	170	2,900
NCL-19	Hastelloy N	Ti-modified Hastelloy N; Hastelloy N controls[c,d]	Fertile-fissile	LiF-BeF_2-ThF_4-UF_4 (68-20-12-0.3) plus bismuth in molybdenum hot finger	704	170	3,600
NCL-20	Hastelloy N	Ti-modified Hastelloy N; Hastelloy N controls[c,d]	Coolant	$NaBF_4$-NaF (92-8)	675	265	Under construction

[a] Permanent specimens.
[b] Hot leg only.
[c] Removable specimens.
[d] Hot and cold legs.
[e] Reworked – operating as NCL-13A.
[f] Repaired – operating as NCL-15A.

Table 18.7. Composition of Hastelloy N

Alloy	Chemical Content (wt %)						
	Ni	Mo	Cr	Fe	Si	Mn	Ti
Standard Hastelloy N	70	17.2	7.4	4.5	0.6	0.54	0.02
Titanium-modified Hastelloy N	78	13.6	7.3	<0.1	<0.01	0.14	0.5

18.6.3 Blanket Salts

Loop NCL-15A, formerly NCL-15 (ref. 16), constructed of standard Hastelloy N with removable specimens in each leg, has operated for 4700 hr with the blanket salt. The chromium concentration in the salt has increased from 25 to only 110 ppm in 2100 hr,

[16] J. W. Koger and A. P. Litman, *MSR Program Semiann. Progr. Rept. Aug. 31, 1968*, ORNL-4344, p. 262.

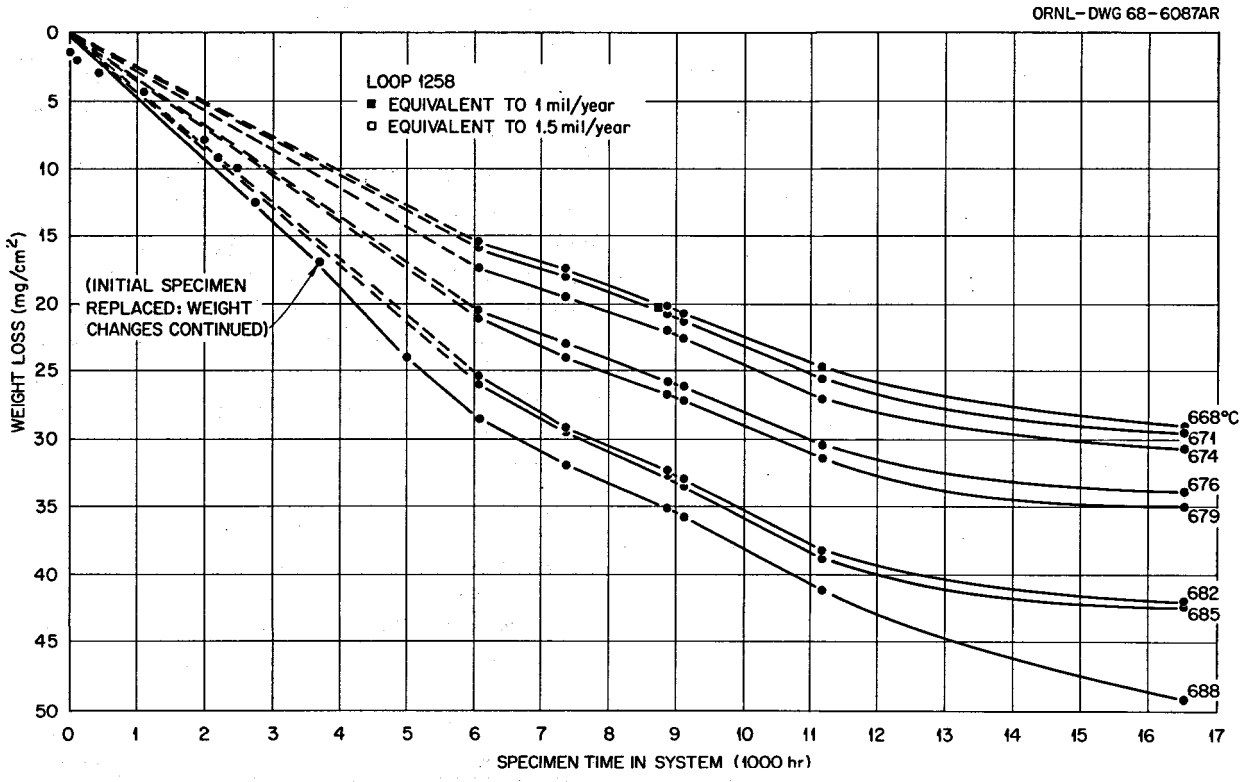

Fig. 18.11. Weight Loss of Type 304L Stainless Steel Specimens as a Function of Operation Time at Various Temperatures in $LiF\text{-}BeF_2\text{-}ZrF_4\text{-}ThF_4\text{-}UF_4$ (70-23-5-1-1 Mole %) Salt.

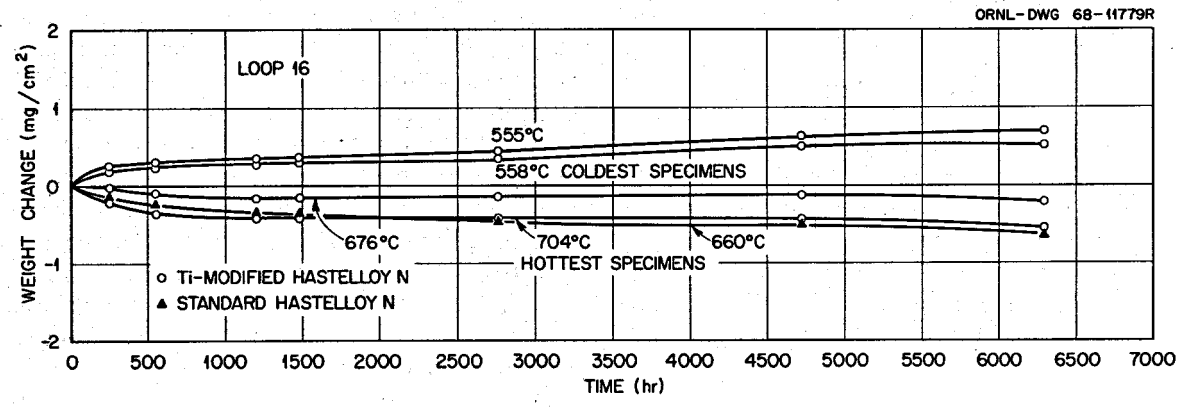

Fig. 18.12. Weight Change vs Time for Standard and Ti-Modified Specimens in Loop NCL-16 Exposed to Fuel Salt ($LiF\text{-}BeF_2\text{-}UF_4$, 65.5-34.0-0.05 Mole %) at Various Temperatures.

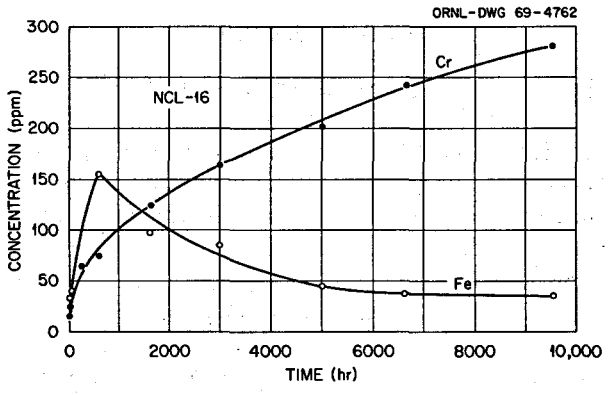

Fig. 18.13. Concentration of Iron and Chromium in the Fuel Salt in Loop NCL-16.

Table 18.8. Bismuth Concentration in LiF-BeF_2-ThF_4-UF_4 (68-20-12-0.3 Mole %) Salt from NCL-19 as a Function of Operating Time

Time (hr)	Sample Weight (g)	Bismuth Concentration[a] (ppm)
0	1	<25
	1	<50
20	1	35
840	1	2200
	0.5	1200
	0.1	<60
1485	1	100
	1	140
	1	73
1633	1	60
2499	1	<20

[a]Polarographic method.

indicating that the specimens are quite compatible with the salt. The weight changes of the removable samples indicate that the average corrosion rate at the maximum temperature of 663°C is <0.05 mil/year.

18.6.4 Coolant Salts

Loop NCL-13A, formerly NCL-13 (ref. 17), constructed of standard Hastelloy N with removable specimens in each leg, has operated for 3100 hr with the fluoroborate coolant salt.

After new fluoroborate salt was added to loop NCL-13A in August, circulation could not be achieved. Our analysis of the situation led us to conclude that previous overheating of the loop had caused BF_3 to evolve and had changed the composition of salt from $NaBF_4$-NaF (92-8 mole %) to a composition much richer in NaF. This in turn would cause the higher-melting NaF to segregate in the loop. To bring the composition back to normal, we added BF_3 gas through the surge tank until a slight overpressure built up over the salt. (No devices were available to measure the amount of BF_3 gas added.) Circulation of the salt was then started. Only a small ΔT (55°C) was obtained at first. Further additions of BF_3 lowered the temperature of the salt in the cold leg and increased the ΔT to about 125°C. Since more BF_3 did not cause immediate changes, the additions of gas were stopped. The loop is now operating satisfactorily with a ΔT of 125°C and a maximum temperature of 607°C.

Figure 18.15 gives the weight changes of specimens at various temperatures as a function of operating time. These initial values are relatively high, with the average corrosion rate over the first 2200 hr being about 1 mil/year at the maximum temperature of 605°C. Analysis of the salt has shown evidence of a large amount of water, 900 ppm, which, because of HF formation, could contribute to a high rate of corrosion. However, these high rates may also be the result of inserting new specimens into a loop system which already had operated 5000 hr. Future measurements will better determine the true corrosion rate in this system. A "cold-finger" device, which will continuously remove corrosion products from the salt, is scheduled to be used on this loop.

Loop NCL-14, constructed of standard Hastelloy N with removable specimens in each leg, has operated for 11,600 hr with the fluoroborate coolant salt. The weight changes of the specimens at the various positions in the loop and at different times are given in Fig. 18.16. This loop operated about 3500 hr with the H_2O content in the salt between 500 and 1000 ppm. During that period the weight changes were small and predictable as a function of time. Wet air then came in contact with the salt through a defective gas line, and the water content and corrosion rate increased dramatically. During the last 5000 hr the H_2O content of the salt has decreased, and the corrosion rate has again decreased as a function of time. The rate of maximum weight loss over the last 5000 hr has been $\sim 1.5 \times 10^{-3}$ mg cm^{-2} hr^{-1} (~0.65 mil/year). This corrosion rate is higher by a factor of 2 than that measured during the earlier operating period when the H_2O content was between 500 and 1000 ppm.

The concentration of impurities in the salt in loop NCL-14 is given as a function of operating time in Fig.

[17]J. W. Koger and A. P. Litman, *MSR Program Semiann. Progr. Rept. Aug. 31, 1968*, ORNL-4344, p. 264.

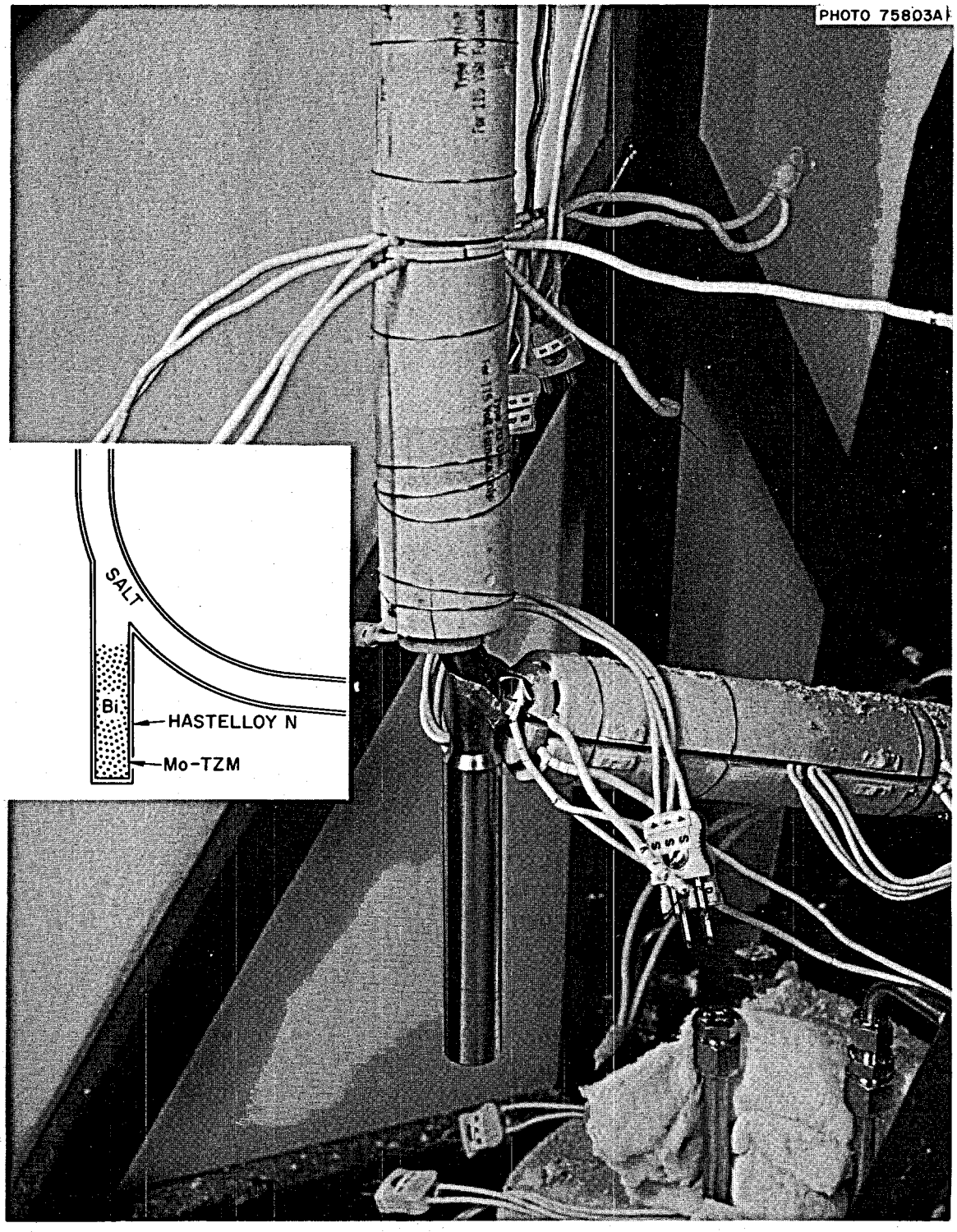

Fig. 18.14. Bismuth "Hot Finger" Contained in Molybdenum with Hastelloy N Jacket on NCL-19.

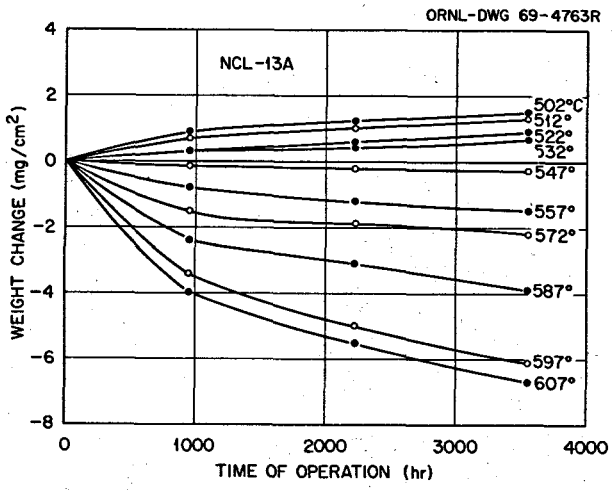

Fig. 18.15. Weight Change vs Time for Standard Hastelloy N Specimens in NCL-13A Exposed to Fluoroborate Salt at Various Temperatures.

18.17. It is obvious that the nickel and molybdenum concentration increased significantly during the time of water ingestion. Nickel and molybdenum are normally not oxidized by fluoride salts, and their increase in the salt is evidence of a generalized HF attack.[18]

Four standard Hastelloy N capsules were operated with $NaBF_4$-NaF (92-8 mole %) fluoroborate salt at 607°C with BF_3 overpressures of 200 torrs, 50 psig, 100 psig, and 400 psig respectively. A typical capsule system is shown in Fig. 18.18. Examination after 6800 hr disclosed that the capsules and specimens were clean and that no corrosion products were visible in the salt. The largest weight loss, equivalent to a uniform loss of 0.02 mil/year, was seen on a specimen exposed to the 100-psig BF_3 vapor in capsule 3. Of particular interest is the observation that all the specimens exposed to the salt gained weight. We believe that this can be explained by the salt analyses, which show an increase of chromium in the salt from 20 to 75 ppm and a decrease in iron from 220 to 20 ppm. This implies that the iron fluoride initially in the salt oxidized chromium from the Hastelloy N to form chromium fluoride, and the reduced iron was deposited on the metal. The water content of the salt remained 400 ppm during the test, while the oxygen increased from 200 to 1400 ppm. Since the largest amount of oxygen was found in the salt of the capsule which had the largest BF_3 pressure, we believe that the oxygen entered as an impurity in the BF_3 gas. Equating the chromium loss from the alloy to the chromium gain by the salt gave a bulk diffusion coefficient for chromium in Hastelloy N of 1.0×10^{-15} cm^2/sec. This value is in reasonable agreement with previous diffusion measurements.[19,20] The most significant result of this experiment is the relatively low corrosion rate observed for Hastelloy N in sodium fluoroborate that contains <500 ppm H_2O. This emphasizes the importance of water vapor in fluoroborate salt corrosion.

Loop NCL-17 will be used to investigate the influence of water content on the corrosion rate of Hastelloy N in sodium fluoroborate. This loop will be constructed of standard Hastelloy N and will contain the fluoroborate salt at the conditions of loop NCL-14. Known amounts of wet helium will be added to the salt, and the resulting changes in the corrosion rate will be measured.

A new standard Hastelloy N loop, NCL-20, which will contain fluoroborate salt, is being constructed. This loop will operate at the temperature extremes of the salt-metal interfaces in a 1000 Mw (electrical) MSBR, namely, 675 to 410°C. The object of this experiment will be to determine whether these temperatures will lead to more unfavorable corrosion than that already observed in tests where we have simulated the bulk fluid temperatures of 605 and 460°C.

18.6.5 Comparison of the Kinetic Behavior of Nickel- and Iron-Based Alloys in Molten Fluoride Salts

The above results allow us to examine the kinetics of the dissolution processes in iron- and nickel-base alloys exposed to fuel and coolant salts. The weight losses of type 304L stainless steel and of standard and titanium-modified Hastelloy N in fuel salt as a function of time at temperature between 660 and 704°C are presented in Fig. 18.19. The plots assume a time dependence of the form

$$W = at^b , \qquad (1)$$

where W is the weight loss in milligrams per square centimeter of surface area, a and b are constants, and t is the time in hours. Terms for this equation are given for each material in Table 18.9.

Similar weight changes are plotted in Fig. 18.20 for standard and modified Hastelloy N at 555 and 604°C in

[18] J. W. Koger and A. P. Litman, *Compatibility of Hastelloy N and Croloy 9M with $NaBF_4$-NaF-KBF_4 (90-4-6 Mole %) Fluoroborate Salt*, ORNL-TM (to be published).

[19] R. B. Evans, J. H. DeVan, and G. M. Watson, *Self-Diffusion of Chromium in Nickel-Base Alloys*, ORNL-2982 (January 1961).

[20] W. R. Grimes *et al.*, *Radioisotopes in Physical Science and Industry*, vol. 3, pp. 559–74, IAEA, Vienna, Austria, 1962.

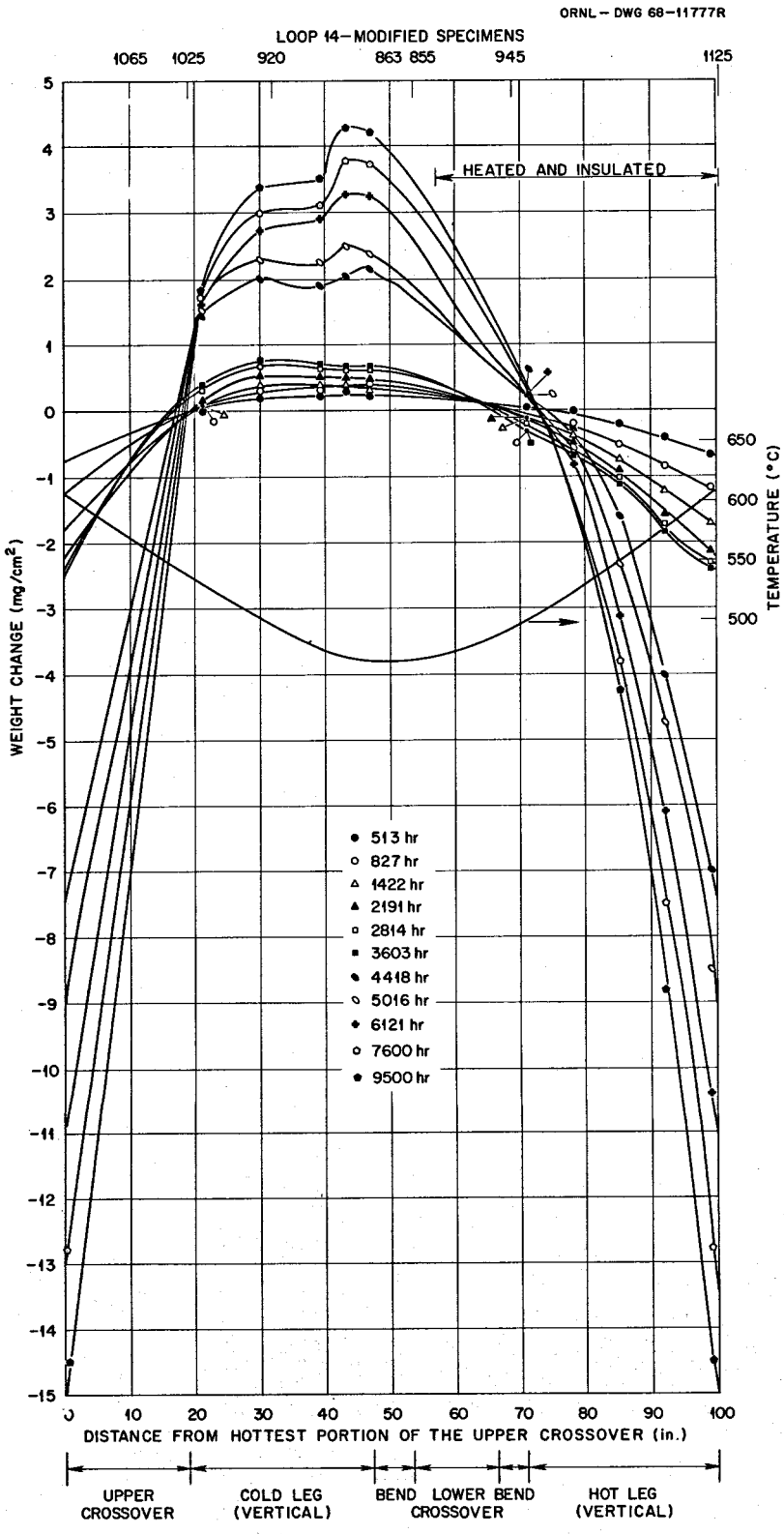

Fig. 18.16. Weight Change as Function of Position (Temperature) for Titanium-Modified Hastelloy N Exposed to Sodium Fluoroborate Salt in Loop NCL-14.

sodium fluoroborate. Again the values were plotted using Eq. (1), and the resultant parameters are shown in Table 18.10.

We next considered the temperature dependence of the weight changes by calculating an average corrosion rate for each test. Arrhenius plots of these average rates are presented in Fig. 18.21. Activation energies indicated by the average slopes of these plots are 36,000 cal/g-mole for the type 304L stainless steel systems and 27,000 cal/g-mole for standard and modified Hastelloy N. It is interesting to compare these results with weight loss behavior based on the assumption of a solid-state diffusion-limited corrosion process. Assuming that the surface concentration of the diffusing species remains constant during test, the resultant weight change expression would be of the form

$$W = \frac{2}{\sqrt{\pi}} \sqrt{Dt}\,(C_0 C_s)\,, \qquad (2)$$

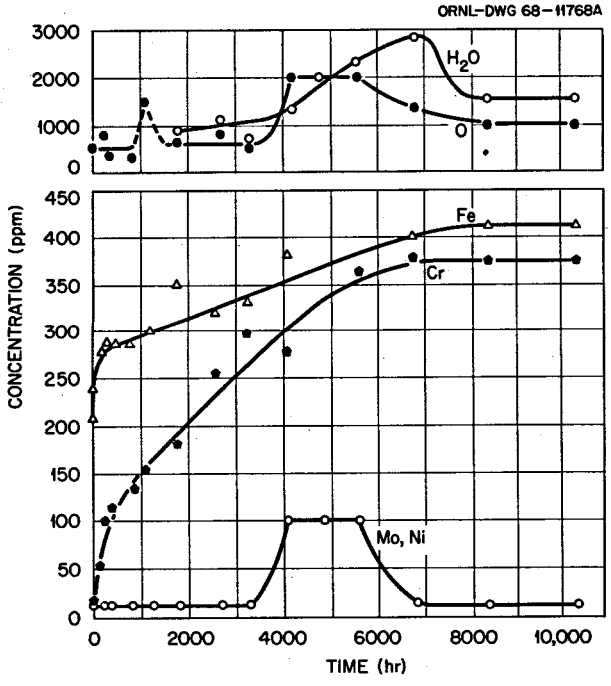

Fig. 18.17. Variation of Impurities with Time in $NaBF_4$-NaF (92-8 Mole %) Thermal Convection Loop NCL-14.

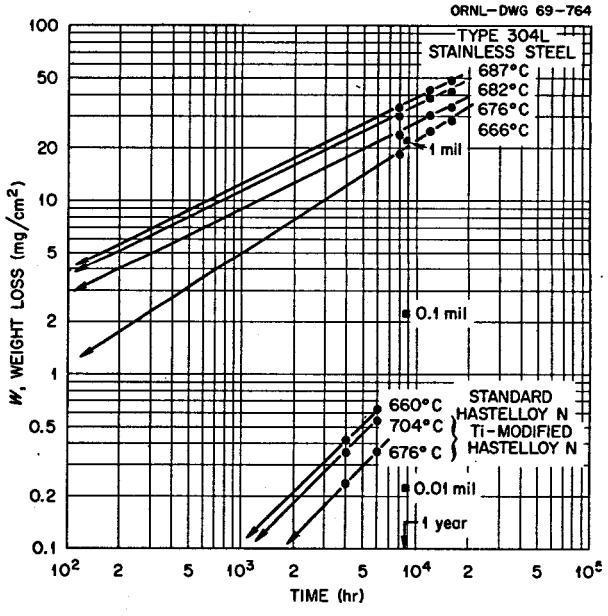

Fig. 18.19. Weight Loss for Type 304L Stainless Steel and Hastelloy N Alloys in Fuel Salts.

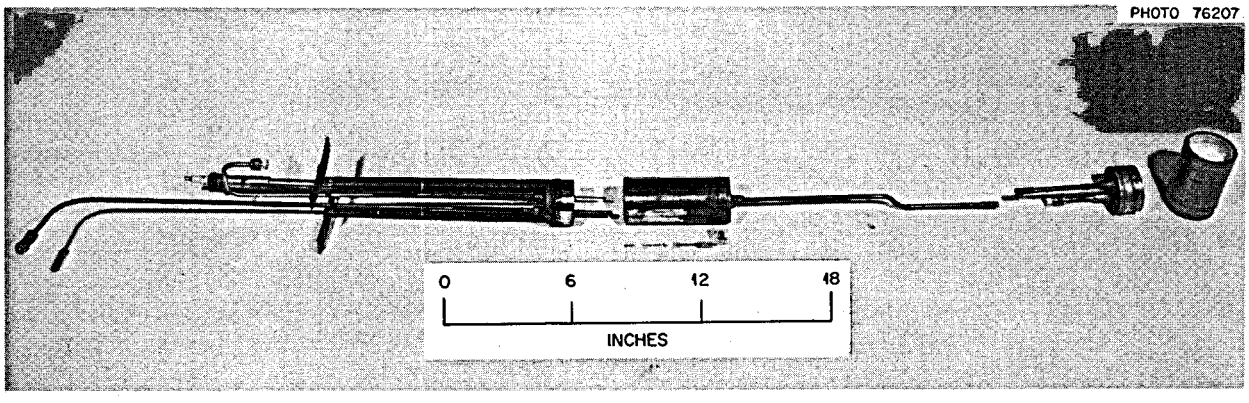

Fig. 18.18. One of Four Standard Hastelloy N Capsules Which Contained $NaBF_4$-NaF (92-8 Mole %) Salt for 6800 hr at BF_3 Pressures of 200 Torrs, 50 psig, 100 psig, and 400 psig. Note the whiteness of the salt in the opened capsule.

Table 18.9. Rate Expressions for Materials in Fuel Salts[a]

Loop Material	Salt	Temperature (°C)	Weight Change Constants[b]		Rate Constants[c]	
			a	*b*	*A*	*Q*
Type 304L stainless steel	1	687	0.33	0.5	8×10^5	36,800
		682	0.31	0.5		
		676	0.26	0.5		
		666	0.25	0.45		
Titanium-modified Hastelloy N	2	704	0.027	0.35	1×10^2	27,000
		676	0.012	0.35		
Standard Hastelloy N	2	660	0.03	0.35	2×10^2	27,000

[a]Salt 1 – LiF-BeF_2-ZrF_4-ThF_4-UF_4 (70-23-5-1-1 mole %); salt 2 – LiF-BeF_2-UF_4 (65.5-34.0-0.5 mole %).

[b]Constants for equation $W = at^b$, where W is weight change, mg/cm^2, and t is time, hr.

[c]Constants for equation $dW/dt = Ae^{-Q/RT}$, where R is gas constant, cal (g-mole)$^{-1}$ (°K)$^{-1}$, and T is absolute temperature, °K.

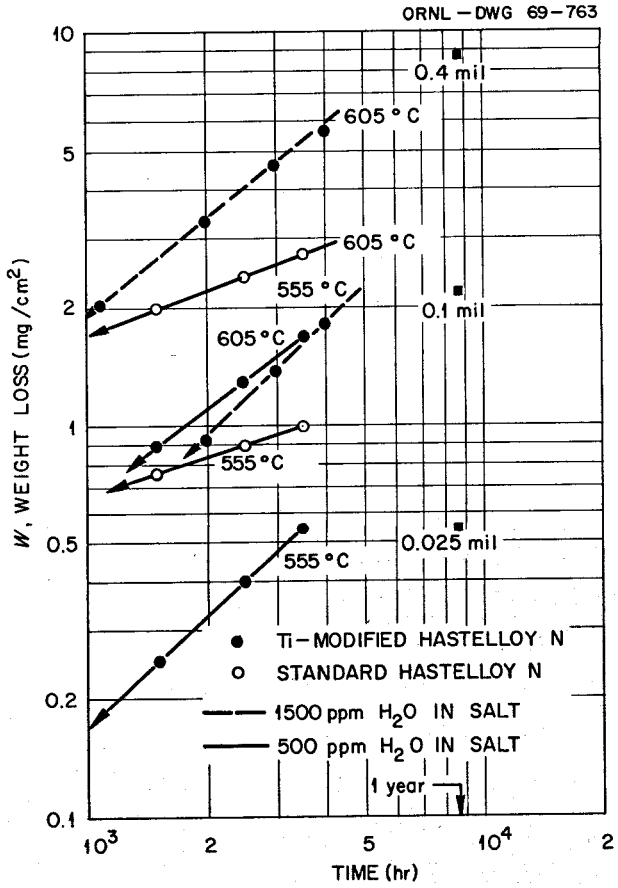

Fig. 18.20. Weight Loss for Hastelloy N Alloys in Sodium Fluoroborate Coolant Salts.

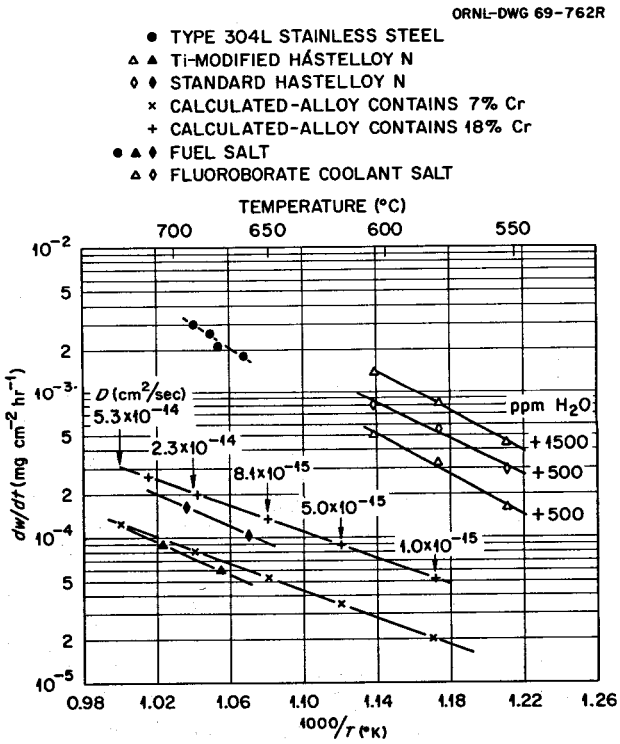

Fig. 18.21. Arrhenius-Type Plot for Materials in Fluoride Salts.

where

W = weight loss, mg/cm^2,

D = diffusion coefficient, cm^2/sec,

t = time, sec,

C_0 = initial uniform concentration, mg/cm^3,

C_s = surface concentration, mg/cm^3 (assumed to be zero).

We assumed that all weight loss was due to the removal of chromium, and, using this expression and published diffusivities for chromium in Hastelloy N, we calculated the weight losses of chromium that should have resulted if the chromium concentration at the surface had been reduced to zero.

As shown in Fig. 18.21, corrosion rates calculated in this manner are in close agreement with results for the modified Hastelloy N–fuel-salt system. The calculations are slightly lower than the observed rates in the standard Hastelloy N–fuel-salt system and very much lower than the observed rates for any of the fluoroborate systems. Assuming that iron, as well as

Table 18.10. Rate Expressions for Materials in Coolant Salts[a]

Loop Materials	Salt	Temperature (°C)	Weight Change Constants[b]		Rate Constants[c]	
			a	b	A	Q
Ti-modified Hastelloy N	3	604	0.0036	0.7	8×10^4	32,200
		579	0.0025	0.7		
		555	0.00032	0.9		
Standard Hastelloy N	3	604	0.15	0.37	3×10^4	29,900
		579	0.16	0.30		
		555	0.063	0.35		
Ti-modified Hastelloy N	4	604	0.0085	0.75	1×10^5	32,200
		579	0.007	0.75		
		555	0.00015	0.1		
		524	0.000055	1.35		

[a]Salt 3 – $NaBF_4$-NaF (92-8 mole %), 500 ppm H_2O; salt 4 – $NaBF_4$-NaF (92-8 mole %), 1500 ppm H_2O.

[b]Constants for equation $W = at^b$, where W is weight change, mg/cm^2, and t is time, hr.

[c]Constants for equation $dW/dt = Ae^{-Q/RT}$, where R is gas constant, cal (g-mole)$^{-1}$ (°K)$^{-1}$, and T is absolute temperature, °K.

Table 18.11. Chemical Analyses of Salt Samples

Element	Composition After Indicated Operating Time					
	0	191 hr	365 hr	633 hr	796 hr	1519 hr
Na[a]	21.8	21.0	23.2	22.5	20.9	22.8
B[a]	9.14	9.23	9.12	9.22	9.22	9.25
F[a]	67.9	68.4	67.9	66.6	67.8	68.3
Fe[b]	407	346	266	280	222	374
		351	257	256	219	
Cr[b]	66	170	124	131	114	272
		156	118	133	117	
Ni[b]	53	4	<20	<20	<10	<15
Mo[b]	41	<10	<15	<20	<10	<6
H_2O[b]	<100	400	1100	600	1400	820
O_2[b]	<50	<50	<50	<50	660	390

[a]Values given in weight percent.

[b]Values given in parts per million.

chromium, has diffused from the standard Hastelloy N alloy brings the calculations in much closer agreement with experimental results for the fuel salt. However, corrosion rates for the fluoroborate loops suggest that solid-state diffusion was not the controlling process in these experiments.

18.7 FORCED CONVECTION LOOP

P. A. Gnadt W. R. Huntley

The MSR-FCL-1 forced convection loop is being operated to evaluate the compatibility of standard Hastelloy N with $NaBF_4$-NaF (92-8 mole %) coolant salt at conditions similar to those which would exist with fluoroborate in the MSRE coolant circuit. During this report period the test loop ran for approximately 2000 hr at design conditions.

For most of the period the system operated at 588°C maximum bulk fluid temperature and 510°C minimum bulk fluid temperature. Figure 18.22 is a typical temperature profile of the system; this profile is based on a computer plot of the temperature information from the test loop and on heat transfer calculations which estimate the inner wall temperatures. Information for this and other computer plots is gathered by the Dextir data logging equipment in Building 9201-3.

Salt samples were taken at the start of the test run and at periodic intervals. The results of the salt analyses are listed in Table 18.11. The salt charge used in this experiment contained more metallic impurities (Fe, Ni, Cr, Mo) than are usually found.[21] The changes in concentrations of impurities, especially Fe, Cr, and H_2O, have been rather erratic as a function of operating time. Further operating time will be required to separate the true chemical changes from the random scatter of analyses.

The pump has been operated with a helium purge through the pump seal (oil) catch basin. The original intent[22] was to add BF_3 to the pump bowl to make up any BF_3 which diffused into the seal catch basin and was swept away by the helium purge. The BF_3 losses, however, are so small that the BF_3 addition system is not being used.

Measurements of the BF_3 in the seal purge gas indicate that the helium (80 cm^3/min) leaving the pump oil catch basin is contaminated with approximately 0.01% BF_3. Analytical results of oil samples for

[21] *MSR Program Semiann. Progr. Rept. Aug. 31, 1968,* ORNL-4344, p. 265.

[22] *MSR Program Semiann. Progr. Rept. Aug. 31, 1968,* ORNL-4344, p. 268.

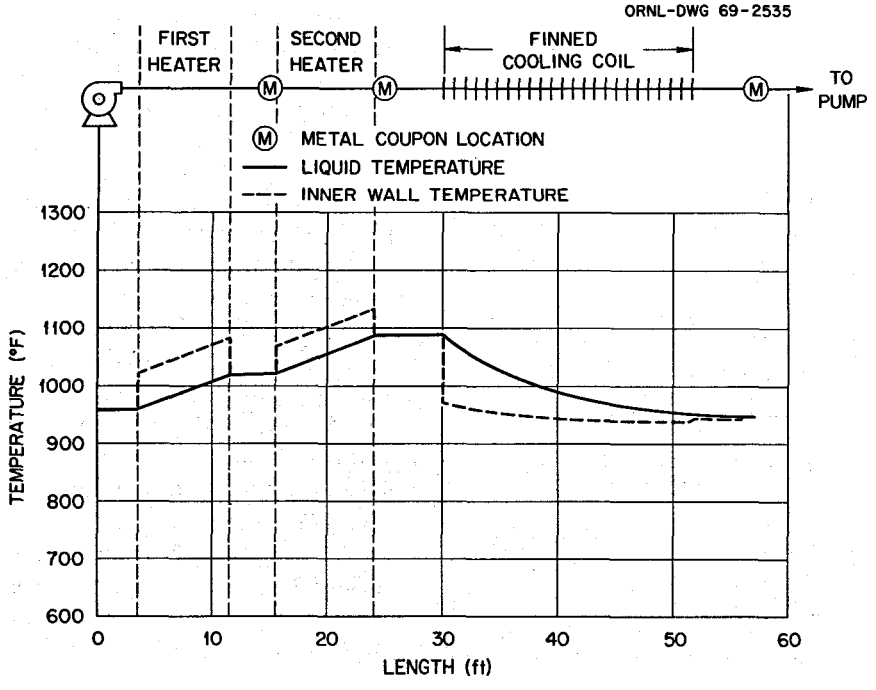

Fig. 18.22. Temperature Profile of Molten-Salt Forced-Convection Corrosion Loop, MSR-FCL-1, at Typical Operating Conditions.

dissolved boron in the seal leakage oil also indicate an extremely small amount of boron dissolved in the oil. These preliminary results indicate that the BF_3 losses from the salt will be insignificant for the scheduled 5000-hr operating period.

The low BF_3 concentration in the helium purge has resulted in little acid accumulation at the gas purge line outlets. Inversion of the purge line and a bucket-type catch basin have also helped to reduce the plugging problem at the end of the purge line. Only a few cubic centimeters of the acid have accumulated in the bucket. No new accumulation of acid on the air exhaust ducts has been noted; however, acid reaction products are noted at the end of the purge line.

Heat transfer performance of the $NaBF_4$-NaF (92-8 mole %) salt was observed in a resistance-heated section of the corrosion loop that was 0.410 in. in inside diameter and 105 in. long. Performance data were obtained at heater inlet temperatures from 521 to 571°C, heater exit temperatures from 566 to 632°C, over a Reynolds modulus range of 4750 to 47,000, and at heat fluxes from 15,750 to 160,000 Btu hr^{-1} ft^{-2}. The data obtained were correlated quite well by the Dittus-Boelter equation, as shown in Fig. 18.23. Although no statistical analysis has been made, we estimate that the error in the measurements on the test loop does not exceed 20%. The data of Fig. 18.23 were plotted using recent[23] physical property values, and it is significant that the use of available physical property data results in agreement with a standard heat transfer correlation equation in our engineering system.

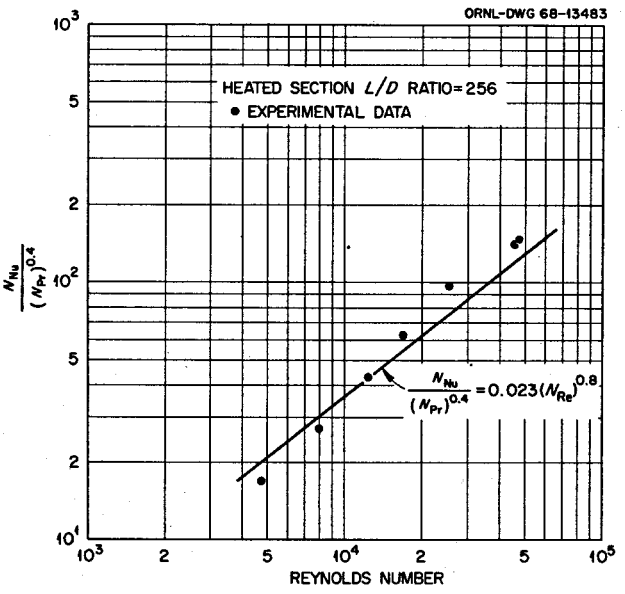

Fig. 18.23. Heat Transfer Characteristics of $NaBF_4$-NaF (92-8 Mole %) Flowing in 0.410-in.-ID Tube.

18.8 OXIDATION OF HASTELLOY N

B. McNabb

We are studying the oxidation and scaling resistance of Hastelloy N and various modified alloys. The main objective of this work is to determine the importance of various elements in controlling oxidation and scaling so that we can obtain a modified alloy with adequate oxidation resistance.

We found that commercial heats of Hastelloy N with only minor differences in composition can have large differences in scaling resistance. Heat 5065 had about 1% weight loss in tests where it was heated for 1000 hr at 982°C and cycled to room temperature every 25 hr, whereas heat 2477 had about 49% weight loss under the same conditions. The major differences in composition are in manganese and silicon, with heat 5065 having 0.55 and 0.57% and heat 2477 having 0.055 and 0.0475% respectively. Alloy No. 10, a laboratory remelt of heat 2477 with 0.5% silicon added, had negligible weight loss under the above conditions.

After determining the importance of silicon, we used the electron microprobe analyzer to determine the distribution of silicon in oxidized samples. An accelerating voltage of 20 kv and a specimen current of 0.02 μa were used to determine the Si $K\alpha$ x-ray intensities. Spot counts were made at various locations in the samples, and a silicon enrichment was noted at the oxide-metal interface and in some of the grain boundary penetrations. To graphically display this, we made a CRT (cathode ray tube) display of Si $K\alpha$ x rays at the surface. Figure 18.24 shows such a display compared with an optical photomicrograph of the same area. By studying the two displays, one can see that silicon is concentrated at grain boundaries and along the interface between the metal and the oxide. We thought at first that the round voids in the optical photomicrograph also had silicon, but the CRT display indicates that this is not true.

Heat 5065 had some large cracks that were filled with oxidation product, and some of these were scanned to see the distribution of the major alloying elements and silicon (Fig. 18.25).

The silicon and chromium were enriched at the oxide-metal interface, and molybdenum, nickel, and

[23] S. Cantor, *Physical Properties of Molten-Salt Reactor Fuel, Coolant, and Flush Salts*, ORNL-TM-2316 (August 1968).

Y-65767

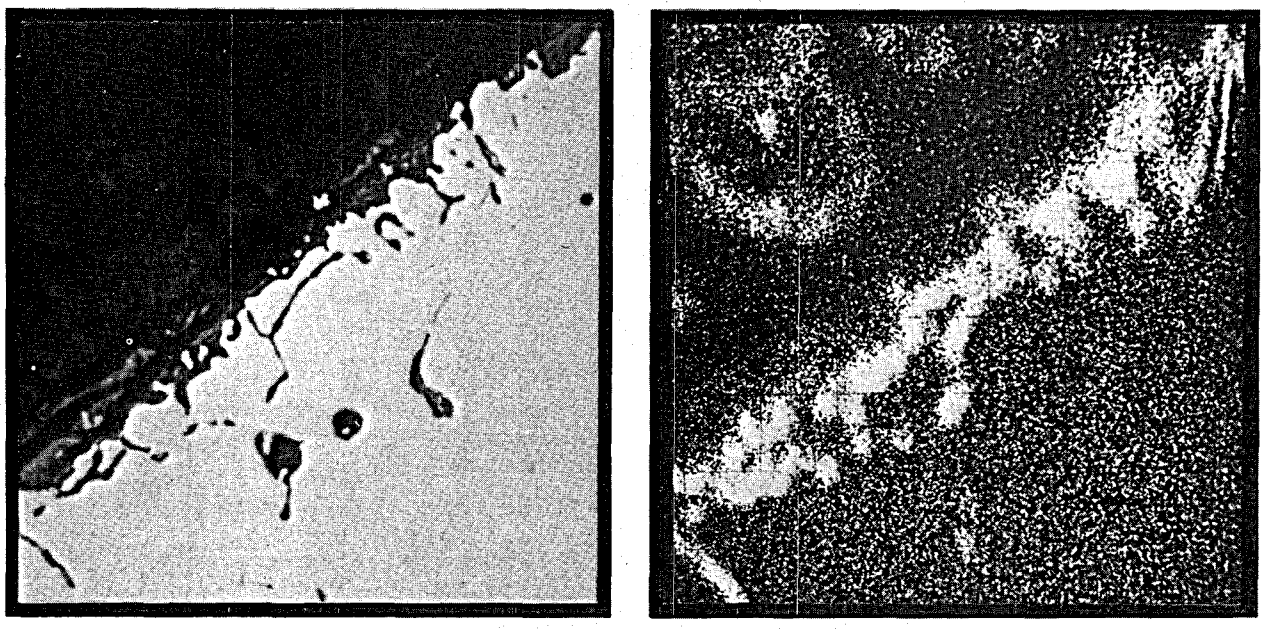

OPTICAL

Si $K\alpha$ X-RAYS

Fig. 18.24. Optical and X-Ray Display Showing the Enrichment of Silicon at the Oxide-Metal Interface of a Hastelloy N (Heat 2477 with 0.5% Si Added) Sample After Oxidation.

iron were depleted. Some areas in the oxide were enriched in nickel and iron, while others were enriched in molybdenum. The significance of this distribution of alloying elements is not known. Figure 18.26 shows the areas of major silicon concentration. The clear zone below the specimen surface is depleted in chromium, and this probably accounts for some of the subsurface voids that do not contain silicon.

The sample of heat 2477 with low silicon, which showed poor oxidation resistance, did not show any silicon enrichment. Figure 18.27 is a CRT display showing the distribution of silicon, chromium, molybdenum, nickel, and iron. It appears that molybdenum and chromium are concentrated at the surface and that nickel and iron are depleted in the same areas. The silicon-rich areas seen just off the surface are due to the silicon naturally occurring in the pelletized alumina used in mounting the metallographic sample.

Figure 18.28 shows the distribution of the major alloying elements in heat 2477 after 1000 hr cycling to 982°C in air with cycles of 15 min heating and 5 min cooling. There are no appreciable concentration differences of any of the elements. This is in contrast to the sample cycled on a frequency of 1 cycle per 25 hr, which showed marked concentration differences near the metal-oxide interface (Fig. 18.27).

Figure 18.29 shows the distribution of the major alloying elements in heat 5067 after cycling in air for 1000 hr at 982°C (15-5 cycle). Heat 5067 has intermediate amounts of manganese and silicon, 0.48 and 0.42% respectively. In this sample the molybdenum and silicon seem to be enriched together in the precipitates, and iron, nickel, and manganese are depleted in the same areas.

The reason for the different morphologies of the oxides is not understood, but may be related to the manganese and silicon content, which could affect the solubilities of other alloying elements. Wasielewski[24] has shown that by adding 0.2% lanthanum to Hastelloy X, the surface oxide can be changed from predominantly Cr_2O_3 to $MnCr_2O_4$, which gives increased oxidation resistance and spalling resistance. Gehlbach and McCoy[25] have found that the silicon content affects the amount and form of precipitates found in Hastelloy N. The high silicon content favors the formation of M_6C carbides; the low silicon content

[24] G. E. Wasielewski, *Nickel-Base Superalloy Oxidation*, AFML-TR-67-30 (January 1967).

[25] R. E. Gehlbach and H. E. McCoy, *MSR Program Semiann. Progr. Rept. Feb. 29, 1968*, ORNL-4254, pp. 209–12.

Y-85764

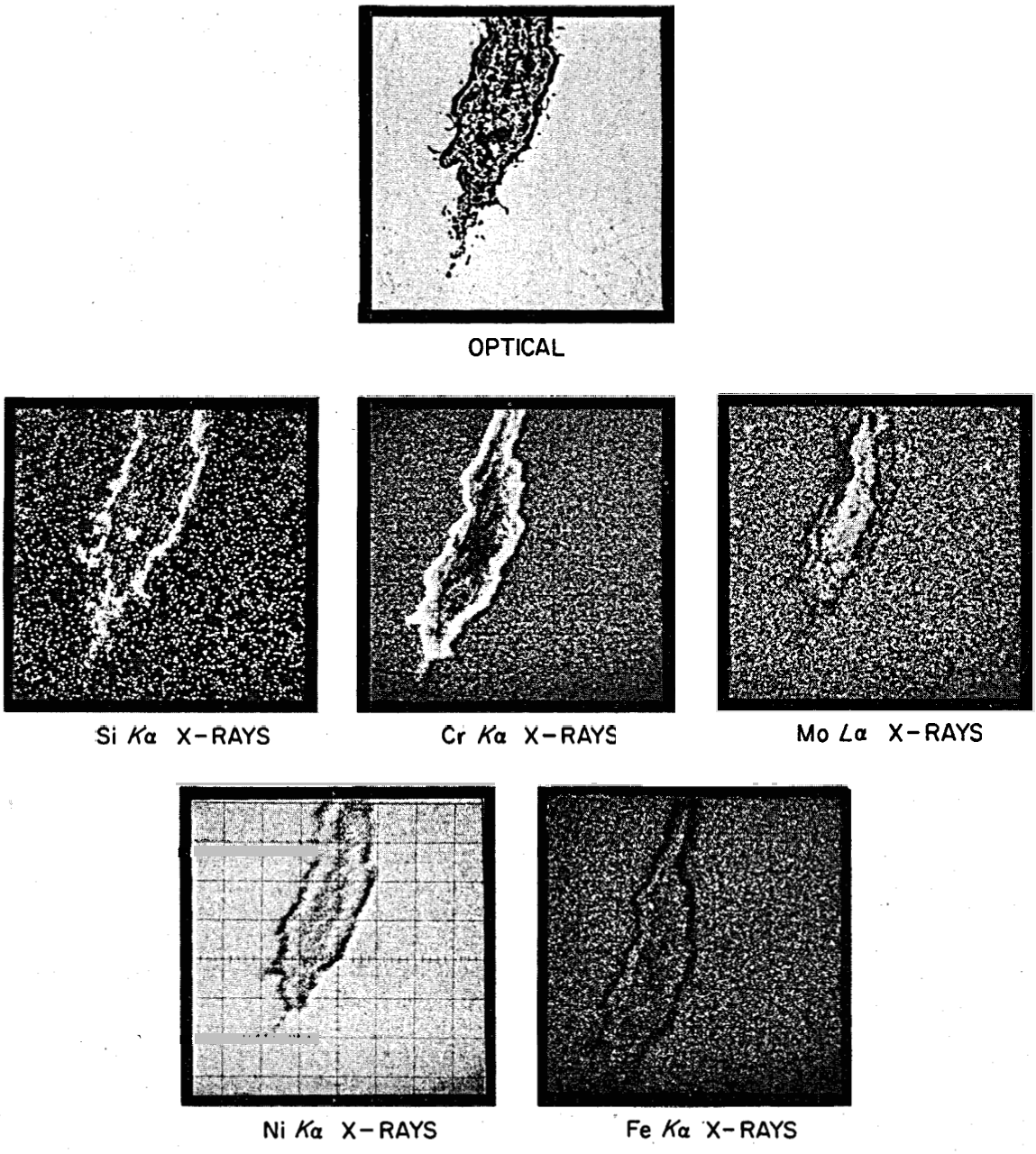

Fig. 18.25. Optical and X-Ray Displays Showing the Distribution of Various Elements in Hastelloy N (Heat 5065) During Oxidation.

favors M_6C primary carbides and $(Mo,Cr)_2C$ precipitates.

Table 18.12 shows the distribution of the major alloying elements in the matrix in the metal near the oxide-metal interface and in the oxide of heats 2477 and 5067. This shows some enrichment of silicon and some depletion of nickel in the oxide and increases near the oxide-metal interface of chromium and iron in heat 5067 and of chromium in heat 2477.

These results show that silicon plays an important role in the oxidation of Hastelloy N. The concentration of this element at the oxide-metal interface may be responsible for the lower oxidation and scaling rate of high-silicon alloys. However, the lower silicon level may be necessary to obtain the desired destruction of precipitates for optimum resistance to irradiation damage. The oxidation resistance at the design temperature of an MSBR of 704°C would be adequate at any silicon level, and the higher oxidation rate of the low-silicon alloy would only be important during unexpected transients.

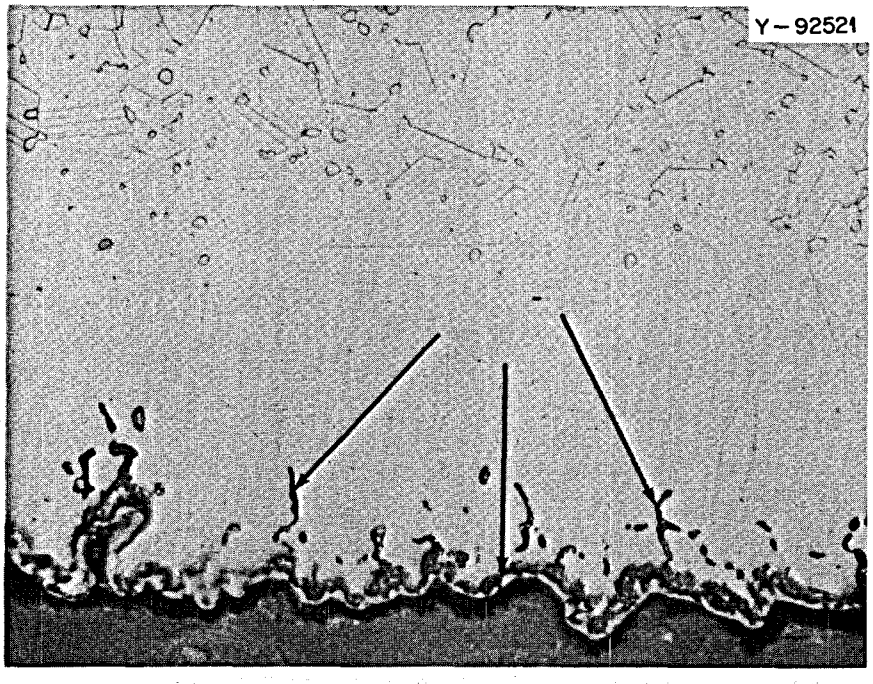

Fig. 18.26. Optical Photomicrograph Showing the Area That Is Enriched in Silicon. The arrows show areas of silicon concentration. Magnification: 500X.

Table 18.12. Results of Semiquantitative Analyses on Oxidized Samples

Heat No.	Location of Sample	Composition (%)					
		Ni	Mo	Fe	Cr	Mn	Si
2477	Matrix	40–80	10–25	5–15	5–10	<1	
	Interface	40–80	10–25	5–15	5–10	<1	
	Oxide	20–50	10–25	5–15	10–30		
5067	Matrix	40–80	10–25	5–15	5–10	0.2–2	
	Interface	40–80	10–25	5–15	5–10	0.2–2	
	Oxide	10–30	10–30	10–30	10–30	0.2–2	0.2–2

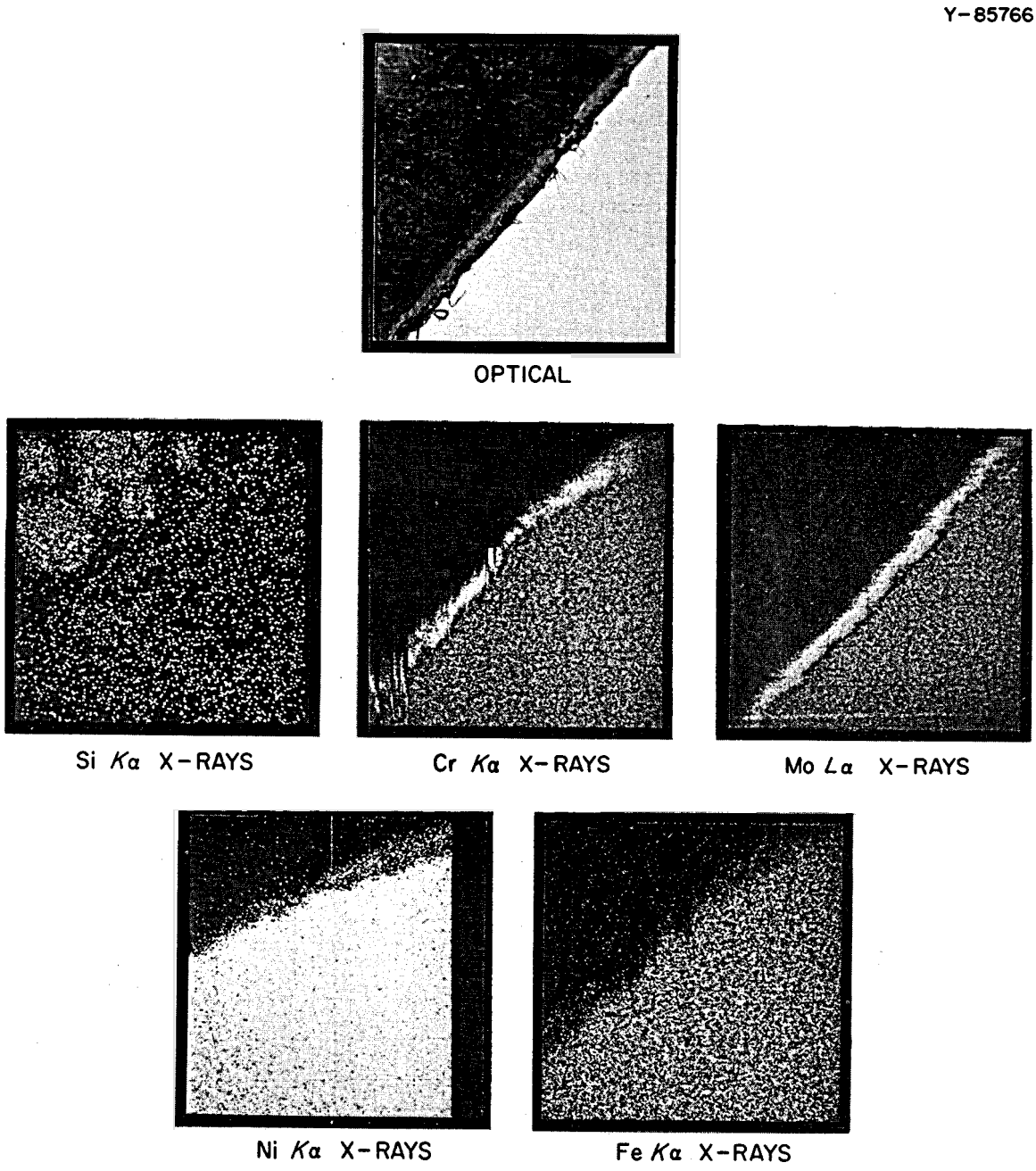

Fig. 18.27. Optical and X-Ray Displays Showing the Distribution of Various Elements in Hastelloy N (Heat 2477) After Oxidation.

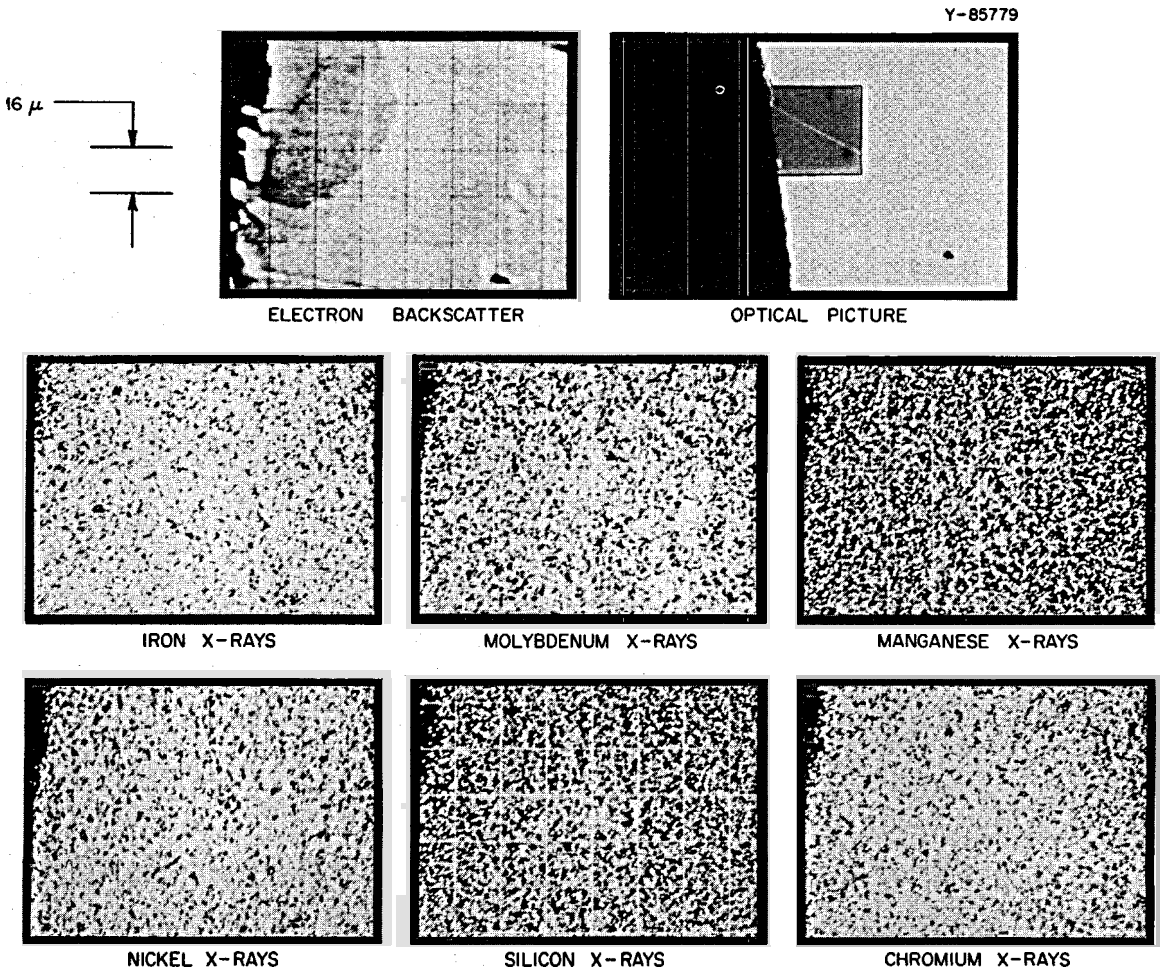

Fig. 18.28. Optical and X-Ray Displays Showing the Distribution of Various Elements in Hastelloy N (Heat 2477) That Has Been Oxidized at 982°C for 1000 hr with Cycles of Heating for 15 min and Cooling to 25°C for 5 min. The x-ray displays cover the shaded area in the optical picture.

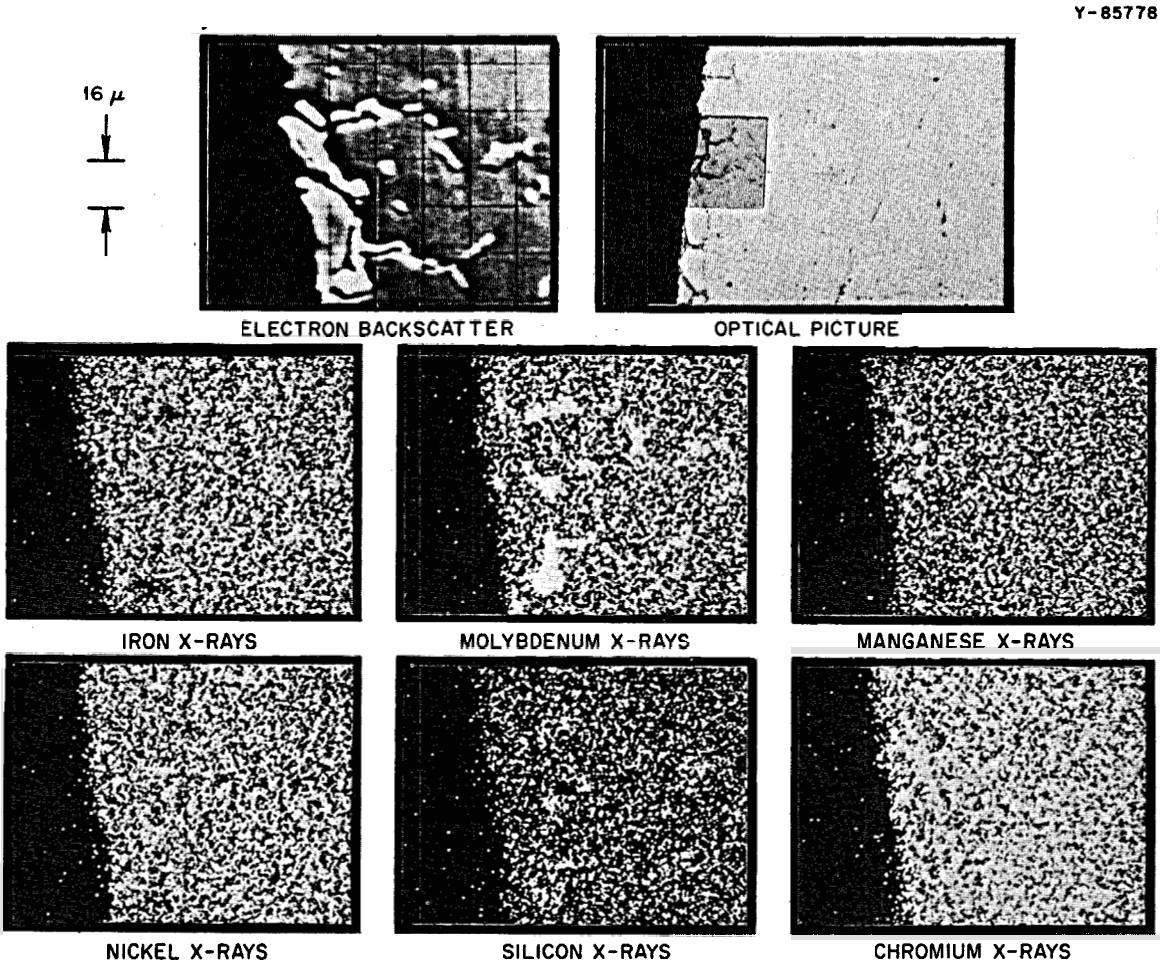

Fig. 18.29. Optical and X-ray Displays Showing the Distribution of Various Elements in Hastelloy N (Heat 5067) That Has Been Oxidized at 982°C for 1000 hr with Cycles of Heating for 15 min and Cooling to 25°C for 5 min. Note from Fig. 18.28.

19. Support for Chemical Processing

19.1 GRAPHITE–HASTELLOY N TRANSITION JOINT DEVELOPMENT

J. P. Hammond

Work continues on graded transition joints for joining graphite to Hastelloy N. These joints, described in detail previously,[1] comprise a series of tungsten-rich, nickel-matrix dispersion alloys brazed together to span the large gap in thermal expansion coefficients between nuclear graphite and Hastelloy N. Premium grades of graphite are also introduced adjacent to the nuclear graphite to reduce the dimensional instability associated with irradiation of nuclear graphite.

Several of these transition joints were prepared using processes and materials developed previously.[2] A minimum of intervening segments was employed in an attempt to reduce fabrication costs; the construction of the joints is illustrated in Fig. 19.1. The coefficients of thermal expansion of the individual segments in relation to those for nuclear graphite and Hastelloy N are given in Fig. 19.2. The Poco graphite segment, inserted to impart irradiation stability, has an expansion coefficient about midway between that for nuclear graphite and for Hastelloy N. This leaves a much narrower gap to be bridged by heavy-metal alloy segments. This bridging is done with two heavy-metal segments, one containing 80% tungsten (matching the Poco graphite) and the other containing 60% tungsten (intermediate between the 80% tungsten segment and the Hastelloy N terminal piece). We matched the expansion coefficients of the Poco graphite and the adjoining heavy metal, since failures often occurred at this interface.

Calculations indicated that the very low modulus of elasticity of graphitic materials[3] would allow composites of nuclear graphite bonded to Poco graphite to be cycled between 650°C and room temperature without straining the materials above their elastic limits. The couplings between the metallic components of this joint should undergo moderate plastic strain in such thermal cycling; however, we expected that they might sustain it without failing because of the good ductilities of the materials involved.

Two three-segment joints were subjected to twenty-four 20-min cycles of heating and cooling between 750°C and room temperature without producing any detectable cracks. Copper between the Cr_2C_3-coated graphite members remained intact and did not appear to react or alloy in any way with the chromium carbide. The overall results are encouraging and indicate that the joints should show excellent behavior under service conditions.

19.2 DEVELOPMENT OF CORROSION-RESISTANT BRAZING ALLOYS FOR MOLYBDENUM

R. W. Gunkel N. C. Cole

Molybdenum seems to be compatible with fluoride salts and with bismuth and would appear to be a good structural material for an MSBR processing plant were it not for its relatively poor weldability. This problem could be circumvented if we could develop a brazing alloy that was compatible with fluoride salts and bismuth and had a flow temperature low enough to prevent recrystallization and subsequent embrittlement of the molybdenum. A small program is under way to develop suitable brazing alloys for this application.

A literature survey showed that most refractory metals were resistant to bismuth and could therefore be considered as candidate materials for formulation of experimental brazing alloys. About 15 refractory-metal-base brazing filler metals were formulated and evaluated, but the lowest melting temperature obtained was 1525°C. For lower-melting filler metals, iron appeared to be the most promising candidate material. Brazing temperatures in the range of 1140 to 1180°C have been

[1] *MSR Program Semiann. Progr. Rept. Feb. 29, 1968*, ORNL-4254, p. 235.

[2] *MSR Program Semiann. Progr. Rept. Aug. 31, 1968*, ORNL-4344, p. 273.

[3] The moduli of elasticity of graphites range between 0.25 and 0.80 × 10^6 psi, as compared with values around 0.55 × 10^8 psi for tungsten heavy-metal alloys.

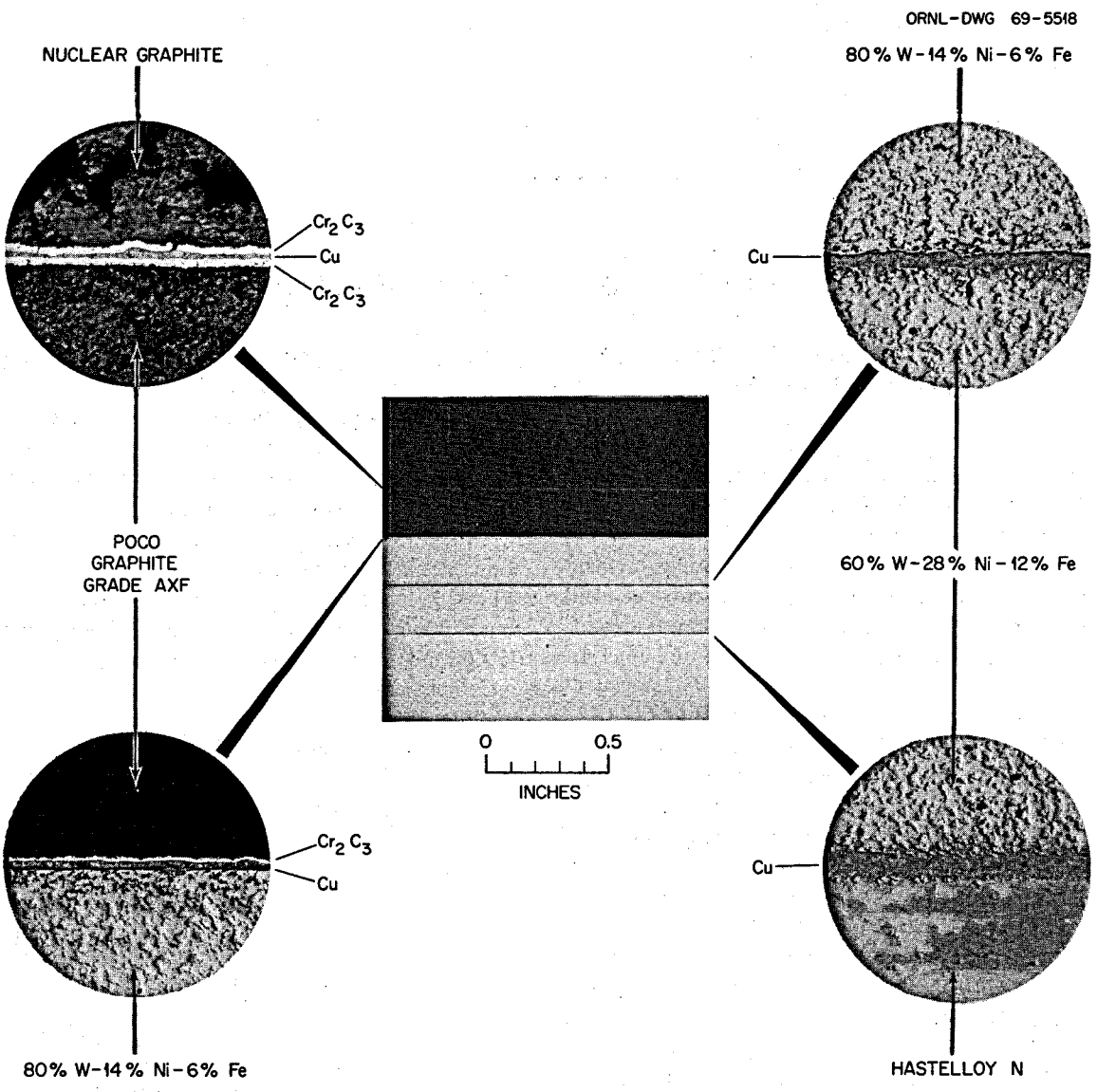

Fig. 19.1. Three-Segment Transition Joint Showing Microstructures in Bond Regions. As polished, oblique illumination. 250X. Reduced 46%.

obtained with three iron-base alloys, and they appear attractive as materials for brazing molybdenum-base alloys below their recrystallization temperatures. One disadvantage of the filler metals investigated to date is their low ductility; therefore one very important phase of our future work will be to obtain more-ductile alloys.

The excellent flowability of these iron-base filler metals on molybdenum has been demonstrated on T-joints. Figure 19.3 is a photomicrograph of a molybdenum-TZM T-joint brazed with one of these alloys, and the excellent wetting properties of the brazing are apparent. Only minor reaction with the base material is evident. Figure 19.4 shows a higher-magnification view of the microstructure of the brazed fillet and illustrates the heterogeneity of the structure. Tests will be run on these joints to determine their compatibility with bismuth and fluoride salts and their shear strengths by using Miller-Peaslee-type specimens.

19.3 EXAMINATION OF Mo-TZM CAPSULE

J. W. Koger A. P. Litman

The capsule test in support of MSR fuel processing by vacuum distillation was completed. A capsule constructed of Mo-TZM (Mo–0.5 Ti–0.08 Zr) and containing Mo-TZM specimens was exposed to LiF-BeF_2-ThF_4-UF_4 (68-20-12-0.3 mole %) salt at 1100°C

(2010°F) for 1011 hr. The chemical composition of the salt before and after test is given in Table 19.1. Small increases in the titanium, zirconium, and chromium concentration in the salt were noted as the result of the test. All three of these elements were present initially in the Mo-TZM. Weight changes of the specimens were negligible (<0.03 mg/cm^2).

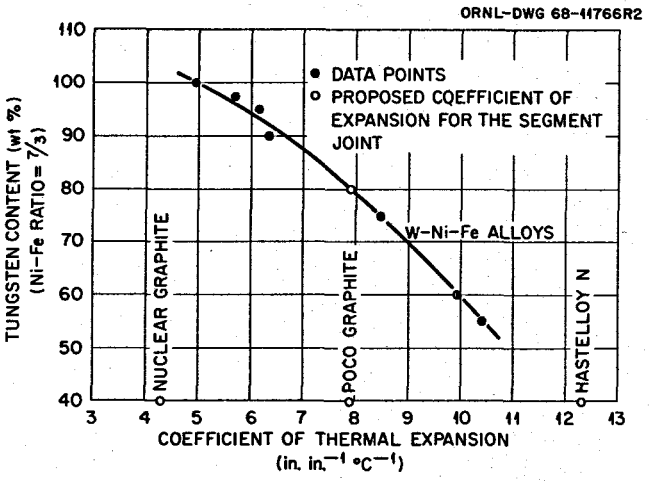

Fig. 19.2. Expansion Coefficients of Three-Segment Joint Materials as a Function of Composition. Coefficients are mean values between room temperature and 600°C and were determined on an optical interferometer.

Figure 19.5*a* shows the typical cold-worked structure of the specimens and the capsule before test. This microstructure is also typical of the specimen exposed to the salt vapor where no microstructural change was noted. A specimen exposed to the salt shows no attack at the surface in the as-polished condition (Fig. 19.5*b*). The same specimen etched (Fig. 19.5*c*) shows recrystallization for a maximum depth of about 4 mils. Examination of this specimen at a lower magnification (Fig. 19.5*d*) shows that both surfaces recrystallized as the result of the test. The capsule wall also recrystallized in the same manner. It is customary for Mo-TZM to be annealed 30 min at 1540°C to produce complete recrystallization.[4] An increase in annealing time from 30 min to 1000 hr should not lower the recrystallization temperature much over 100°C. However, it is

[4]R. L. Stephenson, private communication.

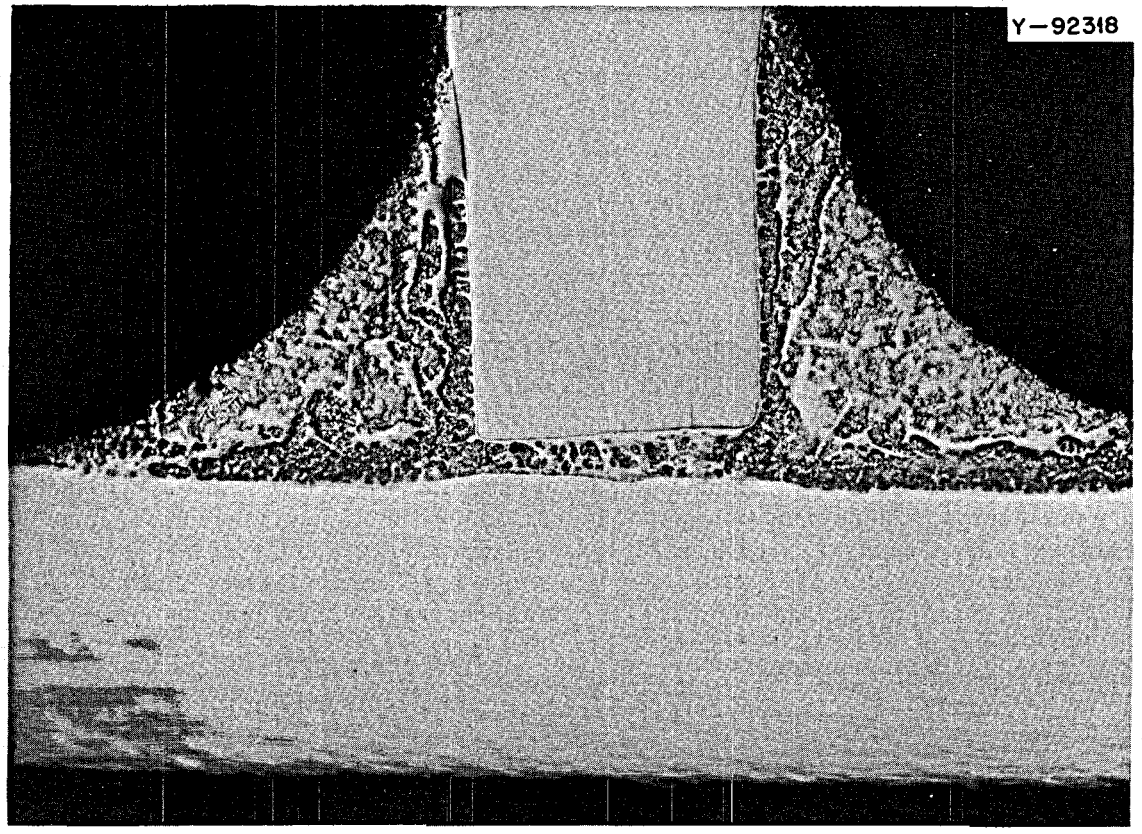

Fig. 19.3. Photomicrograph of a Molybdenum-TZM T-Joint Brazed with an Iron-Base Alloy. Magnification: 60X.

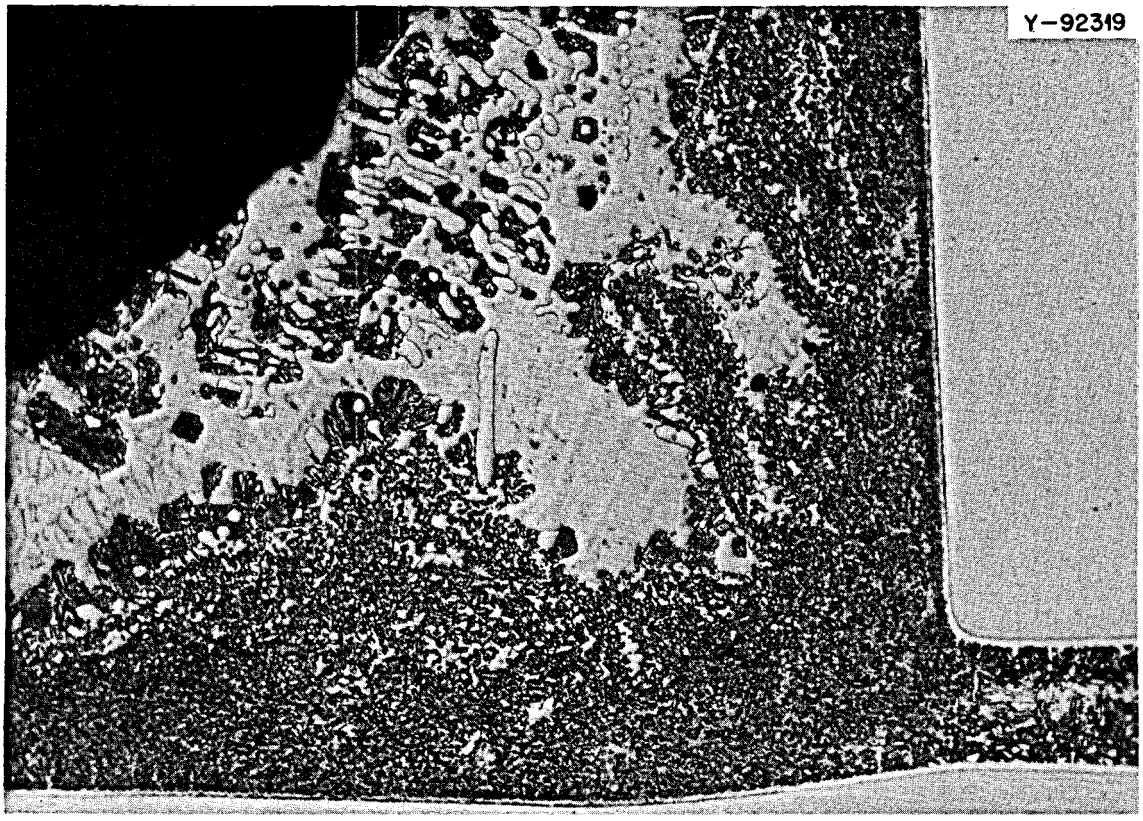

Fig. 19.4. Microstructure of an Iron-Base Brazing Alloy Showing a Heterogeneous Fillet. Magnification: 200X.

Table 19.1. Chemical Analyses of Fertile-Fissile Salt Exposed to TZM Capsule for 1011 hr at 1100°C (2010°F)

	Parts per Million							Weight Percent				
	Mo	Zr	Ti	Fe	Cr	O_2	H_2O	Li	Be	Th	U	F
Before test	<5	37	74	40	20	58	40	6.71	2.65	43.1	1.75	45.5
After test	<10	134	151	38	97	<50	70	7.01	2.55	42.6	1.93	45.7

known that the presence of small concentrations of a foreign element in solid solution can raise the recrystallization temperature as much as several hundred degrees.[5] Thus the enhanced recrystallization (lower recrystallization temperature) in the samples and capsule at 1100°C is very likely due to the removal of the titanium and zirconium from the alloy. This removal would have the effect of freeing the grains and allowing them to grow.

This experiment has shown that zirconium, titanium, and chromium are selectively removed from Mo-TZM during exposure to fluoride salt at 1100°C. This removal results in a change in the microstructure near the surface, but the mechanical property changes should not be deleterious.

19.4 BISMUTH CORROSION STUDIES

J. W. Koger A. P. Litman
B. Fleischer

In flowing bismuth, when even a small temperature difference exists (such as in the proposed MSBR re-

[5]R. E. Reed-Hill, *Physical Metallurgy Principles*, p. 198, Van Nostrand, Princeton, N.J., 1964.

PHOTO 95519

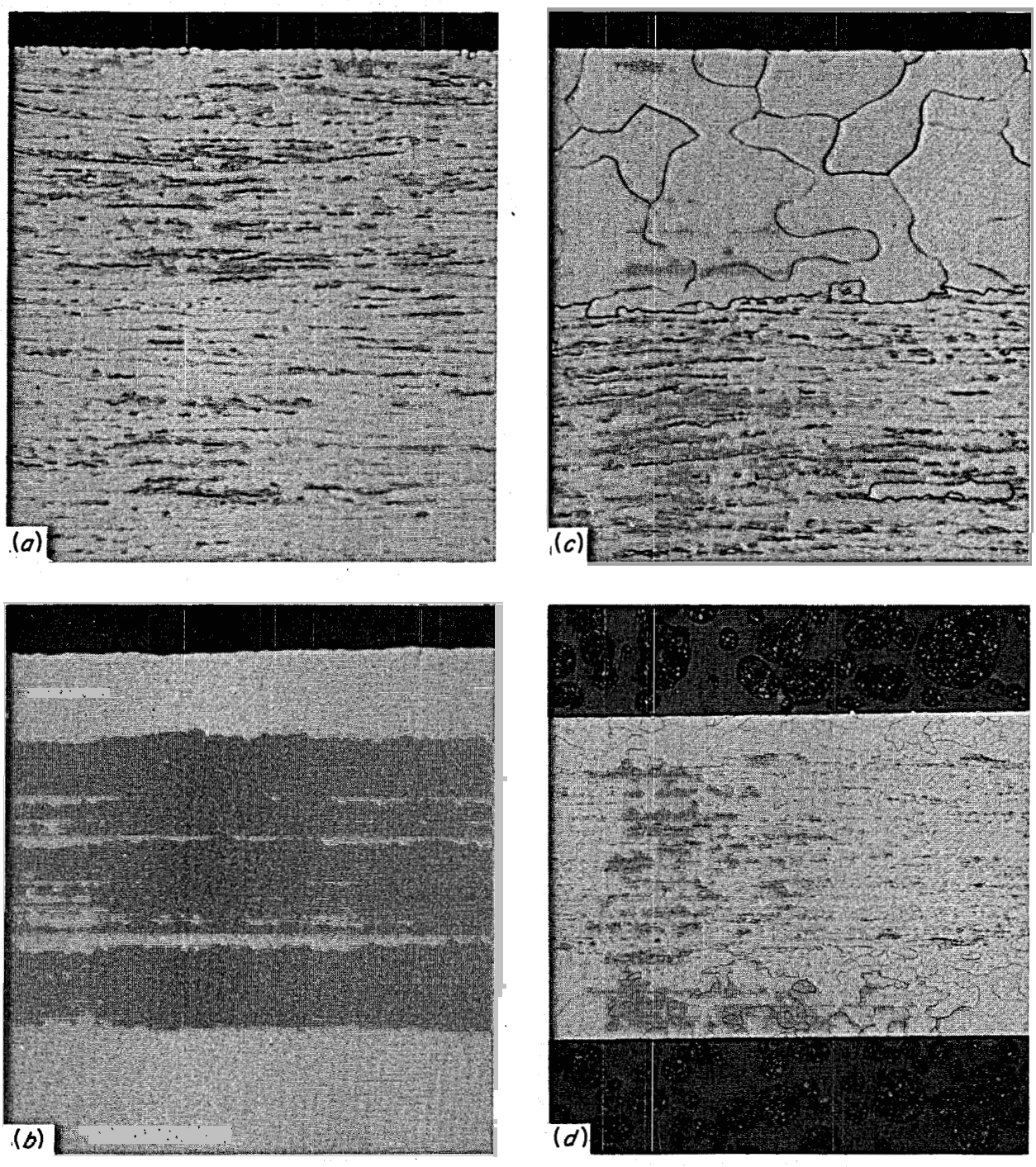

Fig. 19.5. Molybdenum-TZM Alloy Exposed to Fertile-Fissile Salt, LiF-BeF_2-ThF_4-UF_4 (68-20-12-0.3 Mole %), for 1011 hr at 1100°C. (*a*) Microstructure typical of the cold-worked material before test and the specimen exposed to the vapor during test. 500X. Etchant: H_2O, H_2O_2, H_2SO_4. (*b*) Typical of as-polished capsule and specimen exposed to salt. 500X. (*c*) Typical of capsule and specimen surfaces exposed to salt. 500X. Etchant: H_2O, H_2O_2, H_2SO_4. (*d*) Specimen exposed to salt. 100X. Etchant: H_2O, H_2O_2, H_2SO_4.

processing plant), excessive temperature-gradient mass transfer seriously limits the usefulness of container systems fabricated from nickel, iron, and chromium alloys.[6] This rules out most conventional materials for long-term service in the processing plant. Relief in this situation is seen in the refractory alloys, especially molybdenum, that are much more compatible with liquid bismuth. The fabrication of these refractory metals in a large engineering system, however, poses many problems. A very desirable combination of materials would be an iron-base alloy for the exterior and a thin coating or liner of molybdenum on the interior where it would be exposed to salt and bismuth.

The first experiments in the program will consist of a study of the feasibility of exchanging molybdenum from a molten fluoride salt with more active elements (viz., chromium and iron) of the container material by activity-gradient mass transfer. We plan to add a small amount of MoF_6 (gas) to an $LiF\text{-}BeF_2$ salt and pretreat the iron-base loop before the bismuth is added. Equation (1) describes the reaction:

$$MoF_6 + 3Cr \rightarrow 3CrF_2 + Mo\downarrow . \qquad (1)$$

The CrF_2 is soluble in the salt, and the molybdenum should be deposited on the metal wall.

Since molybdenum looks very promising from the standpoint of compatibility but very discouraging from a fabricability standpoint, a practical solution to the materials problem would be available if molybdenum could be applied to conventional materials in the manner described above. Such a treatment could be applied to the processing equipment after welding, and the equipment could be re-treated in place as required.

[6] J. R. Weeks and D. H. Gurinsky, "Solid Metal–Liquid Metal Reactions in Bismuth and Sodium," pp. 106–61 in *Liquid Metals and Solidification*, American Society for Metals, Cleveland, Ohio, 1958.

20. Support for Components Development Program

20.1 REMOTE WELDING DEVELOPMENT

L. C. Williams T. R. Housley R. W. Gunkel

Our efforts on this program have been on a cooperative basis with the Reactor Division and have consisted of work in two areas: (1) equipment procurement for general welding studies, and (2) consultation with Reactor Division personnel on actual remote welding applications. In the first area, we have procured a digital-controlled automatic welding system and an MIG wire feeder and controller; purchase orders are out for a welding head positioner. In the second area of work, we are providing advice and assistance in the construction of a remote-controlled orbital carriage welding head, a device for producing circumferential tungsten-arc welds in large pipe (see Sect. 7.8).

When the general welding equipment is received and assembled, we will be in a position to do detailed welding studies to permit optimum welding process and parameter selection.

20.2 THERMAL CYCLING TESTS ON COATED BEARING SPECIMENS

W. H. Cook L. R. Trotter

The hard-surface coatings are of interest for bearing and valve applications because they are relatively easy to apply. Several coatings have been applied to Hastelloy N cylinders for evaluation. The thermal cycling tests have been completed.

The coatings were applied to the sides of cylinders of Hastelloy N 1 in. in diameter by 1 in. long. Each cylinder had a ½-in.-diam by ½-in.-long handling spindle on one end. The coatings were surface ground to produce the best surface obtainable and to make them 3 mils thick. These surfaces, as measured by Mechanical Technology Inc. (MTI), were found to have surface roughnesses of 0.6 to 9, 1.4 to 2.3, 42 to 125, and 30 to 63 μin. for LW-1, LW-5, MTI, and Metco 81 NS respectively. The NDT fluorescent dye penetrant examinations of them prior to the thermal cycling tests did not reveal any flaws in the coatings.

A thermal cycle nominally required 20 min to heat up from 100 to 700°C and 40 min to cool back down to 100°C. The cycling atmosphere was pure argon. An attempt was made to monitor the sounds during the cycles in order to determine the moment of failure during the 100 thermal cycles. This technique showed some promise, but it requires further development in an area other than a conventional laboratory area. Six specimens of each coating were thermal cycled.

The coatings evaluated were (1) Linde LW-5, 25% tungsten carbide and mixed W-Cr carbides plus 7% nickel, (2) Linde LW-1, tungsten carbide plus 7–10% cobalt, (3) Metco 81 NS, 75% chromium carbide plus 25% nickel-chromium alloy, and (4) MTI, 84% tungsten carbide–10% molybdenum plus 6% cobalt. They survived 100 thermal cycles between 100 and 700°C in the order listed. None of the coatings spalled, but all showed some degree of failure in the fluorescent dye penetrant examinations made on them for us by the Nondestructive Testing Group.

One of the six specimens of the Linde LW-5 developed very fine cracks and some pinholes. This may be because the coating was inferior and/or was thicker in the region of failure.

Two of the specimens of the Linde LW-1 developed pinholes as a result of the thermal cycling. This, I believe, is the result of lack of quality control in fabrication.

The Metco 81 NS and the MTI specimens had heavy backgrounds in the NDT posttest examinations, which suggests a fine network of cracks and/or porosity. This is probably a reflection of lower bonding strength between the carbide particles that make up part of these coatings.

It is interesting to note that we rated these in the order of decreasing resistance to the thermal cycling as Linde LW-5, Linde LW-1, Metco 81 NS, and MTI and that this parallels their bond strengths at room temperature: 6330, 6060, 5400, and 4270 psi, respectively, as determined by MTI.

We shall examine the microstructures of the coatings to determine the nature and causes of the failures and to determine if there are hidden failures such as separation of the coatings from the substrate, Hastelloy N, as a result of the thermal cycling tests.

The results are encouraging, but much work would be required to fully evaluate the potential of the coatings that survived the thermal cycling tests without serious damage. For example, for heat-treating work and design, one should find what upper temperature will cause the coatings to fail; their corrosion resistance to molten salts should be determined; and bearing tests in molten salts involving boundary lubrication (rubbing) and hydrodynamic lubrication tests should be made.

Part 6. Molten-Salt Processing and Preparation

M. E. Whatley

Part 6 deals with the work toward the development of processes for the isolation of protactinium and the removal of fission products from molten-salt reactors. The work is oriented around processing concepts which are gradually achieving maturity. Protactinium is to be isolated by a reductive extraction scheme which traps it in an extraction cascade between thorium, which is less noble, and uranium, which is more noble. The rare earths are to be removed by a reductive extraction operation on a salt stream from which the uranium and protactinium have already been removed. Our technique for determining the distribution of materials between molten salt and bismuth as a function of the reducing power of the bismuth have become quite good, and we can now present reliable distribution coefficients for all the interesting components including lithium, thorium, protactinium, plutonium, zirconium, and uranium. The separation factors for protactinium continue to look attractive, and those for the rare earths appear adequate. The major engineering problems are associated with the development of an electrolytic cell, which is necessary both to provide extractant and to oxidize the extracted uranium, and liquid-liquid contactors which must be effective in this system. We have operated small electrolytic cells made of quartz where, under static conditions, current densities of over 4000 amp/ft^2 were easily achieved. We have yet to demonstrate that these cells can be operated at steady state with flowing fluids and that they can be constructed of metal protected by dynamically cast frozen salt. A system has been installed to study contactors using salt and bismuth, and it is presently in the early stages of shakedown operation. Our work with mercury and water to simulate salt-bismuth systems is progressing well.

We have found that dissolved nickel in the bismuth phase reduces the solubility of thorium, which in turn affects the distribution coefficients in the system. Current versions of our flowsheet now show a bismuth cleanup operation which removes nickel, tin, a variety of seminoble fission products, and zirconium at a rate comparable to a 200-day reactor cycle.

We have gained more detailed information on the distribution coefficients of the rare earths in the salt system presently considered for the MSBR. Europium will be separated from thorium only slightly, but the rest of the rare earths show separation factors over 1.5. Our calculations indicate that this is a useful separation factor if high flow rate ratios can be tolerated. We have yet to undertake contactor studies at high flow rate ratios. Our work on alternative processes for rare-earth separation is still an important part of the program.

The demonstration experiment to distill 48 liters of MSRE carrier salt is now ready to begin. The preparation and installation of this experiment were delayed from various causes, but the experiment can be performed while the reactor is operating and should establish the feasibility of this important tool in molten-salt technology.

21. Flowsheet Analysis

21.1 PROPOSED REDUCTIVE EXTRACTION PROCESSING FLOWSHEET FOR A SINGLE-FLUID MSBR

M. E. Whatley L. E. McNeese

The process flowsheet envisioned for a single-fluid MSBR is based on reductive extraction and processes the reactor salt volume through the protactinium isolation system on a 3-day cycle and through the rare-earth removal system on a 30-day cycle. The present version of the process flowsheet is shown in Fig. 21.1 and is scaled for a 1000 Mw (electrical) MSBR. The protactinium isolation system has been described earlier.[1] The rare-earth removal system will be described in more detail in a later section.

The protactinium isolation system exploits the fact that protactinium is intermediate in nobility between uranium and thorium. A molten-salt stream is withdrawn from the reactor on a 3-day cycle (2.5 gpm) and fed countercurrent to a 5.3-gpm liquid bismuth stream in a 12-stage contactor. If the reductant (thorium and lithium) flow in the bismuth stream entering the contactor is correct, the uranium in the salt will transfer to the downflowing bismuth stream in the lower part of the contactor. The protactinium, however, will concentrate midway up the cascade, where most of the protactinium in the reactor system can be held by diverting the salt through a suitably large volume (200 ft^3). At steady state the ^{233}Pa decays to ^{233}U at the same rate that it is brought into the tank from the reactor. Calculated concentration profiles in the extraction column are discussed in a later section. The concentrations of both protactinium and uranium in the salt leaving the column are negligible; however, the concentration of rare earths at this point is roughly the same as in the reactor. Approximately 10% (0.25 gpm) of the salt stream leaving the protactinium isolation column will be processed for removal of rare earths. The remaining salt passes through an electrolytic oxidizer-reducer where lithium and thorium are reduced into a flowing bismuth cathode to provide the metal stream fed to the column. At the anode of the cell, bismuth is oxidized to BiF_3, which will be soluble in the molten salt. The salt stream, containing BiF_3, is countercurrently contacted with the bismuth stream leaving the extraction column in order to oxidize uranium, protactinium, and other materials, which then transfer to the salt stream and return to the reactor.

The concentration of uranium or protactinium must be known at a point in the column in order to control the reductant concentration in the bismuth stream fed to the column. The uranium concentration is determined by fluorinating approximately 5% of the salt entering the protactinium decay tank and analyzing the resulting gas stream for UF_6. Means for collecting the UF_6 from this operation as well as from other fluorination operations and for returning this material to the fuel salt are provided. The UF_6 is simultaneously absorbed into the molten salt and reduced to UF_4 by a hydrogen sparge. A bismuth removal step will also be provided before salt returns to the reactor.

Approximately 1.5% (0.08 gpm) of the bismuth stream leaving the extraction column will be hydrofluorinated in the presence of a salt stream for removal of the seminoble metals (Ga, Ge, Cd, In, Sn, and Sb), corrosion products (Fe, Ni, and Cr), and fission product Zr. The salt is recycled between the hydrofluorinator and a fluorinator, where uranium is removed. The principal components which build up in this salt are ^7LiF and ZrF_4, and the expected steady-state composition is 47-53 mole % LiF-ZrF_4, which has a liquidus of 520°C.

Salt which is free of uranium and protactinium but which contains rare earths is fed to the center of a 24-stage extraction column at a rate of about 0.25 gpm, sufficient to process a reactor volume in 30 days. The salt flows countercurrent to a bismuth stream containing thorium and lithium. Typically, 60% of the rare earths are extracted from the salt stream in the upper

[1] L. E. McNeese and M. E. Whatley, *MSR Program Semiann. Progr. Rept. Feb. 28, 1968*, ORNL-4254, p. 248.

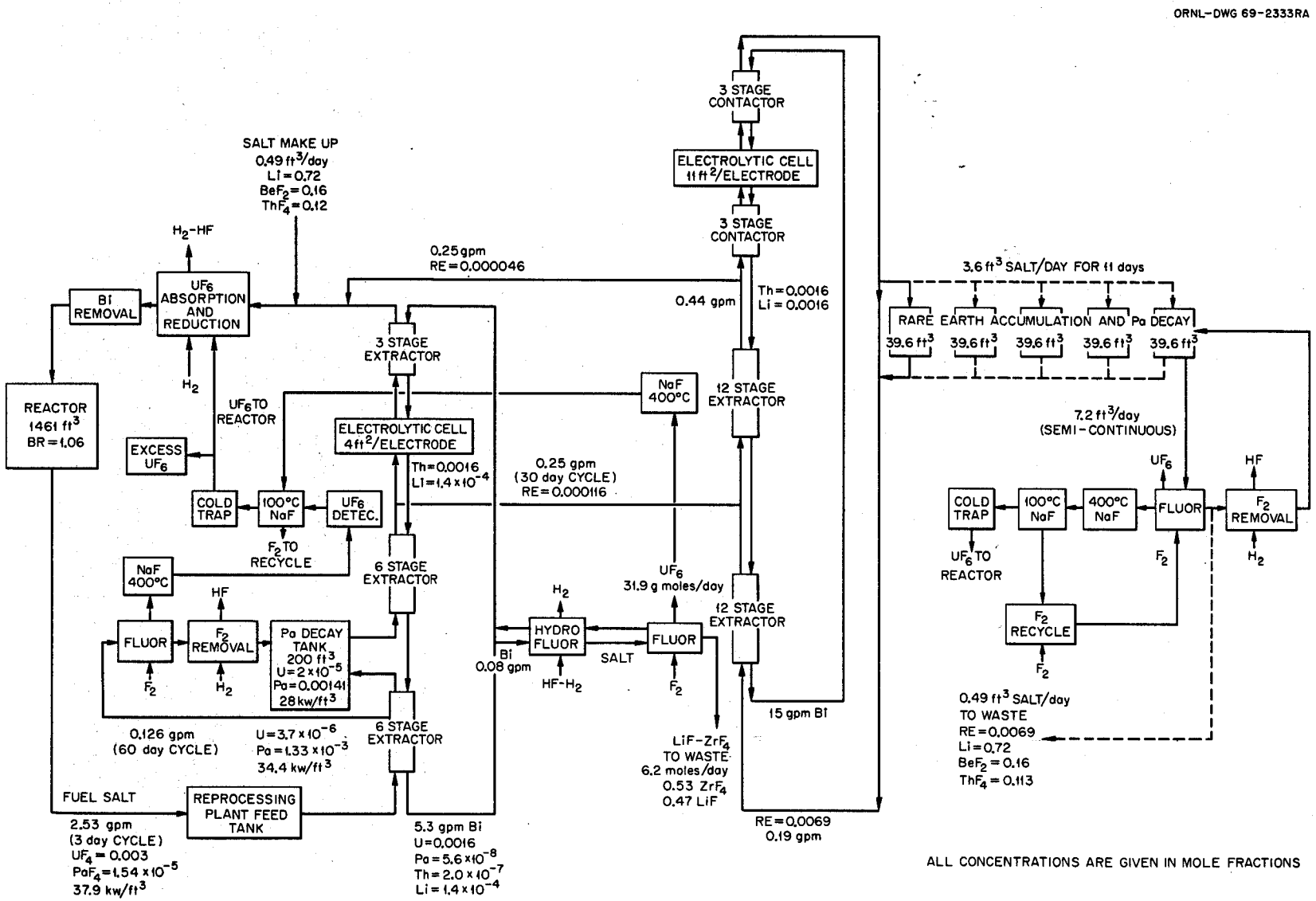

Fig. 21.1. Proposed Reductive Extraction Processing Flowsheet for a Single-Fluid MSBR. All concentrations are in mole fraction.

column (making the effective removal time 50 days), and the rare-earth concentration is increased to approximately 0.69 mole % in the lower column. The bismuth flow rate through the column is 15 gpm. Part of the salt leaving the column returns to the reactor, and the remaining salt is fed to the electrolytic cell complex, the net effect of which is to put thorium and lithium into bismuth and to turn the extracted rare earths around as reflux from the bismuth phase to the returning salt. Both anode and cathode are flowing streams of bismuth. A Bi-Li stream generated at the cathode of the cell is fed to the 3-stage contactor, which effectively removes the ThF_4 from the incoming salt. The salt then picks up BiF_3 as it passes the anode. The salt stream containing BiF_3 is passed countercurrent to the bismuth stream entering the complex from the rare-earth removal column to oxidize the rare earths, thorium, and lithium from the bismuth.

Salt containing rare earths at a concentration of 0.69 mole % is withdrawn from the system at a rate of 0.49 ft^3/day. The active-metal fission products (Sr, Cs, Ba, Rb, and Eu) are also present in the stream at a concentration equal to that in the reactor and are removed on a 3000-day cycle. Salt withdrawal is through a set of tanks used sequentially and each having a volume of about 40 ft^3. This limits the rate at which rare earths could inadvertently return to the reactor. This salt will be fluorinated for uranium recovery when necessary.

21.2 PROTACTINIUM REMOVAL FROM A SINGLE-FLUID MSBR

L. E. McNeese

A method for isolating protactinium from a single-fluid MSBR has been described earlier.[2] Steady-state concentration profiles in the isolation column at the optimum operating conditions have been recalculated using current data on reduction potentials and thorium solubility. For the calculations, assumed values were: a fuel salt composition of 71.7-16-12-0.3 mole % LiF-BeF_2-ThF_4-UF_4, a reactor volume of 1461 ft^3, a processing rate of 2.5 gpm (three-day cycle), an operating temperature of 600°C, a reactor power of 1000 Mw (electrical), and a protactinium decay tank volume of 200 ft^3. The thorium and lithium concentrations in the bismuth stream fed to the column were 0.0016 and 1.4×10^{-4} mole fraction respectively.

A typical calculated profile is shown in Fig. 21.2. The uranium concentration in the salt decreases from the inlet value of 0.003 mole fraction to negligible values at the salt outlet. The concentration of protactinium in the salt increases from the inlet value of 1.39×10^{-5} mole fraction to a maximum of 0.002 mole fraction, after which it drops to negligible values near the salt outlet. The concentration of thorium in the bismuth stream drops from about 0.00132 mole fraction in the upper part of the column to 2×10^{-7} mole fraction near the bismuth outlet. The concentration of lithium in the bismuth decreases from about 0.00127 mole fraction in the upper part of the column to about 0.000142 mole fraction at the bottom of the column.

The concentrations of uranium and protactinium in the salt entering the decay tank are 3.69×10^{-6} and 1.326×10^{-3} mole fraction respectively. The concentrations of uranium and protactinium in the decay tank

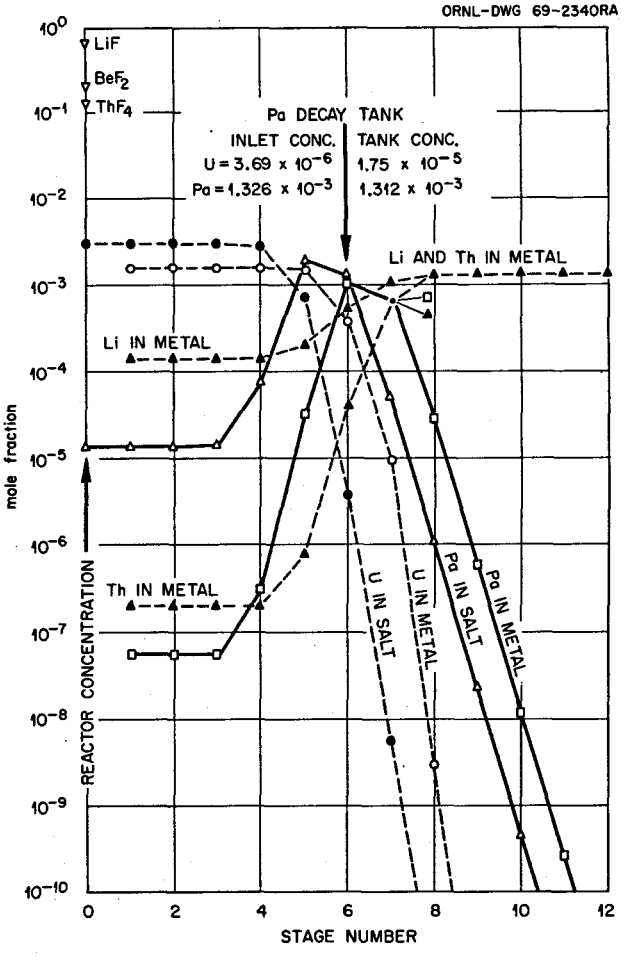

Fig. 21.2. Calculated Concentration Profiles in Protactinium Isolation Column.

[2]L. E. McNeese and M. E. Whatley, *MSR Program Semiann. Progr. Rept. Feb. 28, 1968*, ORNL-4254, p. 248.

are 1.75×10^{-5} and 1.312×10^{-3} mole fraction respectively. Under ideal steady-state operating conditions, approximately 93% of the protactinium present in the reactor system would be held in the decay tank. It is likely that the actual amount of protactinium isolated from the reactor will be somewhat below this value, however, because of inability to maintain optimum operating conditions.

21.3 REMOVAL OF RARE EARTHS FROM A SINGLE-FLUID MSBR

L. E. McNeese

The rare-earth fission products are among the more important neutron absorbers in an MSBR, and operation of this system requires removal of these materials on a cycle of approximately 50 days. Removal of rare earths from a single-fluid MSBR is complicated by the need for separating the rare earths from thorium, which is a major component of the salt.

The proposed method for rare-earth removal is based on differences in the extent to which the rare earths and thorium distribute between molten salt and liquid bismuth containing a reductant. The removal system is shown in its simplest form in Fig. 21.3. A molten-salt stream consisting of fluorides of lithium, beryllium, and thorium and which also contains rare-earth fluorides is fed to the center of an extraction column. The salt flows countercurrent to a stream of liquid bismuth containing thorium and lithium. In the upper part of the column, a large fraction of the rare earths is reduced and transfers to the downflowing metal stream. Below the feed point, the concentration of rare earths is increased in the salt and metal streams in order to produce a concentration suitably high for disposal.

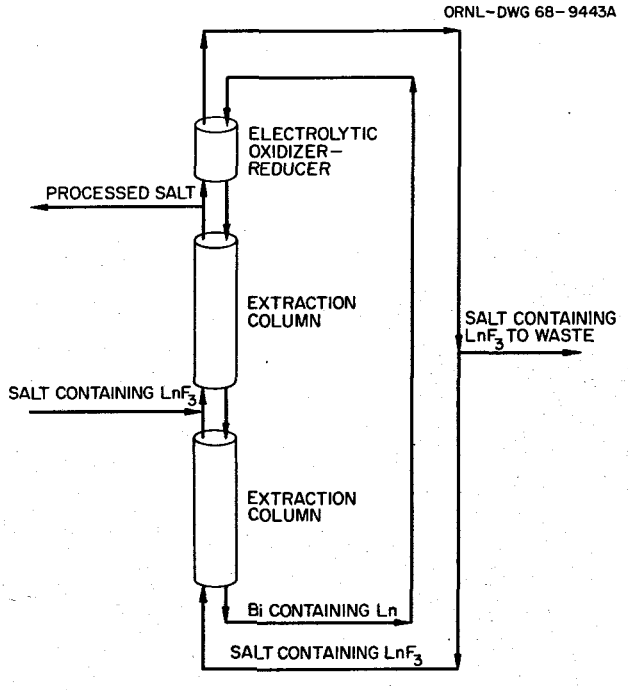

Fig. 21.3. Rare-Earth Removal from a Single-Fluid Reactor by Reductive Extraction.

Molten salt leaving the top of the column contains rare earths at a low concentration. Part of this salt is returned to the reactor, and the rest is sent to an electrolytic cell complex, the net effect of which is to put thorium and lithium into bismuth for use as extractant and to return the extracted rare earths, entering the complex with bismuth from the bottom of the cascade, to the cascade as reflux, oxidizing them out of the bismuth and moving them to the returning salt stream. The complex consists of an electrolysis cell with contactors above and below it. Both the anode and the cathode of the cell are pools of flowing bismuth, and the electrolyte is salt containing neither larger amounts of rare earths nor thorium. The cathode puts lithium into the bismuth stream which flows into the lower contactor, extracting essentially all (about 99%) of the thorium out of the entering salt. The anode puts BiF_3 into the salt which flows into the upper contactor and oxidizes essentially all of the rare earths out of the entering bismuth.

Rare-earth removal efficiencies were calculated for a range of operating conditions to establish the importance of number of stages, separation factor, metal-to-salt flow ratio, rare-earth concentration in the discard stream, location of the feed point, and the fraction of ThF_4 which is reduced in the electrolytic cell. Assumed operating conditions included a reactor volume of 1461 ft^3, a salt processing rate of 0.25 gpm (30-day cycle), an operating temperature of 600°C, and a reactor power of 1000 Mw (electrical). The thorium and lithium concentrations in the bismuth stream fed to the extraction column were both 0.0016 mole fraction.

It was found that the optimum feed location was at the center of the column for most operating conditions, and all results to be presented are based on this feed location. System performance is shown in Fig. 21.4 for a 24-stage column for a range of metal-to-salt flow ratios and for rare-earth–thorium separation factors which range from 1.2 to 6. The fraction of the ThF_4 which is reduced in the electrolytic cell is 99%. It should be noted that for the assumed operating conditions the metal-to-salt flow ratio in the lower part of the column is only dependent on the fraction of ThF_4 reduced and is 85.4 for the present case. For the assumed operating conditions, a bismuth flow rate of

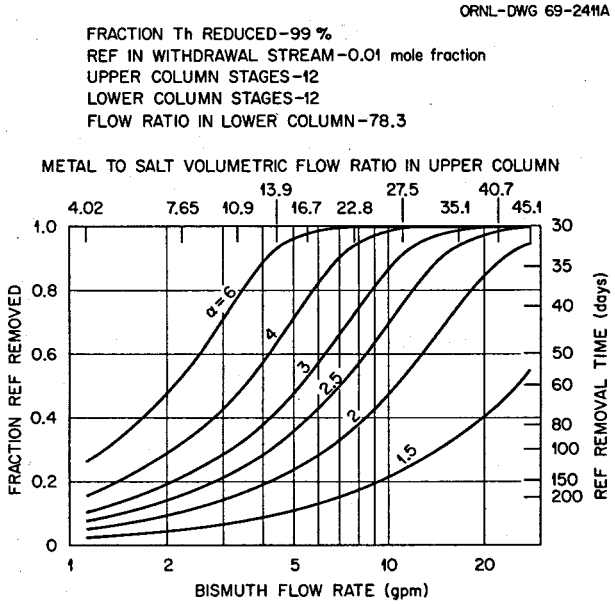

Fig. 21.4. Metal-to-Salt Volumetric Flow Ratio in Upper Column.

15 gpm will result in a rare-earth removal efficiency of 69% (44-day removal time) for a separation factor of 2 and a removal efficiency of 31% (95-day removal time) for a separation factor of 1.5. The metal-to-salt flow ratio in the upper column is about 34 for this bismuth flow rate.

System performance is shown in Fig. 21.5 for the same operating conditions except that a 12-stage extraction column is used. A bismuth flow rate of about 23 gpm is required for roughly the same removal efficiency for a separation factor of 2.

The effect of fraction of ThF_4 reduced in the electrolytic cell is shown in Fig. 21.6 for a separation factor of 2 with a 24-stage column and a rare-earth concentration in the withdrawal stream of 0.0069 mole fraction. It should be noted that this parameter is equal if not greater in importance than the other parameters considered. A significant decrease in removal efficiency results from the fraction of ThF_4 reduced being decreased from 99 to 90%, and the system becomes ineffective if less than 50% of the ThF_4 is reduced. There is essentially no effect of the rare-earth concentration in the withdrawal stream on removal efficiency in the range of interest.

The separation factors for several of the rare earths have been determined for bismuth saturated with thorium in contact with 72-16-12 mole % LiF-BeF_2-ThF_4. The separation factors[3] are 1.3 for Eu, 1.7 for Pm, 1.8 for La, 2.0 for Sm, 3.0 for Nd, and 3.5 for Ce. The removal times for these materials at the reference conditions (24 total stages and 15 gpm Bi) are given in Table 21.1. The removal times range from about 225 days for europium to approximately 30 days for neodymium and cerium and are considered adequate. The rare earth which will set the operating conditions for the removal system is promethium (which has a separation factor of 1.7), since it is one of the more important rare earths. Lanthanum is less important, and the resulting removal time (~100 days) is satisfactory. The removal times for rare earths having separation factors greater than 2, such as neodymium and cerium, will be shorter than required.

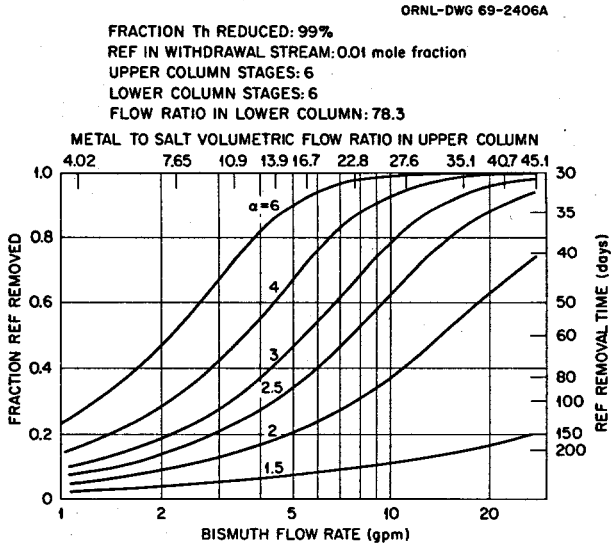

Fig. 21.5. Metal-to-Salt Volumetric Flow Ratio in Upper Column.

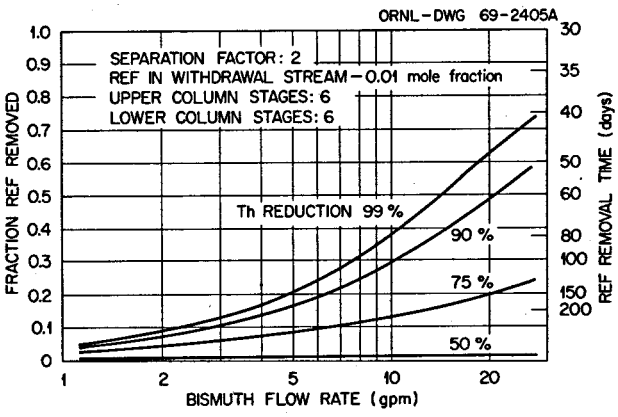

Fig. 21.6. Rare-Earth Removal System Performance as a Function of Bismuth Phase Flow Rate and the Thorium Removal in the Electrolytic Cell Complex.

[3]Fig. 21.6, this report.

Table 21.1. Removal Times for Various Rare Earths at Reference Conditions[a]

Rare Earth	Separation Factor	Removal Time (days)
Pm	1.7	63.8
Nd	3.0	30.6
Sm	2.0	43.5
La	1.8	47.7
Eu	1.3	222.0
Ce	3.5	30.3

[a]Reference conditions include a total of 24 stages and a bismuth flow rate of 15 gpm.

21.4 MATERIAL BALANCE CALCULATIONS

M. J. Bell L. E. McNeese

A computer code has been developed to perform steady-state material balance calculations which describe in detail the nuclear, chemical, and physical processes taking place in the fuel stream of an MSBR. Such calculations are necessary to determine fission product inventories and heat generation rates, to specify flow rates of streams in the chemical processing plant, and to investigate the effects of changes in chemical processing on the nuclear performance of the MSBR. The code also takes into account the buildup of transuranium isotopes, the production of activation products by neutron capture in the carrier salt, and chain branching in the fission product decay schemes not included in earlier investigations.[4]

21.4.1 MSBR Nuclear Data Compilation

In order to perform these calculations, a library of nuclear data for MSBR applications has been compiled. This library contains half-lives and radioactive decay schemes, three-group neutron capture cross sections, and beta and gross gamma disintegration energies for 687 nuclides. Of these, 178 are isotopes of elements which comprise the carrier salt, graphite, and structural materials and their activation products, 461 are fission products and their daughters, and 48 are isotopes of the actinide elements and their daughters. The radioactive decay schemes include beta and positron emission to isomeric states and ground states of daughter nuclides, alpha emission, and isomeric transition. These decay schemes are based primarily on the compilation of Lederer *et al.*[5] The three-group cross-section library consists of a thermal cross section, a resonance integral, and a fast cross section which was generated by averaging a cross section over an MSR spectrum given by Prince for $E > 1$ Mev.[6,7] Where possible, the thermal cross sections and resonance integrals have been corrected for non-$1/v$ behavior, also using the data of Prince.[6,7] In addition to total neutron absorption cross section, the library also contains, for each group, the fraction of neutron captures which lead to fission and n-γ, n-α, n-p, and n-$2n$ reactions. These data are based primarily on the compilations of Stehn *et al.*[8] and Drake.[9] The fission product library includes a compilation of direct fission yields from five fissile species, ^{233}U, ^{235}U, ^{238}U, ^{232}Th, and ^{239}Pu, based on the data of Katcoff.[10] The beta plus gamma disintegration energies were calculated using the computer code SPECTRA written by E. D. Arnold to compute the average energy of a beta particle by integration of the Fermi beta-ray spectrum taking into account changes in spin and parity.[11] A computer code has been written which reads the data in this nuclear library from cards and prepares an array of transition coefficients to be used in the material balance calculations to be described below.

21.4.2 MSBR Material Balance Calculations

For many purposes it is adequate to consider the recirculating fuel salt in a proposed MSBR to be a well-mixed fluid at steady state in which the average concentration of a nuclide i is given by the equation

$$0 = FN_{i0} + V\sum_j e_{ij}\lambda_j N_j + \phi V_c \sum_k f_{ik}\sigma_k N_k + \phi V_c \sum_m y_{im}\sigma_{fm}N_m - (\lambda_i V + \sigma_i \phi V_c + F + P_i)N_i . \quad (1)$$

[4]J. S. Watson, L. E. NcNeese, and W. L. Carter, *MSR Program Semiann. Progr. Rept. Aug. 31, 1967*, ORNL-4191.

[5]C. M. Lederer, J. M. Hollander, and I. Perlman, *Table of Isotopes*, 6th ed., Wiley, New York, 1967.

[6]B. E. Prince, *MSR Program Semiann. Progr. Rept. Feb. 28, 1967*, ORNL-4119, pp. 79–83.

[7]B. E. Prince, *MSR Program Semiann. Progr. Rept. Aug. 31, 1967*, ORNL-4191, pp. 50–58.

[8]J. R. Stehn *et al.*, BNL-325, 2d ed., Suppl. No. 2, vols. I–III (1964).

[9]M. K. Drake, *Nucleonics* 24, 108 (1966).

[10]S. Katcoff, *Nucleonics* 18, 163 (1960).

[11]E. D. Arnold, *Handbook of Shielding Requirements*, ORNL-3576, pp. 21 ff. (1964).

where

N_i = concentration of species i, atoms/cc,

N_{i0} = feed concentration of species i, atoms/cc,

F = volumetric flow rate of fuel salt, cc/sec,

V = fuel salt volume, cc,

V_c = reactor core volume, cc,

ϕ = volume- and energy-averaged neutron flux, barns^{-1} sec^{-1},

λ_i = radioactive disintegration constant of species i, sec^{-1},

σ_i = total spectrum-averaged neutron cross section, barns,

σ_{fi} = fission cross section of species i, barns,

e_{ij} = fraction of disintegrations by species j which lead to formation of species i,

f_{ik} = fraction of neutron captures by species k which lead to formation of species i,

y_{im} = fission yield of species i from fission of species m,

P_i = effective chemical processing rate for species i, cc/sec.

This equation is a generalization of that given in ref. 1 and is a statement of the fact that at steady state the rate of input of species i into the system by direct feed, radioactive decay of precursors, neutron capture, and fission must equal the rate of loss of species i by radioactive decay, neutron capture, flow out of the system, and chemical processing. In addition to the terms given in Eq. (1) the code also provides for loss of isotopes of xenon and krypton by diffusion into the graphite moderator followed by neutron capture or radioactive decay, and production of isotopes of xenon and krypton in the fuel salt by migration of gaseous neutron capture products out of the graphite, using a model developed by Kedl and Houtzeel.[12] Provision is also made in the code for migration of noble gases and noble metals to recirculating bubbles in the fuel salt.[13] The bubbles are treated as a separate well-mixed region of fixed residence time in which radioactive decay may take place. Daughters which are not themselves noble gases or noble metals are assumed to return to the fuel salt.

The volume-averaged thermal flux and the ratio of the resonance flux per unit lethargy to the thermal flux, which are required to compute the spectrum-average cross sections for use in Eq. (1), are obtained from the output of the ROD reactor design code for a given reactor configuration and fuel processing scheme.[14] The ROD code is a multiregion, six-group neutron diffusion code used for the primary design and evaluation calculations for the MSBR. For these conditions Eq. (1) is a coupled system of N linear algebraic equations in N unknowns of the form

$$0 = \sum_{k=1}^{N} a_{ik}X_k + b_i, i = 1, 2, \ldots, N. \qquad (2)$$

The steady-state code which has been developed to solve the system of equations (2) employs the Gauss-Seidel interaction technique, a well-known numerical method which can be shown to converge provided the coefficients a_{ik} fulfill certain restrictions.[15]

The code requires as input the fuel salt volume, core volume, graphite volume, removal times of the elements by chemical processing, and solubility and mass transfer coefficients for migration of the noble gases to the graphite in addition to the nuclear library and the three-group weighting factors for the reactor spectrum described above. The code gives as output the composition of the fuel stream in gram-moles per cubic centimeter and mole fraction of each isotope, the neutron poisoning, and the beta and gamma specific power for each nuclide in watts per cubic centimeter. The code also gives the flow rates, in grams per day, the compositions, and the power of the various streams of fission products leaving the primary fuel-salt loop.

A synthesis of this material balance code with a version of the ROD reactor design code has been developed in order that calculations can be performed for a given reactor configuration over a range of processing conditions. This combined code uses ROD to determine the absorption rates in thorium and uranium for an assumed lumped fission product poisoning. The converged absorption rates for the actinide elements from ROD are then used by the material balance code, which computes inventories and poisoning for the individual fission product nuclides and calculates a new lumped fission product poisoning which is then used by ROD. This process is repeated until the lumped fission

[12] R. J. Kedl and A. Houtzeel, *Development of a Model for Computing ^{135}Xe Migration in the MSRE*, ORNL-4069 (1967).

[13] F. N. Peebles, *Removal of ^{135}Xe from Circulating Fuel Salt of the MSBR by Mass Transfer to He Bubbles*, ORNL-TM-2245 (1968).

[14] O. L. Smith, W. R. Cobb, and H. T. Kerr, *MSR Program Semiann. Progr. Rept. Aug. 31, 1968*, ORNL-4344, p. 68.

[15] L. Lapidus, *Digital Computation for Chemical Engineers*, McGraw-Hill, New York, 1967.

product poisoning calculated by the two codes is satisfactorily close, at which point all concentrations, absorption rates, etc., are known for the assumed operating conditions.

21.4.3 MSBR Processing Plant Design Calculations

Calculations were made for a 2250-Mw (thermal) single-fluid reactor containing 1460 ft^3 of fuel salt of approximate composition 71.7-16-12-0.3 mole % LiF-BeF_2-ThF_4-UF_4. The gases xenon, krypton, and tritium have low solubilities in the fuel salt and can be removed by sparging the salt with helium.[13,16] The noble metals (As, Se, Nb, Mo, Tc, Ru, Rh, Pd, Ag, and Te) do not form fluorides in the salt environment but appear in the gas space of the fuel pump bowl and plate out on the graphite and vessel walls as free metals.[17] A 50-sec residence time in the fuel salt was assumed for the noble gases and noble metals as they migrated to the helium bubbles. It was assumed that these materials circulate in the gas space, which was treated as a well-mixed volume which was stripped on a 110-sec cycle. Plating out of the noble metals on surfaces was not treated as a separate removal mechanism; that is, all noble metals removed from the fuel salt were assumed to be present in the stream resulting from stripping the gas space on a 110-sec cycle. A 200-day removal time was assumed for zirconium and the seminoble metals (Ga, Ge, Cd, In, Sn, and Sb).

The rare-earth fission products with the exception of europium were removed on a 50-day cycle; europium was removed on a 225-day cycle. The active metals (Rb, Cs, Sr, and Ba) were removed by salt discard on a 3000-day cycle. The halogens (I and Br) will be removed from the salt during fluorination on a 50-day cycle.

Table 21.2 gives the processing cycle times, flow rates, and heat generation rates of the principal groups of fission products being withdrawn from the primary-salt loop of the MSBR. It is seen that these streams contain about 1.5% of the reactor power and that 90% of this power is generated in the noble gas and noble metal streams. Table 21.3 gives the chemical composition of these streams of fission products, and the most important fission product poisons are listed in Table 21.4. Studies are now being performed which will give additional information on the effect of chemical processing rates on the nuclear performance of the MSBR.

[16] R. J. Kedl, *MSR Program Semiann. Progr. Rept. Aug. 31, 1968*, ORNL-4344, pp. 72–75.

[17] S. S. Kirslis and F. F. Blankenship, *MSR Program Semiann. Progr. Rept. Aug. 31, 1968*, ORNL-4344, pp. 115–42.

Table 21.2. Processing Cycle Times, Flow Rates, and Power of Fission Product Streams in a 2250 Mw (Thermal) MSBR

Chemical Group	Processing Cycle Time[a]	Flow Rate		Power (Mw)
		Grams per Day	Moles per Day	
Noble gases	50 sec[b]	496.3	4.337	11.37
Noble metals	50 sec[b]	685.4	6.173	16.03
Halogens	50 days	1.9	0.016	0.02
Rare earths	50 days	718.6	5.245	1.29
Zirconium and seminoble metals	200 days	299.5	3.193	0.43
Active metals	3000 days	79.9	0.740	0.94
Total		2281.6	19.70	30.08

[a] The removal times of all elements except europium are assumed to be equal to the processing time for their chemical group. Europium is removed from the fuel salt on a 225-day cycle.

[b] In addition to a 50-sec residence time in the salt, the noble gases and noble metals are assumed to circulate in helium bubbles with 110 sec residence time.

Table 21.3. Chemical Composition of MSBR Processing Streams

Noble Gases		Noble Metals		Halogens	
Element	Mole Fraction	Element	Mole Fraction	Element	Mole Fraction
Xe	0.556	Te	0.391	I	0.764
Kr	0.443	Nb	0.317	Br	0.236
T	0.001	Mo	0.174		
		Others	0.118		
Rare Earths		**Zirconium and Seminoble Metals**		**Active Metals**	
Element	Mole Fraction	Element	Mole Fraction	Element	Mole Fraction
Ce	0.382	Zr	0.986	Sr	0.603
Nd	0.250	Sn	0.008	Cs	0.242
Y	0.111	Sb	0.005	Ba	0.141
La	0.103	Others	0.001	Rb	0.014
Pr	0.094				
Others	0.060				

Table 21.4. Fission Product Poisons in a 2250 Mw (Thermal) Single-Fluid MSBR

Nuclide	Poisoning (absorptions per fissile absorption)	Concentration (mole fraction)
	$\times 10^{-2}$	$\times 10^{-6}$
^{149}Sm	0.631	0.15
$^{135}Xe^{a}$	0.500	9.0×10^{-5}
^{143}Nd	0.160	9.1
^{147}Pm	0.150	3.0
^{151}Sm	0.146	0.43
^{153}Eu	0.044	1.2
^{90}Sr	0.044	608.0
^{155}Eu	0.039	0.050
^{152}Sm	0.037	0.81
^{145}Nd	0.035	8.0
^{143}Pr	0.025	3.8
^{148}Pm	0.025	0.038
^{93}Zr	0.024	64.0
^{154}Eu	0.022	0.26
^{137}Ba	0.013	46.0
^{150}Sm	0.013	1.6
^{148m}Pm	0.012	6.6×10^{-3}
^{141}Ce	0.011	7.2
^{149}Pm	0.010	0.11
^{139}La	0.006	12.0

[a] A ^{135}Xe poison fraction of 0.005 is a fixed design value.

22. Measurement of Distribution Coefficients in Molten-Salt–Metal Systems

L. M. Ferris

During this reporting period, chemical development of the reductive extraction method[1-3] for the processing of single-fluid MSBR fuels was continued. The experimental work consisted mainly in the measurement of the equilibrium distribution of uranium, zirconium, protactinium, plutonium, and rare earths between LiF-BeF_2-ThF_4 solutions and liquid bismuth solutions; the effect of nickel on the solubility of thorium in bismuth was also studied. The distribution coefficients,

$$D_M = \frac{\text{mole fraction of component } M \text{ in the metal phase}}{\text{mole fraction of component } M \text{ in the salt phase}},$$

at a given temperature can be expressed as

$$\log D_M = n \log C_{Li} + \log I ;$$

C_{Li} is the lithium concentration in the metal phase (at. %), I is a constant, and n is the valence of the species in the salt phase. This expression comes directly from the thermodynamic treatment[4] of the equilibria involved in the two-phase systems. The ease with which two components can be separated is indicated by the separation factor $\alpha_{AB} = D_A/D_B$. The higher the separation factor, the easier the separation.

In addition to the main effort on the reductive extraction process, preliminary results were obtained on a metal-transfer method for the separation of rare earths from thorium. If successful, this technique would provide an alternative to the reductive extraction method.

22.1 EXTRACTION OF URANIUM, ZIRCONIUM, PROTACTINIUM, AND PLUTONIUM FROM SINGLE-FLUID MSBR FUELS

J. C. Mailen F. J. Smith
J. F. Land

The equilibrium distribution of uranium, zirconium, protactinium, and plutonium between several typical LiF-BeF_2-ThF_4 single-fluid MSBR fuel salts and liquid bismuth solutions has been measured. The behavior of these elements is of primary interest in the protactinium isolation portion of the reference reductive extraction flowsheet.[3] Prior studies[2,3] utilizing LiF-BeF_2-ThF_4 (69.2-19.4-11.4 mole %) as the salt phase established that the extractability of protactinium was between that of uranium and thorium and that the respective separation factors were high enough to allow isolation of the protactinium. Extraction of zirconium (a major fission product) from LiF-BeF_2-ThF_4 salts has received little, if any, attention. Preliminary work[5] with LiF-BeF_2 (66-34 mole %) indicated that zirconium would behave like a rare-earth fission product. Data obtained in the present study using LiF-BeF_2-ThF_4 (72-16-12 mole %) show that this is not the case. The possibility of using plutonium as a fuel in an MSBR (particularly during startup) has often been considered;[6] consequently its behavior in a reductive extraction process required study.

All experiments involving zirconium, and some of those with uranium, were conducted in mild steel

[1] L. E. McNeese and M. E. Whatley, *MSR Program Semiann. Progr. Rept. Feb. 29, 1968*, ORNL-4254, p. 248.

[2] L. M. Ferris, *MSR Program Semiann. Progr. Rept. Aug. 31, 1968*, ORNL-4344, p. 292.

[3] D. E. Ferguson, *Chem. Technol. Div. Ann. Progr. Rept. May 31, 1968*, ORNL-4272, p. 14.

[4] J. H. Shaffer *et al.*, *Reactor Chem. Div. Ann. Progr. Rept. Dec. 31, 1966*, ORNL-4076, p. 34.

[5] D. M. Moulton *et al.*, *Reactor Chem. Div. Ann. Progr. Rept. Dec. 31, 1967*, ORNL-4229, p. 41.

[6] R. E. Thoma, *Chemical Feasibility of Fueling Molten Salt Reactors with PuF_3*, ORNL-TM-2256 (June 20, 1968).

apparatus using the procedure described previously.[2,3] The other experiments were conducted in a system in which the components that contacted the salt and bismuth (crucible, sparge tube, thermowell) were all fabricated of molybdenum. Use of molybdenum allowed simultaneous HF-H_2 treatment of the salt and bismuth, making it possible to conduct several experiments in sequence in the same apparatus using only one initial charge of protactinium. In a typical experiment, 100 to 150 g of salt and about 200 g of bismuth were loaded into the molybdenum crucible. A few milligrams of ^{231}Pa contained in hydrofluoric acid solution was evaporated onto about 1 g of LiF and added to the system along with any uranium or plutonium desired. In several experiments in which uranium was present, the ^{233}U isotope was used to facilitate accurate analysis. The salt and bismuth were sparged first with 50% HF–50% H_2 for about 24 hr to remove oxide impurities and then for 3 to 4 hr with pure hydrogen to reduce noble-metal fluorides (Ni, Bi, Mo, etc.). The two phases were then sparged with purified argon to remove all residual hydrogen. Extraction of the various components (U, Pa, Pu, etc.) from the salt into the bismuth was effected by the incremental addition of crystal-bar thorium to the system. The first piece of thorium added usually had been irradiated to contain about 1 mc of ^{233}Pa; the presence of the ^{233}Pa tracer in the system allowed immediate gamma counting of the samples, giving a rapid indication of the progress of the experiment. Filtered samples of each phase were taken at least 4 hr after each addition of thorium. Analyses of these samples provided the data necessary for the calculation of the distribution coefficients. In each experiment the system was equilibrated under an argon atmosphere. The argon was purified by passage through two traps filled with uranium turnings; the first trap was held at about 625°C and the second at 200 to 300°C.

In most of the previous studies[2,3,5,7] the valence of the uranium species in the salt phase during extraction was taken to be 4. Thermodynamic considerations[8,9] using data for LiF-BeF_2 systems indicate that at 600°C the valence of the uranium should be very close to 3 when the lithium concentration in the bismuth phase is greater than about 2 wt ppm (0.006 at. %). The results of our recent experiments using refined analytical methods show that this is generally true for uranium in LiF-BeF_2-ThF_4 solutions at 600°C. This is illustrated by the plot of log D_U vs log D_{Li} shown in Fig. 22.1; these data were obtained in two separate experiments at 600°C using LiF-BeF_2-ThF_4 (72-16-12 mole %). The line has a slope of 3. Similar data were obtained in experiments with other salt compositions. Further evidence for the trivalency of uranium in the salt phase is provided by plots of log D_U vs either log D_{Zr} or log D_{Pa}. Uranium and zirconium data from two experiments at 600°C using LiF-BeF_2-ThF_4 (72-16-12 mole %) are shown in Fig. 22.2. The slope of this plot of log D_{Zr} vs log D_U is 1.33, as would be expected if the uranium existed as a trivalent species in the salt. More

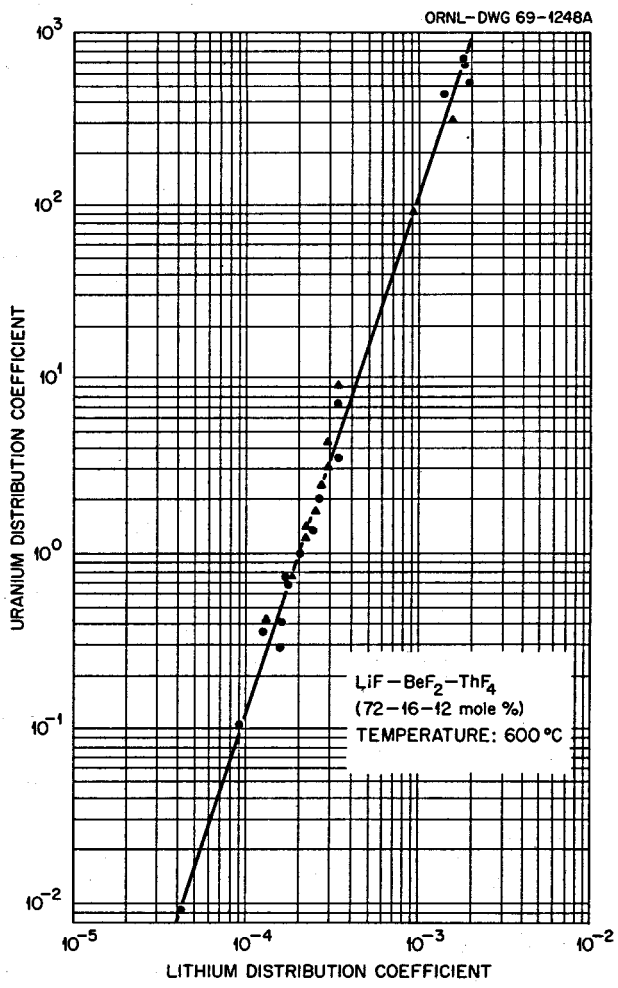

Fig. 22.1. Equilibrium Distribution of Uranium Between LiF-BeF_2-ThF_4 (72-16-12 Mole %) and Bismuth Solutions at 600°C.

[7] D. M. Moulton, W. R. Grimes, and J. H. Shaffer, *MSR Program Semiann. Progr. Rept. Feb. 29, 1968,* ORNL-4254, p. 152.

[8] L. M. Ferris, *Some Aspects of the Thermodynamics of the Extraction of Uranium, Thorium, and Rare Earths from Molten LiF-BeF_2 into Liquid Li-Bi Solutions,* ORNL-TM-2486 (in press).

[9] C. F. Baes, Jr., "The Chemistry and Thermodynamics of Molten Salt Reactor Fluoride Solutions," in *Thermodynamics,* vol. II, p. 409, IAEA, Vienna, 1966.

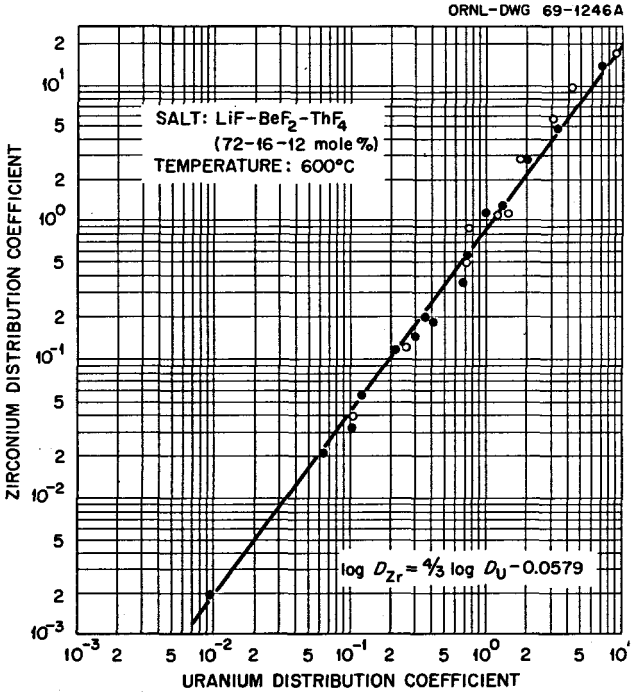

Fig. 22.2. Equilibrium Distribution of Uranium and Zirconium Between LiF-BeF_2-ThF_4 (72-16-12 Mole %) and Bismuth Solutions at 600°C.

importantly, these data show that uranium and zirconium will behave almost identically in the proposed reductive extraction process. Undoubtedly, special provision will have to be made to remove zirconium from the system at one point in the process.

The results of previous studies[2] indicated that protactinium existed as a tetravalent species in the salt phase in a reductive extraction system. Additional experimentation has verified this conclusion. This is illustrated by the plots of log D_{Pa} vs log D_U and log D_{Th} shown in Fig. 22.3. These data were obtained with LiF-BeF_2-ThF_4 (72-16-12 mole %) at 600°C. The slope of the Pa-Th line is 1, as expected from two tetravalent species; the slope of the Pa-U plot is 1.33, which is consistent with the presence of tetravalent protactinium and trivalent uranium in the salt phase. Plutonium was expected to be trivalent in these systems. This expectation was confirmed, as illustrated by the plots of log D_{Pa} and log D_{Th} vs log D_{Pu} shown in Fig. 22.4; the slope of each line is 1.33.

Most of the distribution coefficient data obtained so far for uranium, protactinium, zirconium, plutonium, and thorium are compiled in Table 21.1 in the equation form: $\log D = n \log C_{Li} + \log I$. The data were not analyzed statistically; the equations were obtained by visually fitting what appeared to be the best line through the experimental data. Close inspection of these equations reveals that the distribution coefficients vary as the composition of the salt is changed. The difference in Pa-Th behavior is most noticeable; for example, with the salts containing about 12 mole % ThF_4, the Pa-Th separation factor increased from about 2100 to 4400 as the "free fluoride" equivalence[2] of the salt increased from −4 to +13 (see also Fig. 22.6; Sect. 22.3). "Free fluoride" equivalence (FF) is defined by

$$FF = LiF\ (\text{mole \%}) - 2BeF_2\ (\text{mole \%}) - 3ThF_4\ (\text{mole \%}) .$$

The fact that the Pa-Th separation factors obtained with LiF-BeF_2 (66-34 mole %) and LiF-ThF_4 (73-27 mole %) do not correlate with those obtained with salts containing about 12 mole % ThF_4 emphasizes that the "free fluoride" model is far from ideal. The U-Pu separation factor was about 10 in the two systems in which plutonium was present. Both the U-Pa and Pu-Pa separation factors are variable since the valences of the

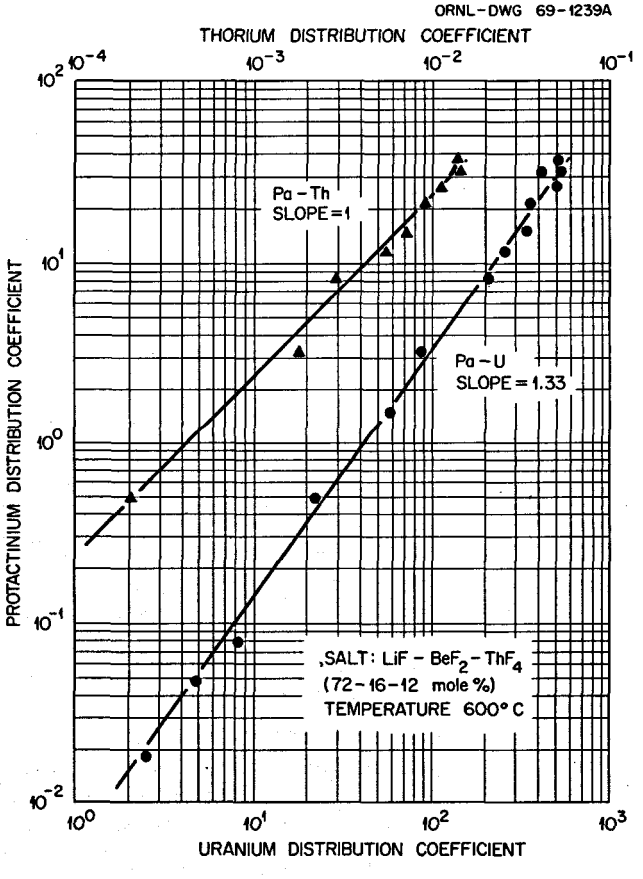

Fig. 22.3. Equilibrium Distribution of Protactinium, Thorium, and Uranium between LiF-BeF_2-ThF_4 (72-16-12 Mole %) and Bismuth Solutions at 600°C.

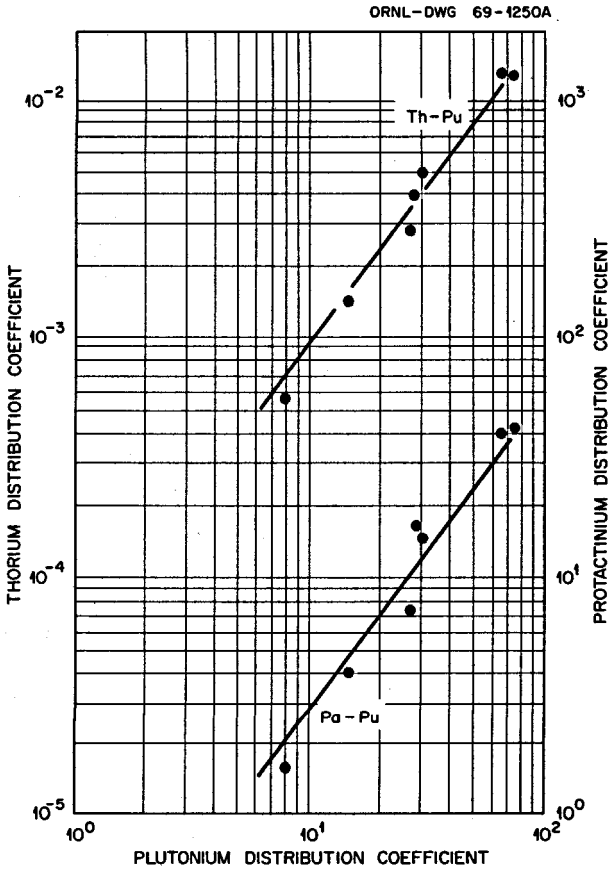

Fig. 22.4. Equilibrium Distribution of Thorium, Protactinium, and Plutonium Between LiF-BeF_2-ThF_4 (72-16-12 Mole %) and Bismuth Solutions at 600°C.

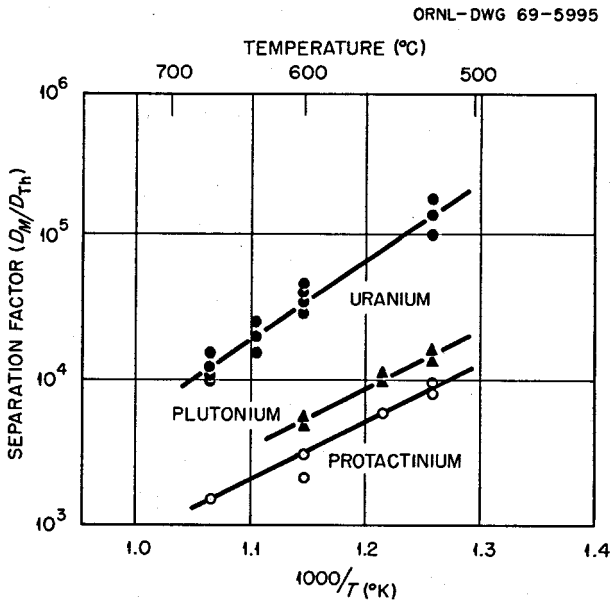

Fig. 22.5. Variation of Metal-Thorium Separation Factors with Temperature. Data obtained with LiF-$BeF_2$$ThF_4$ (72-16-12 mole %). Bismuth phase was saturated with thorium at each temperature.

species are different. When the bismuth phase was saturated with thorium (D_{Th} = 0.0145 for salts in which the ThF_4 concentration is 12 mole %), the U-Pa separation factor was about 15 to 20 regardless of the salt composition. These data show that, for MSBR fuel salts containing about 12 mole % ThF_4, separation of uranium from protactinium should be relatively easy, especially if the reductant concentration in the metal phase is kept low. The Pu-Pa separation is not so easy, but separation factors greater than 10 can probably be achieved by maintaining a very low reductant concentration in the metal phase.

In several experiments, distribution coefficients for the various components were determined as a function of temperature under conditions where the metal phase was saturated with thorium. The effect of temperature on the metal-thorium separation factors obtained with LiF-BeF_2-ThF_4 (72-16-12 mole %) is shown in Fig. 22.5. As seen, these separation factors increase regularly with decreasing temperature.

22.2 SOLUBILITY OF PROTACTINIUM IN BISMUTH

J. C. Mailen F. J. Smith

In the last semiannual report,[2] we gave preliminary results for an experiment (PE7) that was designed to demonstrate that protactinium was sufficiently soluble in bismuth solutions for the reductive extraction process to be practicable. Complete results are now available for this experiment and are presented in Table 22.2. During the present reporting period, we found that the original thorium analyses of the metal phase were in error and, because of the loss of the samples, could not be corrected. Also, distribution coefficients for protactinium and thorium were determined with LiF-BeF_2 (66-34 mole %), the same salt used in experiment PE7. The thorium concentrations in the metal phase given in Table 22.2 were calculated using the measured equilibrium data (Table 22.1; Sect. 22.1), the protactinium distribution coefficients obtained in experiment PE7, and the thorium analyses of the salt samples taken in experiment PE7. These corrected results show that one objective of experiment PE7, the demonstration of the mutual solubility of protactinium and thorium at the 1000-ppm level, was not met. Since thorium and lithium were present in amounts much less than originally thought, the reported number of 1200

Table 22.1. Equilibrium Distribution of Uranium, Protactinium, Plutonium, Thorium, and Zirconium Between LiF-BeF_2-ThF_4 Salts and Bismuth Solutions

Salt Composition (mole %)			"Free Fluoride" Equivalence	Temperature (°C)	Equilibrium Expression[a]	Pa-Th Separation Factor, D_{Pa}/D_{Th}
LiF	BeF_2	ThF_4				
69.2	19.4	11.4	−4	600	$\log_{10} D_{Th} = 4 \log_{10} C_{Li} + 2.077$	2100
					$\log D_{Pa} = 4 \log C_{Li} + 5.398$	
					$\log D_{U} = 3 \log C_{Li} + 5.817$	
					$\log D_{Pu} = 3 \log C_{Li} + 4.796$	
66.0	34.0	0	0	600	$\log D_{Th} = 4 \log C_{Li} + 2.453$	3700
					$\log D_{Pa} = 4 \log C_{Li} + 6.026$	
					$\log D_{U} = 3 \log C_{Li} + 5.971$	
72.0	16.0	12.0	4	600	$\log D_{Th} = 4 \log C_{Li} + 1.653$	3000
					$\log D_{Pa} = 4 \log C_{Li} + 5.144$	
					$\log D_{U} = 3 \log C_{Li} + 5.484$	
					$\log D_{Pu} = 3 \log C_{Li} + 4.518$	
					$\log D_{Zr} = 4 \log C_{Li} + 7.254$	
75.0	13.0	12.0	13	600	$\log D_{Th} = 4 \log C_{Li} + 1.152$	4400
					$\log D_{Pa} = 4 \log C_{Li} + 4.798$	
					$\log D_{U} = 3 \log C_{Li} + 5.231$	
73.0	0	27.0	−8	650	$\log D_{Th} = 4 \log C_{Li} + 0.849$	2360
					$\log D_{Pa} = 4 \log C_{Li} + 4.222$	
					$\log D_{U} = 3 \log C_{Li} + 4.655$ ($D_U > 1$)	

[a] C_{Li} is the lithium concentration in the metal phase in atom percent.

Table 22.2. Results of Experiment PE7, Demonstrating the High Solubility of Protactinium and Uranium in Bismuth

Sample	Temperature (°C)	Total Time (days)	Concentration in Metal Phase (wt ppm)		
			Pa	Th[a]	U
1[b]	600	0.16	1124		
2	600	3.0	1874		
3	600	5.0	2078	60	
4	650	5.1	2078	60	
5	560	6.0	2078		
6	500	7.0	1199	40	
7	550	7.3	2059	60	
8[c]	600	9.0	668	17	1090

[a] These thorium concentrations were calculated from the measured protactinium distribution coefficient and the Pa-Th separation factor determined in a separate experiment with LiF-BeF_2 (66-34 mole %) (Table 21.1, Sect. 21.1).

[b] A small amount of thorium was added to the metal phase after this sample was taken.

[c] A small amount of UF_4 was added before this sample was taken.

ppm is probably very close to the true solubility of protactinium in bismuth at 500°C. Furthermore, the original conclusion that the solubility of protactinium in bismuth is high enough for process application is still valid.

Toward the end of experiment PE7, sufficient UF_4 was added to the system to effect oxidation of some of the protactinium from the metal phase. Under the equilibrium condition established, the metal phase contained about 668 ppm Pa and 1090 ppm U, with corresponding uranium and protactinium material balances of nearly 100%. Thus the mutual solubility of uranium and protactinium in bismuth appears to be high.

22.3 EXTRACTION OF THORIUM AND RARE EARTHS FROM SINGLE-FLUID MSBR FUELS

L. M. Ferris J. J. Lawrance
J. F. Land

Distribution coefficients for thorium and several rare earths have been measured at 600 to 700°C using a variety of LiF-BeF_2-ThF_4 solutions in which the ThF_4 concentration was about 12 mole %. The experimental procedure used was described in a previous report.[2] In each experiment the bismuth phase could be saturated with thorium without changing the composition of the salt detectably. The highest distribution coefficients for the respective components in the system are attained

Table 22.3. Distribution of Thorium, Rare Earths, and Lithium Between LiF-BeF_2-ThF_4 Salts and Thorium-Saturated Bismuth Solutions at 600 and 700°C

Salt Composition (mole %)			"Free Fluoride" Equivalence	Temperature (°C)	Rare Earth	D^{max}			α^*
LiF	BeF_2	ThF_4				Li	Th	Rare Earth	
						× 10^{-3}	× 10^{-2}	× 10^{-2}	
69.2	19.4	11.4	−4	600	Eu^{2+}	1.45	1.35	1.3	0.96
					Eu^{2+}	1.59	1.30	1.5	1.2
					La^{3+}	1.61	1.51	2.0	1.3
					La^{3+}	1.49	1.44	2.1	1.5
					Nd^{3+}	1.65	1.53	4.2	2.7
					Nd^{3+}	1.62	1.49	3.8	2.5
				700	La^{3+}	4.60	4.0	6.0	1.5
					Nd^{3+}	4.23	4.94	13.9	2.8
72.0	16.0	12.0	+4	600	La^{3+}	1.88	1.45	2.3	1.6
					Sm^a	1.88	1.54	3.2	2.1
					Nd^{3+}	2.16	1.40	4.2	3.0
				700	Sm^a	5.02	4.55	9.7	2.1
					Nd^{3+}	5.29	4.41	8.6	1.9
75.0	13.0	12.0	+13	600	Eu^{2+}	2.28	1.49	2.8	1.9
					Eu^{2+}	2.33	1.50	2.6	1.7
					La^{3+}	2.43	1.40	3.5	2.5
					La^{3+}	2.40	1.36	3.3	2.4
					Nd^{3+}	2.40	1.50	5.6	3.7
				700	Eu^{2+}	6.19	3.92	6.7	1.7
					La^{3+}	6.48	4.35	7.6	1.8
					Nd^{3+}	6.95	4.11	14.0	3.4

[a]The average valence of Sm in this experiment was 2.7, indicating that both Sm^{2+} and Sm^{3+} were present in the salt.

when the metal phase is saturated with thorium. This condition provides a convenient reference point for the correlation of the data. Following the convention used previously,[2] distribution coefficients obtained when the metal phase is saturated with thorium are designated at D^{max}, and the rare-earth–thorium separation factors (D_{RE}/D_{Th}) determined at D_{Th}^{max} are denoted by α^*.

The data obtained so far are given in Table 22.3. As illustrated in Fig. 22.6 the data correlate well with the calculated "free fluoride" equivalence of the salt.

The rare-earth–thorium separation factors generally were in the range of 1 to 3.5 over the range of conditions investigated. Increasing the temperature from 600 to 700°C usually produced a small decrease in the separation factor; this is consistent with the earlier observation[2] that temperature had very little effect on α^*. The results obtained in this study are in good agreement with those obtained by other workers.[10]

It is interesting to note that the average values of D_{Th}^{max} obtained at 600 and 700°C correspond to thorium concentrations in the bismuth of about 1850 and 5600 wt ppm respectively. These values are in excellent agreement with those obtained by direct measurement of the solubility of thorium in bismuth.[2]

between the respective salts and the metal phase must be satisfied. Differences in the chemical activities of the various species in the two salts provide the driving force for the transfer of a given component, starting with nonequilibrium conditions. Ideally, the equilibria would favor transfer of a large fraction of the rare earths to the acceptor salt, with little attendant transfer of thorium.

Experimentally this technique was tested using an apparatus similar to that shown schematically in Fig. 22.7. The LiF-BeF_2-ThF_4 donor salt, which initially contained the rare earth, was separated from the acceptor salt by a thorium-saturated bismuth phase. In each experiment the number of moles of donor salt was equal to the number of moles of acceptor salt. The equilibrium distribution of thorium, lithium, and the rare earth among the three phases was then determined at about 600°C. (Beryllium and the anionic species do not transfer in these systems.) In each system tested, equilibrium was reached in less than 48 hr without agitation of any of the phases. The desired equilibrium conditions are those where (1) a large fraction of the rare earth is present in the acceptor salt and (2) the thorium decontamination factor (DF),

$$DF_{Th} = \frac{(\text{mole fraction RE in acceptor})/(\text{mole fraction Th in acceptor})}{(\text{mole fraction RE in donor})/(\text{mole fraction Th in donor})},$$

Although the rare-earth–thorium separation factors increased slightly with increasing "free fluoride" equivalence of the salt, no significant enhancement of the separation factors over those obtained with the reference carrier salt, LiF-BeF_2-ThF_4 (72-16-12 mole %), appears to be possible by changing the salt composition.

22.4 METAL TRANSFER PROCESS STUDIES

F. J. Smith J. J. Lawrance
C. T. Thompson

Because the rare-earth–thorium separation factors attainable by reductive extraction are somewhat lower than desired, alternative methods for effecting this separation are being sought. One possibility is the selective transfer of the rare earths from the LiF-BeF_2-ThF_4 donor salt through a liquid metal phase to an acceptor salt. All oxidation-reduction equilibria is high, hopefully greater than 100.

The results of the experiments conducted to date are given in Table 22.4. It is seen that none of the acceptor

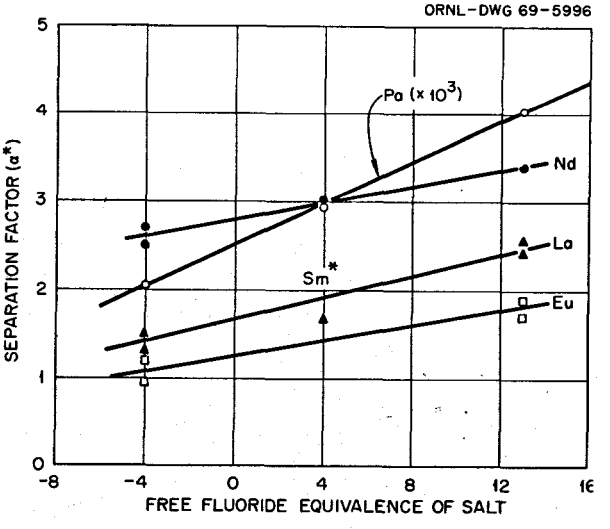

Fig. 22.6. Effect of "Free-Fluoride" Equivalence of LiF-BeF_2-ThF_4 Salts on Rare-Earth–Thorium and Protactinium-Thorium Separation Factors (α^*) at 600°C. ThF_4 concentration in the salts, about 12 mole %).

[10] D. M. Moulton, W. R. Grimes, and J. H. Shaffer, *MSR Program Semiann. Progr. Rept. Aug. 31, 1968*, ORNL-4344, p. 174.

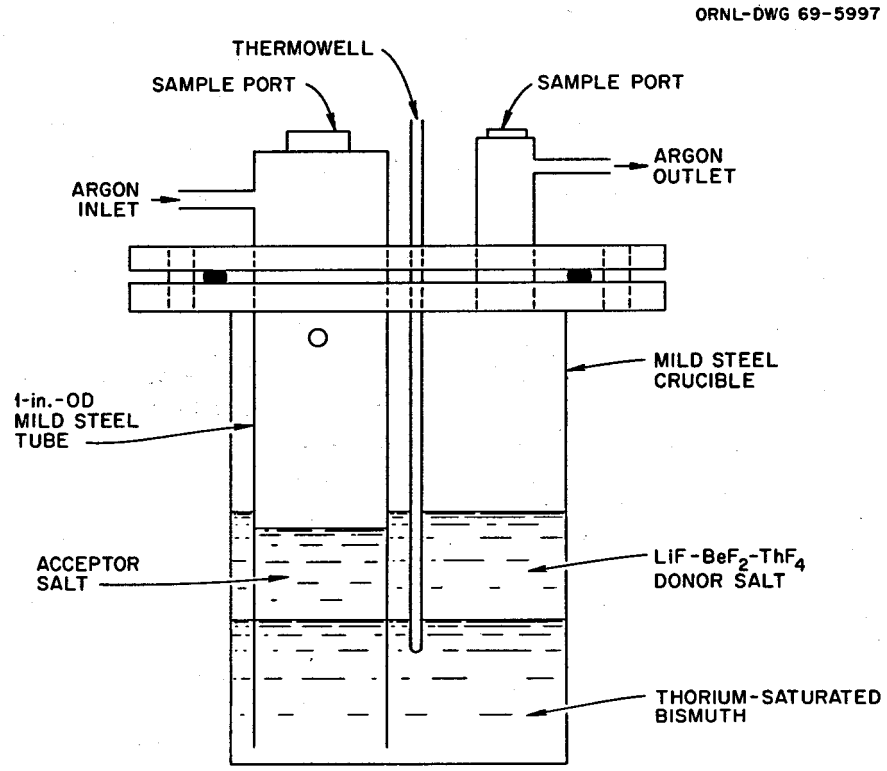

Fig. 22.7. Schematic Diagram of Reaction Vessel Used in Metal-Transfer Experiments.

Table 22.4. Rare-Earth–Thorium Separations in Metal Transfer Experiments

At equilibrium, with equal moles of donor and acceptor salts; bismuth phase saturated with thorium

Donor Salt	Acceptor Salt	Temperature (°C)	Rare Earth	Amount of Rare Earth Transferred (%)	Thorium DF
$LiF-BeF_2-ThF_4$ (75-13-12 mole %)	$LiF-BeF_2$ (66-34 mole %)	600	Eu(II)	39.0	21.0
$LiF-BeF_2-ThF_4$ (75-13-12 mole %)	$LiF-BeF_2$ (66-34 mole %)	600	La(III)	6.4	3.5
$LiF-BeF_2-ThF_4$ (72-16-12 mole %)	$LiF-BeF_2$ (57-43 mole %)	600	La(III)	5.0[a]	3.0[a]
$LiF-BeF_2-ThF_4$ (72-16-12 mole %)	LiCl	640	La(III)	4.1	*b*
$LiF-BeF_2-ThF_4$ (72-16-12 mole %)	LiCl-LiF (90-10 mole %)	640	La(III)	20.0	23.0
$LiF-BeF_2-ThF_4$ (72-16-12 mole %)	LiCl-LiF (80-20 mole %)	640	La(III)	35.0	12.0
$LiF-BeF_2-ThF_4$ (72-16-12 mole %)	LiCl-LiF (80-20 mole %)	600	La(III)	34.0	10.0
$LiF-BeF_2-ThF_4$ (72-16-12 mole %)	LiBr	600	La(III)	1.4	
$LiF-BeF_2-ThF_4$ (72-16-12 mole %)	LiBr-LiF (90-10 mole %)	600	La(III)	9.0	20.0

[a]Calculated from distribution coefficient data from separate experiments with the respective salts.

[b]Contamination of the LiCl with a trace of the $LiF-BeF_2-ThF_4$ salt precluded determination of this value. The thorium DF should be greater than 300, based on the distribution coefficient data obtained in other experiments.[11]

salts used fulfilled both of the desired criteria. Significant transfer of the trivalent rare earth lanthanum was achieved using LiCl-LiF solutions as the acceptor; however, the thorium decontamination factor was only in the range of 10 to 20. Other studies[11] with pure LiCl indicate that high thorium decontamination factors could be achieved but that only a small fraction of a trivalent rare earth such as lanthanum or neodymium would be transferred. The search for an acceptor salt that provides the desired results is continuing.

22.5 EFFECT OF OTHER COMPONENTS ON THE SOLUBILITY OF THORIUM IN BISMUTH

F. J. Smith J. F. Land
C. T. Thompson

Throughout our studies we have been constantly alert to solute interactions in the bismuth phase that could decrease the solubility of thorium and/or result in the formation of an insoluble intermetallic phase. The data obtained in this program show that the thorium solubility at 600°C (about 2000 wt ppm) is not affected by the presence of uranium and zirconium at concentrations of 2000 ppm, either singly or in combination. Similar results were obtained with uranium, plutonium, and thorium; solutions containing about 2000 ppm thorium and at least 2000 ppm uranium and plutonium have been produced. Lithium and lanthanum, in concentrations up to about 1000 ppm, had no detectable effect on the thorium solubility. Nickel was the only element encountered in this work that had a marked effect.

The effect of nickel on the solubility of thorium in bismuth at 600°C was investigated in two experiments. The system was contained under an argon atmosphere in a mild steel crucible in experiment 5639 and in a molybdenum crucible in experiment LA-1. Initially, sufficient crystal-bar thorium was added to just saturate the bismuth at 600°C; lanthanum, at a concentration of about 1000 ppm, was also present in experiment LA-1. Then, small portions of nickel were added to the systems. After each addition, at least 4 hr was allowed for the attainment of equilibrium before a filtered sample of the liquid phase was taken for analysis. The results are shown in Fig. 22.8. The solid circles were obtained in experiment 5639 by back titration with crystal-bar thorium. The data from these experiments can be expressed as a mole fraction solubility product,

$$K_{xp} = X_{Th} X_{Ni} = 6.2 \times 10^{-7} ,$$

over the range of concentrations investigated. This is the type of behavior expected if the Th/Ni atom ratio in the solid phase were 1. This appeared to be the case; by material balance calculations, the Th/Ni atom ratio in the solid phase was 0.90 to 0.99 throughout each experiment. No attempt was made to isolate and identify the solid phase. It could be ThNi (which would not be inconsistent with the reported[12] Th-Ni phase diagram), or it could be a ternary bismuthide, $ThNiBi_x$. The data indicate that a bismuth solution saturated with thorium at 600°C could accommodate up to about 100 ppm nickel before precipitation of a thorium- and nickel-containing solid would occur. It was also of interest to note that the lanthanum concentration in the liquid phase remained unchanged, even when the nickel concentration was 5000 ppm.

[11] F. J. Smith, Chemical Technology Division, unpublished data.

[12] M. Hansen, *Constitution of Binary Alloys*, 2d ed., p. 1048, McGraw-Hill, New York, 1958.

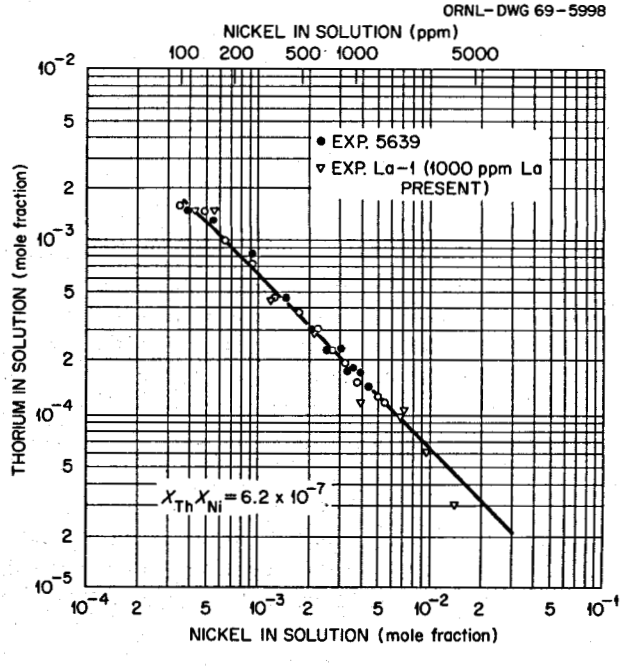

Fig. 22.8. Mutual Solubility of Thorium and Nickel in Bismuth at 600°C.

23. Engineering Development of Process Operations

L. E. McNeese

23.1 ELECTROLYTIC CELL DEVELOPMENT

M. S. Lin L. E. McNeese

Electrolytic cells will be required for operation of reductive extraction systems in an MSBR fuel processing plant. The cell will be used to oxidize uranium or other materials in bismuth streams effluent from extraction contactors as well as for reducing lithium and thorium into flowing bismuth streams to prepare feed for the contactors. The concentrations of materials to be oxidized from the bismuth at the anode are low, so the current density would be limited by the rate at which these materials could be transported to the anode surface. The diffusion-limited current density for oxidation of uranium from bismuth at a uranium concentration of 0.0016 mole fraction was estimated to be 0.15 amp/cm^2 (based on uranium diffusivity in bismuth of 2.5×10^{-5} cm^2/sec,[1] diffusion layer thickness of 5×10^{-3} cm, and bismuth volume of 21.3 cc/g-atom). A current density this low would require an anode area of 21.7 ft^2 for the protactinium isolation system, an area much larger than desired. The area is decreased considerably by oxidizing bismuth, the major component present in the anode. Although this produces a corrosive material, BiF_3, it is more desirable than using very large anode areas. The BiF_3 dissolves in the molten fluoride electrolyte, which is countercurrently contacted with the bismuth stream containing metals to be oxidized. The overall reaction thus is still the oxidation of materials from the metal stream.

To date, two series of experiments have been carried out in two static cells made of quartz. Another static cell made entirely of metal was also recently installed. Results of experiments with these cells will be discussed.

[1] J. C. Hesson, H. E. Hootman, and L. Burris, Jr., *Electrochem. Technol.* 3, 240 (1965).

23.1.1 Quartz Static Cell Experiments

The quartz cell, shown in Fig. 23.1, consists of a flat-bottomed quartz tube (4 in. OD) with metal flanges. The bottom of the cell contains a quartz divider, which results in two compartments equal in size and about 3 in. deep. The compartments were filled with bismuth to within about ½ in. of the top of the divider to produce the electrodes with an exposed area of about 30 cm^2 each. A 3.5-in. layer of molten salt (66-34 mole % LiF-BeF_2) covered the electrodes and served as the electrolyte. Two molybdenum tubes contained within quartz sleeves were introduced from the top of the vessel through the molten salt and terminated near the bottom of the electrode compartments to serve as the electrode leads as well as gas sparge lines. Means for obtaining filtered samples of salt or bismuth were provided.

Prior to each series of experiments the bismuth was sparged with hydrogen at 700°C for about 16 hr. About 1.8 kg of molten salt which had been previously purified by hydrofluorination, hydrogen reduction, and filtration was then introduced into the cell. Viewing slits were provided in the furnace to allow observation of the salt-bismuth interface in the vicinity of the quartz divider. Prior to transfer of molten salt to the cell, the bismuth surfaces were shiny, although a small amount of surface film on the bismuth was noted. After transfer of salt to the cell, the salt was colorless and quite transparent. A flow of argon cover gas was maintained through the gas space above the salt, and a slight positive pressure was maintained in order to prevent air inleakage. The quartz cell is shown after installation in Fig. 23.2. A 0 to 12 v dc power supply was used which had a maximum output of 250 amp. Both the cell current and the potential difference between the electrodes were recorded continuously.

During both series of experiments the voltage applied across the electrodes was increased incrementally from

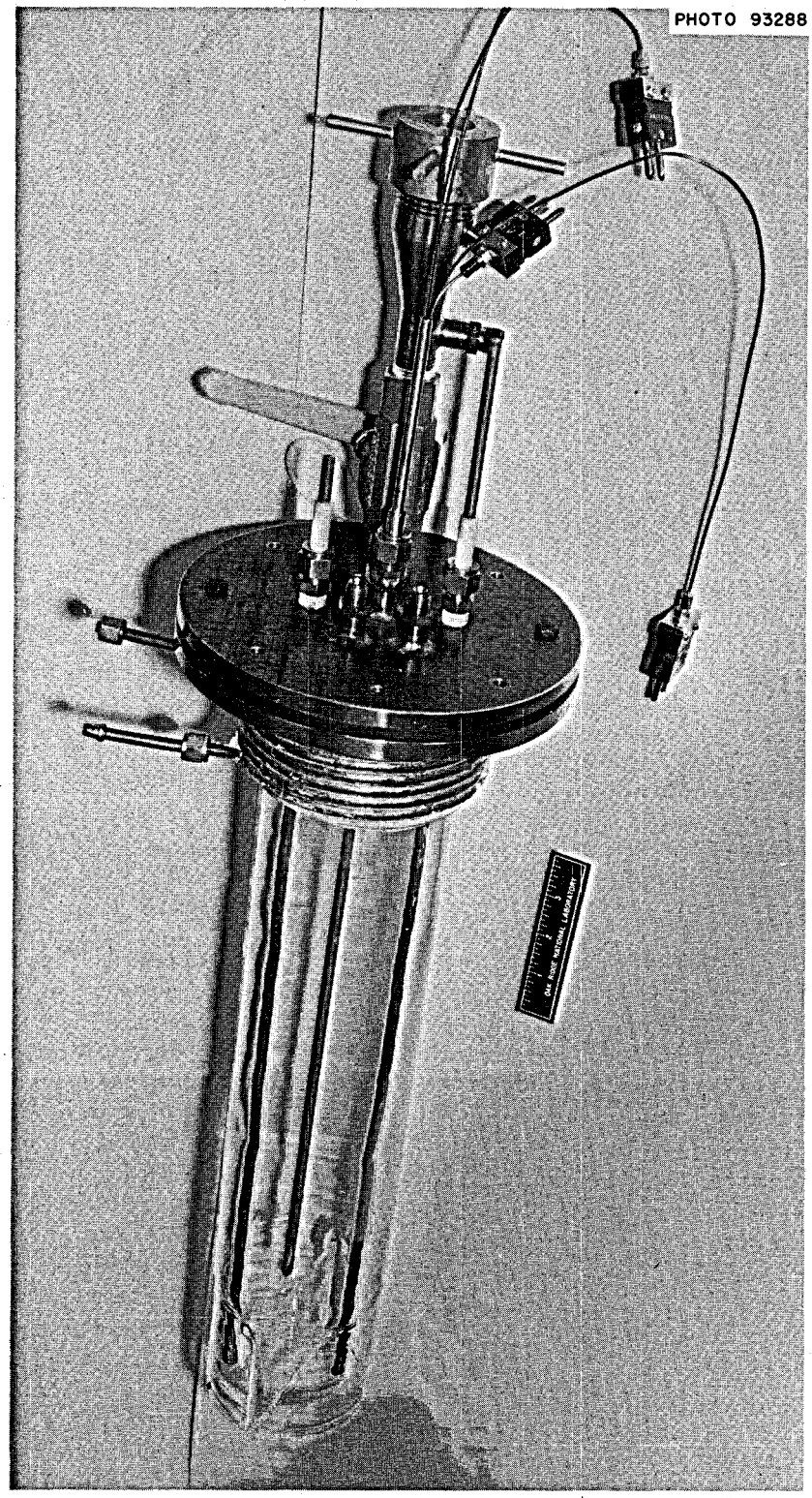

Fig. 23.1. The Static Quartz Electrolytic Cell.

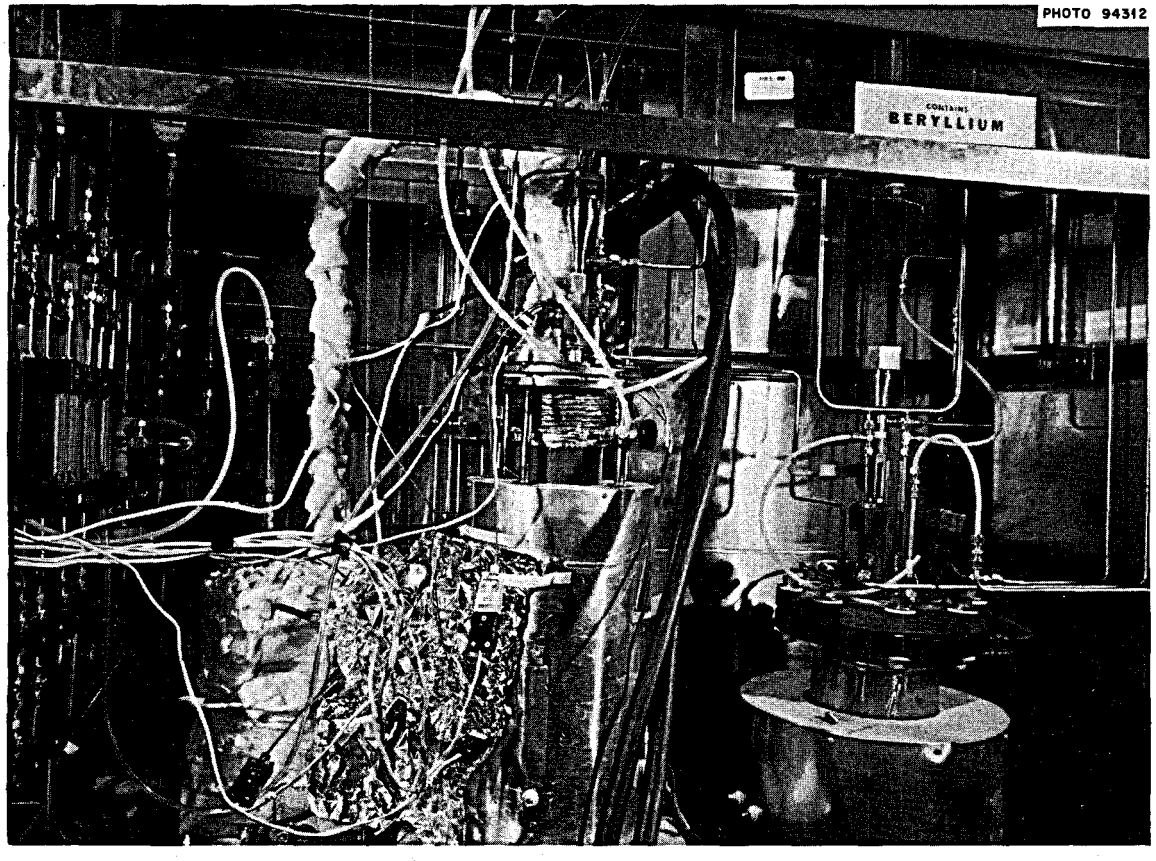

Fig. 23.2. Experimental Electrolytic Installation.

an initial value of 2.6 v in steps of about 0.6 v, and operation of the cell was observed. No gas sparging of the salt or the bismuth electrodes was used during the first series of experiments, but the cathode was sparged with argon during most of the second series of experiments, as will be discussed. The results can be summarized as follows:

1. The initial potential difference between the bismuth electrodes was <0.05 v (below recorder sensitivity). The cell potential increased rapidly to 2 v after passage of 60 coulombs in 10 sec, to 2.1 v after 625 coulombs in 125 sec, and to 2.25 v after 9300 coulombs in 61 min. The cell potential remained at about 2.2 v thereafter. The potential was lowered by mixing the cathode by argon sparging; however, sparging the anode produced no change in cell potential.

2. The current-vs-voltage plot of the experiments (Fig. 23.3) suggests that there is essentially no limiting current in the range covered by the experiments. The slight decrease in cell resistance shown in one of the curves was due to the increase in cell temperature and is consistent with values calculated from the published equation[2] for specific conductivity of molten $2LiF\text{-}BeF_2$ as a function of temperature. The highest current density obtained was 4.5 amp/cm^2 (4180 amp/ft^2). Higher current densities would be expected as the applied potential is increased.

3. During both series of runs, formation of very finely divided dark material was noted at the anode. The material was observed to spread slowly throughout the salt during the first 10 min of operation with the first cell. Circulation of the salt during this period was slight and resulted from thermal convection. Although the salt remained opaque during the remaining cell operation, the salt was transparent after the cell had stood overnight, and only a small amount of dark material was noted at the salt-bismuth interface. During operation of the second cell, the salt immediately above the anode appeared light brown after 10 sec of cell operation (60 coulombs passed). At this point the anode and the salt

[2] J. W. Cooke, ORNL-TM-2316, p. 14.

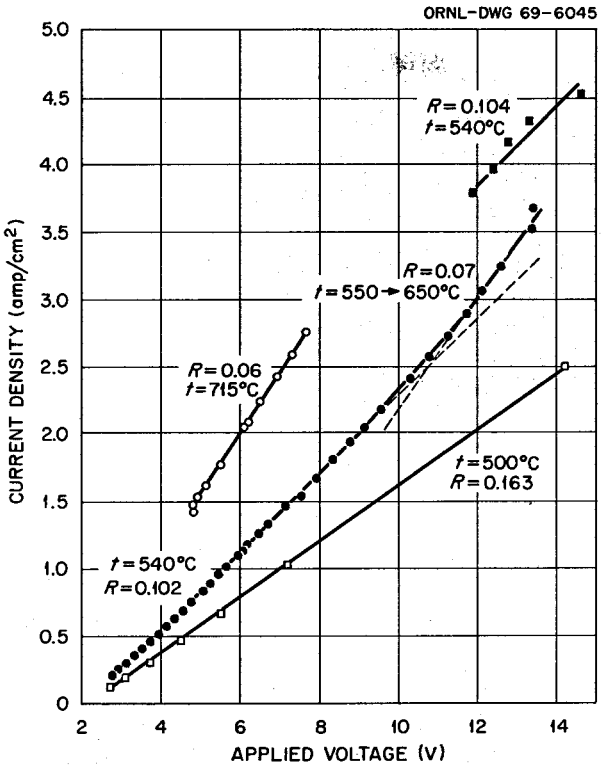

Fig. 23.3. Current-Voltage and Current-Density–Voltage Plot.

above it were stirred by an argon sparge; this resulted in dispersion of the material above the anode throughout the salt, which then appeared light brown. The formation of black material at the anode continued for an additional 125 sec (625 additional coulombs). After standing overnight the salt was clear, with a small amount of black material in it. No further formation of black material was noted during several hours of cell operation which followed. During this time, salt circulation was promoted by an argon sparge in the cathode chamber.

4. Gas was evolved from the anode during the electrolytic process, even at a current density as low as 0.15 amp/cm^2. Mass spectrometric analysis of off-gas samples showed the gas to be SiF_4. The SiF_4 concentration in the samples increased as the cell current density was increased. The gas was produced on the anode side of the quartz divider which separated the bismuth anode and cathode and was produced only during or immediately after current passage. These observations strongly suggest that the gas evolution was the result of reaction of BiF_3 produced at the anode with the quartz divider.

5. There was no evidence of fluorine evolution during most of the cell operation. Only after the cell had shorted internally (arcing was noted between the electrodes) did the KI-starch solution (through which the cell off-gas passed) become lightly tinted.

6. The bismuth concentrations in the salt (probably BiF_3) increased with the number of coulombs passed through the cell, although the concentration was only 10 to 50% of that which would result if only BiF_3 were produced and it all remained in the salt.

23.1.2 All-Metal Static Cell Experiment

Although the initial experimental work on electrolytic cell development utilized quartz as a convenient container material, this material will not be suitable for long-term usage. The most corrosive condition in a cell will be in the vicinity of anodic surfaces, where an oxidizing condition exists. Cathodic surfaces must resist attack by liquid bismuth, but the corrosion problem at this point is not considered severe. It is planned that all anodic surfaces other than liquid bismuth surfaces will be protected by a frozen salt layer. A small all-metal static cell has been installed for study of this method of operation.

The main body of the cells is a 6-in. sched 40 mild steel pipe 18 in. long with a flat, ¼-in.-thick bottom. The cell body is the cathode container. The upper part of the cell is flanged, and the upper flange is electrically insulated from the cell body. The anode of the cell, shown in Fig. 23.4 before assembly, is a double-walled fluid-cooled cup having an inside diameter of 1.75 in. (15.5 cm^2 gross electrode area) and an outside diameter of 2.75 in. The cup is suspended from the top flange by two ¼-in. tubes, which serve as the coolant (nitrogen and water) inlet and outlet as well as the electrical connection to the anode. Provision was made for raising and lowering the anode cup. Viewing ports are provided on the top flange, and provision is made for sampling the salt or bismuth without introducing air into the system. The cell is shown after installation in Fig. 23.2.

The cell has been charged with 16.3 kg of bismuth treated with hydrogen at 700°C for 16 hr and molten salt (4.5 kg of 66-34 mole % LiF-BeF_2) which had been purified by hydrofluorination, hydrogen reduction, and filtration. The system will be tested initially for formation of a frozen salt layer on the outer surfaces of the anode cup, and electrolysis experiments will follow.

23.2 REDUCTIVE EXTRACTION ENGINEERING STUDIES

L. E. McNeese B. A. Hannaford
H. D. Cochran, Jr. W. F. Schaffer, Jr.
E. L. Youngblood

Equipment designed for semicontinuous engineering experiments on reductive extraction was described in an

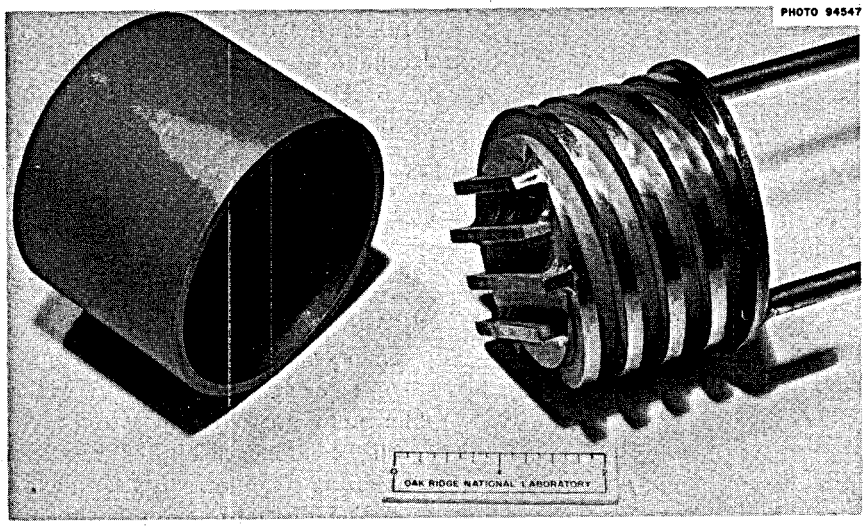

Fig. 23.4. Photograph of Anode Cup Before Assembly.

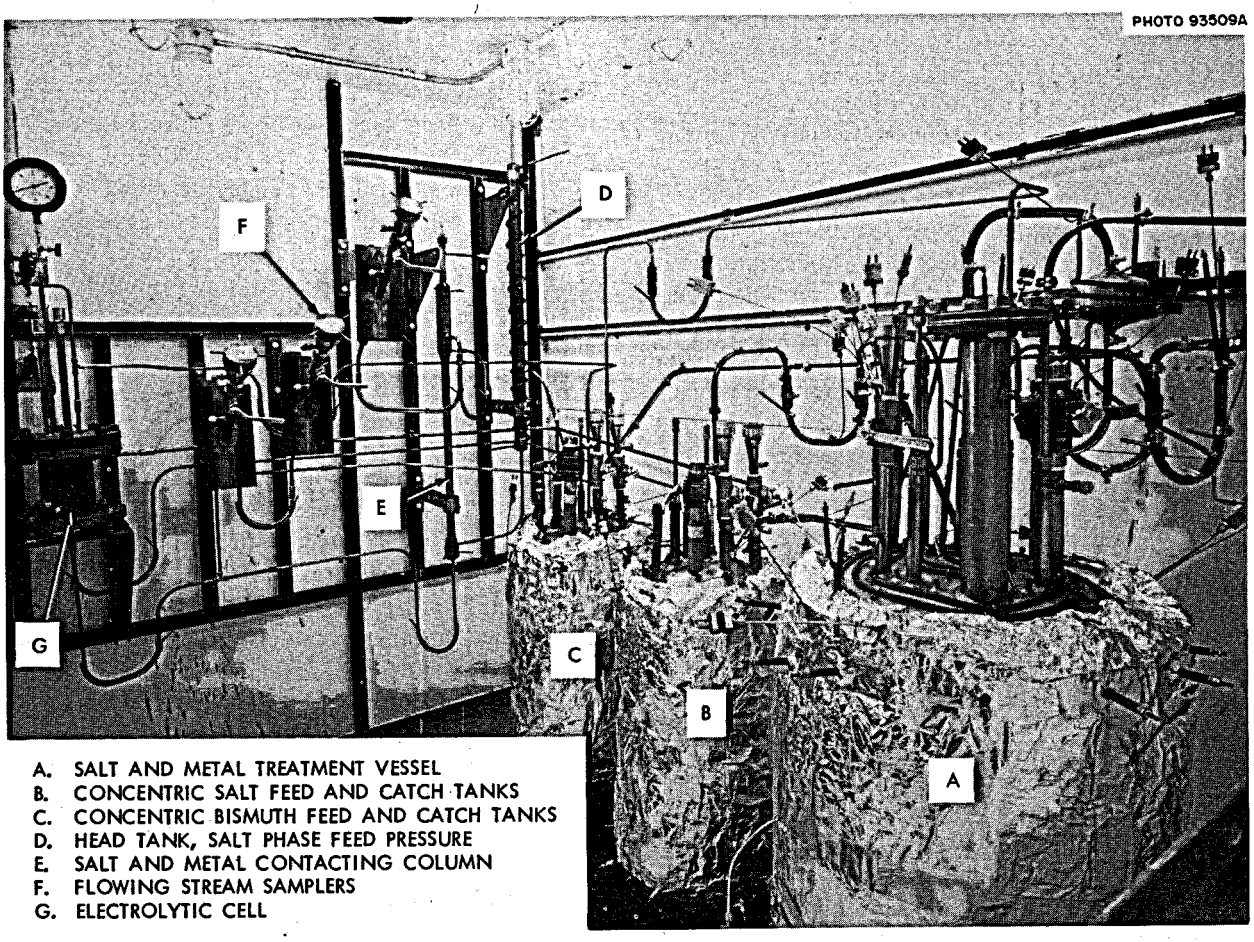

Fig. 23.5. Engineering Facility for Testing Molten-Salt–Molten-Metal Contactors.

earlier report.[3] The contacting column is 0.82 in. ID by 2 ft long, packed with ¼-in. right circular cylinders. The feed and catch tanks for the molten salt and bismuth hold about 20 liters each. The graphite crucible in the salt and metal treatment vessel holds about 50 liters. About 15 liters of each phase will be used during experimentation. Installation of the equipment in Building 3592 has been completed.

Figure 23.5, taken during installation, shows most of the major process components: *A*, salt and metal treatment vessel containing graphite crucible; *B*, concentric feed and catch tanks for the salt phase; *C*, concentric feed and catch tanks for the bismuth phase; *D*, head tank for monitoring salt phase feed pressure; *E*, salt and metal contacting column packed with ¼-in. molybdenum cylinders; *F*, flowing stream samplers; and *G*, electrolytic cell connected in parallel to column. Also visible in the photograph are five tank samplers, salt and metal transfer lines, freeze valves, and one of the two fritted molybdenum filters. Except for the treatment vessel, which is of stainless steel, the equipment is constructed of mild steel.

Preliminary testing and degassing of the equipment has begun, charging of bismuth and salt (LiF-BeF_2-ThF_4, 72-16-12 mole %) will be completed shortly, and experiments should begin within six weeks. The first experiments will be hydrodynamic studies in which the pressure drop across the column will be measured under various flow conditions. After we are confident in the operation of the system, about 0.3 mole % UF_4 will be added to the salt phase. Mass transfer studies can then be performed by adding thorium as reductant to the metal phase. Mass transfer performance will be analyzed and correlated with hydrodynamic conditions in the column.

23.3 SIMULATED MOLTEN-SALT–LIQUID-BISMUTH CONTACTOR STUDIES

J. S. Watson L. E. McNeese

Methods being considered for processing molten-salt breeder reactors require the use of devices for the continuous countercurrent contact of molten salt with liquid bismuth. The hydrodynamic properties of such contactors are being studied at low temperatures in simulated systems using water and mercury rather than molten salt and liquid bismuth. Quantitative measurements have been made of flooding rates, pressure drop, and dispersed phase (Hg) holdup. Quantitative information was also obtained on flow patterns and drop sizes (or interfacial area). Four different packing materials and one baffled cartridge have been studied in a 1-in.-ID column.

As noted in the previous semiannual report, drop behavior and hence interfacial area are dramatically affected by packing sizes. The ⅛-in. Raschig rings caused the mercury to coalesce into streams with low interfacial area, while ¼-in. solid cylindrical packing allowed the mercury to remain dispersed into small droplets with a large interfacial area. The more recent data continue to confirm this dependence of droplet behavior on packing size – mercury is dispersed into small drops by ¼-in. Raschig rings but coalesced by ⅛-in. solid cylindrical packing.

We have also observed a similar dependence of drop behavior upon total column throughput. With packed columns the effect of flow rate on drop size is relatively small and probably can be ignored in most cases. The effect, however, was dramatic with the baffled cartridge. Figure 23.6 shows a photograph of the baffled column with a mercury flow rate of 480 ml/min and a water rate of 200 ml/min. The mercury is well dispersed into small droplets. However, when the mercury rate was increased to 660 ml/min, the mercury coalesced essentially completely, as shown in Fig. 23.7.

Pressure drop and holdup data for a 2-ft length of the 1-in. column packed with ¼-in. Raschig rings are shown in Figs. 23.8 and 23.9. These results are similar to all the data obtained with other packing materials. Pressure drop and holdup for larger packing sizes (where the mercury is well dispersed) may be related by the semiempirical equations

$$\frac{\Delta P}{L} = k_1 V_s X + k_2 \left(\frac{C}{1-X}\right) X$$

and

$$V_s = \frac{g}{g_c}\frac{\Delta\rho}{k_1} - \frac{1}{k_1}\frac{\Delta P}{L} - k_3 D ,$$

where

ΔP = pressure drop due to flow (e.g., total pressure drop across the column less the static head),

L = length of column,

V_s = superficial slip velocity,

X = holdup,

C, D = continuous- and dispersed-phase superficial velocities,

[3] *MSR Program Semiann. Progr. Rept. Aug. 31, 1968*, ORNL-4344, p. 301.

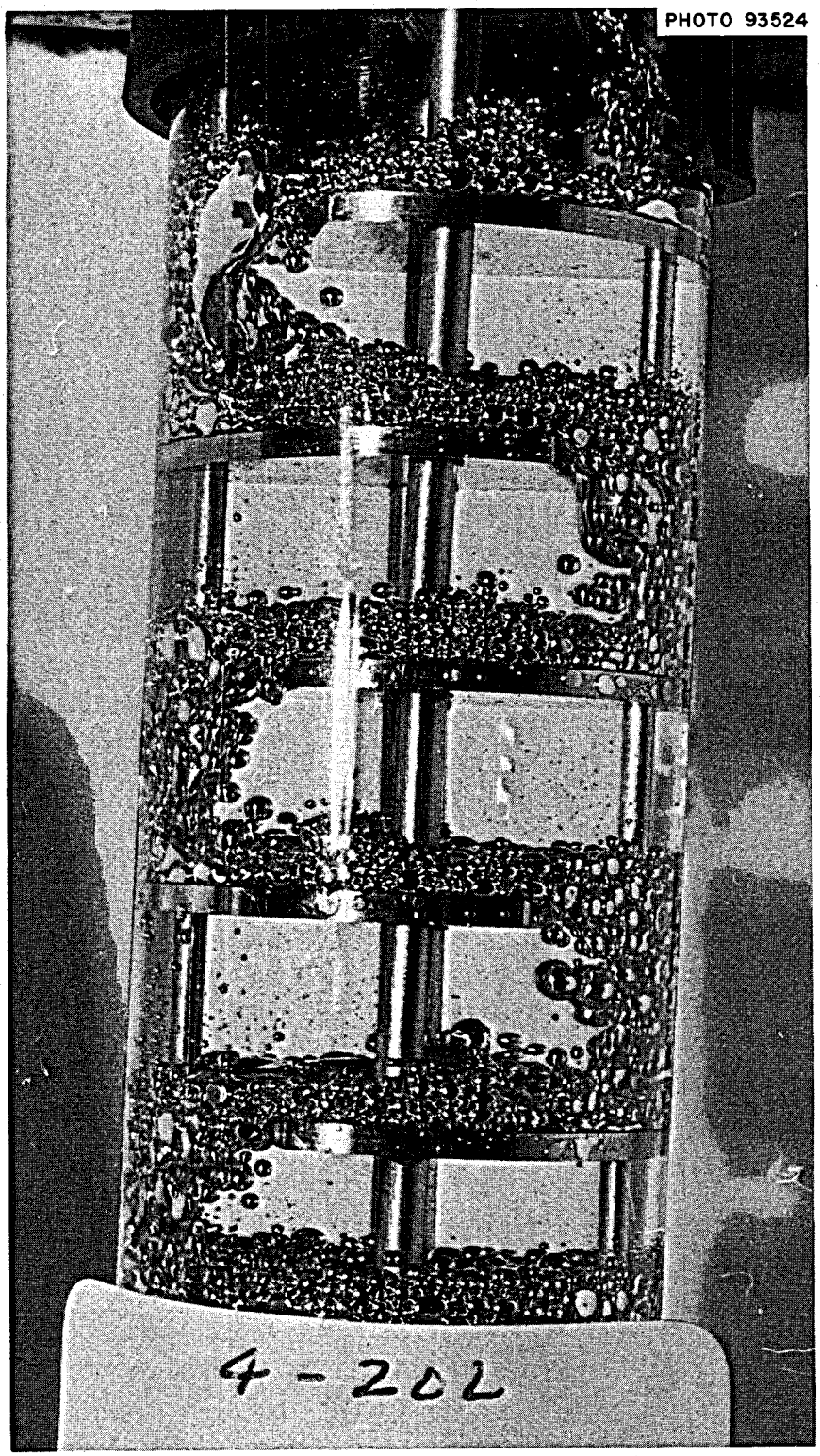

Fig. 23.6. Baffled Column with 480 ml/min of Water.

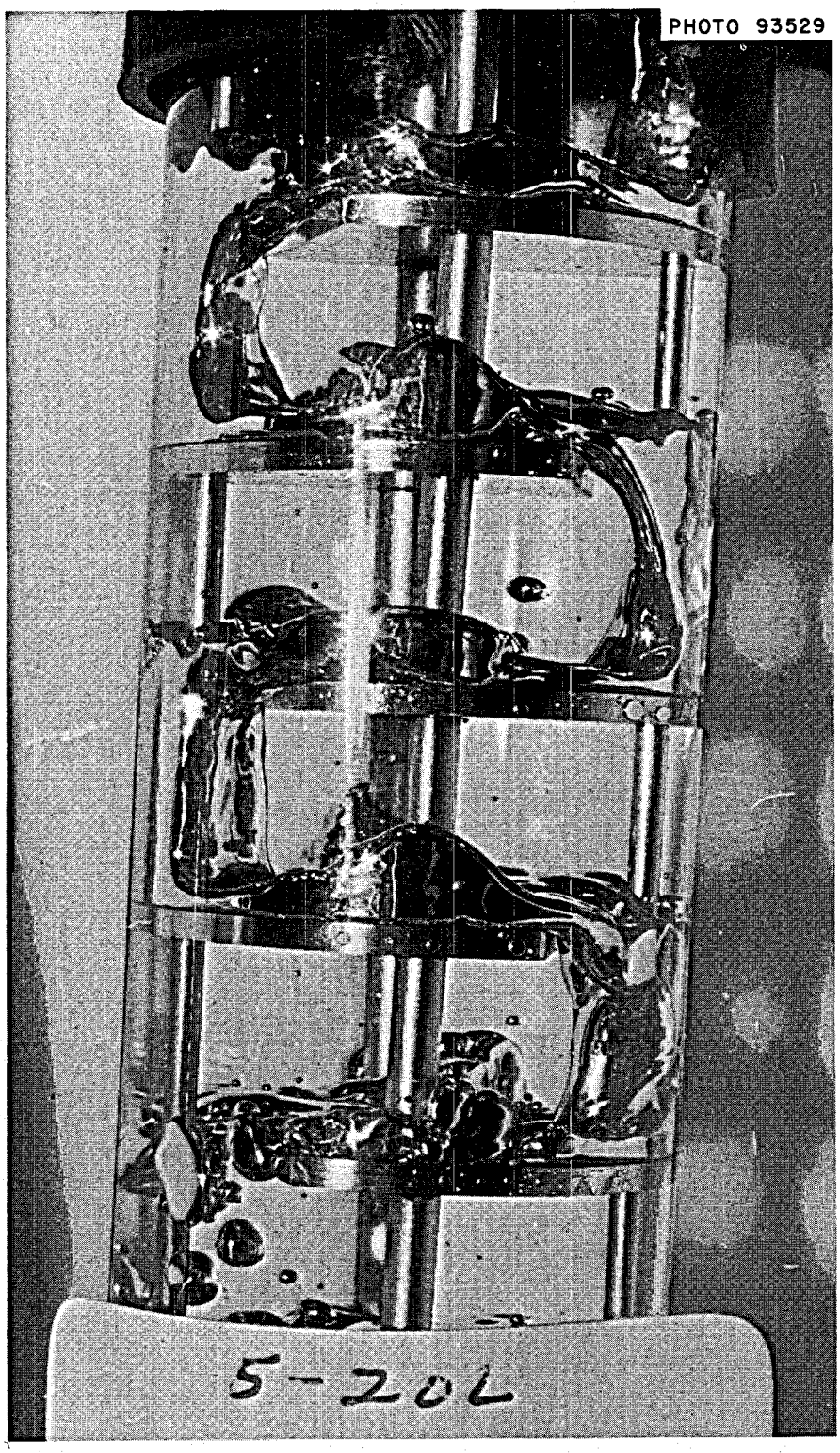

Fig. 23.7. Baffled Column with 660 ml/min of Mercury and 200 ml/min of Water.

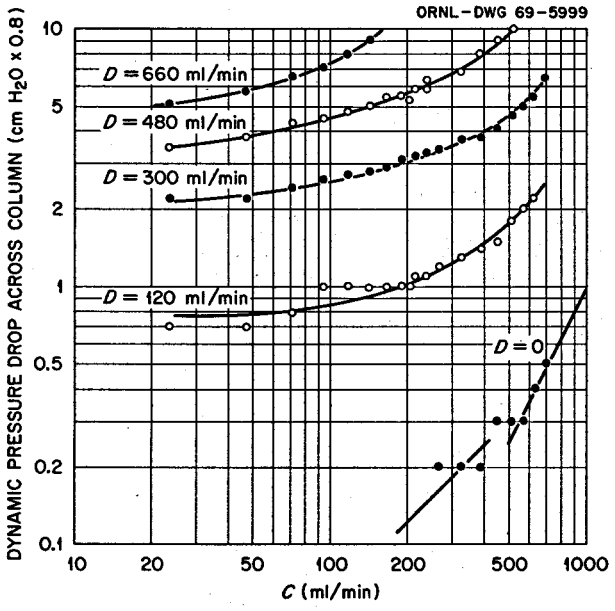

Fig. 23.8. Pressure Drop Across the 1-in. Mercury-Water Column Packed with ¼-in. Raschig Rings.

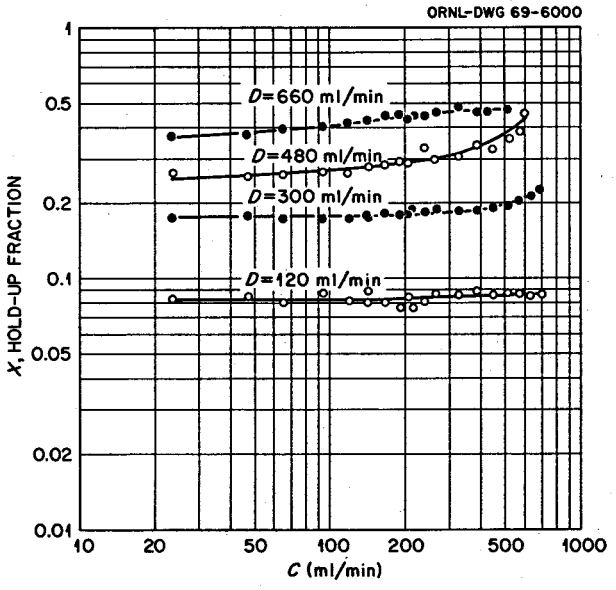

Fig. 23.9. Dispersed Phase Holdup in the 1-in. Mercury-Water Column Packed with ¼-in. Raschig Rings.

$\Delta\rho$ = density difference,

k_1, k_2, k_3 = constants.

Thus with three constants (k_1, k_2, and k_3) the hydrodynamic aspects (holdup, pressure drop, and, by implication, flooding rates) of a dispersed-flow column can be related. Unfortunately, only two of the four packing materials tested gave dispersed flow, and to adequately evaluate any relationship between the hydrodynamic variables will require data from more packing materials. Since we are now also considering larger packing materials for the processing system, a 2-in.-ID column and a larger mercury pump have been installed so that ⅜-in. and possibly ½-in. packing materials can be tested.

The equipment necessary to study back mixing in packed columns has been fabricated and assembled. Ordinary packed columns as well as special columns modified to reduce back mixing will be tested.

23.4 DESIGN OF A CONTINUOUS ELECTROLYTIC CELL TESTING SYSTEM

E. L. Nicholson L. E. McNeese
M. S. Lin W. F. Schaffer
E. L. Youngblood

A system is being built to continuously circulate molten salt and bismuth through an electrolytic cell at 550 to 600°C (Fig. 23.10). The electrolytic cell containment vessel will permit testing a variety of cell designs and has provisions for cooling, sampling, and visually observing the cell. Criteria for the cells are being developed based on tests of static cells that are under way. Tentatively, the cell will have anode and cathode areas of about 0.1 ft² each and will be supplied with approximately 1500 amp at 10 to 20 v. Flows are to be up to 0.5 gpm of bismuth and 0.25 gpm of salt. The system external to the cell consists of a mixer-settler tank to equilibrate the salt and bismuth streams from the cell and gas lift pumps and gravity-head-type orifice flowmeters for return of the streams to the cell. Low-carbon steel will be used for most of the system in contact with salt or bismuth. The agitator shaft and impeller will be made of molybdenum, as will several of the transfer lines and the internal piping in the electrolytic cell containment vessel. Outlet nozzles on the mixer-settler vessel have been coated with vapor-deposited tungsten. Provisions have been made for inserting corrosion test coupons in the system.

Gas lifts were selected as the simplest method for pumping salt and bismuth. Gas lift performance data could not be found for high-density liquids such as bismuth, so tests were made on gas lift pumping of mercury. For a total lift height of 34 in., a lift tube diameter of 0.3 in., and a fractional submergence of 0.54, the maximum pumping rate was 0.26 gpm with a gas consumption of 4.0 std liters/min (1.3 std liters/min at operating temperature). Two lift tubes will be operated in parallel on the bismuth stream to get the desired capacity because a single large-diameter lift tube had excessive gas consumption. One small-

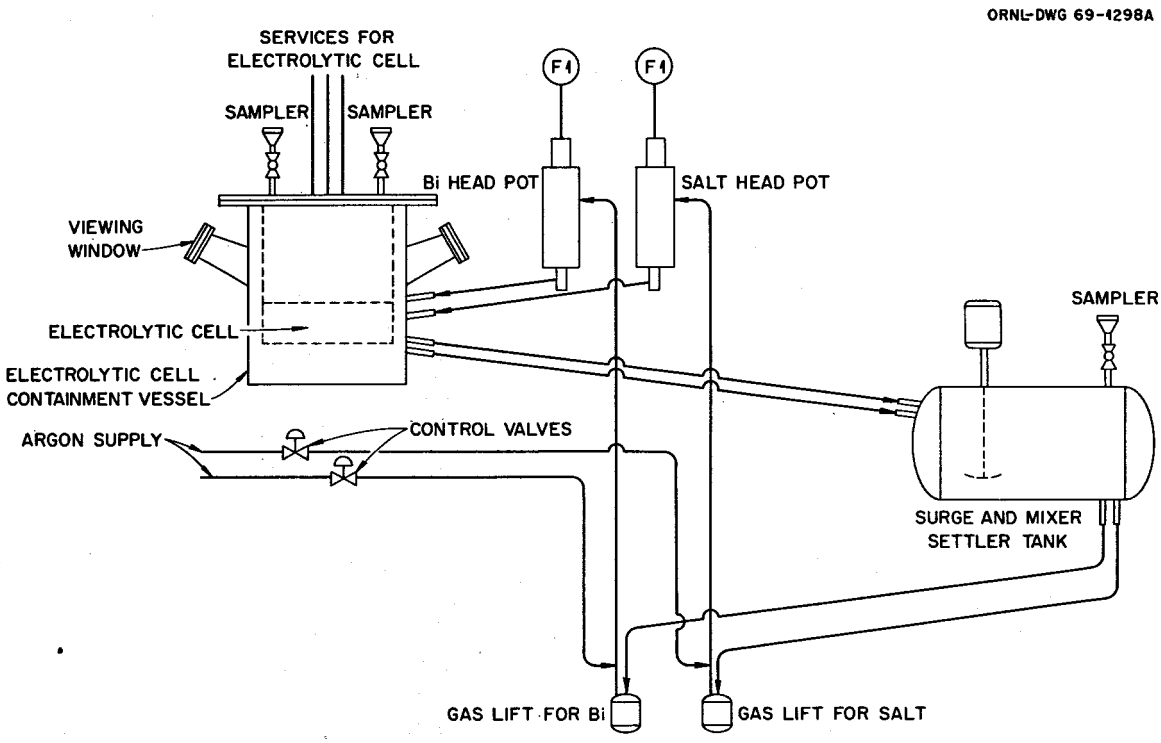

Fig. 23.10. Continuous Electrolytic Cell Testing System.

diameter lift tube will be required for the salt stream. Flow regulation will be obtained by varying the gas flow to the lift. Entrainment and liquid surging was a problem in the gas lift disengagement head pot. A head pot with a baffled annulus was developed that eliminated the entrainment problem and dampened the surges in gas lift liquid discharge so that a quiet pool was maintained in the orifice meter compartment. Tests are under way to determine the required orifice sizes.

The vessels and equipment stand are being fabricated, and modifications to the walk-in hood in Building 3541, where the unit will be installed, are under way.

23.5 EXPERIMENTAL FACILITIES FOR REDUCTIVE EXTRACTION DEVELOPMENT WORK

E. L. Nicholson B. B. Klima
E. L. Youngblood

A request for a directive is being prepared to obtain approval for modification of cell 2, Building 3019, so that it can be used for engineering-scale reductive extraction experiments with protactinium or other alpha emitters. The cell is 19 X 20 X 27 ft high and will have three working levels which are independently ventilated and isolated from each other by air locks so that each level can function as an independent alpha laboratory. Alternatively, removable floor panels will permit installation of large full-height experiments such as a demonstration of reductive extraction using full-height packed columns. Conceptual engineering work is under way, so that the cost estimate can be prepared for the preliminary project proposal that must accompany the directive request.

24. Distillation of MSRE Fuel Carrier Salt

J. R. Hightower H. D. Cochran
B. A. Hannaford L. E. McNeese

The molten-salt still is presently being installed in the spare cell at the MSRE for demonstrating low-pressure, high-temperature distillation of the MSRE carrier salt. Tests with nonradioactive salt mixtures have shown[1] that the equipment is suitable for operation with the irradiated fuel carrier salt.

The nonradioactive tests suggested minor equipment changes for operation at the MSRE. Since we had experienced restrictions in the still pot feed line and in the vacuum line from the receiver, we replaced all lines to ensure that no obstructions existed. Additional thermocouples were installed on the feed line to the still pot, on argon feed lines, and on off-gas lines to give better coverage of temperatures. Lines heated with Calrods were electrically insulated from the heater sheath to prevent the heated line from being accidentally placed in the electrical circuit in the event of a Calrod failure. The configuration of the feed line to the still pot was changed to minimize the length of line heated by the still pot heaters to temperatures near 1000°C. This change could reduce the rate of metal deposition below that seen in the nonradioactive experiments. Improved electrical insulation and shielding were added to the still pot liquid level instrumentation to improve the performance of these instruments.

A new condensate sampler was designed and built. It is similar to equipment used to add ^{233}U to the fuel drain tanks but has modifications to allow samples to be taken without disturbing operation of the still. The sampler is shown schematically in Fig. 24.1. The sample capsules (10-g MSRE capsules) will be placed in holders on the turntable in the containment vessel prior to the experiment. At the end of the experiment the capsules will be withdrawn through the removal tube into a carrier for analysis.

Presently, installation of the still has been completed except for connecting the transfer line from the fuel storage tank to the feed tank and attaching the sampler to the sample line. A filter will be installed in the transfer line to avoid the transfer of solid material. Before completing these items, we introduced about 16 liters of nonradioactive salt into the system to test the liquid probes in the still pot and to ensure that all installed components were working properly. We heated the still pot to 900°C, pumped the condenser down to 0.1–1 mm Hg, and distilled about 2 liters of the test salt. All parts of the system performed satisfactorily. The test salt was then discharged from the still. Connection of the transfer line and attachment of the sampler are under way.

[1] J. R. Hightower and L. E. McNeese, *MSR Program Semiann. Progr. Rept. Aug. 31, 1968*, ORNL-4344, p. 306.

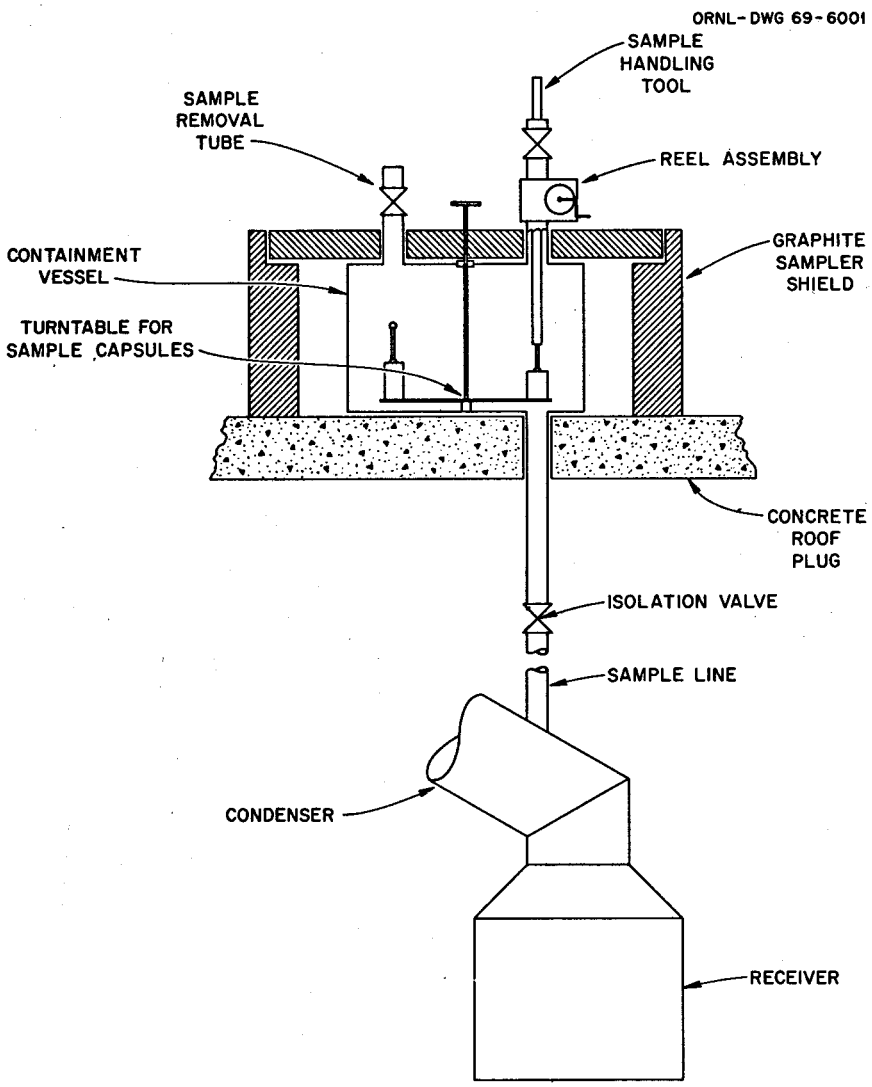

Fig. 24.1. Condensate Sampler for MSRE Distillation Experiment.

OAK RIDGE NATIONAL LABORATORY
MOLTEN-SALT REACTOR PROGRAM

FEBRUARY 28, 1969

M. W. ROSENTHAL, DIRECTOR R
R. B. BRIGGS, ASSOCIATE DIRECTOR D
P. R. KASTEN, ASSOCIATE DIRECTOR R

W. P. EATHERLY, GRAPHITE PROGRAM R
R. B. KORSMEYER, PLANS AND BUDGET R

MSBR DESIGN STUDIES
E. S. BETTIS R

C. E. BETTIS* GE
W. L. CARTER* CT
C. W. COLLINS R
W. K. FURLONG R
E. C. HISE* R
N. A. McLAIN R
J. R. McWHERTER R
H. A. NELMS* R
R. C. ROBERTSON R
J. R. TALLACKSON I&C
L. V. WILSON** R
M. L. WATTS R
W. TERRY R
W. C. GEORGE R
N. M. POLY R

HEAT TRANSFER AND PHYSICAL PROPERTIES
H. W. HOFFMAN* R

J. J. KEYES* R
J. W. COOKE* R
B. COX R
T. S. KRESS R
S. J. CLAIBORNE R
R. L. MILLER R

COMPONENTS & SYSTEMS DEVELOPMENT
DUNLAP SCOTT R

PUMP DEVELOPMENT
A. G. GRINDELL R

C. K. McGLOTHLAN R
P. G. SMITH R
L. V. WILSON** R
H. C. YOUNG R
D. D. OWENS R

COMPONENTS AND SYSTEMS
DUNLAP SCOTT

R. B. GALLAHER R
R. E. HELMS* R
R. J. KEDL R
A. N. SMITH R
C. A. GIFFORD R
F. E. LYNCH R

REMOTE MAINTENANCE
R. BLUMBERG R
P. P. HOLZ* R
J. R. SHUGART R
C. M. SMITH R

CONSULTANT
F. N. PEEBLES UT

INSTRUMENTATION AND CONTROLS
S. J. DITTO I&C

PROCESS INSTRUMENTATION
R. L. MOORE I&C

P. G. HERNDON* I&C
R. J. JONES* I&C

NUCLEAR INSTRUMENTATION AND CONTROL ANALYSIS
J. L. ANDERSON I&C

O. W. BURKE* I&C
F. H. CLARK* I&C
W. H. SIDES I&C

PHYSICS
A. M. PERRY* R

MSRE PHYSICS
B. E. PRINCE R

MSBR ANALYSIS
G. L. SMITH R
W. R. COBB R

MSBR EXPERIMENTAL PHYSICS
G. L. RAGAN R

MSBR CORE DESIGN
H. F. BAUMAN R

CONSULTANT
T. W. KERLIN UT

FUNDAMENTAL RADIATION DAMAGE
D. K. HOLMES SS

W. E. ATKINSON SS
T. S. NOGGLE SS
S. M. OHR SS

MATERIALS
J. R. WEIR, JR. M&C
H. E. McCOY, JR. M&C

MASTER LOOP N STUDIES

D. A. CANONICO* M&C
A. G. CEPOLINA* M&C
R. E. GEHLBACH* M&C
R. W. GUNKEL* M&C
J. W. KOGER M&C
A. P. LITMAN* M&C
C. E. SESSIONS M&C
G. M. SLAUGHTER M&C

GRAPHITE STUDIES

R. L. BEATTY* M&C
O. B. CAVIN M&C
W. H. COOK M&C

C. R. KENNEDY M&C
D. V. KIPLINGER* M&C
R. W. McCLUNG* M&C
W. C. ROBINSON* M&C

GRAPHITE-METAL JOINING

K. V. COOK* M&C
J. P. HAMMOND* M&C
W. J. WERNER M&C
H. L. WHALEY* M&C

TECHNICAL SUPPORT

M. D. ALLEN* M&C
E. R. BOYD* M&C
S. W. COOK* M&C
R. W. CUNNINGHAM* M&C
C. E. DUNN* M&C
J. C. FELTNER M&C
J. W. GEER* M&C
F. D. HARVEY* M&C
J. N. HIX* M&C
C. W. HOUCK M&C

V. G. LANE M&C
E. J. LAWRENCE M&C
E. H. LEE* M&C
W. J. MASON* M&C
B. McNABB M&C
N. O. PLEASANT M&C
R. S. PULLAM* M&C
T. E. SCOTT* M&C
W. H. SMITH, JR.* M&C
L. D. STACK* M&C
G. D. STONLER* M&C

H. R. TINCH* M&C
L. R. TROTTER* M&C
W. H. WARWICK* M&C
J. J. WOODHOUSE M&C
B. C. WILLIAMS M&C
R. W. WILLIAMS M&C

MSBR PROCESSING DEVELOPMENT
M. E. WHATLEY CT

CHEMICAL DEVELOPMENT
L. M. FERRIS CT

J. J. LAWRANCE† CT
J. C. MAILEN CT
C. E. SCHILLING CT
F. J. SMITH CT
J. F. LAND CT
C. T. THOMPSON CT

EXPERIMENTAL ENGINEERING
L. E. McNEESE CT

H. D. COCHRAN, JR. CT
B. A. HANNAFORD CT
J. R. HIGHTOWER, JR. CT
C. W. KEE CT
M. S. LIN CT
J. S. WATSON CT
J. BEAMS CT
V. L. FOWLER CT
R. O. PAYNE CT

PROCESS DESIGN
E. L. NICHOLSON CT

M. J. BELL CT
W. L. CARTER CT
W. F. SCHAFFER CT
E. L. YOUNGBLOOD CT

MSRE PROCESSING
R. B. LINDAUER** CT

CHEMISTRY
W. R. GRIMES* RC

REACTOR CHEMISTRY

F. F. BLANKENSHIP RC
E. G. BOHLMANN* RC
R. E. THOMA** RC

MSRE ON-SITE CHEMISTRY

R. E. THOMA** RC
E. G. BOHLMANN* RC
E. L. COMPERE RC
J. W. MYERS RC
J. C. RUTHERFORD RC

PHYSICAL AND INORGANIC CHEMISTRY

C. F. BAES, JR.* RC
C. E. L. BAMBERGER* RC
C. J. BARTON* RC
J. BRAUNSTEIN* RC
G. D. BRUNTON* RC
S. CANTOR RC
F. A. DOSS RC
M. A. FRIEDMAN RC
L. O. GILPATRICK* RC
B. F. HITCH RC
S. S. KIRSLIS RC
H. W. KOHN RC
D. M. MOULTON RC
J. D. REDMAN* RC
G. D. ROBBINS RC
D. M. RICHARDSON RC
K. A. ROMBERGER* RC
R. G. ROSS RC
H. C. SAVAGE* RC
J. H. SHAFFER* RC
L. M. TOTH RC
C. F. WEAVER* RC
C. R. BENSON RC
L. L. FAIRCHILD RC
W. R. FINNELL RC
J. W. GOOCH, JR. RC
J. R. HART RC
W. JENNINGS, JR. RC
A. L. JOHNSON RC
W. P. TEICHERT RC

MSRE OPERATIONS
P. N. HAUBENREICH R

OPERATION

R. H. GUYMON R
J. L. CROWLEY R
J. K. FRANZREB R
P. H. HARLEY R
T. L. HUDSON R
A. I. KRAKOVIAK R
T. ARNWINE R
R. E. CARNES R
J. P. CULP R
S. J. DAVIS R
W. H. DUCKWORTH R
J. D. EMCH R
E. H. GUINN R
T. G. HILL R
C. C. HURTT R
J. C. JORDAN R
H. J. MILLER R
W. E. RAMSEY R
R. SMITH, JR. R
J. L. STEPP R
S. R. WEST R
J. E. WOLFE R

NUCLEAR AND MECHANICAL ANALYSIS

J. R. ENGEL R
C. H. GABBARD R
A. HOUTZEEL R
R. C. STEFFY R
J. A. WATTS R

MAINTENANCE AND MODIFICATIONS

M. RICHARDSON R
B. H. WEBSTER*** R
A. F. GILLEN R
L. P. PUGH R
J. R. SHUGART R

CHEMICAL PROCESSING

R. B. LINDAUER** CT

INSTRUMENTS AND CONTROLS

S. J. DITTO** I&C

C. D. MARTIN* I&C
J. L. REDFORD I&C
R. W. TUCKER I&C
J. CAMPBELL I&C
C. E. KIRKWOOD I&C

ANALYTICAL CHEMISTRY DEVELOPMENT
J. C. WHITE* AC

RESEARCH AND DEVELOPMENT

A. S. MEYER AC
R. F. APPLE AC
C. M. BOYD AC
J. M. DALE AC
T. H. HANDLEY* AC
D. L. MANNING* AC
T. R. MUELLER* AC
A. L. TRAVAGLINI* AC
J. P. YOUNG* AC

ANALYSES

L. T. CORBIN* AC
G. GOLDBERG* AC
F. K. HASCKER AC
C. E. LAMB* AC
P. F. THOMASON* AC

SPECIAL ASSISTANCE

M. A. BREDIG* C
H. R. BRONSTEIN* C
A. S. DWORKIN* C
G. P. SMITH* M&C

AC ANALYTICAL CHEMISTRY DIVISION
CT CHEMICAL TECHNOLOGY DIVISION
D DIRECTORS DIVISION
GE GENERAL ENGINEERING DIVISION
I&C INSTRUMENTATION AND CONTROLS DIVISION
M&C METALS AND CERAMICS DIVISION
R REACTOR DIVISION
RC REACTOR CHEMISTRY DIVISION
UT UNIVERSITY OF TENNESSEE

* PART TIME ON MSRP
** DUAL CAPACITY
† GUEST SCIENTIST FROM AUSTRALIA

*** TEMPORARILY ASSIGNED TO TVA BROWN'S FERRY NUCLEAR PLANT
SS SOLID STATE

INTERNAL DISTRIBUTION

1. R. K. Adams
2. G. M. Adamson
3. H. I. Adler
4. R. G. Affel
5. J. L. Anderson
6. R. F. Apple
7. C. F. Baes
8. J. M. Baker
9. S. J. Ball
10. C. E. Bamberger
11. C. J. Barton
12. H. F. Bauman
13. S. E. Beall
14. R. L. Beatty
15. M. J. Bell
16. M. Bender
17. C. E. Bettis
18. E. S. Bettis
19. D. S. Billington
20. R. E. Blanco
21. F. F. Blankenship
22. J. O. Blomeke
23. R. Blumberg
24. A. L. Boch
25. E. G. Bohlmann
26. C. J. Borkowski
27. G. E. Boyd
28. J. Braunstein
29. M. A. Bredig
30. E. J. Breeding
31–45. R. B. Briggs
46. H. R. Bronstein
47. W. E. Browning
48. F. R. Bruce
49. G. D. Brunton
50. G. H. Burger
51. D. A. Canonico
52. S. Cantor
53. D. W. Cardwell
54. W. H. Carr
55. W. L. Carter
56. G. I. Cathers
57. J. E. Caton
58. O. B. Cavin
59. A. Cepolino
60. J. M. Chandler
61. F. H. Clark
62. W. R. Cobb
63. H. E. Cochran
64. C. W. Collins
65. E. L. Compere
66. J. A. Conlin
67. K. V. Cook
68. W. H. Cook
69. J. W. Cooke
70. L. T. Corbin
71. W. B. Cottrell
72. B. Cox
73. G. A. Cristy
74. S. J. Cromer (K-25)
75. J. L. Crowley
76. F. L. Culler
77. D. R. Cuneo
78. J. M. Dale
79. D. G. Davis
80. W. W. Davis
81. R. J. DeBakker
82. J. H. DeVan
83. S. J. Ditto
84. R. G. Donnelly
85. I. T. Dudley
86. N. E. Dunwoody
87–88. A. S. Dworkin
89. D. A. Dyslin
90–91. W. P. Eatherly
92. J. R. Engel
93. E. P. Epler
94. W. K. Ergen
95. D. E. Ferguson
96. L. M. Ferris
97. A. P. Fraas
98. J. K. Franzreb
99. H. A. Friedman
100. J. H Frye, Jr.
101. W. K. Furlong
102. C. H. Gabbard
103. W. R. Gall
104. R. B. Gallaher
105. R. E. Gehlbach
106. J. H. Gibbons

107. R. G. Gilliland
108. L. O. Gilpatrick
109. W. R. Grimes
110. A. G. Grindell
111. R. W. Gunkel
112. R. H. Guymon
113. J. P. Hammond
114. R. P. Hammond
115. B. A. Hannaford
116. P. H. Harley
117. D. G. Harman
118. W. O. Harms
119. C. S. Harrill
120. P. N. Haubenreich
121. F. A. Heddleson
122. R. E. Helms
123. P. G. Herndon
124. D. N. Hess
125. R. F. Hibbs
126. J. R. Hightower
127. M. R. Hill
128. E. C. Hise
129. H. W. Hoffman
130. D. K. Holmes
131. V. D. Holt
132. P. P. Holz
133. R. W. Horton
134. A. S. Householder
135. A. Houtzeel
136. T. L. Hudson
137. W. R. Huntley
138. H. Inouye
139. W. H. Jordan
140. P. R. Kasten
141. R. J. Kedl
142. M. T. Kelley
143. M. J. Kelly
144. C. R. Kennedy
145. T. W. Kerlin
146. H. T. Kerr
147. J. J. Keyes
148. D. V. Kiplinger
149. S. S. Kirslis
150. D. J. Knowles
151. J. W. Koger
152. R. B. Korsmeyer
153. A. I. Krakoviak
154. T. S. Kress
155. J. W. Krewson
156. C. E. Lamb
157. J. A. Lane
158. E. J. Lawrence
159. J. J. Lawrence
160. M. S. Lin
161. T. A. Lincoln
162. R. B. Lindauer
163. A. P. Litman
164. J. L. Liverman
165. R. S. Livingston
166. G. H. Llewellyn
167. E. L. Long
168. A. L. Lotts
169. M. I. Lundin
170. R. N. Lyon
171. R. L. Macklin
172. H. G. MacPherson
173. R. E. MacPherson
174. F. C. Maienschein
175. J. C. Mailen
176. D. L. Manning
177. C. D. Martin
178. W. R. Martin
179. H. V. Mateer
180. C. E. Mathews
181. T. H. Mauney
182. R. W. McClung
183. H. E. McCoy
184. D. L. McElroy
185. C. K. McGlothlan
186. C. J. McHargue
187. H. A. McLain
188. L. E. McNeese
189. J. R. McWherter
190. H. J. Metz
191. A. S. Meyer
192. E. C. Miller
193. C. A. Mills
194. R. L. Minue
195. W. R. Mixon
196. R. L. Moore
197. K. Z. Morgan
198. D. M. Moulton
199. J. C. Moyers
200. T. R. Mueller
201. H. A. Nelms
202. H. H. Nichol
203. J. P. Nichols
204. E. L. Nicholson

205. L. C. Oakes
206. W. R. Osborn
207–210. R. B. Parker
211. L. F. Parsly
212. P. Patriarca
213. H. R. Payne
214. A. M. Perry
215. T. W. Pickel
216. H. B. Piper
217. B. E. Prince
218. H. P. Raaen
219. G. L. Ragan
220. J. L. Redford
221. M. Richardson
222. G. D. Robbins
223. R. C. Robertson
224. W. C. Robinson
225. K. A. Romberger
226–400. M. W. Rosenthal
401. R. G. Ross
402. H. C. Savage
403. A. W. Savolainen
404. W. F. Schaffer
405. C. E. Schilling
406. Dunlap Scott
407. J. L. Scott
408. H. E. Seagren
409. C. E. Sessions
410. J. H. Shaffer
411. E. D. Shipley
412. W. H. Sides
413. M. J. Skinner
414. G. M. Slaughter
415. A. N. Smith
416. F. J. Smith
417. G. P. Smith
418. O. L. Smith
419. P. G. Smith
420. A. H. Snell
421. W. F. Spencer
422. I. Spiewak
423. R. C. Steffy
424. C. E. Stevenson
425. W. C. Stoddart
426. H. H. Stone
427. R. A. Strehlow
428. D. A. Sundberg
429. J. R. Tallackson
430. E. H. Taylor
431. W. Terry
432–433. R. E. Thoma
434. P. F. Thomason
435. L. M. Toth
436. D. B. Trauger
437. R. W. Tucker
438. W. C. Ulrich
439. W. E. Unger
440. D. C. Watkin
441. G. M. Watson
442. J. S. Watson
443. H. L. Watts
444. C. F. Weaver
445. B. H. Webster
446. A. M. Weinberg
447. J. R. Weir
448. W. J. Werner
449. K. W. West
450. M. E. Whatley
451. J. C. White
452. R. P. Wichner
453. L. V. Wilson
454. G. J. Young
455. H. C. Young
456. J. P. Young
457. E. L. Youngblood
458. F. C. Zapp
459. Biology Library
460–462. ORNL – Y-12 Technical Library Document Reference Section
463–464. Central Research Library
465–619. Laboratory Records Department
620. Laboratory Records, ORNL R.C.

EXTERNAL DISTRIBUTION

621. W. O. Allen, Atomics International, P.O. Box 309, Canoga Park, California 91304
622. A. Amorosi, LMFBR Program Office, Argonne National Laboratory, Argonne, Illinois 60439
623. J. G. Asquith, Atomics International, P.O. Box 309, Canoga Park, California 91304
624. David Bendaniel, General Electric Co., R&D. Center, Schenectady, N.Y.
625. J. C. Bowman, Union Carbide Technical Center, 12900 Snow Road, Parma, Ohio 44130
626. G. D. Brady, Materials Systems Division, UCC, Kokomo, Indiana 46901
627. Paul Cohen, Westinghouse Electric Corp., P.O. Box 158, Madison, Pennsylvania 15663
628. D. F. Cope, Atomic Energy Commission, RDT Site Office (ORNL)
629. J. W. Crawford, Atomic Energy Commission, Washington 20545
630. M. W. Croft, Babcock and Wilcox Company, P.O. Box 1260, Lynchburg, Virginia 24505
631. D. A. Douglas, Materials Systems Division, UCC, Kokomo, Indiana 46901
632. H. L. Falkenberry, Tennessee Valley Authority, 303 Power Building, Chattanooga, Tenn. 37401
633. C. W. Fay, Wisconsin Michigan Power Company, 231 W. Michigan Street, Milwaukee, Wisconsin 53201
634. A. Giambusso, Atomic Energy Commission, Washington 20545
635. Gerald Golden, Argonne National Laboratory, 9700 S. Cass Avenue, Argonne, Illinois 60439
636. W. W. Grigorieff, Assistant to the Executive Director, Oak Ridge Associated Universities
637. J. T. Kehoe, Burns and Roe, Inc., 700 Kinderkamach, Oradell, New Jersey 07649
638. E. E. Kintner, U.S. Atomic Energy Commission, Washington, D.C.
639. P. M. Krishner, Pioneer Service and Engineering, 400 W. Madison St. Chicago, Illinois 60606
640. J. Ladesich, Southern California Edison Co., P.O. Box 351, Los Angeles, California 90053
641. L. W. Lang, Douglas United Nuclear, 703 Bldg., Richland, Washington 99352
642. R. A. Langley, Bechtel Corp., 50 Beale St., San Francisco, California 94119
643. W. J. Larkin, Atomic Energy Commission, ORO
644. R. A. Lorenzini, Foster Wheeler, 110 S. Orange, Livingston, N.J. 07039
645. W. D. Manly, Material Systems Division, UCC, 270 Park Avenue, New York, New York 10017
646. J. P. Mays, Great Lakes Carbon Co., 299 Park Avenue, New York, New York 10017
647. W. B. McDonald, Battelle-Pacific Northwest Laboratory, Hanford, Washington 99352
648–649. T. W. McIntosh, Atomic Energy Commission, Washington 20542
650. W. J. Mordarski, Nuclear Development, Combustion Engineering, Windsor, Connecticut
651. Sidney Parry, Great Lakes Carbon, P.O. Box 667, Niagara Falls, New York 14302
652. G. J. Petretic, Atomic Energy Commission, Washington 20545
653. A. J. Pressesky, U.S. Atomic Energy Commission, Washington, D.C.
654. D. J. Rose, Department of Nuclear Engineering, Room 24–207, Massachusetts Institute of Technology, Cambridge, Massachusetts 02139
655. M. A. Rosen, Atomic Energy Commission, Washington 20545
656. H. M. Roth, Atomic Energy Commission, ORO
657. R. W. Schmitt, General Electric Co., Schenectady, New York 12301
658. R. N. Scroggins, U.S. Atomic Energy Commission, Washington, D.C.
659. M. Shaw, Atomic Energy Commission, Washington 20545
660. Remo Silvestrini, United Nuclear Corporation, Grasslands Road, Elmsford, New York 10523
661. E. E. Sinclair, Atomic Energy Commission, Washington 20545
662. W. L. Smalley, Atomic Energy Commission, ORO
663. T. M. Snyder, General Electric Co., 175 Curtner Ave., San Jose, California 95103
664. L. D. Stoughton, UCC, P.O. Box 500, Lawrenceburg, Tennessee 38464
665. Philip T. Stroup, Alcoa, P.O. Box 772, New Kensington, Pennsylvania
666. J. A. Swartout, UCC, 270 Park Avenue, New York, New York 10017

667. Richard Tait, Poco Graphite, P.O. Box 1524, Garland, Texas 75040
668. D. R. Thomas, Commonwealth Associates, Inc., 209 E. Washington Ave., Jackson, Michigan 49201
669. M. Tsou, General Motors, 12 Mile and Mound Roads, Warren, Michigan 48089
670. J. W. Ullmann, UCC, P.O. Box 278, Tarrytown, New York 10591
671. C. H. Waugaman, Tennessee Valley Authority, 303 Power Building, Chattanooga, Tenn. 37401
672. D. B. Weaver, Tennessee Valley Authority, New Sprankle Building, Knoxville, Tennessee
673. G. O. Wessenauer, Tennessee Valley Authority, Chattanooga, Tennessee 37401
674. M. J. Whitman, Atomic Energy Commission, Washington 20545
675. H. A. Wilber, Power Reactor Development Company, 1911 First Street, Detroit Michigan
676. James H. Wright, Westinghouse Electric, P.O. Box 355, Pittsburgh, Pennsylvania 15230
677. A. Goldman, Union Carbide Corporation, New York, N.Y.
678. J. C. Robinson, Dept. of Nuclear Engineering, University of Tennessee Knoxville, Tennessee
679. D. E. Erb, Battelle Memorial Institute, 505 King Ave., Columbus, Ohio 43201
680. W. H. Danker, Jr., Westinghouse Electric Corp. P.O. Box 19218, Tampa, Florida 33616

681–682. Laboratory and University Division, AEC, ORO

683–898. Given distribution as shown in TID–4500 under Reactor Technology category (25 copies – CFSTI)